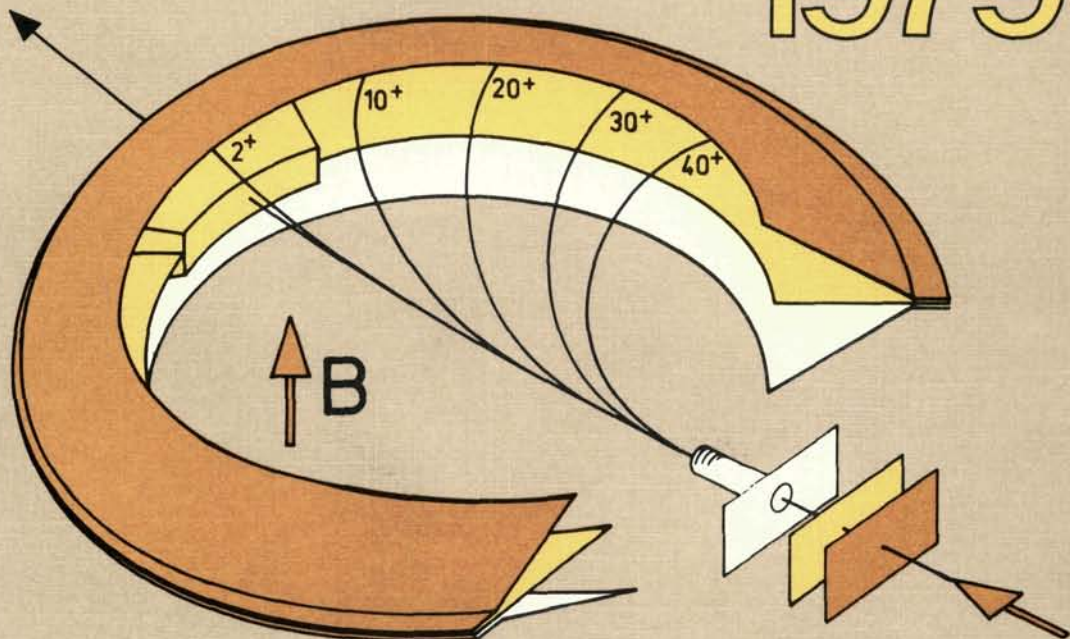


INDC SPECIAL 4

# Physics and Chemistry of Fission 1979



Proceedings of a Symposium, Jülich, 14-18 May 1979

Vol.I



INTERNATIONAL ATOMIC ENERGY AGENCY, VIENNA, 1980



**PHYSICS AND CHEMISTRY  
OF FISSION 1979**

**VOL. I**

The following States are Members of the International Atomic Energy Agency:

AFGHANISTAN	HOLY SEE	PHILIPPINES
ALBANIA	HUNGARY	POLAND
ALGERIA	ICELAND	PORTUGAL
ARGENTINA	INDIA	QATAR
AUSTRALIA	INDONESIA	ROMANIA
AUSTRIA	IRAN	SAUDI ARABIA
BANGLADESH	IRAQ	SENEGAL
BELGIUM	IRELAND	SIERRA LEONE
BOLIVIA	ISRAEL	SINGAPORE
BRAZIL	ITALY	SOUTH AFRICA
BULGARIA	IVORY COAST	SPAIN
BURMA	JAMAICA	SRI LANKA
BYELORUSSIAN SOVIET SOCIALIST REPUBLIC	JAPAN	SUDAN
CANADA	JORDAN	SWEDEN
CHILE	KENYA	SWITZERLAND
COLOMBIA	KOREA, REPUBLIC OF	SYRIAN ARAB REPUBLIC
COSTA RICA	KUWAIT	THAILAND
CUBA	LEBANON	TUNISIA
CYPRUS	LIBERIA	TURKEY
CZECHOSLOVAKIA	LIBYAN ARAB JAMAHIRIYA	UGANDA
DEMOCRATIC KAMPUCHEA	LIECHTENSTEIN	UKRAINIAN SOVIET SOCIALIST REPUBLIC
DEMOCRATIC PEOPLE'S REPUBLIC OF KOREA	LUXEMBOURG	UNION OF SOVIET SOCIALIST REPUBLICS
DENMARK	MADAGASCAR	UNITED ARAB EMIRATES
DOMINICAN REPUBLIC	MALAYSIA	UNITED KINGDOM OF GREAT BRITAIN AND NORTHERN IRELAND
ECUADOR	MALI	UNITED REPUBLIC OF CAMEROON
EGYPT	MAURITIUS	UNITED REPUBLIC OF TANZANIA
EL SALVADOR	MEXICO	UNITED STATES OF AMERICA
ETHIOPIA	MONACO	URUGUAY
FINLAND	MONGOLIA	VENEZUELA
FRANCE	MOROCCO	VIET NAM
GABON	NETHERLANDS	YUGOSLAVIA
GERMAN DEMOCRATIC REPUBLIC	NEW ZEALAND	ZAIRE
GERMANY, FEDERAL REPUBLIC OF	NICARAGUA	ZAMBIA
GHANA	NIGER	
GREECE	NIGERIA	
GUATEMALA	NORWAY	
HAITI	PAKISTAN	
	PANAMA	
	PARAGUAY	
	PERU	

The Agency's Statute was approved on 23 October 1956 by the Conference on the Statute of the IAEA held at United Nations Headquarters, New York; it entered into force on 29 July 1957. The Headquarters of the Agency are situated in Vienna. Its principal objective is "to accelerate and enlarge the contribution of atomic energy to peace, health and prosperity throughout the world".

(C) IAEA, 1980

Permission to reproduce or translate the information contained in this publication may be obtained by writing to the International Atomic Energy Agency, Wagramerstrasse 5, P.O. Box 100, A-1400 Vienna, Austria.

Printed by the IAEA in Austria  
January 1980

**PROCEEDINGS SERIES**

**PHYSICS AND CHEMISTRY  
OF FISSION 1979**

PROCEEDINGS OF AN INTERNATIONAL SYMPOSIUM  
ON PHYSICS AND CHEMISTRY OF FISSION  
ORGANIZED BY THE  
INTERNATIONAL ATOMIC ENERGY AGENCY  
AND HELD AT  
JÜLICH, 14–18 MAY 1979

*In two volumes*

**VOL. I**

INTERNATIONAL ATOMIC ENERGY AGENCY  
VIENNA, 1980

PHYSICS AND CHEMISTRY OF FISSION 1979, VOL. I  
IAEA, VIENNA, 1980  
STI/PUB/526  
ISBN 92-0-030080-4

## FOREWORD

The Kernforschungsanlage Jülich is among the leading nuclear research centres in the world. It provided a suitable and hospitable meeting-place for the Fourth International Symposium on the Physics and Chemistry of Fission, held from 14 to 18 May 1979.

Previous symposia in this series (Salzburg 1965, Vienna 1969, and Rochester 1973) had set the pace for these IAEA-organized meetings, which summarize the important advances in the field during the last twenty years. From one symposium to the next the scientific emphasis is shifted, new ideas and new experimental approaches being assimilated from year to year, such that it has become difficult to accommodate all the different lines of research under the roof of one meeting. To make the working hours at the Fourth Symposium acceptable, approximately two-thirds of the submitted papers could not be accepted for oral presentation; they were made available at the Symposium in the form of extended summaries. These are included in the Book of Extended Synopses made available to all the participants. Further copies can be obtained from the Physics Section, Department of Research and Laboratories, IAEA.

Many pages in the present Proceedings are taken up with review papers, on the assumption that in this way a more complete and unbiased coverage of many different orientations in fission research could be obtained. The contributed papers have been selected to illustrate or complement the extensive reviews.

The interest in the 1979 Symposium, the number of excellent contributions and the lively discussions during the meeting demonstrate the vitality of fission research. Both theoretical and experimental studies reported at the symposium indicate that fission studies have provided many valuable solutions to problems, but clearly other problems are still open and much work remains to be done.

## **EDITORIAL NOTE**

*The papers and discussions have been edited by the editorial staff of the International Atomic Energy Agency to the extent considered necessary for the reader's assistance. The views expressed and the general style adopted remain, however, the responsibility of the named authors or participants. In addition, the views are not necessarily those of the governments of the nominating Member States or of the nominating organizations.*

*Where papers have been incorporated into these Proceedings without resetting by the Agency, this has been done with the knowledge of the authors and their government authorities, and their cooperation is gratefully acknowledged. The Proceedings have been printed by composition typing and photo-offset lithography. Within the limitations imposed by this method, every effort has been made to maintain a high editorial standard, in particular to achieve, wherever practicable, consistency of units and symbols and conformity to the standards recommended by competent international bodies.*

*The use in these Proceedings of particular designations of countries or territories does not imply any judgement by the publisher, the IAEA, as to the legal status of such countries or territories, of their authorities and institutions or of the delimitation of their boundaries.*

*The mention of specific companies or of their products or brand names does not imply any endorsement or recommendation on the part of the IAEA.*

*Authors are themselves responsible for obtaining the necessary permission to reproduce copyright material from other sources.*

## CONTENTS OF VOL. I

### **FISSION BARRIERS AND PROBABILITIES (Session A)**

<p>Experimental survey of the potential energy surfaces associated with fission (IAEA-SM-241/A1) .....</p> <p><i>H.C. Britt</i></p> <p>Discussion .....</p> <p>Низкоэнергетическое фотоделение тяжелых ядер (IAEA-SM-241/A2) .....</p> <p><i>Г.Н. Смирекин, Ю.М. Ципенюк</i></p> <p>(<i>Low-energy fission of heavy nuclei: G.N. Smirenkin, Yu.M. Tsipenyuk</i>)</p> <p>Discussion .....</p> <p>Sub-threshold photofission of <math>^{238}\text{U}</math> in the (3.6–6.0)-MeV energy range (IAEA-SM-241/A3) .....</p> <p><i>R. Alba, G. Bellia, L. Calabretta, A. Del Zoppo, E. Migneco, G. Russo, R.C. Barnà, D. De Pasquale</i></p> <p>Discussion .....</p> <p>Combined analysis of the prompt-fission, delayed-fission, photofission and angular-distribution data from <math>^{234,236}\text{U}</math> and <math>^{238,240}\text{Pu}</math> (IAEA-SM-241/A4) .....</p> <p><i>M. Just, U. Goerlach, D. Habs, V. Metag, H.J. Specht</i></p> <p>Discussion .....</p> <p>La réaction (<math>n, \gamma f</math>) dans les résonances induites par neutrons lents dans <math>^{239}\text{Pu}</math>, <math>^{235}\text{U}</math> et <math>^{241}\text{Pu}</math> (IAEA-SM-241/A5) .....</p> <p><i>J. Trochon</i></p> <p>Discussion .....</p> <p>Несохранение четности при делении ядер <math>^{234}\text{U}</math>, <math>^{236}\text{U}</math> и <math>^{240}\text{Pu}</math> (IAEA-SM-241/A6) .....</p> <p><i>Г.В. Данилян, Б.Д. Водеников, В.П. Дроняев, В.В. Новицкий, В.С. Павлов, С.П. Боровлев</i></p> <p>(<i>Non-conservation of parity in fission of <math>^{234}\text{U}</math>, <math>^{236}\text{U}</math> and <math>^{240}\text{Pu}</math> nuclei: G.V. Danilyan, B.D. Vodennikov, V.P. Dronyaev, V.V. Novitskij, V.S. Pavlov, C.P. Borovlev</i>)</p>	<p>3</p> <p>28</p> <p>31</p> <p>58</p> <p>61</p> <p>69</p> <p>71</p> <p>85</p> <p>87</p> <p>108</p> <p>111</p>
---	--

## SPONTANEOUS FISSION AND FISSION BARRIERS (Session B)

Исследование спонтанного деления изотопов некоторых тяжелых элементов и закономерностей реакций слияния в области сильно делящихся компаунд-ядер (IAEA-SM-241/B1) .....	129
<i>Ю.Ц. Оганесян, О.А. Орлова, Г.М. Тер-Акопьян, Ю.А. Музычка, А.А. Плеве, Б.И. Пустыльник, В.И. Чепигин, Г.Н. Флеров</i>	
( <i>A study of spontaneous fission in the isotopes of some heavy elements and the laws governing fusion reactions in connection with intensely fissile compound nuclei: Yu.Ts. Oganesyan, O.A. Orlova, G.M. Ter-Akop'yan, Yu.A. Muzychka, A.A. Pleve, B.I. Pustyl'nik, V.I. Chepigin, G.N. Flerov</i> )	
Discussion .....	141
Dynamical calculations of spontaneous-fission half-lives (IAEA-SM-241/B2) .....	143
<i>A. Baran, K. Pomorski, S.E. Larsson, P. Möller, S.G. Nilsson, J. Randrup, A. Łukasiak, A. Sobczewski</i>	
Discussion .....	150
Spectroscopic properties of fission isomers (IAEA-SM-241/B3) .....	153
<i>V. Metag</i>	
Discussion .....	174
Beta-delayed fission and low-lying structures in the beta strength function (IAEA-SM-241/B4) .....	175
<i>H.V. Klapdor, C.-O. Wene, I.N. Isosimov, Yu. V. Naumov</i>	
Discussion .....	186
Etude de résonances de vibration dans la réaction $^{231}\text{Pa}(n, f)$ (IAEA-SM-241/B5) .....	187
<i>A. Sicre, F. Caïtucoli, G. Barreau, T.P. Doan, T. Benfoughal, B. Leroux</i>	
Discussion .....	205
Bandes de rotation dans la structure intermédiaire (IAEA-SM-241/B6) ....	207
<i>D. Paya</i>	
Discussion .....	219

## SHELL EFFECTS IN POTENTIAL ENERGIES AND LEVEL DENSITIES (Session C)

Static deformation energy calculations from microscopical to semiclassical theories (IAEA-SM-241/C1) .....	227
<i>M. Brack</i>	
Discussion .....	262

○ Calculs de surfaces d'énergie potentielle par la méthode Hartree-Fock-Bogolyubov (IAEA-SM-241/C2) .....	265
<i>J.F. Berger, M. Girod</i>	
Discussion .....	280
○ Macroscopic-microscopic calculation of fission barriers and masses for heavy elements with a Yukawa-plus-exponential model for the macroscopic energy (IAEA-SM-241/C3) .....	283
<i>P. Möller</i>	
Discussion .....	300
○ Shell structure at high spins (IAEA-SM-241/C4) .....	303
<i>S. Åberg, S.E. Larsson, P. Möller, S.G. Nilsson, G. Leander, J. Ragnarsson</i>	
Discussion .....	358
○ The fission barrier of nuclei at very high angular momenta (IAEA-SM-241/C5) .....	361
<i>M.E. Faber, A. Faessler, M. Ploszajczak</i>	
Discussion .....	371
○ Nuclear friction and giant resonance characteristics observed in fission of heavy nuclei (IAEA-SM-241/C6) .....	373
<i>P. David, J. Debrus, J. Schulze, J. Van der Plicht, M.N. Harakeh, A. Van der Woude</i>	
Discussion .....	384
○ The role of blocking life-time measurements in the study of heavy-ion- induced fission (IAEA-SM-241/C7) .....	387
<i>J.U. Andersen, A.S. Jensen, E. Laegsgaard, K.O. Nielsen, J.S. Forster, I.V. Mitchell, D. Ward, W.M. Gibson</i>	
Discussion .....	406
○ Experimental determination of fission probabilities for proton-rich nuclei near the $N = 126$ shell (IAEA-SM-241/C8) .....	409
<i>K.-H. Schmidt, W. Faust, G. Münzenberg, W. Reisdorf, H.-G. Clerc, D. Vermeulen, W. Lang</i>	
Discussion .....	419
○ Плотность уровней и вероятность деления сферических и деформированных ядер (IAEA-SM-241/C9) .....	421
<i>A. В. Игнатюк, К. К. Истеков, В. Н. Околович, Г. Н. Смирненкин (Level density and fission probability in spherical and deformed nuclei: A. V. Ignatyuk, K. K. Istekov, V. N. Okolovich, G. N. Smirenkin)</i>	
Discussion .....	443

② Theory of intrinsic state density calculations in the shell-correction approach (IAEA-SM-241/C10) .....	445
<i>K. Junker, J. Hadermann, N.C. Mukhopadhyay</i>	
Discussion .....	459
③ A many-body model study of fragment formation in fission (IAEA-SM-241/C11) .....	461
<i>W. Bauhoff, H. Schultheis, R. Schultheis, K. Wildermuth</i>	
Discussion .....	472
④ Shell structure in fission (IAEA-SM-241/C12) .....	475
<i>V.M. Strutinsky</i>	
⑤ On the shell correction energy at doubly magic nuclei (IAEA-SM-241/C26) .....	501
<i>E. Werner, K.M. Dietrich, P. Möller, R. Nix</i>	
Discussion .....	516
<b>FISSION AND HEAVY IONS (Session D)</b>	
Heavy-ion-induced fission following fusion (IAEA-SM-241/D1) .....	521
<i>F. Plasil, R.L. Ferguson</i>	
Discussion .....	549
Mass and kinetic-energy distribution of fragments formed in the heavy-ion-induced fission of $^{208}\text{Po}$ (IAEA-SM-241/D2) .....	551
<i>J.G. Cunningham, J.A.B. Goodall, J.E. Freeman, G.W.A. Newton, V.J. Robinson, J.L. Durell, G.S. Foote, I.S. Grant, J.D. Hemingway</i>	
Discussion .....	561
Influence du moment angulaire sur la largeur des distributions de masse de fission induite par ion lourds: existe-t-il un troisième mécanisme entre la fission et les collisions très inélastiques? (IAEA-SM-241/D3) .....	563
<i>F. Hanappe, J. Peter, B. Tamain, C. Lebrun, J.F. Lecolley, F. Lefebvres, C. Ngô</i>	
Discussion .....	572
Fission properties of very heavy nuclei produced in deep-inelastic collisions (IAEA-SM-241/D4) .....	575
<i>D. v. Harrach, P. Glässel, Y. Civelekoglu, R. Männer, H.J. Specht, J.B. Wilhelmy, H. Freiesleben, K.D. Hildenbrand</i>	
Discussion .....	585
Relations entre les propriétés des collisions très inélastiques et la fission (IAEA-SM-241/DS) .....	587
<i>J. Peter, B. Tamain</i>	
Discussion .....	628
Programme of Sessions .....	629
Secretariat of the Symposium .....	629

**FISSION BARRIERS AND PROBABILITIES**  
**(Session A)**

**Chairman**

**A.F. MICHAUDON**  
France

# EXPERIMENTAL SURVEY OF THE POTENTIAL ENERGY SURFACES ASSOCIATED WITH FISSION\*

H.C. BRITT

Los Alamos Scientific Laboratory,  
University of California,  
Los Alamos, New Mexico,  
United States of America

## Abstract

### EXPERIMENTAL SURVEY OF THE POTENTIAL ENERGY SURFACES ASSOCIATED WITH FISSION.

Progress in the experimental determination of the properties of the potential energy surface associated with fission is reviewed. The importance of nuclear symmetry effects on the calculation of fission widths is demonstrated. Evidence is presented for the fragmentation of the mass-asymmetric second barrier in the thorium region and the axial asymmetric first barrier in the californium region. Detailed analyses of experimental data suggest the presence of two parallel second barriers; the normal mass-asymmetric, axial-symmetric barrier and a slightly higher mass-symmetric, axial-asymmetric barrier. Experimental barrier parameters are determined systematically and compared with calculations from various theoretical models. Techniques for expanding fission probability measurements to higher energies are discussed.

## 1. INTRODUCTION

The IAEA symposia on the physics and chemistry of fission have served both as periodic reviews of fission research and as a source for creating new perspectives and insights to influence further research. In these symposia a major topic has always been the experimental and theoretical attempts to define the characteristics of the potential energy surfaces that control fission decay rates. Progress in this field has generally been marked by occasional giant leaps in the qualitative nature of the theories followed by increasingly detailed experimental investigations. As in many fields the experiments tended to support the current theoretical concepts but at the same time they gradually contributed evidence that the theories were incomplete. In particular, the evolution in our understanding of fission has been steadily in the direction of demonstrating increasing complexity in the potential energy surfaces.

Shortly after the discovery of fission Bohr and Wheeler [1] showed that the fission barrier obtained from a liquid drop nuclear model when coupled with the concept of a fission width controlled by transition states at the barrier could explain the general properties of the

---

\* Work supported by the US Department of Energy.

fission process as then known. This simple liquid drop model was used as the foundation for the interpretation of fission thresholds and decay rates for almost twenty-five years. However, at the first IAEA fission symposium there were just beginning to be signs of experimental phenomena that could not be understood in terms of the current theories. The most dramatic of the new observations were the discovery of fission isomers in americium isotopes [2]. The existence of fissioning isomers with excitation energies of 2-3 MeV and millisec half lives was qualitatively inconsistent with the then current theories of fission. In addition, later experiments showed subbarrier resonances in fission probability distributions [3] and the existence of intermediate structure in low energy ( $n,f$ ) resonance studies for some actinide nuclei [4,5]. These results all pointed to inadequacies in the simple liquid drop theory of fission.

The key to the understanding of these puzzling phenomena came when Strutinski and collaborators in Copenhagen [6] and Nilsson and his group [7] in Lund followed up on an idea originally proposed by Swiatecki [8] that nuclear shells may have important effects in deformed as well as spherical nuclei. Using the method developed by Strutinski for applying shell corrections to a liquid drop potential energy surface it was shown that in the actinide region fission barriers should be double peaked with a well developed second minimum. This result gave a natural explanation for the experimentally observed isomeric phenomena and the 1969 IAEA conference was dominated by reports of theoretical calculations exploiting this new technique and experiments which showed that isomers and resonant structures were a common feature throughout the actinide region [9]. At this point the theory had jumped considerably ahead of the current experiments and it appeared that a quantitative understanding of the fission decay process in terms of basic physical concepts was at hand.

The period between the 1969 and 1973 IAEA fission conferences was one of intense activity by experimental and theoretical groups throughout the world. The theorists discovered the importance of triaxial and mass asymmetric degrees of freedom in their calculations [10-13] and the experimental groups developed methods for estimating fission barrier parameters from the growing volume of experimental results [14-16]. The 1973 conference included the first broad comparisons between theory and experiments [17-19]. It was found that good agreement was obtained in the middle of the actinide region (i.e. uranium and plutonium) but there were quantitative discrepancies between theory and experiment in the light actinides (thorium) and hints of problems in the heavy actinides (curium). Furthermore, there seemed to be a puzzling problem in the normalizations of the supposedly realistic microscopic statistical models that were used to analyse the experimental fission probability results [17].

In this review we will attempt to cover the major experimental results in this area since the last symposium in 1973. The major conceptual breakthrough came as a result of the observation by Bjornholm, Bohr, and Mottleson [20] that nuclear shape symmetries have fundamental effects on the magnitudes of the nuclear level densities. Incorporation of these symmetry effects into the current microscopic statistical models led to a model that could quantitatively reproduce the absolute magnitude of measured fission probabilities [21]. Armed with more realistic models and a continually expanding base of experimental data we are rapidly

discovering that the potential energy surfaces associated with fission must be much more complex than previously believed[ 22-25]. In particular, we may be discovering a new set of smaller shell corrections which produce 1-2 MeV fluctuations in the potential energy surface.

In the remainder of this paper we will present a discussion of the importance of nuclear symmetry effects for understanding fission probability distributions (Section 2); evidence for increased complexity of the potential energy surfaces associated with fission (Section 3); a re-analysis of existing experimental data in terms of our current concepts with a comparison to various theoretical predictions (Section 4) and a sample of some new experimental techniques that may be useful in expanding the measurements of  $\Gamma_f/\Gamma_n$  to higher excitation energy regions (Section 5). We will present and draw conclusions from current experimental data but the reader is referred to the original papers for discussions of the experimental techniques.

## 2. EXPERIMENTAL DETERMINATION OF FISSION BARRIER PARAMETERS

### 2.1. General Considerations

One of the major reasons for pursuing experimental programs to measure fission probability distributions and fission isomer excitation functions is to try to deduce the gross properties of the potential energy surface associated with fission. These "experimental" fission barrier parameters can then be compared with various theoretical calculations.

Figure 1 illustrates schematically the two types of experiment that have been used to obtain most of the current information on fission barrier heights [5]. In a direct reaction fission experiment a direct reaction (or neutron absorption reaction) is used to excite a residual nucleus to a particular excitation energy and the branching ratio for decay by fission relative to neutron or gamma ray deexcitation (or the fission cross section) is measured. This type of experiment [17,18,26,27] gives information on the height and curvature of the highest peak in the fission barrier. In addition, for cases where  $E_A \approx E_B$  or where fission transmission resonances are observed estimates can be obtained for the parameters of both barriers. In the case of fission isomer experiments the results depend most sensitively on  $E_B$  and  $E_{II}$  [14]. Since most isomers occur for heavy actinides (Pu, Am, Cu) where  $E_A > E_B$ , the direct reaction and isomer experiments tend to be complementary. During the last several years data have been obtained on fission probability distributions for most of the actinide nuclei which can be reached using available target isotopes and a wide variety of direct and neutron capture reactions. In addition, excitation functions for most of the accessible fission isomers have been measured. Thus, we now have an almost complete set of experimental data for use in systematizing the gross properties of fission barriers throughout the actinide region.

During the last several years considerable progress has also been made in the development of microscopic statistical models which could be used to extract barrier parameter estimates from fits to experimental data. The major inputs to these models for the analysis of nonresonant data are the level densities as a function of excitation energy at the

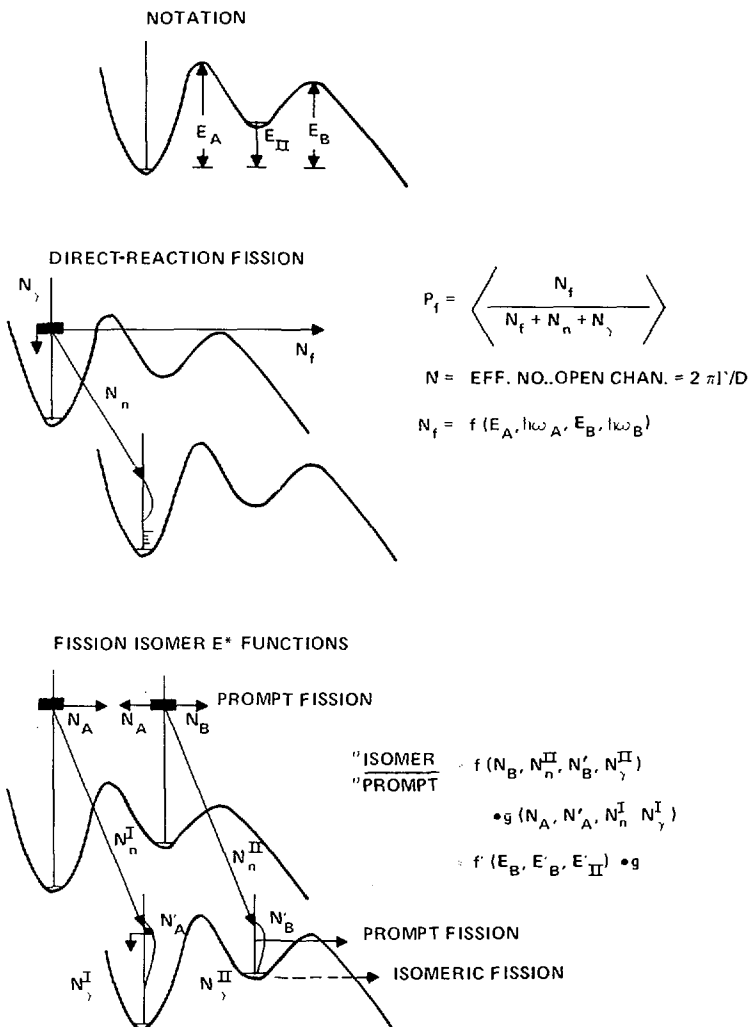


*FIG.1. Systematic illustration of the major features of the direct-reaction fission and fission isomer population processes.*

saddle points and minima of the potential energy surface. These level densities are used for the estimate of the relevant decay widths,  $\Gamma_f$ ,  $\Gamma_n$ , and  $\Gamma_\gamma$ . A major advance in the development of more realistic models was the incorporation of microscopic level densities which could be obtained directly from the relevant single particle spectra that were used to calculate the potential energy surfaces [14,27]. This approach gives more realistic estimates for the slope of the level density function in the critical energy region of 0-5 MeV and eliminates the need for arbitrary parameters that were necessary in previous statistical models.

When resonance structures are observed in the experimental data more detailed information on the potential energy surface can be extracted. In these cases experimental data have been most commonly analysed using models which incorporate resonances generated by the penetrability through a one-dimensional double-peaked fission barrier that has been parameterized by a smooth joining of three parabolic sections [28]. Models of this type are qualitatively successful in reproducing the experimental results. However, there is increasing evidence for the importance of deviations in barrier shapes from simple parabolas, and the variation of the barrier shapes with spin, parity and K value. Also, as we begin to accumulate evidence for increased complexity in the potential energy surfaces the adequacy of a simple one-dimensional approach for the quantitative analysis of resonance phenomena becomes more doubtful. Some of these points will be discussed in more detail in subsequent sections.

## 2.2 Nuclear Symmetry Effects on Level Densities

In the calculations of fission probabilities,  $P_f$ , the important quantities are branching ratios between fission, neutron emission and gamma de-excitation and these ratios generally involve ratios of level densities and not their absolute magnitudes. In the first attempt to use microscopic level densities for  $P_f$  calculations, a single normalization factor (determined from comparison to measured level spacing at the neutron binding energy) and an empirical spin distribution were used to generate level densities from the calculated microscopic state densities [27]. It was felt that any errors in this simplified approach would tend to cancel out in the ratios that come into the  $P_f$  calculations. When this model was applied to the analysis of fission probability data it was found that the shapes of the distributions near threshold could be reproduced but an arbitrary normalization of  $\Gamma_f/\Gamma_n$  was necessary to reproduce the absolute magnitudes of the measured  $P_f$  values. Furthermore, this normalization factor varied from a value of  $\approx 1$  for thorium isotopes to a value of  $\approx 0.1$  for heavy actinides. A more serious difficulty with this model became apparent when comparisons were made to new data taken to higher excitation energies using  $(^3\text{He},\text{df})$  and  $(^3\text{He},\text{tf})$  reactions. It was found that the microscopic statistical model could not in many cases reproduce the shapes of the measured  $P_f$  distributions in the excitation energy region from threshold to  $\approx 5$  MeV above threshold. In particular the model when normalized in the threshold region would tend to seriously underestimate  $P_f$  at higher excitation energies.

The clue toward understanding the major deficiency of this model came from a paper at the 1973 conference where Bjornholm, Bohr and Mottelson [20] pointed out that at low energies nuclear symmetry effects have a very important influence on the level densities for deformed systems. In particular they showed the necessity of combining low lying rotational excitations with the single particle state densities obtained from microscopic calculations. Since the density of these rotational excitations depends on the degree of symmetry in the nuclear system, this approach leads to a dependence of the nuclear level density on the symmetry of the nucleus at the relevant minimum and saddle points in the potential energy surface. This effect is not important when considering the ratio of neutron to gamma ray decay where both decays occur from the nucleus in the same configuration (i.e. in the first potential minimum). However, there is a large effect when comparing the decay of neutrons or gamma rays from the axially and mass symmetric first minimum to fission which

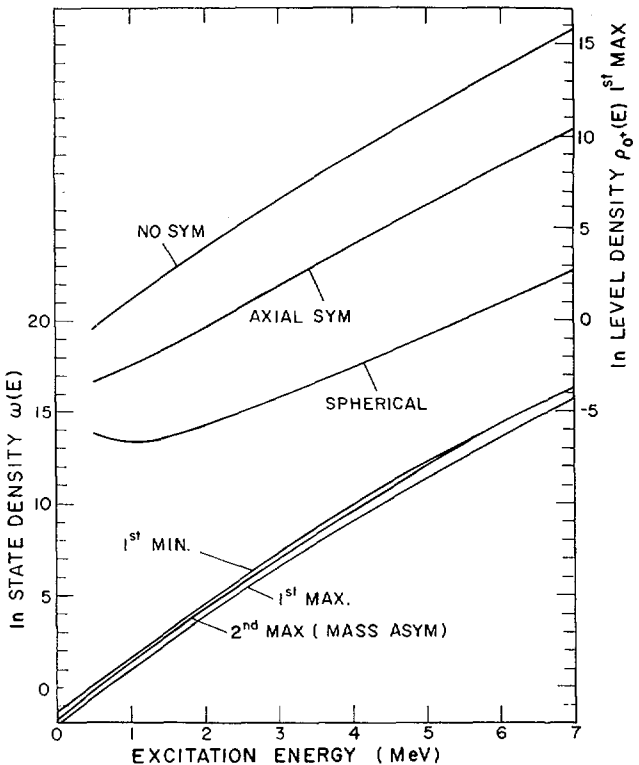


*FIG.2. Calculated nuclear state densities at the first minimum, first axially asymmetric saddle and second mass-asymmetric saddle (lower portion). Calculated nuclear level densities at the first saddle assuming various nuclear symmetries [37].*

involves the passage over two saddle points the first with a triaxial shape and the second with a mass asymmetric, axial, symmetric shape [21].

Figure 2 shows examples of microscopic state densities at the three points in the potential energy surface that are important in determining  $P_f$ . In addition, the level density at the first saddle point is shown for various assumptions about the symmetry of the nuclear shape. The results show that the state density,  $\omega(E^*)$ , is very similar at the first minimum, the axially asymmetric first saddle and the mass asymmetric second saddle. The similarity in  $\omega(E^*)$  is partly due to the similar shell corrections at all three points but is also due to the fact that at low energies the shell and pairing corrections tend to have opposite effects on  $\omega(E^*)$  and lead to a function which is relatively insensitive to the single particle spectrum used to generate the state density. In contrast, there is a large dependence of the nuclear level density,  $\rho(E^*)$ , on the nuclear symmetry. The large change comes about from a breaking of the  $m$ -state degeneracy when a spherical nucleus is deformed

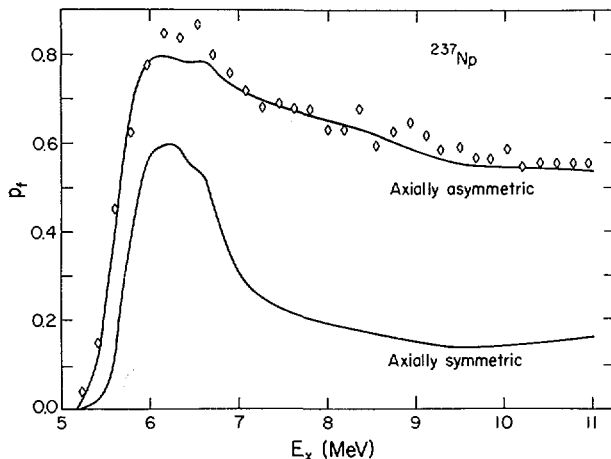


*FIG.3. Fission probabilities for  $^{237}\text{Np}$ . Calculations show fit assuming an axially asymmetric first saddle point and the change when the first barrier is assumed to have an axially symmetric shape.*

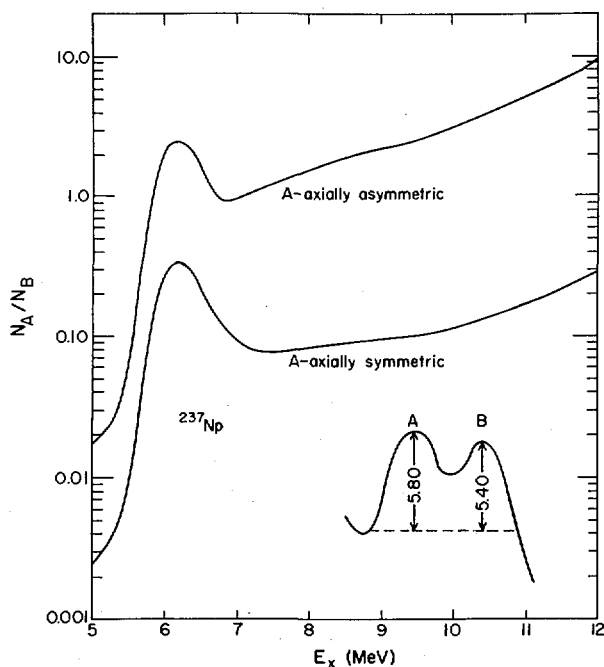


*FIG.4. Ratio of the number of open channels available at each saddle point when different assumptions are made for the shape symmetries at the first saddle (A).*

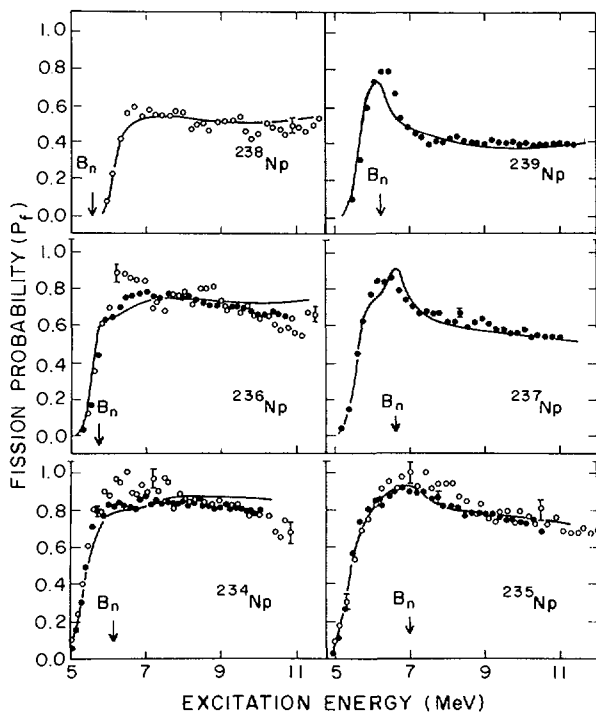


FIG. 5. Fission probability data for a series of neptunium isotopes. Solid lines are fits from the microscopic statistical model described in the text [21].

and the coupling to low lying rotational excitations. The level density for a system with no symmetries (i.e. triaxial with no point group symmetries) is enhanced over an axially symmetric prolate deformation due to the increased number of independent rotational excitations that become possible.

The effect of these level density enhancements on the calculated fission probabilities is shown in Fig. 3 for a model fit to  $P_f$  data for  $^{237}\text{Np}$ . If it is assumed that the first saddle has an axially asymmetric shape a good fit can be obtained. Using the same barrier parameters but assuming an axially symmetric shape at the first saddle leads to a significant reduction in the calculated  $P_f$  and change in shape so that even if the calculations are renormalized the data can not be fit in both the barrier and 8-10 MeV excitation energy regions. The reason for the change in shape of the calculated  $P_f$  distributions is illustrated in Fig. 4. In the case where  $E_A$  is greater than  $E_B$  by a small amount (0.4 MeV in this case) if symmetry effects are neglected the fission probability is always determined by the level density at the first saddle (i.e.  $N_A$  is always less than  $N_B$ ). However, for an axially asymmetric first barrier  $N_A$  increases more rapidly than  $N_B$  so that near threshold  $P_f$  depends most sensitively on  $E_A$  while at higher energies  $E_B$

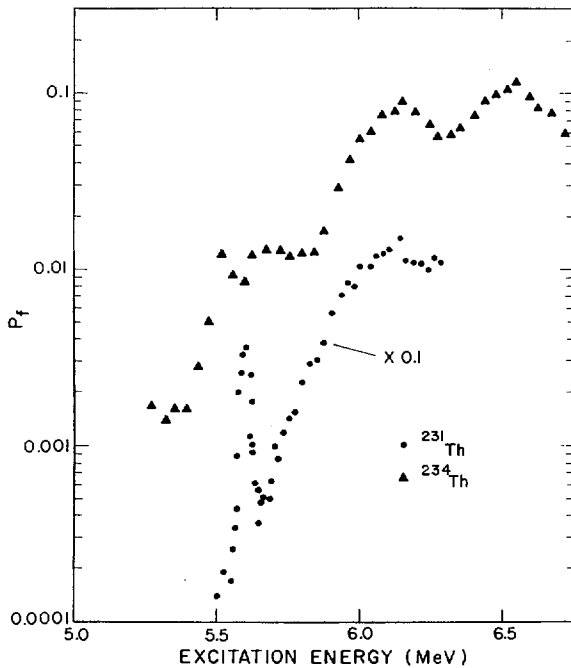


FIG. 6. Fission probability data for compound systems  $^{231}\text{Th}$  and  $^{234}\text{Th}$  [26].

is the most important parameter. Assuming an axially asymmetric first barrier made it possible to obtain qualitatively good fits to fission probability data throughout the actinide region for excitation energies up to  $\approx 12$  MeV without introducing any arbitrary normalization parameters. Typical fits for a series of Np isotopes are shown in Fig. 5. These results provide indirect but compelling evidence that the first barrier is in fact axially asymmetric for most of the actinide region as was predicted by theoretical calculations of the potential energy surface [12,13].

### 3. EVIDENCE FOR INCREASED COMPLEXITY IN THE POTENTIAL ENERGY SURFACE

#### 3.1. The Ra-Th Anomaly

At the 1973 Fission Conference detailed comparisons of fission barrier parameters from fits to experimental data were compared to results from various theoretical calculations of the potential energy surfaces [17-19]. These comparisons showed qualitative agreement in the U-Pu region but there seemed to be a serious disagreement for some thorium isotopes. In particular most theoretical calculations [19,29-31] indicated that the first saddle should be 2-3 MeV lower than the second saddle and, thus, the observed fission probability distributions should be smooth and structureless reflecting the smooth dependence for the

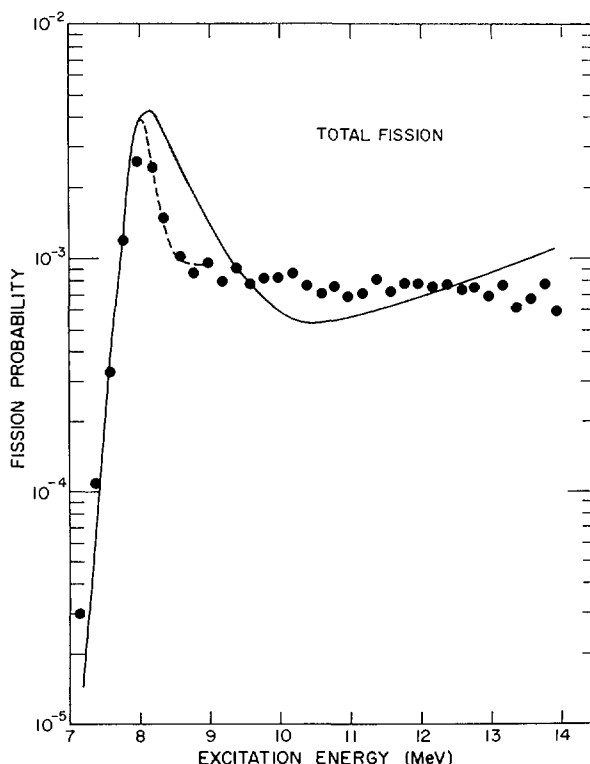


FIG. 7. Fission probability for  $^{228}\text{Ra}$  with model fits as described in the text [23].

penetrability through a single peaked fission barrier. In contrast Fig. 6 shows  $P_f$  distributions for  $^{231}\text{Th}$  and  $^{234}\text{Th}$  where very dramatic resonance phenomena are observed. These results indicate the peaks of the two barriers are of approximately equal height and the very sharp resonance in  $^{231}\text{Th}$  indicates much less damping than is present in heavier actinide nuclei where only the even-even nuclei show resonance structures. A detailed analysis of the  $^{231}\text{Th}$  data [32] indicated the potential minimum between the two barriers had a depth of less than 2 MeV as compared to  $\approx$  3-4 MeV for Pu and Am isotopes.

A possible explanation for the apparent qualitative difference between experimental results and theoretical calculations was suggested by Moller and Nix at the 1973 Conference [19] and shown to be qualitatively reasonable in a later publication [31]. They suggested that the two peaks responsible for the observed resonance phenomena might be due to the development of a third potential minimum in the region of the second mass-asymmetric saddle point. If this explanation were correct it would represent the first case in which secondary shell fluctuations (1-2 MeV) have been observed in the potential energy surface. The region of the

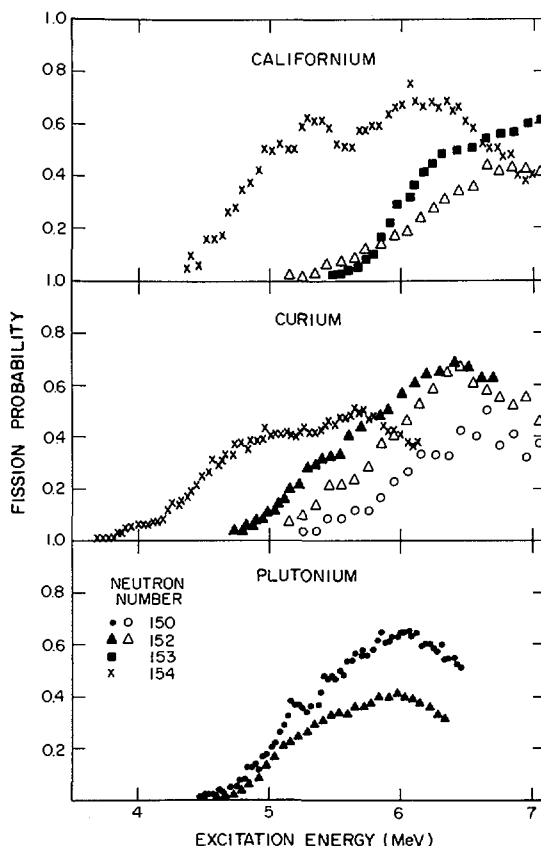


FIG. 8. Fission probabilities for plutonium, curium and californium isotopes [25].

second saddle for thorium isotopes is the most likely place to observe those smaller shell structures because a very broad second barrier is produced by the overlap of the peak of the liquid drop saddle with the major antishell that creates the second barrier in actinide nuclei.

Since 1973 two different experimental investigations have led further credence to the postulate of a third potential minimum for light actinides. Figure 7 shows the fission probability obtained for  $^{228}\text{Ra}$  [23]. In this case it was shown that the sharp structure at  $\approx 8$  MeV could only be reproduced by assuming a resonant penetration of two barriers at  $\approx 8$  MeV separated by a shallow minimum. Theoretical calculations [29] predicted  $E_A \approx 4.2$  MeV and  $E_B \approx 8.7$  MeV so that the most reasonable interpretation of the resonance phenomena was in terms of the postulated third minimum. Finally, very recent high resolution experiments on the  $^{231}\text{Th}$  resonance [33] have indicated complex fine structure which can be most simply interpreted in terms of a

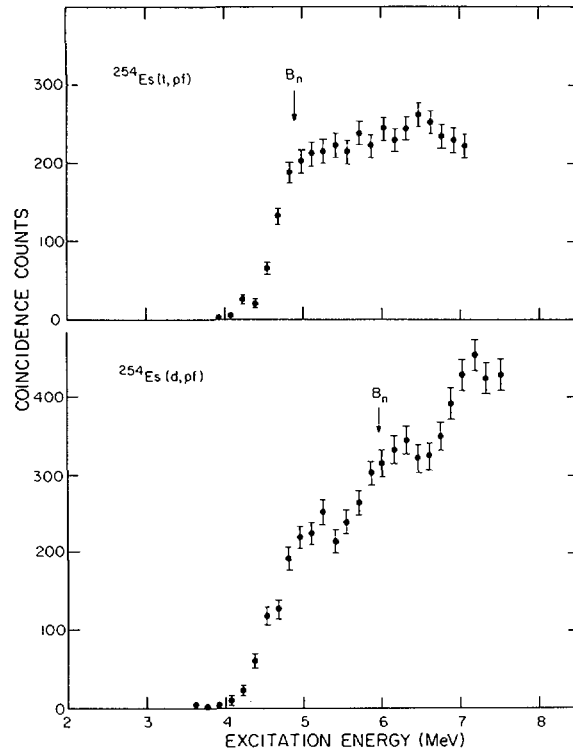


FIG. 9. Measured fission coincidence spectra for reactions on  $^{254}\text{Es}$  [36].

level structure in the third minimum that consists of two overlapping  $K = 1/2$  rotational bands with the opposite parity and essentially no mixing or damping into underlying compound states. The moment of inertia and decoupling parameter of these two bands are found to be the same and are consistent with the deformations expected for the second saddle point rather than the normal second minimum. Since two identical almost degenerate bands of opposite parity are a signature for a mass asymmetric shape these results would seem to give the final experimental confirmation of the third minimum postulate.

### 3.2. Barriers for nuclei with $N = 150-156$

Another region where fission thresholds show an unexpected behavior is near the  $N = 152$  shell [22,25]. It has long been known that ground state masses indicate an apparent shell closure for  $N = 152$  [34] and that there is a sharp discontinuity in the trend of spontaneous fission half lives at this neutron number [35]. The presence of shell effects in this region are also indicated by fission probability measurements (Fig. 8) where it has been shown that for both curium and californium isotopes

there is a drop in the fission threshold when the neutron number is increased from  $N = 152$  to  $N = 154$ . Additional measurements [36] on einsteinium nuclei (Fig. 9) with  $N = 156$  and  $N = 157$  indicate values for  $E_A$  of 5.4 MeV and 4.8 MeV, respectively, which are rather similar to  $^{250}\text{Cm}$  and  $^{252}\text{Cf}$ . These results taken together suggest a significant decrease in  $E_A$  for  $N > 152$ . Furthermore, in the case of  $^{250}\text{Cm}$  a weak resonance at 4 MeV established the height of the second barrier at 4.4 MeV [37] in qualitative agreement with fission isomer results for lighter curium isotopes and with theoretical predictions.

The most surprising aspect of these data is the appearance of resonance like structures in  $^{252}\text{Cf}$  at excitation energies in the region 5-5.5 MeV and the hint of similar structure in  $^{255}\text{Es}$ . These resonances are broader and occur with much larger fission probabilities than any of the transmission resonances observed for lighter actinides. Such a structure could occur from a double peaked fission barrier if the two peaks were very sharp. The appearance of resonant structure for both even-even and odd mass nuclei suggest a shallow minimum as in the case of thorium isotopes. Furthermore, the two apparent resonances in  $^{252}\text{Cf}$  have quite different anisotropies suggesting that there may be closely spaced resonances with different  $K$  values. Closely spaced resonances in an even-even system with different  $K$  values have not been previously observed and are consistent with the presence of an axially asymmetric system which would be expected to show approximately degenerate rotational bands with  $K = 0$  and  $K = 2$ .

In analogy to the thorium results these data appear consistent with the postulate that in this region secondary shell effects have caused the first axially asymmetric saddle point to break into two sharp barriers or at least to become lumpy enough that it deviates significantly from a parabolic shape. A fragmentation of the first barrier would most likely occur in this region since the liquid drop saddle has approximately the same deformation as the first strong antishell. Thus, this is a region where conditions for the first barrier are very similar to those encountered in thorium for the second barrier. The conclusions can not be made as strongly as for thorium but in one respect the situation is somewhat clearer. In this case it seems clear that we are not seeing transmission resonances through the same two barriers as for lighter actinides because for  $^{250}\text{Cm}$  a resonance that can be associated with the "normal" second barrier is observed at a much lower energy. Thus, these results again point to the presence of secondary shell structure on the potential energy surface which can be observed under the appropriate experimental conditions.

### 3.3. The Symmetric Second Saddle Point

For many years there has been considerable interest in the fission of radium and actinium isotopes. In this region fission mass distributions show distinctly separable symmetric and asymmetric components [38], the excitation functions for these components are quite different, and they seem to indicate different thresholds for the two mass components [39]. Attempts have been made to try to correlate this behavior with characteristics of the second saddle point in the potential energy surface [40, 41]. These attempts were, in general, not very convincing because the theoretical calculations of the potential energy surface as a function of mass asymmetry did not show evidence for a separate saddle point at symmetry.

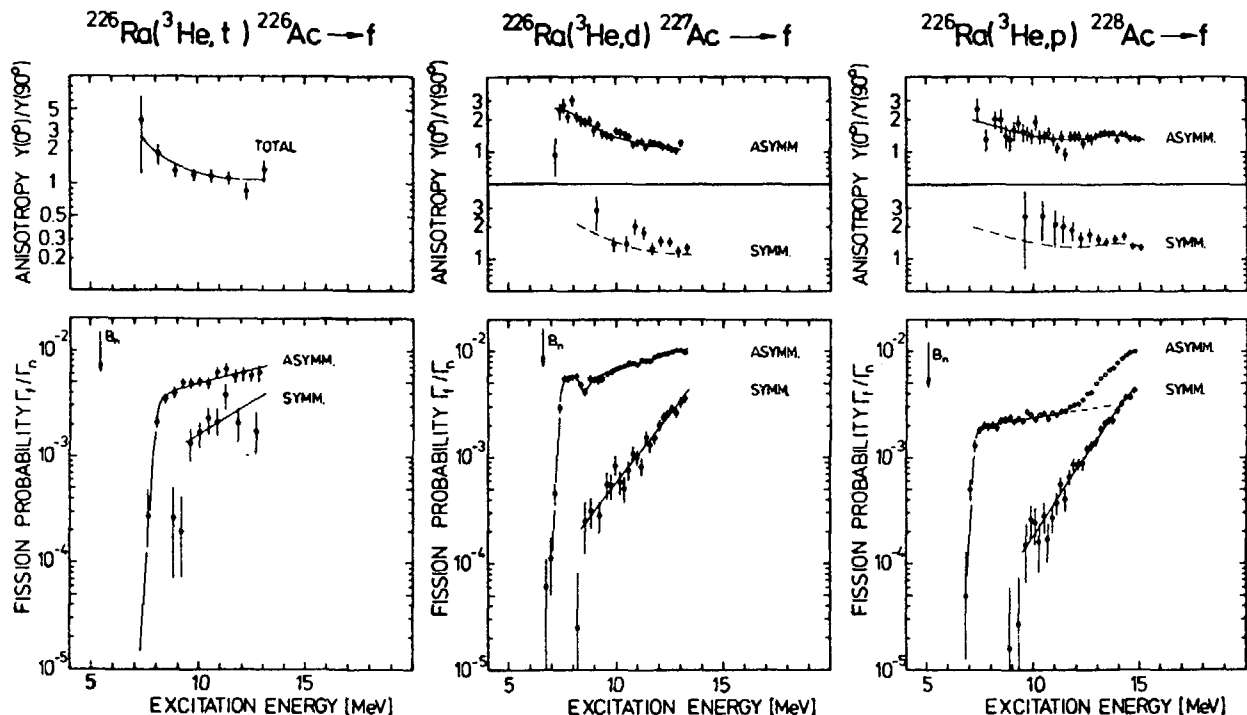


FIG.10. Fission probabilities and fragment anisotropics for  $^{226}\text{Ac}$ ,  $^{227}\text{Ac}$  and  $^{228}\text{Ac}$  [39].

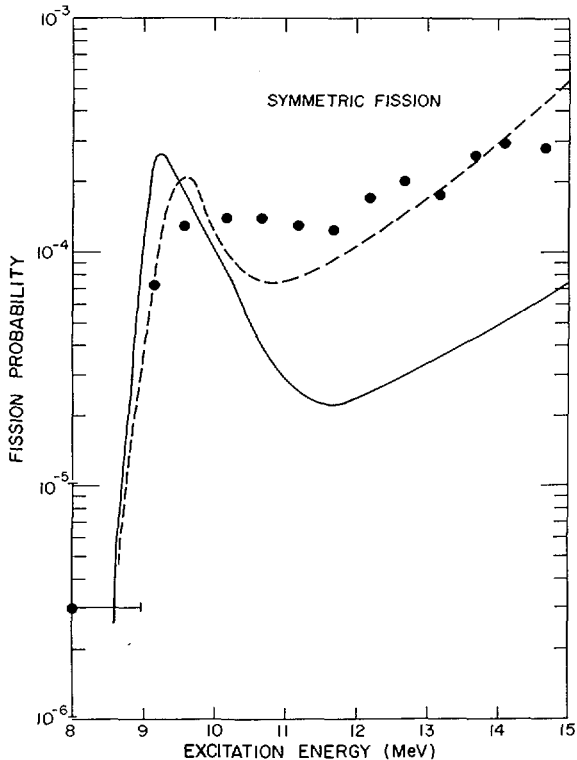


FIG.11. Fission probability for the symmetric fission component of  $^{228}\text{Ra}$ . Lines are model fits as described in the text [23].

Figure 10 shows excitation functions for symmetric and asymmetric mass components [39] for a series of actinium nuclei. The results indicate a threshold for the symmetric component that is 1-2 MeV higher than for the asymmetric component [39]. Similar results have been obtained for  $^{228}\text{Ra}$  [23] and Fig. 11 shows the excitation functions for the symmetric component along with the results obtained from attempts to fit the data with the microscopic statistical model described in Section 2. The solid line represents the best fit that can be obtained if it is assumed that the fission barrier is axially symmetric and mass asymmetric. It is seen that the model is unable to reproduce the rather slowly rising fission probability that is observed both for this case and for the previous actinium data [39]. However, if we arbitrarily assume that symmetric fission involves a separate barrier that is axially asymmetric then the dashed curve is obtained which gives a much better characterization of the experimental data.

At about the same time as the attempt to analyse the  $^{228}\text{Ra}$  data, results became available on the fission probability for  $^{238}\text{U}$  in the excitation energy region 6 - 12 MeV from studies with monoenergetic photons [42].  $^{238}\text{U}$  is a particularly interesting case because previous

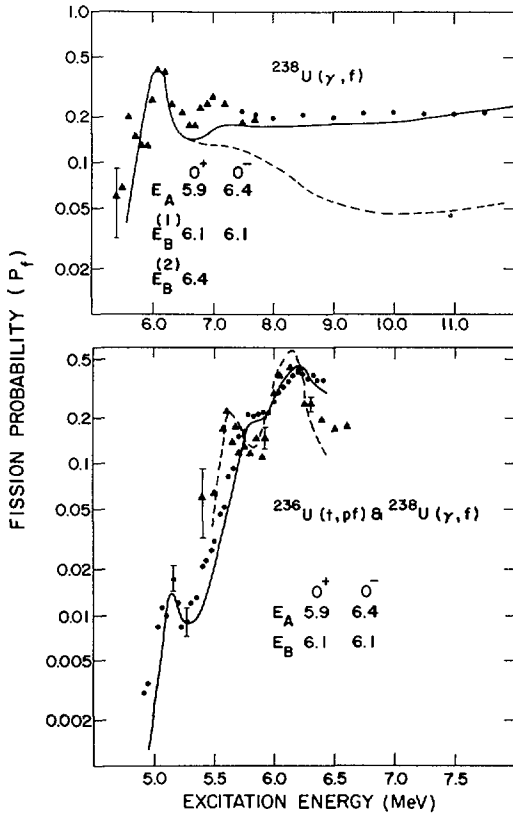


FIG.12. Fits to resonant ( $t, \text{pf}$ ) and  $(\gamma, \text{f})$  data for  $^{238}\text{U}$  (lower portion) and to higher-excitation-energy  $(\gamma, \text{f})$  data. Characteristics of fits are described in the text [24].

data from  $(t, \text{pf})$  [26] and  $(\gamma, \text{f})$  [43] studies near threshold could be used to establish the parameters of the fission barrier for both positive and negative parity transition state bands. The results of these fits [24] are shown in Fig. 12 and the dashed curve in the top portion shows the extrapolation of the fit to higher energies. It is seen that the model calculations underestimate  $P_f$  by about a factor of 4 at excitation energies above 10 MeV. In analogy to our conclusions for  $^{228}\text{Ra}$  we decided to investigate the result of adding another parallel second barrier which was axially asymmetric so that at higher excitation energies it would provide an enhanced fission probability. The solid curve in Fig. 12 shows that adding a parallel second barrier which is 0.3 MeV above the "normal" mass asymmetric barrier yields a good fit for the higher energy  $P_f$  measurement.

In order to test the credibility of this postulate of two parallel second barriers detailed potential energy calculations were done in the mass asymmetry-axial asymmetry plane in the region of the second saddle. The results are shown in Fig. 13. These results show two distinct saddle

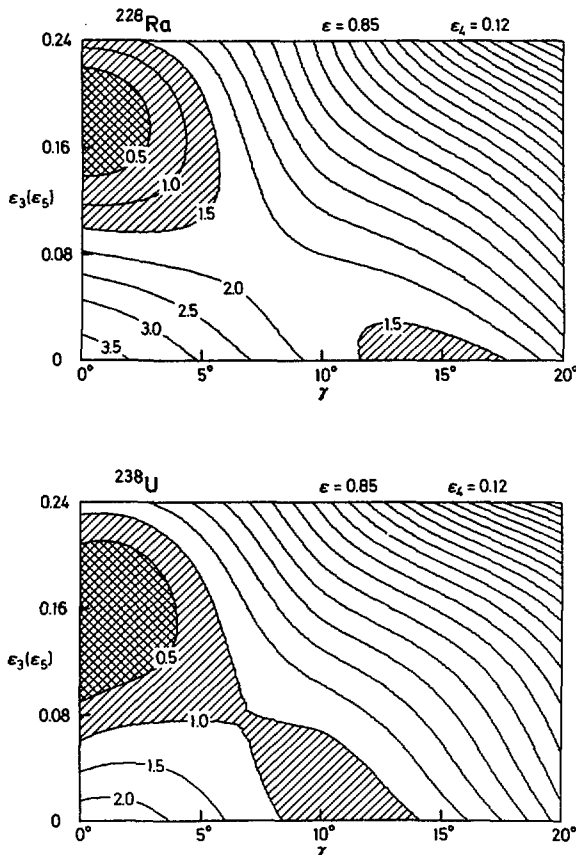


FIG.13. Calculated potential energy as a function of axial ( $\gamma$ ) and mass ( $\epsilon_3 \epsilon_5$ ) degrees of freedom in the vicinity of the second saddle point [24].

points separated by  $\approx 1$  MeV for  $^{228}\text{Ra}$  in agreement with the conclusions from the model fits. For  $^{238}\text{U}$  there is also evidence for two saddles with a separation of  $\approx 0.5$  MeV. In the  $^{238}\text{U}$  case the ridge between the two saddles is not as distinct as for  $^{228}\text{Ra}$ .

Recent attempts to systematically refit the Pf data [37] for actinide nuclei have also shown that the inclusion of an axially asymmetric parallel second barrier which is  $\approx 0.5$  MeV above the normal mass asymmetric barrier either improves the quality of the fit or gives a more consistent set of values for the height of the mass asymmetric barriers. Taken together these results indicate both experimentally and theoretically the existence of two parallel second barriers one of which is mass asymmetric, axially symmetric and the other at an excitation energy about 0.5 MeV higher is mass symmetric and axially asymmetric.

It is interesting to note that while the two mass components for  $^{228}\text{Ra}$  can be approximately identified with fission over the two parallel saddle points the same is not true for  $^{238}\text{U}$ . For  $^{238}\text{U}$  such a correlation would predict predominately symmetric fission at excitation energies above 10 MeV and this is not observed experimentally. For  $^{238}\text{U}$  the lack of a sharp ridge between the two saddles probably means that the nucleus can travel over the mass symmetric saddle and later on the descent toward scission it can go over to a mass asymmetric configuration.

#### 4. SYSTEMATICS OF FISSION BARRIER PARAMETERS

As has been shown in the preceding sections our perceptions of the general characteristics of the potential energy surfaces and the level density functions associated with the fission process have sharpened considerably over the past five years. In addition, the data base on fission probabilities for actinide nuclei has broadened and we are now at the point where data near threshold for most of the fissioning systems that can be conceivably investigated are available. Thus, this seems an appropriate time to attempt a reanalysis of all the available data in a consistent manner using our current version of a microscopic statistical model as described qualitatively in Section 2 and in previous papers [21,26,27].

The details of the model, fitting criteria, input data and the fits to various data sets will be described in a forthcoming comprehensive review [37]. In this section we will only describe some very general features and then compare the barrier parameters extracted from the experimental data with results obtained in other ways with the theoretical predictions of several groups.

In fitting the experimental data we have assumed that the first barrier has no symmetry except for the lightest actinides (Th, Pa) where reasonable fits could be obtained with the assumption of axial symmetry. For cases where the data extended to energies well above threshold we have assumed two parallel second barriers with a separation of 0.5 MeV. In general, we have tried to find a systematic set of parameters where  $E_A$ ,  $E_B$  and the curvatures  $\hbar\omega_A$  and  $\hbar\omega_B$  vary smoothly. From a study of the fits and a comparison to previous analyses we believe that the systematic uncertainties in the determination of barrier parameters from experimental fission probabilities are of the order  $\approx 0.3$  MeV for the higher of the two barriers or for both barriers when  $E_A \approx E_B$ . For a difference of 0.5 - 1.0 MeV between the two barriers the uncertainty on the lower one may be as large as  $\approx 0.5$  MeV and for a difference greater than 1 MeV the lower barrier can not be reliably determined except in cases where transmission resonances are observed.

The results from this systematic analysis of experimental data are shown in Fig. 14. In general, the dependence of  $E_A$  and  $E_B$  on neutron number for a particular element is relatively smooth. The occasional fluctuations with odd or even masses are relatively small and could be due to systematic uncertainties in the relative  $\Gamma_Y$  and  $\Gamma_n$  calculations since the fission thresholds systematically fluctuate from above to below the neutron binding energy as the neutron numbers change from odd to even. Also shown in Fig. 14 are values for  $E_B$  that have been previously obtained from the analysis of fission isomer excitation functions [44] and barrier parameters for Pu and Am isotopes deduced by the Bordeaux

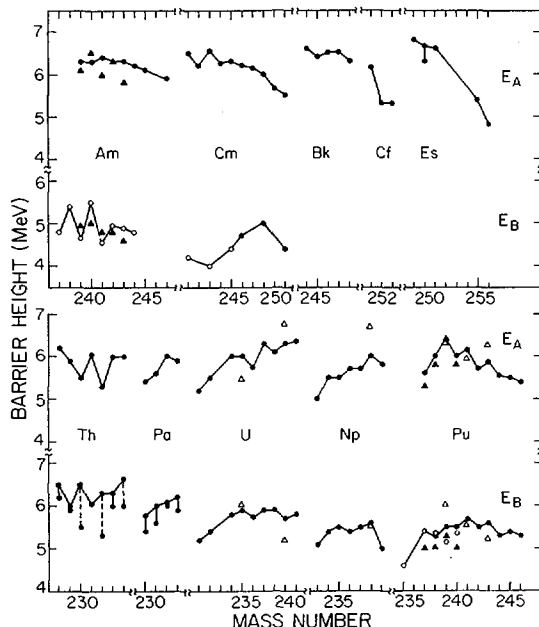


**FIG. 14.** Fission barrier heights ( $E_A$ ,  $E_B$ ) from fits to experimental data. Solid points from fits to fission probability data [37]. Open points from fits to fission isomer excitation functions [14]. Solid triangles are from Refs [44-47]. Open triangles are from analyses of fission widths for sub-barrier fission resonances [48].

- Stony Brook collaboration [44-47] from systematic fits to fission probabilities, fission isomer excitation functions and excitation functions for  $xn$  reactions. The various results are all internally consistent to within an average of  $\approx 0.2$ - $0.3$  MeV which is consistent with our estimates of the reliability of current measurement and analysis techniques. In Fig. 14 we also show estimates for  $E_A$  and  $E_B$  that are obtained from an analysis [48] of the widths of sub-barrier fission resonances for a series of U, Np and Pu isotopes excited in  $(n,f)$  resonances. On the average these results are in good agreement with the results from excitation function analyses. Individual deviations are observed up to  $\approx 0.5$  MeV but some of this could be due to the different spin states excited in the direct reaction and low energy  $(n,f)$  experiments. In general the agreement for values of the barrier parameters extracted from fission probability data,  $xn$  isomer and ground state excitation functions and sub-barrier resonance widths indicate that most of the systematic errors have been eliminated in the current analyses. For the thorium and proto-actinium nuclei both barriers should probably be associated with the second saddle and they are plotted that way in the lower portion of the figure.

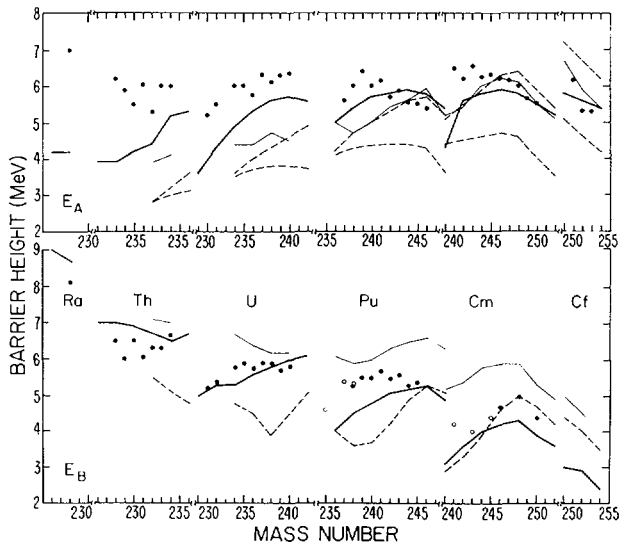


*FIG. 15. Comparison of experimental fission barriers [37] to various theoretical calculations from Möller [29] (solid line), Pauli and Leddergerber [30] (thin solid line) and Möller and Nix [31] (dashed lines).  $E_A$  has been corrected for effect of axial asymmetry as described in the text.*

In Fig. 15 the experimental barrier parameters are compared to predictions from three theoretical calculations. The calculations by Möller [29] use a modified harmonic oscillator potential and the Lysekil liquid drop constants. The first barrier has been lowered to account for the effects of axial asymmetric deformations using the energy differences calculated by Larsson and Leander [49]. The calculations of Möller and Nix [31] use a droplet model for the underlying liquid drop surface and a folded Yukawa potential. In both of these calculations the potentials are fitted to obtain the best representation of known single particle levels for a variety of deformed actinide nuclei. The third set of calculations from Pauli and Leddergerber [30] are most similar to the folded Yukawa model except that in this case the authors: 1) adjusted the parameters of the liquid drop to obtain an approximate fit to fission barrier parameters rather than fixing them with a fit to ground state masses and 2) a Woods-Saxon potential was fitted to the known single particle spectrum of  $^{208}\text{Pb}$ . For the last two calculations the effects of axial deformation at the first saddle were not systematically studied. In the results shown in Fig. 15 the corrections of Larsson and Leander [49] have been applied to the  $E_A$  values from both Möller and Nix, and Pauli and Leddergerber. The Möller and Nix uncorrected values of  $E_A$  are also shown to illustrate the magnitude of this correction.

From Fig. 15 it is seen that the calculations agree with each other and with the experimental barriers to an accuracy of  $\approx 1\text{-}2$  MeV. The overall agreement appears best with the calculations of Möller but there

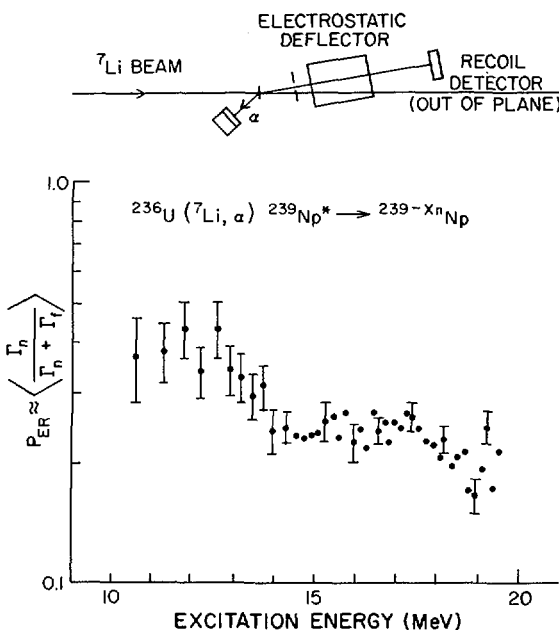


FIG. 16. Evaporation residue probability for  ${}^{236}\text{U}({}^7\text{Li}, \alpha)$  reaction [52].

are noticeable local and systematic deviations that could be a basis for further study. The results shown in Figs. 14 and 15 indicate that we have now evolved to a point where the experiments give a broad survey of barrier parameters with a systematic accuracy ( $\approx 0.3$  MeV) that is considerably better than the theoretical predictions ( $\approx 1-2$  MeV). There has been very little work done recently on refining the theoretical calculations and these results suggest that the experimental situation may now have evolved to a point where a new systematic theoretical study would be profitable. Because of the many differences in the theoretical models used in the calculations shown in Fig. 15 it is not possible to pinpoint whether current difficulties lie primarily in the single particle shell corrections or in the underlying macroscopic liquid drop model. A comprehensive study of the macroscopic liquid drop part of this theory is planned in the near future to see if this might be a major cause of the systematic deviations between theory and experiment [50].

##### 5. $\Gamma_f/\Gamma_n$ MEASUREMENTS TO HIGHER ENERGIES

In the preceding sections we have seen that the experimental studies of fission probabilities for actinide nuclei in the excitation energy range from threshold to the onset of second chance fission (11-12 MeV) has been rather systematically and completely investigated. In this region we also understand in reasonable detail the interpretation of the data in terms of the properties of the underlying potential energy surface and microscopic level density functions.

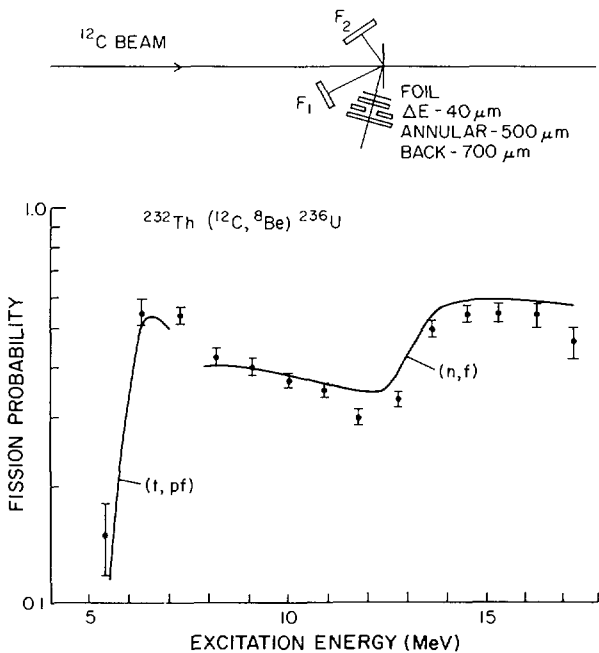


FIG. 17. Fission probability for  $^{232}\text{Th}/(^{12}\text{C}, ^8\text{Be})$  reaction [52].

In this section we will briefly describe some new feasibility studies aimed at investigating whether other types of direct reactions can be used to obtain fission probability data for excitation energies in the region of 10-20 MeV. From a detailed analysis of systematic data in this region it might be possible to obtain a more comprehensive view of several interesting aspects of the fission process. In the higher excitation energy regions it appears that a simple extrapolation of the model described in Section 2 gives too large a value of  $\Gamma_f$ . There are two general effects which should become important at higher excitation energies. First, the relative insensitivity of the microscopic state densities to the input single particle levels (see Fig. 2) tends to diminish and it may be possible from a systematic analysis to test various theoretical models in a new way. A second and more complex effect is that at higher energies the shell effects should start to wash out and cause a shift in the minimum of the level density functions away from the static saddle points [52] so that at a sufficiently high energy the deformation which gives the state density appropriate for an estimate of  $\Gamma_f$  would correspond to the liquid drop saddle. A related and possibly more complex effect is that as the level density minimum shifts toward the liquid drop saddle the symmetry enhancement effects will change.

Systematic data to higher excitation energies have been previously obtained for a series of neptunium isotopes from studies of ( $p,f$ ) reactions on uranium isotopes [52]. One difficulty with this or with direct-reaction fission techniques is that at higher energies in many cases  $P_f$  tends to approach 1 so that the requirements for experimental accuracy in order to obtain useful information become very severe. In an attempt to try to get around this difficulty we have been studying a new technique that involves the detection of evaporation residuals following a direct reaction [53,54]. These are the actinide nuclei which survive fission and decay by  $\alpha$  evaporation. The measurement gives a probability  $P_{ER} = 1 - P_f$  which has greater sensitivity for cases where  $P_f$  approaches 1. A recent experiment of this type [54] is illustrated in Fig. 16. Evaporation residuals are deflected out of plane to eliminate elastic  $^7\text{Li}$  particles and a coincidence required with backward reaction alpha particles. The  $(^7\text{Li}, \alpha)$  reaction leads primarily to residual excitations in the region 14-20 MeV. Thus, this technique seems to be a reasonable candidate for extending our detailed knowledge of  $\Gamma_f / \Gamma_n$  up to the next higher region of excitation energies.

Another reaction that has been recently studied [54] is the  $(^{12}\text{C}, ^8\text{Be})$  reaction where the two alpha particles from the  $^8\text{Be}$  breakup are detected in a semiconductor detector telescope. This reaction yields residual excitations in the 6-16 MeV region and, thus, is very good for studying the region of the onset of second chance fission. Results for the excitation of  $^{236}\text{U}$  are shown in Fig. 17 and it is seen that the data are in good agreement with previous ( $t,pf$ ) and ( $n,f$ ) results

## 6. SUMMARY

This seems like a particularly good time to attempt a summary of our understanding of the potential energy surfaces that govern the fission process and in this review we have tried to accomplish this task. The data set on fission properties is qualitatively complete in the sense that we have information on fission probabilities and fission isomer properties for almost all nuclei that can be realistically investigated. These data have been analysed in a variety of models and yield a set of barrier parameters,  $E_A$  and  $E_B$  to an approximate accuracy of about 0.3 MeV. Thus, a reasonable data set exists for use in testing future theories. Comparisons to presently available theoretical calculations indicate a reliability of the order of 1-2 MeV.

Among the more interesting developments of the last few years has been the development of a very strong experimental case for the fragmentation of the second barrier in the Ra-Th region, evidence for more structures in the first barrier in the Cm-Cf region, and evidence that there are probably two parallel paths to fission in the region of the second barrier for most actinide nuclei. The parallel paths simply indicate that there is more than one way for the nucleus to avoid the large antishell region that occurs for axial and mass symmetric shapes. The increased structure in the potential energy surface is most probably just due to the influence of small second order shells which will tend to produce 1-2 MeV "wiggles" that are then superimposed on the "normal" two peaked fission barrier. We should expect that further more detailed experiments will shed more light on both of these effects.

Finally, the extension of fission probability measurements to higher energies is discussed. This represents another promising area for continuing experimental and theoretical research.

#### ACKNOWLEDGMENT

It is a pleasure to acknowledge useful discussion and critical comments from many colleagues and collaborators. In particular, B. B. Back, E. Cheifetz, J. R. Nix, H. Weigmann and J. B. Wilhelmy have contributed very substantially to the ideas and insights presented in this manuscript.

#### REFERENCES

- [1] N. BOHR and J. A. WHEELER, Phys. Rev. 56 (1939) 426.
- [2] S. M. POLIKANOV, V. A. DRUIN, V.A. KARNAUKOV, V. L. MIKHEEV, A. A. PLEVÉ, N. K. SKOBELEV, V. G. SUBBOTIN, G. M. TER-AKOP'JAN, and V. A. FOMICHEV, Zh. Eksp. Teor. Fiz. 42 (1962) 1464; G. N. FLEROV, A. A. PLEVÉ, S. M. POLIKANOV, E. IVANOV, N. MARTALOGU, D. POENARU and N. VILCOV, Physics and Chemistry of Fission (International Atomic Energy Agency, Vienna, 1965) 307.
- [3] H. C. BRITT, F. A. RICKY, JR., AND W. S. HALL, Phys. Rev. 175 (1968) 1525.
- [4] E. MIGNECO AND J. P. THEOBALD, Nucl. Phys. A112 (1968) 603.
- [5] A. FUBINI, J. BLONS, A. MICHAUDON, and D. PAYA, Phys. Rev. Lett. 20 (1968) 1373.
- [6] V. M. STRUTINSKI, Nucl. Phys. A95 (1967) 420; A122 (1968) 1; M. BRACK, J. DAMGAARD, A. STEHOLM-JENSEN, H. C. PAULI, V. M. STRUTINSKI, and C. Y. WONG, Rev. Mod. Phys. 44 (1972) 320.
- [7] S. G. NILSSON, C. F. TSANG, A. SOBICZEWSKI, Z. SZYMANSKI, S. WYCECH, C. GUSTAFSON, I. L. LAMM, P. MOLLER and B. NILSSON, Nucl. Phys. A131 (1969) 1.
- [8] W. J. SWIATECKI, Phys. Rev. 100 (1955) 937.
- [9] Second IAEA Symposium on Physics and Chemistry of Fission, (International Atomic Energy Agency, Vienna, 1969) Sections C, D, E.
- [10] P. MOLLER and S. G. NILSSON, Phys. Lett. 31B (1970) 283.
- [11] H. C. PAULI, T. LEDERGERBER and M. BRACK, Phys. Lett. 34B (1971) 264.
- [12] S. E. LARSSON, I. RAGNARSSON and S. G. NILSSON, Phys. Lett. 38B (1972) 269.
- [13] U. GOTZ, H. C. PAULI, and K. JUNKER, Phys. Lett. 39B, (1972) 436.
- [14] H. C. BRITT, M. BOLSTERLI, J. R. NIX and J. L. NORTON, Phys. Rev. C7 (1973) 801; H. C. BRITT, S. C. BURNETT, B. H. ERKKILA, J. E. LYNN and W. E. STEIN, Phys. Rev. C4 (1971) 1444.
- [15] J. E. LYNN, Second IAEA Symposium on Physics and Chemistry of Fission (International Atomic Energy Agency, Vienna, 1969) 249.
- [16] B. B. BACK, J. P. BONDORF, G. A. OTROSCHENKO, J. PEDERSEN and B. RASMUSSEN, Nucl. Phys. A165 (1971) 449.
- [17] B. B. BACK, OLE HANSEN, H. C. BRITT, J. D. GARRETT, and B. LEROUX; Physics and Chemistry of Fission, 1973 (IAEA, Vienna, 1974) I 3.
- [18] B. B. BACK, OLE HANSEN, H. C. BRITT, and J. D. GARRETT, ibid I 25.
- [19] P. MOLLER and J. R. NIX, ibid I 103
- [20] S. BJORNHOLM, A. BOHR, B. R. MOTTELSON, ibid I 367.

- [21] A. GAVRON, H. C. BRITT, E. KONECNY, J. WEBER, and J. B. WILHELMY, Phys Rev. C13 (1976) 2374.
- [22] B. B. BACK, OLE HANSEN, H. C. BRITT, and J. D. GARRETT, Phys. Lett. 46B (1973) 183.
- [23] J. WEBER, H. C. BRITT, A. GAVRON, E. KONECNY, and J. B. WILHELMY, Phys. Rev. C13 (1976) 2413.
- [24] A. GAVRON, H. C. BRITT, P. D. GOLDSTONE, J. B. WILHELMY, S. E. LARSSON, Phys. Rev. Lett. 38 (1977) 1457.
- [25] H. C. BRITT, A. GAVRON, P. D. GOLDSTONE, R. SCHOENMACKERS, J. WEBER, and J. B. WILHELMY, Phys. Rev. Lett. 41 (1978) 1010.
- [26] B. B. BACK, OLE HANSEN, H. C. BRITT, and J. D. GARRETT, Phys. Rev. C9 (1974).
- [27] B. B. BACK, H. C. BRITT, OLE HANSEN, B. LEROUX, and J. D. GARRETT, Phys. Rev. C10 (1974) 1948.
- [28] J. D. CRAMER and J. R. NIX, Phys. Rev. C2 (1970) 1048.
- [29] P. MOLLER, Nucl. Phys. A192 (1972) 529.
- [30] H. C. PAULI and T. LEDERGERBER, Nucl. Phys. A175 (1971) 545.
- [31] P. MOLLER and J. R. NIX, Nucl. Phys. A229 (1974) 269.
- [32] J. D. JAMES, J. E. LYNN, and L. EARWAKER, Nucl. Phys. A189 (1972) 225.
- [33] J. BLONS, C. MAZUR, D. PAYA, M. RIBRAG, and H. WEIGMANN, Phys. Rev. Lett. 41 (1978) 1282.
- [34] N. B. GOVE and A. H. WAPSTRA, Nucl. Data Tables 11 (1972) 127.
- [35] M. NURMIA, T. SIKKELAND, R. SILVA, and A. GHIORSO, Phys. Lett. 26B (1967) 78.
- [36] H. C. BRITT, E. CHEIFETZ, and J. B. WILHELMY, to be published.
- [37] H. C. BRITT and B. B. BACK, to be published.
- [38] H. C. BRITT, H. E. WEGNER, and J. C. GURSKY, Phys. Rev. 129 (1963) 2239.
- [39] E. KONECNY, H. J. SPECHT, and J. WEBER, Physics and Chemistry of Fission, 1973 (IAEA, Vienna, 1974) I I3.
- [40] C. F. TSANG and J. B. WILHELMY, Nucl. Phys. A184 (1972) 417.
- [41] A. S. JENSEN and T. DOSSING, Physics and Chemistry of Fission, 1973 (IAEA, Vienna, 1974) I 409.
- [42] J. T. CALDWELL, E. J. DOWDY, B. L. BERMAN, R. ALVAREZ, and P. MEYERS, Los Alamos Scientific Laboratory Report No. LAUR-76-1615.
- [43] P. A DICKEY and P. AXEL, Phys. Rev. Lett. 35 (1975) 501.
- [44] J. GILAT, A. FLEURY, H. DELAGRANGE, and J. M. ALEXANDER, Phys. Rev. C16 (1977) 694.
- [45] H. DELAGRANGE, A. FLEURY, and J. M. ALEXANDER, Phys. Rev. C17, (1978) 1706.
- [46] A. FLEURY, H. DELAGRANGE, and J. M. ALEXANDER, Phys. Rev. C17 (1978) 1721.
- [47] J. P. GIROME, M. GRAFFEUIL, H. DELAGRANGE, and A. FLEURY, in preparation.
- [48] H. WEIGMANN, private communication.
- [49] S. E. LARSSON and G. LEANDER, Physics and Chemistry of Fission, 1973 (IAEA, Vienna, 1973) 177.
- [50] J. R. NIX, private communication.
- [51] V. S. RAMAMURTHY, S. S. KAPOOR, and S. K. KATARIA, Phys. Rev. Lett. 25 (1970) 386.
- [52] J. R. BOYCE, T. D. HAYWARD, R. BASS, H. W. NEWSON, E. G. BILPUCH, F. O. PURSER, and H. W. SCHMITT, Phys. Rev. C10 (1974) 231.
- [53,54] P. D. GOLDSTONE, H. C. BRITT, R. SCHOENMACKERS, and J. B. WILHELMY, Phys. Rev. Lett. 38 (1977) 1262.

## DISCUSSION

H.J. SPECHT: You have shown great caution in drawing conclusions from the observed structures in fission probabilities for radium-228 and californium-252 in terms of the double-humped barrier, further split by secondary shell effects. I fully agree with your approach. I would point out, in fact, that there are at least two other origins for structure. One is simply a matter of the wave-like nature of the quantum-mechanical penetration process — it was pointed out years ago by Hoffmann and Dietrich that penetration of a barrier more ‘squared’ than an inverted parabola leads to structure — and the other possibility is fluctuation in the vibrational strength in the first well, which we have tended to ignore in our enthusiasm for transmission resonances in the second well. Could you comment on that?

H.C. BRITT: I feel that, at the present time, we can only conclude with reasonable confidence that the outer barrier in the case of thorium and the inner barrier for californium have a non-parabolic shape. I think that californium may be the best candidate for reflection-type effects, suggested earlier by Dietrich as a possible effect to look for. The sharp resonance in  $^{231}\text{Th}$  suggests a third shallow minimum, but I agree that so far the evidence is still somewhat ambiguous.

Yu.M. TSIPENYUK: You have endeavoured to describe fission of a nucleus by changing the symmetry of its barriers. In such a case, however, the spectrum of the lower states is altered, and I do not think you can describe the angular distributions under those conditions.

H.C. BRITT: The angular distributions are much more difficult to calculate, since in principle we have to use a different set of barrier parameters for each K state, and the number of parameters involved becomes unreasonable. We have not attempted any such calculations in recent times.

Yu.M. TSIPENYUK: A further point is that the existence of resonances in the case of the light actinides greatly alters analysis of the height of the first barrier, a possible explanation for which is that the resonances relate to the third barrier. Do you not think that in such a case your experimental values would be inaccurate?

H.C. BRITT: We think that in the thorium region both barriers obtained from the analysis are probably associated with the outer barrier.

K.W. GOEKE: At the present time theoretical calculations for evaluating potential energy surfaces suffer from two basic shortcomings. First, there is considerable ambiguity in parametrizing the single-particle potential, for example in the case of the Saxon-Woods potential, or the harmonic oscillator, and so we should look for theories which determine, self-consistently and without parameter fit, the potential energy surface, which will then be based only on the inner dynamics of the process. The present theories of this type are the time-dependent Hartree-Fock theory (TDHF) and, especially for sub-barrier processes,

the adiabatic time-dependent Hartree-Fock theory (ATDHF), which also provides correct values for collective masses. Both these theories have recently been developed to such an extent that we can expect explicit calculations for realistic cases in the near future.

The second disadvantage is that the potential surfaces are basically classical quantities and therefore have to be corrected for quantum effects before being compared with experimental data. The corrections are actually very simple and require only the evaluation of some easily accessible zero-point energies. They can be shown to have a considerable effect, for example, on barrier heights. I think that unless we take both these effects into account we should not wonder at discrepancies between theory and experiment.

H.C. BRITT: I certainly agree that the pursuit of different versions of the Hartree-Fock theory may show the most promise for future progress. I am not certain of the relative importance of quantum corrections, but I agree that they should be carefully looked at.

In any case, your comments support my basic conclusion that now is the right time for new theoretical initiatives in the study of potential energy surfaces.

R.H. IYER: Do the 'wiggles' that one sees in the potential energy barrier have any effect on the mass distribution in fission? The reason I ask is that we have obtained experimental evidence for the existence of some new 'wiggles' or 'bumps' in the highly asymmetric region of fission mass distribution.

H.C. BRITT: As I mentioned in my presentation, there is reasonable correlation between mass asymmetry at the second saddle point and the final mass distribution at infinity for the case of radium, where we really do see separable symmetric and asymmetric mass components. However, for the heavier actinide nuclei I do not believe there is any convincing evidence of a relationship between the saddle-point properties and the details of the final mass distributions.

A. FAESSLER: The main point brought out by what you have told us seems to be that the fission deformation energy surface cannot be described by smoothly joined parabolas. On the other hand, you have obtained discrepancies between theory and experiment for the barrier heights, although in fact the experimental barrier heights were determined on the assumption of parabolas. Do you think that a more realistic assumption with regard to the form of the barrier would change the experimental barrier heights obtained?

H.C. BRITT: No, I do not think that the barrier heights would change very significantly with a more sophisticated model, but other properties, such as the curvature ( $\hbar\omega$ ), are certainly model-dependent. The major problem involved in adding further sophistication is that the models become intractable and we then need some more theoretical guidance on the most profitable direction to take.



# НИЗКОЭНЕРГЕТИЧЕСКОЕ ФОТОДЕЛЕНИЕ ТЯЖЕЛЫХ ЯДЕР

Г.Н.СМИРЕНКИН  
Г.Н.СМИРЕНКИН

Физико-энергетический институт  
Государственного комитета по использованию  
атомной энергии СССР,  
Обнинск

Ю.М.ЦИПЕНЮК  
Институт физических проблем Академии наук СССР,  
Москва,  
Союз Советских Социалистических Республик

## Abstract—Аннотация

### LOW-ENERGY PHOTOFISSION OF HEAVY NUCLEI.

The paper summarizes the results of studies on low-energy photofission of heavy nuclei, mainly in the sub-barrier region of excitation energies. The following aspects of angular anisotropy of fission fragment separation and channel structure are discussed in detail: the spectrum of transition states of a fissionable nucleus, the role of nuclear symmetry in the shaping of angular distribution, mass distributions of fragments and fissionabilities of nuclei. The results of experimental studies on the properties of spontaneously fissionable isomers in reactions with  $\gamma$ -quanta are presented. An analysis is made of data from a study on deep sub-barrier photofission and on the new phenomena discovered in this connection (the isomeric shelf, anomalies in the isotropic component of angular distribution and the resonance structure of the cross-section).

### НИЗКОЭНЕРГЕТИЧЕСКОЕ ФОТОДЕЛЕНИЕ ТЯЖЕЛЫХ ЯДЕР.

В работе подытожены результаты исследований низкоэнергетического фотоделения тяжелых ядер — преимущественно в подбарьерной области энергий возбуждения. Подробно обсуждаются вопросы угловой анизотропии разлета осколков и каналовой структуры: спектр переходных состояний делящегося ядра, роль симметрии ядра в формировании углового распределения, массовых распределений осколков, делимостей ядер. Приводятся результаты экспериментов по изучению свойств спонтанно делящихся изомеров в реакциях с  $\gamma$ -квантами. Анализируются данные по изучению глубоко подбарьерного фотоделения и обнаруженных в этой области новых явлений — изомерного шельфа, аномалий изотропной составляющей углового распределения, резонансной структуры сечения.

## 1. ВВЕДЕНИЕ

Интерес к явлению деления атомных ядер обусловлен не только его практической значимостью, но и уникальными возможностями для изучения свойств силь-

но деформированной ядерной материи. Если колебания ядер, изучаемые спектропией, представляют собой небольшие отклонения от равновесной деформации, то физика деления имеет дело с процессом, в котором энергия также концентрируется на колебательной степени свободы, но деформация возрастает настолько, что завершается развалом ядра. Область вершины возникающего при этом барьера, с которой связано так называемое переходное состояние делящегося ядра, — самое узкое место в процессе деления, определяющее многие его свойства: делимость, угловые распределения осколков и др. Изучение последних, в свою очередь, позволяет делать заключения о свойствах этого состояния, отличающегося от равновесных аномально большой деформацией.

Деление ядер — один из типов ядерного превращения, и экспериментальные методы его изучения, по существу, не отличаются от соответствующих методов ядерной физики. Самым простым способом внесения энергии в ядро является облучение его  $\gamma$ -квантами — безмассовыми частицами, для взаимодействия с которыми характерен очень ограниченный спектр орбитальных угловых моментов. В этом одновременно преимущества и недостаток такого способа возбуждения. Мы не можем таким способом исследовать сложные типы движения нуклонов в ядре, однако в применении к изучению процесса деления атомных ядер, который сам по себе необычайно сложен и многогранен, этот недостаток (простота) является в данном случае преимуществом. Именно с этой точки зрения привлекательно изучение фотodelения тяжелых ядер при энергиях, близких к пороговым.

Гамма-кванты с энергией 5-7 МэВ испытывают на тяжелых ядрах в основном электрические дипольное и квадрупольное поглощения. Для четно-четных ядер-мишеней это приводит преимущественно к образованию составных ядер лишь в двух возможных состояниях:  $2^+$  и  $1^-$ , причем, из-за того, что длина волны  $\gamma$ -квантов в рассматриваемой области энергий значительно превышает размеры ядра, сечение дипольного поглощения должно быть значительно больше сечения квадрупольного поглощения. Моменты четно-четных составных ядер после поглощения  $\gamma$ -квантов с разной мультипольностью оказываются по-разному выстроеными вдоль направления пучка фотонов, и это обеспечивает высокую чувствительность угловых распределений осколков к квантовым характеристикам состояний, через которые происходит деление. Более того, только с помощью  $\gamma$ -квантов осуществляется возможность изучения вероятности деления через состояния с определенными комбинациями спина и четности в широкой области энергий. Этими обстоятельствами обусловлена преимущественная направленность исследования фотodelения именно четно-четных ядер.

Данный обзор не претендует на всеобъемлющий охват всех работ по изучению деления ядер  $\gamma$ -квантами низких энергий ( $\lesssim 10$  МэВ). Мы ставили перед собой задачу анализа экспериментальных результатов, затрагивающих принципиальные свойства процесса деления. Естественно, что этот обзор во многом отражает направление исследований фотodelения на электронном ускорителе — микротроне, проводимых в Институте физических проблем АН СССР в течение последних 15 лет совместно с Физико-энергетическим институтом ГКАЭ СССР.

## 2. УГЛОВАЯ АНИЗОТРОПИЯ ФОТОДЕЛЕНИЯ И ГИПОТЕЗА О.БОРА

Явление угловой анизотропии деления было впервые обнаружено Уинхолдом, Демосом и Халпероном в 1952 г. именно в реакции ( $\gamma$ , f). Эксперимент [1] показал, что при фотodelении  $^{232}\text{Th}$  осколки разлетаются преимущественно под прямым углом к пучку  $\gamma$ -квантов тормозного излучения, их угловое распределение следует закону  $W(\theta) = a + b \sin^2 \theta$ , а отношение коэффициентов  $b/a = W(90^\circ)/W(0^\circ) - 1$ , характеризующее угловую анизотропию, возрастает по мере приближения граничной энергии  $\gamma$ -квантов  $E_{\max}$  к порогу деления. Через пять лет наличие этих свойств было установлено еще у нескольких четно-четных ядер [2].

Для объяснения угловой анизотропии разлета осколков О.Бор [3] выдвинул в 1955 г. идею о каналах деления – квантовых (переходных) состояниях ядра в седловой точке. Гипотеза О.Бора предполагает, что каждому каналу деления отвечает своя поверхность потенциальной энергии деформации, определяемая набором квантовых характеристик:  $J$  – углового момента ядра,  $K$  – его проекции на направление деления, совпадающее с осью симметрии (как и в равновесном состоянии, ядро предполагается аксиально симметричным),  $\pi$  – четности состояния. Предполагается, что величина  $K$  может оказаться достаточно "хорошим" приближенным квантовым числом в процессе спуска делящегося ядра с седловой точки к точке разрыва. Возникающая таким образом зависимость высоты барьера  $E_f^\lambda$  от квантовых характеристик  $\lambda = (J, \pi, K)$  обеспечивает неоднородность распределения  $J$ , что при наличии определенной выстроенности угловых моментов составного ядра  $K$  в пространстве приводит к угловой анизотропии разлета осколков относительно направления падающего пучка.

Фотodelение четно-четных ядер представляет собой исключительно благоприятную возможность для изучения следствий гипотезы О.Бора. Если энергия  $\gamma$ -квантов близка к порогу, то доминирующая роль в делении будет принадлежать каналам  $J^\pi = 2^+$  и  $1^-$ ,  $K=0$ , которые, как отмечалось, возбуждаются при электрических квадрупольном ( $E2$ ) и дипольном ( $E1$ ) поглощениях. Это первые возбужденные состояния именно тех нижайших вращательных полос каналов деления, которые предсказал О.Бор. Парциальный вклад каждого из них может быть надежно установлен

$$\text{экспериментально по виду углового распределения } W_{JK}(\theta) \sim \left| D_{MK}^J(\theta) \right|^2 + \left| D_{MK'}^J(\theta) \right|^2$$

для заданных  $J$  и  $K$ , а именно:  $W_{20} \sim \sin^2 2\theta$  и  $W_{10} \sim \sin^2 \theta$ , где  $D_{MK}^J(\theta)$  – функция Вигнера,  $M$  – проекция  $J$  на направление пучка, равная для  $\gamma$ -квантов  $\pm 1$ . В общем случае угловое распределение осколков описывается выражением

$$W(\theta) = a + b \sin^2 \theta + c \sin^2 2\theta \quad (1)$$

где изотропная компонента  $a$  связана с каналами  $K \neq 0$ , в основном  $K^\pi = 1^-$ .

Следуя неравенствам

$$E_f^{20} < E_f^{10}, \quad E_f^{10} < E_f^{JK}$$

которыми выражено содержание гипотезы О.Бора и

$$\sigma_{\gamma}^{M_Q} \lesssim \sigma_{\gamma}^{E2} \ll \sigma_{\gamma}^{E1}$$

которые описывают соотношение между сечениями фотопоглощения разной мультипольности, отношения коэффициентов (1) можно выразить через проницаемости барьера  $T(E, E_f^{\lambda})$  для отдельных каналов:

$$2 \frac{b}{a} + 1 \approx T(E, E_f^{10}) / T(E, E_f^{11}) \quad (2)$$

$$\frac{a}{b} = \frac{5 \sigma_{\gamma}^{E2} P_f^{20}}{4 \sigma_{\gamma}^{E1} P_f^{10}} \approx \frac{5}{4} \frac{\sigma_{\gamma}^{E2}}{\sigma_{\gamma}^{E1}} \frac{T(E, E_f^{20})}{T(E, E_f^{10})} \quad (3)$$

$$\frac{T(E, E_f^{\lambda})}{T(E, E_f^{\lambda'})} = \begin{cases} 1, & E > E_f^{\lambda} \\ \exp \left[ \frac{2\pi}{\hbar\omega} (E_f^{\lambda'} - E) \right], & E_f^{\lambda} < E < E_f^{\lambda'} \\ \exp \left[ \frac{2\pi}{\hbar\omega} (E_f^{\lambda'} - E_f^{\lambda}) \right], & E < E_f^{\lambda} \end{cases} \quad (4)$$

где, ради простоты, мы предположили  $\hbar\omega_{\lambda} = \hbar\omega_{\lambda'} = \hbar\omega < 2\pi (E_f^{\lambda'} - E_f^{\lambda})$  и игнорировали в (3) разницу в отношениях делимостей  $P_f^{\lambda}$  и проницаемостей  $T(E, E_f^{\lambda})$  для двух каналов с разными комбинациями  $J''$ . Из соотношений (2)-(4) вытекают следующие свойства угловых распределений осколков фотоделения четно-четных ядер, которые можно рассматривать как характерные признаки "каналовой" структуры барьера  $E_f^{JK}$  по О.Бору:

- 1) экспоненциальное увеличение отношений (2) и (3) в области  $E_f^{\lambda} < E < E_f^{\lambda'}$ ;
- 2) существование излома этой зависимости в окрестности энергий  $E \approx E_f^{\lambda} < E_f^{\lambda'}$ , ниже которой она резко ослабевает или исчезает совсем, если  $\hbar\omega_{\lambda} = \hbar\omega_{\lambda'}$ .

Впервые совокупность указанных свойств  $W(\theta)$  наблюдалась в работе [4] при изучении фотоделения  $^{238}\text{U}$  на пучке тормозного излучения микротрона ИФП АН СССР. На рис.1 приведены экспериментальные данные и результаты разложения  $W(\theta)$  по компонентам согласно (1), которые были получены в [4] и при аналогичных измерениях для  $^{232}\text{Th}$  и  $^{240}\text{Pu}$  [5-7]. Несмотря на разницу в соотношении компонент, обсуждаемую нами позже, общим для всех ядер является качественное соответствие энергетической зависимости их вклада в  $W(\theta)$  предсказанию, выраженному соотношениями (2)-(4).

Для установления адекватности представлений модели каналов деления О.Бора решающее значение имеет полученная в [4] информация о квадрупольном фотоде-

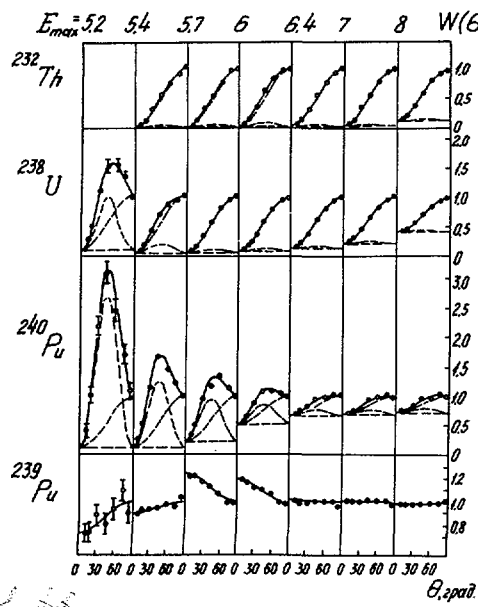


Рис. 1. Угловое распределение осколков при фотоделении  $^{232}Th$ ,  $^{238}U$ ,  $^{239}Pu$ ,  $^{240}Pu$  тормозными  $\gamma$ -квантами при различных энергиях электронов, указанных на рисунке (в МэВ). Данные взяты из работ [4-7, 14]. Пунктиром показаны компоненты  $W(\theta)$ .

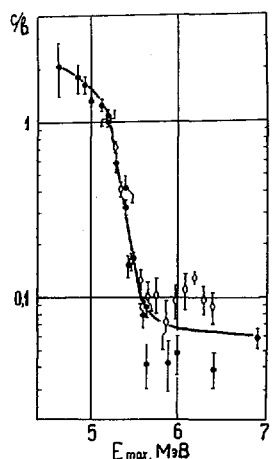


Рис. 2. Относительный вклад квадрупольной компоненты углового распределения для  $^{238}U$  зависимости от граничной энергии тормозного спектра: ● – [4-7], ◇ – [9].

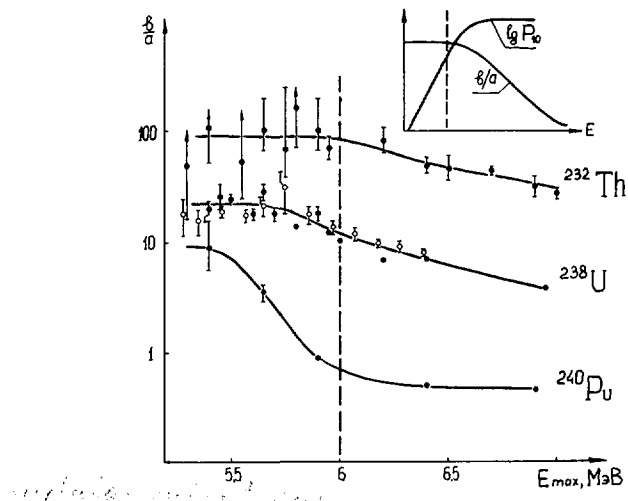


Рис. 3. Энергетическая зависимость угловой анизотропии – отношения  $b/a$  для ядер  $^{232}\text{Th}$ ,  $^{238}\text{U}$ ,  $^{240}\text{Pu}$ : ● – [4-7], ○ – [9]. На вставке: зависимость делимости и угловой анизотропии в модели одногорбого барьера. Пунктиром показано положение наблюдаемого порога.

ления, поскольку до этого спорным был даже сам факт наблюдения компоненты  $\sim \sin^2 2\theta$ , не говоря уже о свойствах отношения  $c/b$ , по которым можно было бы судить о предполагаемой структуре спектра состояний делящегося ядра и связи их с седловой точкой.

В подбарьерной области энергий экспоненциальное падение проницаемости  $T(E, E_f^{10})$  компенсирует малость отношения  $\sigma_\gamma^{E2}/\sigma_\gamma^{E1}$  настолько, что квадрупольная компонента  $c$ , с трудом выделяемая в  $W(\theta)$  в надбарьерной области, глубоко под порогом становится преобладающей. Этот механизм подбарьерного "усиления" относительного вклада квадрупольной компоненты  $W(\theta)$ , который впервые обсуждался Гриффином [8], "работает" согласно (4) лишь при достаточном расстоянии между каналами  $E_f^{10} - E_f^{20} > \hbar\omega/2\pi$ . Из рис. 2, на котором для  $^{238}\text{U}$  приведены данные [4-7] вместе с результатами недавних измерений в Швеции [9], видно, что поведение отношения  $c/b$  находится в согласии с выражениями (3) и (4), согласно которым по наклону экспоненциального участка легко оценить  $\hbar\omega \simeq 0,9$  МэВ, а по величине "усиления" –  $E_f^{10} - E_f^{20} \simeq 0,6-0,7$  МэВ. Аналогично, т.е. в соответствии с (2) и (4), ведет себя угловая анизотропия фотоделения  $b/a$ , энергетическая зависимость которой показана на рис. 3.

Зависимость от энергии анизотропных составляющих углового распределения  $W(\theta)$  в районе порога не только подтверждает конкретную структуру спектра каналов фотоделения четно-четных ядер  $(J^\pi, K) = (2^+, 0), (1^-, 0), (1^-, 1)$ , но и является важным свидетельством того, что характеристика  $K$  в процессе разделения сохра-

няется, т.е. является достаточно хорошим квантовым числом: наблюдаются практически "чистые"  $D_{MK}^J$ -функции  $|D_{\pm 1,0}^2(\theta)|^2$  и  $|D_{\pm 1,0}^1(\theta)|^2$ . Смешивание К, если бы оно было существенным при спуске с вершины барьера, привело бы к значительному вкладу изотропной компоненты (при однородном распределении К деление изотропно).

Угловые распределения осколков фотodelения, согласующиеся с изложенными представлениями, изучены для восьми четно-четных ядер от  $^{226}\text{Ra}$  до  $^{242}\text{Pu}$  [2, 4-7, 9-11]. Фотodelение ядер с нечетным числом нуклонов практически изотропно [2, 12]. Этот результат также предсказал О.Бор [3], связав его с большим набором доступных состояний по J, меньшей выстроенностью угловых моментов вследствие наличия хаотически распределенного спина ядра-мишени, более высокой плотностью каналов деления ( $E_f^\lambda - E_f^\lambda \gtrsim \hbar\omega/2\pi$ ). Исключение составляет ядро  $^{239}\text{Pu}$ , имеющее минимальный спин 1/2, угловые распределения для которого показаны в нижней части рис.1 [13, 14].

### 3. АНОМАЛИЯ ОТНОШЕНИЯ b/a И ДВУГОРБАЯ СТРУКТУРА БАРЬЕРА

В предыдущем разделе для иллюстрации следствий гипотезы О.Бора и обсуждения экспериментальных данных мы фактически использовали представления об одногорбом барьере, которые мотивировались в прошлом моделью жидкой капли и просуществовали без малого 30 лет. Рассчитанные для такого барьера зависимости

$$\text{делимости } P_{10} = \frac{\sigma_{\gamma}^{10}}{\sigma_{\gamma}^{E1}} = \frac{T_{10}}{T_{10} + 2T_{11} + T_{\gamma}^1} \quad \text{и отношения } b/a = (T_{10} - T_{11})/2T_{11} \text{ от энер-}$$

гии возбуждения показаны на вставке к рис.3, откуда следуют описанные выше свойства угловой анизотропии фотodelения. Одно из них удобно использовать при качественном анализе экспериментальных данных как характерный признак классической каналовой структуры: каналовые эффекты в угловой анизотропии (подъем и перегиб b/a) в случае одногорбого барьера должны быть в надпороговой по сечению деления области энергий.

На рис.3 для трех ядер  $^{232}\text{Th}$ ,  $^{238}\text{U}$  и  $^{240}\text{Pu}$ , некоторые угловые распределения для которых показаны на рис.1, приведены данные об угловой анизотропии деления b/a. Пунктиром на вставке рис.3 показано положение наблюдавшегося порога, который с точностью до 0,1-0,2 МэВ одинаков у этих ядер. Хорошо видно, что если в случае  $^{232}\text{Th}$  реализуется "классическая картина", т.е. ожидаемая в соответствии с результатами расчета на вставке, то для более тяжелых ядер положение излома (максимума) b/a находится в противоречии с ней, оно находится не справа от наблюдавшегося порога, а слева, причем расхождение тем сильнее, чем выше Z ядра. Интерпретация этого неожиданного свойства в рамках существовавших представлений вызвала значительные трудности [5, 15], которые удалось преодолеть лишь на основе теоретического предсказания о существовании двугорбой структуры барьера деления тяжелых ядер в работах Струтинского [16].

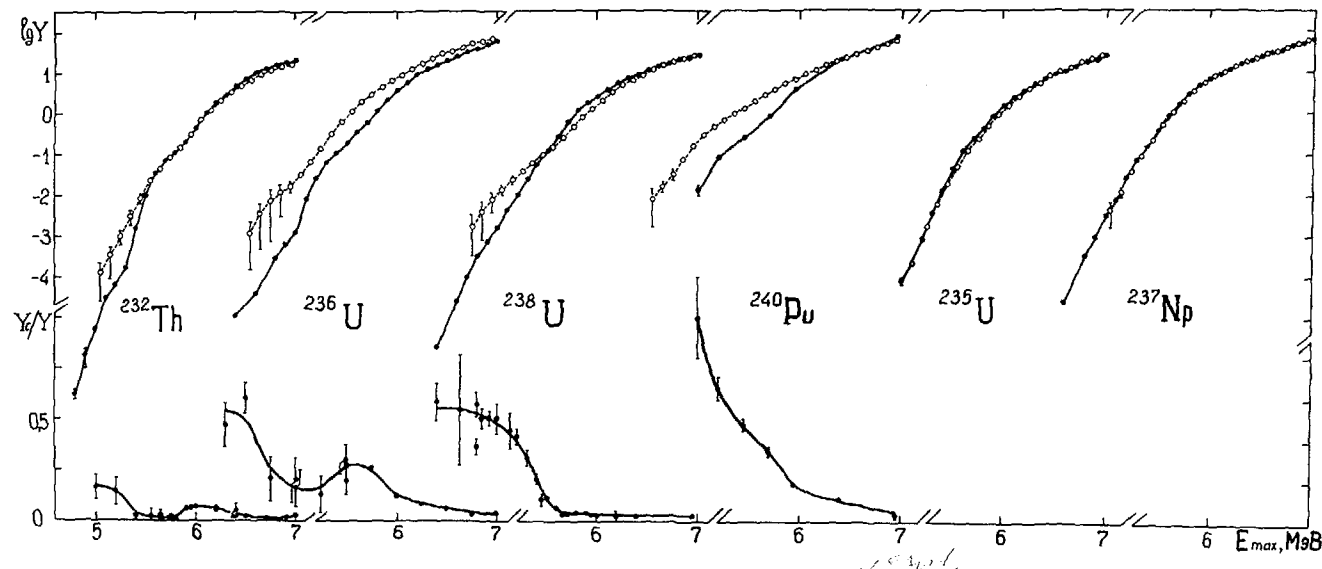


Рис. 4. Сравнение выходов реакций  $(\gamma, f)$  (на рисунке обозначены  $\bullet$ ) с результатами расчетов с  $\sigma_f(E) = \sigma_{\gamma}^{EI}(E) \cdot P_f(t, p_f)$  (на рисунке обозначены  $\circ$ ). В нижней части рисунка приведены экспериментальные данные об относительном вкладе квадрупольной компоненты в полный выход реакции фотоделения.

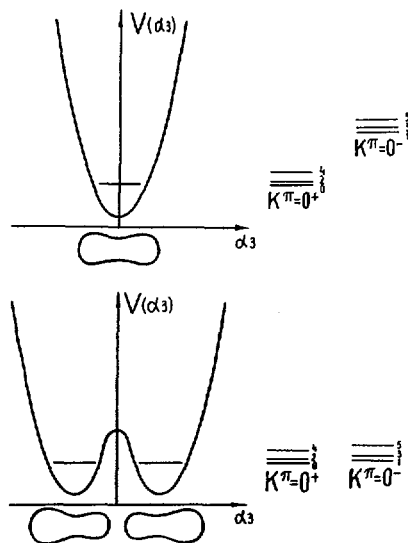


Рис. 5. Схематическое расположение полос положительной и отрицательной четностей у зеркально симметричного (верхняя часть рисунка) и асимметричного (нижняя часть рисунка) ядер.

Объяснение аномалии угловой анизотропии фотоделения четно-четных ядер в рамках модели двугорбого барьера состоит в следующем [6, 15]. С точки зрения факторов, формирующих угловые распределения осколков, новое в модели двугорбого барьера заключается в существовании не одной, как прежде, а двух систем каналов деления  $E_{fA}^\lambda$  и  $E_{fB}^\lambda$ , соответствующих двум горбам (седловым точкам), между которыми в минимуме ядро может жить достаточно долго. Если это время достаточно велико в сравнении с периодом миграции величины  $K$ , то ядро будет фактически "забывать", по какому из дипольных каналов,  $(1^-, 0)$  или  $(1^-, 1)$ , оно прошло через внутренний барьер A, и угловая анизотропия разлета осколков будет определяться спектром каналов на внешнем барьере B. Поскольку порог, наблюдаемый в сечении, определяется высотой наибольшего из горбов, ожидаемая картина будет зависеть от соотношения между их величинами. Если порогом является горб B ( $E_{fB} > E_{fA}$ ), то ситуация будет близкой к той, которая ожидается в модели одногорбого барьера, и она реализуется в случае  $^{232}\text{Th}(y, f)$ . У изотопов плутония, в частности  $^{240}\text{Pu}$ , выше горб A, вследствие чего канальные эффекты в угловой анизотропии из-за механизма "забывания" (смешивания) K смещаются в подбарьерную по сечению деления область энергии, в соответствии с высотой горба B. На этом этапе работ по фотоделению, по-видимому, впервые удалось получить прямое экспериментальное подтверждение одного из наиболее важных предсказаний модели двугорбого барьера — зависимости высот горбов A и B от Z делящегося ядра [16, 17].

#### 4. КВАДРУПОЛЬНОЕ ФОТОДЕЛЕНИЕ И СИММЕТРИЯ ДЕЛЯЩЕГОСЯ ЯДРА

Возвратимся к квадрупольному фотоделению с тем, чтобы обсудить долгое время остававшуюся загадочной сильную  $Z$ -зависимость вклада квадрупольной компоненты  $W(\theta)$ , которая хорошо видна на рис.1. Почему она разыгрывается в узком интервале ядер Th-Pu, однотипных по нуклонному составу и мало отличающихся свойствами равновесных состояний? Так, у четно-четных изотопов плутония (рис.1 и 4) квадрупольная компонента уже отчетливо видна вблизи наблюдаемого порога и ее поведение соответствует расстоянию между каналами  $1^-$  и  $2^+$ ,  $K = 0$ , составляющему, как у обычных ядер, несколько сотен кэв, тогда как у  $^{232}\text{Th}$  вклад ее еще заметен в широкой области подбарьерных энергий возбуждения. Почему механизм подбарьерного "усилений" квадрупольной компоненты, предсказанный Гриффином [8] на основе гипотезы О.Бора, получил подтверждение в реакциях ( $\gamma, f$ ) на всех изотопах урана и плутония, но не "работает" в случае  $^{232}\text{Th}$ ?

Разумного ответа эти вопросы не находили, пока не были развиты представления о двугорбой структуре барьера и получено теоретическое предсказание, что его второй седловой точке (барьеру В) соответствует энергетически более выгодная грушевидная конфигурация ядра [18]. Последнее обстоятельство влечет за собой изменение спектра именно тех каналов деления, которые ответственны за отношение с/б. У ядра, не обладающего симметрией отражения, расстояние между уровнями  $K^\pi = 0^+$  и  $0^-$  быстро уменьшается с высотой барьера для инверсионных переходов между зеркально противоположными конфигурациями, как схематически показано в нижней части рис.5. Роль двугорбой структуры в формировании обсуждаемого свойства состоит в том, что в области горба А ядро сохраняет зеркальную симметрию, т.е. имеет нормальное расщепление полос  $K^\pi = 0^+$  и  $0^-$  (рис.5, верхняя часть), вследствие чего наблюдаемая картина околовороговых канальных эффектов будет сильно зависеть от того, какой из горбов выше. У изотопов плутония первый горб А выше, он определяет порог, наблюдаемый в сечении, и благодаря значительной разнице  $E_{fA}^{10} - E_{fA}^{20} > \hbar\omega/2\pi$  "нормальную" энергетическую зависимость отношения с/б. В случае  $^{232}\text{Th}$  ответственным за порог, наблюдаемый в сечении деления, является второй горб В, при прохождении которого утрачивается зеркальная симметрия ядра, а с ней — расщепление  $E_{fB}^{10} - E_{fB}^{20}$  и связанный с ним механизм подбарьерного "усилений" квадрупольной компоненты.

Рассмотренная интерпретация, основные идеи которой принадлежат Ванденбушу [19], непринужденно объясняет долго ставившую в тупик зависимость вклада квадрупольной компоненты от  $Z$  делящегося ядра, объединяя в одной непротиворечивой картине все основные аспекты структуры барьера: двугорбую форму, дискретную структуру спектра каналов, асимметрию ядра на разных стадиях деления ядра. Однако в рамках данной интерпретации оставался вопрос, почему в случае  $^{232}\text{Th}$  не виден эффект, обусловленный вступлением дискретных каналов  $K^\pi = 0^-$  и, затем,  $K^\pi = 0^+$  барьера А при уменьшении энергии  $\gamma$ -квантов? Тривиальный ответ: "не достигнута в измерениях высота барьера  $E_{fA}$ ", — находился в противоречии

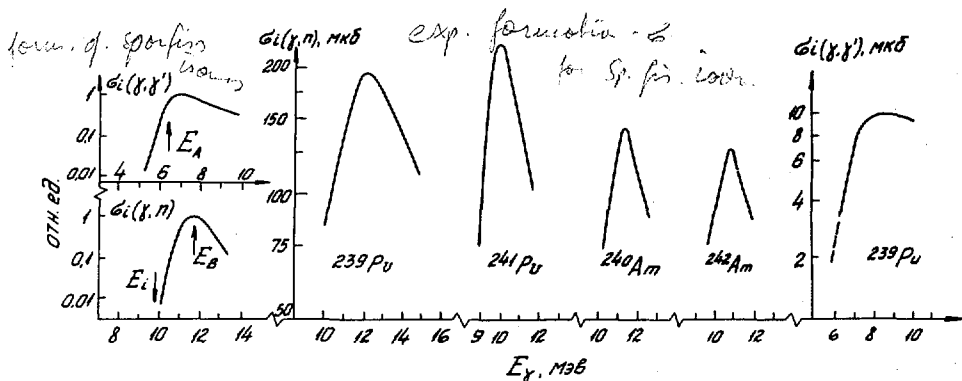


Рис. 6. В левой части рисунка: результаты расчета сечения образования спонтанно делящихся изомеров в реакциях  $(\gamma, \gamma')$  и  $(\gamma, n)$ ; стрелками указаны характерные точки на кривых. В правой части рисунка: экспериментально измеренные сечения образования спонтанно делящихся изомеров  $\text{Pu}$  и  $\text{Am}$  в реакциях  $(\gamma, \gamma')$  и  $(\gamma, n)$  [29]. Ошибки в сечениях всюду составляют  $\sim 30\%$ .

Этот факт также

с результатами анализа других реакций для  $^{232}\text{Th}$  и соседних с ним изотопов, которые приводили к величинам  $E_{fA} \sim E_{fB} = 6.6,5 \text{ МэВ}$  [20]. Между тем, именно он, по-видимому, является правильным.

Трудности определения высоты меньшего из горбов у тяжелых ( $E_{fA} > E_{fB}$ ) и легких ( $E_{fA} < E_{fB}$ ) актинидов неравнозначны. В последнем случае эта задача немного труднее. Во-первых, горб А значительно тоньше, примерно в два раза. Это практически исключает возможность наблюдения эффекта вступления барьера А по изменению наклона проницаемости. Во-вторых, нет таких надежно идентифицируемых способов распада в первую яму, какими явились спонтанно делящиеся изомеры при определении  $E_{fB}$ . Наконец, в-третьих, в связи с предсказанием дополнительной структуры барьера В, приводящей к трехгорбой потенциальной кривой, становится неопределенным анализ резонансов сечения, поскольку при наличии третьего минимума нелегко решить, к какому из них они относятся. Тем не менее, именно это обстоятельство явилось одним из аргументов, которые позволили понять, что прежний анализ подбарьерных резонансов, и связанные с ним значения  $E_{fA}$ , недостоверны [20, 21]. Таким образом, экспериментальной информации о барье-ре А ториевых ядер фактически нет, существуют лишь результаты теоретических расчетов, которые систематически показывают, что  $E_{fA} < E_{fB}$  и составляет менее 5 МэВ [20]. Значительная разница в спектре нижайших каналов  $K = 0$  для барь-ров А и В может явиться как раз тем свойством, используя которое, наконец, удастся с помощью реакции  $(\gamma, f)$  определить высоту барьера А и в этом случае. Недавно [22] у  $^{232}\text{Th}$  было наблюдано, хотя и меньшее в сравнении с более тяже-лыми четно-четными ядрами, но вполне заметное, возрастание квадрупольной ком-поненты (см рис.6), которое можно трактовать, как "включение в игру" барьера А.

Однако оценка  $E_{fA}^{10}$  и  $E_{fB}^{20}$  из хода с/б препятствует сильная резонансная структура проницаемости обоих каналов. Для этой цели требуются экспериментальные данные об угловых распределениях осколков при еще более низких энергиях  $\gamma$ -квантов  $E_{max} < 5$  МэВ.

Итак, установление закономерности  $Z$ -зависимости квадрупольной компоненты  $W(\theta)$ , поиск которой производился в соответствии с конкретным предсказанием О.Бора о подобии спектров нижайших возбужденных состояний ядер равновесной формы и в седловой точке, привело в конечном счете к обнаружению исключения из этого правила. Оно связано с нарушением одного из исходных предположений модели — симметрии инверсии делящегося ядра, свойством неожиданным, но не только не опровергающим, а подтверждающим общую концепцию о каналах деления четно-четных ядер. Более того, поскольку это уточнение касается только каналов деления одного из горбов барьера — внешнего В, для внутреннего А, обладающего зеркальной симметрией, как и для всего барьера в целом, конкретное предсказание О.Бора (в оригинале) остается в силе. Остается в силе и общее указание о том, что увеличение отношения должно происходить в подбарьерной, по отношению к наблюдаемому в полном сечении деления порогу, области. Уточняется лишь то, что этот эффект связан с энергетическим расщеплением  $E_f^{10} - E_f^{20}$  в спектре каналов только одного из барьеров — барьера А.

## 5. ДЕЛИМОСТЬ ЯДЕР В РЕАКЦИЯХ $(\gamma, f)$ и $(t, pf)$

Для изучения свойств каналов деления значительный интерес представляет сравнение характеристик фотоделения и прямых реакций — двух способов возбуждения, наиболее широко используемых при изучении низкоэнергетического деления тяжелых ядер. Существенное их отличие состоит в том, что, если при делении вблизи порога после прямой реакции вследствие достаточно широкого распределения передаваемых орбитальных угловых моментов  $\ell$  доступны целые полосы каналов (для четно-четных ядер это  $K'' = 0^+$  и  $0^-$ ), то при фотоделении — только по одному из них  $J'' = 2^+$  и  $1^-$ . Для такого сравнения более всего подходит реакция  $(t, pf)$ , в которой, как и при фотоделении в случае четно-четного ядра,  $J = \ell$  и  $\pi = (-1)^\ell$ . Делимость такого ядра  $\gamma$ -кантами можно представить как

$$P_f^{(\gamma, f)} = \frac{\sigma_\gamma^{E1} P_f^- + \sigma_\gamma^{E2} P_f^+}{\sigma_\gamma^{E1} + \sigma_\gamma^{E2}} \simeq P_f^- + \frac{\sigma_\gamma^{E2}}{\sigma_\gamma^{E1}} P_f^+ \quad (5)$$

где  $P_f^\pm$  — делимости ядер при делении через состояния  $J'' = 2^+$  и  $J'' = 1^-$ , вблизи порога, осуществляющимся, главным образом, через каналы нижайших полос  $K'' = 0^+$  и  $0^-$ . В той же области энергий деление в  $(t, pf)$ -реакции происходит пре-

имущественно через каналы, принадлежащие тем же полосам  $0^+$  и  $0^-$ , причем, если разницей в делимости для состояний в пределах одной полосы можно пренебречь, то

$$P_f^{(t, pf)} \simeq \frac{\alpha^+}{\alpha} P_f^+ + \frac{\alpha^-}{\alpha} P_f^- \simeq \frac{P_f^+ + P_f^-}{2} \quad (6)$$

где  $\alpha^+ = \sum_{J, \pi=+1} a_{J\pi}$ ,  $\alpha^- = \sum_{J, \pi=-1} a_{J\pi}$ , а последнее приближение в (6) соответствует

предположению об одинаковых вероятностях заселения состояний составного ядра положительной и отрицательной четности  $\alpha^-$  и  $\alpha^+$ .

При энергиях выше барьера с характеристикой  $K'' = 0^-$   $P_f^+ \simeq P_f^- \approx P_f^{(t, pf)}$ , а в фотodelении, вследствие  $\sigma_\gamma^{E2} \ll \sigma_\gamma^{E1}$ ,  $P_f^{(\gamma, f)} \approx P_f^- = P_f^{(t, pf)}$ . Это объясняет отсутствие существенных расхождений экспериментальных данных о делимости при разных способах возбуждения реакции деления ядер вблизи порога, что отмечалось еще в [23]. Однако, ситуация должна измениться достаточно глубоко под барьером, когда благодаря разнице высот барьеров с характеристиками  $K'' = 0^+$  и  $K'' = 0^-$  заметно возрастет отношение  $P_f^+ / P_f^-$ . Тенденцию легко увидеть, рассмотрев предельный случай, соответствующий такому сильному неравенству  $P_f^- \ll P_f^+$ , чтобы можно было пренебречь  $P_f^-$  в сравнении с  $P_f^+ \cdot \sigma_\gamma^{E2} / \sigma_\gamma^{E1}$ . Из (5) и (6) следует, что тогда

$$P_f^{(t, pf)} / P_f^{(\gamma, f)} \simeq \sigma_\gamma^{E1} / \sigma_\gamma^{E2} \gg 1 \quad (7)$$

т.е. делимость в  $(t, pf)$ -реакции может превосходить фотоделимость примерно на порядок. В общем случае должна быть корреляция с вкладом квадрупольного фотodelения.

Для ряда ядер на рис.4, взятом из [24], приведены (нижняя часть рисунка) данные об относительном вкладе квадрупольной компоненты в полный выход

$$\frac{Y_c}{Y} = \frac{\frac{8}{15} c}{a + \frac{2}{3} b + \frac{8}{15} c}$$

в верхней части рисунка приведены данные о самом выходе, который сравнивается с аналогичной величиной, полученной из наблюдаемой делимости [25] интегрированием по тормозному спектру сечения, равного  $\sigma_\gamma^{E1}(E) \cdot P_f^{(t, pf)}$ . Данные о выходах как четно-четных ядер над порогом, так и нечетных во всей перекрывающейся области энергий совпадают, в связи с чем отметим, что никакой нормировкой "сконструированного" выхода к измеренному выходу  $(\gamma, f)$ -реакции не производилось. В случае нечетных ядер набор каналов, участвующих в делении, в обоих реакциях, по-видимому, достаточно велик, чтобы существенно не сказывалась разница в ширине распределения  $\ell$ . Однако, для четно-четных ядер в подбарьерной области энергий везде, где значителен вклад  $Y_c$  в  $Y$ ,  $Y_{t,p}$  отклоняется от  $Y$ , как того требует соотношение (7). Особенно

эффектно сопоставление крайних случаев:  $^{240}\text{Pu}$ , у которого вклад  $Y_c$  в  $Y$ , и отступления  $Y_{t,p}$  от  $Y$  заметны уже вблизи порога ( $\sim 6$  МэВ) и быстро возрастают с уменьшением энергии, и  $^{232}\text{Th}$ , где небольшой эффект намечается лишь глубоко под порогом — вблизи границ чувствительности методик измерения  $P_f^{(t,pf)}$  и  $W(\theta)$  в реакции  $(\gamma, f)$ .

Результаты этого анализа важны в двух отношениях. Во-первых, они свидетельствуют о хорошей взаимосогласованности разнородных экспериментальных данных и соответствия всей использованной информации единым представлениям о спектре каналов деления четно-четных тяжелых ядер, рассмотренным раньше. Во-вторых, удовлетворительное количественное согласие делимостей  $P_f^{(\gamma,f)}$  и  $P_f^{(t,pf)}$  в околовороговой области в случае четно-четных ядер, позволяет, основываясь на (5) и (6), заключить, что каналам одной полосы  $K''$  свойственна примерно одинаковая делимость (по-видимому, с точностью до зависимости  $E_f$  от  $J$ ). Это следствие можно рассматривать как экспериментальное подтверждение идей модели каналов не только в применении к состояниям из разных полос с большой разницей в барьерах  $E_f^\lambda$ , но и к "не-разрешенным" каналам одной полосы.

Завершая обсуждение вопросов, связанных с квантовой структурой барьера, в исследовании которых реакции  $(\gamma, f)$  принадлежит значительная роль, обратимся еще раз к самой концепции каналов деления. Хотя последовательного теоретического обоснования модель каналов деления не имеет, в основе ее лежат самые общие соображения о квантовой природе спектра энергии системы, находящейся в холодном состоянии. Специфика каналов деления состоит в том, что это уровни не в потенциальной яме, а в седловой точке, где потенциальная энергия как функция основного параметра деформации, ведущего к делению, имеет не минимум, а максимум. Представления о каналах деления, правда, без такой конкретизации их спектра, как у О.Бора, были введены еще в 1939 г. Н.Бором и Уиллером [26] при рассмотрении вероятности деления по аналогии с описанием явлений, связанных с диссоциацией молекул (квазимолекулярная модель деления). При решении этой задачи используется так называемый статистический метод переходного состояния, для которого, как подчеркивают Мотт и Месси [27], предположения о квазистационарности переходных состояний не требуется. Из трех квантовых характеристик  $J$ ,  $\pi$  и  $K$ , характеризующих по О.Бору каналы деления, первые две подчинены законам сохранения, а последняя в период эволюции составного ядра может много раз изменить значение, но в то же время быть больше, чем время прохождения через седловую точку. Вероятность преодоления барьера при фиксированном значении  $K$  определяется спектром  $E_f^{J''K}$ . Никаких иных предположений о каналах основанное на гипотезе О.Бора описание вероятности деления не использует.

## 6. ИССЛЕДОВАНИЕ СПОНТАННО ДЕЛЯЩИХСЯ ИЗОМЕРОВ ИЗОТОПОВ Ru и Am С ПОМОЩЬЮ ФОТОЯДЕРНЫХ РЕАКЦИЙ

Обнаружение в Дубне в 1962 году спонтанно делающихся изомеров [28] явилось одним из основополагающих экспериментальных фактов при создании Струтинским мо-

дели двугорбого барьера деления, и именно в ней они нашли свое естественное объяснение как квазистационарные состояния во второй яме. Сейчас накоплен большой экспериментальный материал об энергиях возбуждения, периодах полураспада и других свойствах примерно 40 обнаруженных в области U-Cm изомерных состояниях. Какое место занимают в этих исследованиях  $\gamma$ -лучи?

Развитие исследований спонтанно делящихся изомеров шло от изучения реакций с тяжелыми ионами к реакциям с более легкими частицами. Эксперименты показали, что с уменьшением массы и заряда бомбардирующих частиц возрастает сечение образования ядра в изомерном состоянии. Это объясняется сокращением числа каналов конкурирующих реакций. В этом отношении в фотоядерных реакциях сводится к минимуму число промежуточных ступеней процесса, ведущего к заселению изомерного уровня, так как отсутствие кулоновского барьера и энергии связи для  $\gamma$ -квантов дает возможность получать составные ядра с низкой энергией возбуждения сразу после поглощения излучения. Еще одно неоспоримое преимущество использования  $\gamma$ -квантов — малый вносимый угловой момент по сравнению с реакциями на заряженных частицах.

В экспериментах [29, 30] исследовались спонтанно делящиеся изомеры Ru и Am, образующиеся в результате фотоядерных реакций  $(\gamma, \gamma')$ ,  $(\gamma, n)$  и  $(\gamma, 2n)$ . Реакции образования изомеров получают физически наглядное, но несколько упрощенное описание в модели, рассматривающей возбуждение ядра в первой и второй ямах, заселение изомера (задержанное деление) и конкурирующее с ним мгновенное деление как двухстадийный процесс, в которой сечение фотodelения имеет вид

$$\sigma_f = \sigma_\gamma \frac{T_A}{T_A + T_{\gamma 1}} \left( \frac{T_B}{T_A + T_B + T_{\gamma 2}} + \frac{k T_{\gamma 2}}{T_A + T_B + T_{\gamma 2}} \right) \quad (8)$$

где  $\sigma_\gamma$  — сечение образования составного ядра,  $T_A$ ,  $T_B$  — проницаемости внутреннего и внешнего барьеров;  $T_{\gamma 1}$ ,  $T_{\gamma 2}$  — вероятности  $\gamma$ -распада в первой и второй потенциальных ямах,  $k$  — коэффициент ветвления распада из изомерного состояния. Первый член в скобках описывает мгновенное, а второй — задержанное деление. Сечение образования изомера должно вначале расти, пока энергия возбуждения не превысит барьер деления, а затем падать, повторяя, по крайней мере, качественно, сечение соответствующей парциальной реакции, приводящей к образованию изомера.

Исходя из формулы (8) можно рассчитать зависимости от энергии возбуждения сечений реакции образования изомеров в реакциях  $(\gamma, \gamma')$  и  $(\gamma, n)$ . Эти зависимости представлены на рис. 6. Для нас интересны характерные точки в сечениях образования изомеров.

**Реакция  $(\gamma, \gamma')$ .** Если барьер A выше барьера B (именно эта ситуация характерна для ядер Ru и Am), то по мере снижения под барьер A мы будем наблюдать резкое уменьшение сечения образования изомера, так как радиационная ширина, как и соответствующая ей проницаемость  $T_{\gamma 2}$ , слабо зависит от энергии. Таким образом, мы получаем величину  $E_{fA}$  для  $^{239}\text{Pu}$  и  $^{243}\text{Am}$ . Оценка высоты барьера B получается из изомерного отношения и известной плотности уровней во второй яме.

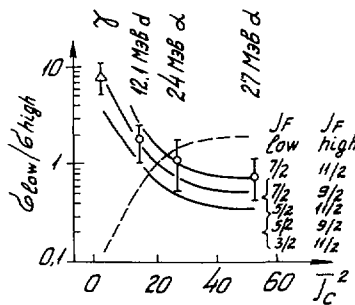


Рис. 7. Относительные вероятности заселения двух изомеров  $^{237}\text{Ru}$  в зависимости от вносимого момента  $J$  [30]. Сплошные линии – результаты расчетов, штрихпунктирные линии – ход зависимости при обратном сочетании спинов  $5/2, 11/2$ .

**Реакция ( $\gamma, n$ ).** Максимум функции возбуждения – это энергия, при которой равны делительная и радиационная ширины во второй яме. Реальная высота барьера больше этой эффективной на 0,7-0,8 МэВ. Энергия второго минимума (точнее энергия изомерного состояния) определяется не столь однозначно, так как пороги реакций определяются путем экстраполяции функций возбуждения к нулевому значению сечений. Естественно, что, как и в реакциях с заряженными частицами, значение порога зависит от выбора модели, определяющей зависимость сечения от энергии, и возникающая при этом неопределенность в величине  $E_{\text{Д}}$  составляет 0,3-0,5 МэВ.

Экспериментальные результаты по изучению спонтанно делящихся изомеров Ru и Am представлены на рис. 6. Согласно указанным характерным точкам можно получить параметры барьеров исследуемых ядер. Нам хотелось бы отметить здесь два факта: во-первых, экспериментальное подтверждение максимума в сечении возбуждения изомеров в реакции ( $\gamma, n$ ), обусловленное конкуренцией мгновенного и задержанного делений, и, во-вторых, возбуждение изомеров в реакции неупругого рассеяния  $\gamma$ -квантов, т.е. в максимально простой ядерной реакции. Изомерные отношения  $\sigma_i/\sigma_f$  составляют по порядку величины при низких энергиях  $10^{-3}$ . При высоких энергиях это отношение намного меньше, так как парциальное сечение реакции, приводящее к образованию изомера, в этой области мало. При измерениях на тормозном пучке эти отношения в выходах оказываются еще меньшими за счет малой доли  $\gamma$ -квантов, участвующих в реакции. Изомерные отношения, полученные в этих экспериментах с  $\gamma$ -лучами, практически такие же, как и в реакциях с заряженными частицами [31]. Эти результаты свидетельствуют в пользу объяснения спонтанно делящихся изомеров как изомеров формы, так как вероятность заселения высокоспиновых состояний в реакциях с  $\gamma$ -квантами сильно подавлена по сравнению с реакциями с заряженными частицами.

Недавно группой немецких физиков исследовалось образование изомеров  $^{237}\text{Ru}$  в реакции ( $\gamma, 2n$ ) при энергии электронов 45 МэВ [30]. Как известно, у этого изотопа

Ри наблюдалось два изомерных уровня с временами жизни 100 нс и 1,1 мкс, причем более короткоживущим оказался изомерный уровень с энергией, меньшей примерно на 0,3 МэВ. Второй уровень рассматривается как одиночестичное возбуждение неспаренного нейтрона. Естественно желание найти соответствующую ему нильсоновскую орбиту, но для этого надо знать J и K этого уровня. В силу малости вносимого углового момента, эксперименты с  $\gamma$ -лучами должны приводить к более определенным выводам, чем в реакциях с заряженными частицами типа ( $\alpha$ , xn) или (d, xn). Это обстоятельство хорошо видно на рис. 7.

Согласно результатам этой работы изомерное отношение  $Y_i/Y_f \approx (6,4 \pm 1,7) \cdot 10^{-6}$  и  $(0,83 \pm 0,22) \cdot 10^{-6}$ , соответственно для короткоживущего и длинноживущего изомера; отсюда извлечены данные о спинах: 5/2 и 11/2 и даже сделана попытка определить соответствующие им нильсоновские орбиты — по мнению авторов, это  $[615]_{11/2^+}$  и  $[862]_{5/2^+}$ . Изомерный уровень с большим спином имеет более высокий барьер B, и этим объясняется значительно (~100 раз) большее его время жизни, чем низколежащего.

## 7. ГЛУБОКО ПОДБАРЬЕРНОЕ ФОТОДЕЛЕНИЕ – КАЧЕСТВЕННО НОВАЯ ОБЛАСТЬ ИССЛЕДОВАНИЙ

Большинство работ по низкоэнергетичному делению ядер проводится в области энергий возбуждений, отстоящих примерно на 1 МэВ от барьера, в которой мы имеем дело со средними величинами, т.е. усредненными в пределах энергетического разрешения эксперимента, а также в пределах ширины уровней (в зависимости от их соотношения со средним расстоянием между уровнями). На процесс деления тяжелых ядер большое влияние оказывает взаимодействие двух систем уровней в первой и второй ямах. Закономерности этого взаимодействия, определяемые природой уровней (компаунд-состояния и вибрационные уровни) и структурой самого барьера, существенно изменяются при продвижении вглубь в подбарьерную область энергий.

Качественно проследить изменение соотношений для средних ширин и расстояний между уровнями можно на рис.8, где схематически показано несколько характерных ситуаций. Если в надбарьерной области I уровни составного ядра в обеих ямах перекрыты, то с уменьшением энергии мы сначала попадаем в промежуточную область II, где  $D_I < \Gamma_D < D_{II}$ , и, наконец, приходим к случаю III неперекрывающихся уровней  $\Gamma_D < D_I$ . Картина изменяется достаточно быстро вследствие экспоненциальной зависимости плотности уровней. Принципиальную роль в процессе деления играют вибрационные состояния во второй яме, сила которых вначале равномерно распределена по всем компаунд-состояниям (полное затухание). В этой ситуации применимо то статистическое описание, в рамках которого мы рассматривали обсуждавшиеся выше вопросы. Под барьером, вследствие уменьшения ширины, вибрационные уровни отчетливо проявляются как резонансы делимости, а при достаточном энергетическом разрешении распадаются на компаунд-состояния во второй яме, играя для

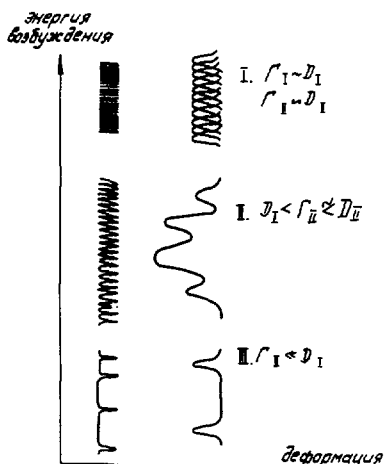


Рис. 8. Схематическое соотношение между ширинами и расстояниями между уровнями в первой и во второй ямах при разных энергиях возбуждения.

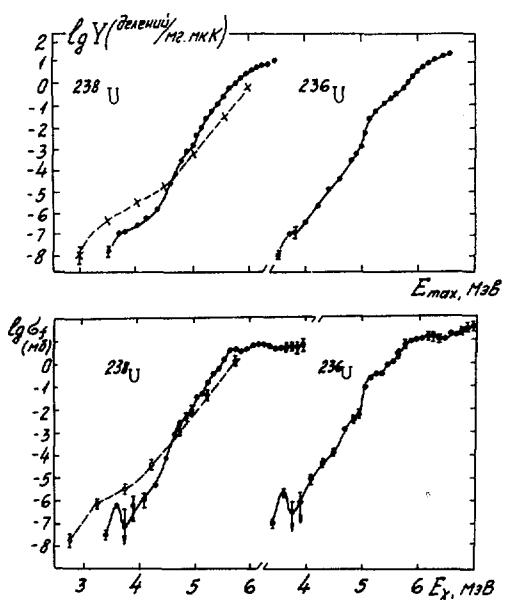


Рис. 9. В верхней части рисунка: выход реакции  $(\gamma, f)$  для ядер  $^{236}, ^{238}\text{U}$ . В нижней части рисунка: сечение реакции  $(\gamma, f)$  для изотопов урана. ● — [36-38], ○, X — [35].

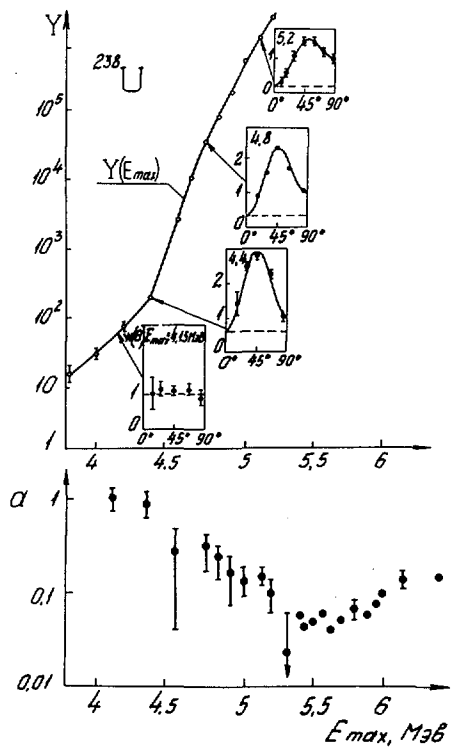


Рис. 10. В верхней части рисунка: изменение характера углового распределения осколков по мере уменьшения энергии возбуждения [41]. В нижней части рисунка: энергетическая зависимость изотропной составляющей  $W(\theta)$  у  $^{238}U$  [37].

них роль огибающей, например, как в хорошо известном случае  $^{240}\text{Pu}$  [32]. В области неперекрывающихся уровнейи вибрационные уровни могут наблюдаться как сильные изолированные резонансы. Начало развитию теоретического описания деления в глубоко подбарьерной области энергий, где обычный статистический подход неприемлем, было положено в рамках теории возмущения Линном [33], а затем Линном и Баком [34].

Экспериментальные исследования процесса фотоделения при энергиях, меньших 5 МэВ, позволили обнаружить три принципиально новых эффекта:

- 1) замедление экспоненциального спада выхода  $(\gamma, f)$ -реакции при  $E_{max} \sim 4,5$  МэВ [35, 36],
- 2) аномальное поведение анизотропии разлета осколков в этой же области [37],
- 3) появление сильных резонансов при  $E_\gamma \simeq 3,6$  МэВ, т.е. при энергии, на 1-1,5 МэВ выше дна второй ямы [37, 38].

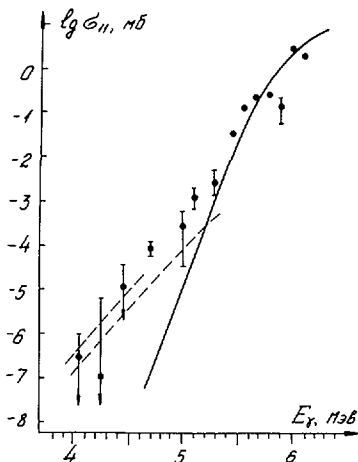


Рис. 11. Изотропная компонента сечения фотоделения  $^{238}U$ , полученная на основе измерения выходов и угловых распределений осколков. Сплошная кривая – расчет сечения через канал  $(1^-, 1)$  в модели с полным затуханием [34] с параметрами, описывающими компоненты  $(2^+, 0)$  и  $(1^-, 0)$ . Пунктирная кривая – расчет вклада задержанного деления (изомерного шельфа) для различных каналов деления [42].

На первый из перечисленных эффектов, являющийся следствием конкуренции прямого и задержанного делений, впервые обратил внимание Бауман [39]. Экспериментально, действительно, в 1975 г. в работах [35, 36] наблюдалось в выходах фотоделения ряда ядер при энергии электронов 4,5 МэВ довольно резкое уменьшение скорости спада, получившее название изомерного шельфа (см. рис.9). Результаты работы [36] были подтверждены в экспериментах итальянских физиков [40].

Качественно появление изомерного шельфа вполне понятно. Для ядер тяжелее тория вероятность разделиться из состояния во второй яме (т.е. уже обладающих деформацией, соответствующей второму минимуму) определяется конкуренцией радиационной и делительной ширин. По мере уменьшения энергии возбуждения может наступить ситуация, когда радиационная ширина станет сравнима или даже больше делительной, и в этом случае ядро будет переходить в основное состояние во второй яме преимущественно путем радиационных переходов, а не мгновенно делиться (с этим же эффектом и было связано появление максимума в сечении образования спонтанно делящихся изомеров в реакции  $(\gamma, n)$ ). Если запрет для переходов обратно в первую яму достаточно велик, то в дальнейшем ядро будет испытывать деление из этого изомерного состояния с периодом, соответствующим проницаемости через барьер В. Если отбор актов деления по времени в эксперименте не происходит, то мы будем наблюдать в сечении проницаемость лишь первого барьера, что и приводит к появлению изомерного шельфа.

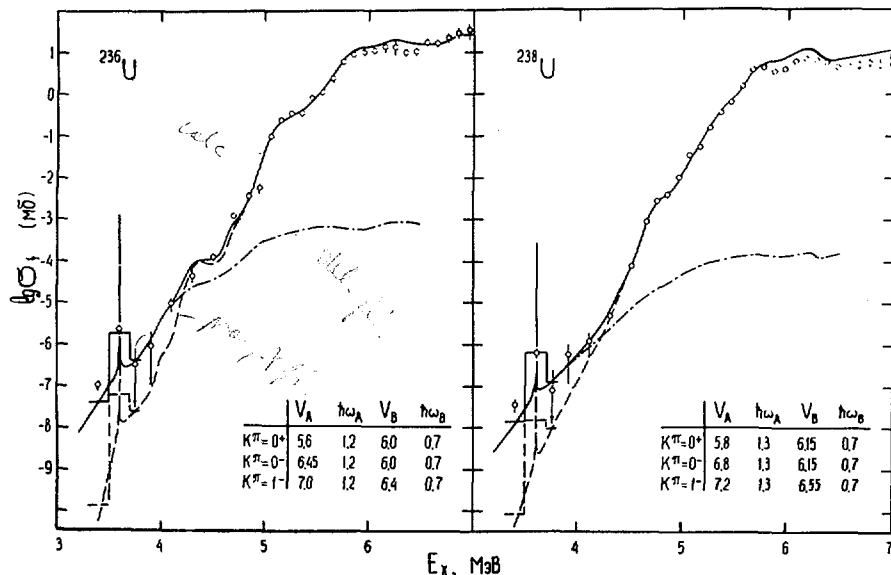


Рис. 12. Сечения реакции  $(\gamma, f)$  для ядер  $^{236}\text{U}$  и  $^{238}\text{U}$  [38]. Сплошные кривые – расчет по методу входных состояний; пунктирные кривые – сечение мгновенного деления, штрихпунктирные кривые – сечение задержанного деления. Гистограммами показаны результаты усреднения кривых по интервалам, соответствующим шагу в измерениях выходов.

Обнаружение нерегулярности в ходе интегральных выходов фотоделения еще не доказывает, что в области изомерного шельфа деление ядер является задержанным.

В случае четно-четных ядер квантовые характеристики нижайшего состояния во второй яме –  $(0^+, 0)$ , и поэтому угловое распределение осколков при делении из изомерного состояния должно быть полностью изотропным. Экспериментальная проверка этого факта, проведенная для ядра  $^{238}\text{U}$  [41], действительно показала, что в области изомерного шельфа фотоделение изотропно, тем самым подтверждая указанную выше интерпретацию (см. рис. 10).

Изотропия деления через изомерное состояние является той особенностью, по которой можно проследить вклад задержанного деления во всей области подбарьерных энергий. Изотропная компонента углового распределения осколков при фотоделении четно-четных ядер возникает при низких энергиях только за счет деления через канал  $(1^-, 1)$  и ей соответствует коэффициент  $a$  в угловом распределении осколков  $W(\theta)$ . На рис. 10 показана зависимость этого коэффициента  $a = (b/a - 1)^{-1}$  (в нормировке  $a + b = 1$ ) от энергии электронов для ядра  $^{238}\text{U}$  [37].

Как видно из представленных данных, изотропная составляющая углового распределения осколков фотоделения в подпороговой области вначале уменьшается по мере уменьшения энергии, и такое поведение  $a(E_{\max})$  непосредственно определяется

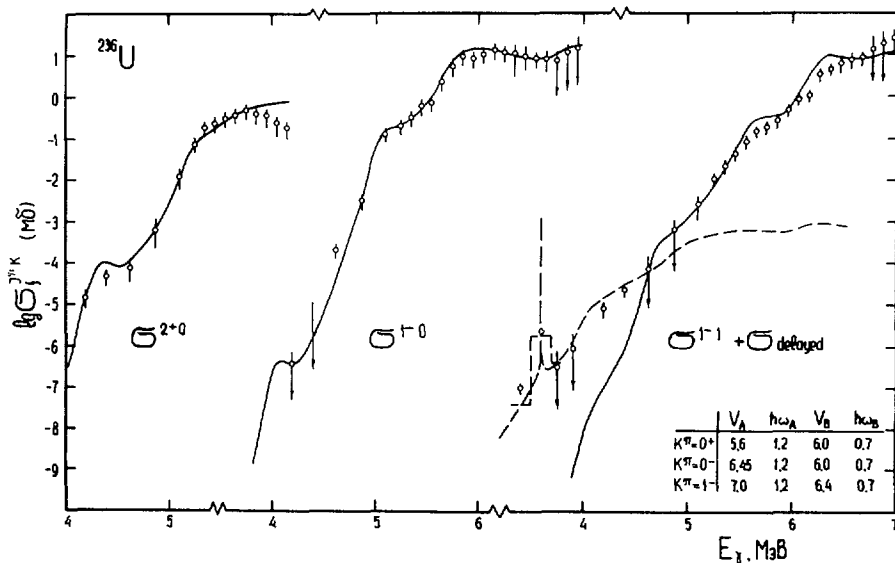


Рис. 13. Угловые компоненты сечения реакции  $(\gamma, f)$  для  $^{236}\text{U}$ . Сплошные кривые – расчет по методу входных состояний сечений мгновенного деления в каналах  $(2, 0)$ ,  $(1^-, 0)$  и  $(1^+, 1)$ ; пунктирная кривая – расчет вклада задержанных делений из этих каналов. Гистограммой показана усредненная кривая задержанного деления.

различием высоты барьеров для каналов дипольного деления с  $K^\pi = 0^-$  и  $1^-$ . При одинаковой кривизне барьеров величина  $\alpha$  должна была бы стремиться к постоянному значению. Однако, вопреки ожидаемой тенденции, обсуждавшейся выше (рис.3), начиная с 5,5 МэВ вклад изотропной компоненты быстро растет, и эта компонента становится доминирующей при  $E_\gamma < 4,5$  МэВ.

Зависимость сечения изотропной компоненты фотodelения для ядра  $^{238}\text{U}$  приведена на рис. 11 [42]. Теоретическая кривая, рассчитанная в предположении полного затухания во второй яме (без учета резонансной структуры) согласно [34] с параметрами, хорошо описывающими компоненты сечения  $(2^+, 0)$  и  $(1^-, 0)$ , показана сплошной линией. Как видно, энергетическая зависимость компоненты  $\sigma_{11}$  при энергиях  $E_\gamma < 5,3$  МэВ резко отклоняется от экспериментальных данных вниз. С этим отступлением, как и с аномальным поведением анизотропии разлета осколков, связано явление, называемое нами [37] "нормальный изомерный шельф" за сходство со свойством, которое обсуждалось Бауманом с соавторами [35]. На этом же рисунке показаны парциальные компоненты сечения задержанного деления, рассчитанные теоретически. Они правильно передают абсолютную величину и наклон нормального шельфа.

Подробное исследование сечения фотodelения  $^{236}\text{U}$  и  $^{238}\text{U}$  в области энергий возбуждения 3,5–4,5 МэВ (рис. 9) привело к еще одному упомянутому вначале эффекту – появлению сильных резонансов при  $E_\gamma \approx 3,6$  МэВ, названному аномальным изо-

мерным шельфом [37]. Аналогичную резонансную структуру имеет и непосредственно измеренное деление в ( $\alpha$ , pf)-реакции на ядре  $^{240}\text{Pu}$  [43] в том же диапазоне энергий. Наблюдающийся резонанс расположен вблизи, если даже не внутри, энергетической щели в спектре возбуждений четно-четных ядер, т.е. мы имеем дело, скорей всего, с одиночным уровнем во второй яме.

Таким образом, в глубоко подбарьерной области возбуждений мы сталкиваемся с целым рядом новых явлений. Принципиальным пунктом в понимании деления ядер в этой области является правильный учет роли вибрационных состояний во второй яме, их ширины и связи со сложными уровнями другой природы. В этом отношении очень интересны появившиеся недавно работы [43-45], в которых развиваются идеи и методы входных состояний (door-way state) применительно к делению.

На рис. 12 и 13 приведены результаты анализа сечения фотоделения  $^{236}\text{U}$  и  $^{238}\text{U}$ , который был выполнен в рамках данного подхода Ю.Б.Остапенко. Рис. 12 показывает вклад в наблюдаемое сечение составляющих, связанных с мгновенным и задержанным делениями. Характерно усиление резонансной структуры (уменьшение затухания вибрационных резонансов) по мере приближения к дну второй ямы. Участок в окрестности сильного и узкого нижайшего резонанса, который проявляется в области, где доминирует задержанное деление, и соответствует чистому вибрационному состоянию, показан гистограммой, шаг в которой есть интервал между экспериментальными точками в полном выходе. Теоретические кривые на рис. 12 представляют сумму парциальных угловых компонент – анизотропных, соответствующих каналам  $(2^+, 0)$  и  $(1^-, 0)$  и изотропной, которая, кроме сечения мгновенного деления через канал  $(1^-, 1)$ , включает в себя вклад задержанного деления из всех каналов. Для ядра  $^{236}\text{U}$  они отдельно показаны на рис. 13. В отличие от реакций ( $\alpha$ , pf), анализировавшихся методом входных состояний в [43, 45], где данные об угловой анизотропии деления привлекались только для оценки вклада отдельных каналов, простота взаимодействия  $\gamma$ -квантов позволяет с помощью непосредственной экспериментальной информации о вкладе всех доминирующих каналов получить практически полное описание интегральных и дифференциальных характеристик вероятности низкоэнергетического деления ядер.

## 8. МАССОВОЕ РАСПРЕДЕЛЕНИЕ ОСКОЛКОВ В ОКОЛОБАРЬЕРНОЙ ОБЛАСТИ

Механизм формирования осколков деления по массам до сих пор остается одним из основных невыясненных вопросов, хотя в этом направлении нет недостатка ни в теоретических, ни в экспериментальных работах. Дело в том, что здесь воедино связывается целый круг нерешенных вопросов, таких, как роль изменения поверхности потенциальной энергии при включении асимметричных деформаций, динамика процесса деления, сам акт раз渲ла ядра, роль структурных особенностей осколков деления и каналов деления.

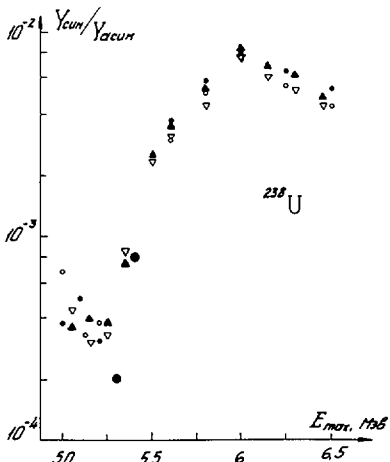


Рис. 14. Энергетическая зависимость отношения выхода симметричных ( $^{115}, ^{117}\text{Cd}$ ) к асимметричным ( $^{139}, ^{140}\text{Ba}$ ) осколкам при фотоделении  $^{238}\text{U}$ . ○, ● — [48]; ▽, ▲ — [49].

Первые работы по массовому распределению осколков при фотоделении  $^{232}\text{Th}$  и  $^{238}\text{U}$  при  $E_{\max} > 5,5$  МэВ были выполнены Даффилдом и Шмиттом в 1957 г. [46], затем аналогичные измерения были проведены Форкманом и Кивикасом [47] в 1965 г. Несмотря на разногласие этих результатов, в них отчетливо был выявлен ряд нерегулярностей в околоспороговом массовом распределении осколков. Нами в 1967 г. совместно с радиохимиками Института атомной энергии им. И. В. Курчатова были проведены измерения выхода осколков  $^{238}\text{U}$  в симметричной и асимметричной частях, вплоть до энергии возбуждения 5 МэВ [48]. Эти измерения были повторены в 1973 г. в Швеции Альмом и Кивикасом [49], которые полностью подтвердили наши измерения. Экспериментально можно сейчас считать установленным три удивительных факта (рис. 14):

- 1) в области  $E_{\max} = 6$  МэВ наблюдается максимум выхода симметричных осколков, которому в сечении соответствует отчетливый резонанс;
- 2) с уменьшением энергии  $\gamma$ -квантов относительный выход симметричного деления резко снижается, уменьшаясь в 30 раз в интервале 5,3-5,8 МэВ так, что отношение выходов осколков в пике и впадине достигает нескольких тысяч;
- 3) при дальнейшем уменьшении энергии  $\gamma$ -квантов отношение выходов симметричных и асимметричных осколков прекращает уменьшаться и выходит на плато.

Прежде чем обсуждать обнаруженные особенности массового распределения, рассмотрим результаты еще одного эксперимента — определения фазы формирования симметричного деления. Как уже подчеркивалось выше, анизотропия разлета осколков деления легких актинидов формируется зависимостью высоты внешнего барьера В от квантовых характеристик. Если внешний барьер для симметричных конфи-

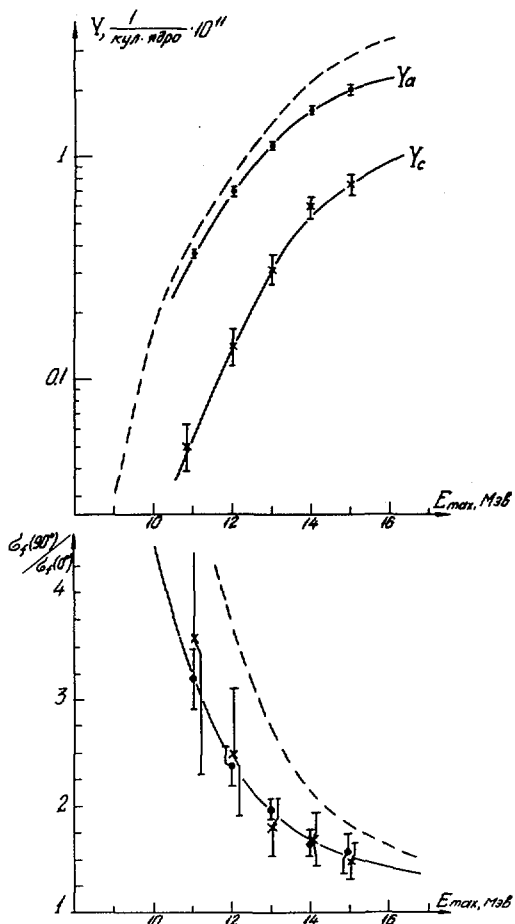


Рис. 15. В верхней части рисунка: зависимость выхода симметричных и асимметричных осколков в реакции  $^{226}\text{Ra}(\gamma, f)$  от граничной энергии тормозного спектра. В нижней части рисунка: анизотропия симметричных ( $\times$ ) и асимметричных ( $\circ$ ) осколков. Пунктирная кривая — кривая анизотропии, смещенная на 1,5 МэВ.

тации делящегося ядра выше, чем для асимметричных ( $E_{\text{fb}}^s > E_{\text{fb}}^a$ ), как показывают теоретические расчеты [20], они определяют соответствующие способы разделения и в этих случаях должны быть разными и угловые анизотропии разлета осколков. И наоборот, если обоим типам деления отвечает единая внешняя седловая конфигурация, а реализующееся распределение масс осколков формируется на спуске с горба В, то угловые анизотропии должны совпадать. Такой эксперимент был проведен на ядре  $^{226}\text{Ra}$  [50].

Результаты этих измерений показаны на рис.15. Приведенный на этом рисунке ход интегральных выходов симметричного  $Y_c$  и асимметричного  $Y_a$  делений в принципе не противоречит предположению о различии высот барьеров симметричного и асимметричного делений  $E_{FB}^s - E_{FB}^a \simeq 1,5$  МэВ. В этом случае при идентичности других характеристик кривая анизотропии симметричного деления должна быть смещена относительно анизотропии разлета асимметричных осколков на те же 1,5 МэВ. Эта смещенная кривая показана на рис.15 пунктиром. Экспериментальные точки тем не менее как для симметричного, так и асимметричного делений практически совпадают, т.е. обеим компонентам соответствует одна и та же седловая точка.

Таким образом, данные об угловой анизотропии свидетельствуют, что реализуется вторая из рассмотренных возможностей: распределение масс формируется при спуске с барьера к точке разрыва, а асимметричная конфигурация ядра в седловой точке, соответствующей барьеру В, лишь облегчает перестройку нуклонов в ядре. С другой стороны, при различных способах возбуждения легких актинидов и Ra [51, 52] выход симметричного деления с уменьшением энергии возбуждения ведет себя так, как если бы ему соответствовал барьер на 1-2 МэВ выше, чем у асимметричного. Казалось бы, что наличие резонанса в отношении выходов симметричного и асимметричного фотodelений  $^{238}\text{U}$  также свидетельствует о различии соответствующих поверхностей потенциальной энергии деформации, что придает им черты независимых способов деления. Объединить в одной непротиворечивой картине свойства распределения масс осколков и угловой анизотропии деления пока не удалось.

## 9. ЗАКЛЮЧЕНИЕ

В этом обзоре мы попытались проанализировать накопленный к настоящему времени экспериментальный материал по низкоэнергетическому фотodelению тяжелых ядер, затрагивая лишь принципиальные вопросы, возникшие и решенные, либо оставшиеся открытыми, на основе современных представлений о двугорбом барьере деления. Эта модель, основанная на результатах расчета потенциального барьера деления по методу оболочечной поправки Струтинского, оказалась весьма плодотворной в физике деления атомных ядер. Объяснив подавляющую совокупность экспериментальных данных, она явилась в то же время и мощным стимулом для постановки новых экспериментальных и теоретических работ.

Эксперименты по фотodelению занимают особое место в исследовании структуры барьера. Благодаря исключительной простоте спектра вносимых в ядро угловых моментов, исследование процесса фотodelения явилось решающим в выяснении достоверности концепции каналов деления. Особую ценность представили  $\gamma$ -кванты и при изучении двугорбой формы барьера. Наблюдаемая Z-зависимость отношений b/a и c/b относится к категории немногих экспериментов, в которых непосредственно и в одном опыте проявляются две разные высоты барьеров А и В. По-видимому, только в фотodelении мы сейчас видим проявление нарушения зеркальной симметрии

ядра на барьере В. Наконец, в экспериментах с  $\gamma$ -лучами впервые началось изучение качественно новой области энергий возбуждения — глубоко подбарьерного деления, в которой удалось продвинуться до энергетической щели в спектре состояний во второй яме. Установлен ряд явлений, связанных с преобладающим при этих энергиях задержанным делением. В ходе его сечения при самых низких достигнутых энергиях обнаружены резонансы, которые соответствуют одному из первых вибрационных состояний во второй яме.

Во многих вопросах простота ядерных реакций с  $\gamma$ -квантами оказалась решающей для выяснения различных аспектов физики деления ядер. В то же время следует отметить, что в вопросе о массовых распределениях осколков фотоделение не дало возможности продвинуться вперед в понимании закономерностей явления и даже выдвинуло ряд новых непонятных его сторон. С точки зрения эксперимента тут прежде всего необходима постановка широкого круга исследований, в том числе и корреляционных, таких, как одновременное измерение массового и углового распределений. Несомненно требуется как увеличение точности экспериментальных данных в области глубоко подбарьерного деления, так и продвижение в область еще более низких энергий, несмотря на всю сложность таких работ.

Авторы глубоко признательны своим коллегам по работе Ю.П.Гангрскому, В.Е.Жучко, А.В.Игнатюку, С.П.Капице, Ю.А.Селицкому, Ю.Б.Остапенко, А.С.Солдатову, многочисленные дискуссии с которыми и их непосредственное участие во многом способствовали успеху обсуждавшихся выше работ по фотоделению.

## ЛИТЕРАТУРА

- [ 1 ] WINHOLD, E.I., DEMOS, P., HALPERN, J., Phys. Rev. 87 (1952) 1139.
- [ 2 ] KATZ, L., BAERG, A.E., BROWN, F., Proc. 2nd Int. Conf. PUAE, Geneva 1958, 15 (1958) 188.
- [ 3 ] BOHR, A., PUAE 2 (1955) 151.
- [ 4 ] SOLDATOV, A.S., SMIRENKIN, G.N., KAPITZA, S.P., TSIPENYUK, Yu.M., Phys. Lett. 14 (1965) 217.
- [ 5 ] РАБОТНОВ, Н.С., СМИРЕНКИН, Г.Н., СОЛДАТОВ, А.С. и др., Proc. Int. Conf. Phys. Chem. Fission, Salzburg, 1 (1965) 217.
- [ 6 ] РАБОТНОВ, Н.С., СМИРЕНКИН, Г.Н., СОЛДАТОВ, А.С. и др., Ядерная физика 11 (1970) 285.
- [ 7 ] ИГНАТЮК, А.В., РАБОТНОВ, Н.С., СМИРЕНКИН, Г.Н. и др., ЖЭТФ 61 (1968) 1284.
- [ 8 ] GRIFFIN, J.J., Phys. Rev. 116 (1959) 107.
- [ 9 ] LINDGREN, L.J., ALM, A., SANDELL, A., Nucl. Phys. A298 (1977) 43.
- [ 10 ] ЖАГРОВ, Е.А., НЕМИЛОВ, Ю.А., СЕЛИЦКИЙ, Ю.А., Ядерная физика 7 (1968) 264.
- [ 11 ] ALM, A., LINDGREN, L.J., Nucl. Phys. A271 (1976) 1.
- [ 12 ] ЖУЧКО, В.Е., ОСТАПЕНКО, Ю.Б., СМИРЕНКИН, Г.Н. и др., Ядерная физика 27 (1978) 1420.
- [ 13 ] RABOTNOV, N.S., SMIRENKIN, G.N., SOLDATOV, A.S., et al., Nucl. Phys. 77 (1966) 92.
- [ 14 ] СОЛДАТОВ, А.С., ЦИПЕНЮК, Ю.М., СМИРЕНКИН, Г.Н., Ядерная физика 11 (1970) 992.
- [ 15 ] RABOTNOV, N.S., SOLDATOV, A.S., SMIRENKIN, G.N., et al., Phys. Lett. 26B (1968) 218.
- [ 16 ] STRUTINSKY, V.M., Nucl. Phys. A95 (1967) 420; A122 (1968) 1.
- [ 17 ] STRUTINSKY, V.M., BJØRNHOLM, S., Nucl. Phys. A136 (1968) 1.

- [18] BRACK, M., DAMGAARD, J., JENSEN, E.S., et al., Rev. Mod. Phys. 44 (1972) 320.
- [19] VANDENBOSCH, R., Phys. Lett. 45B (1973) 207.
- [20] MÖLLER, P., NIX, J.R., Proc. Int. Symp. Phys. Chem. Fission, Rochester, 1 (1974) 103.
- [21] GAVRON, A., BRITT, H.C., WILHELMY, A., Phys. Rev. C13 (1976) 2577.
- [22] ЖУЧКО, В.Е., КАПИЦА, С.П., ОСТАПЕНКО, Ю.Б. и др., Письма в ЖЭТФ 26 (1977) 718.
- [23] HUIZENGA, J.R., BRITT, H.C., Proc. Int. Conf. Photonuclear Reactions, Asilomar (1973).
- [24] ЖУЧКО, В.Е., ОСТАПЕНКО, Ю.Б., СМИРЕНКИН, Г.Н. и др., Ядерная физика 28 (1978) 1170.
- [25] BACK, B.B., HANSEN, O., BRITT, H.C., et al., Proc. Int. Symp. Phys. Chem. Fission, Rochester, 1 (1974) 3; 1 (1974) 25.
- [26] BOHR, N., WHEELER, J.A., Phys. Rev. 56 (1939) 426.
- [27] МОТТ, Н., МЕССИ, Т., Теория Атомных Столкновений, М., Мир, 1969.
- [28] ПОЛИКАНОВ, С.М. и др., ЖЭТФ 42 (1962) 1464.
- [29] GANGRSKY, Yu.P., MARKOV, B.N., TSIPENYUK, Yu.M., Fortschr. Phys. 22 (1974) 199.
- [30] GÜNTNER, W., HUBER, K., KNEISSL, U., et al., Phys. Rev. C19 (1979) 433.
- [31] ФЛЕРОВ, Г.Н., ГАНГРСКИЙ, Ю.П., МАРКОВ, Б.Н. и др., ОИЯИ, Р7-5018, Дубна, 1970.
- [32] GLÄSSEL, P., RÖSSLER, H., SPECHT, H.J., Nucl. Phys. A256 (1976) 220.
- [33] LYNN, J.E., IAEA 2nd Symp. Phys. Chem. Fission, Vienna (1969) 249.
- [34] LYNN, J.E., BACK, B.B., J. Phys. A7 (1974) 39.
- [35] BOWMAN, C.D., SCHRÖDER, T.G., DICK, C.E., JACKSON, H.E., Phys. Rev. C12 (1975) 863.
- [36] ЖУЧКО, В.Е., ИГНАТЮК, А.В., ОСТАПЕНКО, Ю.Б. и др., Письма в ЖЭТФ 22 (1975) 255.
- [37] ZHUCHKO, V.E., IGNATYUK, A.V., SMIRENKO, G.N., et al., Phys. Lett. 68B (1977) 323.
- [38] ЖУЧКО, В.Е., ОСТАПЕНКО, Ю.Б., СМИРЕНКИН, Г.Н. и др., Ядерная физика 28 (1978) 1185.
- [39] BOWMAN, C.D., Bull. Am. Phys. Soc. 18 (1973) 627.
- [40] BELLIA, G., DEL ZOPPO, A., INGRAO, G., et al., Proc. Int. Conf. Nucl. Structure, Tokyo (1977) 753.
- [41] ЖУЧКО, В.Е., ОСТАПЕНКО, Ю.Б., ИГНАТЮК, А.В. и др., Письма в ЖЭТФ 24 (1976) 309.
- [42] ЖУЧКО, В.Е., ЦИПЕНЮК, Ю.М., ИГНАТЮК, А.В. и др., в сб. "Нейтронная физика", М., Атомиздат, 3 (1977) 21.
- [43] GOERLACH, U., HABS, D., JUST, M., et al., Z. Phys. A287 (1978) 171.
- [44] GOLDSTONE, P.D., HOPKINS, F., MALMIN, R.E., PAUL, P., Phys. Rev. C18 (1979) 1706.
- [45] GOLDSTONE, P.D., PAUL, P., Phys. Rev. C18 (1979) 1733.
- [46] SCHMITT, R.A., DUFFIELD, R.B., Phys. Rev. 105 (1957) 1277.
- [47] KIVIKAS, T., FORKMAN, B., Nucl. Phys. 64 (1965) 420.
- [48] КУРЧАТОВ, Б.В., НОВГОРОДЦЕВА, В.И., ПЧЕЛИН, В.А. и др., Ядерная физика 7 (1968) 326.
- [49] ALM, A., KIVIKAS, T., Nucl. Phys. A215 (1973) 461.
- [50] БАЖАНОВ, Е.В., ЖАГРОВ, Е.А., НЕМИЛОВ, Ю.А. и др., Ядерная физика 22 (1975) 36.
- [51] KONECNY, E., SPECHT, H.J., WEBER, J., Phys. Lett. 45B (1973) 329.
- [52] WEBER, J., BRITT, H.C., GAVRON, A., Phys. Rev. C13 (1976) 2413.

## DISCUSSION

H.J. SPECHT: Ever since A. Bohr's original suggestion that the fission channels available at the saddle point determined the fragment angular distributions there has been speculation to what extent  $K$  is really quantitatively conserved during the descent from saddle to scission. Photofission appears to be one of the few relatively 'clean' processes suited to a study of the problem,

both at low and high excitation energies. On the basis of your attempts to fit your impressive data quantitatively, what is your view of the degree of possible non-conservation of K?

Yu.M. TSIPENYUK: Experimentally we find virtually 'clean' Wigner functions beneath the barrier, for example  $D_{\pm 1,0}^1$  for  $^{232}\text{Th}$ , and  $D_{\pm 1,0}^2$  for  $^{242}\text{Pu}$ . The accuracy in the case of D functions is of the order of a few per cent, which in fact indicates the conservation of K. At high excitation energies, conservation of K is more complicated from the standpoint of experimentation, since we find the introduction of new channels with different K, which in turn, in the same way as non-conservation, leads to isotropization of the angular distribution.

S. POLIKANOV: You mentioned briefly the problem of transition states in your presentation. These states were introduced by A. Bohr for cases where the fission barrier in the liquid drop model can be considered rather flat. Nowadays we have to consider the transition states found at the top of both inner and outer narrow fission barriers, corresponding to a highly unstable state of equilibrium. In what sense, therefore, are you using the term transition states at the present time?

Yu.M. TSIPENYUK: The saddle point has always been unstable. As I stressed, a description of fission probability based on Bohr's hypothesis does not require quasi-stationary transition states. This applies as well to the double-humped fission barrier, the only difference being that the shaping of the angular distribution is transposed to the outer barrier.



# SUB-THRESHOLD PHOTOFISSION OF $^{238}\text{U}$ IN THE (3.6–6.0)-MeV ENERGY RANGE

R. ALBA, G. BELLIA, L. CALABRETTA, A. DEL ZOPPO,  
E. MIGNECO, G. RUSSO

Istituto di Fisica dell'Università di Catania,  
Istituto Nazionale de Fisica Nucleare – Sezione Catania,  
Centro Siciliano di Fisica Nucleare e Struttura della Materia,  
Catania, Italy

R.C. BARNA, D. DE PASQUALE  
Istituto di Fisica dell'Università di Messina,  
Istituto Nazionale di Fisica Nucleare,  
Messina, Italy

## Abstract

### SUB-THRESHOLD PHOTOFISSION OF $^{238}\text{U}$ IN THE (3.6–6.0)-MeV ENERGY RANGE.

$^{238}\text{U}$  photofission yield measurements in the 3.6–6.0-MeV range and angular distribution results in the 5.1–6.0-MeV range are presented. A preliminary analysis of the data within the framework of the double-humped barrier model is reported. Fission barrier parameters of the  $2^+0$  channel are obtained. At low energy, the shelf effect is detected in the total photofission yield.

## 1. INTRODUCTION

The ( $\gamma$ ,f) reaction induced by intense bremsstrahlung beams allows the study of the fission process at very low excitation energy and is particularly useful because of its high selectivity in terms of parity and angular momentum. In the particular case of an even-even compound nucleus at low excitation energy, the spin and parity quantum numbers are  $J^\pi = 1^-$  and  $J^\pi = 2^+$ , corresponding to absorption of multipolarities E1 and E2, respectively. In these conditions, an investigation of the properties of deep sub-threshold fission barriers can be made.

In this paper, we present photofission yield measurements of  $^{238}\text{U}$  in the 3.6–6.0-MeV energy range and angular distribution results in the 5.1–6.0-MeV range. As  $\gamma$ -source the bremsstrahlung beam from a microtron has been used. Because of the strong decrease of the photofission cross-section with decreasing energy, two different experimental procedures have been used.

A preliminary analysis of the data provides information on the transition states. Interesting features of the low-energy total photofission yield are discussed.

## 2. EXPERIMENTAL PROCEDURES

The experiments were performed with the 13.5-MeV microtron of Catania University, which has been improved to obtain an average current of 40  $\mu\text{A}$  at 5 MeV [1]. The electron energy was determined with an uncertainty of  $\pm 25$  keV by measuring the magnetic field with an accuracy of 0.1% by means of a Hall effect gaussmeter and using the microtron as a magnetic spectrometer.

The bremsstrahlung converter consisted of a 1-mm-thick tungsten plate and a 10-mm-thick Al electron absorber. The net current on the target was integrated automatically and used for normalization. The position of the electron beam on the converter was defined by a circular copper aperture, with a diameter of 4 mm, placed in front of the bremsstrahlung converter.

The uranium oxide samples consisted of a circular deposit with a diameter of 10 mm, 99.98%  $^{238}\text{U}$ -enriched, on an Al-backing, 25  $\mu\text{m}$  thick; the fission fragments were detected by using makrofol foils as track detectors.

We measured the fission fragment angular distributions and the fission yields in steps of 0.1 MeV from 5.1 MeV to 6.0 MeV. The thickness of the target was

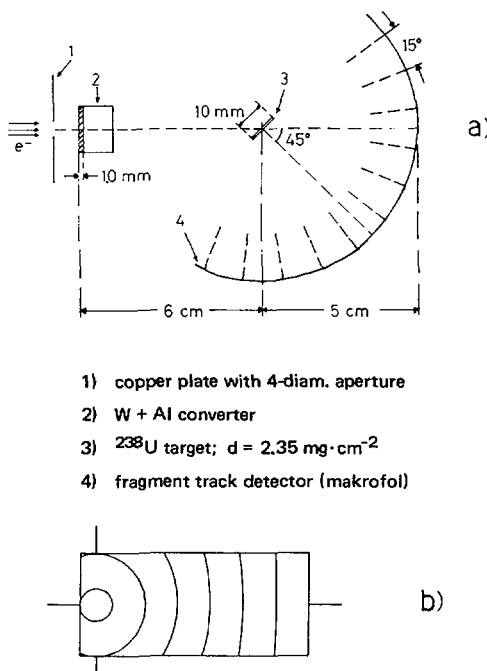


*FIG.1. a) Experimental arrangement for measurement of photofission angular distributions.  
b) Planar view of the angular bins as described in the text.*

2.35 mg U·cm<sup>-2</sup> and the thickness of the makrofol was 10 µm, which is less than the range of the fission fragments. A 41 mm X 91 mm foil of makrofol was mounted on the circumference of a cylindrical aluminium cassette. The fission fragment tracks were counted by dividing the makrofol foil into parts defined as intersections among the cylindrically shaped detector and the beam co-axial conical surfaces starting from the centre of the target and having angular widths of  $\theta_n = 7.5^\circ + (n-1)15^\circ$  with n = 1.7. A schematic view of the experimental arrangement is shown in Fig.1. After the irradiation, the makrofol foils were etched in 6N-NaOH at 70°C for half an hour and analysed by the spark-scanning method.

Moreover, the total fission yields were measured in the 3.6–5.6-MeV range. To increase the fragment yield, ten sample makrofol sandwiches were piled up along the electron beam axis at a distance of 17 mm from the tungsten converter. The thickness of the samples and of the detector foils were 2.3 mg U·cm<sup>-2</sup> and 60 µm, respectively. The plastic foils, etched in 6N-NaOH at 70°C for one hour, were scanned optically.

Both experiments were performed inside the microtron vacuum chamber.

### 3. EVALUATION OF EXPERIMENTAL DATA

The differential photofission yield of an even-even target for combined dipole and quadrupole absorption is theoretically described by the expression [2]

$$W(\theta) = a + b \sin^2 \theta + c \sin^2 2\theta \quad (1)$$

However, because of the finite angular resolution in the actual experiment, the measured distribution of counts N<sub>j</sub> is given by

$$N_j = \int_{\Omega_\gamma} \int_{\Omega_j} W(\theta) d\Omega_\gamma d\Omega_j \quad (2)$$

where dΩ<sub>γ</sub> and dΩ<sub>j</sub> are the solid-angle elements constructed, respectively, on the vectors from the photon emission point to the fission point and from the fission point to the detection point on the makrofol. The integrals above were calculated by a Monte-Carlo method. In this calculation, the finite dimension of the electron beam and the gamma angular distribution were taken into account. Also, the energy loss of the fission fragment in the finite thickness of the target was simulated in order to account for the detection efficiency of the

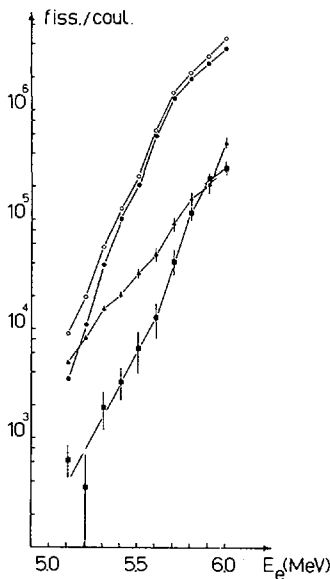


FIG. 2. Experimental yields:  $\blacksquare Y_a$ ;  $\blacktriangle Y_c$ ;  $\bullet Y_b$  and  $\circ$  total yield as function of electron energy.

makrofol foils. The results of a similar calculation are in good agreement with the  $^{236}\text{U}$  fission angular distribution from thick target measured by Alm and Lindgren at 100-MeV gamma energy [3].

The a, b and c values, together with their standard deviations, were obtained from Eq.(2) by means of the least-squares method.

We define

$$Y_a = 4\pi a$$

$$Y_b = \frac{8\pi}{3} b \quad (3)$$

$$y_c = \frac{32\pi}{15} c$$

the isotropic, dipole and quadrupole components, respectively.

The results of the evaluation are shown in Figs 2 to 4.

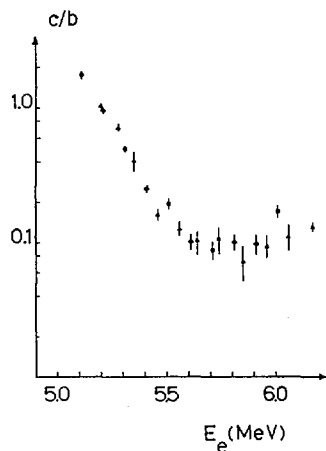


FIG.3.  $c/b$  as a function of the electron energy:  $\diamond$  our measurements;  $\blacktriangle$  measurements of Ref. [4].

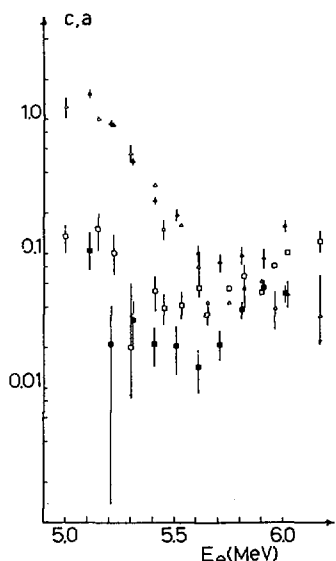


FIG.4. Quadupole and isotropic coefficients as functions of electron energy normalized at  $a + b = 1$ ;  $\blacktriangle$ ,  $\blacksquare$  our  $c$  and  $a$ ;  $\blacktriangledown$ ,  $\lozenge$   $c$  and  $a$  from Ref. [5].

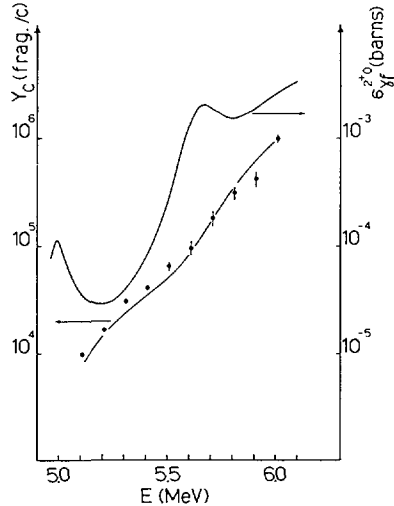


FIG. 5. Quadrupole component as obtained by experimental angular-distribution analysis ( $\bullet$ ); the solid curve is the fit to the yield points. The following parameters were used:  $E_A = 5.95 \text{ MeV}$ ,  $\hbar\omega_A = 1.0 \text{ MeV}$ ,  $E_{II} = 2.17 \text{ MeV}$ ,  $\hbar\omega_{II} = 0.82 \text{ MeV}$ ,  $E_B = 6.22 \text{ MeV}$ ,  $\hbar\omega_B = 0.82 \text{ MeV}$ ,  $W_0 = 0.0 \text{ MeV}$ ,  $W = 0.05 \text{ MeV}$ . The upper curve shows the corresponding evaluated cross-section.

#### 4. ANALYSIS OF THE PHOTOFISSION YIELDS

In this section, we discuss the general trend of the low-energy photofission of  $^{238}\text{U}$  as deduced from a preliminary analysis of the experimental data based on the double-humped fission barrier model [6].

We assume that  $Y_a$ ,  $Y_b$  and  $Y_c$  components represent the fission yields via the  $J^\pi K = 1^-1$ ,  $J^\pi K = 1^-0$  and  $J^\pi K = 2^+0$  transition states, respectively. In this hypothesis, we write the photofission cross-section through the  $J^\pi K$  channel as

$$\sigma_{\gamma,f}^{J^\pi K} = \sigma_{abs}^{J^\pi} \frac{P_f^{J^\pi K}}{P_f^{J^\pi K} + P_\gamma^{J^\pi}} \quad (4)$$

where  $\sigma_{abs}$  is the gamma absorption cross-section,  $P_f$  the fission barrier resonant penetrability including vibrational damping [8, 12] and  $P_\gamma$  the radiative penetrability [9].

The energy dependence of the dipole cross-section  $\sigma_{abs}^{1-}$  is taken from Ref.[7], and  $\sigma_{abs}^{2+} = \sigma_{abs}^{1-} R^2/\lambda^2$  is assumed,  $R$  being the nuclear radius and  $\lambda$  the wavelength of the gamma radiation.

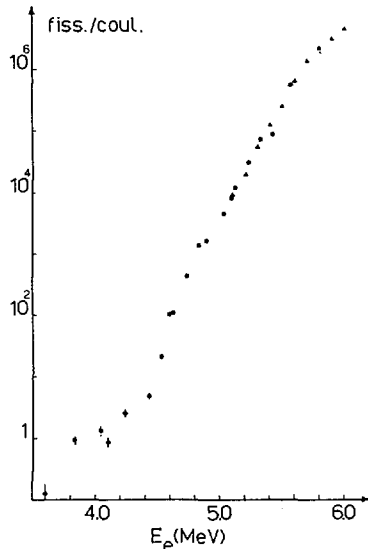


FIG. 6. Total photofission yields in the 3.6–5.6-MeV range ( $\Phi$ ) together with total yield from angular-distribution measurements ( $\Delta$ ) in the 5.1–6.0-MeV range. The curves are normalized to the same value at 5.1 MeV.

An empirical formula for the energy dependence of the bremsstrahlung spectrum is obtained by fitting the experimental data of O'Dell et al. [10] with data corrections taken from Ref.[11].

The photofission yield is, then, obtained by integration of the cross-section (4) over the bremsstrahlung spectrum.

With this model of calculation, we have performed a quantitative analysis of the quadrupole component. As a starting point we have used the  $0^+$  fission barrier parameters deduced from direct relations in Ref. [12]. We find this set of parameters to be consistent with our photofission data. The only difference is in the curvature value  $\hbar\omega_B$  of the external barrier. The calculated  $Y_c$  curve is compared with the experimental points in Fig.5. The same figure shows the calculated  $\sigma_{\gamma,f}^{2+0}$  which is resonant at 5 MeV and 5.7 MeV, in reasonable agreement with the results of Lindgren and Sandell [4].

In this paper a preliminary discussion of the  $Y_a$  and  $Y_b$  curves only is reported.

It has been suggested by Vandenbosch [13] that the relative trend of the  $Y_b$  and  $Y_c$  components, represented by the energy dependence of the c/b ratio in Fig.3, is strongly related to the excitation energy of the  $2^+0$  and  $1^-0$  transition states at the first-barrier deformation. Accordingly, our experimental data provide an additional evidence for  $E_A^{2+0} < E_A^{1^-0}$ . Moreover, the smooth energy

dependence of the  $Y_b$  yield curve does not give significant support to the existence of a resonance at 5.35 MeV in the dipole cross-section indicated in the results of Ref. [4].

The a and c values normalized to  $a + b = 1$  are shown in Fig.4. These experimental values, uncorrected for multiple scattering, are in reasonable agreement with those of Ref.[5]. Nevertheless, our isotropic component lies systematically lower than that of Ref.[5] and, according to our experience, is strongly dependent on the applied correction. Therefore, we think that further measurements with thinner targets are needed for a very accurate multiple-scattering correction and a correct evaluation of the isotropic component.

The results of the integral yield measurements in the energy range 3.6–5.6 MeV are shown in Fig.6. The energy dependence of this yield curve is in good agreement with total yield obtained by the angular distribution measurements. At 4.5 MeV electron energy a dramatic change in the yield slope, already known as the shelf effect [14], is observed. The integral yield curve is in excellent agreement with the data of Ref.[16].

We have also tried to fit the low-energy yield data with  $2^+0$  barrier parameters, assuming that the isomeric shelf is essentially due to the delayed fission of the  $2^+0$  channel. It turns out to be impossible to obtain a reasonable fit of the yield with a resonant cross-section calculated with the parameters of Fig.5. However, at low energy, our model calculation is inadequate and a modified door-way state model including weak and very weak coupling among states in the first and second minima, as described by Lynn [15], is under way.

## REFERENCES

- [1] BARNÀ, R.C., DE PASQUALE, D., ALBA, R., BELLIA, G., CALABRETTA, L., DEL ZOPPO, A., MIGNECO, E., RUSSO, G., Lett. Nuovo. Cim. **24** (1979) 306.
- [2] VANDENBOSCH, R., HUIZENGA, J.R., Nuclear Fission, New York, Academic Press (1973).
- [3] ALM, A., LINDGREN, L.J., Nucl. Phys. **A271** (1976) 1.
- [4] LINDGREN, L.J., SANDELL, A., Z. Phys. **A285** (1978) 415.
- [5] ZHUCHKO, V.E., IGNATYUK, A.V., OSTAPENKO, Yu.B., SMIRENKO, G.N., SOLDATOV, A.S., TSIPENYUK, Yu.M., Phys. Lett. **68B** (1977) 323.
- [6] STRUTINSKY, V.M., Nucl. Phys. **A95** (1967) 420.
- [7] AXEL, P., Phys. Rev. **126** (1962) 671.
- [8] CRAMER, J.D., NIX, J.R., Phys. Rev. **C2** (1970) 1048.
- [9] LYNN, J.E., Systematics for Neutron Reactions of the Actinide Nuclei, Harwell Report AERE-R7468.
- [10] O'DELL, A.A., Jr., SANDIFER, C.W., KNOWLEN, R.B., GEORGE, W.D., Measurements of Absolute Thick-Target Bremsstrahlung Spectra, EGG Report S-380-R (1977).
- [11] FERDINANDE, H., KNUYT, G., VAN DE VIJER, R., JACOBS, R., Nucl. Instrum. Meth. **91** (1971) 135.

- [12] BACK, B.B., HANSEN, O., BRITT, H.C., GARRETT, J.D., Phys. Rev. **C9** (1974) 1924.
- [13] VANDENBOSCH, R., Phys. Lett. **45B** (1973).
- [14] BOWMAN, C.D., Phys. Rev. **C12** (1975) 856.
- [15] LYNN, J.E., Harwell Report AERE R5891 (1969).
- [16] ZHUCHKO, V.E., IGNATYUK, A.V., OSTAPENKO, Yu.B., SMIRENKO, G.N., SOLDATOV, A.S., TSIPENYUK, Yu.M., Sov. Phys.-JETP Lett. 22 (1975) 118.

## DISCUSSION

Yu.M. TSIPENYUK: I am happy to see that your data have confirmed the results we obtained in the experimentally difficult energy region below 4 MeV. The disagreement observed in the isotropic component may be due to the finite dimensions of the target and detectors. There is need for high accuracy in the calculation of the corresponding space intervals.

A. DEL ZOPPO: We are working on this question: an accurate evaluation of the finite-target effect would appear necessary in order to ensure satisfactory determination of the isotropic component.



# COMBINED ANALYSIS OF THE PROMPT-FISSION, DELAYED-FISSION, PHOTOFISSION AND ANGULAR-DISTRIBUTION DATA FROM $^{234,236}\text{U}$ AND $^{238,240}\text{Pu}$

M. JUST, U. GOERLACH, D. HABS, V. METAG, H.J. SPECHT

Physikalisches Institut der Universität Heidelberg

and

Max-Planck-Institut für Kernphysik, Heidelberg,

Federal Republic of Germany

## Abstract

COMBINED ANALYSIS OF THE PROMPT-FISSION, DELAYED-FISSION, PHOTOFISSION AND ANGULAR-DISTRIBUTION DATA FROM  $^{234,236}\text{U}$  AND  $^{238,240}\text{Pu}$ .

Prompt-fission probabilities and angular distributions of fission fragments have been measured for the nuclei  $^{234,236}\text{U}$  and  $^{238,240}\text{Pu}$  down to a probability of  $10^{-4}$  at an excitation energy of approximately 4 MeV using ( $d,p$ ) and ( $^3\text{He},d$ ) reactions, respectively. Fission barrier parameters and excitation energies of  $K^\pi = 0^+, 2^+, 0^-, 1^-$  vibrational states have been deduced from a simultaneous analysis of the prompt-fission probability, the isomeric population probability, and the photofission yields. Difficulties in a quantitative description of the fission fragment angular distributions have not been fully understood.

## Introduction

The heights and widths of the double humped fission barrier and the excitation energies of certain collective states at different deformations are the relevant parameters, which govern the fission probability in actinide nuclei. Fission barrier parameters have been systematically determined from prompt fission probabilities in numerous previous studies <sup>(1-6)</sup>. The ambiguities associated with the extraction of the various parameters can be considerably reduced, if - in addition to the prompt fission probabilities - the probabilities for population of the fission isomer and photofission yields are simultaneously analyzed. We have therefore carefully reinvestigated the even-even nuclei  $^{234,236}\text{U}$  and  $^{238,240}\text{Pu}$ .

The main emphasis has been placed on the following-compared to previous-investigations:

- i) The measurement of the probability for prompt fission following direct reactions has been extended to a level of  $10^{-4}$  not reached before. This value corresponds to a mean excitation energy of about 4 MeV (more than 2 MeV below the highest barrier). Model calculations can thus be compared with experimental fission probabilities over many decades down to a region where calculations are extremely sensitive to the choice of the barrier parameters.
- ii) A doorway state model<sup>(7)</sup> extended to low excitation energies has been used in the analysis of the data. This extended model consistently describes the weak and also the very weak coupling between states in the 1. and 2. minimum at low excitation energies. For further details we refer to ref. 1.
- iii) The analysis simultaneously covers a data set consisting of:
  - a) Prompt fission probabilities;
  - b) Coefficients of angular distributions of fission fragments;
  - c) Probabilities for isomeric population;
  - d) Photofission yields;
  - e) Fission isomer half lives and branching ratio between  $\gamma$ - and fission decay of the isomer.

As a main result of this improved investigation barrier parameters and excitation energies of collective states like  $\beta$ -vibrations ( $K^\pi=0^+$ ),  $\gamma$ -vibrations ( $K^\pi=2^+$ ) octupole vibrations ( $K^\pi=0^-$ ) and the bending mode ( $K^\pi=1^-$ ) have been deduced.

In the next section the experimental method will be briefly described followed by a qualitative discussion of the relevant parameters and their dependence on the different data-sets. Using  $^{240}\text{Pu}$  as an example the model calculations will be outlined. The result of the calculations for all nuclei investigated will then be discussed in the last section.

#### Experimental method

Deuteron and  $^3\text{He}$ -beams from the Heidelberg EN- and MP-Tandem, respectively, were used in the direct reactions  $^{233,235}\text{U}(d,p)$   $^{234,236}\text{U} \rightarrow f$  and  $^{237}\text{Np}(^3\text{He},d)^{238}\text{Pu} \rightarrow f$ .

The beam strikes the target of  $100 \mu\text{g}/\text{cm}^2$  thickness. The direct reaction products are identified in a  $\Delta E-E$  telescope at  $140^\circ$

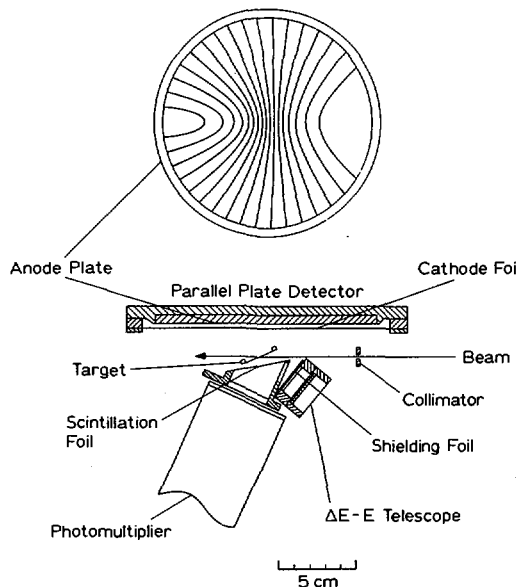


*FIG.1. Scheme of the detector arrangement. The position-sensitive anode is shown on top.*

consisting of a  $200 \mu\text{m}$  thick surface barrier  $\Delta E$ -detector and a  $1500 \mu\text{m}$  surface barrier  $E$ -detector. Fission fragments are registered in a position-sensitive parallel-plate avalanche detector (PPAD), whose anode is subdivided into sections of constant polar angle  $4^\circ$  with respect to the recoil axis of the fissioning nucleus. The two-dimensional read-out problem is thus reduced to a one-dimensional one. The complementary fission fragments are detected in coincidence with the events in the PPAD and the telescope in a scintillation counter placed only 6 mm from the target to minimize the deterioration of the time resolution by differences in the flight times of the fission fragments. The experimental sensitivity is directly proportional to the time resolution since it determines the contribution of chance coincidences. A time resolution of 0.8 ns could be achieved compared to 2-3 ns for the PPAD alone. The efficiency of this detection system for fission fragments amounts to 60% of  $4\pi$  (Fig.1).

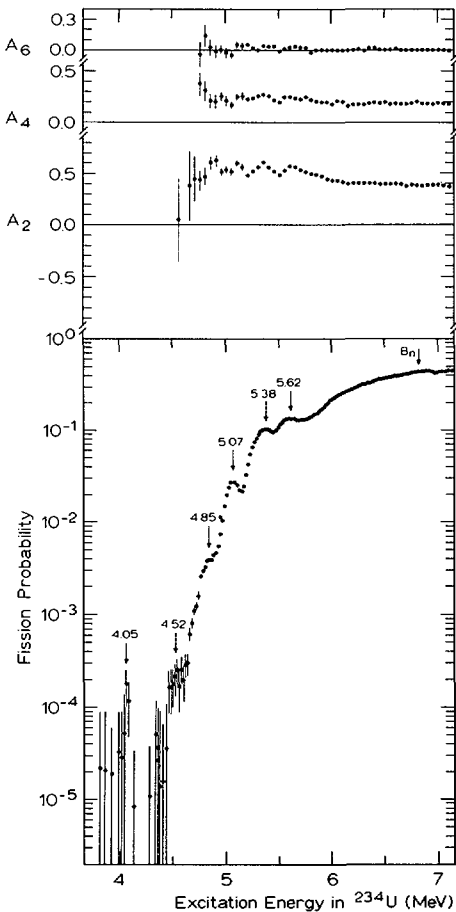


*FIG. 2. Angular correlation coefficients and probability for prompt fission following the reaction  $^{233}\text{U}(d,p)^{234}\text{U} \rightarrow f$ .*

The overall quality of the data is demonstrated for the reaction  $^{233}\text{U}(d,p)^{234}\text{U} \rightarrow f$  in fig. 2. The fission probability as well as the angular correlation coefficients exhibit several pronounced structures, which can be attributed to collective states in the 2. minimum. The prompt fission probability could be followed down to a value of less than  $10^{-4}$ .

Analysis of the Data

The different sets of data used for a more reliable determination of barrier parameters and the spectroscopic properties of the vibrational states are particular sensitive to certain parameters.

## i) Prompt fission probability

These data are most sensitive to the barriers of the  $K^{\pi}=0^+$  state. The location of these states and also higher K-states in the 2. minimum can be identified by the appearance of resonances.

## ii) Angular correlation coefficients

The value of these coefficients can be used in principle for an identification of the K-quantum number of certain collective states.

## iii) Isomeric population probability

Theoretical considerations concerning the actually used doorway state model<sup>(1)</sup> have shown that in the very weak coupling limit the isomeric population probability is directly proportional to the penetrability of the 1. barrier. Therefore it gives quite independent information on the parameters of the 1. barrier for the  $K^{\pi}=0^+, 2^+$  states. Possible resonances provide further details of spectroscopic properties of states in the 2. minimum.

## iv) Photofission data

The different yield curves of photofission induced by bremsstrahlung can also be related to the barrier parameters and excitation energies of distinct K-states. Using the formulas from ref. 2 the isotropic yield  $Y_a$  is determined by the  $K^{\pi}=1^-$  fission channel: the  $Y_b$  component, having an angular distribution proportional to  $\sin^2\chi$ , is governed essentially by the  $K^{\pi}=0^-$  channel and the  $Y_c$  component (proportional to  $\sin^2 2\delta$ ) essentially by the  $K^{\pi}=0^+$  channel, respectively. These simplified relations represent of course only a crude correlation since the calculated yield curves, which contain the complete theoretical formulas, are to some extent sensitive to all parameters under investigation and the change of one parameter will affect the model calculation for all subsets of data.

In the fitting procedure we restrict ourselves to as few variable parameters as possible. To avoid ambiguities all available ex-

perimental information has been used to fix the remaining parameters. Level densities in both wells and  $\gamma$ -widths are thus adjusted to accurately known experimental values<sup>(5,8)</sup>, while other less exactly known parameters like the excitation energy of the lowest state in the second well or the damping width are chosen within reasonable limits, set by experiments<sup>(9,10)</sup>.

Consequently, only the barrier parameters of the different fission channels and the excitation energies of the vibrational states in the 2. minimum essentially remain as variable parameters.

#### Model calculations

For simplicity we shall restrict our discussion to the case of  $^{240}\text{Pu}$ , which represents the most clear-cut example for the interpretation of the data. The prompt fission data are characterized by 3 resonances at 4.2, 4.5 and 5.0 MeV. The resonances at 4.2 and 5.0 MeV are interpreted considering simultaneously the angular distribution data as  $K^\pi=0^+$  resonances in the 2. minimum. There is also a resonance at 4.5 MeV, which can only be a  $K^\pi=0^+$  state because of its strength. If interpreted as an additional  $\beta$ -phonon much more structure due to the higher K-vibrations coupled to it would result in contrast to observation. It is therefore suggested that the resonance at 4.5 MeV might arise from some fragmentation of the  $\beta$ -vibrational strength concentrated at 4.2-4.5 MeV. This fragmentation spreads the  $\beta$ -vibrational strength selectively over several isolated groups of compound states in contrast to a smooth Lorentzian distribution normally used for describing the damping of collective vibrational states into compound states. The lowest-lying resonance in the isomer population probability at 4.0 MeV is probably a  $K^\pi=2^+$  vibration built upon a hypothetical  $\beta$ -vibration at 3.35 MeV. An interpretation as a  $K^\pi=0^+$  resonance would require an unreasonably high  $\gamma$ -width for the decay of the collective state to reproduce the observed yield. The observed spacing of  $K^\pi=0^+$  and  $K^\pi=2^+$  resonances gives a mean energy of about 600-800 keV for the  $\beta$ -vibrational phonon in the 2. minimum. With this interpretation of the observed resonances the barrier parameters were determined considering simultaneously the photofission yields reported in ref. 2. The analysis of these data yields in addition the excitation energies of  $K^\pi=0^-, 1^-$  states relative to the  $K^\pi=0^+$  state at both barriers. The fits to the experimental data for the other 3 nuclei are shown in fig. 3-6.

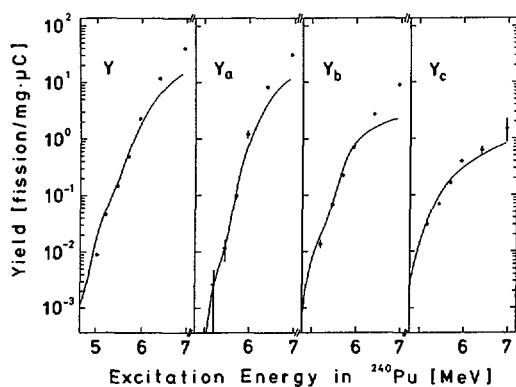
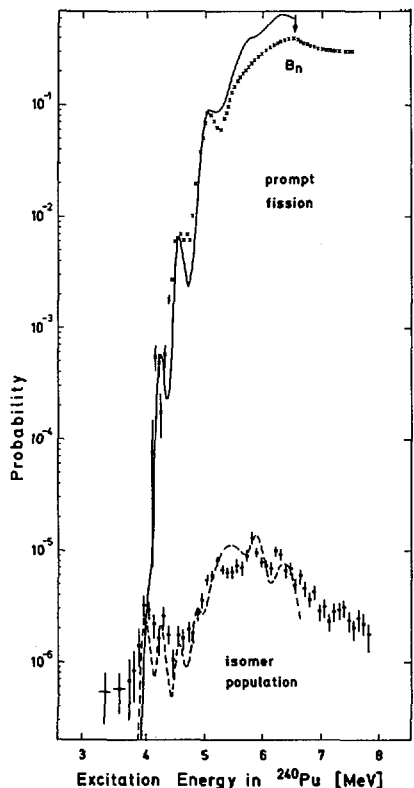


*FIG.3. Comparison between experimental results and model calculations for the prompt fission probability, the isomeric population probability and photofission yields of  $^{240}\text{Pu}$ .*

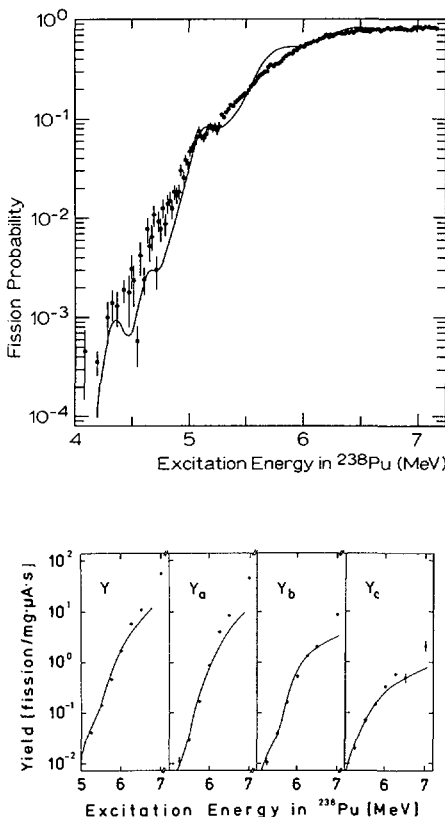


*FIG. 4. Comparison between experimental results and model calculations for the prompt fission probability and photofission yields of  $^{238}\text{Pu}$ .*

It should be pointed out, however, that we did not succeed in a satisfactory quantitative description of the angular distribution data. The reason for this failure is not yet understood.

Two approaches have been used to treat the angular distributions of the fission fragments in the model calculations; the first one assumes a statistical population of compound states in the final nucleus while the other is based on the supposition that the population occurs primarily via only few but relevant single-particle states. In the latter case the specific nuclear structure enters in terms of the Nilsson orbits close to excitation energies of 4-6 MeV. These entrance channel effects, depending

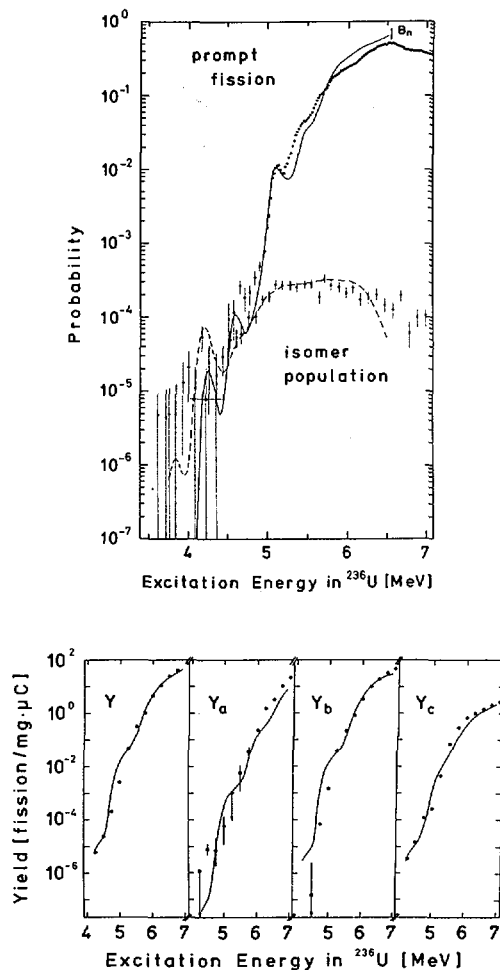


*FIG. 5. Comparison between experimental results and model calculations for the prompt fission probability, isomeric population probability and photofission yields of  $^{236}\text{U}$ .*

on the specific Nilsson orbit the neutron is transferred to, considerably affect the calculated angular distribution coefficients.

An example is given in fig. 7 for the reaction  $^{235}\text{U}(\text{d},\text{p})^{236}\text{U} \rightarrow \text{f}$ . Fig. 7b corresponds to the assumption that for negative-parity states in the final nucleus the transferred neutron is built in the Nilsson orbit  $1/2 [611]$  at all energies, while

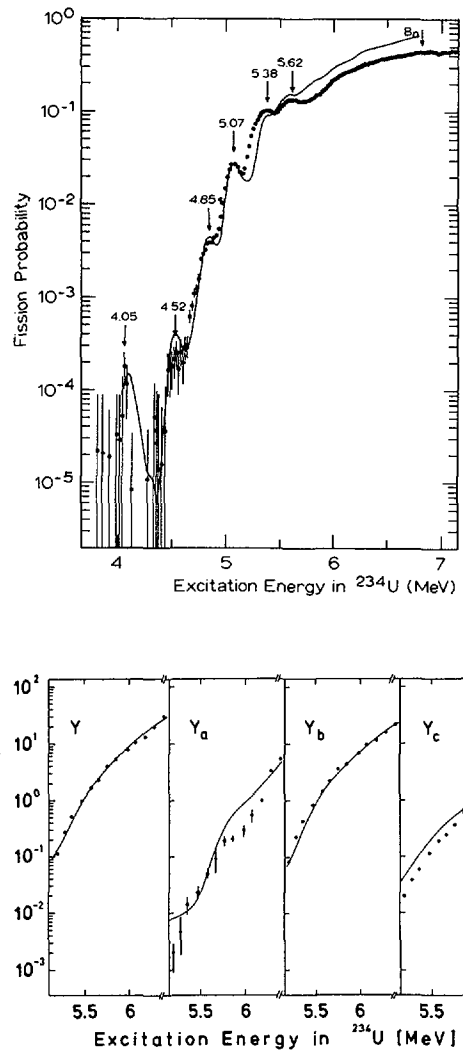
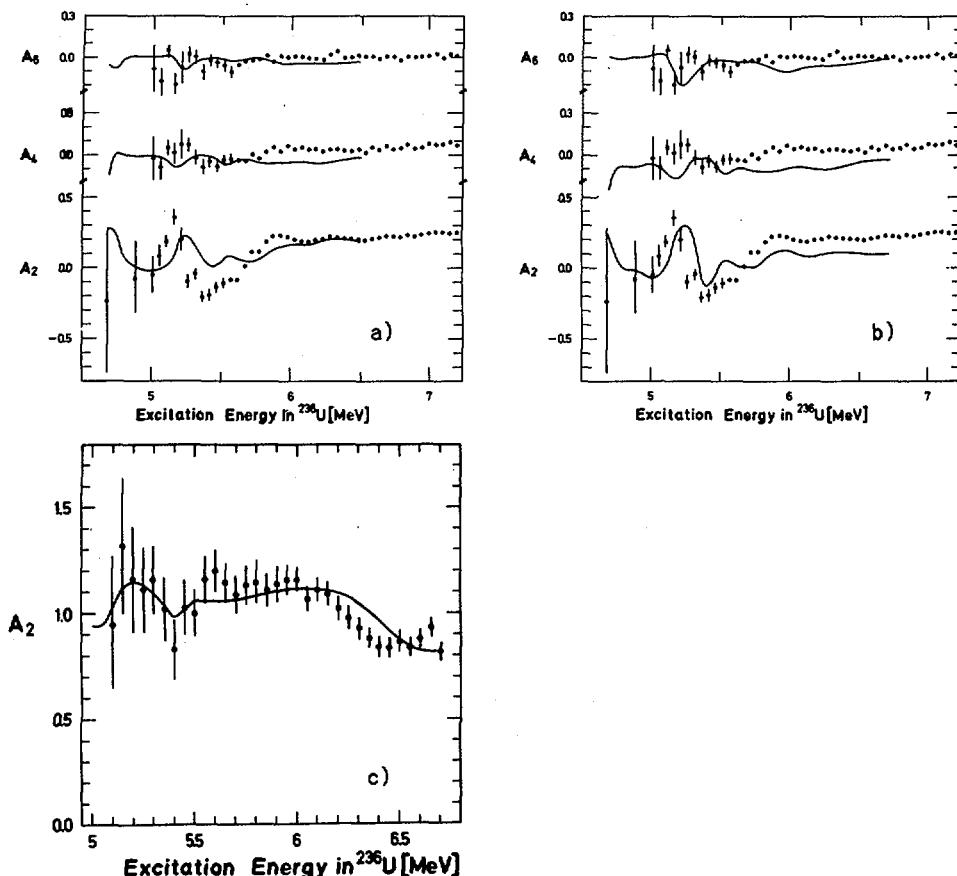


FIG. 6. Comparison between experimental results and model calculations for the prompt fission probability and photofission yields of  $^{234}\text{U}$ .

fig. 7a is based on the argument that the contribution of single Nilsson orbits is smeared out over 1 MeV and therefore many orbits have to be considered simultaneously. This latter treatment uses the formulas from ref. 5. Furthermore the angular correlation coefficients of the reaction  $^{234}\text{U}(\text{t},\text{p})^{238}\text{U} \rightarrow \text{f}$  from ref. 6 have been compared with model calculations using the same set of para-



*FIG. 7. Coefficients of the fission fragment angular distributions for  $^{236}\text{U}$ . The model calculations for the different cases illustrated are discussed in the text.*

meters as in the foregoing cases. Here entrance channel effects are expected to be negligible due to the ground state spin  $0^+$  of the e-e target nucleus  $^{234}\text{U}$ .

The result is given in fig. 7c. The reasonable agreement between experiment and model calculations indicates that entrance channel effects are, indeed, responsible for the deviation in the description of the (d,p) reaction data.

#### Results and Discussion

The resulting values of the heights  $V$  and the widths  $\pi\omega$  of the 2 barriers are shown in fig. 8 for all nuclei investigated. The

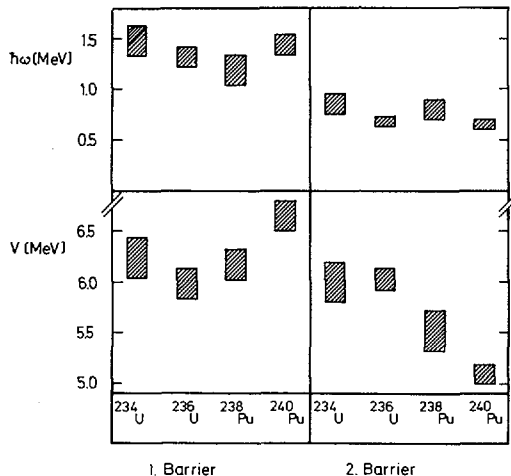


FIG. 8. Barrier parameter for the  $K^\pi = 0^+$  state. The widths  $\hbar\omega$  and the heights  $V$  are given in the upper and lower part of the figure, respectively. Uncertainties within the model are indicated by the hatched area.

widths of 1. and 2. barrier are rather constant for all nuclei and amount to about 1.3 MeV and 0.7 MeV, respectively, while the barrier heights vary from isotope to isotope. The variation of the barrier parameters from isotope to isotope is qualitatively in good agreement with the results of earlier studies<sup>(5)</sup>, but there are quantitative deviations up to 400 keV for the barrier width and 800 keV for the barrier heights. Our values are, however, considered less ambiguous because of the larger body of experimental data reproduced.

New spectroscopic information is obtained from the analysis of the higher  $K$ -states. Their excitation energy relative to the  $K^\pi=0^+$  state at the deformation of the 1. barrier, the 2. minimum and the 2. barrier has been deduced for the first time in a consistent way. These results are shown in fig. 9. The  $K^\pi=1^-$  state is characterized by a rather constant excitation energy of about 700 keV for all investigated nuclei at all deformations. Within the uncertainties of the model calculations the analysis yields the same excitation energy for  $K^\pi=0^-$  vibrations at the 1. barrier and the 2. minimum for the U- and Pu-isotopes separately. However, a remarkable reduction of this energy is found at the deformation of the 2. barrier. This effect has been theoretically expected

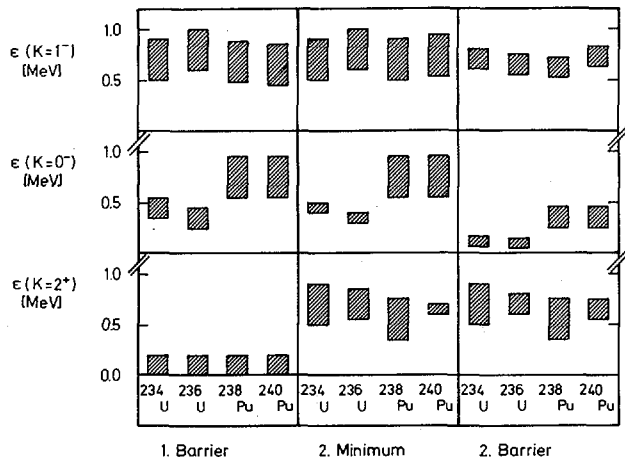


FIG.9. Excitation energies of the  $K^\pi = 2^+, 0^-, 1^-$  states at the deformation of the first barrier, the second minimum and the second barrier. The energies are given relative to the  $K^\pi = 0^+$  state.

and qualitatively explained by an instability of the 2. barrier with respect to pearshaped octupoledeformations. A complete degeneracy between the  $K^\pi=0^+$  and  $K^\pi=0^-$  bands has, however, not been obtained indicating the existence of a well penetrable barrier between the two octupole-deformed minima. Another remarkable result is the large difference between the excitation energy of the octupole vibrations in the U- and Pu-isotopes. While a value of about 350-400 keV is deduced for the U-isotopes, the analysis of the Pu-isotopes gives an excitation energy of about 750 keV. The reason for the large difference is not yet understood, and it cannot be completely ruled out that it is due to some insufficiency in the model description. The low excitation energy of the octupole vibration in the U-isotopes implies that a considerable flux will go through these states in the population of the fission isomer. It may be a challenging experiment to search for the decay of these octupole states applying the techniques of electron or  $\gamma$ -spectroscopy in the 2. well developed recently.

Assuming that the fission isomer is populated via the  $K^\pi=0^+$  and  $K^\pi=2^+$  states, these two states have to be degenerate at the 1. barrier to reproduce the observed flux in the population of the fission isomer. This result might be a more direct experimental indication of the theoretically postulated instability of the 1. barrier with respect to  $\gamma$ -deformation than that deduced from ref. 11.

The excitation energy at the 2. minimum and the 2. barrier again has the same value of about 650 keV for all nuclei investigated.

#### Conclusions

Based on an extended doorway state model a combined analysis of measured prompt and delayed fission probabilities as well as photofission yields has provided a new set of parameters of the double-humped fission barrier for U and Pu isotopes. Because of the larger body of experimental data, which are consistently reproduced, the resulting barrier parameters are considered less ambiguous than those obtained in previous studies. Particular emphasis has been given to the determination of the energies of vibrational excitations at the barriers and the 2. minimum. The deduced excitation energies of vibrational states may be used as a guideline for the observation of their decays by electron or  $\gamma$ -spectroscopy in future experiments.

#### REFERENCES

- 1) U. Goerlach, D. Habs, M. Just, V. Metag, P. Paul, H.J. Specht; Z. Physik A 287 (1978) 171
- 2) N.S. Rabotnov, G.N. Smirenkin, A.S. Soldatov, L.N. Usacher, S.P. Kapitz, Yu.M. Tsipenyuk; Sov. J. Nucl. Phys. 11 (1970) 285
- 3) V.E. Zhuchko, A.V. Ignatyuk, Yu.B. Ostapenko, G.N. Smirenkin, A.S. Soldatov, Yu.M. Tsipenyuk; Phys. Lett. 68 B (1977) 323
- 4) L.J. Lindgren, A. Alm, A. Sandell; Nucl. Phys. A 298 (1978) 43
- 5) B.B. Back, Ole Hansen, H.C. Britt, J.D. Garrett; Phys. Rev. C 9 (1974) 1924
- 6) J.D. Cramer, H.C. Britt; Phys. Rev. C 2 (1970) 2350
- 7) P.D. Goldstone; Thesis (1975), Stony Brook, New York
- 8) D.K. Sood, N. Sarma; Nucl. Phys. A 151 (1970) 532

- 9) H.C. Britt, M. Bolsterli, J.R. Nix, J.C. Norton; Phys. Rev. C 7 (1973) 801
- 10) P. Glässel, H. Rösler, H.J. Specht; Nucl. Phys. A 256 (1975) 220
- 11) A. Garron, H.C. Britt, E. Konecny, J. Weber, J.B. Wilhelmy; Phys. Rev. C 13 (1976) 2374

## DISCUSSION

Yu.M. TSIPENYUK: How different were the barrier parameters obtained from the doorway-state analysis and the statistical model? And which model do you think is better?

M. JUST: In most cases the largest differences are found in the first-barrier parameters. The heights and curvatures of the first barrier are consistently higher than the values obtained from the statistical-model calculations. The advantage of the doorway-state model is that it takes into account the coupling between compound states in the first and second minima.

The strength of the coupling has been found to depend on excitation energy, so a weak coupling region at higher excitation energies, e.g.  $E_x \gtrsim 4.5$  MeV, should be differentiated from the very weak coupling at low excitation energies. In the latter case the extended doorway-state model postulates a steeper decline in the isomeric population and prompt fission probability, together with the occurrence of resonances in the ex-isomeric population probability. This has, in fact, been experimentally observed.

H.C. BRITT: I think that below  $\sim 5$  MeV for d, p reactions there are still large gross structures in the entrance channel on account of the few single-particle excitation modes available. These effects might strongly influence angular distributions and affect the deduced excitation energies for the collective excitations at the barriers.

Sub-barrier calculations are very sensitive to values used for  $\Gamma_\gamma$ , so some of the systematic differences between our barrier parameters might be due to differences in the model for  $\Gamma_\gamma$ .

M. JUST: Yes, I agree. In our model calculations we used the same analytical dependence of the  $\gamma$  width on excitation energy in the first well as you did in your previous work.

S.S. KAPOOR: I would like to comment on the constancy of the K quantum number from saddle to scission in the interpretation of fragment angular-distribution data. This problem is related to the extent of energy dissipation during descent from the saddle. We have to examine carefully whether strong energy dissipation also implies that, due to the strong coupling of the

collective and intrinsic states, constancy of the K quantum number may not be a valid assumption.

J.P. THEOBALD: Dr. Just, did you compare your  $\hbar\omega_A$  values for the widths of the first fission barriers (obtained by interpolation) with those obtained from the related spreading widths  $\Gamma^+$  of intermediate structure in low-energy neutron-induced fission in order to ascertain the effects of single nucleons?

M. JUST: As far as I know, there are no experimental results on neutron widths for the even uranium and plutonium isotopes. Extrapolation from the results of the odd isotopes to the even isotopes seems to be highly critical on account of the influence of the unpaired nucleon.

A.F. MICHAUDON (*Chairman*): Further to Dr. Theobald's question, I think it is true that the widths of the class-II states can help to determine the height and  $\hbar\omega$  of the fission barrier. But when comparing these barrier parameters with those obtained by the combined analysis you have shown us, we have to be sure that the comparison is made for the same fissioning nucleus. For example, you showed us barrier parameters for  $^{240}\text{Pu}$ , whereas the intermediate structure effect in the  $^{240}\text{Pu}$  neutron-induced fission cross-section may give us the  $^{241}\text{Pu}$ , rather than the  $^{240}\text{Pu}$ , fission barrier parameters. Extrapolation of the results from one nucleus to another should be made with great care, since there may be extensive even-odd effects, especially for the parameter  $\hbar\omega$ .

R.L. WALSH: Dr. Just, your Table I shows a difference of  $\sim 1.45$  MeV between the heights of the inner and outer barriers for the  $^{240}\text{Pu}$  compound nucleus. Back et al. at Rochester (BACK, B.B., et al., Physics and Chemistry of Fission (Proc. Symp. Rochester, 1973) Vol.1, IAEA, Vienna (1974) 25), however, found a difference of  $\sim 0.35$  MeV for the  $^{240}\text{Pu}$  barrier height, also using the (d,pf) reaction. Britt (see paper SM-241/A1 in these Proceedings.) reports a difference of  $\sim 0.5$  MeV. How would you explain this discrepancy?

M. JUST: In our analysis we tried to reproduce (d,pf), (d,p isomer) and ( $\gamma$ ,f) data simultaneously. The two sources you quote are limited to the (d,pf) reaction alone. Hence the different values obtained reflect the uncertainties in the analysis, rather than in the actual data. We consider our values more reliable.

# LA REACTION ( $n, \gamma f$ ) DANS LES RESONANCES INDUITES PAR NEUTRONS LENTS DANS $^{239}\text{Pu}$ , $^{235}\text{U}$ ET $^{241}\text{Pu}$

J. TROCHON

Service de physique nucléaire,  
CEA, Centre d'études de Bruyères-le-Châtel,  
Montrouge,  
France

## Abstract-Résumé

THE ( $n, \gamma f$ ) REACTION IN SLOW-NEUTRON-INDUCED RESONANCES IN  $^{239}\text{Pu}$ ,  
 $^{235}\text{U}$  AND  $^{241}\text{Pu}$ .

The ( $n, \gamma f$ ) reaction, a process resulting from competition between gamma ray emission and fission during de-excitation of a compound nucleus, is studied in the resolved-resonance region. After a qualitative study to show the effects of the phenomenon, the experimental data for  $^{239}\text{Pu}$ ,  $^{235}\text{U}$  and  $^{241}\text{Pu}$  are assembled and analysed. It is shown that all the data reflect the effects of that reaction. Experimental values of the product  $\Gamma_{\gamma f} \bar{e}_{\gamma f}$  of the width of the ( $n, \gamma f$ ) reaction and the mean value of the prefission gamma ray energy spectrum are deduced. Next, the theoretical aspects are considered. The calculated values of the energy  $\bar{e}_{\gamma f}$ , combined with the experimental results, enable the values of the width  $\Gamma_{\gamma f}$  to be derived. The usefulness of this reaction for studying fission barriers and class-II vibrational states is demonstrated and discussed.

## LA REACTION ( $n, \gamma f$ ) DANS LES RESONANCES INDUITES PAR NEUTRONS LENTS DANS $^{239}\text{Pu}$ , $^{235}\text{U}$ ET $^{241}\text{Pu}$ .

La réaction ( $n, \gamma f$ ) est étudiée dans la région des résonances résolues en tant que processus résultant de la compétition entre l'émission de rayonnement  $\gamma$  et la fission au cours de la désexcitation du noyau composé. Après une étude qualitative pour montrer les effets du phénomène, les résultats expérimentaux sur  $^{239}\text{Pu}$ ,  $^{235}\text{U}$  et  $^{241}\text{Pu}$  sont rassemblés et analysés. Il est montré que tous présentent les effets de cette réaction. Des valeurs expérimentales du produit  $\Gamma_{\gamma f} \bar{e}_{\gamma f}$  de la largeur de la réaction ( $n, \gamma f$ ) par la valeur moyenne du spectre en énergie du rayonnement  $\gamma$  de pré-fission en sont déduites. L'aspect théorique est ensuite abordé. Les valeurs calculées de l'énergie  $\bar{e}_{\gamma f}$ , combinées avec les résultats expérimentaux, permettent de donner des valeurs de la largeur  $\Gamma_{\gamma f}$ . L'intérêt de cette réaction pour l'étude des barrières de fission et des états vibrationnels de classe II est montré et discuté.

Un noyau composé formé par capture d'un neutron de basse énergie peut se désexciter soit en émettant un neutron (diffusion élastique et éventuellement inélastique), soit un rayonnement  $\gamma$  (capture radiative), soit par fission si ce processus est énergétiquement possible. La réaction

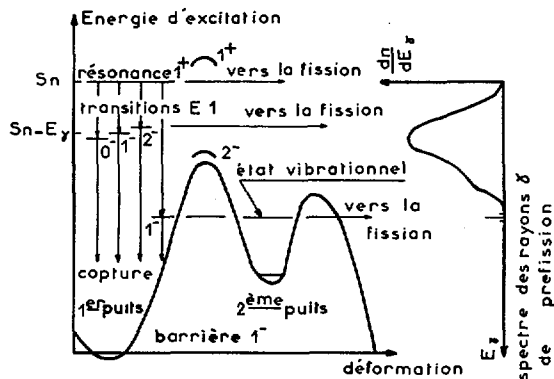


*FIG.1. Description schématique du mécanisme de la réaction  $^{239}\text{Pu}(n, \gamma f)$  dans les résonances  $I^+$ .*

$(n, \gamma f)$  provient de la compétition entre la capture radiative et la fission au cours de cette désexcitation. La région des résonances est la plus favorable à son observation car, par le jeu des fluctuations de PORTER et THOMAS des largeurs de fission, son importance peut varier considérablement d'une résonance à l'autre.

L'existence de la réaction  $(n, \gamma f)$  a été prévue théoriquement en 1965 par STAVINSKY et SHAKER [1] et par LYNN [2] mais ce n'est qu'en 1972 qu'elle a été mise en évidence expérimentalement dans la fission de  $^{239}\text{Pu}$  par neutrons lents [3].

### 1. LE PROCESSUS $(n, \gamma f)$

Après émission d'un rayon  $\gamma$  primaire, le noyau composé formé par capture d'un neutron peut se trouver dans un état d'énergie, de spin et de parité tels que la fission est encore fortement probable. Il fissionnera alors, plutôt que d'émettre un nouveau rayonnement  $\gamma$ .

Cette situation est décrite dans la fig. 1 qui illustre le cas typique des résonances  $I^+$  de  $^{239}\text{Pu}$ . Après capture d'un neutron d'onde "s", le noyau composé  $^{240}\text{Pu}$  se trouve dans un état de spin et parité  $J^\pi = 0^+$  ou  $1^+$ . Dans ce dernier cas la fission est peu favorisée car elle se produit par effet "tunnel" à travers la barrière ( $\langle\Gamma_f\rangle 1^+ = 33,4 \text{ meV}$  [4]). Cependant, après une transition  $E1$ , le noyau résiduel est dans un état  $J^\pi = 0^-$ ,  $1^-$  ou  $2^-$ ; dans le cas d'une transition  $M1$  il est dans un

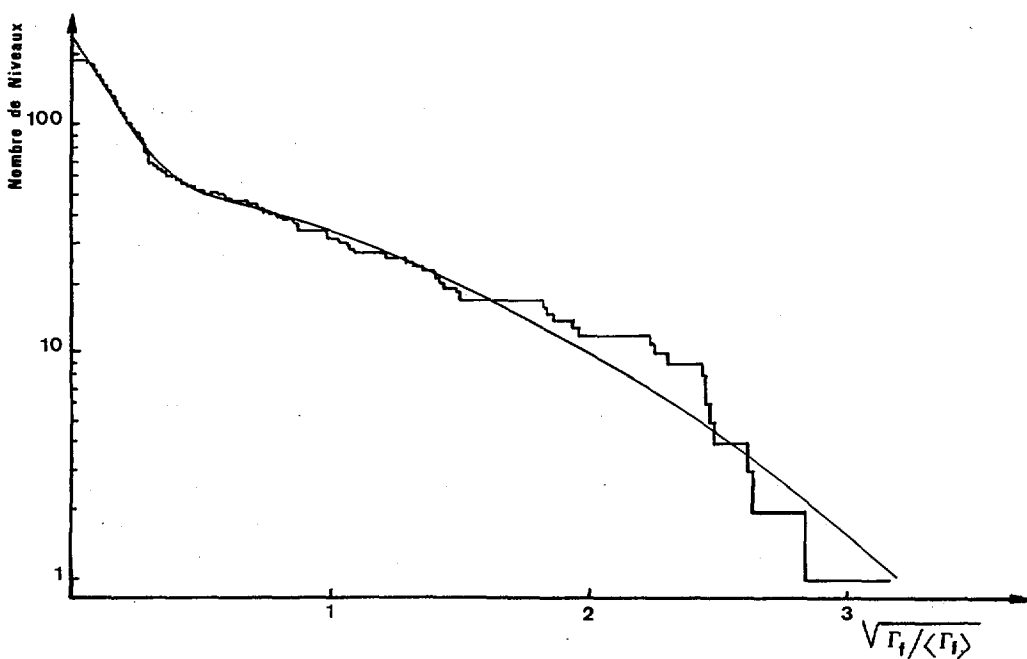


FIG. 2. Distribution intégrale des largeurs de fission  $\Gamma_f$  des résonances de  $^{239}\text{Pu}$  analysées entre 1 et 660 eV (d'après [4]). La courbe théorique est une somme de deux lois en  $\chi^2$  à  $v$  degrés de liberté. Elle fait apparaître un plateau au début de l'histogramme expérimental dû à un manque de faibles largeurs  $\Gamma_f$  attribué à la présence de la réaction  $(n, \gamma f)$ .

état  $J^\pi = 0^+, 1^+$  ou  $2^+$  pour se limiter à ces deux types de transition. Mais les barrières de fission de ces nouveaux états sont très différents de celle de l'état  $1^+$ . En particulier, les états de transition  $0^+, 2^+, 1^-$  et  $2^-$  sont beaucoup plus bas. Si l'énergie du rayon  $\gamma$  émis n'est pas trop importante, la voie de fission peut même être ouverte. Le noyau se désexcite alors par fission au lieu de continuer à se désexciter par cascade de rayons  $\gamma$ . Par contre, le noyau dans des états  $0^-$  ou  $1^+$  poursuit sa désexcitation dans la voie de capture radiative car les barrières de fission correspondant à ces états sont beaucoup plus élevées que l'énergie d'excitation du noyau composé à ce moment là.

Les largeurs  $\Gamma_{\gamma f}$  de ce processus peuvent être considérées comme constantes pour des états initiaux de spin et parité donnés car le nombre de voies de sortie du processus est grand. C'est en s'appuyant sur cette propriété que LYNN a donné une limite supérieure de la plus petite des

deux largeurs  $\Gamma_{\gamma f}$  possibles dans les résonances de  $^{239}\text{Pu}$  [2,5] ( $\Gamma_{\gamma f} < 5 \text{ meV}$ ) (voir fig. 2).

Cependant, cette propriété doit être utilisée avec précaution car la détermination des petites largeurs  $\Gamma_f$  est très sensible aux effets expérimentaux. Ainsi, de faibles fluctuations des largeurs de fission avaient été observées dans la fission sous le seuil de  $^{238}\text{Pu}$  [6]. Il semble maintenant que cet effet soit d'origine expérimentale [5]. De même le manque de largeur  $\Gamma_f < 10 \text{ meV}$  observé dans les résonances de  $^{241}\text{Pu}$  [7] ne peut pas être expliqué par la réaction  $(n, \gamma f)$  (voir § suivants).

## 2. MISE EN EVIDENCE EXPERIMENTALE DE LA REACTION $(n, \gamma f)$ ; INFLUENCE SUR LES CARACTERISTIQUES DE LA FISSION

La difficulté de distinguer un rayon  $\gamma$  de préfission d'un rayon  $\gamma$  émis par les fragments ou une fission "directe" d'une fission précédée d'un rayonnement  $\gamma$  ne permet pas une observation directe de la réaction  $(n, \gamma f)$ . Si à cet obstacle on ajoute la faible amplitude du phénomène, on comprend la difficulté de mettre cette réaction en évidence. En fait les expériences réalisées sont basées sur deux effets :

### 2.1. Effets du rayonnement $\gamma$ de préfission sur le cortège électronique des atomes

Cette méthode a été utilisée à Doubna pour  $^{235}\text{U}$  [8]. Elle consiste à mesurer les événements fission en coïncidence avec les rayons X caractéristiques du noyau fissionnant qui proviennent de la conversion interne du rayonnement  $\gamma$  de préfission. Malheureusement, les fragments de fission peuvent aussi induire indirectement de tels rayons X par action sur les atomes voisins.

Le rapport K de l'aire d'une résonance de fission observée en coïncidence avec les rayons X de la raie  $K_{\alpha_1}$ , à l'aire de la même résonance observée sans coïncidence peut s'écrire :

$$K = A \frac{\Gamma_{\gamma f}}{\Gamma_f} + B \quad (1)$$

A est une constante proportionnelle à l'efficacité du détecteur de rayons X, au pourcentage de transition  $K_{\alpha_1}$  dans l'ensemble des raies K, à la probabilité de remplir un trou dans la couche K et au coefficient de conversion interne. Le terme B provient des effets parasites des fragments de fission.

## 2.2. Influence de la réaction ( $n, \gamma f$ ) sur les propriétés des fragments de fission

Après émission d'un rayonnement  $\gamma$ , le noyau fissioneer a une énergie d'excitation plus faible. Le nombre moyen  $\bar{v}_p$  de neutrons émis est donc également plus faible. Par contre, l'énergie totale moyenne  $\bar{E}_\gamma$  emportée par les rayons  $\gamma$  est plus élevée car à l'énergie des rayons  $\gamma$  de fission qui ne varie que très faiblement avec l'énergie d'excitation, s'ajoute l'énergie emportée par le (ou les) rayon (s)  $\gamma$  précédant la fission. Il en est de même de la multiplicité de ces rayons  $\gamma$ .

On s'attend également à une incidence sur l'énergie cinétique totale  $\bar{E}_K$  des fragments de fission lorsque la variation de cette énergie avec l'énergie d'excitation du noyau composé est importante. C'est le cas des plutonium [39] : des variations  $\Delta E_K \sim -400$  keV sont prévues pour certaines résonances  $1^+$  de  $^{239}\text{Pu}$  de très faible largeur  $\Gamma_f$ .

Expérimentalement, la détection des rayons  $\gamma$  émis en coïncidence avec la fission ne permet que l'observation d'un mélange de fission directe et de réaction ( $n, \gamma f$ ). Dans les résonances pour lesquelles la fission directe est le processus de loin le plus probable (résonances ayant une grande largeur de fission  $\Gamma_f$ ), la réaction ( $n, \gamma f$ ) sera masquée ; les valeurs de  $\bar{v}_p$  et  $\bar{E}_\gamma$  seront à peu près constantes. Au contraire, lorsque la largeur totale de fission  $\Gamma_f$  est suffisamment faible, comparable à la largeur  $\Gamma_{\gamma f}$ , cette réaction contribuera beaucoup à la résonance. Ainsi les largeurs de fission  $\Gamma_f$  des résonances et la largeur  $\Gamma_{\gamma f}$  peuvent être reliées aux grandeurs mesurées par les relations :

$$\bar{E}_\gamma = \bar{E}_{\gamma 0} + \frac{\Gamma_{\gamma f}}{\Gamma_f} \bar{e}_{\gamma f} \quad (2)$$

$$\bar{E}_v = \bar{E}_{v0} - \frac{\Gamma_{\gamma f}}{\Gamma_f} \bar{e}_{\gamma f} \quad (3)$$

où  $\bar{E}_\gamma$  et  $\bar{E}_v$  correspondent à l'énergie emportée par les rayons  $\gamma$  et les neutrons de fission respectivement et  $\bar{E}_{\gamma 0}$  et  $\bar{E}_{v0}$  sont les valeurs de  $\bar{E}_\gamma$  et  $\bar{E}_v$  dans le cas de la fission directe pure.  $\bar{e}_{\gamma f}$  est la valeur moyenne du spectre en énergie des rayons  $\gamma$  de pré-fission. Cette grandeur est, comme la largeur  $\Gamma_{\gamma f}$ , constante pour les résonances de même spin. On peut donc écrire :

$$\bar{E}_\gamma - \bar{E}_{\gamma 0} = - (\bar{E}_v - \bar{E}_{v0}) = \frac{\Gamma_{\gamma f} \cdot \bar{e}_{\gamma f}}{\Gamma_f} = \frac{\text{constante}}{\Gamma_f} \quad (4)$$

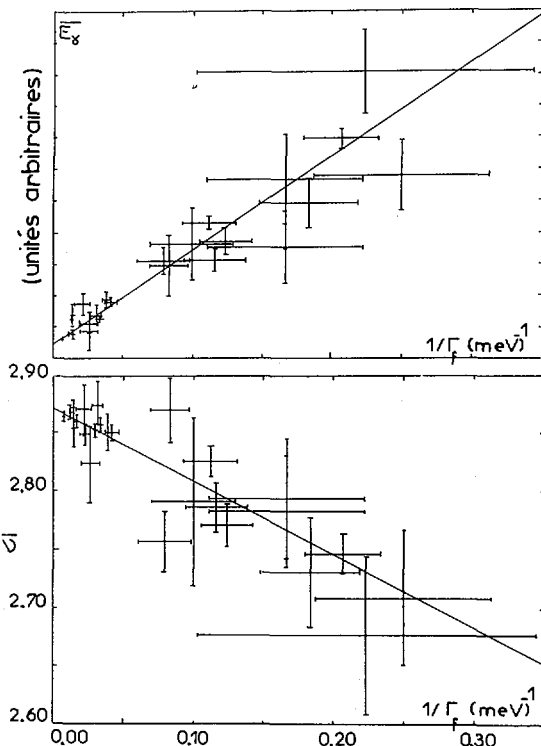


FIG.3. Variations de l'énergie  $\bar{E}_\gamma$  des rayons  $\gamma$  et du nombre  $\bar{\nu}_p$  de neutrons de fission en fonction de l'inverse de la largeur  $\Gamma_f$  des résonances  $I^+$  de  $^{239}\text{Pu}$  (d'après [16]). L'attribution du spin des résonances provient de [10].

Ces différentes équations présentent toutes une dépendance linéaire entre les grandeurs mesurées et l'inverse de la largeur  $\Gamma_f$ . Il suffira donc de tracer les valeurs expérimentales en fonction de  $1/\Gamma_f$  pour faire apparaître, si ils existent, les effets de la réaction  $(n,\gamma f)$ .

### 3. EVIDENCES EXPERIMENTALES DE LA REACTION $(n,\gamma f)$ DANS LA FISSION DE $^{239}\text{Pu}$ DANS LES RESONANCES

Le nombre  $\bar{\nu}_p$  de neutrons émis par fission a fait l'objet de nombreuses mesures dans les résonances. Elles ont été faites dans différents laboratoires par des techniques souvent différentes. Dans les mesures de Saclay par exemple, les neutrons sont détectés dans un gros scintillateur liquide chargé au gadolinium dans lequel ils perdent toute leur énergie

avant d'être capturés, puis comptés [11]. A ORNL, par contre, les détecteurs employés sont suffisamment minces pour que la probabilité de déetecter simultanément deux neutrons soit négligeable [12]. Ainsi le nombre de neutrons détectés est proportionnel à  $\bar{v}_p$ . Ces dispositifs expérimentaux permettent aussi de mesurer l'énergie moyenne  $\bar{E}_\gamma$  des rayons  $\gamma$  émis à la fission.

Après quelques curieux désaccords entre les premières mesures du nombre  $\bar{v}_p$  [13, 14] la situation est maintenant claire grâce aux derniers résultats qui comprennent aussi les valeurs de l'énergie  $\bar{E}_\gamma$  [15, 16].

Les résultats expérimentaux sont portés sur les figures 3 et 4 pour les résonances  $1^+$  et sur la figure 5 pour les résonances  $0^+$ . La dépendance avec  $1/\Gamma_f$  est particulièrement nette dans le premier cas. Elle l'est beaucoup moins dans le second car la fission directe est très importante. Les valeurs du produit  $\Gamma_{\gamma f} \cdot \bar{E}_{\gamma f}$  déduites de ces mesures sont données dans le tableau I.

#### 4. EVIDENCES EXPERIMENTALES DE LA REACTION ( $n, \gamma f$ ) DANS LA FISSION DE $^{235}\text{U}$

Le noyau composé formé par capture d'un neutron d'onde "s" dans  $^{235}\text{U}$  a pour spin de parité  $J^\pi = 3^-$  ou  $4^-$ . Cependant la fission directe est beaucoup plus importante pour ce noyau que pour les résonances  $1^+$  de  $^{239}\text{Pu}$  [20].

La première tentative de mise en évidence expérimentale de la réaction ( $n, \gamma f$ ) fut réalisée par PANTELEEV et Coll. qui mesurèrent une grandeur dont la racine carrée est approximativement proportionnelle à la multiplicité des rayons  $\gamma$  de fission [21]. Les résultats semblent refléter la présence de cette réaction, selon une relation similaire à (2), bien qu'un seul point contribue à obtenir une pente positive pour les résonances  $4^-$  [17].

Plus récemment DLOUHY et Coll. ont détecté le rayonnement X de réarrangement des couches électroniques de l'atome  $^{236}\text{U}$  après conversion d'un rayon  $\gamma$  de pré-fission [8] (voir chapitre précédent). Les résultats (fig. 6) présentent une dépendance linéaire en fonction de  $1/\Gamma_f$  mais seulement par le poids d'une résonance.

De nombreux laboratoires ont effectué la mesure du nombre  $\bar{v}_p$  de neutrons de fission. Après des résultats non concordants [13, 14], un accord est maintenant obtenu sur les résultats plus récents [22, 23, 24] et deux caractéristiques peuvent être dégagées.

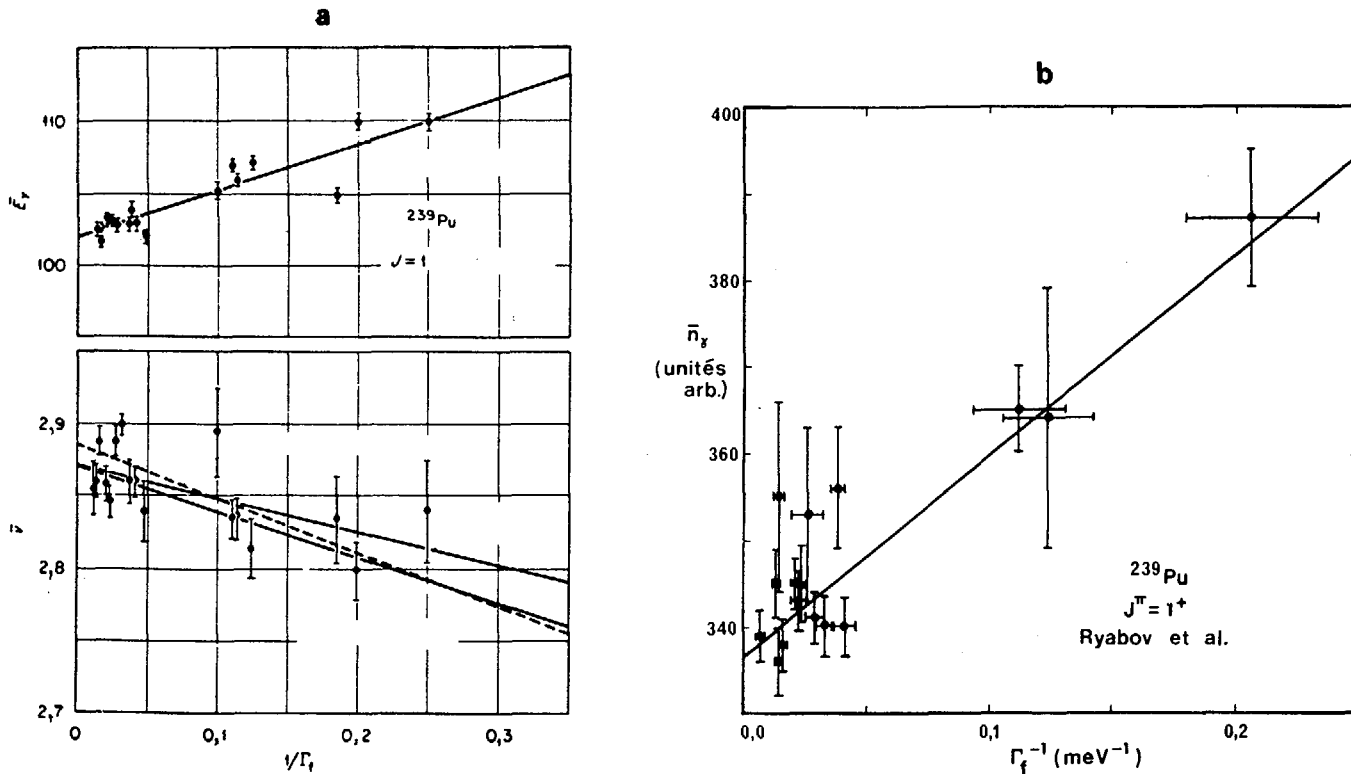


FIG.4. a) Variations de l'énergie  $\bar{E}_\gamma$  des rayons  $\gamma$  et du nombre  $\bar{n}_p$  de neutrons de fission en fonction de l'inverse de la largeur  $\Gamma_f$  des résonances de  $^{239}\text{Pu}$  (d'après [15]). b) Multiplicité des rayons  $\gamma$  émis à la fission en fonction de l'inverse de la largeur de fission des résonances  $1^+$  de  $^{239}\text{Pu}$  (d'après [19]).

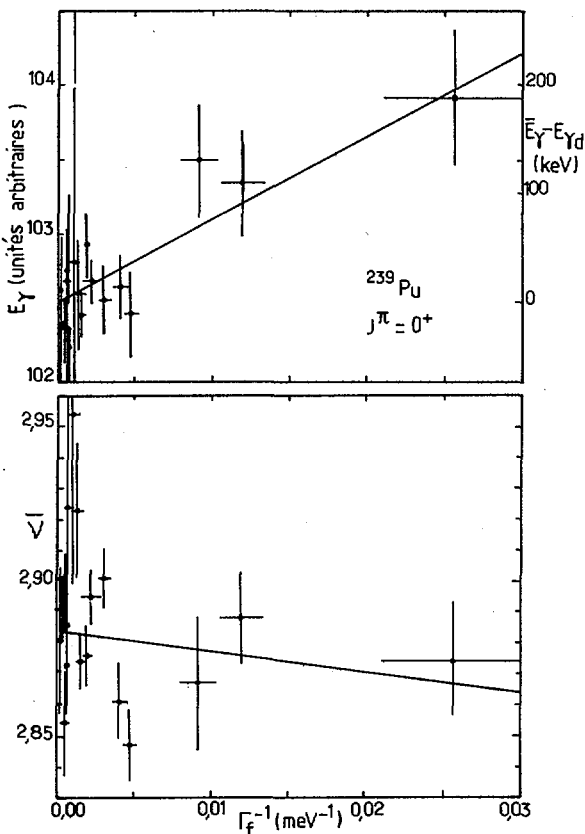


FIG. 5. Variations de  $\bar{E}_\gamma$  et de  $\bar{v}_p$  en fonction de  $1/\Gamma_f$  pour les résonances  $0^+$  de  $^{239}\text{Pu}$  (d'après [16]).

i) les trois plus importantes résonances observées en fission (à 8,8 - 12,4 et 19,3 eV) présentent des variations significatives qui ne semblent corrélées avec aucune des grandeurs caractéristiques de la fission actuellement connues (spin, largeur  $\Gamma_f$ , distribution en masse des fragments de fission, etc....) [24]. Nous n'avons pour l'instant aucune explication à donner à ces résultats.

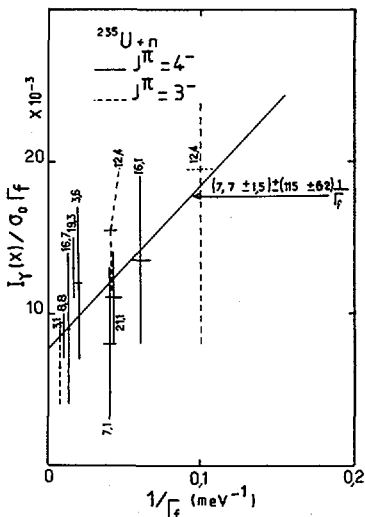
ii) les résonances de petite largeur  $\Gamma_f$  présentent systématiquement des valeurs de  $\bar{v}_p$  plus faibles que celles de grand  $\Gamma_f$ . Elles font apparaître une pente négative de la courbe  $\bar{v}_p = f(1/\Gamma_f)$  (voir figs. 7 et 8).

TABLEAU I. VALEURS EXPERIMENTALES DU PRODUIT  $\Gamma_{\gamma f} \cdot \bar{e}_{\gamma f}$   
DETERMINEES A PARTIR DES MESURES DU NOMBRE  $\bar{\nu}_p$  DE NEUTRONS  
ET DE L'ENERGIE  $\bar{E}_\gamma$  DES RAYONS  $\gamma$  DE FISSION.  $d\bar{\nu}_p/dE^*$  EST LA PENTE  
DE CONVERSION UTILISEE POUR LE CALCUL DE  $\bar{E}_\nu$  A PARTIR DES  
VALEURS DE  $\bar{\nu}_p$

noyau étudié	$J\pi$	mesure	$d\bar{\nu}_p/dE^*$	$\Gamma_{\gamma f} \cdot \bar{e}_{\gamma f} (\text{eV}^2)$	$\langle \Gamma_{\gamma f} \cdot \bar{e}_{\gamma f} \rangle (\text{eV}^2)$
$^{239}\text{Pu}$	$1^+$	$\bar{\nu}_p$ [17]	$0,131 \pm 0,004$	$4800 \pm 530$	$4600 \pm 300$
		$\bar{E}_\gamma$ [17]	[18]	$4490 \pm 400$	
	$0^+$	$\bar{\nu}_p$ [17]		$6600 \pm 9400$	$8000 \pm 1900$
		$\bar{E}_\gamma$ [17]		$8000 \pm 1900$	
$^{235}\text{U}$		$\bar{\nu}_p$ [24]	$0,135 \pm 0,07$	$2920 \pm 1400$	
	$4^-$	$\bar{\nu}_p$ [22]	[18]	$1563 \pm 1090$	$1730 \pm 590$
		$\bar{E}_\gamma$ [22]		$1437 \pm 806$	
		$\bar{\nu}_p$ [24]		$3500 \pm 2500$	
	$3^-$	$\bar{\nu}_p$ [22]		$4222 \pm 4502$	$4020 \pm 2030$
$^{241}\text{Pu}$		$\bar{E}_\gamma$ [22]		$6256 \pm 5515$	
	$2^+$	$\bar{\nu}_p$ [22]	$0,153 \pm 0,02$	$7932 \pm 5158$	$6982 \pm 3819$
		$\bar{E}_\gamma$ [22]	[18]	$5830 \pm 5680$	
	$3^+$	$\bar{\nu}_p$ [22]		$1750 \pm 789$	$1714 \pm 664$
		$\bar{E}_\gamma$ [22]		$1627 \pm 1229$	

Ces résultats, associés à ceux de l'énergie  $\bar{E}_\gamma$  des rayons  $\gamma$  de fission [17,22] (voir fig. 7), permettent de déduire des valeurs du produit  $\Gamma_{\gamma f} \cdot \bar{e}_{\gamma f}$  (voir tableau I).

En conclusion, nous pouvons dire qu'aucune des expériences réalisées n'apporte seule une preuve irréfutable de la présence de la réaction  $(n,\gamma f)$  dans  $^{235}\text{U}$  tant elle est masquée par la fission directe et peut-être par des effets encore non expliqués. Mais toutes ces expériences, pourtant très différentes, recèlent des indices qui forment un faisceau de présomptions tel que l'on peut affirmer que ce processus existe réellement dans ce noyau.



*FIG. 6. Variations de l'intensité du rayonnement X émis en coïncidence avec la fission en fonction de  $1/\Gamma_f$  pour les résonances de  $^{235}\text{U}$  (d'après [8]). L'énergie de la résonance (en eV) est indiquée à côté de la valeur correspondante.*

## 5 - EVIDENCES EXPERIMENTALES DE LA REACTION $(n,\gamma f)$ DANS LA FISSION DE $^{241}\text{Pu}$

Les résonances formées par capture de neutrons "s" ont pour spin et parité  $J'' = 2^+$  ou  $3^+$ . Malheureusement, en l'absence de mesure directe l'attribution du spin de ces résonances repose seulement sur la position relative des états de transition [25] et est très incertaine.

Les seuls résultats sur la réaction  $(n,\gamma f)$  dont on dispose proviennent d'une mesure simultanée de  $\bar{\nu}_p$  et de  $\bar{E}_\gamma$  [22] (voir fig. 9). Ils présentent les effets attendus de la réaction  $(n,\gamma f)$ , fournissant ainsi des valeurs du produit  $\Gamma_{\gamma f} \cdot \bar{e}_{\gamma f}$  (voir tableau I).

Cependant les variations observées sur les résonances supposées  $3^+$  sont bien plus faibles que celles attendues.

### 6. DETERMINATION DE LA LARGEUR $\Gamma_{\gamma f}$ ET DE L'ENERGIE MOYENNE $\bar{e}_{\gamma f}$ DU SPECTRE DES RAYONS $\gamma$ DE PRE-FISSION

Les seules expériences qui ont donné jusqu'à présent des grandeurs quantitatives sur la réaction  $(n,\gamma f)$  sont les mesures du nombre  $\bar{\nu}_p$

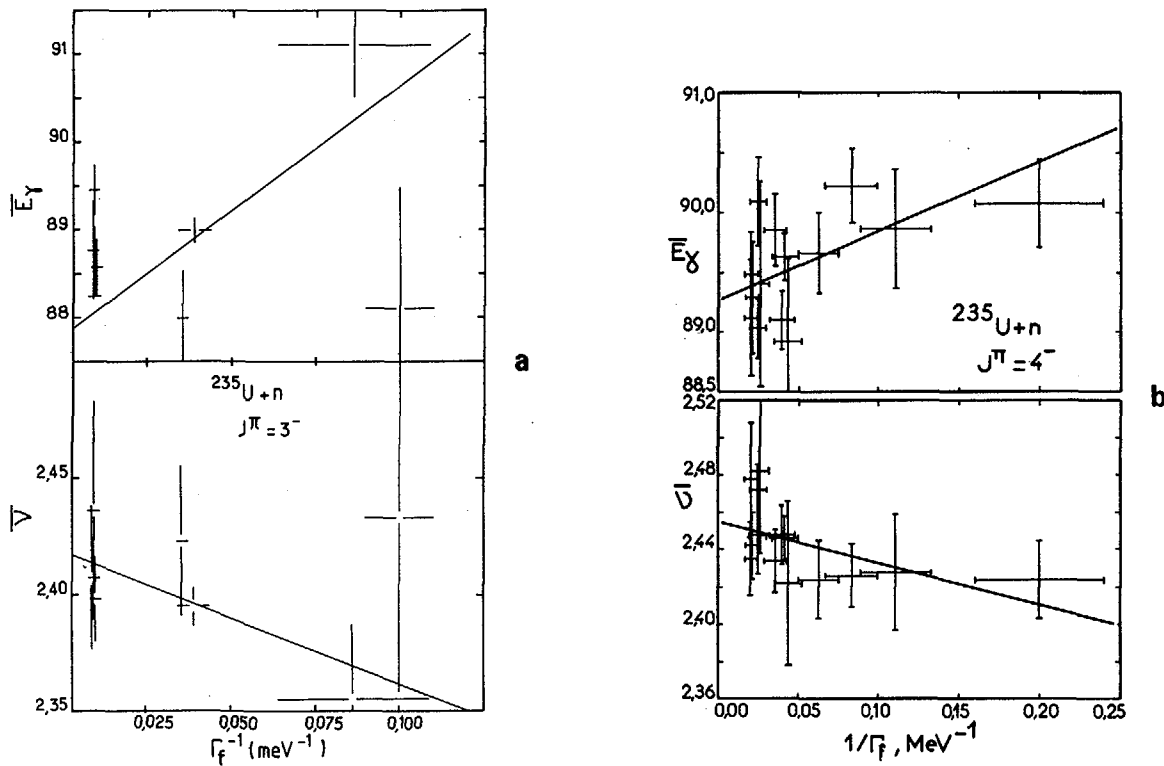
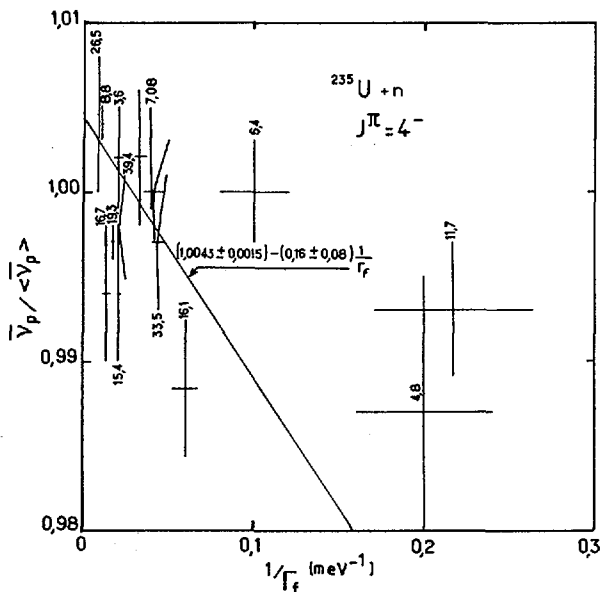


FIG. 7. a) Variations de  $\bar{E}_\gamma$  et de  $\bar{\nu}_p$  en fonction de  $1/\Gamma_f$  pour les résonances  $3^-$  de  $^{235}\text{U}$  (d'après [22]). b) Idem pour les résonances  $4^-$ .



**FIG. 8.** Variations de  $\bar{v}_p$  en fonction de  $1/\Gamma_f$  pour les résonances de  $^{235}\text{U}$  (d'après [24]). L'énergie de la résonance (en eV) est indiquée à côté de la valeur correspondante.

et de l'énergie  $\bar{E}_\gamma$ . Malheureusement, elles ne fournissent que la valeur du produit  $\Gamma_{Yf} \cdot e_{Yf}$  pour chaque état de spin. Un calcul est donc nécessaire pour déterminer chacun de ces paramètres. Un tel travail a été effectué dans différents laboratoires [2,26,27,28] mais les résultats obtenus sont assez dispersés à cause des différences dans les paramètres et les formalismes utilisés.

### 6.1. Formulation générale

Dans la formulation qui suit, on suppose le noyau composé formé dans un état d'énergie  $S_n$  et de spin et parité  $J''$ . Après une transition  $\gamma$  de nature  $\lambda$  et d'énergie  $E_\gamma$ , il se trouve dans un nouvel état d'énergie  $E^* = S_n - E_\gamma$ , de spin et parité  $J'^\pi$  définis par les règles usuelles de sélection.

Dans le cas de l'émission d'un seul rayon  $\gamma$  de pré-fission, la largeur  $\Gamma_{\gamma f}$  a pour expression :

$$r_{\gamma f} = \int_0^U P(E_\gamma) dE_\gamma \quad (5)$$

avec  $U = E^* - \Delta$  où  $\Delta$  est l'énergie d'appariement.

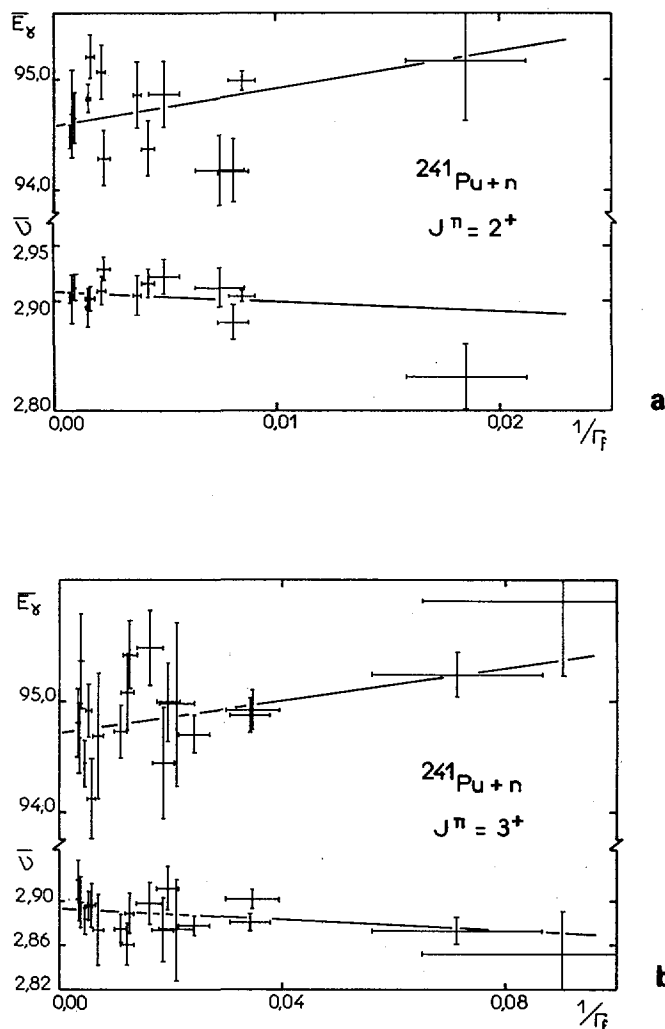


FIG. 9. a) Variations de  $\bar{E}_\gamma$  et de  $\bar{V}_p$  en fonction de  $1/\Gamma_f$  pour les résonances  $2^+$  de  $^{241}\text{Pu}$  (d'après [22]). b) Idem pour les résonances  $3^+$ .

$P(E_\gamma)$  est la probabilité d'observer un rayon  $\gamma$  d'énergie  $E_\gamma$  et a pour expression :

$$P(E_\gamma) = \frac{1}{\rho(Sn, j)} \sum_{\lambda} \sum_{J'=J-1}^{J+1} k_{ij}^{\lambda} \rho(E^*, J') F \frac{\langle \Gamma_f \rangle (E^*, J' \pi')}{\Gamma_\gamma(E^*) + \langle \Gamma_f \rangle (E^*, J' \pi')} \quad (6)$$

Dans cette expression :

$\rho(E^*, J)$  : densité des niveaux de spin  $J$  à l'énergie  $E^*$

$k_{ij}^{\lambda}$  : fonction densité de capture radiative pour un noyau passant d'un état  $i$  vers un état  $j$  par une transition  $\lambda$

$F$  : coefficient tenant compte des fluctuations statistiques. Il peut être calculé analytiquement [22, 26]

$\langle \Gamma_f \rangle (E^*, J' \pi')$  : largeur moyenne de fission d'un état de spin et parité  $J'$   $\pi'$  et d'énergie  $E^*$

$\Gamma_\gamma(E^*)$  : largeur radiative à l'énergie  $E^*$

Les largeurs de fission  $\langle \Gamma_f \rangle_{\alpha}$  d'une voie  $\alpha$  sont déduites de la pénétrabilité  $T_f^{\alpha}$  de la barrière de fission correspondante par la relation de BOHR et WHEELER. Mais les paramètres des barrières choisis pour ce calcul sont eux-mêmes déterminés à partir de réactions de fission avec des particules chargées [32, 34, 35] ou par réaction  $(\gamma, f)$  [36] et varient sensiblement suivant ces réactions ou le formalisme utilisé pour l'analyse. Il en résulte une dispersion importante des largeurs  $\langle \Gamma_f \rangle_{\alpha}$  calculées.

Suivant le formalisme utilisé pour le calcul de l'élément matrice qui donne la probabilité de transition,  $k_{ij}^{\lambda}$  suit une loi en  $E_\gamma^3$  (loi de WEISSKOPF) ou en forme de résonance géante. Or, nous ne disposons d'aucune donnée expérimentale pour trancher dans la gamme d'énergie qui nous intéresse ( $0 < E < 3$  MeV).

Les largeurs  $\Gamma_{\gamma f}$  étant particulièrement sensibles aux variations des différents paramètres utilisés, nous avons effectué ce calcul seulement pour les valeurs moyennes  $\bar{\epsilon}_{\gamma f}$  du spectre en énergie des rayons  $\gamma$  de pré-fission.

## 6.2. Calcul de $\bar{\epsilon}_{\gamma f}$ et résultats

La fonction densité  $k_{ij}^{\lambda}$  utilisée suit une loi en forme de résonance géante  $E_1$  [30] et  $M_1$  [31] dont le rapport vaut  $k_{ij}^{E_1}/k_{ij}^{M_1} = 6,8 \pm 2,1$  [29].

TABLEAU II. CALCUL DE  $\bar{e}_{\gamma f}$ , VALEUR MOYENNE DU SPECTRE EN ENERGIE DES RAYONS  $\gamma$  DE PREFISSION. LES PARAMETRES DES BARRIERES DE FISSION UTILISES SONT DONNES DANS LA PREMIERE PARTIE DE CE TABLEAU. LES PARAMETRES DE LA RESONANCE GEANTE E1 DE LA PROBABILITE DE TRANSITION  $\gamma$  PROVIENNENT DE LA REF.[30]

	$E_A$ (MeV)	$E_B$ (MeV)	$\hbar w_A$ (MeV)	$\hbar w_B$ (MeV)	$E_0^-$ (MeV)	$E_1^-$ (MeV)	$E_2^+$ (MeV)	réf.	$E1/M1^{J1}$	$\bar{e}_{\gamma f}$ (MeV)	$E1/M1^{J2}$	$\bar{e}_{\gamma f}$ (MeV)
$^{239}\text{Pu}$	5,80	5,45	0,82	0,60	0,6	0,7	0,4	[33]	~ 3000	0,850	3	0,756
	6,10	5,60	1,10	0,75	0,15	0,85	0,7	[35]	~ 5000	1,040	4,5	1,032
	6,10	5,60	1,15	0,8	0,15	0,65	0,7		~ 5000	1,150	7	1,136
$^{235}\text{U}$									0 <sup>+</sup>		1 <sup>+</sup>	
	5,70	5,68	0,9	0,5	0,15	0,45	0,18	[33]	43	0,795	16	0,757
	6,20	6,10	1,1	0,85	0,26	0,45	0,38	[35]	60	0,835	20	0,788
$^{241}\text{Pu}$									65	0,920	25	0,847
	5,60	5,63	0,82	0,59	0,5	0,8	0,25	[33]	2 <sup>+</sup>		3 <sup>+</sup>	
	5,60	5,70	1,1	0,75	0,25	0,85	0,60	[35]	8	0,760	2	0,720
									9	0,830	2,5	0,820

TABLEAU III. CARACTERISTIQUES DE LA REACTION ( $n, \gamma f$ ) DANS LES RESONANCES DE  $^{239}\text{Pu}$ ,  $^{235}\text{U}$  ET  $^{241}\text{Pu}$  (VOIR LE TEXTE). LES BARRES D'ERREURS ASSOCIEES AUX ENERGIES  $\bar{e}_{\gamma f}$  CALCULEES PROVIENNENT D'UNE ESTIMATION FAITE A PARTIR DE TESTS DE LA SENSIBILITE AUX PARAMETRES UTILISES

noyau cible	$J\pi$	$\Gamma_{\gamma f} \cdot \bar{e}_{\gamma f}$ (eV <sup>2</sup> )	$\bar{e}_{\gamma f}$ (keV)	$\Gamma_{\gamma f}$ (meV)
$^{239}\text{Pu}$	$0^+$	$8000 \pm 1900$	$1100 \pm 50$	$7,3 \pm 1,8$
	$1^+$	$4600 \pm 300$	$1080 \pm 50$	$4,2 \pm 0,4$
$^{235}\text{U}$	$3^-$	$4020 \pm 2030$	$850 \pm 50$	$4,7 \pm 2,3$
	$4^-$	$1730 \pm 590$	$800 \pm 50$	$2,1 \pm 0,7$
$^{241}\text{Pu}$	$2^+$	$6982 \pm 3819$	$800 \pm 100$	$8,7 \pm 4,9$
	$3^+$	$1714 \pm 664$	$800 \pm 100$	$2,1 \pm 0,8$

La pénétrabilité des barrières de fission à deux bosses a été déterminée par une méthode d'analyse numérique [37] voisine de celle utilisée par BACK [32]. Un potentiel imaginaire simule l'amortissement des états vibrationnels de classe II par les états intrinsèques. Il a été ajusté de façon à reproduire la largeur des résonances à 4,5 et 5,0 MeV de  $^{240}\text{Pu}^*$ .

Les résultats sont portés dans le tableau II avec les paramètres des barrières de fission utilisés.

a) Cas de  $^{239}\text{Pu}$

Les résultats pour l'état de spin  $1^+$  constituent un bon test de cohérence des paramètres car la limite supérieure de la largeur  $\Gamma_{\gamma f}$  est connue (voir 2e chapitre). Dans l'hypothèse où  $\Gamma_{\gamma f} < 5$  meV, on déduit des valeurs du tableau I :  $\bar{e}_{\gamma f} > 860$  keV. Il apparaît que la valeur de  $\bar{e}_{\gamma f}$  calculée avec les barrières déterminées par BACK à partir de la réaction ( $t, pf$ ) [38] est trop faible.

Les paramètres utilisés par GOLDSTONE pour ajuster la section efficace  $^{239}\text{Pu}(d, pf)$  donnent de bien meilleurs résultats car l'état de transition  $K'' = 0^-$  a été abaissé et placé à 150 keV seulement au dessus de l'état fondamental [35]. Compte tenu des imprécisions, on déduit de ce jeu de paramètres les valeurs de  $\Gamma_{\gamma f}$  données dans le tableau III.

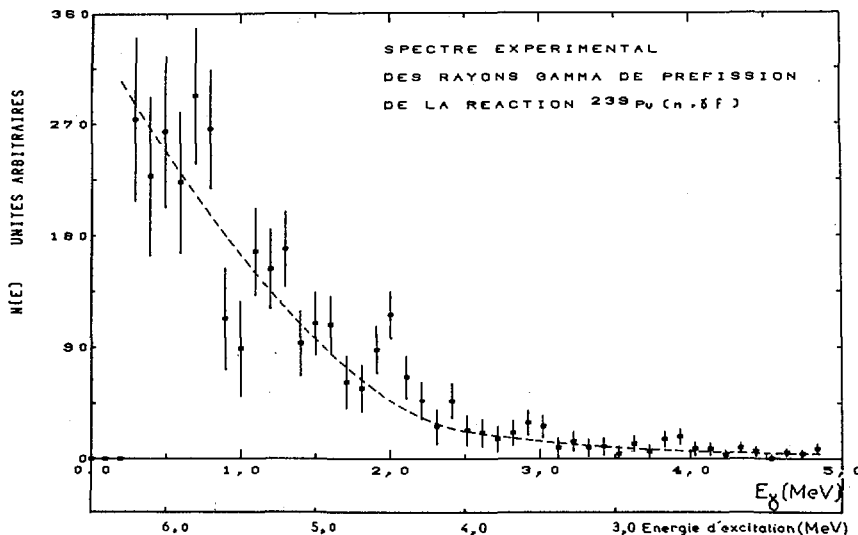


FIG.10. Spectre expérimental brut des rayons  $\gamma$  de pré-fission de la réaction  $^{239}\text{Pu}(n,\gamma f)$  (d'après [38]).

#### b) Cas de $^{235}\text{U}$ et $^{241}\text{Pu}$

La valeur moyenne  $\bar{\epsilon}_{\gamma f}$  obtenue est sensiblement plus faible pour ces deux noyaux. Les valeurs de  $\Gamma_{\gamma f}$  qui en sont déduites sont également données dans le tableau III.

#### 7. ETUDE DU SPECTRE DES RAYONS $\gamma$ DE PRE-FISSION

Par l'intermédiaire de la réaction  $(n,\gamma f)$ , il est possible d'étudier la fission d'un noyau à une énergie d'excitation inférieure à l'énergie de liaison d'un neutron. En particulier, il peut être possible d'observer ainsi des états vibrationnels dans le second puits de la barrière de fission.

Malheureusement, cette mesure est extrêmement difficile à réaliser par la détection directe du rayonnement  $\gamma$  à cause de la fission directe qui masque le phénomène, des rayons  $\gamma$  de fission qui s'ajoutent au rayonnement de pré-fission et du bruit de fond de rayons  $\gamma$  détectés par effet Compton. Une tentative a néanmoins été faite sur la résonance à 44,48 eV de  $^{239}\text{Pu}$  ( $\Gamma_f = 4 \pm 1 \text{ meV}$ ) dont on a comparé le spectre des rayons  $\gamma$  émis en coïncidence avec la fission à celui des résonances de "fission directe" pure [38].

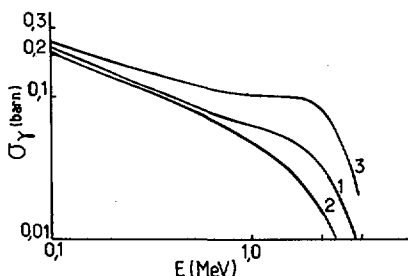


FIG.11. Section efficace de capture radiative de  $^{239}\text{Pu}$  calculée en fonction de l'énergie des neutrons incidents (d'après [28]):

- 1 – en prenant en compte les réactions  $(n, \gamma f)$  et  $(n, \gamma n')$ ; la probabilité de transition  $\gamma$  utilisée suit la résonance géante dipolaire électrique;
- 2 – de même mais en utilisant une probabilité de transition  $\gamma$  suivant la loi en  $E_\gamma^3$ ;
- 3 – sans prendre en compte la réaction  $(n, \gamma f)$ ; la probabilité de transition  $\gamma$  est la même qu'en 1.

Les résultats sont donnés sur la fig. 10 : après une région continue principalement due aux rayons  $\gamma$  détectés par effet Compton, une résonance se dégage vers  $E_\gamma = 2$  MeV (soit  $E^* = (4,52 \pm 0,05$  MeV). Le spin de la résonance à  $E_n = 44,48$  eV étant  $J = 1^+$ , l'état observé est très probablement  $J = 1^-$  ou  $2^-$ . Le nombre quantique  $K$  associé est donc  $K = 0$  ou  $1$ .

Ce résultat est en bon accord avec ceux de la mesure de GOLDSTONE [35] qui par l'intermédiaire de la réaction  $(d, pf)$  observe différentes résonances dont une à 4,70 MeV attribuée  $K = 0^-$ . Le décalage en énergie peut être un effet de normalisation en énergie des deux expériences.

#### CONCLUSION

Le processus  $(n, \gamma f)$  résulte de la compétition entre les différentes voies de sortie lors de la désexcitation d'un noyau composé. Il ne peut être décelé expérimentalement que par ses effets secondaires : effets électroniques ou effets liés aux propriétés du nouvel état dans lequel se trouve le noyau composé après émission d'un rayonnement  $\gamma$ . Ainsi, le nombre  $\bar{n}_p$  de neutrons prompts de fission décroît tandis que l'énergie et la multiplicité des rayons  $\gamma$  émis par fission augmentent. Cependant, quelle que soit la grandeur mesurée, seule la proportion  $\Gamma_{\gamma f}/\Gamma_f$  de cette grandeur pourra être détectée (voir équations 1,2,3).

TABLEAU IV. DIMINUTION  $\Delta\alpha/\alpha$  DE LA VALEUR DE  $\alpha$  DE  $^{239}\text{Pu}$  DUE A LA REACTION  $(n, \gamma f)$  POUR QUELQUES ENERGIES DE NEUTRONS INCIDENTS

énergie $E_n$	thermique	1 keV	30–40 keV	100 keV	300 keV	500 keV	700–800 keV
$\Delta\alpha/\alpha$ réf. [26]	15%	15%	15%	20%		28%	35%
$\Delta\alpha/\alpha$ réf. [28]		15%	10%		20%		50%

Dans la région des résonances la réaction  $(n, \gamma f)$  est en moyenne un processus secondaire par rapport à la fission directe. Mais, par le hasard des fluctuations statistiques de PORTER et THOMAS, quelques résonances ont une largeur  $\Gamma_f$  beaucoup plus faible que les autres. La réaction  $(n, \gamma f)$  dont la largeur  $\Gamma_{\gamma f}$  est constante pour les résonances de même spin, peut alors devenir le processus dominant. C'est ainsi qu'elle a pu être mise en évidence.

Le cas le plus favorable est constitué par les résonances  $1^+$  de  $^{239}\text{Pu}$ . Il est illustré par la fig. 3.

La situation n'est pas aussi claire pour les autres noyaux étudiés mais cependant tous les résultats expérimentaux présentent les effets de la réaction  $(n, \gamma f)$ . Ainsi, les valeurs du produit  $\Gamma_{\gamma f} \cdot \bar{e}_{\gamma f}$  ont pu être déterminés pour les deux états de spin initiaux de chaque noyau, grâce aux mesures du nombre de neutrons et de l'énergie des rayons  $\gamma$  de fission (voir tableau I).

En l'absence de détermination directe de la largeur  $\Gamma_{\gamma f}$ , nous avons été conduits à déterminer cette grandeur en combinant les produits expérimentaux  $\Gamma_{\gamma f} \cdot \bar{e}_{\gamma f}$  et les valeurs calculées de l'énergie  $\bar{e}_{\gamma f}$ . Les largeurs obtenues (voir tableau III) sont en très bon accord avec les prédictions de LYNN basées sur un calcul avec des barrières de fission à une bosse [2].

Le calcul fait aussi ressortir la très grande sensibilité de la réaction  $(n, \gamma f)$  à la position de certains états de transition (par exemple les états  $K^\pi = 0^-$  et  $1^-$  dans le cas des noyaux composés  $^{240}\text{Pu}$  et  $^{242}\text{Pu}$ ).

Les résultats présentés ici apportent donc des éléments importants pour la détermination des paramètres des barrières de fission correspondantes.

Maintenant, il serait très intéressant de pouvoir mesurer le spectre des rayons  $\gamma$  de pré-fission au moins partiellement. Cela permettrait d'estimer la probabilité de transition  $\gamma$  à très basse énergie et de tester la pénétrabilité des barrières de fission en fonction de l'énergie.

Enfin, il faut remarquer que si la contribution de la réaction  $(n, \gamma f)$  dans les résonances est faible, elle peut devenir à plus haute énergie très importante par rapport à la capture radiative. Ainsi, après LYNN [2] et LECOQ [26], différents auteurs [28] ont montré qu'il faut prendre cette réaction en considération pour le calcul de la section efficace de capture radiative  $\sigma_\gamma$  et du nombre  $\alpha = \sigma_\gamma / \sigma_f$ , rapport des sections efficaces de capture et de fission. La fig. 11 et le tableau IV illustrent cet effet qui peut être extrêmement important.

## REFERENCES

- [1] STAVINSKY, V., SHAKER, M.O., Nucl. Phys. 62 (1965) 667.
- [2] LYNN, J.E., Phys. Lett. 18 (1965) 31.
- [3] SHACKLETON, D., TROCHON, J., LEBARS, M., FREHAUT, J., Phys. Lett. 42B (1972) 344.
- [4] DERRIEN, H., Thèse de Doctorat, Paris (1974), non publiée.
- [5] LYNN, J.E., The Theory of Neutron Resonances Reactions, Clarendon Press, Oxford (1968) 432–450.
- [6] BOWMAN, C., AUCHAMPAUGH, G.F., STUBBINS, W.F., YOUNG, T.E., SIMPSON, F.B., MOORE, M.S., Phys. Rev. Lett. 18 (1967) 15.
- [7] BLONS, J., DERRIEN, H., C.R. Conf. nationale soviétique sur la physique du neutron, Kiev, II (1967) 263.
- [8] DLOUHY, Z., KRISTIÁK, J., PANTELEEV, T.S., Czech. J. Phys. B26 (1976) 1334.
- [9] DERRIEN, H., BLONS, J., EGGERMAN, C., MICHAUDON, A., PAYA, D., RIBON, P., «Sections efficaces totale et de fission du  $^{239}\text{Pu}$  – Etude statistique des paramètres de résonances», Nuclear Data for Reactors (C.R. Conf. Paris, 1966), AIEA, Vienne, II (1967) 195.
- [10] TROCHON, J., DERRIEN, H., LUCAS, B., MICHAUDON, A., «Détermination du spin des résistances induites par des neutrons lents dans le plutonium-239», Nuclear Data for Reactors, (C.R. Conf. Helsinki, 1970), AIEA, Vienne, I (1970) 495.
- [11] SOLEILHAC, M., FREHAUT, J., GAURIAU, J., J. Nucl. Energy 23 (1969) 495.
- [12] WESTON, L.W., TODD, J.H., Proc. Conf. on Neutron Cross Sections and Technology, Knoxville, II (1971) 861.
- [13] RYABOV, Yu., Réunion internationale sur la structure nucléaire, Doubna, URSS, Contribution 88.
- [14] WEINSTEIN, S., REED, R., BLOCK, R.C., «Neutron multiplicity measurements for  $^{233}\text{U}$ ,  $^{235}\text{U}$  and  $^{239}\text{Pu}$  resonance fission», Physics and Chemistry of Fission (C.R. Coll. Vienne, 1969), AIEA, Vienne (1969) 477.

- [15] WESTON, L.W., TODD, J.M., Phys. Rev. **C10** (1974) 1402.
- [16] FREHAUT, J., SHACKLETON, D., «Mesure du nombre moyen de neutrons prompts et de l'énergie moyenne des rayons gamma prompts émis lors de la fission induite par neutrons de résonance dans  $^{235}\text{U}$  et  $^{239}\text{Pu}$ », Physics and Chemistry of Fission 1973 (C.R. Coll. Rochester, New York, 1973), AIEA, Vienne, II (1974) 201.
- [17] SHACKLETON, D., Thèse de Doctorat, Paris (1974) non publiée.
- [18] FREHAUT, J., MOSINSKI, G., SOLEILHAC, M., Rapport EANDC (E) 154 "U" (1973).
- [19] RYABOV, Yu., TROCHON, J., SHACKLETON, D., FREHAUT, J., Nucl. Phys. **A216** (1973) 395.
- [20] MOORE, M.S., MOSES, J.D., KEYWORTH, G.A., DABBS, J.W.T., HILL, Phys. Rev. **C18** (1978) 1328.
- [21] PANTELEEV, T., RYABOV, Yu., TSAN SAN KMAK, BORUKHOVICH, G.Z., PETROV, G.A., TETEREV, E.N., Phys. Lett. **35B** (1971) 507.
- [22] SIMON, G., Thèse de Doctorat, Paris (1975), non publiée.
- [23] REED, R.L., HOCKENBURY, R.W., BLOCK, R.C., Rapport COO 3058-29 (RPI) III (1972).
- [24] HOWE, R.E., PHILIPS, T.W., BOWMAN, C.D., Phys. Rev. **C13** (1976) 195.
- [25] BLONS, J., DEBRIL, G., FERMANDJIAN, J., MICHAUDON, A., «Mesure et analyse des sections efficaces de fission de l'uranium-235 et du plutonium-241», Nuclear Data for Reactors (C.R. Conf. Helsinki, 1970), AIEA, Vienne, I (1970) 469.
- [26] LECOQ, G., Thèse de Doctorat, Paris (1967) non publiée.
- [27] TROCHON, J., PRANAL, Y., SIMON, G., SÜKOŠD, C., Conférence nationale soviétique sur la physique du neutron, Kiev (1975)
- [28] SUKHOVITSKIJ, E.S., KLEPATSKIJ, A.B., KON'SHIN, V.A., ANTSIPOV, G.V., Conférence nationale soviétique sur la physique du neutron, Kiev, n° 77-3806.
- [29] BOLLINGER, L.M., THOMAS, G.E., Phys. Rev. **C6** (1972) 1322.
- [30] VEYSSIERE, A., BEIL, H., BERGERE, R., CARLOS, P., LEPRETRE, A., Nucl. Phys. **A199** (1973) 45.
- [31] HANNA, S.S., C.R. Ecole internationale sur les réactions électro- et photonucléaires et leurs applications, Erice, Italie (1976), non publié.
- [32] BACK, B.B., BONDORF, J.P., OSTROCHENKO, G.A., PEDERSEN, J., RASMUSSEN, B., Nucl. Phys. **A165** (1971) 449.
- [33] BACK, B.B., BRITT, H.C., HANSEN, O., LEROUX, B., GARETT, J.D., Phys. Rev. **C10** (1974) 1948.
- [34] GLÄSSEL, P., RÖSLER, H., SPECHT, M.J., Nucl. Phys. **A265** (1976) 220.
- [35] GOLDSTONE, P.D., HOPKINS, F., MALMIN, R.E., PAUL, P., Phys. Rev. **18C** (1978) 1706.
- [36] VANDENBOSCH, R., Phys. Lett. **45B** (1973) 207.
- [37] THOMET, P., Rapport CEA-R-4631 (1974).
- [38] TROCHON, J., Thèse de Doctorat, Paris (1978), non publiée.
- [39] LACHKAR, J., PATIN, Y., SIGAUD, J., J. Phys. Lett. **36** (1975) 79.

## DISCUSSION

J.P. THEOBALD: What is the smallest resonance fission width  $\Gamma_f$  that you have measured?

J. TROCHON: The smallest fission we have measured is  $\Gamma_f = (4 \pm 1)$  meV for some  $1^+$  resonances of  $^{239}\text{Pu}$ .

C.M.C. WAGEMANS: In support of the experimental data you have shown us, I would like to report that we have observed a small ( $n, \gamma f$ ) effect on the average kinetic values for the  $^{239}\text{Pu}$  ( $n, f$ ) resonances, which I will describe in a paper I am going to present later (see SM-241/F7 in these Proceedings). This point is illustrated by Fig.A, which shows a linear least-square fit to the  $\bar{E}_k^*$  data

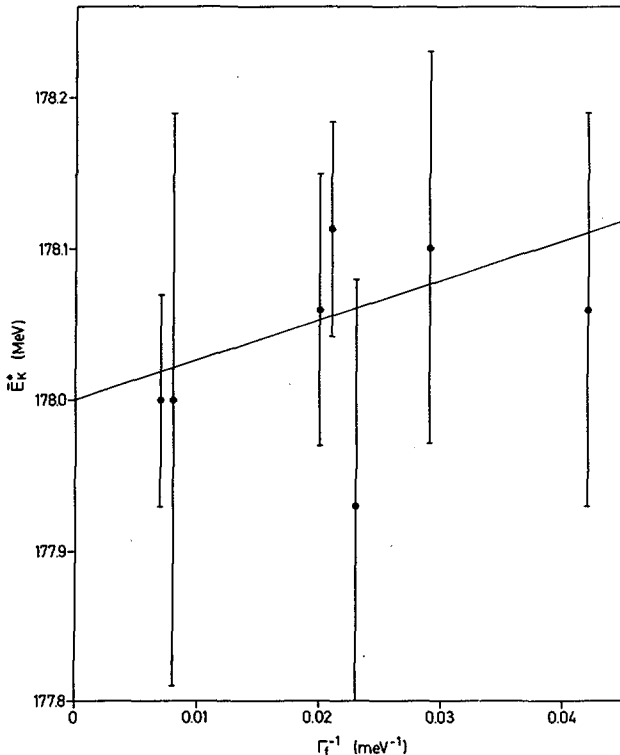


FIG.A.  $\bar{E}_k^*$  versus  $\Gamma_f^{-1}$ .

as a function of  $\Gamma_f^{-1}$  for the  $1^+$  resonances. The slope is slightly positive, as might be expected in the presence of a ( $n, \gamma f$ ) effect.

J.W. BOLDEMAN: For the neutron fission of  $^{239}\text{Pu}$  near thermal energies the fission cross-section is dominated by two resonances — an  $0^+$  resonance at negative neutron energy, and the  $1^+$  resonance at 0.296 eV. In this energy region very accurate  $\bar{\nu}_p$  measurements have been made showing excellent agreement. They can be analysed to obtain the difference  $\bar{\nu}_p(0^+) - \bar{\nu}_p(1^+)$  of 0.060 neutrons following the removal of ( $n, \gamma f$ ) process effects. In other words, strong channel effects are observed in this case. On the other hand, from the analysis of the resonance fluctuations at higher neutron energies a difference of

approximately 0.014 neutrons has been determined, i.e. there is an absence of channel effects. Can you comment on this discrepancy and say to what extent it might effect your analysis?

J. TROCHON: Yes, a difference has been found between the  $\bar{\nu}_p$  for the  $0^+$  and  $1^+$  resonances in the very-low-energy neutron-induced fission of  $^{239}\text{Pu}$ , corroborated by the measurement of the fission-fragment kinetic energy.

Alternatively, extrapolation to  $1/\Gamma_f = 0$  of the Saclay data for  $\bar{\nu}_p$  and  $\bar{E}_\gamma$  yields a small value for the difference in the average fission fragment excitation energy for  $0^+$  and  $1^+$  resonances ( $\Delta E_{\text{frag},0^+}^* - \Delta E_{\text{frag},1^+}^* \approx (100 \pm 50)$  keV). The Saclay measurement, however, did not include the very low-neutron energy region.

I would like to make two comments in this connection. First, as already mentioned, for the three strongest fission resonances in  $^{235}\text{U}$ ,  $\bar{\nu}_p$  fluctuations have been observed that do not correlate with any known fission characteristic. The  $1^+$  resonance in  $^{239}\text{Pu}$  at 0.296 eV is perhaps an example of this.

Second, this phenomenon does not affect the method of deducing the presence of the  $(n, \gamma f)$  reaction. The linear dependence with opposite signs for the  $\bar{\nu}_p$  and  $\bar{E}_\gamma$  values with  $1/\Gamma_f$  is the real indication of this reaction. Variation in  $\bar{\nu}_p$  simply shifts the absolute magnitude of the slope of the linear dependence. This dependence is very clearly observed in the  $1^+$  resonances of  $^{239}\text{Pu}$ .

# НЕСОХРАНЕНИЕ ЧЕТНОСТИ ПРИ ДЕЛЕНИИ ЯДЕР $^{234}\text{U}$ , $^{236}\text{U}$ И $^{240}\text{Pu}$

Г.В.ДАНИЛЯН, Б.Д.ВОДЕННИКОВ, В.П.ДРОНЯЕВ,  
Б.В.НОВИЦКИЙ, В.С.ПАВЛОВ, С.П.БОРОВЛЕВ

Институт теоретической и экспериментальной физики,  
Москва,  
Союз Советских Социалистических Республик

## Abstract—Аннотация

### NON-CONSERVATION OF PARITY IN FISSION OF $^{234}\text{U}$ , $^{236}\text{U}$ AND $^{240}\text{Pu}$ NUCLEI.

A study was made of the P-odd angular correlation  $W(\theta) = \text{const} (1 + a \vec{\sigma} \cdot \vec{P})$  between the direction of emission of a light (or, where appropriate, a heavy) fragment  $\vec{P}$  and the direction of polarization of a nucleus  $\vec{\sigma}$  in the fission of  $^{233}\text{U}$ ,  $^{235}\text{U}$  and  $^{239}\text{Pu}$  nuclei by polarized thermal neutrons. Targets, which contained approximately  $100 \mu\text{g} \cdot \text{cm}^{-2}$  fissionable material placed on both sides of an aluminium backing and were 0.1–0.15 mm wide, were arranged in a vacuum chamber along the axis of the neutron beam. Silicon surface-barrier detectors were arranged on each side of the target to detect fission fragments emitted by the target either in the direction of neutron polarization or away from it, depending on the direction of neutron-beam polarization at the moment of fragment detection. The direction of polarization could be reversed once per second; however, it was reversed not regularly but stochastically. An electronic circuit separated out pulses from light and heavy fragments and channelled them into scaling circuits corresponding to the two opposing directions of polarization. After each measurement cycle a computer connected on line with the experiment calculated the asymmetry in the number of light and heavy fragments counted by a given detector when the direction of neutron beam polarization was reversed. The measurement cycle lasted approximately 17 min, during which time the direction of polarization was reversed on average approximately 600 times. Measurements on a polarized beam alternated with measurements on a depolarized beam. Control measurements excluded the possibility of instruments affecting the results. After averaging of independent measurements, introduction of corrections for the polar solid angle of fragment detection and expression of results in terms of 100% neutron polarization, the following asymmetry coefficients were found:

$$a(^{234}\text{U}) = (2.8 \pm 0.3) \times 10^{-4}; \quad a(^{236}\text{U}) = (1.7 \pm 0.4) \times 10^{-4}; \quad a(^{240}\text{Pu}) = (-4.8 \pm 0.8) \times 10^{-4}.$$

The positive sign of asymmetry signifies that a light fragment is emitted preferentially in the direction of spin of a neutron captured by a nucleus.

### НЕСОХРАНЕНИЕ ЧЕТНОСТИ ПРИ ДЕЛЕНИИ ЯДЕР $^{234}\text{U}$ , $^{236}\text{U}$ И $^{240}\text{Pu}$ .

Исследовалась Р-нечетная угловая корреляция  $W(\theta) = \text{const} (1 + a \vec{\sigma} \cdot \vec{P})$  между направлением вылета легкого (или, соответственно, тяжелого) осколка,  $\vec{P}$ , и направлением поляризации ядра,  $\vec{\sigma}$ , при делении ядер  $^{233}\text{U}$ ,  $^{235}\text{U}$  и  $^{239}\text{Pu}$  поляризованными тепловыми нейтронами. Мишени, содержащие примерно по  $100 \mu\text{г}/\text{см}^2$  делящегося вещества, нанесенного на обе стороны алюминиевой подложки, толщиной 0,1–0,15 мм, располагались в вакуумированной камере вдоль оси пучка нейтронов.

нов. По обе стороны от мишени располагались кремниевые поверхностно-барьерные детекторы, регистрировавшие осколки деления, вылетевшие из мишени либо по направлению поляризации нейтронов, либо против, в зависимости от направления поляризации пучка нейтронов в момент регистрации осколка. Направление поляризации могло реверсироваться ежесекундно, однако реверс осуществлялся не периодически, а стохастически. Электронная схема выделяла импульсы от легких и тяжелых осколков и направляла их в пересчетные схемы, соответствующие двум противоположным направлениям поляризации. Электронно-вычислительная машина, подключенная в линию с экспериментом, после каждого цикла измерений вычисляла асимметрию счета легких и тяжелых осколков данным детектором при реверсировании направления поляризации пучка нейтронов. Цикл измерений продолжался примерно 17 мин, в течение которых происходило в среднем около 600 реверсов направления поляризации. Измерения на поляризованном пучке чередовались с измерениями на деполяризованном. Контрольные измерения исключали возможные аппаратурные эффекты. После усреднения независимых результатов измерений, внесения поправок на конечный телесный угол регистрации осколков и приведения результатов к 100%-ной поляризации нейтронов, получены следующие значения для коэффициентов асимметрии:

$$a(^{234}\text{U}) = (2,8 \pm 0,3) \cdot 10^{-4}; \quad a(^{236}\text{U}) = (1,7 \pm 0,4) \cdot 10^{-4}; \quad a(^{240}\text{Pu}) = (-4,8 \pm 0,8) \cdot 10^{-4}.$$

Положительный знак асимметрии означает, что легкий осколок преимущественно вылетает по направлению спина захваченного ядром нейтрона.

## 1. ВВЕДЕНИЕ

Гипотеза универсального слабого взаимодействия [1] предсказала существование слабого межнуклонного потенциала. Отношение его к сильному потенциальному в ядре может быть порядка  $G/\hbar c \bar{r}^2 \approx 10^{-7}$ , где  $G$  – константа слабого взаимодействия,  $\bar{r}$  – среднее расстояние между нуклонами в ядре. Часть этого потенциала нарушает четность и, следовательно, наличие его в гамильтониане ядра приводит к смешиванию ядерных состояний с одним и тем же полным моментом, но противоположной четностью. Вследствие этого в различных ядерных процессах должны проявляться Р-нечетные эффекты. Такие эффекты действительно наблюдались. В работе [2] впервые наблюдалась асимметрия излучения  $\gamma$ -квантов относительно направления поляризации ядер. Другой Р-нечетный эффект – циркулярную поляризацию  $\gamma$ -квантов, излучаемых неполяризованными ядрами, обнаружили в работе [3]. Сообщалось также о наблюдении запрещенного по четности  $\alpha$ -распада [4]. Наиболее надежные результаты получены в экспериментах со сложными ядрами, количественная интерпретация которых затруднена из-за незнания структуры ядер. Но такие данные могут оказаться полезными именно для понимания структуры ядра и механизмов протекания ядерных реакций. Благоприятным обстоятельством здесь является то, что Р-нечетные эффекты в сложных ядрах усилены по сравнению с аналогичными эффектами в NN-взаимодействиях на несколько порядков величины.

В этой связи нам представлялось интересным исследовать несохранение четности в процессе деления ядер. Впервые на такую возможность обращалось внимание в работе [5], в которой предполагалось исследовать корреляцию вида

$$W(\theta) = \text{Const} (1 + a \vec{\sigma} \vec{P}) \sim 1 + a \cos \theta \quad (1)$$

между направлением вылета легкого (или, соответственно, тяжелого) осколка  $\vec{P}$ , и направлением поляризации ядра  $\vec{\sigma}$  при спонтанном делении поляризованных ядер. Авторы ожидали, что в благоприятном случае возможно значительное усиление наблюдаемого эффекта из-за зависимости барьера деления от четности. В работе [6] рассмотрено усиление для случая двухгорбого барьера. В этом случае фактор усиления может содержать резонансный член, если имеет место случайное перекрытие уровней противоположной четности соответственно в первой и второй ямах. При надбарьерном делении таких ядер, как  $^{233}\text{U}$ ,  $^{235}\text{U}$ ,  $^{239}\text{Pu}$ , тепловыми нейтронами, можно ожидать значительное усиление, обусловленное высокой плотностью уровней компаунд-ядра [7]. По крайней мере, именно этим фактором можно объяснить наблюдавшиеся Р-нечетные эффекты в  $(n, \gamma)$ -реакциях [8-10]. В отличие от  $(n, \gamma)$ -процесса, где определяющей, вероятно, является стадия образования компаунд-ядра, в процессе деления есть еще две стадии – до седловой точки и от седловой точки до точки разрыва, на каждой из которых может происходить перемешивание состояний противоположной четности с соответствующими факторами усиления [11].

Корреляция вида (1) в принципе может возникнуть вследствие интерференции амплитуд переходов из состояний основной и примесной четности в определенное конечное состояние.

Действительно, законы сохранения полного момента и четности в процессе деления требуют выполнения равенств:

$$\vec{I}_C = \vec{I}_L + \vec{I}_T + \vec{L} \equiv \vec{F} + \vec{L} \quad (2)$$

$$\Pi_C = (-1)^L \Pi_L \Pi_T \quad (\text{все } L \text{ одинаковой четности}) \quad (3)$$

где  $I_C$ ,  $I_L$  и  $I_T$  – спины компаунд-ядра, легкого и тяжелого осколков, соответственно,  $L$  – орбитальный момент двух осколков,  $\Pi_C$ ,  $\Pi_L$ ,  $\Pi_T$  – внутренние четности компаунд-ядра, легкого и тяжелого осколков, соответственно.

Если в равенстве (3)  $\Pi_C$  – неопределенное, то в рассматриваемом процессе разрешены как четные, так и нечетные значения орбитального момента. Интерференция амплитуд с  $L$  и  $L'$ , равными  $\pm 1$ ;  $\pm 3$ ;  $\pm 5$  и т.д. (с ограничениями, накладываемыми значениями  $L$ , и центробежным барьером), приводит к корреляции (1) для определенного конечного состояния ( $\Pi_L^{\pm}$ ,  $\Pi_T^{\pm}$ ). Коэффициент асимметрии определяется выражением

$$a(I_L^{\Pi_L}, I_T^{\Pi_T}) = \sum_{I_C, F, K, L, L'} B(I_C) C(I_C K; I_L I_T F L L') b_L b_{L'}^* \quad (4)$$

где  $B(I_C)$  – мера поляризации компаунд-ядра, образованного при захвате поляризованного нейтрона

$$B(I_C) = \pm \left( \frac{I_C}{3(I_C + 1)} \right)^{1/2} \frac{I_C + 1}{I_i + \frac{1}{2}} P_n \quad (\text{знак } \pm \text{ для } I_C = I_i \pm \frac{1}{2}) \quad (5)$$

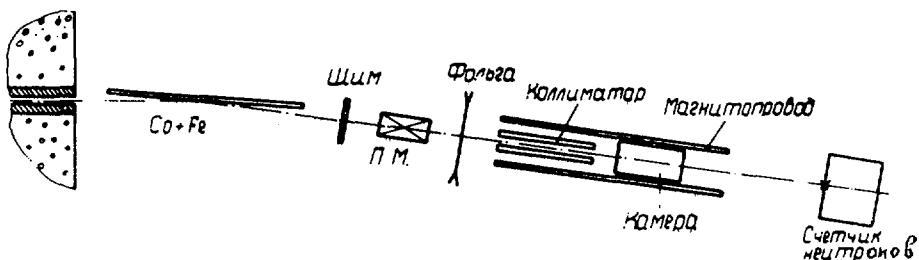


Рис. 1. Схема экспериментальной установки.

где  $I_i$  — спин ядра мишени,  $P_n$  — степень поляризации пучка нейtronов,  $F$  — спин канала,  $K$  — проекция полного момента ядра на ось разлета осколков,  $C(I_C K; I_D I_T F L' L)$  — геометрический коэффициент,  $b_L$  и  $b_{L'}$  — амплитуды переходов в данное конечное состояние из состояний основной и примесной четности.

Для околобарьерного деления можно ожидать, что число членов суммы в (4) невелико, и коэффициент асимметрии в какой-то мере будет характеризовать примесь состояния противоположной четности в состоянии, через которое происходит деление. Однако, выделить определенное конечное состояние в делении практически невозможно, и, следовательно, в любом случае, коэффициент асимметрии будет определяться суммой по некоторому (априори, неизвестному) числу конечных состояний

$$\bar{a} = \sum_{I_D I_T} a(I_D^{\Pi_D} I_T^{\Pi_T}) \quad (6)$$

В методическом отношении эксперимент по измерению Р-нечетной асимметрии в делении имеет определенные преимущества перед другими подобными экспериментами. Во-первых, специфика деления позволяет одновременно измерять асимметрию как для "частицы", так и для "ядра отдачи", причем коэффициенты асимметрии для них должны быть одинаковы по модулю и иметь противоположные знаки. Это — важный контроль достоверности результата. Во-вторых, легкие и тяжелые осколки достаточно хорошо разрешаются и нет обычной для таких экспериментов проблемы перекрытия "линий". И, наконец, что не менее важно, полностью отсутствует проблема фона. Следовательно, измерения Р-нечетной асимметрии в делении могут быть выполнены с достаточно высокой точностью.

## 2. ЭКСПЕРИМЕНТАЛЬНАЯ УСТАНОВКА

На рис. 1 показана схема установки. Коллимированный пучок нейtronов из горизонтального канала тяжеловодного реактора ИТЭФ падал на намагниченное до насыщения кобальтовое зеркало под углом  $6,5'$ . Отраженный поляризованный пучок

тепловых нейтронов (вектор поляризации которого перпендикулярен плоскости рисунка) проходил через устройство, управляющее поляризацией, вновь коллимировался и падал на мишень. На участке от управляющего устройства до мишени пучок пропускался между полюсами "магнитопровода" в слабом постоянном магнитном поле с целью предотвратить деполяризацию пучка "блуждающими" магнитными полями.

Устройство управления поляризацией включало в себя деполяризующий "шум", поворотный магнит и "фольгу". "Шум", представляющий собой прокатанную железную пластину толщиной 0,3 мм, периодически перекрывал пучок нейтронов на участке между зеркалом-поляризатором и поворотным магнитом, благодаря чему пучок нейтронов деполяризовался. Поворотный магнит создавал магнитное поле, в котором вектор поляризации пучка мог адиабатически поворачиваться на угол  $\pm 90^\circ$  вокруг оси пучка, так, что направление поляризации нейтронов оказывалось параллельным или антипараллельным направлению магнитного поля в магнитопроводе. Для предотвращения адиабатического поворота спина в области между поворотным магнитом и магнитопроводом при антипараллельной ориентации создаваемых ими полей в соответствующем месте перпендикулярно к пучку располагалась "фольга", представляющая собой плоскую раму с натянутыми параллельно друг другу тонкими проволоками (диаметром 0,33 мм), по которым пропускался ток в одном направлении при антипараллельной ориентации "сшиваемых" полей. Благодаря тому, что создаваемое "фольгой" поле меняло знак на расстоянии менее 1 мм, происходил неадиабатический переход и спины нейтронов после "фольги" оказывались ориентированными антипараллельно ведущему полю. Как показали измерения, эффективность "фольги" оказалась равной  $0,98 \pm 0,02$ , т.е. степень поляризации пучка нейтронов при реверсировании практически не изменялась. Степень поляризации пучка периодически измерялась с использованием зеркала-анализатора, которое устанавливалось за мишенью. Усредненное по многим сериям измерений значение поляризации оказалось равным  $0,84 \pm 0,04$ . При введении "шима" в пучок поляризация падала примерно на порядок и не превышала 8%. Плотность потока поляризованных нейтронов на мишени составляла  $3 \cdot 10^6$  н/( $\text{см}^2 \text{с}$ ). Интенсивность пучка нейтронов постоянно мониторировалась нейтронным счетчиком с  $\text{BF}_3$ , расположенным на расстоянии 5 м от мишени.

Мишень состояла из пяти алюминиевых дисков диаметром 30 мм, толщиной 0,1 мм (или 0,15 мм), на каждую из сторон которых был нанесен слой делящегося вещества толщиной, соответствующей примерно 100 мкг/см<sup>2</sup>. Метод изготовления мишеней обеспечивал достаточную однородность слоя по толщине. Мишень монтировалась в вакуумированной камере с тонкими входным и выходным окнами из майлара. Поперечное сечение пучка нейтронов было равным  $10 \times 100$  мм<sup>2</sup>. Камера устанавливалась так, что мишень располагалась вдоль пучка нейтронов, перпендикулярно оси поляризации. Использовались два варианта расположения кремниевых поверхностно-барьерных детекторов относительно мишени.

В первом варианте два детектора  $\phi 25$  мм располагались на расстоянии 15 мм по обе стороны от каждого диска, соосно с ним. Между каждым диском и детектором имелась диафрагма, выделявшая конечный телесный угол. Группы из пяти детекторов с каждой стороны от мишени были включены параллельно.

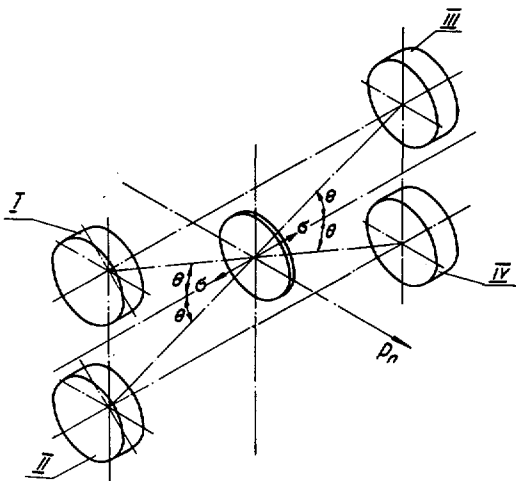


Рис. 2. Геометрия расположения мишени и детекторов относительно пучка нейтронов.

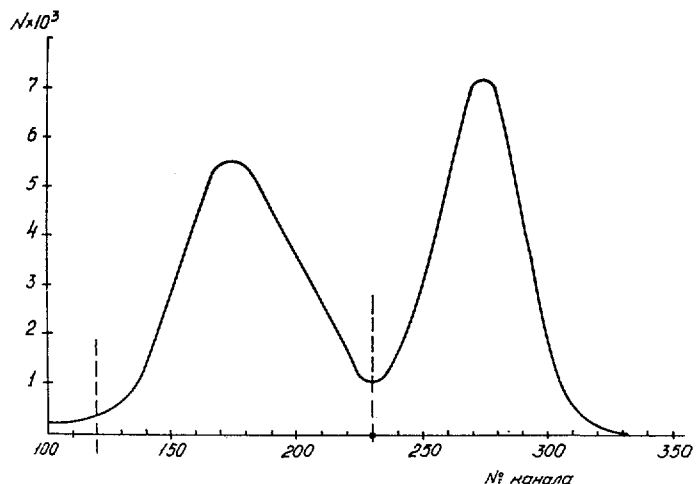


Рис. 3. Типичный амплитудный спектр импульсов от группы детекторов осколков деления  $^{236}U$ . Пунктиром показаны пороги дискриминаторов.

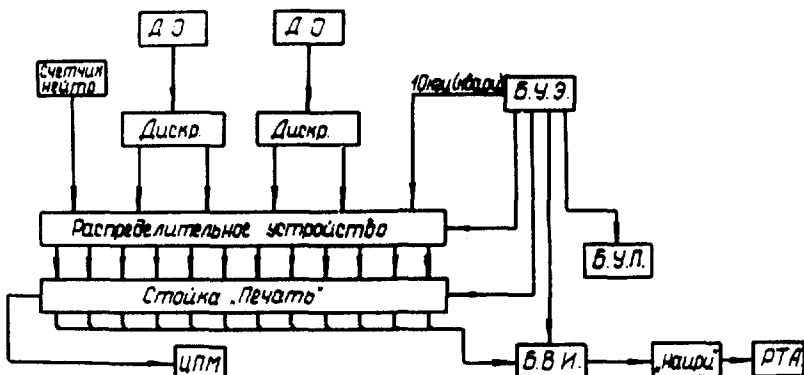


Рис. 4. Блок-схема электронной части установки: Д.О. – детектор осколков, Б.У.Э. – блок управления экспериментом, Б.У.П. – блок управления поляризацией нейтронов, Б.В.И. – блок вывода информации на ЭВМ, Ц.П.М. – цифропечатающая машина, Р.Т.А. – телетайп, стойка "Печать" – пересчетные схемы.

Во втором варианте (рис.2) детекторы (I-IV) смешены на  $\pm 11$  мм относительно плоскости, определяемой векторами  $\vec{d}$  (вектор поляризации пучка нейтронов) и  $\vec{P}_n$  (импульс нейтрона) и проходящей через центр мишени. Плоскость, в которой находились детекторы, отстояла от плоскости мишени на 13 мм. Средний угол между направлением поляризации пучка нейтронов и направлением вылета регистрируемого осколка составлял  $\sim 40^\circ$ . Как и в первом варианте, пять дисков располагались вдоль пучка нейтронов. Диафрагма между детекторами и мишенью исключала попадание осколков, вылетавших из одной мишени, на детекторы соседней мишени. Все детекторы, смешенные относительно мишени в одном направлении, были включены параллельно. На рис.3 показан типичный амплитудный спектр осколков деления  $^{235}\text{U}$ , зарегистрированных группой детекторов. Левый пик соответствует тяжелым осколкам, правый – легким. Импульсы от легких осколков выделялись интегральным дискриминатором, от тяжелых – дифференциальным. Сформированные импульсы поступали на вход распределительного устройства (см. рис.4), которое направляло их в разные группы пересчетных схем в зависимости от направления поляризации пучка нейтронов в момент поступления импульса. Направление поляризации пучка могло реверсироваться ежесекундно, однако реверс осуществлялся не периодически, а стохастически, чтобы избежать приборной асимметрии, обусловленной изменением интенсивности нейтронного потока или дрейфом характеристик электронной аппаратуры. На время переходных процессов при реверсировании поляризации (0,03 с) распределительное устройство блокировалось. На распределительное устройство были заведены также импульсы от нейтронного счетчика и импульсы от кварцевого генератора тактовой частоты. Коррелированный счет последних позволял определять суммарное время измененияй с одним и с другим направлением поляризации с точностью, лучшей чем  $10^{-6}$ .

ТАБЛИЦА I. КОЭФФИЦЕНТЫ АСИММЕТРИИ  
СЧЕТА ДЕТЕКТОРАМИ 1 И 2 ГРУПП ЛЕГКИХ (Л)  
И ТЯЖЕЛЫХ (Т) ОСКОЛКОВ ПРИ ДЕЛЕНИИ  $^{235}\text{U}$   
ПОЛЯРИЗОВАННЫМИ ТЕПЛОВЫМИ НЕЙТРОНАМИ.  
n – АСИММЕТРИЯ СЧЕТА НЕЙТРОНОВ  
МОНИТОРНЫМ СЧЕТЧИКОМ

j	K	$a_{jk} \cdot 10^{-4}$	
		$P_n = 0,84$	$P_n = 0,08$
1	Т	$0,89 \pm 0,34$	$-0,09 \pm 0,31$
	Л	$-0,77 \pm 0,35$	$0,47 \pm 0,38$
2	Т	$-0,59 \pm 0,39$	$-0,04 \pm 0,45$
	Л	$0,83 \pm 0,47$	$-0,65 \pm 0,42$
n		$-0,03 \pm 0,10$	$0,10 \pm 0,10$

Цикл измерений продолжался примерно 17 мин. За это время происходило в среднем около 600 реверсов направления поляризации пучка нейтронов. Измерения на поляризованном пучке чередовались с измерениями на деполяризованном пучке. Чтобы исключить возможную аппаратурную асимметрию, связанную с индивидуальными каналами регистрации, последние от цикла к циклу перекоммутировались также стохастически. После каждого цикла измерений информация с пересчетных схем через блок связи передавалась в электронно-вычислительную машину "Наира" (ЭВМ). Одновременно в ЭВМ передавался код данного измерения (поляризованный или деполяризованный пучок, связь каналов регистрации с направлением поляризации пучка). ЭВМ вычисляла величины

$$a_{jk} = \frac{\vec{n}_{jk} - \vec{n}'_{jk}}{\vec{n}_{jk} + \vec{n}'_{jk}} \quad (7)$$

где  $j$  – индекс группы детекторов,  $K = L, T$  – индекс группы легких или тяжелых осколков,  $\vec{n}, \vec{n}'$  – скорость счета осколков данной группы детекторов при определенном в пространстве направлении поляризации пучка нейтронов.

Все измеряемые величины и вычисленные по ним значения коэффициентов асимметрии пропечатывались телетайпом. Через каждые 10 циклов ЭВМ вычисляла средневзвешенные значения коэффициентов асимметрий и их среднеквадратичные ошибки. В обработку не включались значения асимметрий, выходящие за 5 стандартных отклонений. Такие события пропечатывались в виде условного символа и анализировались нами. Суммарное число их не превышало 1%, и лишь 0,06% таких событий не сопровождалось явной ошибкой при передаче информации в ЭВМ.

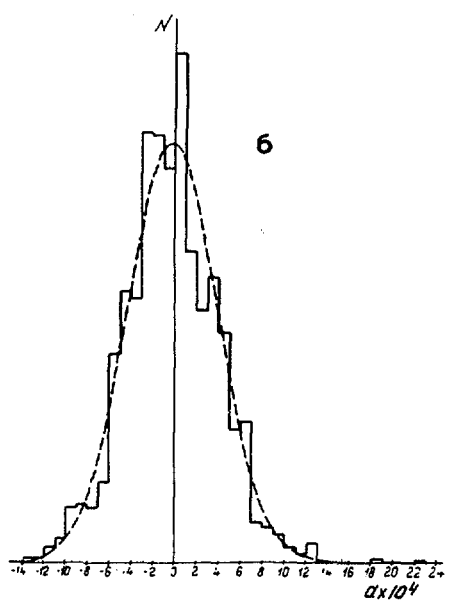
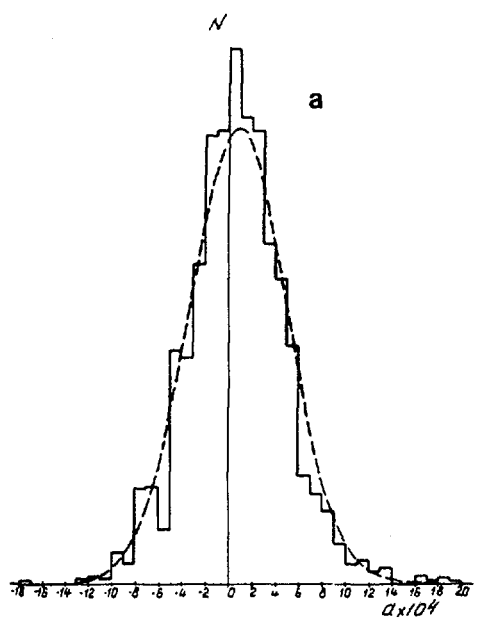


Рис. 5. Распределение коэффициентов асимметрии: а – в измерениях на поляризованном пучке (10131 значение), б – в измерениях на деполяризованном пучке (9826 значений).

ТАБЛИЦА II. КОЭФФИЦИЕНТЫ АСИММЕТРИИ  
СЧЕТА ОСКОЛОКОВ ДЕЛЕНИЯ  $^{236}\text{U}$  ДЕТЕКТО-  
РАМИ I-IV, УСРЕДНЕННЫЕ ПО ГРУППАМ  
ЛЕГКИХ И ТЯЖЕЛЫХ ОСКОЛОКОВ

j	$a_j \cdot 10^4$	j	$a_j \cdot 10^4$
I	$1,85 \pm 1,18$	III	$0,29 \pm 1,23$
II	$1,76 \pm 0,98$	IV	$-2,53 \pm 1,18$

### 2.1. Измерения асимметрии при делении $^{236}\text{U}$

Основные измерения с мишенью из окиси урана, обогащенного изотопом  $^{235}\text{U}$  до 75%, проводились в камере с геометрией варианта 1. Из двухчастичной кинематики деления и геометрии камеры следует, что должны иметь место равенства:

$$\bar{a}_{jT} = -\bar{a}_{jL}; \quad \bar{a}_{IK} = -\bar{a}_{2K} \quad (8)$$

если измеряемые величины обусловлены корреляцией (1).

Усредненные результаты измерений приведены в табл. I. В последней строчке приведены значения асимметрии счета нейтронов мониторным счетчиком.

Из таблицы видно, что действительно наблюдается ожидавшаяся корреляция знаков асимметрий в измерениях на поляризованном пучке ( $P_n = 0,84$ ). Однако статистическая точность результатов недостаточна, чтобы проверить соотношение (8) количественно.

Средневзвешенное значение коэффициентов асимметрий в измерениях на поляризованном пучке оказалось равным  $a' = (0,77 \pm 0,19) \cdot 10^{-4}$ , на деполяризованном —  $a'' = (-0,27 \pm 0,19) \cdot 10^{-4}$ .

На рис.5 показаны распределения измеренных значений коэффициентов асимметрии для поляризованного (рис.5а) и деполяризованного (рис.5б) пучков. Пунктирные кривые — гауссовые распределения с параметрами, определяемыми соответствующими средними значениями. Проверка по критерию Пирсона дала  $\chi^2 = 17,1$  при 17 степенях свободы ( $P = 0,454$ ).

Учитя остаточную поляризацию "деполяризованного" пучка получим:  
 $a = (1,15 \pm 0,34) \cdot 10^{-4}$ . Поправка на конечный телесный угол ( $\cos\theta = 0,9$ ) и приведение результата к 100%-ной поляризации пучка нейтронов дает  $a(^{236}\text{U}) = (1,50 \pm 0,44) \cdot 10^{-4}$ . Положительный знак коэффициента означает, что легкий осколок вылетает преимущественно по направлению спина захваченного нейтрона.

Проведенный нами анализ различных методических и физических факторов показал, что, вероятно, единственным "фоновым" эффектом может быть интерференция

S и P-резонансов при захвате ядром  $^{235}\text{U}$  поляризованных тепловых нейтронов. Угловое распределение осколков в этом случае может содержать член, пропорциональный

$$\vec{\sigma} [\vec{P}_n \vec{P}_f] \quad (9)$$

где  $\vec{\sigma}$  – единичный вектор в направлении спина нейтрона,  $\vec{P}_n$  и  $\vec{P}_f$  – единичные векторы в направлениях импульсов, соответственно нейтрона и легкого (или тяжелого) осколка.

Корреляция (9) приводит к лево-правой асимметрии, которая в ряде случаев может имитировать асимметрию вперед-назад по отношению к направлению поляризации пучка нейтронов. В условиях данного эксперимента такая ситуация может возникнуть, если имеется систематический сдвиг одной группы детекторов относительно мишени вверх, а другой группы – вниз. Хотя оценки показали, что этот эффект не может превышать величину  $10^{-5}$  в использованной геометрии, тем не менее необходимо было убедиться в этом экспериментально. В камере с геометрией расположения детекторов варианта 2 (см. рис.2) созданы условия, при которых вклад от корреляции (9) для отдельных групп детекторов (I-IV) должен возрасти более, чем в 20 раз по сравнению с геометрией варианта 1, если в последнем предполагать наличие систематического перекоса на  $2-3^\circ$ , незаметного на глаз. Более того, если для P-нечетной корреляции  $\vec{\sigma} \vec{P}$  знаки асимметрий для групп детекторов I и II должны быть одинаковы и противоположны знакам для групп III и IV, то для P-четной корреляции (9) знаки для верхних групп детекторов I и III должны быть противоположны знакам для нижних – II и IV. Если в измеряемый эффект дают вклад обе корреляции, то в измерениях с геометрией 2 можно определить величину каждой из этих компонент.

В табл. II приведены результаты измерений асимметрии при делении  $^{235}\text{U}$  поляризованными нейтронами в геометрии 2, усредненные по группам легких и тяжелых осколков с учетом результатов измерений на деполяризованном пучке.

Здесь  $j$  – индекс группы детекторов (см. рис.2). Из этих данных видно, что наблюдаемая асимметрия не возросла в 20 раз (пропорционально  $\sin \theta$ ), а знаки эффектов соответствуют корреляции  $\vec{\sigma} \vec{P}$ , а не корреляции (9). Усреднение данных таблицы II с поправкой на конечный телесный угол ( $\cos \theta = 0,75$ ) и приведением к 100%-ной поляризации нейтронов, дает

$$a(^{236}\text{U}) = (2,5 \pm 1,0) \cdot 10^{-4} \quad (10)$$

что в пределах ошибок согласуется с результатом, полученным в измерениях с геометрией 1. Вклад корреляции (9) не превышает 4% от этой величины, т.е. пренебрежимо мал. Усреднение двух результатов для  $^{236}\text{U}$  приводит к значению:

$$a(^{236}\text{U}) = (1,7 \pm 0,4) \cdot 10^{-4} \quad (11)$$

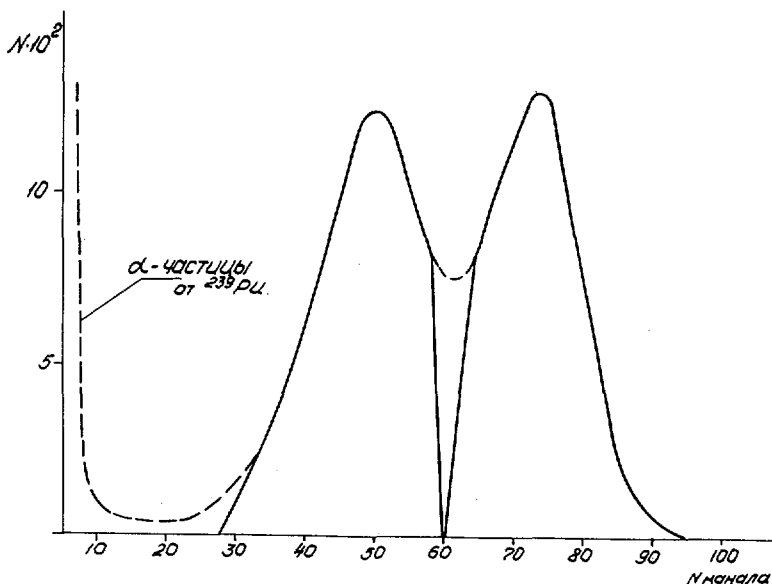


Рис. 6. Амплитудный спектр импульсов от группы детекторов осколков деления  $^{240}\text{Pu}$ .  
Сплошные кривые – участки спектров, выделяемые дискриминаторами.

ТАБЛИЦА III. КОЭФФИЦИЕНТЫ АСИММЕТРИИ СЧЕТА ЛЕГКИХ И ТЯЖЕЛЫХ  
ОСКОЛКОВ ДЕТЕКТОРАМИ I-IV ПРИ ДЕЛЕНИИ  $^{240}\text{Pu}$

j	K	$a_{jk} \cdot 10^4$		j	K	$a_{jk} \cdot 10^4$	
		$P_n = 0,84$	$P_n = 0,08$			$P_n = 0,84$	$P_n = 0,08$
I	Л	$4,17 \pm 0,81$	$1,96 \pm 0,82$	III	Л	$-3,87 \pm 1,16$	$-0,06 \pm 0,93$
	Т	$-3,66 \pm 0,73$	$-0,91 \pm 0,75$		Т	$2,68 \pm 1,05$	$1,89 \pm 0,90$
II	Л	$3,63 \pm 0,85$	$-0,09 \pm 0,66$	IV	Л	$-2,80 \pm 0,91$	$0,38 \pm 1,16$
	Т	$-3,34 \pm 0,80$	$0,74 \pm 0,84$		Т	$2,77 \pm 1,00$	$2,22 \pm 1,14$

ТАБЛИЦА IV. КОЭФФИЦИЕНТЫ АСИММЕТРИИ СЧЕТА ЛЕГКИХ И ТЯЖЕЛЫХ ОСКОЛКОВ ДЕЛЕНИЯ  $^{234}\text{U}$  В ЭНЕРГЕТИЧЕСКИХ ИНТЕРВАЛАХ I-IV

$P_n$	$a \cdot 10^4$			
	тяжелые осколки		легкие осколки	
	I	II	III	IV
0,84	$-2,07 \pm 0,31$	$-1,85 \pm 0,34$	$1,94 \pm 0,32$	$2,39 \pm 0,30$
0,08	$-0,14 \pm 0,35$	$-0,78 \pm 0,31$	$-0,16 \pm 0,35$	$0,06 \pm 0,32$

## 2.2. Измерения асимметрии при делении $^{239}\text{Pu}$

Измерения с мишенью из гидроокиси плутония проводились только в геометрии 2. На рис. 6 показан типичный амплитудный спектр осколков деления  $^{239}\text{Pu}$ , зарегистрированных группой детекторов (пунктир). Сплошные кривые – участки спектров, выделяемые дискриминаторами. Измерения на  $^{239}\text{Pu}$  велись круглосуточно в течение двух месяцев. В ходе эксперимента камера, как целое, периодически поворачивалась относительно оси, перпендикулярной к пучку, на  $180^\circ$ , чтобы дополнительно исключить эффекты, связанные с возможной несимметрией установки.

Результаты измерений приведены в табл. III. Из приведенных данных получаем

$$a(^{240}\text{Pu}) = (-3,1 \pm 0,5) \cdot 10^{-4} \quad (12)$$

Вклад корреляции (9) в асимметрию счета осколков в геометрии 2 равен  $(0,5 \pm 0,5) \cdot 10^{-4}$ . Поправка на конечный телесный угол регистрации осколков ( $\cos \theta = 0,75$ ) и приведение результата к 100%-ной поляризации нейтронов дает

$$a(^{240}\text{Pu}) = (-4,8 \pm 0,8) \cdot 10^{-4} \quad (13)$$

В эксперименте с плутониевой мишенью периодически, вместо регистрации осколков, регистрировались  $\alpha$ -частицы распада  $^{239}\text{Pu}$ . Дифференциальные дискриминаторы настраивались так, чтобы выделять небольшой участок спектра  $\alpha$ -частиц. Все звенья установки при этом функционировали так же, как и в основных измерениях Р-нечетной асимметрии. Поскольку  $\alpha$ -распад никак не связан с нейтронным пучком, то измеряемая асимметрия должна характеризовать приборную асимметрию, связанную с каналами регистрации.

Усредненное значение асимметрии оказалось равным

$$a_{\text{П}}(a) = (0,15 \pm 0,29) \cdot 10^{-4} \quad (14)$$

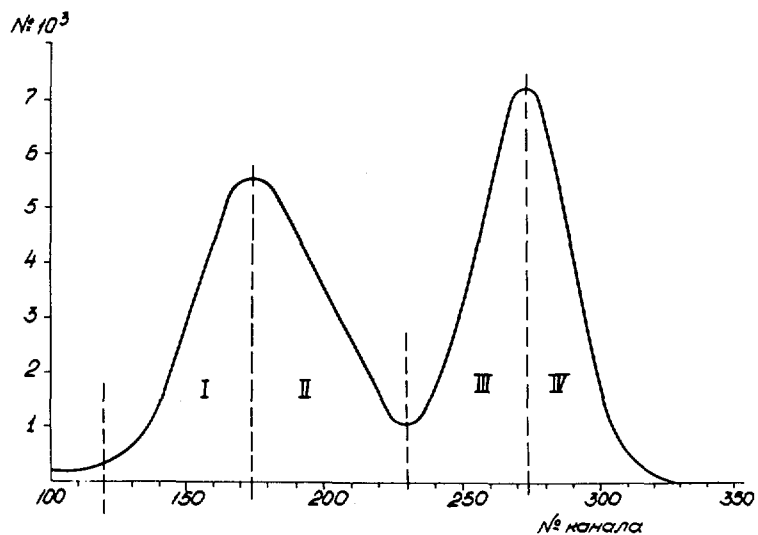


Рис. 7. Схема выделения амплитудных интервалов при делении  $^{234}U$ .

ТАБЛИЦА V. КОЭФФИЦИЕНТЫ  
Р-НЕЧЕТНОЙ АСИММЕТРИИ

Ядро-мишень	$I_i$	$a \cdot 10^4$
$^{239}\text{Pu}$	$\frac{1}{2}$	$-4,8 \pm 0,8$
$^{233}\text{U}$	$\frac{5}{2}$	$2,8 \pm 0,3$
$^{235}\text{U}$	$\frac{7}{2}$	$1,7 \pm 0,4$

Здесь важно отметить, что нижние пороги дифференциальных дискриминаторов устанавливались на крутом участке спектра  $\alpha$ -частиц, и, следовательно, полученный результат характеризует стабильность порогов и отсутствие корреляции между формой аппаратурного спектра частиц и реверсом направления поляризации нейтронов.

### 2.3. Измерение асимметрии при делении $^{233}\text{U}$

Измерения с мишенью из окиси  $^{233}\text{U}$  проводились как в геометрии 2, так и в геометрии 1. Измерения в геометрии 2 проводились лишь с целью выявить вклад корреляции (9) в асимметрию. Величина этого эффекта, так же как и для ядер  $^{235}\text{U}$  и  $^{239}\text{Pu}$ , оказалась в пределах ошибок измерений. С учетом этой неопределенности Р-нечетная асимметрия при делении  $^{233}\text{U}$  в этой серии измерений оказалась равной

$$a(^{234}\text{U}) = (3,6 \pm 1,0) \cdot 10^{-4} \quad (15)$$

Измерения в геометрии 1 были выполнены с большим числом мишеней и детекторов, чем в случае  $^{235}\text{U}$ , с тем, чтобы с достаточной статистической точностью определить коэффициенты асимметрий для каждого из интервалов (I-IV) амплитудного спектра осколков (см. рис. 7). Очевидно, что если нет аппаратурных эффектов, то коэффициенты асимметрий для интервалов III и IV должны быть одинаковы. Если это так, то отличие коэффициентов для интервалов I и II могло бы дать грубые указания о зависимости эффекта от массы осколка. Результаты измерений сведены в табл. IV. Незначительное отличие коэффициентов асимметрий для внутренних интервалов (II и III) по сравнению с внешними (I и IV) можно объяснить частичным перекрытием соответствующих максимумов.

Из этих данных можно сделать два вывода: первый — что наблюдаемая асимметрия не связана с аппаратурными эффектами, и второй — что, вероятно, нет существенной монотонной зависимости эффекта от массы осколка.

Средневзвешенное значение коэффициента асимметрии для ядра  $^{234}\text{U}$  по двум сериям измерений равно

$$a(^{234}\text{U}) = (2,8 \pm 0,3) \cdot 10^{-4} \quad (16)$$

## 3. РЕЗУЛЬТАТЫ И ИХ ОБСУЖДЕНИЕ

Измеренные коэффициенты асимметрии сведены в таблицу V. Приведенные значения не поправлены на фактор, определяющий степень поляризации компаунд-ядер, образованных при захвате поляризованных тепловых нейтронов. Сделать это невозможно, поскольку неизвестен вклад конкурирующих спиновых состояний  $I_i \pm 1/2$  в захват тепловых нейтронов. Как видно из формулы (5), поляризация компаунд-ядра в состояниях  $I_i \pm 1/2$  имеет противоположный знак. Более того, в общем случае вероятность процесса, сопровождающего захват тепловых нейтронов с переходом в данное конечное состояние, должна определяться когерентной суммой четырех амплитуд  $A(I_i + 1/2)^+, A(I_i - 1/2)^+, A(I_i + 1/2)^-, A(I_i - 1/2)^-$ , а величина Р-нечетной асимметрии — соответствующими интерференционными членами.

Тем не менее, обращает на себя внимание регулярная зависимость абсолютной величины измеренной асимметрии от значения спина ядра-мишени,  $I_1$ . Можно предположить, что указанная зависимость отражает лишь зависимость меры поляризации компаунд-ядра от спина ядра-мишени. Тогда, характерная величина асимметрии оказывается порядка  $(5-6) \cdot 10^{-4}$ , что совпадает с величинами Р-нечетных эффектов в  $(n, \gamma)$ -реакциях [8-10]. Если это совпадение не случайное, то можно сделать два вывода:

- a) механизм нарушения четности в процессах  $(n, \gamma)$  и  $(n, f)$  один и тот же, и, вероятно, определяется стадией образования компаунд-состояния;
- b) суммирование по конечным состояниям не нивелирует эффект.

Авторы благодарят И. В. Чувило, В. Г. Шевченко и М. С. Козодаева за постоянный интерес к работе, Л. Б. Окуня, Г. А. Лобова и Е. С. Ржевского за полезные дискуссии, В. А. Емельянова, Р. С. Зинатулина и А. И. Пономарева за помощь в измерениях.

#### ЛИТЕРАТУРА

- [1] FEYNMAN, R.P., GELL-MANN, M., Phys. Rev. 109 (1958) 193.
- [2] ABOV, Yu.G., KRUPCHITSKY, P.A., ORATOVSKY, Yu.A., Phys. Lett. 12 (1964) 25.
- [3] ЛОБАШОВ, В.М., НАЗАРЕНКО, В.А., САЕНКО, Л.Ф., СМОТРИЦКИЙ, Л.М. ХАРКЕВИЧ, Г.И., Письма в ЖЭТФ 3 (1966) 268.
- [4] NEUBECK, K., SCHOBEZ, H., WAFFLER, H., Phys. Rev. C10 (1974) 320.
- [5] ВЛАДИМИРСКИЙ, В.В., АНДРЕЕВ, В.Н., ЖЭТФ 41 (1961) 663.
- [6] BUDNIK, A.P., ROBOTNOV, N.S., Phys. Lett. 46B (1973) 155.
- [7] ШАПИРО, И.С., УФН 96 (1968) 647.
- [8] АБОВ, Ю.Г., ЕРМАКОВ, О.Н., КРУПЧИЦКИЙ, П.А., ЖЭТФ 16 (1973) 1738.
- [9] ДАНИЛЯН, Г.В., НОВИЦКИЙ, В.В., ПАВЛОВ, В.С., БОРОВЛЕВ, С.П., Письма в ЖЭТФ 26 (1976) 380.
- [10] BONKOULA, H., CAVAINAC, J.C., CHARVET, J.L., KAONG, D.H., VIGNON, B., WILSON, R., Phys. Lett. 71B (1977) 287.
- [11] РАБОТНОВ, Н.С., Ядерная физика 26 (1977) 1302.

**SPONTANEOUS FISSION AND FISSION BARRIERS**  
**(Session B)**

**Chairman**

**S.S. KAPOOR**

India

# ИССЛЕДОВАНИЕ СПОНТАННОГО ДЕЛЕНИЯ ИЗОТОПОВ НЕКОТОРЫХ ТЯЖЕЛЫХ ЭЛЕМЕНТОВ И ЗАКОНОМЕРНОСТЕЙ РЕАКЦИЙ СЛИЯНИЯ В ОБЛАСТИ СИЛЬНО ДЕЛЯЩИХСЯ КОМПАУНД-ЯДЕР

Ю.П.ОГАНЕСЯН, О.А.ОРЛОВА, Г.М.ТЕР-АКОПЬЯН,  
Ю.А.МУЗЫЧКА, А.А.ПЛЕВЕ, Б.И.ПУСТЫЛЬНИК,  
В.И.ЧЕЛИГИН, Г.Н.ФЛЕРОВ  
Объединенный институт ядерных исследований,  
Дубна,  
Союз Советских Социалистических Республик

## Abstract—Аннотация

### A STUDY OF SPONTANEOUS FISSION IN THE ISOTOPES OF SOME HEAVY ELEMENTS AND THE LAWS GOVERNING FUSION REACTIONS IN CONNECTION WITH INTENSELY FISSILE COMPOUND NUCLEI.

In the search for an explanation for the failure of many attempts to fuse superheavy elements in complete fusion reactions, fusion experiments on the 108th element are of interest. For this purpose the reactions  $^{207,208}\text{Pb} + ^{58}\text{Fe}$  and  $^{226}\text{Ra} + ^{48}\text{Ca}$  were used. The upper limits were found for the cross-sections of reactions which result in the formation of the following products which undergo spontaneous fission:  $\sigma < 2 \times 10^{-35} \text{ cm}^2$  for nuclei with  $T_{\frac{1}{2}}^{\text{SF}} \geq 0.1 \text{ ms}$  in  $^{207,208}\text{Pb} + ^{58}\text{Fe}$  reactions and  $\sigma < 3 \times 10^{-35} \text{ cm}^2$  for nuclei with  $T_{\frac{1}{2}}^{\text{SF}} \geq 1 \text{ ms}$  in the  $^{226}\text{Ra} + ^{48}\text{Ca}$  reactions. A search was also made for  $^{255}\text{Fm}$ , which is a daughter nucleus of the  $\alpha$ -decay chain of the isotope  $^{271}108$  formed in the reaction  $^{226}\text{Ra}(^{48}\text{Ca}, 3n)$ . The limit obtained is equal to  $\sigma < 10^{-34} \text{ cm}^2$  if the isotope  $^{271}108$  and its daughter nuclei undergo mainly  $\alpha$ -decay. Cross-sections of reactions of the (HI, xn) type were calculated by a method based on statistical examination of the de-excitation of a compound nucleus. The ALICE program was used with the incorporation of a few changes. A semi-empirical ratio for the dependence of the level density parameter on excitation energy and on the structure of nuclei was introduced. At all stages of the evaporation cascade except the last, liquid-drop fission barriers were used as a function of angular momentum. In the final stage they were replaced by a ground-state barrier incorporating shell corrections. Calculated cross-sections for evaporation reactions observed upon the irradiation of natural Tl,  $^{208}\text{Pb}$  and  $^{209}\text{Bi}$  with  $^{48}\text{Ca}$  ions agreed well with experimental values. At the same time, a similar calculation for the  $^{207,208}\text{Pb}(^{58}\text{Fe}, xn)$  and  $^{226}\text{Ra}(^{48}\text{Ca}, xn)$  reactions showed that the cross-sections expected for the formation of isotopes of the 108th element lay beyond the observed limits. Thus, the most plausible assumption is that these isotopes have short half-lives, as follows:  $T_{\frac{1}{2}}^{\text{SF}} < 0.1 \text{ ms}$  for  $^{263-265}108$  and  $T_{\frac{1}{2}}^{\text{SF}} < 1 \text{ ms}$  for  $^{271,272}108$ . The connection between the limits found and the systematics of  $T_{\frac{1}{2}}^{\text{SF}}$  for known atomic nuclei is discussed.

### ИССЛЕДОВАНИЕ СПОНТАННОГО ДЕЛЕНИЯ ИЗОТОПОВ НЕКОТОРЫХ ТЯЖЕЛЫХ ЭЛЕМЕНТОВ И ЗАКОНОМЕРНОСТЕЙ РЕАКЦИЙ СЛИЯНИЯ В ОБЛАСТИ СИЛЬНО ДЕЛЯЩИХСЯ КОМПАУНД-ЯДЕР.

Для выяснения причин многих неудачных попыток синтеза сверхтяжелых элементов в реакциях полного слияния представляют интерес эксперименты по синтезу 108-го элемента. С этой

целью использовались реакции  $^{207,208}\text{Pb} + ^{58}\text{Fe}$  и  $^{226}\text{Ra} + ^{48}\text{Ca}$ . Были получены верхние пределы поперечных сечений реакций, приводящих к спонтанно делящимся продуктам:  $\sigma < 2 \cdot 10^{-35} \text{ см}^2$  для ядер с  $T_{1/2}^{\text{SF}} \geq 0,1 \text{ мс}$  в реакциях  $^{207,208}\text{Pb} + ^{58}\text{Fe}$  и  $\sigma < 3 \cdot 10^{-35} \text{ см}^2$  для ядер  $T_{1/2}^{\text{SF}} \geq 1 \text{ мс}$  в реакции  $^{226}\text{Ra} + ^{48}\text{Ca}$ . Велся также поиск  $^{255}\text{Fm}$ —дочернего ядра цепочки  $\alpha$ -распада изотопа  $^{271}108$ , образующегося в реакции  $^{226}\text{Ra}$  ( $^{48}\text{Ca}, 3\text{n}$ ). Получен предел, равный  $\sigma < 10^{-34} \text{ см}^2$ , если изотоп  $^{271}108$  и его дочерние ядра испытывают главным образом  $\alpha$ -распад. Поперечные сечения реакций типа (HI, xn) рассчитывались по методу, основанному на статистическом рассмотрении деваизбуждения компаунд-ядра. Применялась программа ALICE, которую были внесены некоторые изменения. Было введено полуэмпирическое соотношение для зависимости параметра плотности уровней от энергии возбуждения и структуры ядер. На всех ступенях испарительного каскада, кроме последней, использовались жидкокапельные барьеры деления, зависящие от углового момента. На последней ступени они заменялись барьером для основного состояния, учитывающим оболочечные поправки. Расчет поперечных сечений испарительных реакций, наблюдавшихся при облучении  $^{eCT}\text{Tl}$ ,  $^{208}\text{Pb}$  и  $^{209}\text{Bi}$  ионами  $^{48}\text{Ca}$ , дал хорошее согласие с экспериментом. В то же время аналогичный расчет для реакций  $^{207,208}\text{Pb}$  ( $^{58}\text{Fe}$ , xn) и  $^{226}\text{Ra}$  ( $^{48}\text{Ca}$ , xn) показал, что ожидаемые поперечные сечения для образования изотопов 108-го элемента выше установленных пределов. Поэтому наиболее вероятным является предположение, что эти изотопы имеют короткие периоды полураспада:  $T_{1/2}^{\text{SF}} < 0,1 \text{ мс}$  для  $^{263-265}108$  и  $T_{1/2}^{\text{SF}} < 1 \text{ мс}$  для  $^{271,272}108$ . Обсуждается связь полученных пределов с систематикой  $T_{1/2}^{\text{SF}}$  для известных атомных ядер.

## 1. ВВЕДЕНИЕ

Многочисленные эксперименты, проведенные с целью синтеза сверхтяжелых элементов в реакциях полного слияния с бомбардирующими тяжелыми ионами с  $A \geq 40$  (см., например, [1, 2]), не внесли пока ясность в проблему существования гипотетических нуклидов в новой области стабильности. К сожалению, положение не изменилось после того, как в Дубне и Беркли были получены достаточно интенсивные пучки ускоренных ионов  $^{48}\text{Ca}$  и был выполнен ряд работ по синтезу сверхтяжелых элементов [3-7] с применением этой бомбардирующей частицы. Оба возможных объяснения: слишком короткие времена жизни синтезируемых изотопов или очень малые поперечные сечения реакций, требуют дополнительного изучения. Поэтому представляет интерес исследование стабильности ядер с  $Z \geq 100$  и закономерностей их образования в реакциях слияния с тяжелыми ионами.

Времена жизни этих ядер в отношении  $\alpha$ - и  $\beta$ -распада, включая и область сверхтяжелых элементов, могут быть предсказаны достаточно точно. В то же время теоретические предсказания периодов полураспада для спонтанного деления неизвестных изотопов могут различаться на 3-4 порядка величины в области, непосредственно примыкающей к известным ядрам, а разница в предсказаниях для сверхтяжелых ядер достигает 10 и более порядков. Поэтому представляет интерес получение данных о спонтанном делении новых изотопов.

Систематика известных  $T_{1/2}^{\text{SF}}$  (см. рис. 1) отражает влияние оболочечной структуры на стабильность ядер. Однако, в противоположность изотопам Cf, Fm и 102-го

элемента, для которых проявляется стабилизирующий эффект подоболочки  $N = 152$ , у изотопов  $\text{Ku}$  ( $Z = 104$ ) этот эффект практически отсутствует [8, 9] и наблюдается монотонный рост  $T_{1/2}^{\text{SF}}$  с увеличением числа нейтронов. Можно ожидать, что для более тяжелых элементов также будет наблюдаться рост  $T_{1/2}^{\text{SF}}$  с увеличением  $N$  без выраженного максимума при  $N = 152$ . Это предположение находит подтверждение в соответствующих теоретических расчетах [10, 11], а также в результатах изучения спонтанного деления изотопов  $^{259}\text{Ra}$  [12] и  $^{263}\text{Ra}$  [13].

Важным промежуточным этапом при переходе от указанных изотопов к сверхтяжелым элементам был бы синтез 108-го элемента. С этой целью нами использовались реакции  $^{226}\text{Ra} + ^{48}\text{Ca}$  и  $^{208}\text{Pb} + ^{58}\text{Fe}$ . Эксперименты проводились на внутреннем пучке циклотрона У-300 Объединенного института ядерных исследований (ОИЯИ).

## 2. ЭКСПЕРИМЕНТЫ ПО СИНТЕЗУ ИЗОТОПОВ 108-ГО ЭЛЕМЕНТА

### 2.1. Реакция $^{226}\text{Ra} + ^{48}\text{Ca}$

В этой реакции минимальная энергия возбуждения компаунд-ядра  $E_{\min}^*$  составляет 32 МэВ, поэтому каналы с испарением 2-4-х нейтронов являются наиболее вероятными. В реакции Зп должен получаться нечетный изотоп  $^{271}\text{Ra}$ , для которого можно сделать приближенную оценку  $T_{1/2}^{\text{SF}}$ , используя результаты теоретических расчетов в наиболее близкой области. Согласно работам [10, 11], следует ожидать для этого изотопа период полураспада порядка 10 с. В то же время, если проэкстраполировать результаты расчетов работы [14] в область  $Z = 108$ , значения получаются на 2-3 порядка величины ниже.

Для оценки периода полураспада в отношении к  $\alpha$ -распаду мы воспользовались полуэмпирической формулой [15] и массовой формулой [16]. Полученные оценочные значения  $T_{1/2}^{\text{SF}}$  и  $T_{1/2}^\alpha$  для изотопа  $^{271}\text{Ra}$  и возможных продуктов его  $\alpha$ -распада показаны на рис. 2. Видно, что согласно оценкам, по всей цепочке распада  $T_{1/2}^\alpha < T_{1/2}^{\text{SF}}$ . Простые оценки периодов полураспада для электронного захвата показывают, что этот вид распада для рассматриваемых изотопов маловероятен.

Как следует из рис. 2, целесообразно попытаться зарегистрировать на опыте  $^{255}\text{Fm}$  ( $T_{1/2} = 20,1$  ч,  $E_\alpha = 7,01$  МэВ), как продукт распада  $^{271}\text{Ra}$ . Однако, нельзя исключить и другую возможность, а именно, что изотоп  $^{271}\text{Ra}$  или некоторые продукты его распада испытывают главным образом спонтанное деление. Поэтому схема эксперимента предусматривала возможность наблюдения как  $^{255}\text{Fm}$ , так и регистрацию коротковивущих спонтанно делящихся нуклидов.

В опыте использовалась тонкая мишень ( $0,6 \text{ mg/cm}^2 \text{ RaF}_2$  на подложке из Ni,  $0,9 \text{ mg/cm}^2$ ) и вращающийся сборник в виде Al-фольги (6 мкм), переносящий ядра отдачи к слюдяным трековым детекторам осколков деления за время, равное 1 мс. После облучений продолжительностью по 20 часов Al-сборник подвергался химической переработке и из него выделялась фракция Fm, которая очищалась от примесей Ra, Ac, Th, способных дать фон в районе пика  $\alpha$ -частиц  $^{255}\text{Fm}$ .

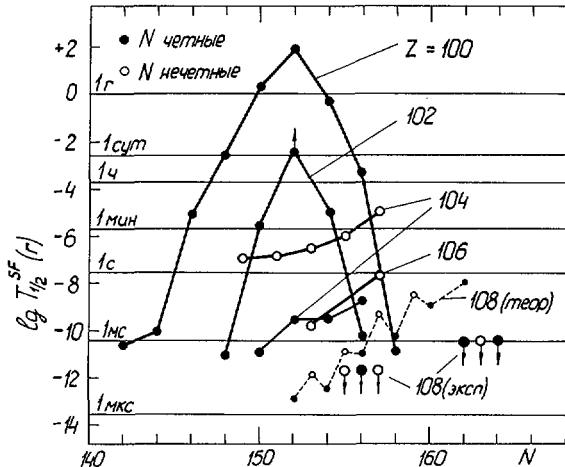


Рис. 1. Систематика экспериментальных значений  $T_{1/2}^{\text{SF}}$  для четно-четных изотопов с  $Z \geq 100$  и для нечетных изотопов с  $Z = 104$  и  $106$ . Пунктиром обозначен расчет для  $Z = 108$  [11].

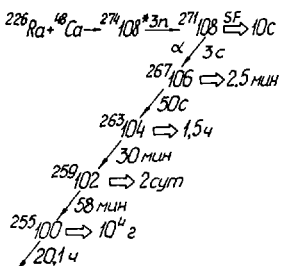


Рис. 2. Схема образования и распада изотопа  $^{271}108$  (см. текст).

$\alpha$ -спектр фракции Fm измерялся с помощью Si-Au-поверхностно-барьерного детектора. Эффективность регистрации  $\alpha$ -частиц составляла около 20 %.

Перед изготовлением мишени радиий очищался от примесей свинца (менее  $10^{-3}$  вес %) и урана (менее  $10^{-1}$  вес %), способных при облучении  $^{48}\text{Ca}$  дать фон спонтанного деления. Общая длительность облучений составила 60 ч при интегральном потоке  $4.5 \cdot 10^{16}$ . Энергия ионов  $^{48}\text{Ca}$  равнялась 235 МэВ на входе в слой Ra и 223 МэВ на выходе из него.

В эксперименте не было зарегистрировано ни одного осколка спонтанного деления. Соответствующая верхняя граница поперечного сечения образования в реакции  $^{226}\text{Ra} + ^{48}\text{Ca}$  спонтанно делящихся продуктов с  $T_{1/2} \geq 1 \text{ мс}$ , в том числе

изотопов  $^{270-272}108$ , составляет  $3 \cdot 10^{-35}$  см $^2$ . Не наблюдался на опыте и  $\alpha$ -распад  $^{255}\text{Fm}$ , что дает верхнюю границу поперечного сечения образования этого изотопа, равную  $10^{-34}$  см $^2$  при условии  $T_{1/2}^\alpha < T_{1/2}^{\text{SF}}$ .

## 2.2. Реакция $^{208}\text{Pb} + ^{58}\text{Fe}$

В ряде экспериментов по синтезу изотопов с  $Z = 100\text{-}107$ , выполненных в Дубне [1, 8, 9, 12, 17, 18], наблюдались продукты испарения компаунд-ядер, образующихся при полном слиянии бомбардирующих ионов от Ag до Mn с ядрами мишней Tl, Pb, Bi. Некоторые эксперименты были выполнены также в Беркли [19]. Поперечные сечения исследовавшихся реакций ( $\text{HI}, 2\text{-}4n$ ) имели величину  $10^{-30} \text{-} 10^{-34}$  см $^2$ , сравнительно большую в масштабах сечений, обычных при синтезе сильно делящихся трансфермийевых ядер. Не исключено поэтому, что использование реакций типа  $^{208}\text{Pb} (^{58}\text{Fe}, \chi n)$  будет эффективным при синтезе изотопов 108-го элемента.

Оценка  $E_{\min}$  показывает, что вблизи кулоновского барьера в этом случае должны протекать реакции с испарением двух, трех, а, возможно, и одного нейтрона. Постая линейная экстраполяция при  $N = 157$  от  $Z = 100, 102, 104$  и  $106$  к  $Z = 108$  дает для изотопа  $^{265}108$  в качестве грубой оценки  $T_{1/2}^{\text{SF}} \approx 1$  мс. Теоретические оценки [10, 11] приводят для изотопов 108-го элемента с числом нейтронов  $N = 155, 156$  и  $157$  к значениям  $T_{1/2}^{\text{SF}} = 0,5; 0,3$  и  $30$  мс, соответственно. Спонтанное деление должно быть основным видом распада указанных изотопов, так как оценки  $T_{1/2}^\alpha$  дают, по крайней мере, на порядок большие времена.

Чтобы иметь возможность получить нечетный изотоп  $^{263}108$  в реакции  $2n$ , в опытах облучалась также мишень из обогащенного  $^{207}\text{Pb}$ .

Мишень представляла собой металлический слой  $^{208}\text{Pb}$  или  $^{207}\text{Pb}$  толщиной 2 мг/см $^2$  на Ni-подложке (1,5 мг/см $^2$ ). Были приняты меры для предотвращения ее испарения под действием пучка. Толщина свинцового слоя контролировалась периодически методом рентгено-флуоресцентного анализа.

Ядра отдачи, выбитые из мишени, тормозились в Al-фольге толщиной 9 мкм, укрепленной по периметру диска диаметром 25 см, вращавшегося со скоростью 11 000 об/мин и переносившего ядра отдачи к слюдяным детекторам за время, равное 0,1 мс. В контрольном эксперименте, в котором мишень из  $^{208}\text{Pb}$  облучалась ионами  $^{54}\text{Cr}$ , с энергией 278 МэВ, при интегральном потоке  $4,8 \cdot 10^{16}$  наблюдалось 11 осколков спонтанного деления изотопа  $^{259}106$ , получавшегося в реакции  $^{208}\text{Pb} (^{54}\text{Cr}, 3n)$  [12]. Измеренное в этом опыте поперечное сечение указанной реакции —  $(2,5 \pm 0,9) \cdot 10^{-34}$  см $^2$ , в пределах экспериментальных ошибок и возможной неточности выбора энергии  $^{54}\text{Cr}$ , совпало с ранее измеренным [12].

В экспериментах с  $^{58}\text{Fe}$  энергия бомбардирующих ионов равнялась 306 МэВ на входе в мишень и 282 МэВ на ее выходе. Средняя интенсивность пучка ионов составляла  $1,5 \cdot 10^{12}$  с $^{-1}$ . В опыте с мишенью из  $^{207}\text{Pb}$  не было зарегистрировано ни одного осколка спонтанного деления при интегральном потоке  $^{58}\text{Fe}$   $6,5 \cdot 10^{16}$ . Это дает верхний предел поперечного сечения  $2 \cdot 10^{-35}$  см $^2$ . Интегральный поток  $^{58}\text{Fe}$  на мишени  $^{208}\text{Pb}$  сос-

ставил  $2,8 \cdot 10^{17}$  ионов. Было зарегистрировано 6 треков осколков деления, происхождение которых может быть объяснено наличием микропримесей урана в слюде. Поэтому может быть указан лишь верхний предел поперечного сечения реакций  $\sim 2 \cdot 10^{-35} \text{ см}^2$ .

### 3. ИЗУЧЕНИЕ ЗАКОНОМЕРНОСТЕЙ РЕАКЦИЙ ПОЛНОГО СЛИЯНИЯ В ОБЛАСТИ СИЛЬНО ДЕЛИЩИХСЯ КОМПАУНД-ЯДЕР

Отсутствие среди продуктов реакций  $^{226}\text{Ra} + ^{48}\text{Ca}$  и  $^{208}\text{Pb} + ^{58}\text{Fe}$  изотопов 108-го элемента можно объяснить одной из двух причин: либо эти изотопы имеют слишком короткие времена жизни, что исключает их наблюдение в описанных экспериментах, либо реальные поперечные сечения соответствующих испарительных реакций меньше установленных пределов. Остановимся несколько подробнее на втором предположении.

Для анализа реакций полного слияния бомбардирующих ионов  $^{48}\text{Ca}$  с различными мишенями нами был применен метод расчета сечений, основанный на статистическом рассмотрении процесса девозбуждения компаунд-ядра, использующем приближение ферми-газа для плотности уровней. Применялась полуэмпирическая зависимость параметра плотности уровней от энергии возбуждения  $E^*$  и структуры ядер [20]

$$a(E^*) = \tilde{a} \left[ 1 + [1 - \exp(-0,054E^*)] \frac{\Delta W(Z, A)}{E^*} \right]$$

где  $\tilde{a}$  изменялось от 22 до 25 МэВ $^{-1}$  в интервале  $A = 250\text{--}300$ . Величина  $\Delta W(Z, A)$  имеет смысл оболочечной поправки к массам основных состояний. Для всей области рассматриваемых ядер ее можно было выбрать около -5 МэВ. В расчетах предполагалось, что  $a_n(E^*) = a_f(E^*)$ .

На всех ступенях испарительного каскада, кроме последней, использовались жидкокапельные барьеры деления  $B_\ell^{LD}$ , зависящие от углового момента [21]. На последней ступени каскада использовались величины барьера для основного состояния  $B_0$ , учитывающие оболочечные эффекты [22]. Такая модификация барьера деления на последней ступени каскада ( $E^* \approx 20\text{--}10$  МэВ) особенно важна при рассмотрении девозбуждения компаунд-ядра с  $Z \geq 100$ , где величина жидкокапельного барьера стремится к нулю. Критический угловой момент определяется тем значением углового момента, при котором жидкокапельный барьер деления становился равным нулю,  $\ell \approx 40\text{--}60 \hbar$ . Парциальные сечения образования компаунд-ядра рассчитывались с использованием действительной части оптического потенциала в параболическом приближении

$$V_{ad} = V_0 \exp \{ [r_0 (A_1^{1/3} + A_2^{1/3}) - r]/d \}$$

где для всей области исследуемых ядер  $V_0 = -67$  МэВ,  $d = 0,4$  фм,  $r_0 = 1,28$  фм.

Энергетическая зависимость сечений обратных реакций захвата ( $n, p, \alpha$ ) вычислялась по оптической модели.

При расчете энергий возбуждения для всех ядер использовались экспериментальные значения масс ядер, если они известны. В тех случаях, когда такие данные отсутствуют, массы ядер вычислялись по формуле [22]. По этой же формуле рассчитывались энергии связи нуклонов и  $\alpha$ -частиц. Энергии вращения для равновесных и седловых фигур вычислялись по формулам работы [21].

В расчетах учитывались каналы деления и испарения нуклонов и  $\alpha$ -частиц. Вычисления проводились для каждого парциального сечения образования компаунд-ядра с шагом, равным 1 МэВ, по энергии возбуждения. За основу была взята программа ALICE [23], в которую были внесены указанные выше изменения.

Описанная модель была применена нами для анализа результатов экспериментов, в которых были получены интегральные выходы изотопов  $^{246}\text{Cf}$ ,  $^{252}\text{Fm} + ^{255}\text{Fm}$  и  $^{254}\text{Fm}$  при облучении ионами  $^{48}\text{Ca}$  толстых мишеней из  $^{208}\text{Pb}$ ,  $^{209}\text{Bi}$  и естественной смеси изотопов Tl. Перечисленные изотопы являлись дочерними продуктами цепочек распада исходных ядер, которые получались в различных каналах девозбуждения компаунд-ядра. Расчетные кривые функций возбуждения для различных испарительных реакций  $^{48}\text{Ca}$  на  $^{205}\text{Tl}$ ,  $^{208}\text{Pb}$  и  $^{209}\text{Bi}$  показаны на рис.3. Каждая из этих кривых интегрировалась от порога соответствующей реакции до максимальной энергии пучка ионов  $^{48}\text{Ca}$  ( $E_0$ ), указанной на рис.3 стрелками. Большинство рассматриваемых функций возбуждения лежит левее максимальной энергии, поэтому неопределенность энергии ионов на входе в толстую мишень (5 МэВ) не влияет существенно на результаты расчета.

Сравнение экспериментальных данных и результатов расчета проведено в табл.I, в первых трех колонках которой перечислены мишени (Tl, Pb, Bi), указаны изотопы, которые наблюдались на опыте и интегральные поперечные сечения их образования ( $\Sigma_{\text{эксп}}$ ) в единицах мкб.МэВ.

В 4 колонке приведены основные каналы девозбуждения компаунд-ядра. Расчетные поперечные сечения в максимумах функций возбуждения этих каналов и расчетные интегральные сечения даны в 5 и 6 колонках. Парциальный вклад  $a_k$  каждого испарительного канала (7 колонка) определялся соответствующими цепочками  $\alpha$ - и  $\beta$ -распадов. В случае  $^{e\pi}\text{Tl}$  в  $a_k$  учитывался состав смеси изотопов тал-

$$\Sigma_{\text{расч}} = \sum_k a_k \int_{E_B}^{E_0} \sigma_k(E) dE,$$

включающие вклад всех испарительных каналов. Каналы испарения, суммарный вклад которых  $\leq 10\%$  от полной величины  $\Sigma_{\text{расч}}$  для простоты не включены в табл.I.

Как видно из табл.I, для всех наблюдавшихся продуктов реакций получено качественное согласие расчетных и экспериментальных интегральных сечений. Интересно, что все три компаунд-ядра образуются в практически совпадающих начальных состояниях по энергии возбуждения и угловому моменту. Действительно, для  $^{205}\text{Tl}$ ,  $^{208}\text{Pb}$  и  $^{209}\text{Bi}$  расчетная величина барьера взаимодействия с  $^{48}\text{Ca}$  равна 172, 172,8 и 175 МэВ и  $E_{\min}^* = 22,3, 18,9$  и 20 МэВ, соответственно. Поэтому из сово-

ТАБЛИЦА I. СРАВНЕНИЕ РЕЗУЛЬТАТОВ ЭКСПЕРИМЕНТОВ С РАСЧЕТОМ. БОМБАРДИРУЮЩИЕ ИОНЫ –  $^{48}\text{Ca}$ , ТОЛСТЫЕ МИШЕНИ. ПОПЕРЕЧНЫЕ СЕЧЕНИЯ ( $\sigma_{\text{расч}}^{\text{макс}}$ ) В мкб (1 барн (б) =  $10^{-28} \text{ м}^2$ ), ИНТЕГРАЛЬНЫЕ ПОПЕРЕЧНЫЕ СЕЧЕНИЯ ( $\Sigma_{\text{эксп}}$ ,  $\sigma_{\text{расч}}^{\text{Инт}}$ ,  $\Sigma_{\text{расч}}$ ) – В мкб · МэВ

Мишень	Продукт	$\Sigma_{\text{эксп}}$	Канал	$\sigma_{\text{расч}}^{\text{макс}}$	$\sigma_{\text{расч}}^{\text{макс}}$	$a_k$	$\Sigma_{\text{расч}}$
$^{232}\text{Th}$	$^{232}\text{Fm}$	$0,20 \pm 0,05$	1n 1p	0,035 0,004	0,24 0,032	0,7 0,7	0,19
	$^{244}\text{Cf}$	$1,3 \pm 0,2$	3n an	0,25 0,11	0,7 0,78	0,69 0,27	0,76
$^{208}\text{Pb}$	$^{232}\text{Fm} + ^{235}\text{Fm}$	$4,2 \pm 0,8$	2n	2,1	15	0,1	1,5
			1n 1a	0,25 0,11	1,8 0,86	0,1 1	1,1
$^{209}\text{Bi}$	$^{244}\text{Cf}$	$40,6 \pm 6$	2n	2,1	15	0,9	14
	$^{232}\text{Fm} + ^{235}\text{Fm}$	$0,93 \pm 0,16$	1n an	0,068 0,037	0,74 0,39	1 1	1,3
	$^{244}\text{Cf}$	$0,39 \pm 0,08$	3n	0,034	0,32	0,99	0,32

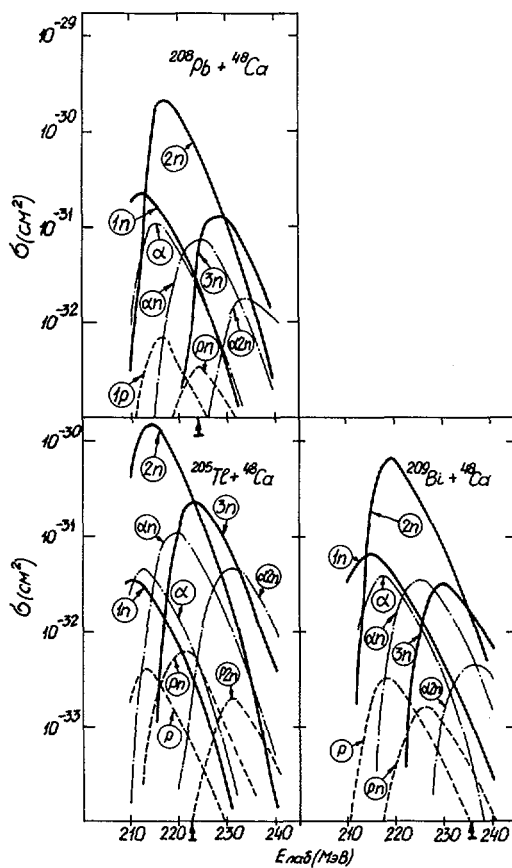


Рис.3. Расчетные функции возбуждения для реакций  $^{208}\text{Pb} + ^{48}\text{Ca}$ ,  $^{205}\text{Tl} + ^{48}\text{Ca}$  и  $^{209}\text{Bi} + ^{48}\text{Ca}$ . Стрелками обозначены значения энергии  $^{48}\text{Ca}$  в лабораторной системе на входе в толстые мишени.

купности данных, представленных в табл.I, можно оценить роль всех основных испарительных каналов.

В данной работе удалось измерить сечение реакции 1n. Именно этот канал обуславливает около 90 % выхода  $^{252}\text{Fm}$  при облучении  $^{ect}\text{Tl}$ . Хорошее согласие измеренного интегрального сечения с расчетным свидетельствует о том, что при переходе от  $^{40}\text{Ar}$  к  $^{48}\text{Ca}$  радиус взаимодействия сталкивающихся ядер практически не изменился. Расчетное сечение в максимуме функции возбуждения реакции  $^{205}\text{Tl}$  ( $^{48}\text{Ca}$ , 1n) равно  $3,5 \cdot 10^{-32} \text{ см}^2$ . Канал реакции 1n вносит примерно 60 %-ный вклад в выход изотопов  $^{252}\text{Fm}$  +  $^{255}\text{Fm}$  в реакции  $^{209}\text{Bi} + ^{48}\text{Ca}$ . В реакции  $^{203}\text{Pb} + ^{48}\text{Ca}$  вклад этого канала выделить трудно, так как большое сечение име-

ТАБЛИЦА II. РАСЧЕТНЫЕ ПОПЕРЕЧНЫЕ СЕЧЕНИЯ РЕАКЦИЙ ПРИ ЗНАЧЕНИЯХ ЭНЕРГИЙ ИОНОВ  $E_{\text{макс}}$ (ЛАБОРАТОРНАЯ СИСТЕМА), СООТВЕТСТВУЮЩИХ МАКСИМУМАМ ФУНКЦИЙ ВОЗБУЖДЕНИЯ.  $Q = M_1 + M_2 - M_{K-\text{я}}$

Реакция	$r_0$ (фм)	$B_0$ (МэВ)	$Q$ (МэВ)	$E_{\text{макс}}$ (МэВ)	$\sigma$ (см $^2$ )
$^{208}\text{Pb}$ ( $^{58}\text{Fe}$ , 1n)	1,28	3,2	-205	283	$2,6 \cdot 10^{-31}$
	1,25	2,2	-203	288	$6,5 \cdot 10^{-35}$
$^{208}\text{Pb}$ ( $^{58}\text{Fe}$ , 2n)	1,28	3,2	-205	293	$3,1 \cdot 10^{-32}$
	1,25	2,2	-203	293	$8,8 \cdot 10^{-33}$
$^{226}\text{Ra}$ ( $^{48}\text{Ca}$ , 2n)	1,28	3,4	-154	224	$1,0 \cdot 10^{-33}$
	1,28	2,4	-152	223	$4,0 \cdot 10^{-35}$
	1,25	2,4	-152	228	$3,0 \cdot 10^{-36}$
$^{226}\text{Ra}$ ( $^{48}\text{Ca}$ , 3n)	1,28	3,4	-154	227	$5,0 \cdot 10^{-33}$
	1,28	2,4	-152	226	$7,0 \cdot 10^{-34}$
	1,25	2,4	-152	230	$1,5 \cdot 10^{-34}$

ет реакция с испарением  $\alpha$ -частицы, а вилка на К-захват у ядра  $^{255}102$  экспериментально не наблюдалась. Для оценок мы приняли ее равной 10 %.

Как видно из рис.3 расчетные сечения испарения двух нейтронов в максимуме являются наибольшими по сравнению с другими каналами испарения. Канал 2n четко проявляется в случае реакции  $^{208}\text{Pb} + ^{48}\text{Ca}$  в выходах изотопов  $^{254}\text{Fm}$  и  $^{246}\text{Cf}$ . На основании наших данных можно утверждать, что у  $^{254}102$  имеется 10 %-ная вилка на К-захват. Расчетный максимум сечения реакции  $^{208}\text{Pb}(^{48}\text{Ca}, 2n)$  равен  $2,1 \cdot 10^{-30}$  см $^2$ , однако, из сравнения  $\Sigma_{\text{эксп}}$  и  $\Sigma_{\text{расч}}$  следует, что экспериментальное сечение примерно в 3 раза больше расчетного.

В реакции  $^{209}\text{Bi} + ^{48}\text{Ca}$  выход  $^{246}\text{Cf}$  полностью обусловлен каналом 3n, расчетное максимальное сечение которого равно  $3,4 \cdot 10^{-32}$  см $^2$ . Этим же каналом определяется около 60 % измеренного выхода  $^{246}\text{Cf}$  в реакции  $^{ect}\text{Tl} + ^{48}\text{Ca}$ .

#### 4. ОБСУЖДЕНИЕ РЕЗУЛЬТАТОВ

Учитывая полученное согласие между теорией и экспериментом (см. табл. I), мы сочли возможным применить описанный метод расчета для оценки поперечных

сечений реакций полного слияния  $^{226}\text{Ra} + ^{48}\text{Ca}$  и  $^{208}\text{Pb} + ^{58}\text{Fe}$ . Результаты расчета представлены в табл. II, из которой видно, что при  $r_0 = 1,28 \text{ fm}$  поперечные сечения испарительных реакций в указанных комбинациях ион – мишень должны быть существенно выше тех пределов, которые были достигнуты в наших экспериментах. Поэтому было целесообразным оценить зависимость предсказываемых поперечных сечений от параметров модели  $r_0$ ,  $B_0$  и от возможных ошибок в Q-реакциях, вызванных неточностью массовой формулы [22]. При этом мы воздержались от радикальных изменений в теории, связанных с предположением о резком уменьшении вероятности слияния тяжелых ядер при переходе от свинцовой мишени к радиевой или от бомбардирующих ионов Ar-Mn к  $^{58}\text{Fe}$ . Величины поперечных сечений для некоторых реакций при измененных параметрах  $r_0$ ,  $B_0$  и Q-реакции, представлены в табл. II.

Как видно из табл. II, эти величины оказываются выше экспериментально установленных пределов. Поэтому отсутствие среди продуктов реакций  $^{207,208}\text{Pb} + ^{58}\text{Fe}$  спонтанно делящихся нуклидов с  $T_{1/2} \geq 0,1 \text{ ms}$ , по всей вероятности, связано с тем, что времена жизни соответствующих изотопов  $^{263,264}108$  меньше 0,1 ms. Исключение, быть может, составляет изотоп  $^{265}108$  с числом нейтронов 157. Он мог образоваться в наших опытах только в реакции  $^{208}\text{Pb}(^{58}\text{Fe}, 1n)$ , для которой при  $r_0 = 1,28 \text{ fm}$  и  $B_0 = 3,2 \text{ MeV}$  предсказывается поперечное сечение в максимуме  $2,6 \cdot 10^{-31} \text{ cm}^2$ . Однако, как видно из табл. II, допустимые изменения в величинах этих параметров и Q-реакции могут объяснить уменьшение величины поперечного сечения этой реакции в 400 раз и более.

Расчеты показывают (см. табл. II), что при постоянном  $r_0 = 1,28 \text{ fm}$  уменьшение  $B_0$  на 1 MeV и переход от  $Q = -154 \text{ MeV}$  к  $Q = -152 \text{ MeV}$  (что является большим изменением для этих параметров) поперечные сечения реакций  $^{226}\text{Ra}(^{48}\text{Ca}, 2n)$  и  $^{226}\text{Ra}(^{48}\text{Ca}, 3n)$  все еще оказываются выше пределов, установленных экспериментально. Особенно слабо зависит от параметров сечение реакции Зп, приводящее к образованию изотопа  $^{271}108$ . Что касается параметра  $r_0$ , для комбинации  $^{226}\text{Ra} + ^{48}\text{Ca}$  его уменьшение по сравнению с величиной 1,28 fm, установленной при анализе данных по реакциям слияния  $^{48}\text{Ca}$  с Tl, Pb и Bi, вряд ли оправдано. Однако, даже заметное его уменьшение, до 1,25 fm, не приводит к снижению предсказываемого сечения реакции Зп ниже экспериментального предела.

Таким образом, наиболее предпочтительным оказывается предположение, что изотопы  $^{271,272}108$  не наблюдались на опыте, так как их периоды полураспада короче, чем 1 ms. Естественно предположить, что основным видом их распада является спонтанное деление.

Пределы периодов полураспада  $T_{1/2}^{\text{SF}}$  для изотопов 108-го элемента, полученные в настоящей работе, показаны на рис. 1. Как видно из рисунка, эти пределы не столь далеки от теоретических предсказаний для легких изотопов  $^{263-265}108$ . Однако, для более тяжелых изотопов они существенно ниже ожидавшихся величин. Например, для нечетного изотопа  $^{271}108$  разница составляет 4 порядка величины. Такое расхождение не является, тем не менее, неожиданным, так как точность расчетов  $T_{1/2}^{\text{SF}}$  невелика. Расхождения расчетных величин  $T_{1/2}^{\text{SF}}$  с экспериментальными

данными в области известных ядер достигает нескольких порядков величины [10, 11, 14, 24]. Оценить неопределенность предсказаний в области неизвестных ядер можно, сравнивая результаты расчетов по различным моделям [10, 11, 14], которые дают близкие результаты в области известных изотопов с  $Z = 100\text{-}102$  и различаются на 2-3 порядка величины в соседней области ( $Z = 104\text{-}108$ ,  $N = 156\text{-}162$ ). Предсказание для изотопов 108-го элемента монотонного роста  $T_{1/2}^{\text{SF}}$  с увеличением числа нейтронов [10, 11] также является неоднозначным [14].

Нам представляется, что необходимо дальнейшее исследование проблемы синтеза 108-го элемента. При изучении реакции  $^{208}\text{Pb} + ^{58}\text{Fe}$  необходим поиск продуктов с  $T_{1/2} < 0,1$  мс. Было бы целесообразным также изучить реакции  $^{249}\text{Cf} + ^{22}\text{Ne}$ ,  $^{210}\text{Pb} + ^{58}\text{Fe}$ ,  $^{204}\text{Hg} + ^{64}\text{Ni}$ , которые позволяют получить, в принципе, более тяжелые изотопы 108-го элемента. Фактически эксперименты по синтезу 108-го элемента являются модельными для перехода к синтезу сверхтяжелых ядер. Такой переход связан с применением тяжелых мишеней и  $^{48}\text{Ca}$  или еще более тяжелых бомбардирующих частиц. Поэтому дальнейшее изучение реакции  $^{226}\text{Ra} + ^{48}\text{Ca}$  при существенно большей быстроте действия и чувствительности методики является очень желательным. С началом работы нового ускорителя тяжелых ионов — циклотрона У-400 ОИЯИ возможности проведения подобных работ резко возросли.

В заключение авторы благодарят В. Зайделя, Ю.А. Селицкого, В.Б. Фунштейна, С.С. Коваленко и К.А. Петржака, участвовавших в экспериментах с радиевой мишенью, Х. Брухертзайфера, О. Константинеску, М. Шварценберг, К.А. Гаврилова и Чой Вал-сека за проведение химических экспериментов, С.П. Третьякову за помощь в расчетной части работы.

#### ЛИТЕРАТУРА

- [1] OGANESSION, Yu.Ts., Nukleonika 22 (1977) 89.
- [2] HULET, E.K., Proc. Int. Symp. on Superheavy Elements, Lubbock, Texac (1978).
- [3] TER-AKOPIAN, G.M., et al., JINR E7-10722, Dubna (1977), Ядерная физика 29 (1979) 608.
- [4] OGANESSION, Yu.Ts., et al., Nucl. Phys. A294 (1978) 213.
- [5] HULET, E.K., et al., Phys. Rev. Lett. 39 (1977) 385.
- [6] OTTO, R.J., et al., J. Inorg. Nucl. Chem. 40 (1978) 589.
- [7] ILLIGE, J.D., et al., Phys. Lett. 78B (1978) 209.
- [8] OGANESSION, Yu.Ts., et al., Nucl. Phys. A239 (1975) 157.
- [9] TER-AKOPIAN, G.M., et al., Nucl. Phys. A255 (1975) 509.
- [10] BARAN, A., et al., Proc. Int. Conf. on Nuclei Far from Stability, CERN 76-13 (1976) 537.
- [11] POMORSKI, K., Nukleonika 23 (1978) 125.
- [12] ОГАНЕСЯН, Ю.Ц. и др., Письма ЖЭТФ, 20 (1974) 580.
- [13] ДРУИН, В.А. и др., ОИЯИ Р7-12056, Дубна (1978).
- [14] RANDRUP, J., et al., Phys. Rev. C13 (1976) 229.
- [15] КОЛЕСНИКОВ, Н.Н., ДЕМИН, А.Г. ОИЯИ Р2-9421, Дубна (1975).
- [16] КОЛЕСНИКОВ, Н.Н., ВЫМЯТНИН, В.М., Изв. АН СССР, сер. физ., 39 (1975) 637.
- [17] OGANESSION, Yu.Ts., et al., Nucl. Phys. A273 (1976) 505.
- [18] FLEROV, G.N., et al., Nucl. Phys. A267 (1976) 359.

- [19] NITSCHKE, J.M., et al., Nucl. Phys. A313 (1979) 236.
- [20] ИГНАТОК, А.В. и др., Ядерная физика 21 (1975) 1185.
- [21] COHEN, S., PLASIL, F., SWIATECKI, W.J., Ann. Phys. 82 (1974) 557.
- [22] MYERS, W.D., SWIATECKI, W.J., Ark. Fys. 36 (1967) 343.
- [23] BLANN, M., PLASIL, F., Report COO-3494-10 (1973).
- [24] LEDERGERBER, T., Reactions of Heavy Ions with Nuclei and Synthesis of New Elements, JINR D7-9734, Dubna (1976).

## DISCUSSION

G.F. HERRMANN: In view of the fact that fission competition is important in evaporation calculations, which approach did you take in estimating the  $\Gamma_n/\Gamma_f$  values?

G.M. TER-AKOP'YAN: We adopted the approach based on a statistical model.

H.J. SPECHT: Do I correctly assume that the effects of angular momentum on the fission barrier were taken into account in the calculations?

G.M. TER-AKOP'YAN: We calculated the fission barrier in accordance with the Cohen, Plasil and Swiatecki method at all the evaporation stages except the last, i.e. we used the liquid-drop approximation and took into account dependence on angular momentum. In the last evaporation stage we introduced a barrier for the ground state, in which we took account of shell effects, disregarding in this case the dependence of the barrier on angular momentum.

P. ARMBRUSTER: How did you make allowance for the disappearance of shell effects with excitation energy? And which damping energy did you use for the last evaporation stage?

G.M. TER-AKOP'YAN: The gradual disappearance of the shell effects with increase in excitation energy was actually taken into account by using liquid-drop fission barriers at all the evaporation stages except the last, as I have explained. This represents a rather crude model, of course, which can be used only as a first approximation. But it accords quite well with the experimental data.

At all evaporation stages we used the same value for the level density parameter, without altering the constants in it.

J. PETER: Do your cross-section calculations take into account the fact that only weak partial waves contribute to fusion, especially in the case of systems such as Pb + Fe with high  $Z_1$  and  $Z_2$ ? Medium and high partial waves produce highly inelastic conditions – which is not envisaged in the ALICE program.

G.M. TER-AKOP'YAN: In the combinations of heavy ions and targets here considered, the condition predominantly causing partial wave cut-off with a high angular barrier is the one imposed by fission at  $B_e^{LD} = 0$ . We did not, therefore, consider cut-off due to the initial conditions.



# DYNAMICAL CALCULATIONS OF SPONTANEOUS-FISSION HALF-LIVES

A. BARAN, K. POMORSKI\*

Institute of Physics,  
The M.Sklodowska-Curie University,  
Lublin, Poland

S.E. LARSSON, P. MÖLLER, S.G. NILSSON

Department of Mathematical Physics,  
Lund Institute of Technology,  
Lund, Sweden

J. RANDRUP\*\*

The Niels Bohr Institute,  
Copenhagen, Denmark

A. ŁUKASIAK, A. SOBICZEWSKI

Institute for Nuclear Research,  
Warsaw, Poland

## Abstract

### DYNAMICAL CALCULATIONS OF SPONTANEOUS-FISSION HALF-LIVES.

Spontaneous-fission half-lives are calculated for the heaviest even-even nuclei ( $Z = 96-110$ ). The penetration of the fission barrier is treated as a one-dimensional problem, in the WKB approximation. The potential energy is calculated as a sum of the Myers-Swiatecki droplet model energy and the shell correction obtained by the Strutinsky method. Quadrupole axial and non-axial deformations and axial deformations of multipolarities three, five and six are considered. The mass tensor (only six components) is calculated in the cranking approximation. All microscopic calculations are based on the modified oscillator single-particle potential. The action integral is minimized by two different variational methods. No free parameters are used. — The calculated half-lives reproduce the experimental values with an accuracy slightly better than two orders (around a factor of 50), on the average.

---

\* Present address: Technische Universität München, Garching, Federal Republic of Germany.

\*\* Present address: Lawrence Berkeley Laboratory, Berkeley, USA.

## 1. INTRODUCTION

There is a continuous interest in the theoretical reproduction of the spontaneous-fission half-lives  $T_{sf}$  for known nuclei and in corresponding predictions for unknown nuclides. This is connected with a continuous progress in the synthesis of new elements and also of new isotopes of already known elements. An important reason for this interest is also the fact that the present description of  $T_{sf}$  is still rather far from satisfactory.

This paper is a continuation of our previous research [1, 2], in which a theoretical reproduction on the half-lives  $T_{sf}$  without making use of any free parameter has been tried. In the earlier, both dynamic (e.g. Ref.[3]) and static (e.g. Ref.[4]), calculations, a free parameter has been used. Henceforth, we shall refer to Ref.[1] as I.

We shall concentrate on even-even nuclei with atomic numbers  $Z = 96-110$ . The half-lives  $T_{sf}$  are calculated dynamically. The main differences with respect to the paper I are: accounting for the  $\epsilon_6$  degree of freedom (describing the deformation of multipolarity 6) in the calculation of the fission barrier, application of the Ritz method in the variational calculation of the barrier penetrability — as a test for the variational method elaborated and applied earlier (see I) — consideration of a larger number of isotopes.

## 2. DESCRIPTION OF THE CALCULATIONS

In the calculation of the half-life,  $T_{sf} = \ln 2/(nP)$ , where  $n$  is the number of assaults of a given nucleus on the fission barrier per unit time, a basic factor is the probability  $P$  of the penetration of the nucleus through the fission barrier for a given assault. Similarly, as in previous investigations [1, 3, 5, 6], the barrier is treated as one-dimensional. A two-dimensional treatment has been studied in Ref.[7] for the case of a simple barrier. In the one-dimensional case, the penetrability calculated in the WKB approximation is [5]

$$P = [1 + \exp S(L_{\min})]^{-1} \quad (1)$$

where

$$S(L) = 2 \int_{s_1}^{s_2} \sqrt{\frac{2}{\hbar^2} [V(s) - E] B(s)} ds \quad (2)$$

with

$$B(s) = \sum_{i,j} B_{\alpha_i \alpha_j}(s) \frac{d \alpha_i}{ds} \frac{d \alpha_j}{ds} \quad (3)$$

is the action integral calculated along a trajectory L given in the deformation space.  $V(s)$  is the potential energy along L, E is the energy of the fissioning nucleus,  $\alpha_i$  and  $\alpha_j$  ( $i, j = 1, \dots, n$ ) are the deformation parameters, and s is the parameter describing the position on the trajectory L.  $B(s)$  is the effective-mass (inertia) parameter of the nucleus 'moving' along L and constructed from the components B of the mass tensor.

By the dynamical calculation of  $T_{sf}$ , we mean that, having both the potential energy  $V(\alpha_1, \dots, \alpha_n)$  and the mass tensor  $B_{\alpha_i \alpha_j} (\alpha_1, \dots, \alpha_n)$  dependent on deformation, we look (by variational methods) for the trajectory  $L_{min}$  for which the action  $S(L)$  becomes minimum.

The deformation of the nucleus is described by the following parameters: (quadrupole)  $\epsilon$ , (hexadecapole)  $\epsilon_4$ , (multipolarity 6)  $\epsilon_6$  (see Ref.[8]) and (reflection-asymmetric)  $\epsilon_{35}$ , being a combination of the parameters  $\epsilon_3$  and  $\epsilon_5$  corresponding to the deformations of multipolarities 3 and 5, respectively [9]. Besides these axially symmetric deformations, the non-axial quadrupole deformation  $\gamma$  [10] is also taken into account. The full dynamical calculation is performed in the  $(\epsilon, \epsilon_4)$  space. Other degrees of freedom are accounted for either in an approximate dynamical way ( $\gamma$ ) (see I) or only statically ( $\epsilon_6, \epsilon_{35}$ ), i.e. only through the potential energy.

The potential energy is calculated as a sum of the smooth part, described by the Myers-Swiatecki droplet model [11, 12] and the shell correction evaluated by the Strutinsky method [13].

The mass tensor is obtained by the cranking model (e.g. Refs [5, 14]). All microscopic calculations (shell correction and mass tensor) are based on the modified oscillator single-particle potential with the 'A = 242 parameters' (see Ref. [8]).

Minimization of the action integral (2) is performed by the variational method. The potential energy and the mass tensor are calculated at 198 grid points in the  $(\epsilon, \epsilon_4)$ -plane, the same as in I, covering a wide region in this plane. A procedure based on dynamical programming methods [15] and elaborated in Ref.[16] allows for a numerically fast choice of the minimal path  $L_{min}$  among all possible zigzag-type trajectories connecting two fixed end points and passing through the grid points situated in the barrier region (i.e. in the region where the potential energy  $V(\alpha_1, \dots, \alpha_n)$  is larger than the energy E of a fissioning

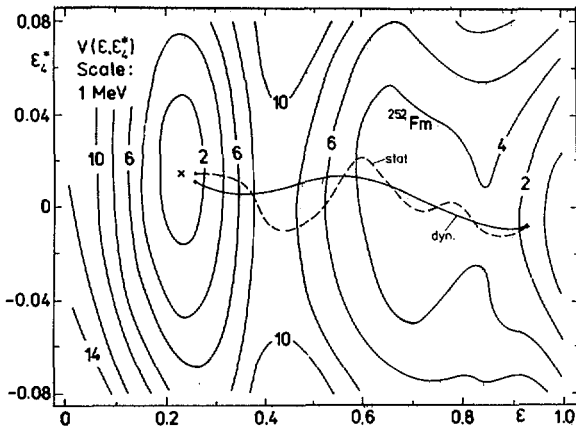


FIG. 1. Potential energy of  $^{252}\text{Fm}$  calculated as a function of the deformation parameters  $\epsilon$  and  $\epsilon_4^*$ . Static and dynamic fission trajectories are indicated.

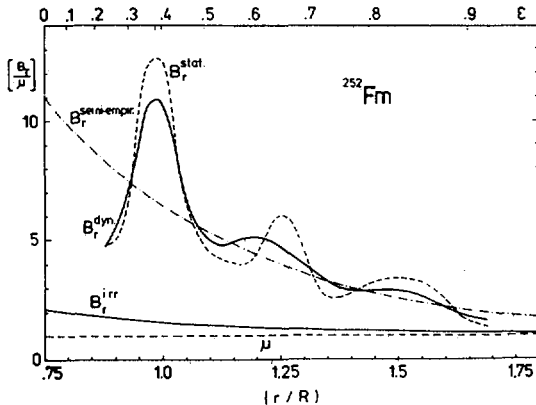


FIG. 2. Effective mass parameter calculated along static and dynamic trajectories for  $^{252}\text{Fm}$ .

nucleus. As the two end points we take the point of minimal potential energy (first minimum), situated before the entrance into the barrier, and a point corresponding to the same potential energy but situated behind the exit point out of the barrier, on the static fission trajectory. The sensitivity to changes in the end points is checked.

As the dynamical fission trajectories are found to be smooth and not to deviate very much from the straight line connecting the end points (Fig.1), we

found it reasonable to use also the following Ritz method for finding  $L_{\min}$  [2]: The deviation of a fission trajectory from the straight line connecting the end points is expanded in a Fourier series (sine functions), and the coefficients of the expansion are treated as the variational parameters. Minimization of the action  $S(L)$  shows that the series is rapidly convergent. The main contribution is obtained from the first two terms; the contribution of the third term is already small and that of the fourth is only of the order of two pro-mille ( $2 \times 10^{-3}$ ). This method, which uses smooth trial trajectories  $L$ , may be considered to be a test of the above method using  $L$  lines of the zigzag-type. The half-lives  $T_{sf}$  obtained by both methods appear to be practically the same.

### 3. RESULTS AND DISCUSSION

An example of the potential energy calculated as a function of  $\epsilon$  and  $\epsilon_4$  (the parameter  $\epsilon_4^* = \epsilon_4 - 0.2 \epsilon + 0.06$ , equivalent to  $\epsilon_4$ , is introduced to make an average fission trajectory for heavy elements especially simple:  $\epsilon_4^* \approx 0$ ) is given in Fig.1. We see that the dynamical trajectory (dyn) is shorter and smoother than the static one (stat), i.e. the trajectory obtained when only the potential energy is minimized or, equivalently, when  $S(L)$  is minimized with the mass tensor independent of deformation. This is typical for all nuclei.

Although the dynamical trajectory deviates considerably from the static one, the corresponding potential barriers (along both trajectories) are close to one another. This is because, when deviating from the static trajectory, we are close to the minimum of the potential energy and the changes of this energy are of second order. The difference in the effective-mass parameter is larger. The parameter calculated along the dynamical path ( $B^{dyn}$ ) is smaller in the region of the largest values of the barrier than that obtained along the static path ( $B^{stat}$ ). This can be seen in Fig.2, where  $B^{dyn}$  is considerably smaller than  $B^{stat}$  in the region of the saddle point which is around  $\epsilon = 0.4$  (as seen in Fig.1). This difference results in the smaller life-times  $T_{sf}$  when calculated dynamically, than those obtained statically; so, it makes dynamics significant. It can also be seen that  $B^{dyn}$  is a smoother function of the deformation than  $B^{stat}$ , and this makes  $B^{dyn}$  somewhat less sensitive to details of the shell structure of the nucleus and, thus, to details of its description, than  $B^{stat}$ . In the figure, we also show a one-parameter semi-empirical effective mass  $B^{semi-empir}$  as introduced in Ref.[17] The parameter is fitted to the experimental  $T_{sf}$  [17] (see also Ref.[4]). We see that  $B^{semi-empir}$  is rather close to our effective  $B$ , when in the latter the shell effects are smoothed out.

The effect of the deformation  $\epsilon_6$  (investigated only statically in this paper) on the fission barrier is considerable. It is illustrated in Fig.3 for  $^{252}\text{Fm}$ . We can see that minimization of the potential energy with respect to this additional degree of freedom decreases the energy mainly in the region of the first minimum.

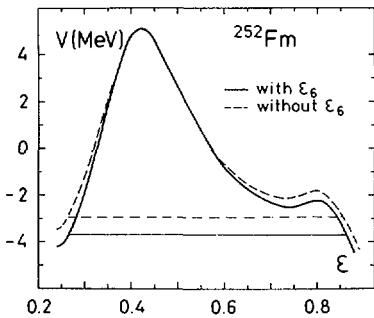


FIG.3. Effect of the inclusion of the deformation  $\epsilon_6$  on the static fission barrier for  $^{252}\text{Fm}$ .

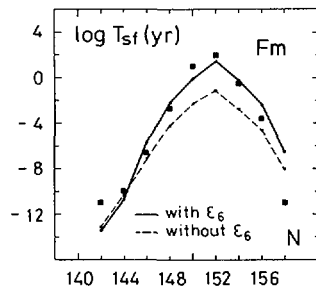


FIG.4. Effect of accounting for  $\epsilon_6$  on the half-lives  $T_{sf}$  for the  $\text{Fm}$  isotopes.

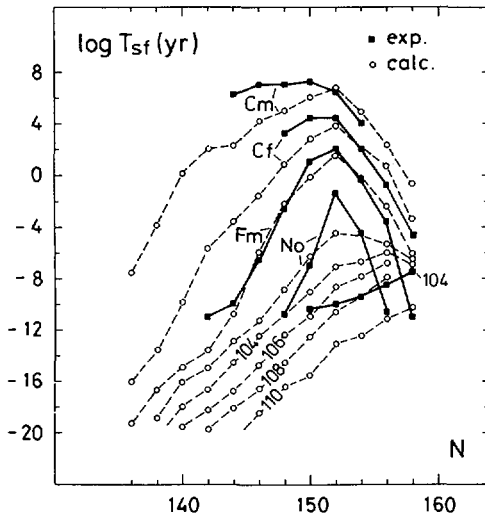


FIG.5. Final results for the calculated half-lives  $T_{sf}$  (in years). The experimental values are also shown.

This increases the barrier for about 0.7–0.8 MeV and results in an increase of the half-life  $T_{sf}$  by about two orders. The changes in  $T_{sf}$ , due to the inclusion of  $\epsilon_6$ , are explicitly given in Fig. 4 for all Fm isotopes for which the experimental  $T_{sf}$  are known. We can see that  $T_{sf}$  is increased for almost all isotopes.

The final results for  $T_{sf}$  are given in Fig. 5. Some more recent experimental points in the figure are taken from Refs [18–21]. We see that the microscopic calculations (with no free parameters!) are able to reproduce the experimental life-times with an accuracy better than two orders (around a factor of 50), on the average. The change in the half-life systematics, seen for  $Z = 102–104$ , is less abrupt in the calculations than in the experiment.

The calculations are performed with the droplet-model parameters of Ref.[11]. A use of the new parameters [12] fitted to the experimental masses and barriers results, as a rule, in life-times  $T_{sf}$  that are one or two orders shorter.

## REFERENCES

- [1] BARAN, A., POMORSKI, K., LARSSON, S.E., NILSSON, S.G., MÖLLER, P., RANDRUP, J., SOBICZEWSKI, A., in Nuclei Far from Stability (Proc. 3rd Int. Conf. Cargèse, 1976), CERN 76–13, Geneva (1976) 537.
- [2] BARAN, A., Phys. Lett. **76B** (1978) 8.
- [3] PAULI, H.C., LEDERGERBER, T., in Physics and Chemistry of Fission (Proc. 3rd Symp. Vienna, 1974) Vol.1, IAEA, Vienna (1975) 463.
- [4] RANDRUP, J., LARSSON, S.E., MÖLLER, P., NILSSON, S.G., POMORSKI, K., SOBICZEWSKI, A., Phys. Rev. **C13** (1976) 229.
- [5] BRACK, M., DAMGAARD, J., JENSEN, A.S., PAULI, H.C., STRUTINSKY, V.M., WONG, C.Y., Rev. Mod. Phys. **44** (1972) 320.
- [6] PAULI, H.C., Physics Reports **7C** (1973) 35; Nukleonika **20** (1975) 601.
- [7] RING, P., MASSMANN, H., RASMUSSEN, J.O., Nucl. Phys. **A296** (1978) 50.
- [8] NILSSON, S.G., TSANG, C.F., SOBICZEWSKI, A., SZYMAŃSKI, Z., WYCECH, S., GUSTAFSON, C., LAMM, I.L., MÖLLER, P., NILSSON, B., Nucl. Phys. **A131** (1969) 1.
- [9] MÖLLER, P., Nucl. Phys. **A192** (1972) 529.
- [10] LARSSON, S.E., Physica Scripta **8** (1973) 17.
- [11] MYERS, W.D., SWIATECKI, W.J., Ann. Phys. (N.Y.) **84** (1974) 186.
- [12] MYERS, W.D., Droplet Model of Atomic Nuclei, IFI/Plenum, New York (1977).
- [13] STRUTINSKY, V.M., Nucl. Phys. **A95** (1967) 420; **A122** (1968) 1.
- [14] KANIOWSKA, T., SOBICZEWSKI, A., POMORSKI, K., ROHOZINSKI, S.G., Nucl. Phys. **A274** (1976) 151; POMORSKI, K., KANIOWSKA, T., SOBICZEWSKI, A., ROHOZINSKI, S.G., Nucl. Phys. **A283** (1977) 394.
- [15] BELLMAN, R.E., KALABA, R.E., Quasi-Linearization and Non-linear Boundary Value Problems, American Elsevier, New York (1965).
- [16] BARAN, A., PhD Thesis (in Polish), Report INR 1803/VII/PL/B, Warsaw, 1979.
- [17] FISET, E.O., NIX, J.R., Nucl. Phys. **A193** (1972) 647.
- [18] HULET, E.K., WILD, J.F., LOUGHEED, R.W., EVANS, J.E., QUALHEIM, B.J., NURMIA, M., GHIORSO, A., Phys. Rev. Lett. **26** (1971) 523.

- [19] OGANESSION, Yu.Ts., DEMIN, A.G., ILJINOV, A.S., TRETYAKOVA, S.P., PLEVE, A.A., PENIONZHKEVICH, Yu.E., IVANOV, M.P., TRETYAKOV, Yu.P., Nucl. Phys. A239 (1975) 157.
- [20] HOFFMAN, D.C., WILMELMY, J.B., WEBER, J., DANIELS, W.R., HULET, E.K., LANDRUM, J.H., LOUGHEED, R.W., WILD, J.F., Report LA-UR-77-2901, Los Alamos, (1977).
- [21] HOFFMAN, D.C., these Proceedings.

## DISCUSSION

H.A.O. NIFENECKER: Moretto and Babinet have pointed out that the pairing gap should be treated dynamically and that the action integral should also be minimized with respect to the pairing gap parameter. Have you included these factors in your calculations or would you consider them irrelevant?

A. SOBICZEWSKI: We did not minimize the action integral with respect to the pairing gap. Pairing is treated in a static (BCS) manner, with the strength of this interaction being fitted to the odd-even mass difference.

F. DICKMANN: I would just like to comment, in connection with whether the pairing gap is used in the calculation of the effective mass parameter, that the gap cannot be chosen freely in the quasi-static cranking model and has to be the same as for the potential energy calculation. If we determine the gap by treating it as a variable free parameter to be determined by minimizing the action integral, then the effective mass is no longer the cranking mass. I think that for the finite deformation velocities, not treated in your paper, anti-pairing effects would reduce the gap parameter below its static value.

A.F. MICHAUDON: I should also like to stress the importance of pairing in calculating the mass inertia parameter and, therefore, the dynamic approach to scission. Usually, simple assumptions are made for the variation in the pairing force with deformation, taken either as a constant or as proportional to the surface of the deformed nucleus. But the truth of the matter seems more complicated.

For example, when pairing is not introduced as a free parameter, but is obtained from the calculation using an adequate effective force, Hartree-Fock calculations actually show that the pairing strength can exhibit large variation as a function of deformation. I refer those who are interested in this point to the paper that Dr. Berger will be presenting at this Symposium (see SM-241/C2 in these Proceedings).

K.W. GOEKE: Dr. Sobiczewski, as far as I understand, you have used the Inglis cranking model for evaluation of the collective mass tensor. This model disregards, however, the rather important residual interaction. Since the mass parameter enters directly into the expression for the life-time, I would expect

your results to change considerably if you applied theories such as self-consistent cranking or the adiabatic time-dependent Hartree-Fock (ATDHF) theory.

A. SOBICZEWSKI: Yes, I agree that the residual interactions which are not included in the cranking model and which could be considered, for example, in the ATDHF treatment, may alter the inertia significantly. It would certainly be a good thing to obtain inertia by using ATDHF. However, before applying the ATDHF to the fission mode it would be worthwhile testing it (with consistently calculated potential energy) by an analysis of the vibrational and rotational modes, which seem to be better suited to testing inertia than fission. For cranking inertia this test has shown that the figure obtained is too small. I refer you to Ref.[14] of my paper.

J.P. THEOBALD: Did you also find evidence for highly asymmetric fission of the No isotopes when one of the fragments is a Ni or Ca isotope, such as has been predicted by Greiner and Sandulescu?

A. SOBICZEWSKI: No, we have not dealt with the fragmentation problem.



# SPECTROSCOPIC PROPERTIES OF FISSION ISOMERS

V. METAG

Max-Planck-Institut für Kernphysik,  
Heidelberg, Federal Republic of Germany

## Abstract

### SPECTROSCOPIC PROPERTIES OF FISSION ISOMERS.

Recent progress in measuring the spectroscopic properties of fission isomers is reviewed. The magic neutron number 146 is deduced for the deformation of the second minimum from the systematics of fission isomeric half-lives. Applying newly developed and improved experimental techniques like the charge plunger method and the recoil distance technique, quadrupole moments, moments of inertia, and spins of fission isomeric states have been determined. All data consistently substantiate the evidence for shape isomerism in the actinide region. The experimental problems encountered in the measurement of magnetic moments are also discussed.

## 1. INTRODUCTION

Since the first observation of fission isomers by S. Polikanov and co-workers [1] in 1962 a large amount of experimental evidence has been accumulated in support of their interpretation as shape isomers associated with a second minimum in the fission potential [2]. This review attempts to cover recent developments in the field of fission isomers with particular emphasis on their spectroscopic properties. Since the last IAEA meeting at Rochester in 1973 several groups have performed experiments aimed at extending the observable range of fission isomeric half-lives, measuring spins, g factors, moments of inertia and quadrupole moments of fission isomers as well as identifying their high-lying vibrational excitations. Some of these experimental developments are discussed in a recent review by R. Vandenbosch [3].

## 2. SYSTEMATICS OF FISSION ISOMER HALF-LIVES

Until 1973 two standard techniques were applied for measuring the half-lives of fission isomers: In pulsed beam experiments [4] the fission fragments from isomeric decays were observed in the intervals between the beam bursts, whereas in recoil distance measurements [5,6] the delayed fission fragments were registered in funnel-type detector arrangements placed along the direction of the fission isomers recoiling from the target. For both arrangements the shortest observable half-lives were of the order of a few nanoseconds as given by the widths of the beam pulses or by the minimum flight times of the recoil ions to the detector arrangement, respectively. The development of the projection method [7,8] extended the range of observable half-lives by about three orders of magnitude to approximately 5 ps. This led to the identification of six sub-nanosecond fission isomers in even-even Pu [9]

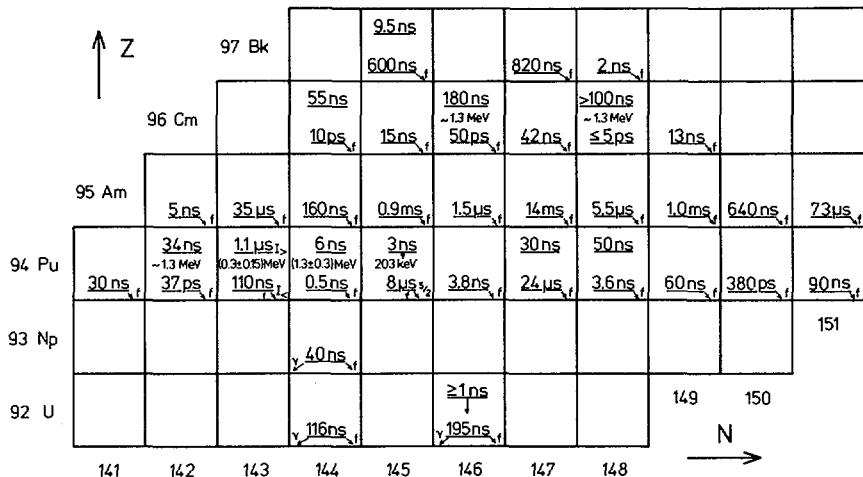


**FIG. 1.** Part of the nuclear chart giving the half-lives of all fission isomers known at present. Two values for the same nucleus indicate spin-isomeric states in the second minimum. In some cases, their excitation energies relative to the lowest states in the second well have been measured. Information on the spins of the isomers in  $^{237}\text{Pu}$  and  $^{239}\text{Pu}$  are also included (see Section 5).

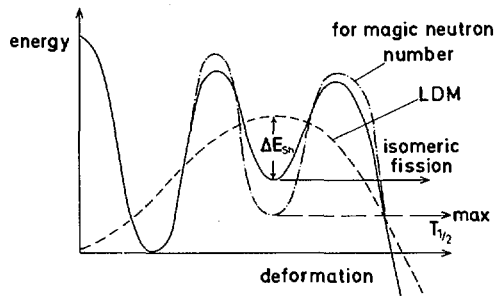


**FIG. 2.** Double-humped fission barriers for a magic and a non-magic actinide nucleus, demonstrating the effect on the fission isomeric half-life.

and Cm [10] isotopes. Together with K isomers in the second well recently discovered [11,12] with the charge plunger technique they are included in an updated tabulation of fission isomeric half-lives given in Fig. 1.

The double isomers in even-even nuclei are interpreted as two quasiparticle excitations [3] of the fission isomers since their excitation energies, measured in four cases, are about 1.3 MeV relative to the lowest state in the second minimum, which is close to the expected pairing gap. Excitation energies of approximately 300 keV and 203 keV have been reported for the K isomers in the odd-even  $^{237}\text{Pu}$  [13] and  $^{239}\text{Pu}$  [14] isotopes, respectively, which are considered to be excited single particle configurations in the second well.

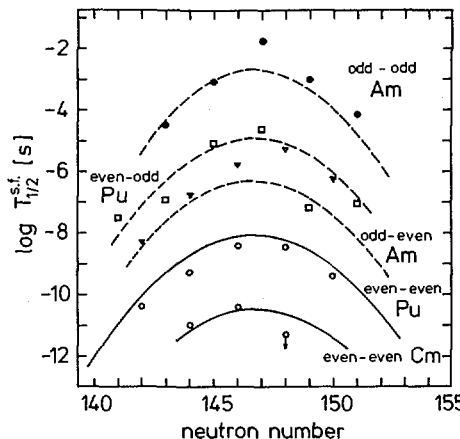


*FIG.3. Half-lives of fission isomers in Pu, Am, and Cm isotopes plotted as a function of the neutron number. The curves are taken from a fit with a semi-empirical formula which parametrizes the dependence of the half-lives on proton and neutron number as well as the odd-even effect.*

Apart from the isomers in  $^{239}\text{Pu}$  [11] and  $^{238}\text{U}$  [12] whose predominant decay to the lowest state in the second minimum has been utilized to study the rotational excitations of the fission isomer (see Sec. 3) it is uncertain whether the decay of the higher lying isomers occurs primarily by electromagnetic transitions or spontaneous fission and which of the two possible decay modes consequently governs the observed half-lives.

The detailed analysis [15] of the half-lives of the lowest states in the second well substantiated the supposition that the dependence of the half-lives on the proton number is mainly determined by the change in the liquid drop model part of the double-humped fission barrier as already noted in [16] and provided a quantitative parametrization of the odd-even effect. The most important result is, however, that the half-lives plotted as a function of the neutron number clearly achieve a relative maximum indicating the influence of shell effects. As illustrated in Fig. 2, the strongest shell effect and thus the most pronounced second minimum is expected for the nucleus with the magic neutron number at the deformation of the second minimum, which is consequently characterized by the relatively longest half-life since an effectively larger barrier has to be penetrated from the isomeric state in the spontaneous fission decay. A fit to the observed fission isomeric half-lives [15] (Fig. 3) yielded a magic neutron number of 146 as compared to 148 which was predicted by most calculated single particle schemes (see Sec. 5). A detailed discussion of the semi-empirical formula used to fit the half-lives is found in Refs. [3,15].

The systematics predicts half-lives of 500 ns, 2  $\mu\text{s}$ , and 50  $\mu\text{s}$  for the isomers in  $^{236},^{238}\text{U}$  and  $^{237}\text{Np}$ , respectively, while the experimental values [17,18,20] are 116 ns, 195 ns, and 40 ns. In addition, delayed fission yields observed in charged particle induced reactions are considerably lower than expected [19]. This experimental information is indicative for an additional decay mode of the isomeric states in these nuclei which may also explain the failure to find fission isomers in odd-even U and in the Np isotopes, except for  $^{237}\text{Np}$  [20]. Already at the third IAEA symposium a direct observation of

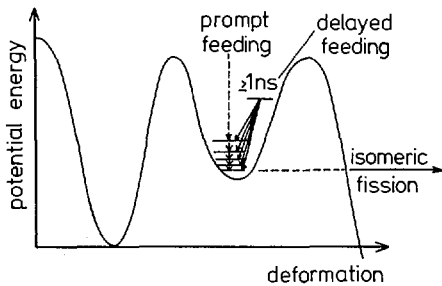


*FIG.4. Schematic illustration of delayed feeding of rotational states in the second minimum which allows the observation of rotational transitions applying the recoil shadow method.*

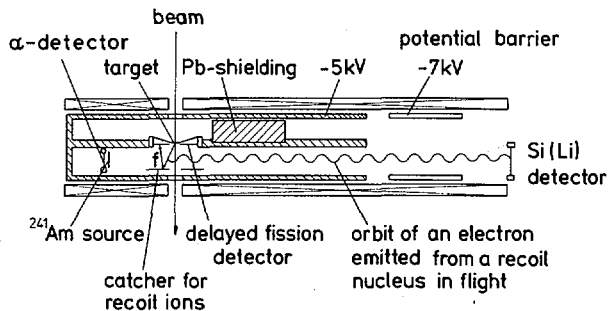


*FIG.5. Experimental arrangement for studying electrons from the decay of short-lived (1–30 ns) K isomers in the second minimum [14]. A voltage of 5 kV is applied to the target area to post-accelerate the emitted electrons. A potential barrier prevents electrons with energies of less than 2 kV from reaching the detector. Conversion electrons from the  $\alpha$ -decay of an  $^{241}\text{Am}$  source provide an on-line energy calibration.*

a  $\gamma$  decay was reported for the isomer in  $^{238}\text{U}$  by Russo et al. [19]. Careful measurements of the cross section for populating the isomer in  $^{236}\text{U}$  in neutron capture [21] and photonuclear reactions [22] have given an indirect estimate of  $(7 \pm 2)$  and approximately 6, respectively, for the branching ratio of gamma-to-fission decay of the  $^{236}\text{U}$  isomer. Preliminary results have been obtained at Heidelberg claiming the de-excitation of this isomer by a 2.215 MeV  $\gamma$  transition [23]. This measurement, however, has been challenged by a recent investigation of the group at Gießen [24] who failed to observe the reported  $\gamma$  line and conclude that the  $\gamma$  decay of the  $^{236}\text{U}$  isomer occurs mainly through several consecutive transitions of low energy. Further experiments with considerably improved detection systems are needed to clarify the situation.

### 3. ROTATIONAL EXCITATIONS OF FISSION ISOMERS

The pioneering experiment of the Munich group [25] on  $^{240}\text{Pu}$  and the analogous measurement of the Copenhagen-Seattle collaboration [26] on  $^{236}\text{U}$  provided proof for the existence of rotational bands based on fission isomeric states. The rotational states were identified by the observation of rotational transitions in delayed coincidence with isomeric fission. The moments of inertia of these bands (see Table II) were found to be more than twice as big as the moments of inertia of the respective ground-state rotational bands and even larger than the moment of inertia of a rigid rotor at ground state deformation, providing the first qualitative evidence for the large deformation of fission isomers.

In both experiments transitions below 40 keV could not be observed due to the rising background of  $\delta$  electrons which are knocked out of the atomic shells by the beam particles with Mb cross sections, as opposed to cross sections of the order of  $\mu\text{b}$  relevant for the population of rotational states in the second minimum. Investigations of rotational excitations of fission isomers have recently been extended to lower transition energies, thus allowing also the study of odd-even nuclei, by utilizing delayed rather than prompt feeding of the rotational states via the decay of a spin isomer in the second minimum as illustrated schematically in Fig. 4. The rotational transitions of interest then occur with some time delay and can consequently be separated from the prompt  $\delta$  electrons by timing or rather by geometrical shielding applying the recoil shadow method [27]. In principle, this technique can be used for studying excited states of fission isomers in several nuclei since the many entries of double isomers in Fig. 1 show that K isomerism is as common in the second as in the first well.

The experimental arrangement used by the Heidelberg-Darmstadt collaboration [14] is shown in Fig. 5. Following the  $^{238}\text{U}(\alpha, 3n)$  reaction  $^{239}\text{Pu}$  nuclei excited in a 2.6 ns spin isomer in the second well recoil from the target. Conversion electrons emitted in flight after some nanoseconds in the decay of the spin isomer are transported through the magnetic field of a Solenoid to a Si(Li) detector. After the de-excitation of the rotational band the recoil nuclei are in the lowest state of the second minimum and their subsequent spontaneous fission decay, determined by the 8  $\mu\text{s}$  half-life, is registered in an annular detector after having stopped the recoil ions on a catcher foil. The electron detector is protected against  $\delta$  electrons from the target as well as the annular detector against prompt fission events by geometrical shielding. A converted transition in the second minimum is identified by requiring a delayed coincidence to occur between the electron and fission detector. To allow in-beam detection of electrons with energies as low as 4 keV an accelerating voltage of 5 kV is applied to the target area. Further details of the experimental arrangement can be found in Ref. [14].

The spectrum of electrons measured in delayed coincidence with isomeric fission and corrected for the chance coincidence background is shown in Fig. 6. The decay curve for the electrons below 31 keV is consistent with the 8  $\mu\text{s}$  half-life of the fission isomer and thus verifies that the observed electron lines originate from transitions in the second minimum of  $^{239}\text{Pu}$ . The spectrum has been analyzed using the known energy and intensity requirements of L, M, and N conversion lines and taking into account that on the average only 1.6 conversion electrons are emitted per spin isomer decay [28]. The interpretation of the spectrum given in Ref. [14] leads to the decay scheme of Fig. 7 establishing two states at 24.3 and 56.2 keV which are fed by a spin isomer tentatively placed at an excitation energy of 203 keV on the basis of only weak feeding transitions.

The low-lying states have been interpreted as rotational excitations of the fission isomer and their energies have been analyzed using the well-known rotational energy expansion

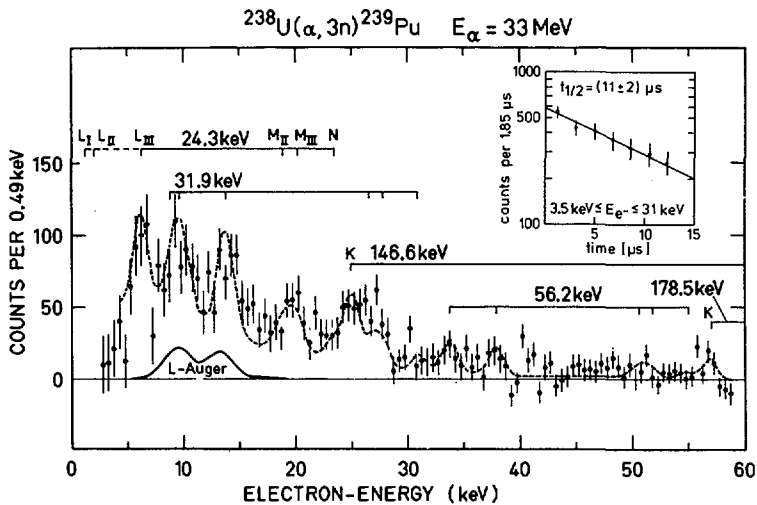


*FIG. 6.* Spectrum of electrons measured in delayed coincidence with isomeric fission of  $^{239}\text{Pu}$  after correction for random coincidences [14]. The inset shows the decay curve measured for the electrons in the energy range from 3.5 to 31 keV. The dashed curve represents a fit to the data. The position of the K, L, M, and N components of the different transitions are indicated. The curve denoted L-Auger is an estimate for the intensity and spectral distribution of Auger electrons which is included in the fit.

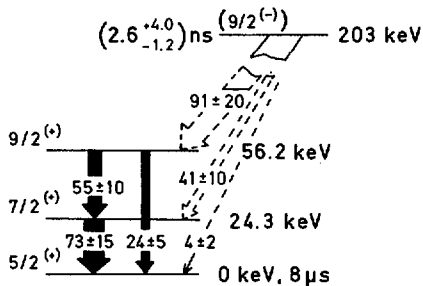


*FIG. 7.* Suggested decay scheme [14] of the 2.6 ns isomer in the second well of  $^{239}\text{Pu}$  showing the transitions feeding and depopulating the rotational band on the 8- $\mu\text{s}$  fission isomer. Transitions given as dashed lines are only tentative. The intensity of each transition is indicated.

$$E_I - E_K = AI(I+1) + BI^2(I+1)^2 \quad (1)$$

which involves three unknown parameters; the spin  $I_o = K$  of the fission isomer, the rotational constant  $A = \hbar^2/2\theta$  related to the moment of inertia  $\theta$ , and the coefficient  $B$  of the second-order term describing the perturbation of the band. A fit of Expression (1) to the observed energies gives  $I_o = 5/2$ ,  $A = (3.36 \pm 0.1)\text{keV}$ ,  $B = (4 \pm 3)\text{eV}$  if one requires in addition that the resulting rotational constant  $A$  be close to the value  $(3.343 \pm 0.003)\text{keV}$  measured [25] for the

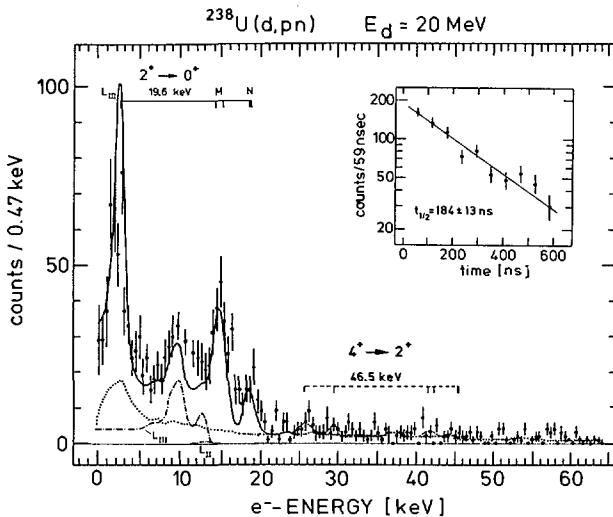


*FIG. 8. Spectrum and decay curve of electrons measured in delayed coincidence with isomeric fission of  $^{238}\text{U}$  [30]. The solid curve represents a fit to the  $L_{\text{III}}$ ,  $M$ , and  $N$  conversion electron lines of the supposed  $2^+ \rightarrow 0^+$  transition. The chance coincidence background (dotted line) and the contribution of Auger electrons (dot-dashed line) are also indicated.*

fission isomer in the neighboring isotope  $^{240}\text{Pu}$ . The odd-even effect in the moment of inertia generally known to be less than 20% at the ground state deformation in the actinide region [29] is expected to be further reduced at the second minimum due to the larger spacing of the relevant single particle orbits and the larger absolute value of the moment of inertia. Assuming different spin values would lead to rotational constants deviating by more than 30% [14] from the value reported for  $^{240}\text{Pu}$ .

Additional information on the wave function of the fission isomer has been obtained from the  $M1/E2$  mixing ratio of the rotational transitions for which an upper limit of  $\delta^{-2} < 1.4$  had been deduced in Ref. [14] from the analysis of the relative intensities of the conversion electron lines shown in the spectrum of Fig. 6. Within the rotational model the mixing ratio is related to the quantity  $[(g_K - g_R)/Q_0]^2$ , and knowing the quadrupole moment of  $Q_0 = (36 \pm 4)\text{b}$  (see Sec. 4) a limit of  $|g_K - g_R| \leq 0.30$  has been determined. Together with the deduced spin of  $5/2$  this result led to the first identification of a single particle state in the second minimum as discussed in Sec. 5.

The recoil shadow method has also been applied to the fission isomer in  $^{238}\text{U}$  [30]. The electron spectrum measured in delayed coincidence with isomeric fission is shown in Fig. 8. The decay curve for the electrons, which is consistent with the known half-life of the fission isomer of 196 ns, again proves that the observed electron lines originate from transitions in the second minimum. Only one transition is observed, most likely the  $2^+ \rightarrow 0^+$  transition, indicating that the isomer feeding the  $2^+$  state is probably of low spin. The isomer was discovered in a charge plunger experiment [12] giving a lower limit of 1 ns for its half-life. The  $L_{\text{III}}$  line of the observed transition has an energy of only 2 keV and could only be observed by applying a postacceleration of 8 kV. If the interpretation given in Ref. [30] is correct, this is the first observation of a  $2^+ \rightarrow 0^+$  transition in the second minimum.

TABLE I. ROTATIONAL PARAMETERS OF BANDS IN THE SECOND WELL

Nucleus	A [keV]	B [eV]	Ref.
$^{236}\text{U}$	$3.36 \pm 0.01$		26
$^{238}\text{U}$	$3.27 \pm 0.03$		30
$^{239}\text{Pu}$	$3.36 \pm 0.1$	$4 \pm 3$	14
$^{240}\text{Pu}$	$3.343 \pm 0.003$	$-(0.28 \pm 0.04)$	25

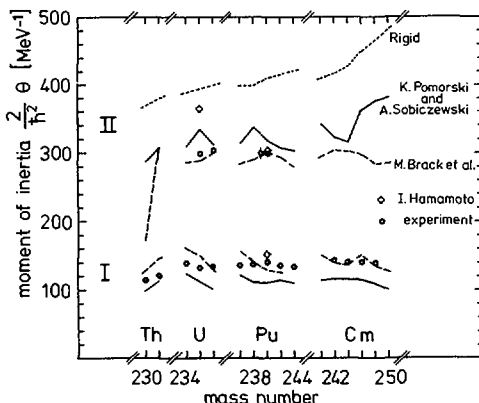


FIG. 9. Moments of inertia of fission isomers and ground states of actinide nuclei in comparison with calculated values [31-33].

In previous investigations of rotational band structure such a low energy transition was always obscured by the  $\delta$  electron background. A rotational constant of  $A = (3.27 \pm 0.03)\text{keV}$  is deduced from the measured transition energy.

The rotational constants measured so far for the bands based on fission isomeric states are listed in Table I. The resulting moments of inertia as well as the experimental values for the ground state rotational bands are compared in Fig. 9 with calculations based on the cranking formalism by Pomorski and Sobiczewski [31], Brack et al. [32], and Hamamoto [33] who have used wave functions of slightly different single particle potentials. There is a reasonable overall agreement although some discrepancies between experimental and calculated moments of inertia are found at the ground state deformation. Slightly reduced moments of inertia are reported in calculations assuming instead of a constant pairing strength one which increases proportionally with the nuclear surface (for clarity not shown in Fig. 9). In view of the non-negligible discrepancies between theory and experiment the present comparison does not allow to favor clearly one of the two assumptions.

#### 4. QUADRUPOLE MOMENTS OF FISSION ISOMERS

Since moments of inertia are model-dependent functions of the deformation,

their measurement establishes the large deformation of fission isomers only qualitatively. The deformation of fission isomeric states, however, can be directly inferred from the lifetimes of the rotational states which are, within the rotational model, determined by the quadrupole moment. Because of the appreciable experimental difficulties encountered in the observation of rotational transitions within the bands on fission isomeric states standard techniques used to measure the lifetimes of excited nuclear states have not been applied. Instead, two completely new experimental techniques have been developed to measure the lifetimes of rotational states in the second minimum: the charge plunger technique [34] utilizing atomic physics effects, and an alternative technique [35] of limited applicability and accuracy based on a modification of the projection method.

The principle of the charge plunger technique developed at Heidelberg is based on the fact that nuclear transitions of low energy are highly converted in heavy nuclei. The emission of a conversion electron creates a vacancy in one of the inner atomic shells which decays either by X-ray emission or by an Auger process occurring in the L shell with a probability of 50% in the actinide region. In the latter case the vacancy is filled with an electron from the M shell while simultaneously another electron (the Auger electron) is emitted from the M or higher shells. With increasing probability for the Auger effect this process proceeds like an avalanche to the outer shells, further complicated by the occurrence of fast Coster-Krönig transitions. If the atom is freely recoiling in a vacuum after a nuclear reaction, the emission of further Auger electrons converts the atom into a highly charged ion with an average charge of  $14^+$  [36] in a time estimated to be less than  $10^{-14}$  s, which is short compared to the nuclear lifetimes of interest.

As described in Ref. [11] this effect can be exploited for measuring the lifetimes of excited nuclear states (Fig. 10). A recoil ion excited in a nuclear reaction leaves the target with an equilibrium charge of  $1^+$  given by the recoil velocity which is typically about 0.2% of the velocity of light for ( $\alpha, xn$ ) reactions. After some picoseconds corresponding to distances of the order of  $\mu m$  a nuclear transition occurs and a conversion electron is emitted followed by a sequence of Auger electrons. The essential point of the technique is that the highly charged recoil ion recaptures all electrons lost in the Auger cascade by passing a thin carbon foil placed downstream at some distance to the target. A low charge recoil ion emerges from the carbon foil and a charge distribution again centered at the equilibrium charge will be observed. If, on the other hand, the carbon foil is placed close to the target and the nuclear transition occurs after passing the carbon foil, there will be no charge resetting and a distribution of highly charged recoil ions is found. Thus, the charge distribution of the recoil ions consists of two completely separate components depending on the time of the nuclear decay. By measuring the relative intensity of the high and low charge recoil ions behind the carbon foil as a function of its distance to the target the de-excitation time of the nuclear level can be determined without ever observing the nuclear transition directly. Because of the obvious analogy of this new technique to the conventional plunger method it was called the charge plunger technique (CPT).

If not only one but rather a sequence of nuclear states is populated in the nuclear reaction as e.g. in a rotational band, several consecutive converted transitions occur leading to even higher atomic charges [37] up to  $40^+$ . Applying the charge plunger technique the analysis described above yields the total de-excitation time of the band which is determined essentially only by the quadrupole moment. Within the rotational model the lifetimes of the individual rotational states are given by

$$T_{1/2}(I_1, K) = \frac{\text{const}}{Q_o^{2.5} E^2 \langle I_1 K | I_2 K \rangle^2 (1+\alpha)}$$

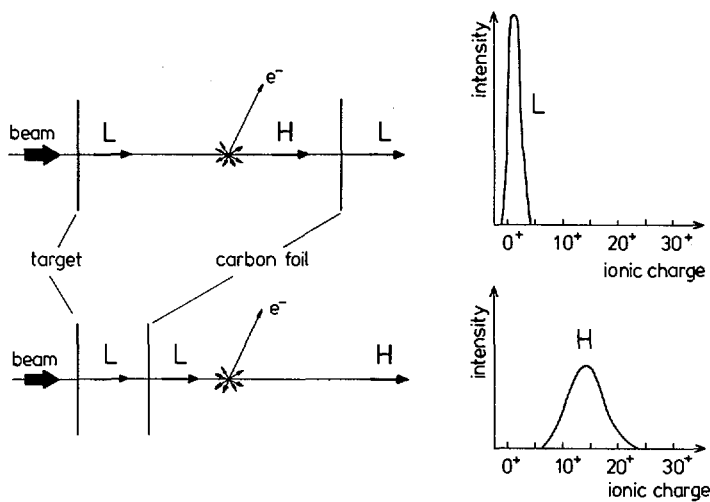


*FIG.10. Principle of charge plunger technique [34]. The charge distributions of recoil ions are schematically sketched for the two possibilities of nuclear transitions occurring before or after passing the charge resetting foil.*

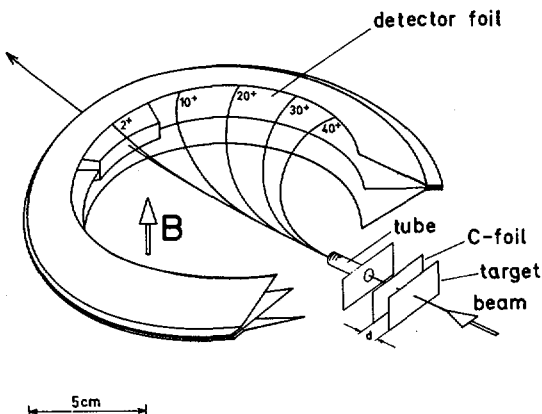
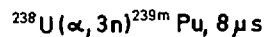


*FIG.11. Experimental arrangement for measuring the charge distribution of long-lived fission isomers ( $T_{1/2} \gg 200$  ns) by deflection in a magnetic field [11]. The flight paths of the isomeric recoil ions are indicated.*

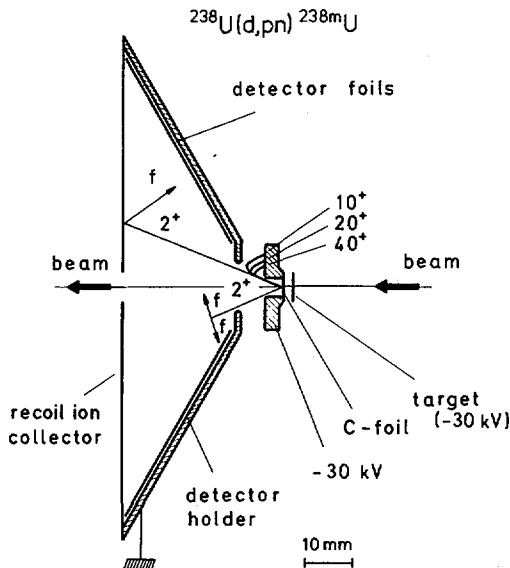


*FIG. 12. Experimental arrangement for separating low- and high-charge recoil ions with short fission isomeric half-lives ( $T_{1/2} \geq 5$  ns) in an electric field [12].*

Spins and transition energies can principally be determined from electron spectroscopy (Sec. 3) leaving the quadrupole moment as the only unknown parameter. Even if the transition energies were not exactly known, their uncertainty does not enter into the analysis since the energy dependence of the half-lives is nearly completely compensated for by the inverse energy dependence of the known conversion coefficients  $\alpha \gg 1$ . Together with the side feeding intensities which can be determined by unfolding the charge distribution as described in Ref. [34] the individual lifetimes are input to a cascade calculation which describes the de-excitation of the rotational band. The quadrupole moment is then deduced from a fit of the calculated overall decay curve to the experimental data. The analysis of charge plunger measurements and the systematic errors involved are discussed in greater detail in Ref. [34].

Although the charge plunger technique is generally applicable to any excited nuclear state with an appreciable electron conversion decay, it has, apart from a test experiment on  $^{240}\text{Cm}$  [34], so far been used only to measure the lifetimes of levels in the second minimum based on a fission isomer.

Depending on the half-life of the fission isomer, deflection of the isomeric recoil ions in either a magnetic or an electric field has been applied to determine their charge distributions. Figure 11 shows the experimental arrangement used for measuring the quadrupole moment of the 8  $\mu\text{s}$  fission isomer in  $^{239}\text{Pu}$  [11]. Fission isomers produced in the  $^{238}\text{U}(\alpha, 3n)$  reaction recoil from the target, and after passing the carbon foil and a collimating tube they are deflected in a magnetic field onto different positions of a recoil ion collector depending on their charge state. Since the time of flight of approximately 200 ns is short compared to the isomeric half-life of 8  $\mu\text{s}$ , most of the spontaneous fission decays occur in the detector foils of the catcher arrangement yielding a direct correspondence between the distribution of fission fragment tracks and ionic charge states.

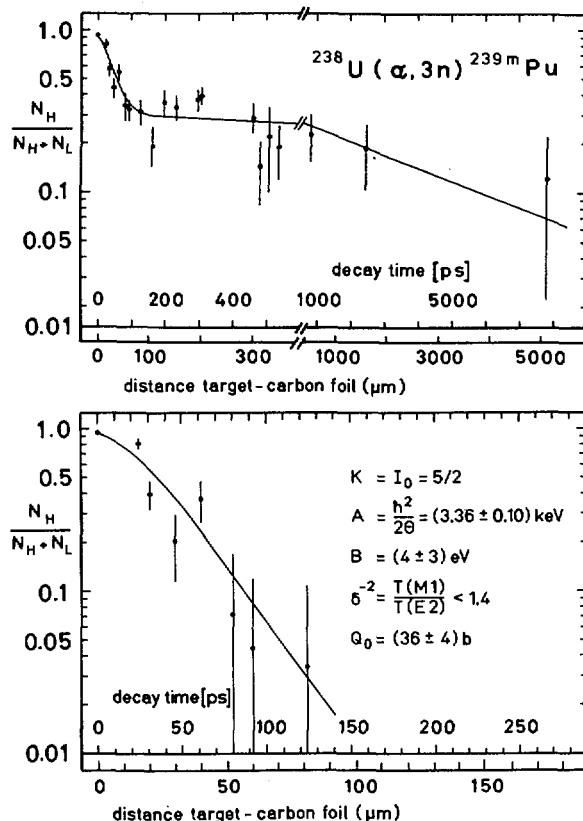


*FIG.13. Fraction of highly charged recoil ions as a function of the distance (or flight time) between target and charge resetting foil [11]. The lower part shows the same quantity plotted versus an expanded distance scale after subtraction of the contribution from the decay of the 2.6 ns spin isomer. The solid curves represent a fit of a cascade calculation to the data points using the known spin, rotational constants and M1/E2 mixing ratio.*

Fission isomers in even-even nuclei with half-lives of  $T_{1/2} \leq 200$  ns are too short-lived to be deflected in a magnetic field since they would fission in flight before reaching the detector. Instead, an electrostatic field has been used [12] to separate low and high charge recoil ions over a distance of only a few millimeters corresponding to flight times of some nanoseconds (Fig. 12). This technique has been applied to measuring the quadrupole moment of the 200 ns fission isomer in  $^{238}\text{U}$  [12]. In passing the carbon foil the fission isomeric recoil ions from the  $^{238}\text{U}(\text{d},\text{pn})$  reaction are slowed down to energies of less than 250 keV. A voltage of -30 kV is applied to the target and the carbon foil enabling only recoil ions with charges of less than  $8^+$  to reach the detector arrangement which is on ground potential. Their fission decay either in flight or after being stopped on a catcher foil is again registered with track detector foils. Recoil ions with higher charges are directly reflected into the target or deflected onto the carbon foil holder.

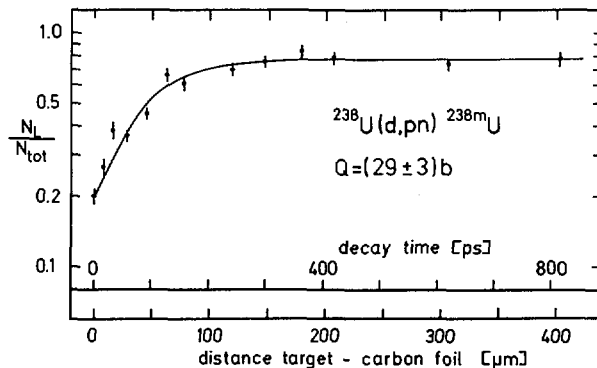


*FIG.14. Fraction of low-charge fission isomeric recoil ions plotted as a function of the distance between target and carbon foil. The solid curve is a fit of a cascade calculation to the data points yielding a quadrupole moment of  $(29 \pm 3) \text{ b}$  [12].*

The total number of recoil ions geometrically accepted in the detector arrangement is determined by running with zero voltage.

In both experiments [11, 12] the fraction of high and low charge recoil ions, respectively, has been measured for increasing distances of the carbon foil to the target. The results are given in Figs. 13, 14. For short distances of  $\lesssim 100 \mu\text{m}$ , corresponding to flight times of  $\lesssim 200 \text{ ps}$ , a rapid variation in the composition of the measured charge distributions is observed due to the de-excitation of the rotational bands based on the fission isomers. The percentage of low charge recoil ions serves as a measure for those nuclei already in the lowest state of the second minimum upon reaching the charge resetting foil, whereas the fraction of high charge recoil ions reflects the number of fission isomers still excited in rotational states. In both experiments a sizable portion of high charge recoil ions is found also for larger distances ( $> 100 \mu\text{m}$ ) indicating the existence of a spin isomer in the second well which feeds the rotational levels with some time delay. A half-life of  $2.6^{+4}_{-1.2} \text{ ns}$  has been found for the spin isomer in  $^{239}\text{Pu}$  [11]; for  $^{238}\text{U}$  only a lower limit of 1 ns can be given [12]. The decay of these spin isomers has been utilized for the direct observation of the converted rotational transitions [14, 30] using the recoil shadow method (Sec. 3).

To determine the quadrupole moments of the fission isomeric states the rapidly varying parts of the charge distributions have been fitted, as discussed above, with cascade calculations which describe the sequence of feeding and depopulating transitions within the rotational band. In both cases transition energies and spins measured by electron spectroscopy have been included in the analysis. Quadrupole moments of  $(36 \pm 4) \text{ b}$  and  $(29 \pm 3) \text{ b}$  are deduced for  $^{239}\text{Pu}$  and  $^{238}\text{U}$ , respectively.

In addition, the decay curves of the individual rotational levels can be obtained by unfolding the charge distributions, measured for various distances of the carbon foil to the target, into the contributions of the individual rotational states. E.g., half-lives of  $(12 \pm 2)$ ,  $(8 \pm 2)$ , and  $(9 \pm 2) \text{ ps}$  have been extracted from a detailed analysis for the first three excited rotational states in the second minimum of  $^{239}\text{Pu}$  [11].

At Copenhagen, a completely different approach to deriving the lifetimes of rotational states in the second minimum has been pursued [35] which is only

TABLE II. QUADRUPOLE MOMENTS AND DEFORMATIONS OF FISSION ISOMERS

Nucleus	Isomer		
	Q [b]	c/a	Ref.
$^{238}\text{U}$	$29 \pm 3$	$1.8 \pm 0.1$	12
$^{236}\text{Pu}$	$37 \pm 1^4$	$2.0 \pm 0.3$	35
$^{239}\text{Pu}$	$36 \pm 4$	$2.0 \pm 0.1$	11

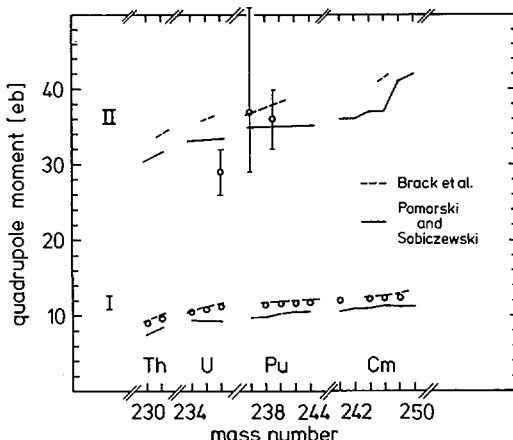


FIG.15. Quadrupole moments of fission isomers and ground states of actinide nuclei in comparison with calculated values [31, 32].

applicable to fission isomers with very short half-lives so that the rotational de-excitation time and fission lifetimes are comparable and fission decays occur already from excited rotational states. The rotational lifetimes have been measured relative to the decay of the fission isomer in  $^{236}\text{Pu}$  with a half-life of 37 ps by determining the branching ratio for spontaneous fission and electromagnetic decay of the rotational levels. The larger the quadrupole moment the faster will be the in-band E2 transitions and the smaller is the contribution of excited rotational levels to the observed delayed fission yield. Fission from excited rotational states and the  $0^+$  ground state of the second well can be separated by measuring the angular distribution of the delayed fission fragments with a modified projection method. The lowest  $0^+$  state decays isotropically whereas the higher spin states, provided that the nuclear alignment is preserved during their lifetimes, contribute increasingly to an anisotropic decay pattern to the extent that they undergo fission. This alignment was studied in a separate experiment [37]. From the measured anisotropy of  $1.48 \pm 0.15$  a quadrupole moment of  $37_{-8}^{+14}$  b has been deduced.

All measured quadrupole moments of fission isomers are listed in Table II. They are compared to the quadrupole moments of the nuclear ground states

and to theoretical predictions [31,32] in Fig. 15. If the shape of the nuclei in the fission isomeric state is approximated by a prolate spheroid, an axis ratio ( $c/a$ ) close to 2:1 is derived from the measured quadrupole moments which systematically exceed the known ground state deformations of approximately  $c/a = 1.3 : 1$ . This result provides the quantitative proof for the interpretation of fission isomers as shape isomers and for the existence of a second minimum in the fission potential. The measured deformation of fission isomers with an axis ratio close to 2:1 has been expected theoretically [38,39] since the shell corrections to the nuclear binding energy which cause the existence of a second minimum are largest for nuclear shapes of high symmetry.

### 5. SPINS AND MAGNETIC MOMENTS OF FISSION ISOMERS

Several attempts have been made to obtain information about single particle states in the second well by measuring their spins and magnetic moments. Altogether three different approaches have been pursued to determine the spins of fission isomers: either by measuring angular distributions of delayed fission fragments or by analyzing the relative population of double isomers as a function of the spin deposited in the nucleus or by direct observation of rotational excitations of fission isomers. Time-dependent perturbed angular distribution (TPAD) experiments have been performed to measure g factors of fission isomers applying different techniques to preserve the nuclear alignment.

In compound reactions the spins of the residual nuclei are aligned in a plane perpendicular to the beam direction. The anisotropy in the angular distribution of fission fragments emitted in the decay of a fission isomer is then given by the angular momentum of the isomeric state and its projection on the nuclear symmetry axis at the second barrier, provided the alignment is maintained for the lifetime of the fission isomeric state. Magnetic moments can be deduced by observing the modulation of the isomeric decay curves due to the time dependence of the anisotropic angular distribution in an external magnetic field applied perpendicular to the plane of the beam and the detectors. Also these experiments require that the orientation of the nuclear spin be not completely randomized by hyperfine interactions during the lifetime of the isomeric state.

Measurements of fission fragment anisotropies [40,41] and g factors [42, 43] have been reported in which fission isomeric recoil ions were implanted in a cubic lattice of Pb in the hope that the recoil ions will come to rest at substitutional sites thus avoiding hyperfine interactions between the large quadrupole moments of fission isomers (Sec. 4) and the electric field gradients which would lead to a de-alignment of the nuclear spin. A different approach has been to heat up thick ( $\approx 5 \text{ mg/cm}^2$ ) metallic U targets close to the melting point to reduce the effect of disturbing hyperfine interactions by an enhanced migration of vacancies [44]. A third approach aimed at decoupling the quadrupole interactions by applying a magnetic field parallel to the direction of the recoiling isomers which were again stopped in a cubic Pb lattice [45].

Despite the numerous efforts statistically convincing and reproducible results have not been obtained so far in any of these experiments indicating that the experimental conditions are not completely controlled and that the solid state effects are not sufficiently understood at present to deduce reliable values for spins and g factors of fission isomers from these types of measurements. It should be noted, however, that the majority of the experiments has been performed on the relatively long-lived fission isomers with half-lives of 0.1  $\mu\text{s}$  and 1.1  $\mu\text{s}$  for  $^{237}\text{Pu}$  and 8  $\mu\text{s}$  for  $^{239}\text{Pu}$ . After a better insight into the hyperfine interactions in the solid state environment has

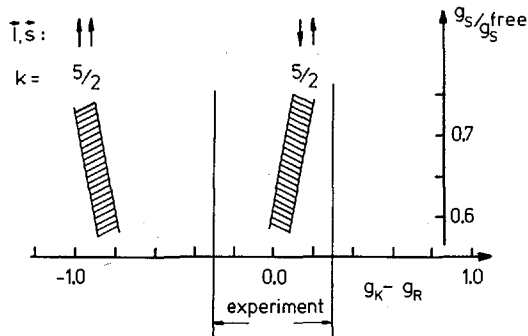


*FIG. 16. The experimental limit of  $|g_K - g_R|$  for the odd-neutron state in the second well of  $^{239}\text{Pu}$  in comparison with the theoretical expectation of the single-particle model for different values of  $g_s/g_s^{\text{free}}$ , allowing for parallel and antiparallel coupling of spin and orbital angular momentum. The hatched areas result from a variation of  $g_R$  in the range  $0.30 \leq g_R \leq 0.40$ .*

been gained, future experiments should rather concentrate on fission isomers with half-lives in the nanosecond range which are less sensitive to de-alignment effects.

Attempts have been made to determine the spins of the two fission isomeric states in  $^{237}\text{Pu}$  by measuring their relative population as a function of the angular momentum deposited in the nucleus in different charged particle induced [46] and photonuclear [47] reactions. Although it is difficult to make definite spin determinations from these types of measurements, a statistical model analysis of the data seems consistent with spin assignments of  $11/2$  to the  $1.1\text{ }\mu\text{s}$  state and  $5/2$  to the  $100\text{ ns}$  state. An interpretation identifying the observed isomers with the Nilsson orbits [615] $11/2^+$  and [862] $5/2^+$  has been suggested tentatively [47, 48]. This assignment can only be considered very speculative since calculated single particle diagrams (see below) give three possible candidates for orbits with spin  $5/2$ .

A more promising approach to obtain information about single particle states in the second minimum seems to be electron spectroscopy. The detailed analysis of the rotational band in  $^{239}\text{Pu}$  yielded a spin of  $5/2$  and  $|g_K - g_R| \leq 0.30$  for the fission isomeric state [14]. In Fig. 16 this experimental result is compared with theoretical expectations for the g factor assuming a pure single particle configuration with

$$g = (1 - \frac{K^2}{K(K+1)})g_R + \frac{K^2}{K(K+1)}g_K$$

$$Kg_K = g_1^{<1_z>} + g_{s\text{eff}}^{<s_z>}$$

allowing for parallel as well as antiparallel coupling of spin and orbital angular momenta and for different values of  $g_R$  and  $g_{s\text{eff}}$ . The comparison shows that the predominant component of the wave function of the isomeric state in  $^{239}\text{Pu}$  has to be an orbit with antiparallel coupling of spin and orbital angular momentum and that the admixture of a component with  $\vec{l}$  and  $\vec{s}$  parallel

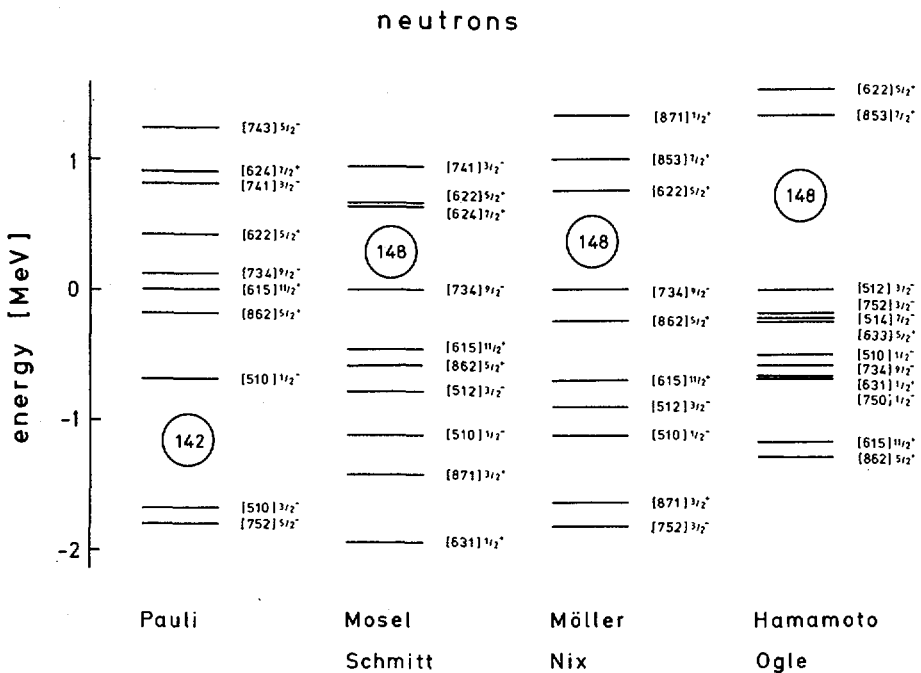


FIG.17. Single-particle diagrams for neutrons at the deformation of the second minimum calculated by different groups [49, 50, 51, 52]. Each state is characterized by the asymptotic quantum numbers  $[Nn_z\Lambda] K^\pi$ . The figure is identical with the one given by R. Vandenbosch [3] except for the level order calculated by Hamamoto and Ogle [52]. This has been plotted for the deformation parameters  $\eta_2 = 0.65$ ,  $\eta_4 = 0.08$  which are consistent with the measured quadrupole moment of the  $^{239}\text{Pu}$  fission isomer and give for its wave function a contribution of less than 40% of the  $[862] 5/2^+$  orbit to the predominant  $[633] 5/2^+$  orbit as required by the observed  $M1/E2$  mixing ratio of the transitions within the rotational band based on this isomer [14]. In case of such strong mixing between different single-particle states of the same spin and parity, the labelling with asymptotic quantum numbers is, however, only of limited validity.

amounts to less than 40%. This signature together with the spin  $I = 5/2$  permits the identification of the odd neutron state at the deformation of the second minimum by comparison with the single particle diagrams in Fig. 17 calculated by various groups [49, 50, 51, 52] using different single particle potentials. The only Nilsson state that meets both requirements is the  $5/2^+ [633]$  orbit. It is found close to the Fermi surface for the neutron number 145 only in the calculation of Hamamoto and Ogle [52] who used a spin-orbit force 20% higher compared to standard parameters. The comparison of experiment and theory suggests that the spin orbit force in the nuclear potential may have to be increased with deformation, as noted already by S.G. Nilsson and coworkers [53] and independently by Dudek and Werner [54] in an attempt to reproduce consistently the experimentally known single particle level order in nuclei close to the doubly magic  $^{208}\text{Pb}$  as well as in the deformed rare earth and actinide nuclei.

## 6. VIBRATIONAL EXCITATIONS OF FISSION ISOMERS

High-lying vibrational excitations of fission isomers have been identified by observing resonances in the probabilities for prompt fission [55,56, 57,58,59,60] and the population of fission isomeric states [61] as well as structures in photofission yields [62,63]. Vibrations along the nuclear symmetry axis ( $\beta$  vibrations with  $K^{\pi} = 0^+$  in even-even nuclei) are closely related to the fission mode and, serving as doorway states for the fission process, lead to an enhanced fission probability. Other collective vibrations such as gamma vibrations ( $K^{\pi} = 2^+$ ) and octupole vibrations ( $K^{\pi} = 0^-$ ) coupled to the beta-vibrational states may give rise to resonances of comparable strength. A systematic and detailed analysis of prompt fission probabilities in the actinide region has been reported by the Los Alamos group [59,60].

A serious problem in the assignment of certain vibrational modes to the observed resonances is caused by the possibility of an irregular fragmentation of the beta-vibrational strength. Reliable interpretations of the data can only be obtained in a combined analysis of the probabilities for prompt and delayed fission as well as fission fragment angular distributions and photofission yields, exploiting the sensitivity of the different sets of data to specific fission channels.  $K^{\pi} = 0^+$  resonances are most pronounced in prompt fission probabilities derived from direct reactions, while  $K^{\pi} = 0^-$  and  $1^-$  vibrations may rather be located by analyzing the structure in photofission yields because of the strong absorption of  $E1$  radiation. Resonances due to  $K = 2^+$  vibrations are observed best in the probability for the population of the fission isomeric states because of the supposed  $\gamma$  instability of the inner fission barrier, leading to a near degeneracy of  $K^{\pi} = 2^+$  and  $0^+$  states, and the relatively higher outer barrier for the  $K = 2^+$  channel. Angular distributions of fission fragments, characteristic of the angular momentum and its projection on the nuclear symmetry axis at the outer barrier, also help in the assignment of particular vibrational modes.

A combined analysis of all available data was performed by Just et al. [64] in the framework of a modified doorway state model [65] extended in its applicability to excitation energies as low as 4 MeV. An average vibrational spacing of the order of 600 keV was deduced. The location of different vibrational states determined relative to the  $K = 0^+$  vibrations at the inner and outer barriers and in the second minimum, respectively, is shown in Fig. 18. The  $K = 2^+$  vibrations at the inner barrier and the  $K = 0^-$  vibrations at the outer barrier, respectively, are found to be nearly degenerate with the  $K = 0^+$  states, giving further support to the supposition of a gamma-unstable inner barrier and a reflection asymmetric outer barrier [66]. The lowest lying vibrational excitations in the second minimum are the octupole vibrations for which excitation energies as low as 300 keV have been inferred for the U isotopes.

Evidence for an asymmetrically deformed outer barrier was also reported by Blons et al. [67,68] who performed high resolution studies of intermediate structure in the neutron fission cross sections of  $^{230}\text{Th}$  and  $^{232}\text{Th}$ . These investigations revealed states which have been interpreted as members of rotational bands based on isomeric states in a third minimum [69] of the fission barrier because of the large moment of inertia associated with these bands. For  $^{231}\text{Th}$  [68] and in Ref. [70] now also for  $^{233}\text{Th}$  the existence of two nearly degenerate rotational bands of opposite parity have been suggested which would strongly support the existence of a reflection asymmetric deformation of the third minimum. This interpretation of the data, however, seems to be inconsistent with careful measurements of fission fragment angular distributions [71,72]. For further details the reader is referred to the review [73] given by D. Paya at this conference.

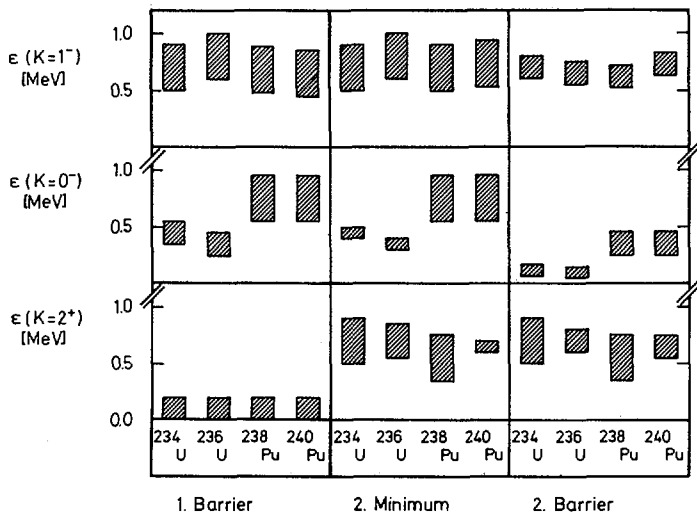


*FIG.18. Excitation energies of vibrational states with  $K^\pi = 2^+, 0^-$  and  $1^-$  relative to the  $K = 0^+$  states at the inner and outer barrier and at the second minimum, respectively, as determined from a combined analysis of prompt and delayed fission probabilities and photofission yields [64]. The hatched areas indicate the uncertainties within the model.*

## 7. CONCLUSION

Since the third IAEA symposium on the physics and chemistry of fission remarkable progress has been achieved in the spectroscopy of fission isomers. In particular, with the invention of the charge plunger technique and the improvement of the recoil shadow method powerful tools have been developed for studying their spectroscopic properties. Systematics of moments of inertia and quadrupole moments begin to emerge. The determination of the spin of a fission isomer has led to the first identification of a single particle state at the deformation of the second minimum providing a sensitive test for the single particle potentials at large deformations. The considerable amount of data accumulated shows that the spectroscopy of fission isomers is no longer in its infancy. Further experiments are needed to establish the  $\gamma$  decay of shape isomers in more nuclei and to settle the dispute on the existence of a third minimum in the fission potential.

## ACKNOWLEDGMENT

It is a pleasure to acknowledge the collaboration with the groups at Heidelberg, Darmstadt, and Copenhagen. In particular, I would like to thank Dietrich Habs, Hartmut Backe, and Geirr Sletten who contributed significantly to the developments described in this review. I am also indebted to Hans Specht for numerous rewarding discussions and many helpful comments.

## REFERENCES

- [ 1] POLIKANOV, S.M., DRUIN, V.A., KARNAUKHOV, V.A., MIKHEEV, V.L., PLEVÉ, A.A., SKOBELOV, N.K., SUBBOTIN, V.G., TER-AKOPYAN, G.M., FOMICHEV, V.A. Sov. Phys. JETP 15 (1962) 1016.
- [ 2] STRUTINSKY, V.M., Nucl. Phys. A95 (1967) 420; Nucl. Phys. A122 (1968) 1.
- [ 3] VANDENBOSCH, R., Ann. Rev. Nucl. Sci. 27 (1977) 1.
- [ 4] VANDENBOSCH, R., WOLF, K.L., 2nd IAEA Symp. Phys. Chem. of Fission, Vienna 1969, p. 439.
- [ 5] METAG, V., REPNOW, R., FOX, J.D., VON BRENTANO, P., Z. Phys. 226 (1969) 1.
- [ 6] LARK, N., SLETTEN, G., PEDERSEN, J., BJØRNHOLM, S., Nucl. Phys. A139 (1969) 481.
- [ 7] LIMKILDE, P., SLETTEN, G., Nucl. Phys. A199 (1973) 504.
- [ 8] METAG, V., LIUKKONEN, E., SLETTEN, G., GLOMSET, O., BJØRNHOLM, S., Nucl. Instr. Meth. 114 (1974) 445.
- [ 9] METAG, V., LIUKKONEN, E., GLOMSET, O., BERGMAN, A., 3rd IAEA Symp. Phys. Chem. of Fission, Rochester, USA, 1973, Vol. I, p. 317.
- [10] SLETTEN, G., METAG, V., LIUKKONEN, E., Phys. Lett. B60 (1976) 153.
- [11] HABS, D., METAG, V., SPECHT, H.J., ULFERT, G., Phys. Rev. Lett. 38 (1977) 387.
- [12] ULFERT, G., METAG, V., HABS, D., SPECHT, H.J., to be published.
- [13] VANDENBOSCH, R., RUSSO, P.A., SLETTEN, G., MEHTA, M., Phys. Rev. C8 (1973) 1080.
- [14] BACKE, H., RICHTER, L., HABS, D., METAG, V., PEDERSEN, J., SINGER, P., SPECHT, H.J., Phys. Rev. Lett. 42 (1979) 490.
- [15] METAG, V., Nukleonika 20 (1975) 789.
- [16] METAG, V., REPNOW, R., VON BRENTANO, P., Nucl. Phys. A165 (1971) 289.
- [17] CHRISTIANSEN, J., HEMPEL, G., INGWERSEN, H., KLINGER, W., SCHATZ, G., WITTHUHN, W., Nucl. Phys. A239 (1975) 253.
- [18] BRITT, H.C., Atom. Nucl. Data Tables 12 (1973) 407.
- [19] RUSSO, P.A., PEDERSEN, J., VANDENBOSCH, R., Nucl. Phys. A240 (1975) 13.
- [20] WOLF, K.L., UNIK, J.P., Phys. Lett. B43 (1973) 25.
- [21] ANDERSEN, V., CHRISTENSEN, C.J., BORGREEN, J., Nucl. Phys. A269 (1976) 338.
- [22] GÜNTHER, W., HUBER, K., KNEISSL, U., KRIEGER, H., Nucl. Phys. A297 (1978) 254.
- [23] HABS, D., METAG, V., SINGER, P., SPECHT, H.J., Max-Planck-Institut für Kernphysik, annual report (1975), p. 55.
- [24] BARTSCH, H., GÜNTHER, W., HUBER, K., KNEISSL, U., KRIEGER, H., MAIER, H.J., Nucl. Phys. A306 (1978) 29.
- [25] SPECHT, H.J., WEBER, J., KONECNY, E., HEUNEMANN, D., Phys. Lett. 41B (1972) 43.
- [26] BORGREEN, J., PEDERSEN, J., SLETTEN, G., HEFFNER, R., SWANSON, E., Nucl. Phys. A279 (1977) 189.
- [27] BACKE, H., RICHTER, L., WILLWATER, R., KANKELEIT, E., KUPHAL, E., NAKAYAMA, Y., MARTIN, B., Z. Phys. A285 (1978) 159.
- [28] ULFERT, G., thesis, University of Heidelberg, 1977 (unpublished).
- [29] ELLIS, Y.A., SCHMORAK, M.R., Nucl. Data B8 (1972) 345.
- [30] BACKE, H., GOERLACH, U., METAG, V., SINGER, P., SPECHT, H.J., to be published.
- [31] POMORSKI, K., SOBICZEWSKI, A., Acta Physica Polonica B9 (1978) 61.
- [32] BRACK, M., LEDERGERBER, T., PAULI, H.C., JENSEN, A.S., Nucl. Phys. A234 (1974) 185.
- [33] HAMAMOTO, I., Phys. Lett. 56B (1975) 431.
- [34] ULFERT, G., HABS, D., METAG, V., SPECHT, H.J., Nucl. Instr. Meth. 148 (1978) 369.
- [35] METAG, V., SLETTEN, G., Nucl. Phys. A282 (1977) 77.

- [36] DE WIECLAWIK, W., Comp. Rend. 266 (1968) 577.
- [37] METAG, V., HABS, D., SPECHT, H.J., ULFERT, G., KOZHUHAROV, C., Hyp. Int. 1 (1976) 405.
- [38] BOHR, A., MOTTELSON, B., Nuclear Structure, Benjamin, New York (1974), Vol. II, p. 609.
- [39] STRUTINSKY, V.M., MAGNER, A.G., OFENGENDEN, S.R., DØSSING, T., Z. Phys. A283 (1977) 269.
- [40] SPECHT, H.J., KONECNY, E., WEBER, J., KOZHUHAROV, C., 3rd IAEA Symp. Phys. Chem. of Fission, Rochester, USA, 1973, Vol. I, p. 285.
- [41] HABS, D., METAG, V., SPECHT, H.J., Max-Planck-Institut für Kernphysik, annual report (1974), p. 1.
- [42] KALISH, R., HERSKIND, B., PEDERSEN, J., SHACKLETON, D., STRABO, L., Phys. Rev. Lett. 32 (1974) 1009.
- [43] HABS, D., HERSKIND, B., METAG, V., PEDERSEN, J., SLETTEN, G., SPECHT, H.J., Max-Planck-Institut für Kernphysik, annual report (1975), p. 57.
- [44] HABS, D., METAG, V., PAUL, P., SCHATZ, G., SPECHT, H.J., Max-Planck-Institut für Kernphysik, annual report (1976), p. 51.
- [45] HABS, D., HANNA, S., METAG, V., PEDERSEN, J., SLETTEN, G., SPECHT, H.J., Max-Planck-Institut für Kernphysik, annual report (1977), p. 48.
- [46] RUSSO, P.A., VANDENBOSCH, R., MEHTA, M., TESMER, J.R., WOLF, K.L., Phys. Rev. C3 (1971) 1595.
- [47] GÜNTHER, W., HUBER, K., KNEISSL, U., KRIEGER, H., MAIER, H.J., Phys. Rev. C19 (1979) 433.
- [48] VANDENBOSCH, R., 3rd IAEA Symp. Phys. Chem. of Fission, Rochester, USA, 1973, Vol. I, p. 251.
- [49] PAULI, H.C., Phys. Rep. C7 (1973) 35.
- [50] MÖLLER, P., NIX, J.R., 3rd IAEA Symp. Phys. Chem. of Fission, Rochester, USA, 1973, Vol. I, p. 103.
- [51] MOSEL, U., SCHMITT, H.W., Nucl. Phys. A165 (1971) 13.
- [52] HAMAMOTO, I., OGLE, W., Nucl. Phys. A240 (1975) 54.
- [53] NILSSON, S.G., private communication, 1978.
- [54] DUDEK, J., WERNER, T., J. Phys. G, Nucl. Phys. 4 (1978) 1543.
- [55] PEDERSEN, J., KUZMINOV, B.D., Phys. Lett. B29 (1969) 176.
- [56] SPECHT, H.J., FRASER, J.S., MILTON, J.C.D., DAVIES, W.G., 2nd IAEA Symp. Phys. Chem. of Fission, Vienna 1969, p. 363.
- [57] GOLDSTONE, P.D., HOPKINS, F., MALMIN, R.E., VON BRENTANO, P., PAUL, P., Phys. Lett. B62 (1976) 280.
- [58] GOLDSTONE, P.D., HOPKINS, F., MALMIN, R.E., PAUL, P., Phys. Rev. Lett. 35 (1975) 1141.
- [59] BACK, B.B., HANSEN, O., BRITT, H.C., GARRETT, J.D., Phys. Rev. C9 (1974) 1924.
- [60] BACK, B.B., BRITT, H.C., HANSEN, O., LEROUX, B., GARRETT, J.D., Phys. Rev. C10 (1974) 1948.
- [61] GOERLACH, U., HABS, D., JUST, M., METAG, V., PAUL, P., SPECHT, H.J., MAIER, H.J., Z. Phys. A287 (1978) 171.
- [62] LINDGREN, L.J., ALM, A., SANDELL, A., Nucl. Phys. A298 (1978) 43.
- [63] DICKEY, P.A., AXEL, P., Phys. Rev. Lett. 35 (1975) 501.
- [64] JUST, M., GOERLACH, U., METAG, V., SPECHT, H.J., this conference, paper IAEA-SM-241/A4.
- [65] GOLDSTONE, P.D., PAUL, P., preprint.
- [66] VANDENBOSCH, R., Phys. Lett. 45B (1973) 207.
- [67] BLONS, J., MAZUR, C., PAYA, D., Phys. Rev. Lett. 35 (1975) 1749.
- [68] BLONS, J., MAZUR, C., PAYA, D., RIBRAG, M., WEIGMANN, H., Phys. Rev. Lett. 41 (1978) 1282.
- [69] MÖLLER, P., NIX, J.R., 3rd IAEA Symp. Phys. Chem. of Fission, Rochester, USA, 1973, Vol. I, p. 140.
- [70] BLONS, J., MAZUR, C., PAYA, D., RIBRAG, M., WEIGMANN, H., this conference, paper IAEA-SM-241/048.

- [71] LEROUX, B., BARREAU, G., SICRE, A., BENFOUGHAL, T., CAITUCOLI, F., DOAN, T.P., JAMES, G.D., this conference, paper IAEA-SM-241/044.
- [72] BOLDEMAN, J.W., WALSH, R.L., DE L. MUSGROVE, A.R., this conference, paper IAEA-SM-241/97.
- [73] PAYA, D., this conference, paper IAEA-SM-241/B6.

## DISCUSSION

S. POLIKANOV: In discussing the rotational levels for  $^{238}\text{U}$  you suggested that there were two isomeric states in the second well. What do you know about the second isomer?

V. METAG: The existence of a higher-lying isomeric state in the second well for  $^{238}\text{U}$  was first deduced from our observation of highly-charged fission isomeric recoil ions at large distances between the carbon foil and the target in our charge plunger experiment based on the  $^{238}\text{U}$  ( $d, pn$ ) reaction. The half-life of the isomer should be in the 1-20 ns range, since transitions from its decay have been seen when applying the recoil shadow method. The fact that we mainly observed only the  $2^+ \rightarrow 0^+$  transition implies that the feeding isomer has low spin. I would imagine that it is the octupole vibration which is the lowest collective vibration in the second well. On this point I refer to the paper given by Dr. Just at this Symposium (see SM-241/A4 in these Proceedings).

H.J. SPECHT: This might be an appropriate moment to ask whether any of the theoreticians present could comment on the significance of a spin-orbit force increasing with deformation. In particular, one wonders whether there might be different Nilsson levels in play at the outer barrier from what would be found without the effect. I should be interested to hear if there has been investigation of the influence that this may have on the stability, i.e. on the barrier heights.

H.C. PAULI: Perhaps I could give an answer. Variation in the spin-orbit force has been considered. In a paper I co-authored a few years ago we treated the spin-orbit coupling as a free parameter. This approach had some effect on the location of super-heavy elements in that it made the 126-shell even stronger than before and, as far as I know, the 114-shell did not change too drastically. But why there should be variation in the spin-orbit force with deformation is not too clear, though there are, of course, speculations on the subject.

# BETA-DELAYED FISSION AND LOW-LYING STRUCTURES IN THE BETA STRENGTH FUNCTION

H. V. KLAUDOR

Max-Planck-Institut für Kernphysik, Heidelberg,  
Federal Republic of Germany

C.-O. WENE

Department of Nuclear Physics,  
Lund Institute of Technology, Lund, Sweden

I.N. ISOSIMOV, Yu. V. NAUMOV

Institute of Physics, University of Leningrad,  
Union of Soviet Socialist Republics

## Abstract

### BETA-DELAYED FISSION AND LOW-LYING STRUCTURES IN THE BETA STRENGTH FUNCTION.

Beta-delayed fission ( $\beta$ DF) gives a possibility of investigating the fission barrier for nuclei far off beta stability. However, before any information on the fission barrier can be extracted, the effect of low-lying structures in the beta strength function ( $S_\beta$ ) on the  $\beta$ DF branching ratio has to be considered. This is in general not being done. In this paper, the low-lying structures that occur in  $S_\beta$  are discussed and microscopic calculations for the Gamov-Teller strength function are presented for  $^{232}\text{Th}$  ( $\beta^-$ -decay) and  $^{232}\text{Pu}$ ,  $^{240}\text{Cm}$ ,  $^{244,248}\text{Cf}$  and  $^{248}\text{Fm}$  ( $\beta^+$ -decay). Using the calculated strength functions,  $\beta^+$ DF branching ratios are calculated and compared with the experimental ones. The sensitivity of the results to different shapes of  $S_\beta$  is investigated. It is concluded that, when the expected structures in  $S_\beta$  are considered, there are, at present, no indications from  $\beta^+$ DF measurements that the errors in the fission barrier calculations are larger than the uncertainty given for those calculations. The difference in magnitude between the  $\beta^-$ DF and the  $\beta^+$ DF branching ratios is also explained by the occurrence of low-lying structures in  $S_\beta$ .

## 1. INTRODUCTION

Beta delayed fission ( $\beta$ DF) was first directly observed in proton-rich nuclides in experiments performed at Dubna [1]. In the experiments using thermonuclear explosives very neutron-rich actinide nuclides are produced [2]. The reversal in the odd-even yield of beta stable nuclides observed in these experiments, [3,4], was interpreted as due to  $\beta^-$ DF [5] in the nuclides beta decaying to the line of beta stability after the neutron exposure. This indicates very large  $\beta^-$ DF branching ratios for nuclides like  $^{252,254,256}\text{Pu}$  and  $^{254,256}\text{Cm}$  [6]. Recently,  $\beta^+$ DF branching ratios have been measured in  $^{232,234}\text{Pu}$  [1,7],  $^{240}\text{Cm}$  [8],  $^{244,246,248}\text{Cf}$  [8,9] and  $^{248,250}\text{Fm}$  [10]. On the neutron-rich side  $\beta^-$ DF in  $^{234,236,238}\text{U}$  [10-12] and  $^{232}\text{Th}$  [10] has been investigated.

In calculations of the  $\beta$ DF branching ratio the beta strength function,  $S_\beta$ , enters

$$S_\beta(E) = b(E)/(f(Q_\beta - E, Z) \cdot T_{1/2}) \quad (1)$$

where  $b(E)$  is the absolute beta intensity to levels at excitation energy  $E$ ,  $Q_\beta$  the total energy available,  $f$  the statistical Fermi function and  $T_{1/2}$  the beta decay half life. The  $\beta$ DF branching ratio is obtained by folding the fission probability over  $S_\beta(E)f(Q_\beta - E, Z)T_{1/2}$ . When  $Q_\beta$  is smaller or about equal to the highest fission barrier, the branching ratio will be very sensitive to the shape of the barrier. Measurements of the ratios can therefore be used to obtain information about the fission barrier for nuclides far off stability [5] which is difficult with other available methods. Data on  $\beta$ DF in  $^{232},^{234}\text{Pu}$  were used by Habs et al. [7] in an attempt to deduce the height of the inner barriers for those nuclides. The results obtained by using an oversimplified assumption on the shape of  $S_\beta$  were taken by these authors as evidence for large deviations from the heights predicted by Strutinsky type calculations.

In order to be able to draw any conclusions about the fission barrier from measured branching ratios, the shape of  $S_\beta$  has to be known [13,14]. Three different assumptions have generally been used for analyzing  $\beta$ -delayed phenomena

- 1)  $S_\beta(E) = \text{constant}$  [15]
- 2)  $S_\beta$  proportional to the level density in the daughter nucleus [16]
- 3) gross theory [17]

Habs et al. [7] base their conclusions on  $S_\beta = \text{constant}$ . The same assumption is used also for calculating the branching ratio in ref. [11].

Neither assumption 1) nor 2) can include any realistic nuclear structure effect in the  $\beta$ -transition matrix elements as they will not fulfill any sum rule. In this respect the gross theory of beta-decay represents an improvement because it considers single particle sum rules and some strongly simplified nuclear structure. However, it has recently been pointed out [18,13,14,19] that all these assumptions ignore the existence of important low-lying structures in  $S_\beta$ . Experimental evidence for these structures is found in high resolution  $\beta$ -delayed neutron work [20,21]. The fact that the corresponding structures expected [18,13] in  $S_\beta$  have not been observed in heavy nuclei by recent total  $\gamma$ -absorption experiments [e.g. ref. 15] is due to the very low efficiency for high energy  $\gamma$ -rays of the detection system used there. The existence of the low-lying structures implies large changes [18,13] in the presently made analysis of beta delayed phenomena, (for detailed discussion see ref. [13]).

It is the purpose of this contribution to discuss the low-lying structures which occur in the actinide region and their influence on beta-delayed fission, especially on the extraction of information about fission barriers from measurements of  $\beta$ DF branching ratios.

## 2. SHAPE OF $S_\beta$ IN THE ACTINIDE REGION

Figures 1 and 2 show in a very schematical way the nuclear configurations giving rise to the low energy structure in  $S_\beta$  for allowed Gamow-Teller and El-like first forbidden transitions. (The figures and the states configurations are discussed in detail in ref. 13).

For  $\beta^-$  GT transitions there are two types of collective states that may lie within the  $\Omega_\beta$ -window: Core Polarized States (CPS) and Back Spin-Flip States (BSFS). Due to the similarities between the GT operator and the M1 isovector operator CPS and BSFS are populated also by M1  $\gamma$ -decay of the isobaric Analogue State (IAS). Such  $\gamma$ -decay studies of the CPS together with the Anti-Analogue State (AIAS) have been made for a long time [see e.g.ref. 22,23] and the information from these investigations can be used to estimate the energies of the different states. Using the Lane potential  $V_1$ , the position of the AIAS centroid is expected at  $E_{\text{AIAS}} = E_{\text{IAS}} - V_1(2T_0+1)/2A$  with  $V_1 = (120 \pm 30)$  MeV.  $E_{\text{IAS}}$  is the excitation energy of the IAS. The simplest CPS configurations lie higher than the AIAS by an amount equal to the pairing energy of the neutron ( $12/\sqrt{A}$  MeV). The simplest spin flip states (SFS) and BSFS lie higher and lower than the CPS by the spin-orbit splitting. BSFS will occur in nuclides where the neutron excess is large enough to make spin-flip transitions between LS-partners in two neighbouring shells possible.

The low energy structures in the Gamow-Teller  $\beta^-$  strength function have been observed directly in high resolution  $\beta^-$  delayed neutron and gamma experiments in medium heavy nuclides up to  $A < 140$  by Kratz et al. [20,21]. The structures appear about the expected energies with widths of 1 MeV. The states forming the GT  $S_\beta^-$  have been observed also in charge exchange reactions (CER) [24].

The first forbidden transitions become increasingly important with increasing  $Z$  and  $A$ . In addition to the high-lying  $El(-1;-1;+1)$  mode, a low-lying  $El(-1;-1;-1)$  mode is expected [25] in nuclei with  $v = (3N)^{1/3} - (3Z)^{1/3} > 1$ , i.e. when the neutron excess is more than one major shell. The  $El(-1;-1;-1)$  is of considerable interest for the neutron-rich nuclides. Its centroid will be at

$$E(El(-1;-1;-1)) = E_{\text{IAS}} - 79 A^{-1/3} - V_{El}(T_0+1)/A \quad (2)$$

where  $V_{El} = (55 \pm 15)$  MeV [26]. The importance of this structure for beta delayed processes has first been pointed out in ref. [13,19]. Apart from the strong first forbidden transitions in the region around  $^{208}\text{Pb}$  there is no direct experimental evidence for  $El(-1;-1;-1)$ . The large  $\beta$ DF branching ratios [6] for the transuranium nuclides synthesized using thermonuclear explosions indicate structures in  $S_\beta$  within the  $\Omega_\beta$ -window, but above the fission barrier. At present it is not possible to tell whether those are due to the BSFS, the El state or some other state excited in first forbidden decay, [13,19].

An estimate for the centroid of  $El(+1;+1;+1)$  is obtained from eq. (2) by changing the signs for the three right hand terms.

Figs. 3,4 show the calculated GT-strength functions for the  $\beta^-$ -decay to  $^{232}\text{Th}$  and the  $\beta^+$ -decay to  $^{232}\text{Pu}$ ,  $^{240}\text{Cm}$ ,  $^{244}$

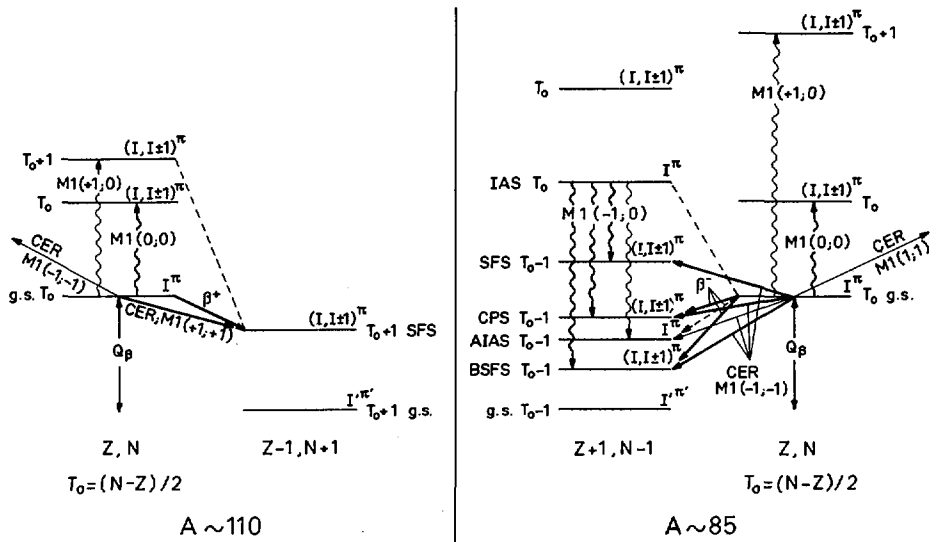


**FIG.1.** Schematic presentation taken from Ref.[13] of the  $M1$  ( $\Delta T; \mu_T$ ) modes and Gamow-Teller beta transitions in a proton-rich ( $\beta^+$  decay) and a neutron-rich ( $\beta^-$  decay) nuclide. Only the lowest-lying CPS and SFS configurations are shown. Weak  $\beta^-$  transitions to the AIAS occur because of mixing with the CPS and SFS configurations.

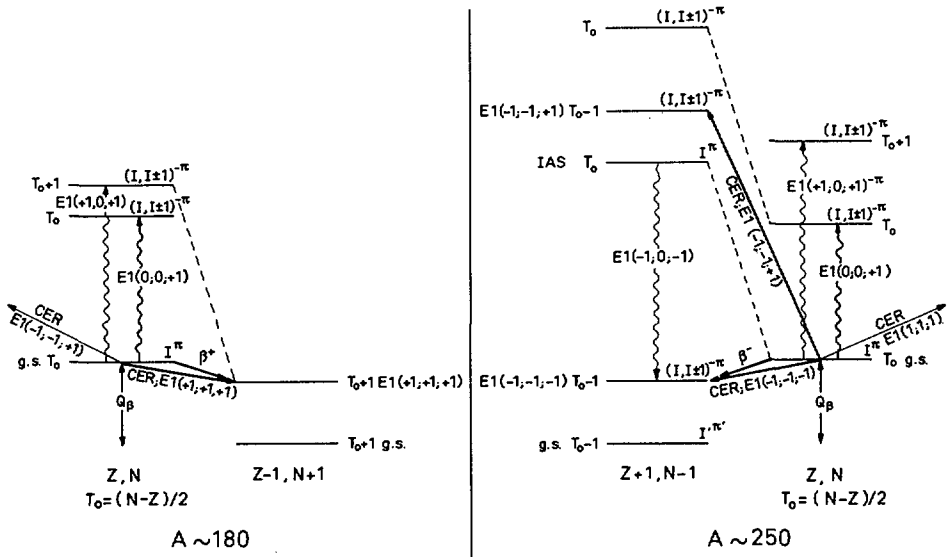


**FIG. 2.** Schematic presentation taken from Ref.[13] of the E1 ( $\Delta T$ ;  $\mu_r$ ;  $\Delta n$ ) modes and E1-like beta transitions in a proton-rich ( $\beta^+$  decay) and a neutron-rich ( $\beta^-$  decay) nuclide. The parameter  $n$  is the harmonic-oscillator quantum number.

$^{248}\text{Cf}$  and  $^{248}\text{Fm}$ . The calculations have been performed neglecting deformation, the order and the position of single particle levels has been taken from Ref. 27.

The calculation of  $S_{\beta^-}$  for  $^{232}\text{Th}$  has been performed by the model used recently [14] for the calculation of  $S_{\beta^-}$  for the decay of  $^{236},^{238}\text{Pa}$ , and used earlier for calculation of the M1 strength distribution in the isovector  $\gamma$ -decay of isobaric analogue states [23, 28, 29]. The matrix of the Hamiltonian  $H = H_{\text{sp}} + H_{\text{GT}}$  with the residual interaction

$$H_{\text{GT}} = \frac{G_0}{2} (\vec{\tau} \cdot \vec{\tau}) + \frac{G_1}{2} (\vec{\tau} \cdot \vec{\tau}) (\vec{\sigma} \cdot \vec{\sigma}) \quad (3)$$

was diagonalized in the basis of proton-particle neutron-hole states that are connected with the  $1^+$ -momentum.

The lowest-lying states in Fig. 3 correspond to back-spin flip transitions [see Refs. 13, 14] and only very little GT- $\beta$ -strength is falling into the  $Q_{\beta^-}$ -window.

The strength functions for electron capture (EC) have been calculated in the following way [see also Ref. 30]. The quasi-particles have been equally distributed over the  $h_{9/2}$ ,  $i_{13/2}$ ,  $f_{7/2}$  proton and  $g_{9/2}$ ,  $i_{11/2}$ ,  $j_{15/2}$  neutron subshells. The Hamiltonian eq. (3) of the system has been diagonalized in the basis of states 1)-4) (setting  $\Delta_n = \Delta_p = \Delta = 0.4$  MeV, a spin  $1^+$  has been assumed for the parent state):

- 1)  $p_{i13/2} \rightarrow (n_{i11/2} \otimes n_{i11/2})_{0^+} \quad (E=0)$
- 2)  $p_{i13/2} \rightarrow (n_{i11/2} \otimes n_{i11/2})_{2^+} \quad (E=2\Delta_n)$
- 3)  $p_{i13/2} \rightarrow (n_{i11/2} \otimes n_{i11/2})_{0^+} \quad (E=2\Delta_n)$   
 $(p_{i13/2} \otimes p_{i13/2})_{2^+}$
- 4)  $p_{i13/2} \left. \begin{array}{l} \\ \\ \end{array} \right\} \rightarrow \left[ (p_{i13/2} \otimes n_{i11/2})_{1^+} \otimes (p_{i13/2} \otimes n_{i11/2})_{1^+} \right]_{0^+, 2^+} \quad (E=2\Delta_p + 2\Delta_n)$

(E corresponds to the unperturbed excitation energies)

The probability for electron capture (EC) can be calculated from the strength functions in fig. 4 by multiplying  $S_{\beta^-}$  with the Fermi function, which for EC is proportional to  $(Q_{\text{EC}} - E)^2$ .

The main uncertainty in the calculated positions of the peaks in  $S_{\beta^+}(E)$  is coming from the pairing energies. The interference between the  $\beta^+$  and  $\beta^-$ -decay (see Ref. 25) is estimated to have a minor effect on these positions, however, it will reduce the calculated strengths. For the calculation

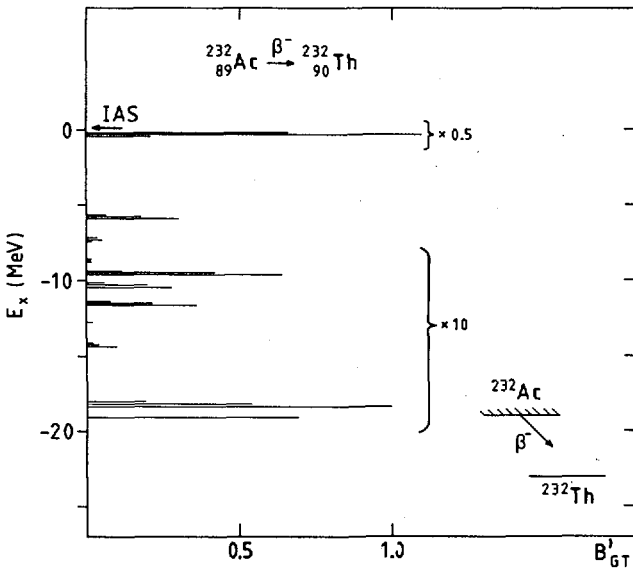


FIG.3. The calculated reduced Gamow-Teller transition probability for  $^{232}\text{Ac} \xrightarrow{\beta^-} {}^{232}\text{Th}$ . The beta strength function is given by  $B'_{\text{GT}}$ .

of  $\beta\text{DF}$  branching ratios, however, the latter is not important since the total strength is normalized by the halflife. Deformation of the nuclei is expected to lead to a spreading of the peaks in  $S_{\beta^+}$  by not more than 1 MeV.

### 3. DETERMINATION OF FISSION BARRIERS

Fission barriers for nuclides close to the stability line have been investigated in direct reactions [31] and by fission isomers [32]. For nuclides far from the stability line beta-delayed fission seems at present to be the only possibility for studying the barriers. However, the results obtained will depend, in general very strongly, on the shape of the beta strength function [13,14].

The large  $\beta\text{DF}$  branching ratios [6],  $P_{\beta\text{DF}}$ , in the beta-decay chains of the products from the thermonuclear experiments, occur in nuclides where  $Q_{\beta}$  is several MeV larger than the maximum fission barrier  $E_{\text{max}}$ . The branching ratio is independent of the details of barrier penetration and is effectively determined by the shape of  $S_{\beta}$  together with the values of  $E_{\text{max}}$  and  $Q_{\beta}$  and eventually the neutron threshold.

At present, the neutron-rich actinide nuclides synthesized in the thermonuclear experiments can not be produced under controlled laboratory conditions although this should in principle be possible [13] using microfission explosives [33]. For the

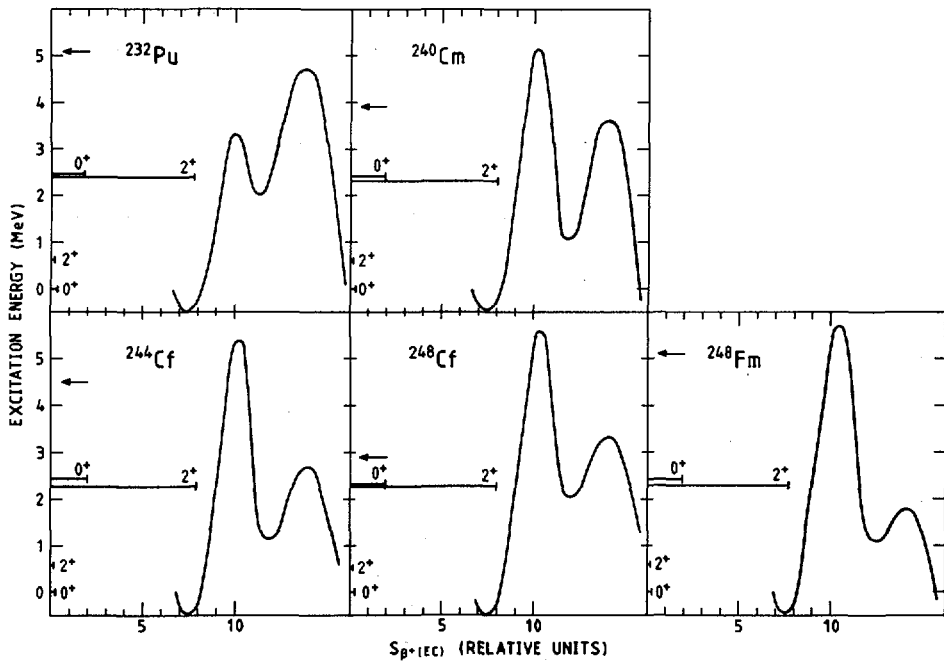


**FIG.4.** Calculated relative beta strength function for electron capture to the indicated nuclei. The fission barriers are from Ref.[35]. The arrows point to  $Q_{EC}$ -values calculated using the Garvey-Kelson mass relationship [38].

nuclides produced in the laboratory where the  $\beta$ DF ratio has been measured,  $Q_\beta \sim E_{\max}$  or  $Q_\beta \ll E_{\max}$ . The possibility of very narrow resonances in the fission probability,  $P_f(E)$ , close to the energy of the second well [34] makes the analysis of the  $P_{\beta DF}$ -values in the latter type of nuclides difficult. For nuclides where  $Q_\beta \sim E_{\max}$  and  $P_{\beta DF}$  is not too small, one would expect most of the fission to come from high-lying levels, where  $P_f(E)$  is better understood which would make it possible to obtain information about the fission barriers if the shape of  $S_\beta$  is known.

Besides the calculated beta strength function, fig. 4 also shows the fission barriers calculated by Möller and Nix [35] with the modified harmonic oscillator potential. Using these fission barriers the  $\beta$ DF branching ratios have been calculated for  $^{232}\text{Pu}$ ,  $^{244}\text{Cf}$ ,  $^{248}\text{Fm}$ , assuming the shape of  $S_\beta$  being a Gaussian peaked at the center of gravity for the upper  $0^+$ ,  $2^+$  states in fig. 4 and with a full width at half maximum of 1 MeV. Such a width is consistent with our estimates above as well as with the results from the delayed neutron experiments [20, 21]. The peak to background ratio is assumed to be 100. For calculating the fission probability a parametrization has been used, that accounts for the only partial overlap

TABLE I. EXPERIMENTAL AND CALCULATED BRANCHING RATIOS

Nuclide	Experimental $P_{\beta DF}$	Calculated $P_{\beta DF}$
$^{232}\text{Pu}$	$(1.3^{+4}_{-0.8}) \times 10^{-2}$ (Ref. [7])	$5 \times 10^{-3}$
$^{244}\text{Cf}$	$5 \times 10^{-4}$ (Ref. [9])	$4 \times 10^{-4}$
$^{248}\text{Fm}$	$3 \times 10^{-3}$ (Ref. [10])	$2 \times 10^{-3}$

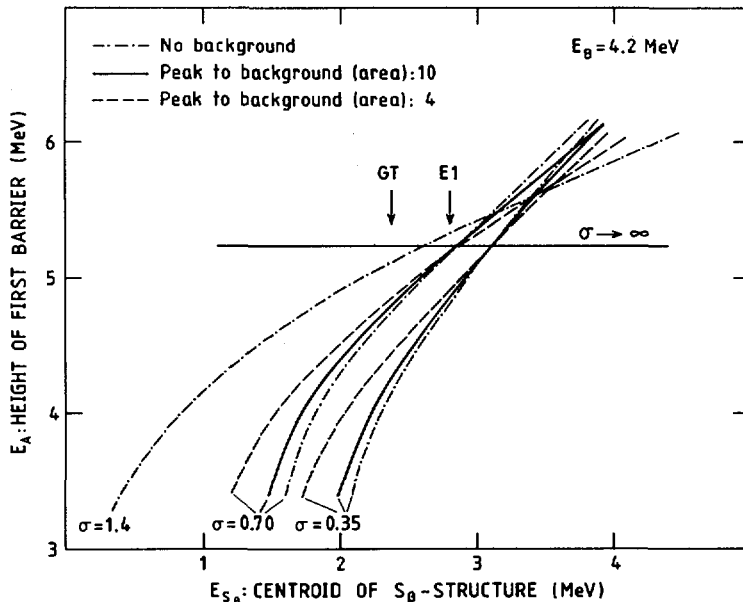


FIG.5. Keeping  $E_B$  fixed at 4.2 MeV, the height of the first barrier ( $E_A$ ) corresponding to the measured branching ratio  $P_{\beta DF} = 1.3 \times 10^{-2}$  [7] has been calculated for different positions ( $E_{S\beta}$ ) of a single structure in the beta strength function. The structure is assumed to have a Gaussian shape. The width,  $\sigma$ , of the Gaussian is varied as well as the ratio between the area in the structure and the area of the background within the  $Q_\beta$ -window from states lying outside this window.  $\sigma = 0.35$  MeV corresponds to a FWHM of 1 MeV.

[36] between the states in the first and second well. The parametrisation is a good approximation for the three nuclei considered in view of the fact that most of the fission only goes through one barrier. It will be discussed elsewhere. For the barrier curvatures the standard values  $\hbar\omega_A = 0.9$  and  $\hbar\omega_B = 0.6$  MeV have been chosen. Table I gives the experimental and calculated ratios.

Although, in view of the large uncertainties involved, agreement within a factor of 2 is rather fortuitous, the table indicates that our calculations of  $S_\beta$ , together with the Strutinsky type fission barrier calculations describe the experimental results fairly well. For  $^{240}\text{Cm}$  and  $^{248}\text{Cf}$  branching ratios of  $10^{-5}$  and  $< 10^{-7}$  have been measured [8,9], while our calculations give  $9 \cdot 10^{-7}$  and  $2 \cdot 10^{-7}$ , respectively. However, for these nuclei a more detailed treatment of the fission probability is necessary.

In figure 5 the sensitivity of the results on the shape of  $S_\beta$  is investigated for  $^{232}\text{Pu}$ . In order to be able to discuss also the results by Habs et al [7] we have kept the height of the second fission barrier fixed at  $E_B=4.2$  MeV, letting the height of the first barrier,  $E_A$ , to be determined by the experimental results and the shape of  $S_\beta$ .  $E_B=4.2$  MeV is within the interval of 4.0-4.5 MeV assumed in ref. 7 but also well within the uncertainty of  $\pm 1$  MeV quoted [35] for the Strutinsky type calculations. Assuming  $S_\beta=\text{constant}$  Habs et al find  $E_A=5.3$  MeV, i.e. a 2 MeV higher barrier than the calculations give, which would indicate that the well-known "Thorium anomaly" could be a general anomaly for proton-rich nuclei. However, as figure 5 shows, using our calculations of  $S_\beta$  and assuming a width consistent with the delayed neutron experiments [20,21] would, even with the lower  $E_B$ , give  $E_A=4.0-4.5$  MeV i.e. within the errors quoted for the Strutinsky procedure. Two conclusions can be drawn from the analysis above:

- If the expected structures in  $S_\beta$  are included, there is at present no indication from the experimental results on  $\beta^+DF$  branching ratios, that the Strutinsky procedure gives barrier heights differing from the experimental ones by more than the errors quoted [35] or  $\pm 1$  MeV.
- Since the results on the barrier heights will depend strongly on the position and width of  $S_\beta$  much more effort has to be made to investigate the details of  $S_\beta$  both experimentally and theoretically.

#### 4. CONCLUSION

For most of the proton-rich nuclei where  $\beta^+DF$  can be observed, the low-lying structures in the Gamow-Teller  $S_\beta$  are expected below the maximum of the calculated fission barriers. The estimate for the  $E1(+1;+1;+1)$ -configuration in sec. 2 indicates that the same is true for first forbidden  $E1$ -like  $\beta^+$ -decay. Thus, the  $\beta^+DF$  branching ratios will in general be small and this effect will first have to be considered before any conclusions are drawn about the height of the fission barriers. As is shown in section 3, if the expected structures in  $S_\beta$  are included, there are no indications from present  $\beta^+DF$  measurements that the calculated fission barriers are wrong by more than  $\pm 1$  MeV.

The situation is different for the neutron-rich nuclei. The simple estimates in ref. [13] indicated that the BSFS will play a large role in these nuclei. Our calculations for  $^{232}\text{Th}$

in this paper and for  $^{236,238}\text{U}$  in ref. [14] show that the BSFS centroid is expected at an excitation energy of 4-6 MeV, i.e. close to or just above the maximum of the calculated fission barriers for the neutron-rich actinides. This leads to very large  $\beta^-$ DF branching ratios when BSFS lies inside the  $Q_\beta$ -window. Such large branching ratios are seen [5,6] for the nuclides produced in the synthesis experiments using the neutron bursts from thermonuclear explosions. For these nuclides the  $E1(-1;-1; -1)$ -states may also occur close to or above  $E_{\max}$  [13] enhancing the ratios. The large  $\beta^-$ DF branching ratios will have drastic effects on the production of neutron-rich actinides and trans-actinides in the astrophysical  $r$  or  $n$ -process or by thermonuclear explosions. These effects are discussed in detail in ref [5,37, 6,18,13,19].

We have here not at all discussed the effect of the low-lying structures in  $S_\beta$  on the beta decay half-life. This is done elsewhere [18,13,19].

#### R E F E R E N C E S

- [1] KUSNETSOV,V.I.,SKOBELEV,N.K.,FLEROV,G.N.,*Sov.J.Nucl.Phys.* 4 (1967) 202, *Sov.J.Nucl.Phys.* 5 (1967) 191
- [2] ECCLES,S.F., Proc.Symp. on Engineering with Nuclear Explosives, Las Vegas, Nevada, (1970), Vol.2, 1269.
- [3] DORN,D.W.,HOFF,R.W., *Phys.Rev.Lett.* 14 (1965) 440
- [4] INGLEY,J.S., *Nucl.Phys.* A124 (1969) 130 (contains all data available up to 1969).
- [5] WENE,C.-O.,JOHANSSON,S.A.E., *Phys.Scripta* 10A (1974) 156
- [6] WENE,C.-O.,JOHANSSON,S.A.E., CERN-Report 76-13,p.584
- [7] HABS,D.,KLEWE-NEBENIUS,H.,METAG,V.,NEUMANN,B.,SPECHT,H.J., *Z.Physik* A285 (1978) 53
- [8] GANGRSKY,Yu.P.,et.al.preprint JINR P7-10797 (1977)
- [9] GANGRSKY,Yu.P.,*Isv.Akad.Nauk SSSR*, in press
- [10] GANGRSKY,Yu.P., priv.communication
- [11] GANGRSKY,Yu.P.,MARINESCU,G.M.,MILLER,M.B.,SAMOSJOK,W.N., KHARISOV,I.F., *Yad.Fiz.* 27 (1978) 894
- [12] BATIST,L.H.,BERLOVICH,E.,GAWRILOW,W.W.,NOVIKOV,Yu.N., ORLOV,C.Yu.,TICHONOW,W.I.,preprint No 363 (1977), Institute of Nucl. Physics, Leningrad.
- [13] Klapdor,H.V.,WENE,C.-O., report MPI-H v25 (1978) Max-Planck-Institut für Kernphysik, Heidelberg, and to be published.
- [14] Klapdor,H.V.,WENE,C.-O.,ISOSIMOW,I.N.,NAUMOW,Yu.W., *Phys.Lett* 78B (1978) 20
- [15] DUKE,C.L.,HANSEN,P.G.,NIELSEN,O.B.,RUDSTAM,G.,*Nucl.Phys.* A151 (1970) 609  
HARDY,J.C.,JONSON,B.,HANSEN,P.G.,*Nucl. Phys.* A305 (1978) 15
- [16] SHALEV,S.,RUDSTAM,G.,*Nucl.Phys.* A230 (1974) 153, A235 (1974) 397, A275 (1977) 76
- [17] TAKAHASHI,K.,*Progr. Theor. Phys.* 47 (1972) 1500
- [18] Klapdor,H.V.,*Phys. Lett.* 65B (1976) 34, CERN-Report 76-13,p.311
- [19] Klapdor,H.V.,WENE,C.-O., *Astrophys.J.Lett.*, in press.
- [20] KRATZ,K.-L.,RUDOLPH,W.,OHM,H.,FRANZ,H.,HERRMANN,G., RISTORI,C.,CRANCON,J.,ASGHAR,M.,CRAWFORD,G.I.,NUH,F.M., PRUSSIN,S.G.,*Phys.Lett.* 65B (1976) 231

- [21] KRATZ, K.-L., RUDOLPH, W., OHM, H., FRANZ, H., ZENDEL, M., HERRMANN, G., PRUSSIN, S.G., NUH, F.M., SHIBAB-ELDIN, A.A., SLAUGHTER, D.R., HALVERSSON, W., Klapdor, H.V., Nucl. Phys. A317 (1979) 335
- [22] Klapdor, H.V., Phys. Lett. 35B (1971) 405  
Schrader, M., Klapdor, H.V., Bergdolt, G., Bergdolt, A.M., Phys. Lett. 60B (1975) 39
- [23] NAUMOW, Yu.W., KRAFT, O.E., Sov.J.Part.Nucl., 6 (1976) 361
- [24] DOERING, R.R., GALONSKY, A., PATTERSON, D.M., BERTSCH, G.F., Phys.Rev.Lett. 35 (1975) 1691
- [25] BOHR, A., MOTTELSON, B., Nucl. Structure, vol I and II, W.A. Benjamin, New York (1969), (1975).
- [26] PAUL, P., in Int. Conf. on Photonuclear Reactions and Applications, U.S. Atomic Energy Commission Office of Information Services, Oak Ridge, Tenn, (1973) vol I, p.407.
- [27] IVANOVA, S.P., KOMOW, A.L., MALOW, L.A., SOLOVIEV, W.G., Sov.J. Part.Nucl., Vol 7:2, (1976)
- [28] NAUMOW, Yu.W., Isv.Akad.Nauk SSSR (ser.fiz) 39 (1975) 1656
- [29] Klapdor, H.V., Schrader, M., Bergdolt, G., Bergdolt, A.M., NAUMOW, Yu.W., Isv.Akad.Nauk SSSR (ser.fiz.) 42 (1978) 64
- [30] BYKOV, A.A., NAUMOW, Yu.W., Isv.Akad.Nauk SSSR (ser.fiz.) 42 (1978) 1911
- [31] BACK, B.B., HANSEN, O., BRITT, H.V., GARRETT, J.D., Phys.Rev. C9 (1974) 1924  
BACK, B.B., BRITT, H.C., HANSEN, O., LEROUX, B., GARRETT, J.D., Phys.Rev. C10 (1974) 1948
- [32] BRITT, H.C., BÖLSTERLI, M., NIX, J.R., NORTON, J.L., Phys.Rev. C7 (1973) 801
- [33] WINTERBERG, F., Nature 241 (1973) 449
- [34] LYNN, J.E., in Nuclear Structure, Dubna Symp. (IAEA, Vienna 1968) p.463
- [35] MÖLLER, P., NIX, J.R., in Proc Third IAEA Symp. on Physics and Chemistry of Fission, Rochester, N.Y. 1973 (IAEA, Vienna, 1974) Vol I, p.103.
- [36] GLÄSSEL, P., RÖSLER, H., SPECHT, H.J., Nucl.Phys. 256 (1976) 220
- [37] WENE, C.-O., Astron. Astrophys. 44 (1975) 233
- [38] Atomic and Nuclear Data Tables, 17 (1976) No 5-6

## DISCUSSION

H.J. SPECHT: I am most interested to hear of your difficulties in attempting to use  $\beta$ -delayed fission probabilities to determine fission barrier heights. But I am afraid I cannot agree with your conclusions. I do not think that you can really claim consistency with the theoretical barriers for  $^{232}\text{Pu}$  in this connection. If I understand correctly, you have adopted a spherical basis for these highly deformed nuclei, but would you not expect the width of the strength function to increase by several MeV if you use a deformed basis? An increase of this kind and/or a shift in the centre of gravity by less than 0.5 MeV would bring us back to our former conclusion that the first barrier height in  $^{232}\text{Pu}$  is  $> 5$  MeV.

C.O. WENE: No, I do not think so. That is in fact one of the main points of my talk. If you shifted the centre of gravity by 0.5 MeV in the other direction, you would see that the barrier height was lower than 3 MeV. So I do not believe that it is possible to extract barrier heights in the way you did in your work, cited as Ref.[7] in our paper. Given the experimental data on  $P_{\beta DF}$  and the  $\beta$  strength function available at present, it is not possible to conclude that there is a 'thorium anomaly' for  $^{232},^{234}\text{Pu}$  as well. We feel that reliable extractions of barrier heights from  $\beta$ -delayed fission measurements can be made only after careful experimental determination of the  $\beta$  strength function.

The effect of deformation on the spreading of the  $\beta$  strength function has been investigated in detail for  $^{117-123}\text{Ba}$  isotopes by Ivanova and co-workers (Yad. Fiz. 24 (1976) 278) and is found to have much less influence on the shape of  $S_\beta$  than you suggest.

G.F. HERRMANN: I would just like to comment that structures in the  $\beta$  strength function of proton-rich nuclei have also been assumed by Khamaukov and co-workers in order to explain the shapes of several  $\beta^+$ -delayed proton spectra. As far as neutron-rich nuclei are concerned, I can also refer you to a paper by S.G. Prussin and co-workers to be published shortly in Nuclear Physics. They show that it is only by the introduction of Gaussian-shaped structures that both the general shape of  $\beta$ -delayed neutron spectra and branching into the final excited states can be understood.

C.O. WENE: Thank you for the comment. We have recently given a detailed review of the theoretical and experimental work being done on the  $\beta$  strength function. For details see Ref.[13] of my paper, and an article by the same authors in the press for the Bulletin of the USSR Academy of Sciences.

# ETUDE DES RESONANCES DE VIBRATION DANS LA REACTION $^{231}\text{Pa}(n,f)$

A. SICRE, F. CAÏTUCOLI, G. BARREAU\*,  
T.P. DOAN, T. BENFOUGHAL, B. LEROUX  
Centre d'études nucléaires de Bordeaux-Gradignan,  
Gradignan, France

## Abstract—Résumé

### **STUDY OF VIBRATIONAL RESONANCES IN THE REACTION $^{231}\text{Pa}(n,f)$ .**

The excitation function of the reaction  $^{231}\text{Pa}(n,f)$  was measured from 130 to 450 keV with a neutron energy resolution of 5 keV. The measurements confirmed the existence of the two structures already observed around  $E_n = 200$  keV and  $E_n = 330$  keV and revealed a narrow resonance around  $E_n = 160$  keV. The use of an energy resolution of only 2 keV showed that the width of this resonance is  $\leq 2$  keV. The angular distributions of the fission fragments were also measured in the vicinity of these three structures with an energy resolution of 5 keV. The excitation function and the angular distributions were reproduced simultaneously with the aid of a statistical model allowing for the competition between the different exit channels (neutron emission, gamma emission, fission through a barrier with two peaks). This analysis shows that the narrow resonance at 160 keV has all the characteristics of a pure vibrational resonance ( $KJ^\pi = (33^+)$ ). The resonances at 200 keV and 330 keV are interpreted as corresponding to the vibrational states  $K^\pi = 0^+$  and  $K^\pi = 0^-$ .

### **ETUDE DES RESONANCES DE VIBRATION DANS LA REACTION $^{231}\text{Pa}(n,f)$ .**

La fonction d'excitation de la réaction  $^{231}\text{Pa}(n,f)$  a été mesurée de 130 à 450 keV avec une résolution en énergie des neutrons de 5 keV. Cette mesure a confirmé l'existence des deux structures déjà observées vers  $E_n = 200$  keV et  $E_n = 330$  keV et mis en évidence une résonance étroite vers  $E_n = 160$  keV. L'utilisation d'une résolution en énergie de 2 keV seulement a montré que la largeur de cette résonance est  $\leq 2$  keV. Les distributions angulaires des fragments de fission ont également été mesurées au voisinage de ces trois structures avec une résolution en énergie de 5 keV. La fonction d'excitation et les distributions angulaires ont été reproduites simultanément à l'aide d'un modèle statistique rendant compte de la compétition entre les différentes voies de sortie (émission de neutrons, émission gamma, fission à travers une barrière à 2 maxima). Cette analyse montre que la résonance étroite à 160 keV présente toutes les caractéristiques d'une résonance de vibration pure ( $KJ^\pi = (33^+)$ ). Les résonances à 200 keV et 330 keV sont interprétées comme correspondant à des états de vibration  $K^\pi = 0^+$  et  $K^\pi = 0^-$ .

---

\* Actuellement à l'Institut Laue Langevin, Grenoble, France.

## 1. INTRODUCTION

Il y a une dizaine d'années, on avait déjà observé que les fonctions d'excitation des réactions ( $n,f$ ) sur les actinides non fissiles présentaient souvent des plateaux ou même des structures résonnantes au voisinage de leurs seuils. Dans le cadre du modèle de la goutte liquide, qui prévoit une barrière de fission présentant un seul maximum, ces structures ne pouvaient être dues qu'à une modification de la compétition entre les différentes voies de sortie (fission, émission de neutrons ou émission de rayonnements  $\gamma$ ), et elles ont généralement été attribuées à l'ouverture soudaine de nouvelles voies de neutrons; mais toutes les tentatives d'interprétation quantitatives basées sur cette hypothèse se sont soldées par des échecs, et il a fallu attendre l'introduction par Strutinsky des effets de couche et d'appariement dans le modèle de la goutte liquide pour expliquer d'une manière cohérente l'existence de ces structures.

En effet l'une des principales conséquences des travaux de Strutinsky [1-4] consiste à prévoir une barrière de fission présentant 2 maxima encadrant un second puits de potentiel capable d'assurer une certaine stabilité à des états très déformés et en particulier à des états de vibration  $\beta$  qui jouent le rôle d'états-porte vers la fission.

Ceci est schématisé sur la figure 1 qui présente la variation du coefficient de transmission à travers la barrière de fission en fonction de l'énergie disponible dans le degré de liberté associé à la fission.

Ce coefficient de transmission présente des résonances pour des énergies correspondant aux états de vibration  $\beta$  du second puits de potentiel. La largeur de ces résonances dépend naturellement de la largeur, donc du temps de vie, des états de vibration qui leur donnent naissance. Comme à chaque état de vibration est associée une bande de rotation, la probabilité de fission présente une série de résonances correspondant aux différents membres de cette bande de rotation. Ces résonances individuelles seront distinctes si leur largeur est faible par rapport à l'énergie de rotation et plus ou moins confondues dans le cas contraire. Leurs intensités relatives dépendent principalement de la distribution en moment angulaire du noyau composé, car la compétition entre les différentes voies de sortie dépend peu du moment angulaire.

L'étude de ces résonances de vibration présente un grand intérêt dans la mesure où il est possible d'en extraire des informations sur la forme de la barrière de fission et sur les caractéristiques spectroscopiques des états de vibration  $\beta$ . Dans certains cas privilégiés, il est également possible de mesurer le moment d'inertie de noyaux très déformés [5], ou d'obtenir des informations sur l'importance de la viscosité nucléaire au niveau du second puits de potentiel [6].

L'obtention de ces informations exige toutefois l'utilisation d'une très bonne résolution en énergie et la mesure simultanée des distributions angulaires des fragments de fission afin de mettre en évidence l'ouverture successive des différentes voies de fission.

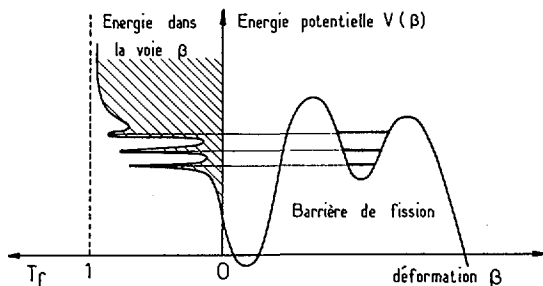


*FIG.1. Variation du coefficient de transmission à travers la barrière de fission en fonction de l'énergie disponible dans le degré de liberté associé à la fission.*

Dans une précédente étude [7], réalisée avec une résolution en énergie de 10 keV, nous avions observé dans la fonction d'excitation de la réaction  $^{231}\text{Pa}(n,f)$  deux structures résonantes situées au voisinage des énergies de neutrons  $E_n=200$  keV et  $E_n=330$  keV; l'interprétation simultanée de la fonction d'excitation et de la forme des distributions angulaires des fragments de fission nous avait conduit à supposer que chacune de ces structures provenait de la superposition d'au moins 2 résonances de vibration. Il nous a donc paru intéressant d'essayer de mettre en évidence ces différentes composantes éventuelles en reprenant nos mesures avec une meilleure résolution en énergie.

## 2. TECHNIQUES EXPERIMENTALES

### *Production des neutrons*

La section efficace de fission de la réaction  $^{231}\text{Pa}(n,f)$  ainsi que les distributions angulaires des fragments de fission ont été mesurées auprès de l'accélérateur Van de Graaff de 4 MV du Centre d'études nucléaires de Bordeaux-Gradignan. Les neutrons incidents sont produits par la réaction  $^7\text{Li}(p,n)$  sur une cible de fluorure de lithium. Un détecteur de neutrons placé dans la direction des protons incidents permet de contrôler le flux de neutrons. Les mesures sont faites point par point en modifiant l'énergie des protons incidents. La calibration en énergie du faisceau de protons est obtenue par la mesure du seuil de la réaction  $^7\text{Li}(p,n)$  qui est pris égal à 1880,6 keV. Au-delà du seuil, la fonction d'excitation de la réaction présente un maximum; l'épaisseur des dépôts de LiF est évaluée à partir de la variation en énergie des protons incidents faisant passer le taux de production de neutrons de 10% à 90% de ce maximum. En utilisant un faisceau de protons de 30  $\mu\text{A}$  sur un dépôt de LiF de  $10 \mu\text{g/cm}^2$ , on obtient un flux de

neutrons de  $10^5 \text{ n} \cdot \text{cm}^{-2} \cdot \text{s}^{-1}$  sur le dépôt fissionnant situé à une distance de 10 cm. La résolution en énergie du faisceau de neutrons est alors de l'ordre de 2 keV.

### *Dépôts de $^{231}\text{Pa}$*

Les deux cibles de  $^{231}\text{Pa}$  que nous avons utilisées proviennent de Harwell et sont constituées d'un dépôt d'oxyde de protactinium sur un disque d'aluminium de 2 cm de diamètre et de 0,25 mm d'épaisseur. Les épaisseurs de  $^{231}\text{Pa}$  sont respectivement égales à  $2,04 \text{ mg/cm}^2$  et  $2,01 \text{ mg/cm}^2$ ; chaque cible contient donc environ 6 mg de  $^{231}\text{Pa}$ . Les dépôts contiennent ( $93,5 \pm 0,2\%$ ) de  $^{231}\text{Pa}$  et ( $6,5 \pm 0,1\%$ ) de descendants. Parmi les descendants seuls les noyaux  $^{227}\text{Ac}$  et  $^{207}\text{Pb}$  ont des périodes suffisamment longues pour assurer leur accumulation, mais ils présentent des seuils de fission beaucoup plus élevés que celui de la réaction étudiée.

### *Détection des fragments de fission*

La section efficace de fission de la réaction  $^{231}\text{Pa}(n,f)$  est faible (inférieure à 100 mb) dans la zone d'énergie étudiée près du seuil. Par contre le  $^{231}\text{Pa}$  présente une très forte radioactivité  $\alpha$  ( $1,8 \times 10^6 \alpha \cdot \text{mg}^{-1} \cdot \text{s}^{-1}$ ). Le taux relatif de fragments par rapport aux particules  $\alpha$  est donc de l'ordre de  $10^{-7}$ . Ces conditions très particulières nous ont conduit à utiliser les détecteurs plastiques de traces. En effet, en choisissant convenablement les paramètres de l'attaque chimique qui permettent de révéler les traces des particules enregistrées (concentration, température, durée), il est possible de faire une discrimination entre les particules  $\alpha$  et les fragments de fission avec une efficacité pratiquement égale à 100%.

Le détecteur utilisé est une feuille de Makrofol suffisamment mince ( $10 \mu\text{m}$ ) pour être traversée de part en part par les fragments de fission dont le parcours est de 15 à 20  $\mu\text{m}$  dans cette matière. Après irradiation, une attaque chimique ( $\text{NaOH } 6\text{N à } 70^\circ\text{C}$  pendant 20 min) permet de produire un trou de 1 à 2  $\mu\text{m}$  de diamètre à l'emplacement de chaque impact d'un fragment de fission sur le détecteur.

Les traces sont ensuite visualisées en utilisant la méthode proposée par Lark [8]: la feuille de Makrofol est placée entre une plaque de cuivre et une feuille de Mylar métallisé dont la couche d'aluminium est portée à la haute tension; les claquages qui se produisent à l'endroit des traces détruisent la couche d'aluminium. On obtient ainsi une image de la distribution de l'impact des fragments de fission sur le détecteur.

## 2.1. Mesure de la section efficace de fission

### *Dispositif expérimental*

Pour cette mesure nous avons utilisé les détecteurs plastiques de traces dans un montage en sandwich comportant un dépôt de  $^{231}\text{Pa}$  et un dépôt de  $^{235}\text{U}$  placés dos à dos. Chaque détecteur est constitué par une feuille de Makrofol de 10  $\mu\text{m}$  d'épaisseur, maintenue face à chaque dépôt à une distance de 1 mm. La géométrie de détection est alors très voisine de  $2\pi$ .

Dans une première expérience, nous avons voulu obtenir une dispersion de l'énergie des neutrons  $\Delta E_n = 5 \text{ keV}$ . Pour cela, nous avons employé une cible de LiF de  $30 \mu\text{g/cm}^2$  d'épaisseur qui produit une dispersion maximale due à la perte d'énergie des protons incidents:  $\Delta E_p^p = 4,2 \text{ keV à } E_n = 150 \text{ keV}$ . Le système dépôts-détecteurs a été placé à 7,5 cm de la cible de LiF; pour cette distance, on a une dispersion due à l'ouverture du faisceau de neutrons  $\Delta E_n^n = 2,2 \text{ keV à } E_n = 150 \text{ keV}$ ; la dispersion totale à 150 keV est alors  $\Delta E_t^t = 4,8 \text{ keV}$ .

Dans une expérience complémentaire, nous avons pu atteindre une dispersion encore plus faible en utilisant une cible de LiF de  $10 \mu\text{g/cm}^2$  et en plaçant le sandwich dépôts-détecteurs à 10 cm de cette cible. On a alors respectivement  $\Delta E_p^p = 1,3 \text{ keV}$  et  $\Delta E_n^n = 1,4 \text{ keV à } 150 \text{ keV}$ , ce qui donne une dispersion totale  $\Delta E_t^t = 2,1 \text{ keV}$  pour cette énergie en évaluant à 1 keV la résolution de l'accélérateur. Une dispersion aussi faible s'obtient bien entendu au détriment du taux de comptage, et il est difficile de l'employer sur d'importantes plages en énergie.

La normalisation des résultats se fait par rapport à la section efficace de fission de la réaction  $^{235}\text{U}(n,f)$  pour laquelle nous avons pris les valeurs de la compilation de Sowerby et al. [9].

### *Résultats*

La section efficace de fission mesurée de  $E_n = 130$  à  $450 \text{ keV}$  par pas de 5 keV avec une résolution en énergie des neutrons de 5 keV est présentée sur la figure 2; les barres d'erreur qui sont portées représentent seulement les fluctuations statistiques sur les nombres de traces comptées. Cette mesure confirme l'existence des deux larges structures centrées sur  $E_n = 200 \text{ keV}$  et  $E_n = 330 \text{ keV}$ , mais la meilleure résolution utilisée ici permet de faire apparaître nettement une résonance très fine à  $E_n = 160 \text{ keV}$ . Cette résonance présente une hauteur de 25 mb et une largeur égale à la résolution en énergie  $\Delta E_n = 5 \text{ keV}$ . Les valeurs de la section efficace au sommet de la résonance et dans le creux, à  $E_n = 175 \text{ keV}$ , sont dans le rapport 3,8.

Afin de préciser la largeur réelle de cette résonance, nous avons fait une nouvelle mesure avec une résolution en énergie  $\Delta E_n = 2 \text{ keV}$  dans une zone très

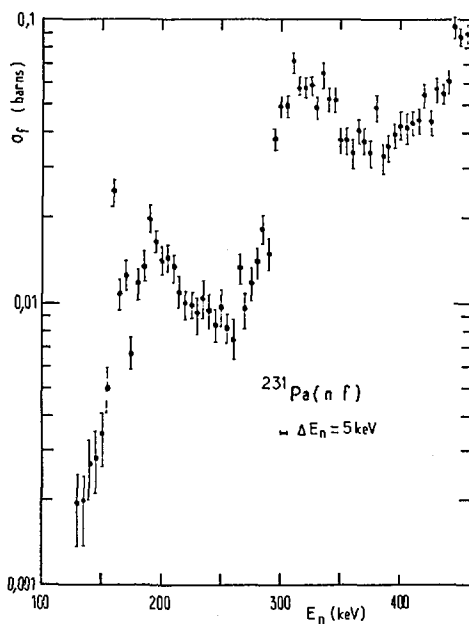


FIG.2. Section efficace de fission entre  $E_n = 130$  et  $450 \text{ keV}$ .

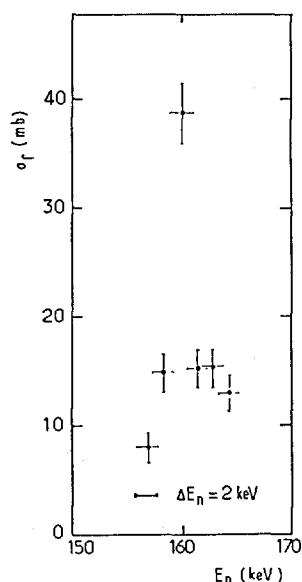


FIG.3. Section efficace de fission dans une zone limitée autour de  $160 \text{ keV}$ .

limitée autour de 160 keV. Le résultat obtenu (fig.3) montre que la largeur de la résonance est encore de l'ordre de la résolution en énergie, c'est-à-dire 2 keV. Par contre, le sommet de la résonance passe de 25 à  $39 \pm 3$  mb; il est donc tout à fait possible que cette résonance soit encore plus haute et plus étroite.

## 2.2. Mesure des distributions angulaires

Pour compléter la mesure de la section efficace de fission, nous avons aussi mesuré les distributions angulaires des fragments de fission avec une résolution en énergie compatible avec la largeur des structures observées.

### *Dispositif expérimental*

Les fragments de fission sont enregistrés par un détecteur plastique cylindrique, de 18 cm de diamètre et de 30 cm de hauteur, dont l'axe est perpendiculaire à la direction moyenne des neutrons incidents; les dimensions de ce cylindre résultent d'un compromis entre la résolution angulaire, l'angle solide de détection, la facilité de manipulation du détecteur et le rapport signal sur bruit du détecteur. Afin de permettre le dépouillement par la méthode des étincelles, le détecteur est une feuille de Makrofol de 10  $\mu\text{m}$  d'épaisseur. Cette feuille est fixée par effet électrostatique sur une feuille plus épaisse de Makrofol. Au centre du cylindre les deux dépôts de  $^{231}\text{Pa}$  sont placés dos à dos, et animés d'un mouvement de rotation autour de l'axe du cylindre. Cette rotation a pour but d'atténuer l'influence sur les distributions angulaires du ralentissement ou de l'absorption des fragments rasants dans l'épaisseur des dépôts de  $^{231}\text{Pa}$ . L'ensemble se trouve dans une chambre cylindrique en acier inoxydable dont la paroi fait 1 mm d'épaisseur; une pompe maintient cette chambre sous un vide primaire. La chambre est placée sur un plateau orientable permettant le positionnement correct de l'ensemble cibles-détecteur par rapport à la direction des neutrons incidents (fig.4).

### *Obtention des distributions angulaires expérimentales*

En première approximation, on peut considérer que les fragments de fission proviennent d'une source ponctuelle. Les fragments dont la direction d'émission fait un angle  $\theta$  donné avec la direction moyenne Oz des neutrons incidents atteignent le détecteur le long d'une courbe décrite par l'intersection du cylindre du détecteur avec le cône de demi-angle au sommet  $\theta$  et d'axe Oz. La figure 5 représente ces courbes sur un demi-cylindre de détecteur déroulé et pour des angles  $\theta$  variant de  $0^\circ$  à  $90^\circ$  par intervalles de  $10^\circ$ . Au moyen d'une grille, on peut compter les traces des fragments dans chaque zone du détecteur ainsi délimitée et obtenir les quantités  $(dN/d\Omega)/(\theta)$ .

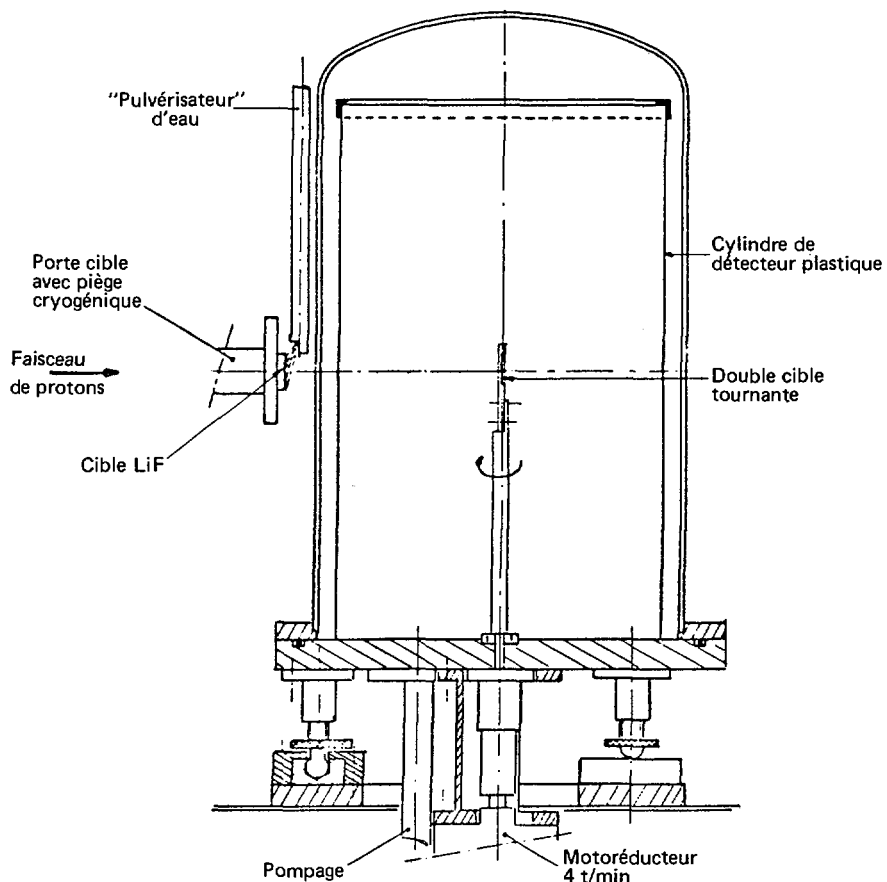


*FIG. 4. Détecteur cylindrique.*

Afin de préciser l'influence des dimensions réelles du dispositif sur les mesures, nous avons effectué un calcul du type Monte Carlo pour simuler la répartition des fragments sur le détecteur pour différentes distributions angulaires théoriques, en tenant compte des dimensions réelles des cibles de LiF et de  $^{231}\text{Pa}$  et de la rotation des cibles de  $^{231}\text{Pa}$ . L'écart entre les distributions angulaires théoriques et simulées reste inférieur à 2%; l'influence de la résolution angulaire est donc négligeable par rapport aux fluctuations statistiques.

#### Résultats

Les distributions angulaires des fragments de fission ont été mesurées de  $E_n = 160 \text{ keV}$  à  $E_n = 350 \text{ keV}$  avec une résolution en énergie des neutrons de

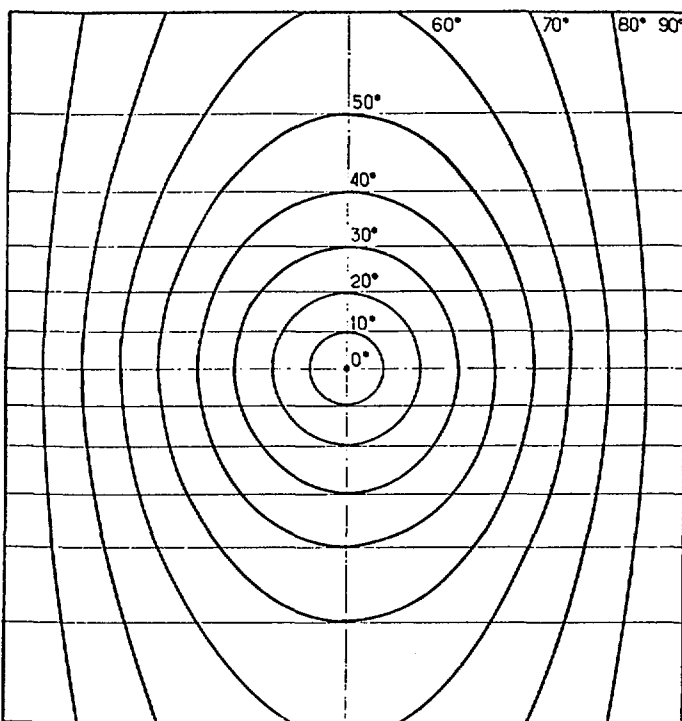


*FIG.5. Courbes décrites par l'intersection du cylindre du détecteur avec le cône de demi-angle au sommet  $\theta$  et d'axe Oz.*

5 keV. Les résultats obtenus sont représentés sur la figure 6 ainsi que le lissage obtenu au moyen d'un développement en polynômes de Legendre:

$$W(\theta) = A_0 \left[ 1 + \sum_n \alpha_{2n} P_{2n}(\cos \theta) \right]$$

Dans le tableau I, nous donnons les valeurs des coefficients  $\alpha_{2n}$  ainsi que les valeurs du rapport  $R = W(0^\circ)/W(90^\circ)$  calculées à partir de ce développement.

L'information la plus intéressante qui ressort de ces mesures est la forme nettement piquée à  $90^\circ$  de la distribution angulaire pour  $E_n = 160$  keV. Lorsque l'énergie croît jusqu'à  $E_n = 225$  keV, les distributions angulaires tendent à devenir isotropes. Dans le domaine de la résonance située autour de  $E_n = 330$  keV, la forme des distributions angulaires varie assez peu autour d'une forme isotrope.

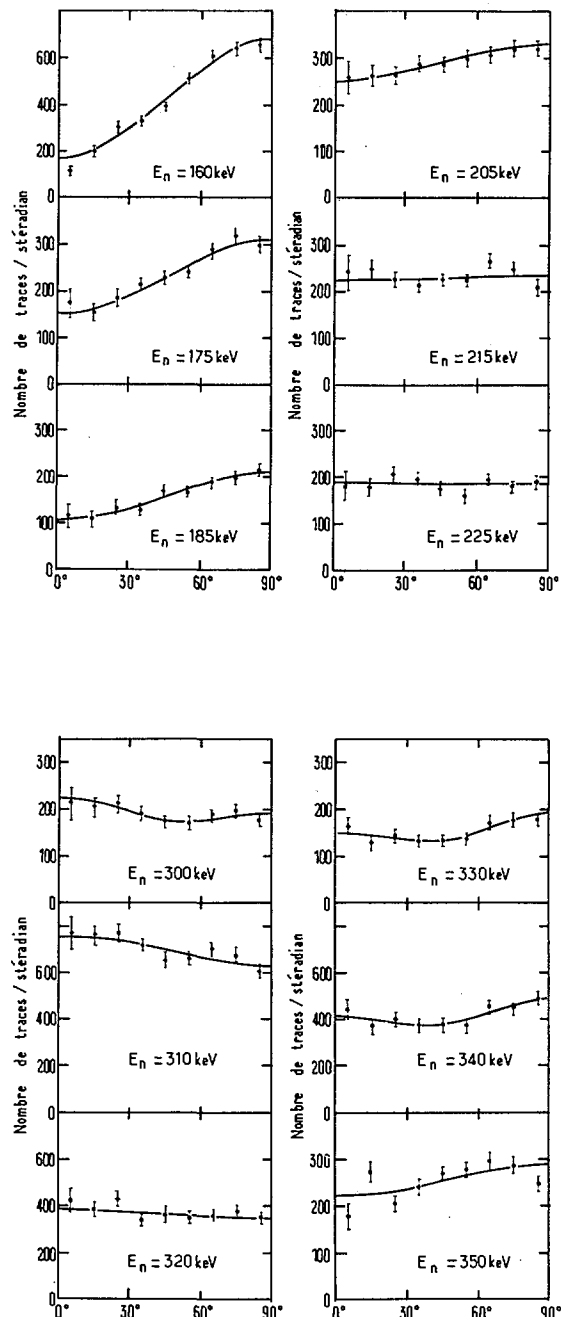


FIG. 6. Distributions angulaires des fragments.

TABLEAU I. COEFFICIENTS  $\alpha_{2n}$  ET R OBTENUS AU MOYEN D'UN DEVELOPPEMENT EN POLYNOMES DE LEGENDRE

$E_n$ (keV)	$\alpha_2$	$\alpha_4$	$R = W(0^\circ)/W(90^\circ)$
160	$-0,656 \pm 0,024$		$0,26 \pm 0,03$
175	$-0,404 \pm 0,039$		$0,50 \pm 0,05$
185	$-0,389 \pm 0,047$		$0,51 \pm 0,06$
195	$-0,113 \pm 0,042$		$0,84 \pm 0,05$
205	$-0,165 \pm 0,039$		$0,77 \pm 0,05$
215	$-0,035 \pm 0,046$		$0,95 \pm 0,06$
225	$0,012 \pm 0,052$		$1,02 \pm 0,07$
300	$0,060 \pm 0,055$	$0,147 \pm 0,068$	$1,18 \pm 0,11$
310	$0,119 \pm 0,028$		$1,19 \pm 0,04$
320	$0,056 \pm 0,038$		$1,09 \pm 0,05$
330	$-0,247 \pm 0,056$	$0,201 \pm 0,072$	$0,80 \pm 0,10$
340	$-0,182 \pm 0,034$	$0,159 \pm 0,044$	$0,85 \pm 0,06$
350	$-0,162 \pm 0,041$		$0,78 \pm 0,05$

### 3. METHODE D'ANALYSE

L'interprétation des résultats expérimentaux est effectuée à l'aide d'un programme d'analyse basé sur les hypothèses suivantes:

— La réaction ( $n,f$ ) est supposée se dérouler en deux étapes successives indépendantes. Dans l'étape initiale, il y a formation d'un noyau composé de moment angulaire  $J$  et de parité  $\pi$  par capture de neutron. Le noyau formé présente une déformation très voisine de la déformation de l'état fondamental du noyau cible. Il se trouve donc dans le premier puits de la barrière de fission avec une énergie d'excitation  $E^* \cong B_n + E_n$ . Dans notre étude de la réaction ( $^{231}\text{Pa} + n$ ) où  $B_n = 5,562$  MeV, cette énergie d'excitation varie entre 5,7 et 6 MeV environ. Dans une deuxième étape le noyau se désexcite suivant l'un des trois modes de désexcitation possibles: émission d'un rayonnement gamma, émission d'un neutron ou fission.

— Nous supposons en outre que la projection  $K$  du moment angulaire total  $J$  du noyau composé sur son axe de déformation principal se conserve au cours du processus de fission et en particulier pendant la transition du point-selle au point de scission. Cette hypothèse peut se justifier par la rapidité de cette

transition ( $10^{-21}$  à  $10^{-22}$  s) qui empêche une action importante des forces de Coriolis. On suppose que les fragments de fission sont émis le long de l'axe de déformation principal du noyau.

La section efficace différentielle de fission correspondant à une voie de fission caractérisée par les nombres quantiques  $KJ\pi$  est alors donnée par l'expression suivante:

$$\frac{d\sigma_f}{d\Omega}(E^*, J\pi K, \theta) = \frac{2J+1}{4\pi} \cdot \frac{T_f^{KJ\pi}(E^*)}{\sum_{K=J}^{+J} T_f^{KJ\pi}(E^*) + N_n^{J\pi}(E^*) + N_\gamma^{J\pi}(E^*)} \times \sum_{M=-J}^{+J} \sigma_c(E^*, J\pi M) \cdot |d_{MK}^J(\theta)|^2$$

Dans cette expression,  $E^*$  est l'énergie d'excitation du noyau composé,  $\theta$  définit l'angle d'émission des fragments de fission par rapport à la direction des neutrons incidents;  $\sigma_c$  est la section efficace de formation du noyau composé;  $T_f$  est le coefficient de transmission à travers la barrière de fission;  $N_n$  et  $N_\gamma$  sont les nombres de voies de sortie effectives respectivement associés à l'émission d'un neutron et à l'émission d'un rayonnement gamma; enfin les fonctions  $d_{MK}^J(\theta)$  sont les fonctions d'onde de la toupie symétrique.

a) La section efficace de formation du noyau composé est calculée en utilisant les coefficients de transmission pour les neutrons  $T_\chi^{\beta \pm 1/2}(E_n)$  obtenus par Perey et Buck [10] au moyen d'un potentiel optique non local.

b) Pour calculer le coefficient de transmission  $T_f$  à travers la barrière de fission  $V(\beta)$ , on ne considère que l'énergie  $E_\beta$ , effectivement disponible dans le degré de liberté  $\beta$  associé à la fission:  $E_\beta = E^* - E^i$  où  $E^i$  est l'énergie «interne» disponible dans les autres degrés de liberté du noyau parmi lesquels on distingue la rotation du noyau autour d'un axe perpendiculaire à son axe de déformation principal:

$$E_\beta = E^* - (E_0^i + E_{\text{rot}})$$

avec

$$E_{\text{rot}} = \frac{\hbar^2}{2I} \left[ J(J+1) - K(K+1) + \delta(K, 1/2) \cdot \alpha \cdot (-1)^{J+1/2} \cdot (J+1/2) \right]$$

où  $\mathcal{J}$  est le moment d'inertie du noyau et  $\alpha$  le paramètre de découpage.

Il s'agit donc de résoudre l'équation de Schrödinger:

$$-\frac{\hbar^2}{2\mu} \frac{\partial^2 \varphi(\beta)}{\partial \beta^2} + \left[ V(\beta) - E_\beta \right] \varphi(\beta) = 0$$

Dans le cas d'une barrière à deux maxima, cette équation se résout numériquement ou analytiquement dans le cadre de l'approximation WKB [11]. Cependant Cramer et Nix [12] ont proposé une méthode de résolution analytique sans aucune approximation pour une barrière représentée par une suite de trois paraboles jointives. Le coefficient de transmission calculé par cette méthode présente des résonances aiguës pour des énergies  $E_\beta$  inférieures au plus bas des deux maxima de la barrière. Ces résonances correspondent aux états de vibration du deuxième puits. La position et la forme des résonances dépendent des six paramètres ( $E_A, \hbar\omega_A$ ), ( $E_B, \hbar\omega_B$ ), ( $E_{II}, \hbar\omega_{II}$ ) qui caractérisent respectivement les hauteurs et les courbures des 2 maxima et la profondeur et la courbure du puits intermédiaire.

Dans le cas d'une barrière présentant 3 maxima, telle que l'ont suggérée Möller et Nix [13], on peut utiliser le calcul analytique généralisé par Bhandari [14], mais comme dans cette hypothèse le premier maximum est faible, on peut se ramener à une double barrière constituée par le second et le troisième maximum de hauteur comparable.

Pour simuler un effet de damping au niveau du second puits, on ajoute, comme l'ont proposé Back et al. [15] au potentiel réel  $V(\beta)$  un terme imaginaire  $W(\beta)$  localisé dans le second puits. Le coefficient de transmission est alors la somme de deux termes: un terme correspondant à la transmission directe sans amortissement  $T_D$  et un terme décrivant la redistribution du flux absorbé. On suppose que cette redistribution se fait indépendamment de la voie d'entrée:

$$T_f^{KJ\pi} = T_D^{KJ\pi} + A^{KJ\pi} \frac{\sum_K^J T_B^{KJ\pi}}{\sum_K^J T_A^{KJ\pi} + \sum_K^J T_B^{KJ\pi}}$$

où  $T_A$  et  $T_B$  sont les pénétrabilités à travers chacun des maxima A et B calculées par la formule de Hill et Wheeler [16].

$$T_{A,B}^{KJ\pi} = \left[ 1 + \exp \left\{ 2\pi (E_{A,B} - E_\beta) / \hbar\omega_{A,B} \right\} \right]^{-1}$$

Dans le cas limite où il y a amortissement complet dans le second puits, le flux transmis directement est nul et le flux absorbé est égal au flux transmis à travers le premier maximum:

$$T_f^{KJ\pi} = T_A^{KJ\pi} \cdot \frac{\sum_K^J T_B^{KJ\pi}}{\sum_K^J T_A^{KJ\pi} + \sum_K^J T_B^{KJ\pi}}$$

c) Les densités de niveaux utilisées dans le calcul sont obtenues à partir des densités d'états  $\omega_{Pu}$  établies par Britt et al. [17] pour le  $^{240}\text{Pu}$ . Ces densités sont déduites directement des spectres théoriques des états de particules indépendantes calculés pour les différentes déformations [18]. Pour une déformation donnée, on a

$$\rho(E^*, J) = C \cdot \omega_{Pu} (E^* + \delta\Delta_n + \delta\Delta_p) \cdot (2J + 1) \exp \left[ \frac{-(J + 1/2)^2}{2\sigma^2} \right]$$

Dans cette expression  $\Delta_n$  et  $\Delta_p$  sont les corrections de pairing pour les neutrons et les protons;  $\sigma$  est le spin cut-off pris égal à 5,45 MeV, et  $C$  est une constante qui est ajustée pour rendre compte de la densité de niveau mesurée pour le  $^{232}\text{Pa}$  au voisinage de l'énergie de liaison du neutron.

#### 4. ANALYSE DES RESULTATS

Le but de cette analyse consiste à déterminer les paramètres qui permettent de reproduire simultanément la section efficace de fission et la forme des distributions angulaires des fragments de fission. Ces paramètres sont:

- la valeur de  $K$  et la parité  $\pi$  des structures internes correspondant aux voies de fission considérées;
- le moment d'inertie  $J$  associé à la bande de rotation construite sur chaque structure interne;
- les hauteurs et les courbures  $(E_A, \hbar\omega_A)$ ,  $(E_{II}, \hbar\omega_{II})$ ,  $(E_B, \hbar\omega_B)$  qui caractérisent la barrière de fission effective associée à chaque structure interne.

La comparaison de la forme très caractéristique de la distribution angulaire mesurée vers  $E_n = 160$  keV avec les distributions angulaires  $W^{KJ\pi}(\theta)$  calculées

TABLEAU II. ENERGIES DES RESONANCES CORRESPONDANT AUX DIFFERENTS MEMBRES DE LA BANDE DE ROTATION ET SECTIONS EFFICACES DE FORMATION DU NOYAU COMPOSE POUR LES DEUX PARITES

J	$E_n$ (keV)	$\sigma_c^{J^+}$ (barns)	$\sigma_c^{J^-}$ (barns)
3	160	1,220	0,055
4	188	0,007	0,032
5	223	0,006	

pour différentes valeurs de K, J,  $\pi$  conduit à attribuer la résonance très étroite observée à cette énergie à un état de vibration pur  $(K, J, \pi) = (3, 3, \pm)$ . Le tableau II donne les énergies auxquelles nous devrions trouver des résonances correspondant aux différents membres de la bande de rotation construite sur le même état de vibration (en donnant au paramètre  $\hbar^2/2J$  la valeur de 3,5 keV mesurée dans le second puits du  $^{240}\text{Pu}$  par Specht et al. [19]) ainsi que les sections efficaces de formation du noyau composé pour les 2 parités. Si on considère la parité négative, la contribution de  $J^\pi = 4^-$  à  $E_n = 188$  keV n'est pas négligeable, et la distribution angulaire à cette énergie devrait avoir une forme correspondant à la forme théorique  $W^{34-}(\theta)$ , c'est-à-dire piquée à  $55^\circ$ ; expérimentalement nous n'observons pas une forme semblable. Nous avons donc choisi la parité positive.

En ce qui concerne les deux résonances à  $E_n = 200$  keV et  $E_n = 330$  keV, pour lesquelles nous n'avons pas observé de sous-structure, il est plus difficile de les interpréter sans ambiguïtés. La forme des distributions angulaires qui leur correspondent ne permet pas de choisir nettement entre les différentes possibilités  $K^\pi = 0^+, 0^-, 2^+, 2^-$ . Nous avons donc essayé de reproduire la section efficace et la forme des distributions angulaires pour les différentes combinaisons possibles. Nous avons obtenu le meilleur accord avec les résultats expérimentaux (fig. 7 et 8) en attribuant la résonance observée vers  $E_n = 200$  keV à un état de vibration pur  $K^\pi = 0^+$ , et la résonance observée vers  $E_n = 330$  keV à un état de vibration  $K^\pi = 0^-$  faiblement amorti.

Les paramètres des barrières de fission effectives utilisées dans cette analyse sont donnés dans le tableau III; ils sont en bon accord avec les valeurs extraites de l'analyse de l'allure générale de la fonction d'excitation [7], et avec les valeurs obtenues à partir de la réaction  $^{231}\text{Pa}(d, pf)$  [20].

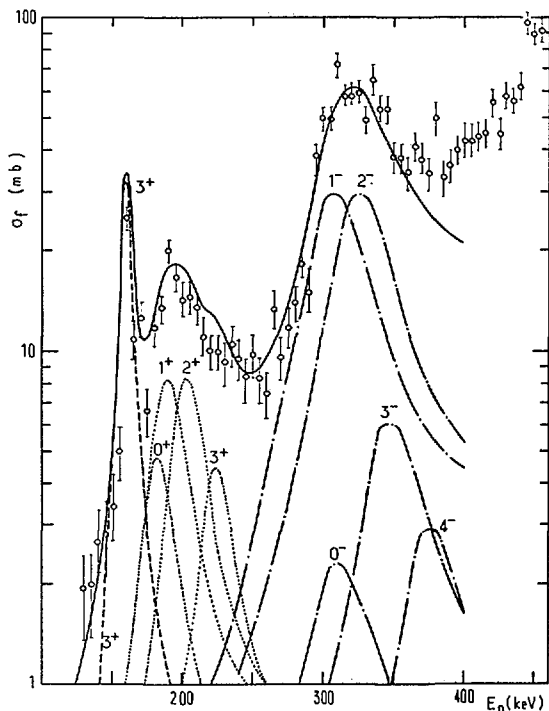


FIG. 7. Sections efficaces pour les différentes combinaisons possibles.

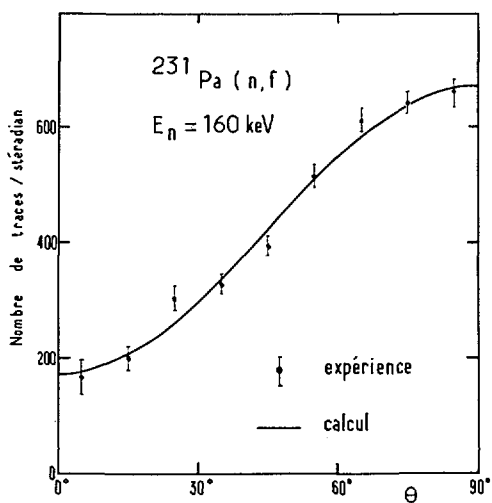


FIG. 8. Distribution angulaire pour  $E_n = 160 \text{ keV}$ .

TABLEAU III. PARAMETRES DES BARRIERES DE FISSION

$E_n$ (keV)	$K^\pi$	$E_A$	$\hbar\omega_A$	$E_B$	$\hbar\omega_B$
160	$3^+$	6,0	0,85	6,15	0,4
200	$0^+$	5,85	0,9	6,20	0,4
330	$0^-$	6,00	0,85	6,15	0,5
$^{231}\text{Pa}(n,f)$		5,95	0,9	6,15	0,4
$^{231}\text{Pa}(d,pf)$		5,75	0,8	6,10	0,45

## 5. CONCLUSION

La fonction d'excitation de la réaction  $^{231}\text{Pa}(n,f)$  a été mesurée de 130 à 450 keV avec un pas en énergie et une résolution en énergie de 5 keV, ce qui a permis de confirmer l'existence des deux structures résonantes observées vers 200 keV et 330 keV et de mettre en évidence une résonance très étroite à 160 keV; une mesure complémentaire effectuée avec une résolution en énergie de 2 keV a montré que la largeur de cette résonance est inférieure ou égale à 2 keV. Les distributions angulaires des fragments de fission ont également été mesurées au voisinage de ces trois structures avec une résolution en énergie de 5 keV. La fonction d'excitation ainsi que les distributions angulaires sont bien interprétées en considérant trois voies de fission caractérisées par  $K^\pi = 3^+, 0^-$  et  $0^+$ ; les 3 résonances sont attribuées à des états de vibration  $\beta$  du puits de potentiel intermédiaire. La forme de la barrière de fission extraite de cette analyse est en bon accord avec la barrière de fission extraite de l'allure générale de la fonction d'excitation et avec la systématique de Los Alamos. Le résultat le plus intéressant de ce travail concerne la résonance très étroite observée à 160 keV, qui a toutes les caractéristiques d'une résonance de vibration pure ( $K^\pi = 3^+$ ). Il s'agit d'une résonance de vibration individuelle correspondant au moment angulaire  $J = 3$ . Les résonances associées aux autres membres de la bande de rotation construite sur l'état de vibration  $K^\pi = 3^+$  ne sont pas observées car les états du noyau composé présentant un moment angulaire supérieur à 3 sont très faiblement peuplés par la capture de neutrons d'aussi faible énergie.

Comme cette résonance est très étroite, l'état de vibration qui en est responsable doit présenter une faible énergie d'excitation effective, et ceci d'autant plus que le noyau  $^{232}\text{Pa}$  est un noyau impair-impar. Une telle situation ne peut exister que si cet état de vibration appartient à un second puits de poten-

tel très peu profond, ou au troisième puits proposé par Nix. Les calculs théoriques prévoient que cet éventuel troisième puits présente une asymétrie de masse, aussi devrait-il exister dans cette hypothèse un autre état de vibration  $K^\pi = 3^-$  au voisinage de l'état de vibration  $K^\pi = 3^+$  mis en évidence; malheureusement il n'est pas possible de l'observer en réaction (n,f) car les états du noyau composé  $J^\pi = 3^-$  sont très peu peuplés. Il serait donc particulièrement intéressant d'étudier la fission du  $^{232}\text{Pa}$  en utilisant une réaction directe pour obtenir une distribution des moments angulaires plus large; en effet une telle étude permettrait de mesurer le moment d'inertie du noyau dans l'état de vibration  $K^\pi = 3^+$ , et de voir s'il existe bien deux bandes de rotation  $K^\pi = 3^+$  et  $3^-$  constituant la signature d'un troisième puits asymétrique dans la barrière de fission de ce noyau.

## REFERENCES

- [1] STRUTINSKY, V.M., *Yad. Fiz.* **3** (1966) 614.
- [2] STRUTINSKY, V.M., *Sov. J. Nucl. Phys.* **3** (1966) 449.
- [3] STRUTINSKY, V.M., *Nucl. Phys. A* **95** (1967) 420.
- [4] STRUTINSKY, V.M., *Nucl. Phys. A* **122** (1968) 1.
- [5] BLONS, J., MAZUR, C., PAYA, D., *Phys. Rev. Lett.* **35** (1975) 1749.
- [6] BARREAU, G., Thèse d'Etat, Bordeaux (1977).
- [7] SICRE, A., BARREAU, G., CHASTEL, R., DOAN, T.P., LEROUX, B., SAGEAUX, J.C., «Etude de la réaction  $^{231}\text{Pa}(n,f)$  induite par neutrons rapides», *Physics and Chemistry of Fission 1973* (C.R. Coll. Rochester, N.Y., 1973) I, AIEA, Vienne (1974) 71.
- [8] LARK, M.L., *Nucl. Instrum. Methods* **67** (1969) 137.
- [9] SOWERBY, M.G., PATRICK, B.H., MATHER, D.S., *Nucl. Sci. Eng.* **17-8** (1974).
- [10] AUERBACH, E.H., PEREY, F.G.J., Rapport BNL (T-286) (1962).
- [11] GAI, E.V., IGNATIOUK, A.V., RABOTNOV, N.S., SMIRENKINE, G.N., «Double-humped barrier in the quasi-classical approximation», *Physics and Chemistry of Fission (C.R. Coll. Vienne, 1969)*, AIEA, Vienne (1969) 337.
- [12] CRAMER, J.D., NIX, J.R., *Phys. Rev. C2* (1970) 1048.
- [13] MÖLLER, P., NIX, J.R., «Calculation of fission barriers», *Physics and Chemistry of Fission 1973* (C.R. Coll. Rochester, N.Y., 1973) I, AIEA, Vienne (1974) 103.
- [14] BHANDARI, B.S., *Nucl. Phys. A* **256** (1976) 271.
- [15] BACK, B.B., HANSEN, O., BRITT, H.C., GARRETT, J.D., *Phys. Rev. C9* (1974) 1924.
- [16] HILL, D.L., WHEELER, J.A., *Phys. Rev.* **89** (1953) 1102.
- [17] BRITT, H.C., BOLSTERLI, M., NIX, J.R., NORTON, J.L., *Phys. Rev. C7* (1973) 801.
- [18] BOLSTERLI, M., FISET, E.O., NIX, J.R., NORTON, J.L., *Phys. Rev. C5* (1972) 1050.
- [19] SPECHT, H.J., KONECNY, E., HEUNEMANN, D., WEBER, J., Proc. Europ. Conf. on Nuclear Physics, Aix-en-Provence, Vol.II (1972) 8.
- [20] BACK, B.B., BRITT, H.C., HANSEN, O., LEROUX, B., GARRETT, J.D., *Phys. Rev. C10* (1974) 1948.

## DISCUSSION

R.H. IYER: You mentioned that you used a  $2 \text{ mg} \cdot \text{cm}^{-2}$  thick  $^{231}\text{Pa}$  target in your cross-section and angular distribution measurements. This corresponds to  $\sim 15 - 20\%$  of the effective range of the fission fragments and is, I think, too thick for good cross-section and angular distribution measurements unless you introduce corrections for self-absorption losses of fission fragments in the actual target. This is particularly true when you are detecting the fission fragments with a Makrofol track detector, and may affect both your cross-section and angular distribution data, particularly the latter.

A. SICRE: In the experimental device that we used to measure the angular distributions, the  $^{231}\text{Pa}$  was deposited at two points in the centre and set in motion by rotation around the vertical axis of the cylinder formed by the detector. This movement was intended to average, in all horizontal directions, the angular distribution effects due to slowing-down or absorption of grazing fission fragments in the deposited material. Vertically, possible effects of this kind are limited, since the detector records only the fragments with an emission angle less than  $60^\circ$  relative to the direction of the incident neutrons.

S.S. KAPOOR (*Chairman*): To ensure that there are no systematic errors in the angular distribution measurements, you could also carry out the experiment by replacing the  $^{231}\text{Pa}$  target with a  $^{235}\text{U}$  target of the same thickness and measuring the angular distributions for thermal neutron fission. If the experiment is carried out with identical geometry, you will then get an isotropic distribution.

A. SICRE: To evaluate the distortion of the shape of the angular distributions due to the use of our method we designed a Monte-Carlo-type calculation to simulate the behaviour of the fission fragments between their emission and their recording by the detector. The calculation results show that the distortions are still very small.

We also recorded the angular distribution of the fission fragments from a  $^{252}\text{Cf}$  source and found, as expected, that the angular distribution was isotropic.



# BANDES DE ROTATION DANS LA STRUCTURE INTERMEDIAIRE

D. PAYA

DPh-N/MF,

CEA, Centre d'études nucléaires de Saclay,

Gif-sur-Yvette,

France

## Abstract—Résumé

### ROTATIONAL BANDS IN INTERMEDIATE STRUCTURE.

The intermediate structure effects observed in the fission cross-section of a large number of isotopes have been attributed to the presence of vibrational states in the second well of the fission barrier. A new phenomenon appears with the isotopes of thorium where the intermediate structure presents rotational bands. Investigation of these bands provides a number of arguments in favour of the existence of a third well, in which the nucleus would take an asymmetric form: the very presence of rotational bands suggests a potential well less deep than the second well, the moment of inertia is the same for the three rotational bands investigated and its value is three times greater than in the ground state, and finally each band is divided into two bands of positive and negative parities separated by 11 keV. The latter characteristic is typical of a nucleus in which the space symmetry inversion is not preserved; it provides information on the potential barrier separating two inverse states from each other. In one of the structures investigated the level  $[981] \frac{1}{2}$  can be identified from the value of the decoupling parameter. Little is known about the other structures but they could consist of rotational bands built on vibrational bands. Finally, the estimation of certain characteristic times — lifetime, rotation period and inversion period — provides the basis for some interesting comparisons.

### BANDES DE ROTATION DANS LA STRUCTURE INTERMEDIAIRE.

Les effets des structures intermédiaires observés dans la section efficace de fission d'un grand nombre d'isotopes ont été attribués à la présence d'états de vibration dans le deuxième puits de la barrière de fission. Un phénomène nouveau apparaît avec les isotopes de thorium où la structure intermédiaire présente des bandes de rotation. L'étude de ces bandes fournit un certain nombre d'arguments en faveur de l'existence d'un troisième puits dans lequel le noyau prendrait une forme asymétrique: la présence même de bandes de rotation suppose un puits de potentiel moins profond que ne l'est le deuxième puits, le moment d'inertie est le même pour les trois bandes de rotation étudiées et sa valeur est trois fois plus grande que dans l'état fondamental, enfin chaque bande est dédoublée en deux bandes de parités positive et négative décalées de 11 keV. Cette dernière propriété est caractéristique d'un noyau dans lequel la symétrie par inversion de l'espace n'est pas respectée; elle fournit des renseignements sur la barrière de potentiel qui sépare deux états inverses l'un de l'autre. Dans l'une des structures étudiées on peut identifier le niveau  $[981] \frac{1}{2}$  grâce à la valeur du paramètre de découplage. On possède encore peu de renseignements sur les autres structures mais elles pourraient être constituées par des bandes de rotation construites sur des bandes de vibration. Enfin, l'estimation de certains temps caractéristiques — durée de vie, période de rotation et période d'inversion — donne lieu à des comparaisons intéressantes.

Les effets de structures intermédiaires dans les sections efficaces de fission sont connus depuis plus de dix ans [1] et il est maintenant bien établi que ce sont des effets de voie de sortie qui prennent naissance lors de la traversée de la barrière de fission. Ils sont dus à la présence de niveaux situés dans un minimum secondaire de la barrière où le noyau peut séjourner dans un état intermédiaire métastable au cours de son chemin vers la fission. En principe, une structure intermédiaire est constituée par un groupe isolé de résonances fines. Cependant, il arrive très souvent que, pour des raisons expérimentales, la structure fine ne soit pas résolue. Le groupe prend alors l'aspect d'une résonance large qui représente la variation de la valeur moyenne de la probabilité de fission le long de la structure. Ces résonances sont d'une grande utilité dans la détermination expérimentale des principales caractéristiques de la barrière de fission. C'est ainsi qu'à la suite de mesures extensives effectuées sur un grand nombre d'isotopes, on a pu dresser une systématique des maximums et des minimums en fonction du nombre de protons et du nombre de neutrons [2].

Comme l'ont montré Möller et Nix [3], les calculs effectués avec une double barrière sont en bon accord avec l'expérience, sauf pour les thoriums où le premier maximum et le second minimum sont bien plus bas que les valeurs mesurées. Cette "anomalie du thorium" pourrait être résolue par le creusement d'un troisième minimum peu profond, à une déformation où la symétrie de masse du noyau n'est pas respectée. Plusieurs expériences ont donc été entreprises sur les thoriums afin de déterminer si ce résultat de calcul pouvait recevoir une confirmation expérimentale ou si, au contraire, on devait le considérer comme un effet artificiel résultant d'un choix trop restreint de paramètres.

#### Hiérarchie des états intermédiaires

La classification des états qui interviennent dans la création de structures intermédiaires a été donnée par Lynn [4] puis par Back [5]. Au départ, l'hamiltonien total du noyau est développé de manière à faire apparaître explicitement un terme  $H_\beta$  associé à la vibration qui permet seule au noyau de franchir la barrière de fission :

$$H = H_\beta + H_i + H_{\beta i}$$

Dans ce développement,  $H_i$  contient tous les autres degrés de liberté, que ce soient les autres paramètres collectifs associés à la forme du noyau ou à sa rotation ou bien les excitations de particules dans le champ nucléaire moyen. L'interaction entre le degré de liberté  $\beta$  et les autres degrés de liberté est incluse dans le terme  $H_{\beta i}$ . En l'absence d'interaction, les fonctions propres  $|\beta i\rangle$  de l'hamiltonien  $H = H_\beta + H_i$  s'écrivent comme des produits des fonctions propres  $|\beta\rangle$  et  $|i\rangle^0$ . Quand la surface de potentiel a deux minimums on peut diviser les fonctions propres  $|\beta\rangle$ , donc aussi les fonctions propres  $|\beta i\rangle$ , en deux classes appelées classe I et classe II suivant que l'amplitude est maximale dans le premier puits ou dans le second.

L'observation de largeurs de fission non nulles montre l'existence d'un couplage entre le mouvement de vibration et les autres degrés de liberté. L'importance du couplage dépend de la densité d'états à l'énergie considérée. Dans le premier puits, aux énergies qui nous intéressent, la densité est très grande puisque l'espacement moyen est d'environ 1 eV. L'énergie de vibration ne peut rester concentrée sur un seul état, elle se répartit rapidement sur les états voisins. Dans ces conditions, on admet généralement que les composantes de vibration dans le premier puits sont uniformément réparties sur les états plus denses du noyau composé. Le mouvement de vibration dans le premier puits sera assimilé à une onde plane. Dans le deuxième puits, une partie de

l'énergie est immobilisée sous forme d'énergie potentielle. L'énergie disponible sous forme d'énergie d'excitation est d'autant plus petite que le minimum est plus élevé. La densité d'états est environ cent fois moins grande que dans le premier puits. Dans ces conditions, les états de vibration seront beaucoup moins dilués et n'auront, en fait, de composantes notables que sur les seuls états voisins. Dans un modèle où les espacements sont constants, la force de la résonance de vibration est distribuée suivant une fonction de Lorentz :

$$P(E) \approx \frac{1}{2\pi} \frac{\Gamma_{II}}{(E - E_{II})^2 + \frac{1}{4} \Gamma_{II}^2}$$

où  $E_{II}$  est l'énergie de l'état de vibration et  $\Gamma_{II}$  représente la largeur de couplage de cet état aux autres états du deuxième puits.

#### Situation expérimentale

L'expérience fournit des exemples de différents amortissements de la résonance de vibration dans les états voisins.

Dans un noyau comme  $^{238}\text{Np}$  la profondeur du deuxième puits de potentiel est d'environ 3 MeV. L'espacement moyen des états au voisinage des sommets de la barrière y est de quelques dizaines d'électronvolts. Le mouvement de vibration est donc complètement amorti et la composante de vibration est distribuée de manière quasi uniforme sur tous les états de classe II. C'est ce qui est observé dans la section efficace de fission induite par neutrons où aucune résonance large n'est visible au voisinage du seuil [6]. On peut estimer la largeur de couplage  $\Gamma_{II}$  à plusieurs centaines de keV. Les états de classe II apparaissent comme des résonances fines dont la largeur est d'environ 10 eV ; leurs espacements obéissent à la loi de Wigner. Les spins de ces états sont distribués de manière statistique suivant une dépendance en  $2J + 1$ . Quand la résolution en énergie devient meilleure que l'espacement des états de classe I, on voit que la probabilité de fission à travers un état de classe II est en fait distribuée sur les états de classe I qui ont le même spin que lui et une énergie voisine [7].

Quand la densité des états de classe II diminue, le mouvement de vibration n'est plus que partiellement amorti dans le second puits. C'est ce qui est observé dans la réaction  $^{239}\text{Pu}(d, pf)$  [8] : entre 4,9 et 5,1 MeV la fonction d'excitation montre un groupe de résonances fines qui résultent du couplage d'un état de vibration aux états de classe II. Comme dans le cas de  $^{238}\text{Np}$ , les espacements sont distribués suivant la loi de Wigner mais l'espacement moyen est plus grand ; il vaut 10,8 keV. Il semble, par contre, que les spins soient tous identiques. Pour expliquer ce résultat surprenant, on a émis l'hypothèse d'un effet de voie d'entrée. Un cas assez semblable a été rapporté dans la réaction  $^{234}\text{U}(n, f)$  [9]. A une énergie de neutron 300 keV, il apparaît un groupe de résonances de classe II avec un espacement moyen de 13 keV. Ce groupe a été analysé en termes de couplage des états de classe II avec un état de vibration et la bande de rotation construite sur cet état. L'analyse conduit à des largeurs de couplage  $\Gamma_I = 800 \pm 300$  keV dans le premier puits et  $\Gamma_{II} = 35 \pm 5$  keV dans le deuxième. Dans ce cas aussi, les distributions angulaires sont très semblables d'une structure fine à l'autre. Elles sont expliquées par un état de vibration  $K^\pi = 1/2^+$  avec des contributions de deux autres états :  $K^\pi = 3/2^+$  et  $K^\pi = 1/2^+$  situés à des énergies d'excitation un peu plus élevées.

Pour les thoriums, les calculs, la systématique et l'analyse des données de photofission sous le seuil [10] prévoient tous un deuxième minimum

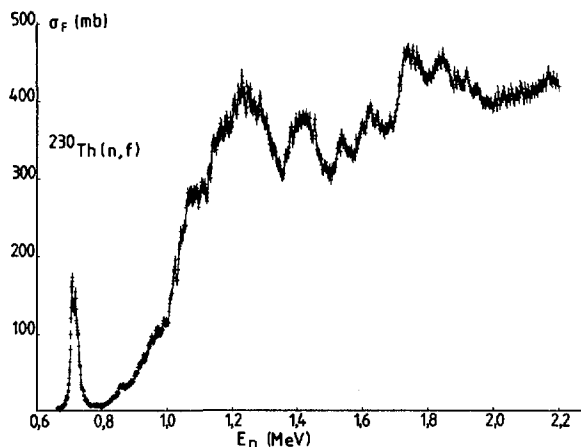


FIG.1. Section efficace de fission de  $^{230}\text{Th}$ .

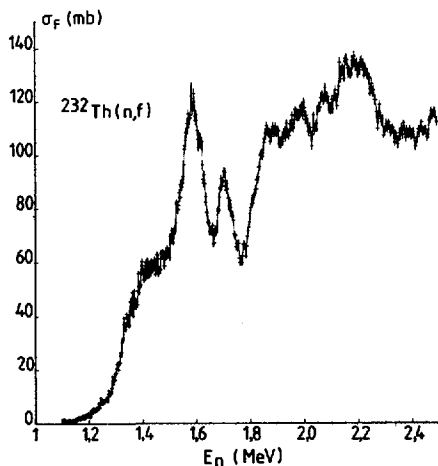


FIG.2. Section efficace de fission de  $^{232}\text{Th}$ .

compris entre 2 et 3 MeV au-dessus du premier, soit un puits au moins aussi profond que pour le neptunium. On s'attend donc à une densité de niveaux importante et à un amortissement complet de la résonance de vibration. Or, la section efficace de  $^{230}\text{Th}$  pour les neutrons de 720 keV présente une résonance isolée avec une largeur de 25 keV qui est citée comme le prototype d'une résonance de vibration peu ou pas amortie [11]. Pour lever la contradiction, il faut admettre que cette résonance n'appartient pas au deuxième puits mais plutôt au troisième qui, lui, est beaucoup moins profond. Un moyen de prouver cette hypothèse est de parvenir à résoudre la structure fine. En effet,

si cette structure fine est causée par les tout premiers niveaux excités, on doit observer, en raison du caractère collectif de ces niveaux, des propriétés fort différentes de celles qui existent dans le second puits où le caractère collectif s'est complètement estompé.

#### La section efficace de fission des thoriums-230 et 232

La détection de niveaux dans un éventuel troisième minimum nécessite une bonne résolution en énergie. C'est le cas des mesures qui ont été effectuées auprès des accélérateurs linéaires de Saclay puis de Geel sur la section efficace de fission des thoriums-230 [12] et 232 [13] pour des neutrons d'énergies comprises entre 0,5 MeV et 3 MeV. La mesure de la section efficace a été complétée, pour ce qui concerne  $^{232}\text{Th}$ , par deux mesures d'anisotropie dans lesquelles une grille placée contre la cible de thorium éliminait les fragments émis à des angles supérieurs respectivement à  $45^\circ$  et  $30^\circ$ ; les angles sont comptés par rapport à la direction du faisceau de neutrons incident. Les principales caractéristiques de ces expériences sont indiquées dans la référence [14].

Les figures 1 et 2 montrent les sections efficaces de fission de  $^{230}\text{Th}$  et  $^{232}\text{Th}$ . Des structures fines apparaissent clairement sur les résonances larges : à 720 keV pour  $^{230}\text{Th}$ , à 1,6 MeV et 1,7 MeV pour  $^{232}\text{Th}$ , et leur espacement moyen est d'environ 10 keV. Cependant, cet effet est notablement différent de ceux qui existent pour les autres noyaux et dont nous avons rappelé les principales propriétés.

i) Ces résonances fines ne peuvent évidemment être des états de classe I dont l'espacement mesuré à l'énergie de liaison d'un neutron est d'environ 10 eV. Peuvent-elles être des états de classe II ? On a vu que le deuxième minimum est situé entre 2 et 3 MeV au-dessus du premier. Dans ces conditions on peut évaluer l'espacement des états de classe II à une énergie de neutrons de 1,6 MeV par exemple, par comparaison avec l'espacement connu des états de classe I à des énergies de neutrons de quelques électronvolts. Par application d'une relation de la forme

$$\frac{D_{II}}{D_I} = \left[ \frac{U_{II}}{U_I} \right]^{5/4} \exp 2\sqrt{a} (\sqrt{U_I} - \sqrt{U_{II}})$$

on trouve un espacement  $D_{II} = 5$  eV pour un deuxième minimum à 2 MeV et  $D_{II} = 38$  eV pour un minimum à 3 MeV. Avec de tels espacements, on ne peut certainement pas expliquer des "fluctuations statistiques" qui auraient un espacement observé de 10 keV.

ii) Dans les structures intermédiaires des autres noyaux, les espacements obéissaient à des lois statistiques (distribution de Wigner). Dans le cas des thoriums, on observe une régularité qui sera analysée en détail au paragraphe suivant.

iii) Les mesures d'anisotropie et les mesures de distributions angulaires montrent que le spin ne reste pas constant pour tous les éléments d'une même structure mais, au contraire, augmente en fonction de l'énergie.

Ces arguments montrent qu'il n'est pas possible d'attribuer les structures intermédiaires observées dans les thoriums à des niveaux du deuxième minimum de la barrière de fission, comme on l'a fait précédemment.

#### Les bandes de rotation

L'influence du second minimum sur la structure intermédiaire étant écartée, on peut se tourner vers le troisième minimum. Dans cette hypothèse, où l'énergie d'excitation est très faible, on ne peut atteindre que les tout

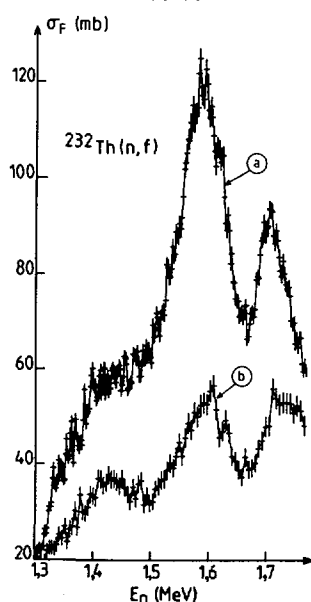


FIG.3. a) Section efficace de fission de  $^{232}\text{Th}$  intégrée sur tous les angles. b) Section efficace dans un angle inférieur à  $45^\circ$  qui favorise les spins élevés.

TABLEAU I. ENERGIES EXPERIMENTALES DES STRUCTURES FINES ET ENERGIES CALCULEES AVEC LE SPIN  $J^\pi$

	$J^+$	$E_{\text{exp}}$ (keV)	$E_{\text{calc}}$ (keV)	$J^-$	$E_{\text{exp}}$ (keV)	$E_{\text{calc}}$ (keV)
$^{230}\text{Th}$ (bande $K = 1/2$ )	$1/2^+$	$708,6 \pm 0,6$	708,7	$1/2^-$	$719,8 \pm 0,4$	719,7
	$3/2^+$	$701,6 \pm 1$	701,4	$3/2^-$	$712,3 \pm 1$	712,4
	$5/2^+$	$733,0 \pm 1$	732,6	$5/2^-$	$743,3 \pm 1$	743,6
	$7/2^+$	$715,5 \pm 1$	715,6	$7/2^-$	$726,6 \pm 1$	726,6
$^{232}\text{Th}$ (bande $K = 3/2$ )	$3/2^+$	$1568,9 \pm 1$	1569,3	$3/2^-$	$1579,8 \pm 0,5$	1579,7
	$5/2^+$	$1581,5 \pm 1$	1581,6	$5/2^-$	$1591,8 \pm 1$	1592,1
	$7/2^+$	$1699,8 \pm 1$	1598,8	$7/2^-$	$1611 \pm 1$	1609,4
	$9/2^+$	$1620,5 \pm 1$	1621,0	$9/2^-$	$1631 \pm 1$	1631,6
				$11/2^-$	$1660 \pm 2$	1658,8
$^{232}\text{Th}$ (bande $K = 1/2$ )	$1/2^+$	$1690,1 \pm 1$	1689,9	$1/2^-$	$1702 \pm 1$	1702
	$3/2^+$	$1680,9 \pm 1$	1680,7	$3/2^-$	$1693 \pm 1$	1693,2
	$5/2^+$	$1714,6 \pm 1$	1715,0	$5/2^-$	$1726 \pm 1$	1726,2
	$7/2^+$	$1693,5 \pm 1$	1693,6	$7/2^-$	$1706 \pm 1$	1705,9

premiers états, très peu denses. Le mouvement de rotation inclus dans le terme  $H_i$  de l'hamiltonien est faiblement couplé au mouvement intrinsèque et peut en être séparé. On s'attend donc à observer des bandes de rotation.

Dans cette hypothèse, Blons a cherché à attribuer aux différentes structures fines un spin  $J$  et une parité  $\pi$  en se basant sur les espacements et les intensités relatives. En effet, les états qu'il est possible de former par capture d'un neutron de moment angulaire  $\ell$  ont le spin et la parité  $J^\pi = (\ell \pm 1/2)(-)^{\ell}$ ; or, la section efficace de formation du noyau composé, très sensible à la valeur de  $\ell$ , détermine généralement une valeur unique. Il est certain que cette attribution constitue une base de travail qui demande à être confrontée aux mesures de distribution angulaire. Malheureusement, une comparaison détaillée s'avère difficile parce que ces mesures souffrent en général d'une résolution en énergie insuffisante pour séparer les structures fines. Toutefois, une mesure à bonne résolution, effectuée récemment à l'Université de Bordeaux sur  $^{230}\text{Th}$ , n'est pas en désaccord avec l'attribution qui a été faite [15]. Dans le cas de  $^{232}\text{Th}$ , la situation est compliquée par la présence, sous les résonances à 1,6 MeV et 1,7 MeV, d'un fond important qui perturbe les distributions angulaires. Néanmoins, on constate une variation du rapport d'asymétrie le long de chaque résonance, en accord qualitatif avec l'hypothèse d'une bande de rotation (figure 3).

L'analyse de Blons montre la nécessité de faire intervenir, pour chaque valeur de  $J$ , à la fois la parité positive et la parité négative. Le tableau I donne, pour les trois groupes de résonances étudiés, les énergies et les attributions de spin et de parité. Les énergies sont comparées aux énergies calculées par la formule habituelle :

$$E(J) = E_{OK} + \frac{\hbar^2}{2J} \left[ J(J+1) - K(K+1) + \delta(K, 1/2)a(-1)^{J+1/2}(J + \frac{1}{2}) \right]$$

L'accord observé entre les valeurs calculées et les valeurs mesurées est excellent. Il montre l'existence d'une grande régularité dans la distribution des espacements (fig. 4). Il faut noter aussi que les valeurs du paramètre de rotation  $\hbar^2/2J$  sont très voisines ( $1,9 \pm 0,1$  keV pour  $^{230}\text{Th}$  à 720 keV,  $2,5 \pm 0,2$  keV pour  $^{232}\text{Th}$  à 1,6 MeV et  $1,9 \pm 0,1$  keV pour  $^{232}\text{Th}$  à 1,7 MeV), ce qui plaide en faveur des bandes de rotation.

### Le troisième minimum

L'existence de bandes de rotation indique la présence d'états collectifs purs ou presque purs. Leur faible largeur montre, d'autre part, que ces états sont peu dilués. Il faut en conclure qu'à l'énergie considérée la densité de niveaux est petite et donc que cette énergie est très voisine de celle du minimum. Le deuxième minimum, trop profond, ne remplit pas cette condition ; par contre, le troisième minimum, avec une profondeur calculée voisine de 1 MeV, semble convenir.

La valeur du moment d'inertie renforce cette interprétation : il est trois fois plus grand que dans l'état fondamental alors qu'il n'est que deux fois plus grand à la déformation du deuxième minimum [16]. Cette dépendance est conforme à celle obtenue par le calcul [17]. On remarque cependant que la valeur obtenue pour les bandes  $K = 1/2$  (qui ont même moment d'inertie et même paramètre de découplage pour les deux isotopes) est légèrement plus grande que celle de la bande  $K = 3/2$ . Cette différence ne permet pas, pour l'instant, de tirer des conclusions définitives concernant la forme de la force d'appariement : le moment d'inertie des bandes  $K = 1/2$  semble indiquer une force d'appariement constante, alors que celui de la bande  $K = 3/2$  supposerait plutôt une force d'appariement proportionnelle à la surface.

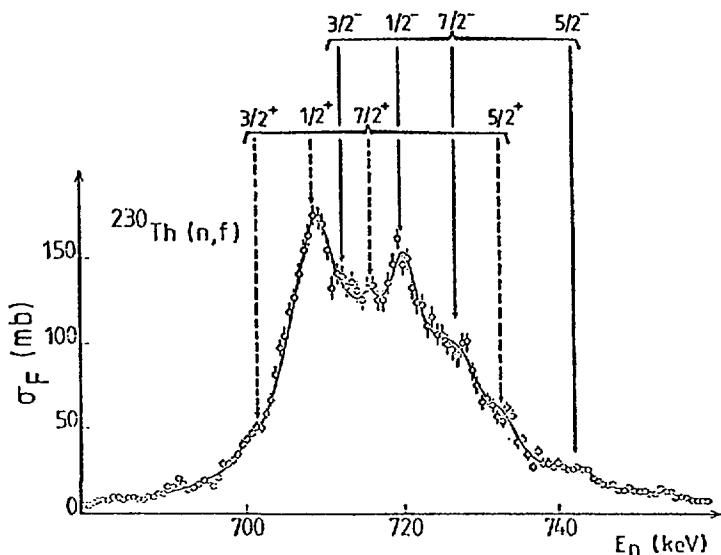


FIG.4. Spins et parités des structures fines de  $^{231}\text{Th}$ .

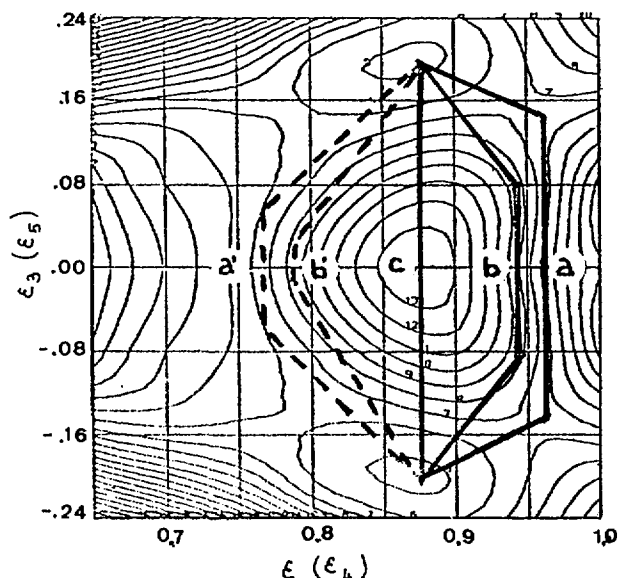


FIG.5. Différents chemins utilisés pour le calcul de l'énergie d'inversion. La surface d'énergie potentielle est tirée de [18].

TABLEAU II. ENERGIE D'INVERSION POUR  
DIFFERENTS CHEMINS TRACES SUR LA  
FIGURE 5

Trajet	$E^- - E^+$ (keV)	S (unités arbitraires)
a	74	104
a'	23	114
b	5	201
b'	0,4	155
c	0,01	422

Enfin, un argument de poids en faveur du troisième minimum est le dédoublement de parité. Le tableau I montre que, dans chaque cas, une bande de rotation de parité positive est accompagnée d'une bande de rotation de parité négative identique, à un décalage près d'environ 11 keV. C'est une propriété bien connue en spectroscopie moléculaire pour les molécules asymétriques dont l'ammoniac est le prototype. L'énergie potentielle d'une telle molécule, tracée en fonction de la distance de l'atome N au plan  $H_3$ , a un double minimum correspondant aux deux configurations d'équilibre droite et gauche équivalentes. Les fonctions d'onde sont des combinaisons linéaires des fonctions d'onde de la molécule dans chacune de ces configurations :

$$\psi_+ = \frac{1}{\sqrt{2}} (\psi_D + \psi_G)$$

$$\psi_- = \frac{1}{\sqrt{2}} (\psi_D - \psi_G)$$

Dans la molécule de  $NH_3$ , les états de parité négative de la bande  $K = 0$  sont décalés vers le haut par rapport aux états de parité positive, la fréquence d'inversion étant de 23 GHz.

L'énergie potentielle  $U$  des noyaux de thorium, tracée en fonction du paramètre d'asymétrie de masse  $\varepsilon_3$ , a le même comportement au niveau du troisième minimum qui, en réalité, se dédouble en deux minimums correspondant aux deux orientations possibles du noyau. Cet effet n'existe pas pour le premier et le deuxième minimum où la symétrie de masse est respectée.

L'énergie d'inversion entre la bande de parité positive et la bande de parité négative dépend de la pénétrabilité de la barrière de potentiel qui sépare les deux trous asymétriques. Dans le cas d'une barrière à une dimension, et en supposant que le mouvement de vibration de masse est découpé des autres mouvements collectifs, on peut calculer cette énergie d'inversion. Cela a été fait pour différents chemins tracés sur la carte d'énergie potentielle calculée par Möller [18] (fig. 5). Les résultats sont rassemblés dans le tableau II ainsi que la valeur correspondante de l'intégrale d'action :

$$S = \int_{(c)} \sqrt{2\mu(E-U) \left[ 1 + \left( \frac{dE}{d\varepsilon_3} \right)^2 \right]} d\varepsilon_3$$

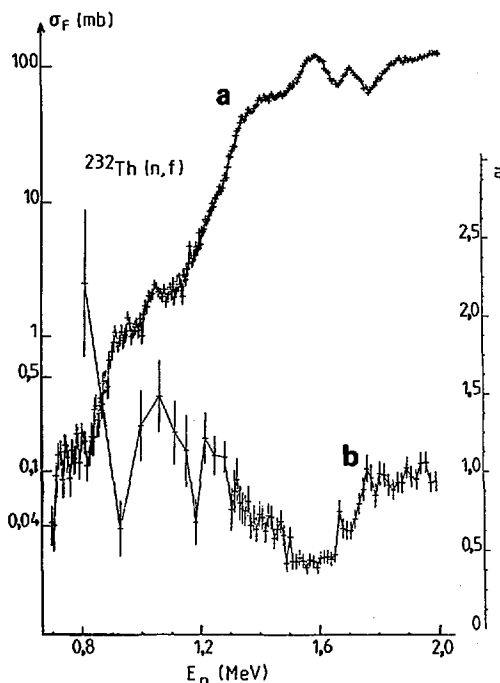


FIG. 6. a) Section efficace de fission de  $^{232}\text{Th}$ . b) Rapport d'anisotropie.

Dans ces calculs on a supposé que le paramètre d'inertie  $\mu$  était constant :  $\mu = 0,0540 \text{ A}^{9/3} \text{ fm}^2 \text{ MeV}^{-1}$ . L'examen du tableau II montre qu'il est possible d'obtenir un bon accord avec l'énergie d'inversion mesurée de 11 keV à condition de ne pas choisir un chemin comme le chemin c qui passe très près du sommet de la barrière et qui d'ailleurs est très peu probable. En fait, on peut envisager deux chemins possibles qui passeraient de part et d'autre du sommet.

L'observation, dans  $^{231}\text{Th}$  et  $^{233}\text{Th}$ , d'une bande de rotation  $K = 1/2$  avec un paramètre de découplage  $a = -2,5$  est intéressante car elle permet de personnaliser le niveau sur lequel est construite la bande de rotation. D'après des calculs effectués par le groupe de Nilsson [19], on peut trouver quatre niveaux de spin  $1/2$  dans un intervalle de 3 MeV autour de l'énergie de Fermi des thoriums à la déformation correspondant au troisième minimum. Tous ces états ont un paramètre de découplage positif ou nul sauf un : l'état [981] situé à environ 700 keV au-dessus de l'énergie de Fermi de  $^{231}\text{Th}$  pour lequel  $a = -2,2$ , valeur remarquablement voisine de la valeur expérimentale. Outre cette bande  $K = 1/2$ , on doit trouver d'autres bandes de rotation associées aux différents états possibles. La plus spectaculaire est celle qui se trouve à 1,6 MeV dans la section efficace de  $^{232}\text{Th}$  et pour laquelle  $K = 3/2$ . Mais il est vraisemblable qu'il en existe d'autres comme, par exemple, dans la section efficace de  $^{230}\text{Th}$  au voisinage de 970 keV et de 1100 keV (fig. 1) ; à ces énergies les structures apparaissent moins distinctement car elles se superposent à l'ouverture de la voie de fission  $K = 1/2$  qui crée une contribution importante à la section efficace et qui perturbe la distribution angulaire.

L'étude et la classification des différentes structures peuvent être facilitées par la remarque suivante : dans un puits de potentiel caractérisé par une courbure  $\omega$ , les états de vibration sont espacés de  $\hbar\omega$ . Cela se traduit dans le coefficient de transmission d'une barrière à deux bosses par l'apparition de résonances à l'énergie de ces états. La largeur de ces résonances est :

$$\Gamma \approx \frac{2}{\pi} \hbar\omega (T_A + T_B)$$

où  $T_A$  et  $T_B$  sont les coefficients de transmission à travers chacune des deux barrières qui encadrent le minimum ; elle diminue donc au fur et à mesure qu'on s'enfonce dans le puits. Si le troisième puits de la barrière de fission a une profondeur d'environ 1 MeV pour une courbure  $\hbar\omega \approx 0,65$  MeV, on peut y construire, sur chaque état intrinsèque, deux résonances de vibration séparées de 0,65 MeV, la plus basse en énergie ayant une intensité beaucoup plus petite que l'autre. Précisément, la section efficace de  $^{232}\text{Th}$  montre, au-dessous de 1,3 MeV, une série de résonances larges qui ne dépassent pas 2 mb (contre plus de 50 mb au-dessus de 1,3 MeV). Ceci apparaît clairement sur la figure 6 et a été rapporté aussi par Androsenko et Smirenkin [20]. En particulier, il existe, à 0,95 MeV et 1,05 MeV, deux résonances dont les mesures d'anisotropie indiquent qu'elles ont précisément les mêmes nombres quantiques  $K = 3/2$  (ou  $5/2$ ) et  $K = 1/2$  que les résonances à 1,6 MeV et 1,7 MeV situées à 0,65 MeV plus haut. De même, on remarque deux résonances  $K = 1/2$  à 0,78 MeV et 1,25 MeV auxquelles pourraient correspondre les structures intermédiaires  $K = 1/2$  situées à 1,43 MeV et 1,90 MeV.

#### Comparaison de quelques temps caractéristiques

En écrivant l'énergie de rotation sous la forme :

$$E_{\text{rot}} = \frac{\hbar^2}{2J} \left[ J(J+1) - K(K+1) \right] = \frac{1}{2} J \hbar^2 \omega^2$$

il est possible d'évaluer la période du mouvement collectif de rotation du noyau dans le troisième puits. Dans la bande  $K = 1/2$  où le moment d'inertie est le plus grand on trouve, pour différentes valeurs du moment angulaire  $J$  :

$J$	$3/2\hbar$	$5/2\hbar$	$7/2\hbar$	$9/2\hbar$	$11/2\hbar$
$T_{\text{rot}} \times 10^{19}\text{s}$	6,28	3,85	2,81	2,22	1,84

(pour la tête de bande  $J = 1/2$  le noyau n'a pas de mouvement de rotation collectif). Il est intéressant de comparer ces valeurs à la durée de vie des états estimée à partir de la relation d'incertitude :

$$\Delta E \cdot \Delta t \approx \hbar$$

Pour une largeur  $\Delta E$  de 7 keV, la durée de vie  $\Delta t$  est de 1'ordre de  $0,94 \times 10^{-19}\text{s}$ . On voit qu'elle est notablement plus petite que la période de rotation. Néanmoins, on conçoit qu'il n'est pas nécessaire que le noyau ait fait un tour complet pour qu'on puisse définir un mouvement de rotation. D'une manière plus précise, il existe une relation d'incertitude :

$$\Delta J \cdot \Delta \theta \approx \hbar$$

qui montre que, pour pouvoir définir le spin  $J$  à une unité h près, il suffit que le noyau ait tourné d'au moins 1 radian. Cette condition est vérifiée même dans le cas où le noyau tourne le plus lentement.

Dans un noyau possédant la symétrie de résolution, la configuration résultante de l'inversion des coordonnées peut aussi bien être obtenue par une rotation de  $\pi$  autour d'un axe perpendiculaire à l'axe de symétrie. Le dédoublement des niveaux en parités positive et négative ne se produit pas dans ce cas. S'il est malgré tout observé dans les thoriums c'est parce que, précisément, le noyau n'a pas le temps de tourner d'un angle égal ou supérieur à  $\pi$ . L'inversion ne peut donc pas se faire au moyen d'une simple rotation tant que le spin est inférieur à  $11/2\hbar$ . Elle nécessite une inversion effective des coordonnées et, par conséquent, le franchissement d'une barrière de potentiel qui est seul responsable du dédoublement de parité. Il serait intéressant d'exciter la même bande de rotation par une réaction de type (d,pf) qui apporte plus de moment angulaire afin d'alimenter des spins supérieurs à  $11/2\hbar$ . On devrait alors observer la disparition du dédoublement.

La période d'inversion peut être estimée à partir de l'espacement de 11 keV entre la bande de parité positive et la bande de parité négative. La valeur trouvée ( $3,76 \times 10^{-19}$ s) est, elle aussi, plus grande que la durée de vie. Cela signifie simplement que le noyau ne franchit pas effectivement la barrière qui sépare les deux puits asymétriques. Au cours de son trajet vers la fission, il passe par un, et un seul, des deux puits.

#### Conclusion

Les structures intermédiaires observées dans les sections efficaces de  $^{230}\text{Th}$  et  $^{232}\text{Th}$  sont donc intéressantes à plus d'un titre. Elles montrent la présence de bandes de rotation qui impliquent l'existence d'un troisième puits de potentiel dans la barrière de fission. Les états de rotation sont situés dans ce puits et c'est la première fois qu'on observe un noyau lourd dans un état où la symétrie de masse n'est pas respectée. L'analyse qui a été limitée, jusqu'à présent, à trois structures principales a déjà fourni un certain nombre de renseignements. Nul doute que l'étude des autres structures apportera plus de précisions et constituera le début d'une véritable spectrométrie dans le troisième puits. On sera alors en possession d'un ensemble de données expérimentales capables d'établir les modèles théoriques.

On peut penser que des effets semblables existent dans les noyaux voisins mais qu'ils sont passés inaperçus jusqu'à présent à cause du manque de résolution en énergie. Déjà, dans la fission de  $^{231}\text{Pa}$  par des neutrons de 160 keV, apparaît une résonance dont la largeur est inférieure à 2 keV. Il est possible qu'elle soit aussi une résonance de vibration pure dans le troisième puits de la barrière de fission [21]. Malheureusement, elle serait la tête d'une bande  $K = 3$  dont les autres composantes sont peu alimentées par des neutrons de 150 keV, ce qui rend difficile leur observation.

#### Remerciements

Cet exposé est le fruit d'une collaboration quotidienne qui se poursuit depuis plusieurs années avec J. Blons. De nombreuses conversations avec M. Martinot et H. Nifenecker ont contribué au fil des mois à résoudre bien des problèmes. Des enseignements fort enrichissants ont jailli de discussions avec B. Leroux et son équipe. Enfin l'intérêt que A. Bohr, B. Mottelson et S.G. Nilsson ont apporté à ce travail, ainsi que leurs encouragements ont été très appréciés.

#### Références

- [1] PAYA, D., BLONS, J., DERRIEN, H., MICHAUDON, A., Physics and Chemistry of fission 1969 (C.R. Coll. Vienne, 1969) AIEA, Vienne (1969) 307.
- [2] BACK, B.B., HANSEN, D., BRITT, H.C., GARETT, J.D., Phys. Rev. C9 (1974) 1924.

- BACK, B.B., BRITT, H.C., HANSEN, D., LEROUX, B., GARETT, J.D., Phys. Rev. C10 (1974) 1948.
- [3] MÖLLER, P., NIX, J.R., Physics and Chemistry of fission 1973 (C.R. Coll. Rochester, 1973) I, AIEA, Vienne (1974) 103 .
- [4] LYNN, J.E., UKAEA Rep. AERE-R-5891 et Physics and Chemistry of fission 1969 (C.R. Coll. Vienne, 1969) AIEA, Vienne (1969) 249.
- [5] BACK, B.B., Nucl. Phys. A228 (1974) 323.
- [6] PLATTARD, S., BLONS, J., PAYA, D., Nucl. Sci. Engin. 61 (1976) 477.
- [7] KEYWORTH, G.A., LEMLEY, J.R., OLSON, C.E., SEIBEL, F.T., DABBS, J.W.T., HILL, N.W., Physics and Chemistry of fission 1973 (C.R. Coll. Rochester, 1973) I, AIEA, Vienne (1976) 85.
- [8] GLÄSSEL, P., RÖSLER, H., SPECHT, H.J., Nucl. Phys. A256 (1976) 220.
- [9] BARREAU, G., Thèse Doct. es Sci., Univ. Bordeaux CENBG 7706 (1977).
- [10] BELLIA, G., Del ZOPPO, A., MIGUECO, E., Proc. Int. Conf. on Nuclear Structure, Tokyo (1977) 754.
- [11] JAMES, G.D., LYNN, J.E., EARAKER, L.G., Nucl. Phys. A189 (1972) 225.
- [12] BLONS, J., MAZUR, C., PAYA, D., RIBRAG, M., WEIGMANN, H., Phys. Rev. 41 (1978) 1282.
- [13] BLONS, J., MAZUR, C., PAYA, D., Phys. Rev. Lett. 35 (1975) 1749.
- [14] BLONS, J., MAZUR, C., PAYA, D., RIBRAG, M., WEIGMANN, H., cette conférence : résumés IAEA-SM-241/B9 et IAEA-SM-241/B10.
- [15] LEROUX, B., communication privée.
- [16] BACKE, H., RICHTER, L., HABS, D., METAG, V., PEDERSEN, J., SINGER, P., SPECHT, H.J., Phys. Rev. Lett. 42 (1979) 490.
- [17] SOBICZEWSKI, A., communication privée.
- [18] MÖLLER, P., Nucl. Phys. A192 (1972) 529.
- [19] NILSSON, S.G., communication privée.
- [20] ANDROSENKO, Kh.D., SMIRENKO, G.N., ZhETF Pis. Red. 19 (1974) 355 ; JETP Lett. 19 (1974) 199.
- [21] SICRE, A., CAITUCOLI, F., BARREAU, G., DOAN, T.P., BENFOUGHAL, T., LEROUX, B., cette conférence : communication IAEA-SM-241/B5.

## DISCUSSION

J.W. BOLDEMAN: Let me preface my remarks by congratulating you, and also Dr. Blons, on a fine series of cross-section measurements for neutron fission of  $^{230},^{232}\text{Th}$ . Because of the difficulty of such measurements and the complexity of the analysis, there has been some debate as to whether the existence of a triple-humped fission barrier has been proved conclusively for thorium isotopes. In the case of the cross-section data for  $^{230}\text{Th}$ , the essence of the argument in favour of the triple-hump has been an attempt to demonstrate that both positive and negative parity  $K = 1/2$  bands are required to fit the experimental data in the vicinity of the large resonance at 715 keV. Blons and co-workers have presented a fit to this cross-section by using a table of parameters including the double-parity option. We have calculated the fission fragment angular distributions that would

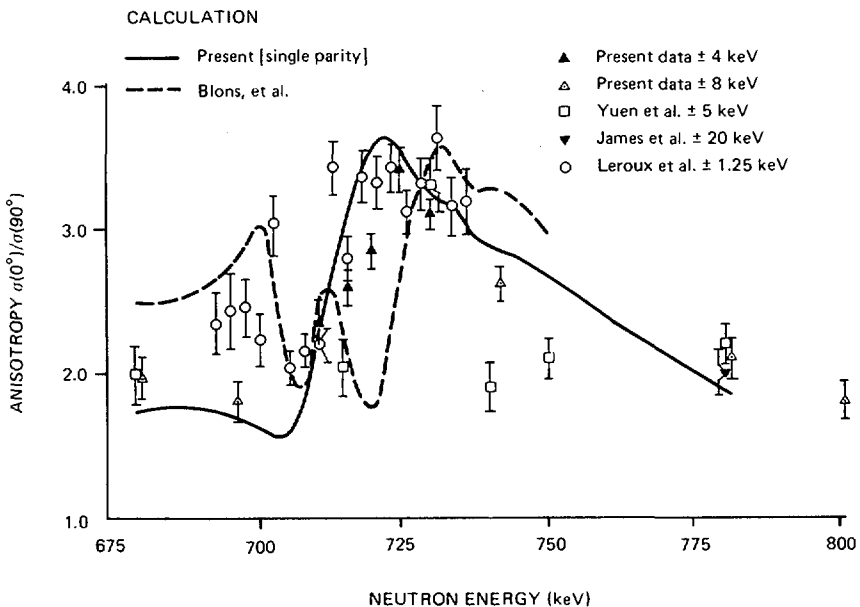


FIG.A. Anisotropy versus neutron energy.

result from the use of this set of parameters, and the anisotropies derived from these calculated angular distributions are shown in Fig.A. Leroux and co-workers have also calculated a similar dependence for the anisotropy, using Blons' parameters.

We have recently completed a series of fission fragment angular-distribution measurements for neutron-induced fission of  $^{230}\text{Th}$ , covering the energy region around the 715 keV resonance, which was also extended to 1100 keV. The anisotropies derived from these measurements, together with data from previous experiments, namely, work by Yuen and co-workers, and James and co-workers, are shown in the figure. It is clear that the experimental data are in disagreement with the calculated anisotropy. This disagreement is most serious at 720 keV, where there is a large peak in the fission cross-section that has been associated with an isotropic channel  $(K, J, \pi) = (1/2, 1/2, -)$ . The disagreement is not particularly important at very low energies since the fission cross-section is very small in such cases and is probably dominated by the tails of the cross-sections through other fission bands that were not included in Blons' parameters.

Faced with this disagreement we have sought an alternative series of parameters providing a better fit to the experimental data. A set of parameters of this kind is shown in a paper that will be presented later in this Symposium

(see IAEA-SM-241/F6 in these Proceedings). The anisotropy derived by means of these parameters is compared with the experimental data in the figure. It is suggested that this set of parameters provides a better fit to the anisotropy in the vicinity of the 715 keV resonance. These parameters also reproduce all the details in the anisotropy up to 1100 keV and most, though perhaps not all, of the significant structure near 715 keV. The unfortunate feature of these parameters is that only one parity is required to fit the resonance at 715 keV.

I personally assume that the fission barriers for the thorium isotopes do have a triple-humped shape. We are preparing a paper with an alternative set of double-parity parameters, which provide a slightly better overall fit. However, despite this improvement, the single-parity option does ensure a reasonable fit and so the argument for the triple-humped shape based on the double-parity requirement cannot be regarded as absolutely conclusive.

J. BLONS: I would say in reply to your comments that the  $^{230}\text{Th}$  (n,f) cross-section was measured in two different runs and that the same fine structures were observed in both cases. Their spacing, number and relative intensities can only be fitted on the assumption of two rotational bands with positive and negative parities. The most probable spin assignment in this hypothesis is the one we propose. Unfortunately, direct comparison with angular distribution results is not very easy since the angular distributions are not measured with an energy resolution as good as ours — 1.7 keV FWHM. When the angular anisotropy is calculated with our parameters and different energy resolutions, the dip at 720 keV diminishes and even disappears for an energy resolution of 8 keV. This is due to the presence of two 7/2 states on both sides of the 1/2 state in our scheme.

Leroux's results, shown in Fig.A, are in agreement with the calculated data, provided that an energy resolution of 8 keV is used for the calculation. This value is larger than the one claimed by the author. On the other hand, Boldeman's results are also in agreement with the same calculation above 710 keV, but below 710 keV they are lower.

B. LEROUX: I would add to Dr. Blons' comments that we made two series of fission fragment angular distribution measurements in the vicinity of the 715 keV resonance for the reaction  $^{230}\text{Th}$  (n,f). The first of these was made with an energy resolution and step of 5 keV, while the second had a step and resolution of 2.5 keV. The data obtained agree well if allowance is made for statistical fluctuations and rapid variation in anisotropy with the incident neutron energy. These angular distributions have been decomposed into Legendre polynomials to extract the fragment anisotropy and the excitation function. The shape of the resonance obtained has a half-height width that is intermediate between the width measured by Blons and that measured a few years ago at Harwell by James.

H.A.O. NIFENECKER: Isomeric shelves have been reported in the  $^{232}\text{Th}(\gamma, f)$  process, and have been interpreted as evidence of a rather deep second minimum and a thin second barrier. They appear to contradict the third-minimum hypothesis. But perhaps Dr. Asghar has something to say on that point?

M. ASGHAR: Yes, I can say that we have analysed the  $^{232}\text{Th}$  sub-barrier photofission data (ZHUCHKO, B., et al., JETP Lett. 22 4 (1975) 118) in terms of the predicted triple-humped barrier (ASGHAR, M., Z. Phys. A 286 (1978) 299). It was shown that these results, particularly the isomeric shelf itself seen in these data, cannot be explained by the second minimum. However, the data can be explained in terms of the third minimum if we assume that  $E_{\text{III}}$  — the energy of the third minimum relative to the ground-state energy — is  $\sim 3$  MeV instead of  $\sim 4.5$  MeV, as generally thought, and, further, that the isomeric state in this well is fed and decays in similar fashion to the heavier actinides with double-humped barriers.

A.F. MICHAUDON: Dr. Asghar, I do not think that the isomeric plateau observed in thorium photofission you report is necessarily in contradiction to the interpretation of the thorium data proposed by Dr. Paya. If this plateau is located at 3 MeV at most, it means that the vibrational class-II states are strongly damped at the excitation energy reached in compound nucleus by the absorption of fast neutrons. So, these class-II vibrational states *cannot* cause the structural effects observed in the neutron-induced fission cross-sections for  $^{230}, 232\text{Th}$ , and another assumption is required — for example, the third well in the fission barrier — to explain these results.

Furthermore, the situation with regard to the structural effects in  $^{230}, 232\text{Th}$  is still rather confusing, both from the theoretical and experimental points of view. I would therefore take a different view from that of Dr. Boldeman, namely I think we first need consistency between good experimental data (fission cross-section and angular distributions) before making sophisticated calculations. I know this is difficult and may not be possible for a long time, since the fine structure in the fission cross-sections is observed only when the resolution is very good and gives us low count rates and long accumulation times, for example, several weeks. The angular distribution data essential for  $J, K$  attribution are obtained at still lower count rates and are therefore available only with poorer resolution that partly smears out the fine structure effects.

J.W. BOLDEMAN: While I would concur that there is some disagreement between our angular distribution measurements and those obtained by Leroux and co-workers at low energies, where measurement is difficult, at the peak in the cross-section near 720 keV, where count rates are high, the measurements are in agreement and both sets of data show very strong forward peaking. Consequently, they disagree to a considerable extent with the location of a  $(K, J, \pi) = (1/2, 1/2, -)$  channel at this energy.

I should also like to point out that there does appear to be some difference between the calculations of different groups based on the same set of parameters. Hence it is clearly of great importance to resolve this discrepancy as soon as we possibly can.

H.J. SPECHT: I am afraid that we are all getting rather confused at this point. The situation seems to be that, disregarding for the moment the experimental discrepancies, we have one group claiming that there is evidence for eight sub-structures in the  $^{230}\text{Th}$  resonance, while the opposing group is happy to have states with just one parity in order to obtain a perfect fit. Why can we not just agree then that the structure is not rotational, but simply due to class-II compound states?

D. PAYA: Well, if the structures were due to such compound states, the angular distribution would vary statistically with energy and be identical on the average. As I stated, this is, in fact, observed in all structures where class-II compound states are involved. On the other hand, all thorium measurements show that angular distributions are not identical on the average, but that they show more forward peaking as the energy increases along the gross structure, as expected for the case of a rotational band.

As far as the fit with one parity is concerned, we know, although we cannot prove it, that it is not quite so 'perfect', since most of the shoulders, namely those at 701, 733 and 743 keV, are disregarded.

D.G. VASS: As a general comment on this unresolved issue, I would point out that the cross-section for fission and the anisotropy of the fission fragments depend on polarization of the neutrons inducing fission as well as on their energy. So discrepancies between the various experimental measurements obtained by different groups may arise through differences in the state of polarization of the incident neutron beam, especially at resonances.

Yu.M. TSIPENYUK: Dr. Paya, I have a question on a different theme. What was the third well depth required to ensure the observed resonance width, and how does the figure agree with the theoretical calculations?

D. PAYA: The observed widths of the fine structures are reproduced with a third minimum, the depth of which ranges from 0.8 to 1. MeV. This value accords with the theoretical data.

P. ARMBRUSTER: Is the decoupling parameter that you have obtained able to reproduce both the level sequence and the feeding and intensities of the different partial cross-sections, especially the increased intensity of the  $1/2^+$  states?

D. PAYA: The relative intensities of the different partial cross-sections are governed by the entrance channels. The relative positions of the different lines are given by the moment of inertia and the decoupling parameter. We are able to reproduce, with our own parameters, both the detailed shape and the intensity of the broad resonance at 720 keV fairly well.



## **SHELL EFFECTS IN POTENTIAL ENERGIES**

**AND LEVEL DENSITIES**

**(Session C)**

**Chairmen**

**K.M. DIETRICH**  
FRG

**H.C. PAULI**  
FRG

# STATIC DEFORMATION ENERGY CALCULATIONS: FROM MICROSCOPICAL TO SEMICLASSICAL THEORIES

M. BRACK

Institute for Theoretical Physics,  
University of Regensburg,  
Regensburg, Federal Republic of Germany

## Abstract

### STATIC DEFORMATION ENERGY CALCULATIONS: FROM MICROSCOPICAL TO SEMICLASSICAL THEORIES.

Various methods of calculating static potential energy surfaces are reviewed. Their uncertainties and limitations for the prediction of fission barriers of heavy nuclei are evaluated. The relations of the Strutinsky shell-correction method to the microscopical Hartree-Fock theory, on the one hand, and to semiclassical approaches, on the other hand, are discussed. Some representative experimental results are compared with the theoretical predictions, and the differences are related to the uncertainties in the theoretical results themselves.

### 1. INTRODUCTION AND SYNOPSIS

It was forty years ago that the fission process was qualitatively understood in terms of a barrier in the static deformation energy surface of the nucleus. The theoretical model which was underlying this interpretation and used in the classical papers by Bohr and Wheeler [1] and Frenkel [2], is the liquid drop model (LDM), familiar to every nuclear physicist. However only thirty years later, the first quantitative agreement between experimental and theoretical fission barrier heights could be achieved due to the shell-correction method (SCM) proposed by Strutinsky [3]. Since then, important progress has been made in the understanding of shell structure effects, especially in heavy deformed nuclei. The SCM has been confirmed by purely microscopical Hartree-Fock calculations with various effective interactions. Some promising progress has also been made in the refinement of semiclassical theories which are closely related to the Strutinsky method.

The aim of this paper is a comparison of the different methods used for the calculation of static deformation energy surfaces of heavy nuclei. In particular we try to give a critical evaluation of their suitability and their limitations for the theoretical prediction of fission barriers. As the title is indicating, we shall not follow the historical development of the theory, but rather start at a purely microscopical level.

In Section 2, microscopical calculations are reviewed. We discuss the constrained Hartree-Fock (CHF) method, its physical and technical limitations, and a recently improved time-saving approximation to it. The semi-microscopical shell-correction method (SCM) still being the most powerful

tool for systematic calculations of deformation energy surfaces, it is natural that an entire Section 3 is devoted to it. Here we first discuss the theoretical and numerical justification of the SCM within the HF framework. Some possible uncertainties inherent in the practical SC-approach, using phenomenological shell model potentials and LDM parameters, are evaluated. Then some extensions of the method applicable to excited nuclei and the possible inclusion of correlations through the Migdal theory are shortly summarized. Finally, the most important practical ingredient of the SCM, namely the Strutinsky energy averaging procedure, is discussed. Though a technical detail, it is essential and has provoked repeated criticism especially in connection with the use of finite depth potentials. Its uncertainties are carefully studied and several alternative methods and recent improvements are reviewed. In particular, we shall emphasize the complete equivalence between the (traditional) Strutinsky energy averaging and the extended Thomas-Fermi (ETF) model. Finally, with the help of some recent experimental results for actinide fission barriers, we shall establish the kind of agreement that is obtained by the most typical shell-correction calculations. The discrepancies are then compared to the uncertainties presented in the theoretical results themselves. The two most persisting cases where the disagreement with experiment clearly exceeds the theoretically expected error limits, namely the so-called Pb-and Th-anomalies, are discussed. We emphasize in particular the connection between the Pb-anomaly and the apparent lack of selfconsistency between the commonly used finite depth shell model potentials and LDM parameters.

In the final section 4 we shall summarize our conclusions and shortly mention some recent progress in the development of semiclassical methods which are very useful in determining average nuclear properties. We will outline an iteration procedure with which it should soon be possible to determine average potentials and deformation energies selfconsistently in a purely semiclassical way.

## 2. MICROSCOPICAL METHODS

### 2.1 Selfconsistent (CHF) calculations

The only practically feasible ways of describing heavy deformed nuclei on a purely microscopical level are using the independent particle (Hartree-Fock, HF) approximation or - when including pairing correlations - the independent quasiparticle (HF-Bogolyubov, HFB) approximation. Even in the HF framework, the technical problems are rather immense due to the non-linearity and the (in general) integro-differential character of the HF-equations. It is therefore only the development of fast computers on one hand and of mathematically sufficiently simple effective nucleon-nucleon interactions on the other hand, that made selfconsistent microscopical calculations possible for heavy deformed nuclei. For an extensive general review of HF-calculations of nuclear properties with phenomenological effective forces, we refer to a recent article of Quentin and Flocard [4].

An important development was initiated some ten years ago with the revival of the effective interaction of Skyrme by Vautherin and Brink [5]. The simplicity of this interaction consists in a zero-range expansion, where the finite range of the force is expressed through gradient dependent terms. The parametrization of the Skyrme force and its application to constrained Hartree-Fock (CHF) calculations was further developed by the Orsay group [6,7,19] and resulted in the first selfconsistently calculated fission barrier of  $^{240}\text{Pu}$  [7]. Although the agreement with the experiment was not too good - several reasons for this will be discussed below

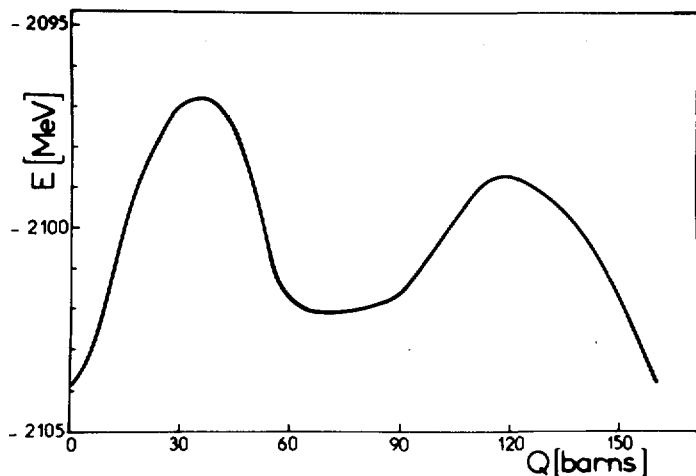


FIG.1. Fission barrier of the hypothetical super-heavy nucleus  $^{298}\text{I}114$ , obtained with the Skyrme force, SIII, and the CHF method [8].  $Q$  is the (mass) quadrupole moment.

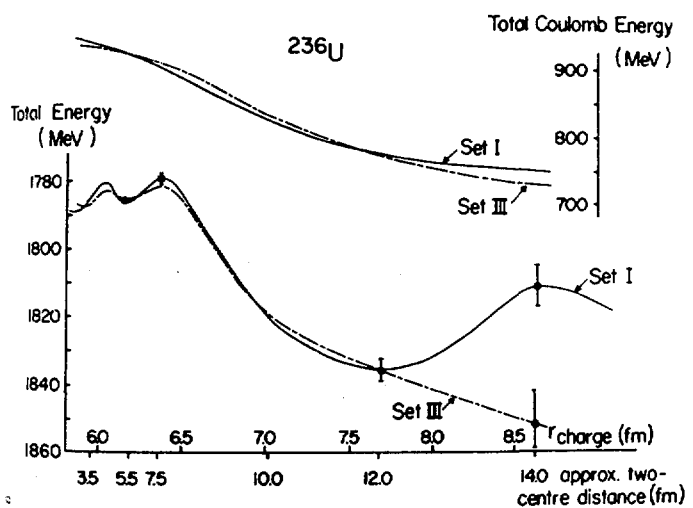


FIG.2. Fission barrier of  $^{236}\text{U}$ , obtained with the self-consistent K-matrix model [12]. Mass asymmetry is included at and beyond the second saddle. Only four points have been calculated.

in sect. 2.2 - it was quite exciting to see the familiar double-humped shape emerging from a purely microscopical calculation. Due to the large computer times needed for these calculations, no systematical CHF-investigation of actinide fission barriers has been performed up to date. However, some selected calculations were done for the barriers of hypothetical superheavy nuclei [8,9]. As an illustration, we show in Figure 1 the barrier of  $^{298}114$  obtained with the Skyrme III force [8]. In refs. [7,9], the dependence of the barrier heights on the force parameters has also been investigated (for some results, see the discussion below).

In another group, a selfconsistent K-matrix model [10] initiated by Meldner [11] was applied to a CHF-calculation for the asymmetric fission of  $^{236}\text{U}$  by Kolb et al. [12]. In this case, the deformation energy curve was continued from the saddle point down to the scission region, see Figure 2. One notes here that two sets of parameters, which give similar results for spherical nuclei [12], lead to different predictions of the barrier heights and, especially, of the deformation energy curve near scission.

In both these sets of calculations, a quadratic constraint was used to obtain points of the deformation energy curves away from local minima. Pairing correlations were included in the BCS approximation using a phenomenological gap parameter  $\Delta$  or an average pairing matrix element  $G$ . This is a rather severe restriction of the consistency of these models: The paring matrix element is added *ad hoc*, and not calculated from the same effective interaction which determines the average (HF) field of the nucleus. As a consequence, the familiar dilemma concerning the deformation dependence of  $G$  (or the average gap  $\bar{\Delta}$ ) arises, which already caused a lot of discussion and uncertainties in the shell-correction calculations of fission barriers (see Sect. 3 below). Indeed, a drastic dependence of the barrier height on constant or surface-pairing was demonstrated in the CHF-calculations [7], too (see also 2.2.d below).

The right thing to do - but a lot more complicated - is to use an effective interaction which allows to perform true HFB calculations. With the present-day Skyrme forces [6] this is not possible due to their unrealistic behaviour at high momentum transfer. (This defect can, however, be removed by adding a few more exchange terms [13].) Recently, Gogny succeeded in designing a phenomenological finite range force (with a zero-range density dependent term) which is suited for HFB-calculations [14,15] in spite of the rather enormous technical problems involved. The results obtained in ref. [15] show a remarkable agreement between theoretical and experimental pairing properties of Sn-isotopes and various rare-earth nuclei. Simultaneously, the total binding energies and density distributions obtained in these calculations for spherical nuclei are at least of the same quality as those of the best earlier HF-calculations with effective forces. The first fission barrier calculations with the Gogny force will be presented in the subsequent paper at this Symposium [16].

## 2.2 Discussion of error sources and limitations

When comparing the fission barriers obtained in CHF calculations to experimental ones, one should consider several restrictions made in the models discussed above. Let us first discuss the physical restrictions.

### a) Spurious energies.

A well-known deficiency of the HF-approximation is the fact that Slater determinants (or BCS wavefunctions) are neither good eigenstates of the total centre of mass momentum  $\vec{P}$  nor of the total angular momentum  $J$ . As a

consequence, the HF energy contains spurious kinetic energy contributions of translational and rotational motion. The former can reasonably well be taken care of (at least in heavy nuclei) by the direct part of

$$\Delta E_{CM} = \langle \vec{P}^2 \rangle / 2mA$$

leading to a slight rescaling of the total single-particle kinetic energy [6,19]. Since this correction is very little deformation dependent (even including the exchange part [17]), it leads to no serious errors in deformation energies. The spurious rotational energy, however, is harder to determine. Exact angular momentum projection being much too cumbersome in heavy nuclei, one often approximates its contribution by the expectation value (see, e.g. [20]):

$$\Delta E_{rot} = \hbar^2 \langle \vec{J}^2 \rangle / 2I$$

where  $I$  is the moment of inertia. In heavy deformed nuclei,  $\Delta E_{rot}$  easily amounts to  $\sim 3\text{-}6$  MeV at the ground state [17,19,21] and further increases with increasing deformation. It thus leads to an overestimation of the fission barriers. Since in the above expression, the moment of inertia is needed, it is cumbersome to calculate and can only approximately be estimated. Using the cranking model values, one obtains for typical actinides a correction of  $\sim 1$  MeV to the inner ( $E_A$ ) and  $\sim 2\text{-}3$  MeV or more to the outer barriers ( $E_p$ ). The safest estimate is perhaps possible for the correction to the isomer excitation energy ( $E_{II}$ ), using the experimental values of  $I$ , and amounting here to  $\sim 1$  MeV. (All these corrections are relative to the ground state energy  $E_I$ ). We anticipate here that the correction  $\Delta E_{rot}$  (as well as  $\Delta E_{CM}$ ) plays no important role in the shell-correction approach, since it can be argued there [21] that only its - safely negligible - fluctuating part must be considered.

b) Coulomb exchange energy.

Since an exact calculation of the Coulomb exchange energy  $E_{CEX}$  is very time-consuming, it has in most cases been taken into account only approximately. In ref. [12] e.g., the statistical estimate

$$E_{CEX} = -\frac{5}{4\pi} \left(\frac{3}{2\pi z}\right)^{2/3} E_{CD}$$

was used, where  $E_{CD}$  is the direct Coulomb energy. A somewhat more refined (local density) Slater approximation is [22,23]

$$E_{CEX} = -\frac{3}{4} e^2 \left(\frac{3}{\pi}\right)^{4/3} \int d^3r \rho_p^{4/3}(r)$$

$\rho_p(r)$  being the proton density, and was used in most of the Skyrme-HF calculations [5-9]. Both these approximations (and others) were checked against exact calculations and found to be satisfactory at ground state deformations [24, 19]. More recent investigations of  $E_{CEX}$  using analytical deformed harmonic oscillator results [25] indicate, however, that the Slater approximation may have the wrong deformation dependence in some cases (namely practically none), whereas the statistical approximation (where  $E_{CEX}$  is proportional to  $E_{CD}$ ) seems more justified. For the Skyrme-HF results, this would lead to a positive correction at the second barrier of  $\sim 0.5 - 1$  MeV for actinides and  $\sim 1\text{-}1.5$  MeV for super-heavy nuclei [9].

c) Dependence of barriers on the force parameters

In most phenomenological effective interactions, there is some freedom left in the choice of the parameters, if one restricts oneself to ground-state properties only. In the case of the Skyrme-forces there is, in fact, an infinite choice of parameters (see Beiner et al. [6]) in the sense that any value of the density dependent term ( $t_3$ ) may be chosen. The rest of the parameters can then still be chosen such as to give reasonably good fits to ground state properties of all spherical

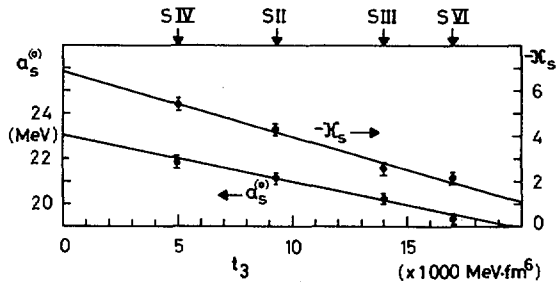


FIG.3. Surface energy  $a_s^{(0)}$  and surface asymmetry coefficients  $\kappa_s$  for different Skyrme interactions (with theoretical error bars), obtained by a semiclassical variational calculation [40]. No spin-orbit contribution is included. Note the linear dependence of  $a_s^{(0)}$  and  $\kappa_s$  on the Skyrme force parameter  $t_3$ .

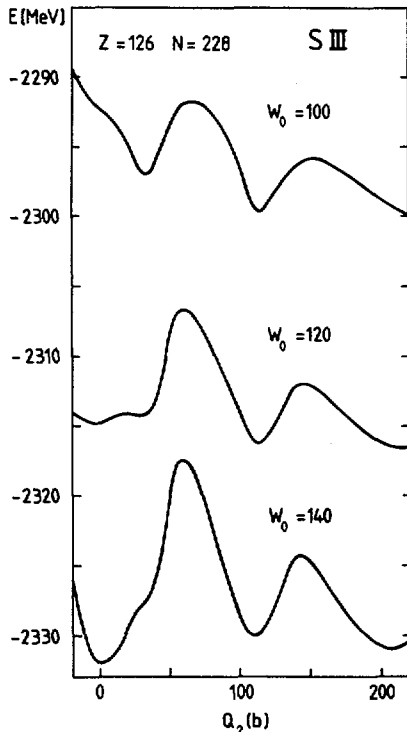


FIG.4. Deformation energy curves for the hypothetical nucleus  $^{354}126$ , obtained with the expectation value method (see Section 2.3). The spin-orbit force parameter  $W_0$  (in units of  $\text{MeV}\cdot\text{fm}^5$ ) is varied, the other parameters of the force Skyrme III are kept constant.  $W_0 = 120 \text{ MeV}\cdot\text{fm}^5$  is the standard value (from Ref. [9]).

nuclei; hereby, the forces with a larger density-dependent term  $t_3$  turn out to have a larger effective nucleon mass  $m^*(r)$ . It is thus important to know how the properties at large deformations depend upon this variation of parameters.

In the thesis of Flocard [7] (p. 37), a comparison is made of the barriers of  $^{240}\text{Pu}$  obtained with the Skyrme forces SIII and SIV. Both barrier heights are larger by  $\sim 5\text{-}6$  MeV with S IV than with S III. A similar difference (6 MeV) was found for the inner barrier of the super-heavy candidate  $^{354}\text{126}$  with the same forces [9]. One may argue that the S III force has to be preferred because of its more realistic value of the effective nucleon mass in the interior of the nucleus ( $m^*/m = 0.75$  for S III and 0.5 for S IV) and its better single-particle spectra of deformed nuclei [19, 26]. Still, the sensitivity of the fission barriers to the force parameters is rather severe. These results are substantiated by independent investigations of the liquid drop parameters inherent in the Skyrme interaction. It was found, indeed, that the surface and surface asymmetry parameters of the different Skyrme forces do vary appreciably, those of S III being very close to the standard LDM values. This is illustrated in Fig. 3.

A similar variation of barrier heights was observed in the calculations of Kolb et al. [12] reported already in Fig. 2 above. In particular, the difference obtained near scission is rather drastic. Note, however, that only four points were calculated along these curves. A more recent calculation, using a newer version of the K-matrix model [27], is reported in ref. [4] (see fig. 11 there). It seems to substantiate the curve labeled "Set III" in Fig. 2, although with a second barrier of more than  $\sim 15$  MeV (as estimated from that figure).

So far, we have been discussing the freedom in the parameters for the central parts of the effective interactions used. An even more drastic - and actually alarming - dependence of the results is found, when it comes to varying the spin-orbit force. The latter has, in all HF (and HFB) calculations mentioned above, been added purely phenomenologically and adjusted such as to give the spin-orbit splittings of the single-particle levels observed experimentally in spherical nuclei. Note that the central part of the Skyrme forces has been linked back to density dependent Brückner-HF calculations with the Reid soft core nucleon-nucleon potential [23], and can therefore be said - as well as the K-matrix models - to be one degree less phenomenological than the spin-orbit force which, in this respect, is to be put at the same level as the simple shell model.

In Figure 4 we show three fission barrier curves for the superheavy nucleus  $^{354}\text{126}$ , obtained with the same force Skyrme III, but with three different values of the spin-orbit parameter  $W_0$  [9]. These curves are not obtained fully selfconsistently, but with the expectation value method [18] to be discussed below. The lack of self-consistency leads to an uncertainty of  $\sim 1\text{-}2$  MeV up to the second minimum and does in any case not affect the dramatic variation of the barrier heights with  $W_0$ . Note that for  $W_0 = 120 \text{ MeV fm}^5$  (the standard value for S III) and  $W_0 = 140 \text{ MeV fm}^5$ , the nucleus is spherical in the ground state, whereas for  $W_0 = 100 \text{ MeV fm}^5$  it becomes deformed. The height of the first barrier varies from 5 to 15 MeV in the three cases. Of course, it is no surprise that the spin-orbit force plays an important - if not the decisive - role for the magnitude and the phase of the shell effects. However, a variation of  $\pm 10\%$  of the constant  $W_0$  could easily be absorbed by a re-adjustment of the other Skyrme parameters without spoiling the nice results for ground-state properties. And its determination by fitting the

HF-levels to experimental single-particle (or hole) states in magic nuclei may be disputed, since the latter are known to receive appreciable contributions from couplings to vibrational modes, which are missing in the HF approach, and which are especially large in spherical closed-shell nuclei (see, e.g. ref. [28]). It is therefore no large overstatement to say that one can obtain almost any barrier one wants by exploiting the freedom in determining the spin-orbit parameter. Taken together with the ambiguities in the rest of the force, uncertainties of many MeV are present in the heights of fission barriers.

In future HF-calculations, fission barriers must definitely be taken into account in pinning down the force parameters. Furthermore, a better understanding of the spin-orbit force is highly desirable. In this respect we refer to an interesting recent attempt to link the spin-orbit force back to simple model nucleon-nucleon potentials by fully relativistic Hartree-calculations [29].

d) Treatment of pairing correlations

We have already discussed the lack of consistency of HF plus BCS calculations as performed by the Orsay group [5-9] and Kolb et al. [10,12]. Of course, for the ground-states this is no severe restriction since their pairing properties can usually be fitted reasonably well by the phenomenological constants  $\Delta$  or  $G$ . The deformation dependence of  $\Delta$  and  $G$  is, however, not known well enough. We may deduce some hints from the result of the Gogny group [15]. There, a deformation energy curve of  $^{152}\text{Sm}$  was obtained in a full HFB-calculation (using a linear constraint) and compared to two approximate (HF plus BCS) calculations. At large deformations, the prescription of a constant gap  $\Delta$  clearly gave a better agreement with the HFB result than a pairing interaction  $G$  proportional to the surface. If this trend persists for heavy nuclei, it might have very interesting consequences for fission barriers. Note that in the Skyrme-HF-BCS calculations of Flocard et al. [7], the constant  $\Delta$  prescription led to a second barrier of  $^{240}\text{Pu}$  which was  $\sim 8$  MeV higher than the one obtained with the other prescription. The newest HFB-results with the Gogny force seem to confirm, indeed, the trend of a constant average pairing gap  $\Delta$  [16]. We also remark here that some interesting attempts have been made to treat the pairing correlation in a classical (Thomas-Fermi) approximation [30]. When applied to deformed nuclei, this approach might also provide some valuable information.

Let us now turn to some technical limitations of the CHF calculations, which are mainly due to their time consuming character.

e) Truncation effects from finite basis expansion

For spherical nuclei, the HF-equation can be solved directly and relatively fast in coordinate space (i.e. in the radial variable) with standard numerical procedures [5,6,10,14,23]. In deformed nuclei, however, the two- or three-dimensional, nonlinear partial (integro-) differential equations pose severe numerical problems. The standard way out is projection on a deformed harmonic oscillator basis and diagonalization of the hamiltonian matrix. We need not explain this method which is well-known from shell-correction calculations (see, e.g. ref. [31]). So far, all CHF calculations for fission barriers with realistic interactions have been performed by this projection method, recently renewed attempts in coordinate space [32] notwithstanding. The difference to the SCM is that the truncation effects are present in the total HF-energies with

their full weight. The time and space limitations of computer calculations set lower bounds on the induced errors. For spherical nuclei, they can be studied carefully by comparison to the exact ( $r$ -space) results (see, e.g. ref. [19]) and extrapolated to small deformations. At large deformations one has to content oneself with observing the convergence of the (relative) deformation energies under variations of the size (number  $N_0$  of major oscillator shells) and the parameters (oscillator strength  $\hbar\omega$  and ratio  $q$  of principal axes) of the deformed basis. In the fission direction (symmetry axis), a single oscillator well (with  $N_0 \approx 13$  to 15) is just about sufficient for deformations up to the second saddle point of actinide nuclei. In ref. [7], the remaining truncation error was estimated to be  $\sim 1$ - $2$  MeV at the second barrier of  $^{240}\text{Pu}$ . When going beyond the outer barrier, a two-center basis of some kind becomes indispensable [8,12,16] (see also refs. [33,34]).

f) Restrictions on symmetries and degrees of freedom

Even with projection on a finite basis, the computer time and space limitations force one to keep some symmetries of the variational space. Whereas left-right (mass) asymmetry can be allowed for at a relatively low cost [12,16], the abandonment of axial symmetry is still too expensive in HF-applications to heavy nuclei. (For triaxial HF-calculations in light nuclei see, e.g. ref. [35].) The corresponding errors in the deformation energies can only be estimated from comparison with the results of SCM-calculations. Thus, in the  $^{240}\text{Pu}$  results of Flocard et al. [7], the first and second barrier heights may be reduced by  $\sim 1$  MeV and  $\sim 4$  to 5 MeV due to the lack of non-axial and left-right asymmetric degrees of freedom, respectively.

For the same practical reasons, more than one constraint can hardly ever be included in full CHF calculations for heavy nuclei. Mainly two physical quantities have been constrained: 1) the quadrupole moment  $Q_2$  [6-9, 15,16] which may be a reasonable fission mode up to the second barrier, and 2) the distance  $r$  between the two halves of the nucleus (i.e. the "nascent fragments") [12] which certainly is more appropriate beyond the saddle and especially around scission. Thus, real deformation energy surfaces have not been obtained with the CHF method, but rather their projections along a one dimensional path which is hoped to be close enough to some adiabatic fission trajectory. The question which constraint to choose in which portion of the deformation space can only be (approximately) answered using a lot of intuition and experience; its ultimate answer can, of course, only be given in the framework of dynamical calculations where the inertial mass tensor is taken into account [36].

g) Final remarks

To conclude this discussion of CHF calculations, we compile in Table I the various corrections, estimated according to a) - f) above, which have to be added to the fission barriers of  $^{240}\text{Pu}$  obtained by Flocard et al. [7]. We see that after these corrections and ignoring the uncertainties in the force parameters themselves, the agreement with experiment is not too bad, if the prescription of an average pairing matrix element  $G$  proportional to the surface is used. With the constant gap  $\Delta$  prescription, much too high barriers would result.

As to the results of Kolb et al. [12] shown in Figure 2, the corrections b) and f) do not apply (mass asymmetry was included and the Coulomb exchange energy taken in the statistical approximation). The truncation error should also be smaller here since a two-center basis was used. Thus, subtracting the spurious rotational energy of  $\sim 2$ - $3$  MeV,

TABLE I. FISSION BARRIERS OF  $^{240}\text{Pb}$  OBTAINED BY FLOCARD ET AL. [7] AND SEVERAL ERROR ESTIMATES (ALL QUANTITIES IN MeV). EXPERIMENTAL RESULTS FROM Ref. [37]. RESULTS IN PARANTHESES ARE OBTAINED WITH A CONSTANT AVERAGE PAIRING GAP  $\Delta$

		$E_A$	$E_B$
	CHF, S III, G=surf. ( $\Delta$ const.)	9 (11)	13 (21)
a)	spur. rotat. energy corr.	- 1	-2 to -3
b)	Coulomb-exch. energy corr.	< + 0.5	+0.5 to +1
e)	truncation error	< - 0.5	-2
f)	$\gamma$ - and mass asymmetry energy	- 1	-4 to -5
c)	uncertainty in force parameters	several MeV	several MeV
	resulting barriers with S III	7 (9)	4-6 (12-14)
	experimental barriers	$6.0 \pm 0.3$	$5.35 \pm 0.2$

a second barrier of  $\sim 4$  to 7 MeV results, depending on the set of parameters. Note that a constant (average) gap was used in this calculation, which thus leads to a lower result than the corresponding one of Flocard et al. [7]. The more recent result of Cusson and Kolb quoted in ref. [4] (Fig. 11), however, would also lead to a barrier of  $E_B$  of  $\sim 13$ -14 MeV.

A similar result has now also been obtained in the newest Gogny-HFB calculations [16]. Together with the other results, this might indicate that an essential component is missing in the large-deformation behaviour of the effective forces in use.

Our conclusions should not be taken from a too pessimistic side: It is true that the experimental fission barriers are not yet well reproduced. On the other hand one should not forget that these CHF calculations represent a completely parameter-free (apart from the pairing problem) extrapolation from calculations where many ground-state properties of most stable nuclei are explained consistently with very few parameters of the effective interaction. As such, and considering the technical problems involved, they represent a remarkable progress.

We have clearly demonstrated that there is by far enough freedom in the force parameters to allow for a simultaneous inclusion of the correct barrier heights in a fit of the ground-state properties. It is also clear that this has to be done in the future - as well as it was necessary in the more phenomenological LDM plus shell-correction calculations. Such new fits in HF-calculations will, of course, require a lot of calculation time. It is therefore important to realize that some much more rapid, but still reasonably accurate approximations to the CHF method exist or are being developed, and will be valuable for the inclusion of

the large deformation behaviour in the selfconsistent description of nuclei with effective interactions. One purely microscopical approximation is discussed in the following subsection, others that make use of semiclassical methods will be presented in Sect. 4.

Finally we should also mention the merit of the CHF calculations to have provided a purely microscopically based quantitative confirmation of the shell-correction approach. This aspect will be discussed in Sect. 3.1 below.

### 2.3. The Expectation-Value Method (EVM)

At the same time as the CHF calculations with Skyrme forces were developed, a non-selfconsistent, but microscopical approach was studied by Ko et al. [17]. This method consists in approximating the total binding energy by the expectation value of the two-body Skyrme Hamiltonian between Slater determinants built of eigenstates of a deformed Woods-Saxon (WS) potential. Practically it corresponds thus exactly to one iteration of a HF-calculation, using a suitably chosen (deformed) potential. In ref. [17], this potential was taken from a standard shell-correction calculation [38] with the generalized WS-Potential of ref. [31], using a two-dimensional (axially and left-right symmetric) family of nuclear shapes  $(c,h)$ . (For details, see ref. [38].) The deformation parameters  $(c,h)$  play in this method the role of the constraint. The deformation energy surfaces obtained this way in ref. [17] for heavy nuclei had the correct shell structure (two saddle points, second isomer minimum). However, the mean part of the deformation energies was increasing too fast, leading to far too high fission barriers.

Recently, we proposed a new version of the EVM [18]. Two essential improvements over ref. [17] were made: 1) An effective mass  $m^*(r)$  was included in the diagonalization of the WS-potential (it was put equal to the free nucleon mass in ref. [17]). 2) The parameters of the WS-potential (as well as effective mass and spin-orbit potential) were fitted to reproduce as well as possible the results of spherical HF calculations. (In this way no free parameters are left, those of the Skyrme force remaining fixed.) Thirdly, an improved relation was used to determine the basis deformation parameter  $q$  at each point  $(c,h)$  instead of the prescription of refs. [31,38].

The method thus consists of the following steps:

- 1) Fit the central nuclear potentials  $V(r)$ , the effective masses  $m^*(r)$  and the spin-orbit potentials  $W(r)$  obtained in a spherical HF-calculation by Woods-Saxon functions, such as to reproduce the correct half-value radii, surface thicknesses and mean values in the interior of the nucleus (independently for protons and neutrons).
- 2) Deform these WS-functions according to the prescription of ref. [31] along a suitable path in deformation space  $(c,h)$  (or any other given shape parametrization).
- 3) Diagonalize the one body-Hamiltonian (for each kind of nucleons)

$$\hat{H} = -\vec{\nabla} \cdot \frac{\hbar^2}{2m^*(\vec{r})} \vec{\nabla} + V(\vec{r}) - i \vec{\nabla} W(\vec{r}) \cdot (\vec{\nabla} \times \vec{\delta})$$

compute the densities  $\rho(r)$  and  $\tau(r)$  and from them the total Skyrme energy. Minimize it with respect to the basis size parameter  $\hbar\omega$  at each deformation. (This can be done analytically, see Vautherin, (1973), ref. [5].)

In order to compare the results to CHF calculations, the quadrupole moment  $Q_2$  is easily computed at each point. We show such a comparison for  $^{240}\text{Pu}$  in Figure 5, taken from ref. [18]. The EVM curve was here obtained by

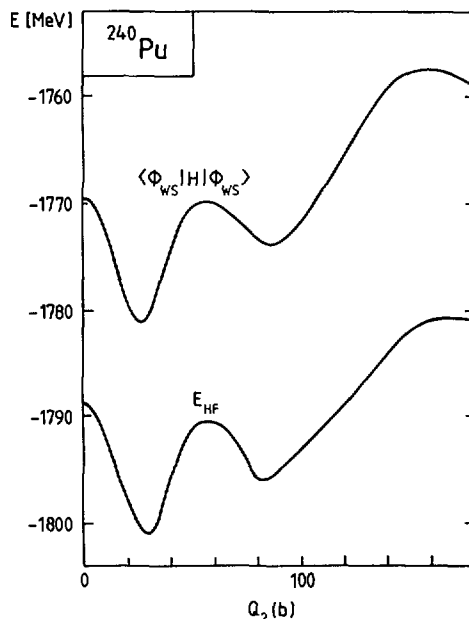


FIG.5. Fission barriers of  $^{240}\text{Pu}$  obtained with the EVM (above) and the CHF method (below) using the force Skyrme III. A constant average pairing gap was used (from Ref. [18]).

minimizing the energy for each  $Q_2$  with respect to the deformation parameters  $c$  and  $h$ . (The lowest path is not far from  $h=0$  as in the results of shell-correction calculations [38].)

We see that up to the second barrier, the deformation energy obtained with this method reproduces the selfconsistent CHF result within  $\sim 1\text{-}2$  MeV. (A constant average pairing gap  $\Delta$  was used here.) Hereby, a factor of at least  $\sim 5$  to 10 was saved in computation time. Similar results were obtained for other nuclei, too [18]. The lack of selfconsistency leads mainly to an almost constant shift of the deformation energy (here of  $\sim 20$  MeV), the local minima and maxima being unaffected.

The error of  $\sim 1\text{-}2$  MeV in the EVM results as compared to the CHF results is reasonably small in view of the various overall uncertainties, which we discussed above. (For the Skyrme force S IV, where the nuclear HF-potential has much larger oscillations in the interior than with S III, the discrepancies are larger,  $\sim 3\text{-}5$  MeV [9].) The EVM is therefore an efficient tool for exploratory calculations in unknown regions of nuclei. It has been applied for an investigation of super-heavy nuclei [9], a result of which was shown in Figure 4 above.

Of course, this method requires some knowledge of the most important deformation degrees of freedom relevant for the desired application. It is therefore especially well suited in connection with a shell-correction calculation. If full selfconsistency is required, the EVM provides an excellent starting point for CHF-iterations. (As a rule, only  $\sim 2\text{-}5$  iterations were required to obtain a well-converged energy.)

Note that in ref. [18], the Coulomb potential was not included in the diagonalization of the proton Hamiltonian  $\hat{H}_p$ . The Coulomb energy was thus treated fully in lowest order perturbation. Including a reasonable (e.g. LDM-) guess for the Coulomb potential in  $\hat{H}_p$  should improve the method and might, in fact, remove most of the remaining smooth error.

The step 1) described above - although it is simple and straight forward - might be a little cumbersome, in particular if many different nuclei and force parameters are investigated. It is hoped that the potentials  $V(r)$ ,  $W(r)$  and  $m^*(r)$  may soon be obtained in semiclassical variational calculations. In fact, for spherical nuclei such investigations have already been performed [39,40] and the EVM was applied there with a similar success.

### 3. THE SHELL-CORRECTION METHOD (SCM)

Swiatecki and Myers [41, 42] emphasized the close connection between the shell-effects in the nuclear binding energies and the non-uniformities of the single-particle spectra of the shell model. In the LDM fits of ref. [42], the energy shell-corrections were phenomenologically parameterized as functions of nucleon masses and deformation.

Strutinsky [3] gave the first microscopical definition of the shell-correction  $\delta E$ , pointing out that it can be extracted from the sum of occupied levels  $\varepsilon_i^{SM}$  of the (deformed) shell model (separately for neutrons and protons):

$$\delta E_{n,p} = \sum_{i=1}^{N(Z)} \varepsilon_i^{SM} - \left\langle \sum_{i=1}^{N(Z)} \varepsilon_i^{SM} \right\rangle_{\text{aver}} \quad (3.1)$$

Here, the second term is a suitably averaged part (see Sect. 3.3) of the single-particle sum. The ansatz

$$E_{\text{tot}} = E_{\text{LDM}} + \delta E \quad (\delta E = \delta E_n + \delta E_p) \quad (3.2)$$

was justified by Strutinsky [3] from HF-theory using a (formal) decomposition of the HF density matrix  $\rho^{\text{HF}}$  into a smooth part  $\bar{\rho}$ , which is responsible for the average (LDM) energy, and a fluctuating part  $\delta\rho$ , which to lowest order is contained in  $\delta E$ :

$$\rho^{\text{HF}} = \bar{\rho} + \delta\rho \quad (3.3)$$

(For simplicity we omit indices for neutrons and protons and consider only one kind of nucleons.)

The shell-correction method (SCM) [3] - on the other side of the Atlantic Ocean also called "microscopic-macroscopic method" - is based on eqs. (3.1,3.2) and the use of phenomenological LD models (e.g. ref. [42]) and deformed shell-model potentials (e.g. of Nilsson [43]). It has initiated a revolutionary development in the understanding of the shell structure in deformed nuclei. In particular, it led to the first qualitative and quantitative explanation of the fission isomers [44] in terms of the by now famous double-humped fission barrier (see also refs. [45, 46]). It is not our aim here to review the numerous calculations made using the SCM with different macroscopic and microscopic ingredients; for that we refer to some representative review articles [38, 47] where many details and applications can be found.

Presently, we shall rather be concerned with the numerical verification of what has been termed the "Strutinsky energy theorem" [48]. Later in this section, some extensions of the method and the technical ways of performing the averaging in eq. (3.1) shall be discussed.

### 3.1 Numerical tests of the SCM within the HF-framework

#### a) The Strutinsky energy theorem

The original derivation of eq. (3.2) from HF-theory by Strutinsky [3] has been discussed and reformulated by numerous authors [38,48-52]. Expanding the HF-energy (in matrix notation)

$$E_{HF} = \text{tr } T\varrho^{HF} + \frac{1}{2} \text{tr } \varrho^{HF} (\text{tr } \varrho^{HF} \bar{\nu}) \quad (3.4)$$

where  $\bar{\nu}$  is the (antisymmetrized) two-body matrix element of the effective interaction, into a Taylor series around the average part  $\bar{\rho}$  in eq. (3.3), one can easily show using perturbation theory arguments that

$$E_{HF} = E[\varrho^{HF}] = E[\bar{\varrho}] + \delta E_1 + \mathcal{O}[(\delta\varrho)^2] \quad (3.5)$$

where

$$E[\bar{\varrho}] = \text{tr } T\bar{\varrho} + \frac{1}{2} \text{tr } \bar{\varrho} (\text{tr } \bar{\varrho} \bar{\nu}) \quad (3.6)$$

and  $\delta E_1$  is the first-order shell-correction, which can be written as in eq. (3.1). Using the occupation numbers  $n_i^{HF}$  and  $\tilde{n}_i$  (see Sect. 3.3), it reads

$$\delta E_1 = \sum_i \hat{\varepsilon}_i n_i^{HF} - \sum_i \hat{\varepsilon}_i \tilde{n}_i = \sum_i \hat{\varepsilon}_i \delta n_i \quad (3.7)$$

Hereby  $\hat{\varepsilon}_i$  are the eigenvalues of the averaged HF-Hamiltonian  $\bar{H}$  defined by

$$\bar{H} = H_{HF}[\bar{\varrho}] = \left. \frac{\partial E_{HF}}{\partial \varrho} \right|_{\bar{\varrho}} \quad (3.8)$$

The point is that the term  $\delta E_1$  in eq. (3.5), and with it the sum of occupied levels  $\hat{\varepsilon}_i$ , contains all contributions of first order in  $\delta\varrho$ . This is true for any density dependent effective interaction, in contrast to the findings of ref. [48] where the rearrangement terms were not correctly included in the definition of the average field (see the detailed discussions in refs. [51,53]).

The practical shell-correction approach consists in the following basic assumptions (see also refs.[3,52]):

1. The average HF energy  $E[\bar{\rho}]$  (3.6) can be approximated by a phenomenological LDM energy  $E_{LDM}$ :

$$E[\bar{\varrho}] \approx E_{LDM} \quad (3.9)$$

2. The levels  $\hat{\varepsilon}_i$  of the averaged HF-Hamiltonian  $\bar{H}$  eq. (3.8) can be approximated by shell-model levels  $\varepsilon_i^{SM}$ :

$$\sum_i \hat{\varepsilon}_i \delta n_i \approx \sum_i \varepsilon_i^{SM} \delta n_i \quad (3.10)$$

3. The "shell-correction expansion" eq. (3.5) is converging fast enough, so that the terms of second and higher order in  $\delta\rho$  can be neglected.
4. In the points 1. and 2. it is assumed that  $\bar{\rho}$  and the corresponding average quantities derived from it are smooth as functions of nucleon numbers and of deformation.

As a particular point of criticism, the argument was made [54] that in the identification (3.10), a constraint should be added to the shell-model potential, since a constraint is also necessary in the HF-calculation to obtain points away from local minima. It was shown, however, in refs. [49, 52, 53, 55] that this is not true. This misunderstanding was based, in fact, upon the erroneous assumption that all first-order shell-effects should be contained in the sum of occupied Hartree-Fock levels  $\epsilon_i^{\text{HF}}$  [50, 54] (which led to much too negative conclusions about the validity of the SCM [50, 54, 56]). That this is not so, is easily seen noting that

$$\delta E_1^{\text{HF}} = \sum_i \epsilon_i^{\text{HF}} n_i^{\text{HF}} - \sum_i \epsilon_i^{\text{HF}} \tilde{n}_i \quad (3.11)$$

does contain all first-order contributions in  $\delta\rho$ . ( $\delta E_1^{\text{HF}}$  differs from  $\delta E_1$  (3.7) only to second order in  $\delta\rho$ .) Since the second sum in eq. (3.11) also contains an oscillating term linear in  $\delta\rho$  (which was actually observed in ref. [50]!), this term is missing - or rather double-counted - in the sum of the occupied HF-levels  $\epsilon_i^{\text{HF}}$ .

Before turning to numerical tests of the energy theorem (3.5), we remark that pairing effects are usually included in the BCS-approximation in the SCM (see, e.g. refs. [3, 38]). A derivation of the energy theorem within the HFB-theory was given by Kolomietz [57].

#### b) Numerical tests.

At the time when the SCM was developed, no reliable HF-calculations were available to test the above assumptions. Bunatian et al. [51] exploited the fact that the second-order shell-correction  $\delta E_2$  (containing all terms quadratic in  $\delta\rho$  in the expansion (3.5)) can be expressed explicitly in terms of the two-body interaction or the scattering amplitude (see also ref. [38]). They calculated the term  $\delta E_2$  in perturbation, using different parameter sets of Migdal's universal quasiparticle amplitude [58] and Woods-Saxon single-particle wavefunctions. In their results for a series of spherical nuclei around  $^{208}\text{Pb}$ , the quantity  $\delta E_2$  did not vary more than by  $\pm \sim 1$  MeV around a mean value of  $\sim 2$  MeV.

Another preliminary test was performed by Bassichis et al. [59], comparing first-order CHF-results for  $^{108}\text{Ru}$  [50] obtained with the Tabakin potential [60] to some ad hoc fits of Nilsson levels and LDM parameters. Their conclusions cannot be taken on their face values due to the lack of self-consistency and the omission of pairing effects in these investigations.

The first consistent test of the energy theorem (3.5) was presented at the Rochester fission symposium by Brack and Quentin [55]. There, CHF-calculations were performed mainly for rare-earth nuclei with the Skyrme force S III. Later, these tests were extended in refs. [61-63] for light and heavy nuclei, using also the Skyrme force S II and the Negele-DME force [23] (see also refs. [4, 19, 53]). In these calculations, the average density matrices  $\bar{\rho}$  were calculated with the Strutinsky averaging procedure, using everywhere the local plateau condition (see Sect. 3.3), so that no single free parameter was used. The averaging of  $\rho$  was done either once on top of the converged CHF results [55, 61] or self-consistently in each iteration [62, 63].

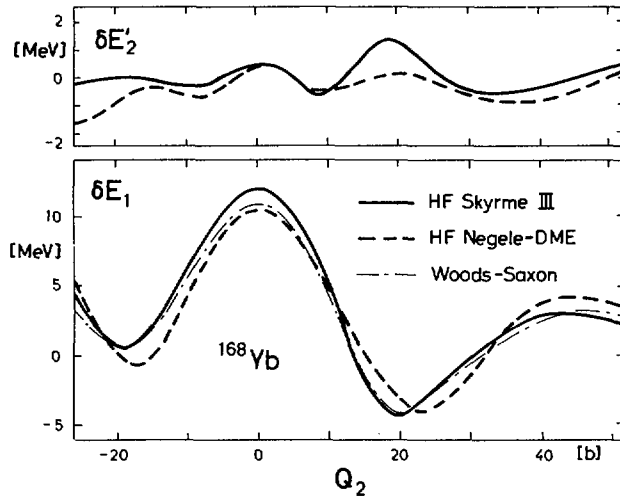


FIG. 6. First-order ( $\delta E_1$ ) and sum of higher-order shell-corrections ( $\delta E'_2$ ) obtained for  $^{168}\text{Yb}$  with the forces S III and Negele-DME using the shell-correction expansion (3.5) of the HF energy [62]. The shell-correction  $\delta E_1$  obtained from a Woods-Saxon potential is shown for comparison. Note that the scale for  $\delta E'_2$  is twice as large as that for  $\delta E_1$ .

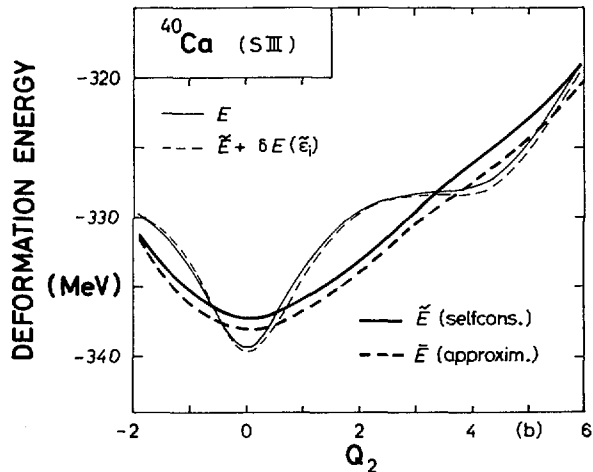


FIG. 7. Deformation energies for  $^{40}\text{Ca}$  obtained with the force S III [61]. Thin solid line: HF energy. Heavy solid line: self-consistently averaged energy. Heavy dashed line: energy, averaged once after HF-iteration. Thin dashed line: 'Strutinsky' approximation to HF energy, differing everywhere less than by 0.5 MeV from the latter.

The quantities  $E[\rho]$  and  $\delta E_1$  were then calculated directly according to eqs. (3.6), (3.7), and the sum of all second and higher order terms was obtained inclusively by the difference

$$\delta E'_2 = E_{HF} - E[\bar{\rho}] - \delta E_1 \quad (3.12)$$

Pairing correlations were included consistently in the BCS-uniform gap method [3,38]. For details of the calculations, see refs. [55,62].

The main results of these investigations can be summarized as follows:

1. The shell-correction series (3.5) indeed converges very rapidly; the sum  $\delta E'_2$  of higher order corrections is (for  $A \gtrsim 100$ ) of the order  $\sim 1-2$  MeV and does not oscillate by more than  $\sim \pm 1$  MeV (both as function of deformation and nucleon number).
2. The first-order shell-correction  $\delta E_1$  depends little on the effective interaction used<sup>1</sup> (this need not be so for  $E[\rho]$ !). It is furthermore well reproduced (within  $\sim 1-2$  MeV) by a phenomenological (Woods-Saxon) potential. (See Fig. 6 below.)
3. The average energy  $E[\bar{\rho}]$  (3.6) has the properties required for a LDM energy: it is smooth and has its minimum at spherical symmetry. If spurious energies and truncation errors are subtracted (see Sect. 2.2), it can well be fitted with suitably chosen LDM parameters. (In particular, the results extracted from the Skyrme III force were closely reproduced by the 1966 parameters of Myers and Swiatecki [42]), see refs. [55,61].) These results may also be viewed as a microscopical derivation of the LDM, which in itself is interesting.
4. An optimal convergence of the series (3.5) is reached, if the average densities  $\bar{\rho}$  are determined selfconsistently. (This has been suggested independently by Tyapin [66] and further discussed by Strutinsky [52,67].) It was achieved in refs. [61-63] by averaging  $\rho$  in each step of the iteration, so that the quantities  $\rho$ ,  $E[\rho]$  and  $H$  after convergence became selfconsistent. It was found, then, that  $\delta E'_2$  is less than  $\sim 0.6$  MeV in magnitude at all deformations, even in such light nuclei as  $^{160}\text{O}$  and  $^{40}\text{Ca}$ . (See also Fig. 7 below.)
5. In light nuclei ( $A \lesssim 40$ ), if the averaging of  $\bar{\rho}$  is not done selfconsistently,  $\delta E'_2$  is up to  $\sim 3-4$  MeV and of the same order as  $\delta E_1$ .
6. The sum of all oscillating terms is also reasonably well reproduced (to within  $\sim 1$  MeV) by the shell-correction  $\delta E_1^{\text{HF}}$  eq. (3.11) [62]. This had also been noted by Krieger and Wong [64].

We illustrate these results in Figs. 6 and 7. The first-order shell-correction  $\delta E_1$  and the sum of all higher-order terms  $\delta E'_2$  are shown for  $^{168}\text{Yb}$  in Figure 6 (from ref. [62], Trieste 1975). The forces Skyrme III and Negele-DME were used. They lead to almost identical results (within  $\sim 1-2$  MeV), although the total energy  $E[\rho]$  is different by several MeV at larger deformations for these two forces [61]. We see also that the resulting  $\delta E_1$  is well reproduced by the shell-correction obtained from a Woods-Saxon potential with the same  $Q_2$ -deformation [38]. (No adjustment was made of the W-S parameters!) Note the correlations between the oscillations in  $\delta E_1$  and  $\delta E'_2$ , which seem to suggest that neglecting  $\delta E'_2$  would affect differences between stationary points of the total energy surface (e.g. barrier heights) only by  $\sim 1$  MeV.

In Figure 7, deformation energies are shown for the nucleus  $^{40}\text{Ca}$  (from ref. [61], Paris 1975), obtained with S III. The once averaged ( $\bar{E}$ ) and self-consistently averaged( $\bar{E}$ ) energies are shown to differ by  $\sim 1-2$  MeV; they

---

<sup>1</sup> Apart from the spin-orbit force, see Section 2.2c and Fig. 4.

are both perfectly smooth. The approximation  $\tilde{E} + \delta E(\tilde{\varepsilon}_i)$ , where the shell-correction (3.7) is now evaluated in terms of the eigenvalues of the self-consistent average field, is very close of the HF energy  $E$  at all deformations. This implies that the sum  $\delta E_1^2$  of higher order corrections is everywhere smaller than  $\sim 0.5$  MeV. The same was found also for medium and heavy nuclei [62,63]. We show the result for  $^{40}\text{Ca}$  here because it demonstrates that the decomposition of the HF energy into a LD and a shell-correction part works even for very light nuclei (including  $^{16}\text{O}$  [62]), which might not have been expected *a priori*.

Similar investigations were made by Bassichis et al. [65] along a program outlined in ref [50] and using the earlier HF-results for  $^{108}\text{Ru}$  [50] mentioned above. However, they used an inconsistent averaging of the density matrix (without curvature-corrections) which, in fact, includes some excitation energy. Consequently, their results depend strongly on the averaging width. Disregarding this fact, they can be said to agree well with our above results.

### c) Discussion of results and conclusions

We should not forget that the above investigations only can test the validity of the SCM within the HF-framework, i.e. to the extent that nature can be replaced by HF-calculations. The effects of correlations are therefore not included, or only as far as they can be mocked up by the effective force used in the HF-approximation. (For extensions beyond HF, see Sect. 3.2 below.).

As we have said in Sect. 2, however, the groundstate energies of most nuclei are very well described in the HF-approximation using the present-day effective interactions. We have also seen that, at least in principle, the deformation energies are reasonably well described. Hereby we emphasize that some of the most pertinent uncertainties of the CHF method discussed in Sect. 2.2, namely the spurious energy contributions and the truncation effects, essentially cancel out in the shell-correction  $\delta E_1$ . As to the uncertainties in the parameters of the (central) force, they are mostly taken care of in the SCM by the LDM parameters which are adjusted to fit experimental results. (The uncertainties in the spin-orbit force and the deformation dependence of the pairing parameters, however, mainly persist in the SCM.)

Keeping this in mind, we may draw the following conclusions from the above HF-tests of the SCM:

1. The rapid convergence of the shell-correction expansion (3.5) has been established. The second and higher-order terms which are neglected in the practical SCM, oscillate not more than  $\sim \pm 1$  MeV. Their mean value depends somewhat on the definition of the average part  $\rho$  of the density matrix and is minimized if the averaging is done selfconsistently.
2. In transitional nuclei, where the first-order shell-correction  $\delta E_1$  is small, the higher order terms might not be negligible, especially if finer details such as e.g. prolate-oblate energy differences are considered. The same is true in light nuclei if LDM and shell-model parameters are not determined selfconsistently.
3. The first-order shell-correction  $\delta E_1$  is a rather stable quantity. It is little sensitive to the effective forces used (apart from the spin-orbit part!) and depends also not much on the selfconsistency of the treatment (see also Sect. 2.3).
4. The average part of the HF-energy is mainly determined by the properties of the force; hereby the selfconsistency is important.
5. Phenomenological LD models can in principle fit the average HF-energies well. For the validity of the SCM, it is essential how good such a fit

- is and whether the average (shell-model) potential is consistent with the LDM parameters. This is, however, not easily checked in actual cases.
6. A particular case of an inconsistency between shell-model potential and LD-energy may be the Pb-anomaly. Since the (selfconsistent) shell-correction  $\delta E_1$  extracted from Skyrme-HF calculations for  $^{208}\text{Pb}$  is in agreement with the value found from a Woods-Saxon potential [38] ( $\sim -18$  to  $-20$  MeV), the anomaly must be due to the LDM parameters used in the SCM calculations. (See also Sect. 3.5.)
  7. We may invert the content of the points 3 and 4 above and state: A self-consistent treatment using effective forces is only necessary for obtaining the average parts of deformation or binding energies. Shell effects can be treated in perturbation, if selfconsistent LD and shell-models are used. (This may be done either with the SCM or with the EVM discussed in sect. 2.3). This gives a strong renewed motivation for the improvement of semiclassical methods, as will be discussed in Sect. 4.
  8. The possibilities of improving the phenomenological shell-model potentials towards selfconsistency in the above average (statistical) sense was discussed by Strutinsky in ref. [52], where also explicit correction formulae were derived. (See also Strutinsky's review talk [67].) These have, however, not yet been used in numerical calculations.

### 3.2 Extensions of the SCM

So far, all our considerations concerned nuclei without excitations. Two extensions of the SCM have been developed which allow to include excitations.

One of them is the treatment of intrinsic excitations within the statistical model [68,69]. It has been widely used in calculations of entropies and level density parameters [70]. The Strutinsky-renormalization eq. (3.2) is thereby usually made at temperature  $T = 0$ . The assumption implicitly made is then that both LDM and shell-model parameters do not depend on the excitation (temperature) of the nucleus. The temperature-dependence of the LDM parameters has been studied [71] and found to be rather weak. The effect of a finite temperature on the (selfconsistent) shell-model potential was investigated in HF-calculations using Skyrme forces by two groups [72,73]. Hereby not the intrinsic energy, but the thermodynamical potential

$$\Omega = \langle H \rangle - TS - \lambda \langle N \rangle$$

is minimized. The main result of these calculations is that, indeed, changes in the selfconsistent potential are negligible. The HF-energies  $\epsilon_i^{\text{HF}}$  depend very little on the temperature up to  $T \sim 5\text{-}6$  MeV. In particular, the physically relevant quantity, namely the entropy  $S$  as a function of the excitation energy  $E^*$ , is extremely well reproduced when calculated from the "cold" spectrum (evaluated at  $T=0$ ). (This result is qualitatively understood by extending the energy theorem (3.5) to finite temperatures, see ref. [72].) Together with the results quoted above in Sect. 3.1, this shows that the usual, non-selfconsistent thermodynamical-statistical approach [70] is well justified. (Strictly speaking, the conclusions of refs. [72,73] are only valid to the extent that the parameters of the effective interaction themselves do not depend on the temperature. As long as  $T$  is much smaller than the Fermi energy, this assumption should however be well fulfilled.)

The idea of renormalizing the grand canonical partition function  $\Phi$ , from which all thermodynamical quantities can be derived consistently, was put forward by Gottschalk and Ledigerber [74]. They derived a shell-correction expansion of  $\Phi$  which is of the same spirit as that of the HF-energy in eq. (3.5). The problem here is how to determine the "empirical"  $\Phi_{LDM}$  by which the average part of the shell-model quantity is replaced. In ref. [74] this was done in terms of an average level density which, however, cannot be determined uniquely.

Another extension is that for nuclei with large angular momentum, which is done by minimizing the expectation value of the cranking Hamiltonian  $H_\omega$ :

$$H_\omega = H - \omega J_x$$

for a rotation about, say, the  $x$ -axis. We do not need to give references to the extensive high-spin studies done by several groups over the past five years; they will be reviewed and discussed in the paper of the Lund group [75]. The selfconsistency of these calculations has not been tested so far. Due to the loss of time reversal symmetry of the cranking Hamiltonian, the corresponding HF-calculations become extremely time consuming for heavy nuclei. (For some cranked HF-calculations for  $^{20}Ne$ , see e.g. ref. [76].) The problem of selfconsistency should, however, be kept in mind when using cranked shell-correction calculations for the prediction of yrast traps, which might depend rather crucially on the shell-model and LDM parameters.

We finally mention an important extension of the SCM which allows to go beyond the HF framework. Bunatian et al. [51] showed that in the Fermi liquid theories of Landau and Migdal (see ref. [58]), the first-order shell correction to the total nuclear binding energy can be cast in the same form as eq. (3.7), where this time  $\varepsilon_i$  are the quasiparticle energies. This has, however, not been used for actual shell-correction calculations so far<sup>2</sup> (apart from the estimation of the second-order terms in ref. [51]), although this would be interesting because it allows the inclusion of correlations (cf. also Dietrich's summary talk of the Rochester conference [77]).

### 3.3 The energy averaging method and alternative suggestions

#### a) Strutinsky energy averaging and the plateau condition

A lot has been published about the method which Strutinsky originally proposed in ref. [3] for the definition of the average part of the single-particle energy sum in eq. (3.1). This method of energy averaging was reformulated in various ways [38,49-51, 78-80] and repeatedly criticized [81] in connection with the so-called plateau-problem. Due to the abundant literature, we will be brief in discussing the method and emphasize those aspects from which new insight has been gained over the past six years.

According to the original prescription [3], the smooth part of the single-particle energy sum is expressed in the following way (for one kind of nucleons, say neutrons):

$$\left\langle \sum_{i=1}^N \varepsilon_i \right\rangle = \tilde{E} \cdot \int_{-\infty}^{\infty} E \tilde{g}(E) dE \quad (3.13)$$

The average level density  $\tilde{g}(E)$  in eq. (3.13) is obtained by folding the level spectrum  $\varepsilon_i$  over an energy range  $\gamma$ :

---

<sup>2</sup> See, however, Werner, E., et al., paper IAEA-SM-241/C26, these Proceedings.

$$\tilde{g}(E) = \frac{1}{\gamma} \sum_i f\left(\frac{E - \varepsilon_i}{\gamma}\right) P_M\left(\frac{E - \varepsilon_i}{\gamma}\right); \int_{-\infty}^{\lambda} \tilde{g}(E) dE = N \quad (3.14)$$

The (symmetric) folding function  $f(x)$  - usually taken as a Gaussian - may be of a rather general form, provided that it falls off sufficiently fast for large  $x$  [80]. The so-called curvature-correction polynomial  $P_M(x)$  ensures that any smooth component of the level density, which is equal to a polynomial of order  $M$  in energy, is identically reproduced by the averaging procedure (3.14) independently of the value of  $\gamma$  and the precise shape of the averaging function  $f(x)$ . Introducing occupation numbers  $\tilde{n}_i$  by

$$\tilde{n}_i = \int_{-\infty}^{(\lambda - \varepsilon_i)/\gamma} f(x) P_M(x) dx; \sum_i \tilde{n}_i = N \quad (3.15)$$

one can rewrite the average energy  $\tilde{E}$  (3.13) in the form [80,38]

$$\tilde{E} = \sum_i \varepsilon_i \tilde{n}_i + \gamma \frac{\partial \tilde{E}}{\partial \gamma} \quad (3.16)$$

For a harmonic oscillator potential, where the true average level density is a parabola (for  $E > 0$ ), the energy  $\tilde{E}$  (3.16) is independent of  $\gamma$  for  $M \geq 4$  as soon as  $\gamma$  is somewhat larger than  $\hbar\omega$ , the level spacing, provided that  $\lambda \gg \hbar\omega$  and sufficiently many levels are included above the Fermi energy  $\lambda$ . The curve  $\tilde{E}(\gamma)$  thus shows an ideal "plateau". This also works approximately for the Nilsson-potential [46,78]. In more realistic potential wells, however, the average part of the level density is no longer a polynomial in  $E$ . Then the infinitesimal plateau conditions must be fulfilled

$$\frac{\partial \tilde{E}}{\partial \gamma} \Big|_{\gamma_0} = 0; \quad \frac{\Delta \tilde{E}(\gamma_0)}{\Delta M} \Big|_{M_0} = 0 \quad (3.17)$$

which corresponds to fitting the (true) average level density locally by an optimal Taylor expansion up to order  $M_0$  [80]. In most cases, the conditions (3.17) can be fulfilled with values of the order

$$\gamma_0 \approx (1.2 - 1.6) \hbar\Omega; \quad M_0 \approx 6-10 \quad (3.18)$$

where  $\hbar\Omega$  is the average distance of the main shells in the spectrum  $\varepsilon_i$ .

Most of the trouble reported [81] was due to neglecting the simultaneous fulfilment of both conditions in eq. (3.17). Another problem is that of the contributions from states in the continuum for the case of finite depth potentials. The usual praxis of including the discrete levels obtained by diagonalisation of these potentials in a harmonic oscillator basis [38,79,80] is rediscussed in the review paper of Strutinsky [67]; we need therefore not discuss it here. We just mention that Ross and Bhaduri [82] showed that rather good plateaux can be obtained for a spherical Woods-Saxon potential, when sufficiently many resonances are included in the continuum region. On the other hand, the discrete states obtained with a typical restricted basis in the lower continuum (up to  $\sim 10 - 15$  MeV in heavy nuclei) rather closely reproduce the positions of the resonances (see, e.g., ref. [72]).

With the plateau conditions (3.17) approximately fulfilled, the second term in eq. (3.16) can be omitted and the shell-correction  $\delta E$  then takes the form of eq. (3.7).

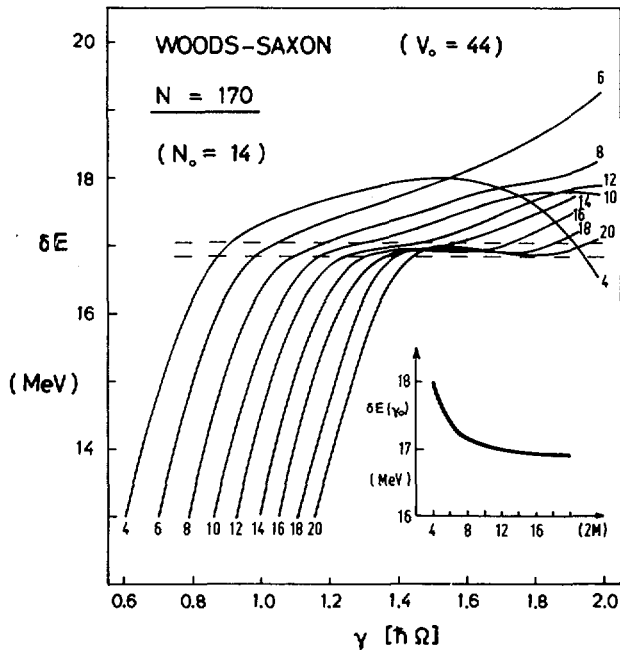


FIG.8. Shell-correction  $\delta E$  in a situation of high local level density (spherical Woods-Saxon potential without spin-orbit term, large positive value of  $\delta E$ ), plotted versus averaging range  $\gamma$  for various orders  $2M$  of the curvature-correction polynomial. Note that for  $2M \gtrsim 12$ , a rather well-defined value  $\delta E \cong (17 \pm 0.15)$  MeV is found. The insert shows the stationary points (or points of deflection)  $\delta E(\gamma_0)$  versus  $2M$ . Using a typical standard value  $\gamma \approx 1.2 \hbar\Omega$  and  $M = 4$  or  $6$ , the error made is still less than 1 MeV (from Ref. [83]).

In ref. [83], the plateau conditions (3.17) were carefully studied for a spherical Woods-Saxon potential (without spin-orbit term). The main results found there may be summarized as follows:

1. For medium and heavy nuclei,  $A \geq 100$ , the conditions (3.17) can usually be fulfilled up to an uncertainty in  $\bar{E}$  of  $\Delta\bar{E} \leq 1$  MeV.
2. For smaller particle numbers ( $N \leq 50$ ) and in cases where the distance of the Fermi level  $\lambda$  from the continuum is smaller than  $\hbar\Omega$ , the uncertainty may be as large as  $\Delta\bar{E} \approx 1-2$  MeV.
3. Difficulties are sometimes met in situations where the local level density at the Fermi energy is large, i.e. when  $\delta E$  is maximal (see also refs. [80,81]). In these cases it may help to go to rather large values of the curvature-correction order  $M$  ( $\sim 14 - 16$ ) to obtain a unique value of  $\bar{E}$ . This is illustrated in Figure 8.
4. The optimal values  $\gamma_0$  and  $M_0$  are not necessarily smooth functions of the nucleon numbers  $N, Z$ . The error made in  $\bar{E}$  is thus discontinuous and rather random. The safest procedure is to determine  $\gamma_0$  and  $M_0$  for a couple of cases in a given region and then to fit a smooth interpolation formula  $\gamma_0(N, Z)$  for systematic shell-correction calculations (see also ref. [80]).

5. In realistic cases, especially when deformations and spin-orbit term are included which tend to remove the largest degeneracies of the spectra  $\varepsilon_i$ , the uncertainty in  $\tilde{E}$  should never be larger than  $\Delta\tilde{E} \approx 1-1.5$  MeV, even if fixed standard values such as  $T_0 \approx 1.2 \text{ h}\Omega$  and  $M_0 = 6$  are used.

b) Alternative methods

Mainly with the intention of overcoming the above-mentioned continuum and plateau problems, several alternative methods have been suggested to extract the smooth part of the sum of occupied levels. We shall here only discuss those methods which are of practical use or which have been studied in sufficient detail.

A modified energy averaging procedure with asymmetric smoothing functions, proposed by Bunatian et al. [51], turned out not to lead to unique values of  $\tilde{E}$  [84].

The so-called temperature-method, proposed by Ramamurthy et al. [85], makes use of the fact that shell effects disappear at large temperatures. The idea is thus to calculate the (intrinsic) energy  $E(T)$  and the entropy  $S(T)$  as function of temperature  $T$  using the thermodynamical-statistical model. (For details see refs. [85-88].) For temperatures larger than  $T_0 \sim 2-3$  MeV ( $k=1$ ), the shell effects disappear (see also refs. [72,73]);  $E(T)$  and  $S(T)$  then become smooth functions  $E(T)$  and  $S(T)$ , respectively. Thus, calculating  $\tilde{E}$  and  $S$  at same finite temperatures

$$T_0 < T \ll |\lambda - V_0|$$

and extrapolating these functions back to zero temperature, one may isolate the energy shell effect at  $T = 0$ :

$$\Delta E_0 = \sum_{i=1}^N \varepsilon_i - \tilde{E}(0) \quad (3.19)$$

It was numerically verified that  $\Delta E_0$  is practically equal to the Strutinsky shell-correction  $\delta E$  (3.7) [85,87,88]. One important detail was to realize [85] that corrections to the asymptotic expansions of  $\tilde{E}(T)$  and  $\tilde{S}(T)$ , containing the local derivatives of the average level density at the Fermi energy  $\tilde{g}'(\lambda)$ ,  $\tilde{g}''(\lambda)$ , ..., must be included in order to obtain unique values of  $\Delta E_0$ . Ignoring these corrections, one just obtains the "back-shifted Fermi gas model" results [86] (see also the discussion in the contribution of Junker et al. to this conference [89]). Including the terms containing derivatives of  $\tilde{g}(E)$  corresponds exactly to the curvature-correction in the Strutinsky averaging method, as shown analytically in refs. [57,90]. We see this also by comparing the equation (3.16) for the Strutinsky-averaged energy  $\tilde{E}$  with the equation for the free energy  $F$ :

$$\begin{aligned} \tilde{E} &= \sum_i \varepsilon_i \tilde{n}_i + \gamma \frac{\partial \tilde{E}}{\partial \gamma} \\ \downarrow &\qquad\qquad\qquad\downarrow\qquad\qquad\qquad\downarrow \\ F &= \sum_i \varepsilon_i n_i(T) + T \frac{\partial F}{\partial T} \end{aligned}$$

Both equations are identical in their form. The important physical difference is, however, that in the thermodynamical equation,  $-\partial F/\partial T = S > 0$  for  $T > 0$ , whereas  $\partial E/\partial \gamma$  is always zero (see eq. 3.17). Due to the curvature-corrections built into the  $\tilde{n}_i$ , the Strutinsky averaging is thus a "cold-averaging" (with zero "entropy"  $\partial E/\partial \gamma$ ), in contrast to the temperature averaging which brings excitation energy into the system.

We see thus that the backward-extrapolated value  $\tilde{E}(0)$  in eq. (3.19) is equal to the Strutinsky averaged energy  $\bar{E}$  of eqs. (3.13, 3.16), and the two methods are completely identical - at least in principle. Practically, some minor differences occur due to the different technical ways of obtaining  $\bar{E}$  resp.  $\tilde{E}(0)$ . In some cases the Strutinsky  $\bar{E}$  is found less accurately than  $\tilde{E}(0)$  with the temperature method, and vice versa [91]. Both methods do depend on the continuum contributions for finite potentials. Their results agree within the overall uncertainty of  $\lesssim 1 - 1.5$  MeV quoted above. A combination of the two methods which diminishes somewhat the influence of the continuum states was recently proposed by Ofengenden et al. [92].

A different approach is replacing in eq. (3.13) the averaged level density  $\tilde{g}(E)$  by an asymptotic expression  $g_{AS}(E)$  valid for large values of  $E$ , i.e. for large nucleon numbers. The problem of finding  $g_{AS}(E)$  for a given potential goes back to Weyl in 1911 [93] and has repeatedly been taken up again [78, 94]. The use of  $g_{AS}(E)$  for calculating the shell-correction was proposed in 1969 by Gaudin and Sajot [95] and applied for finite and infinite square-well potentials. In ref. [80], the case of an infinite box of cubic shape was investigated. It was found that with a careful use of the conditions (3.17) in the Strutinsky averaging (see point 4 in sect. 3.3a), the values for  $\delta E$  obtained by both methods agree within  $\leq 0.2$  MeV for  $N \gtrsim 40$ .

Bohr and Mottelson [69] proposed the direct asymptotic expansion of the single-particle sum:

$$\sum_{i=1}^N \epsilon_i = E_{AS}(N) + \delta E \quad (3.20)$$

$$E_{AS}(N) = a_v N + a_s N^{2/3} + a_c N^{1/3} + a_o + \dots$$

This is completely equivalent to the use of  $g_{AS}(E)$  in eq. (3.13), but demonstrates the analogy with the LDM-expansion of binding energies more readily. The coefficients in  $E_{AS}(N)$  are not easily evaluated in general. The volume term  $a_v$  is given in the Thomas-Fermi model [69], and the surface coefficient  $a_s$  can be related to the phase shifts of the bound state wave functions (due to the surface) in case of a local potential (no spin-orbit term!) [96]. The remaining coefficients must, however, be determined numerically by fitting  $E_{AS}(N)$  to the exact sums of occupied  $\epsilon_i$  for large values of  $N$ . This method was carefully investigated by Sobicewski et al. [83] for a local, spherical Woods-Saxon potential. The asymptotic series was found not to converge fast enough to allow for a unique determination of  $E_{AS}(N)$  for realistic particle numbers. When chosen to fit the Strutinsky-averaged values  $\bar{E}(N)$  for very large  $N$ , however, agreement of  $E_{AS}$  and  $\bar{E}$  within  $\leq 1$  MeV was found for  $N \gtrsim 40$ . Fulfilment of the stationary conditions (3.17) for  $E$  was important here, too (see also the discussion in sect. 3.3a above). This result is interesting because  $E_{AS}$  only depends on occupied states, thus demonstrating the correctness of the continuum treatment in the Strutinsky averaging. The method of the asymptotic expansion in itself is not able to give unique values of shell-corrections; in particular for potentials with spin-orbit terms and deformed shapes, where the phase shifts cannot be given analytically, it is not practically applicable.

The most successful alternative to the Strutinsky averaging, which is free from contributions of unoccupied states and is applicable for realistic deformed potentials, is the semiclassical partition function method proposed by Bhaduri and Ross [97] and further developed by Jennings and

Bhaduri [98,99]. It makes use of a semiclassical expansion of the partition function which goes back to Wigner and Kirkwood [100]:

$$Z(\beta) = Z_{\text{CL}}(\beta) \left\{ 1 + \hbar^2 \chi_2(\beta) + \hbar^4 \chi_4(\beta) + \dots \right\} \quad (3.21)$$

In eq. (3.21),  $\beta$  is the inverse temperature (here simply treated as a mathematical variable);  $\chi_n(\beta)$  are coefficients which depend on the potential and its first  $n$  gradients; and  $Z_{\text{CL}}(\beta)$  is the classical partition function. By inverse Laplace transforming term by term of eq. (3.21), one obtains the smooth part of the level density  $g(E)$ ; the first (classical) term yielding the Thomas-Fermi result  $g_{\text{TF}}(E)$ . Correspondingly one obtains the particle number and the average single particle energy sum in the form

$$\begin{aligned} N &= N_{\text{TF}} + N_2 + N_4 + \dots \\ E_{\text{ETF}} &= E_{\text{TF}} + E_2 + E_4 + \dots \end{aligned} \quad (3.22)$$

where the indices refer to the order of the corresponding terms in eq. (3.21) ( $E_{\text{TF}} = E_{\text{CL}}$ , etc.). For details of this method, we refer to refs. [98 - 101]. Since semiclassical corrections to the Thomas-Fermi expressions are evaluated here, the method is also referred to as the extended Thomas-Fermi (ETF) model; identical results can also be derived by other techniques [102,103]. The series for  $E_{\text{ETF}}$  (3.22) was shown in ref. [101] to converge very rapidly for realistic Woods-Saxon potentials; the term  $E_4$  is of order  $\sim 1$  MeV (for each kind of particles). The energy  $E_{\text{ETF}}$  can thus easily be evaluated to at least the same accuracy as the Strutinsky-averaged quantity  $\bar{E}$ . Hereby, the spectrum  $\varepsilon_i$  need not be known and only the classically allowed region  $V(r) \leq \lambda$  is used to evaluate  $E_{\text{ETF}}$ .

The close connection between the Strutinsky energy averaging and WKB- or ETF-like methods was pointed out early [3,38,103]. In ref. [80] it was shown analytically that for a (deformed) harmonic oscillator potential,  $E_{\text{ETF}}$  and  $\bar{E}$  are identical (independently of the exact shape of the averaging function  $f(x)$  in eq. (3.14)). Jennings [98,99] demonstrated the equivalence of the two methods for any (smooth) infinite potential, provided that a plateau can be found in the Strutinsky averaging. For realistic Woods-Saxon potentials, including spin-orbit term and deformations relevant for fission, the two methods have been compared carefully in ref. [101]. In all cases,  $E_{\text{ETF}}$  and  $\bar{E}$  agree within  $\leq 1 - 1.5$  MeV, thus within the overall uncertainty of either method. This result not only demonstrates the complete equivalence of the two methods in the most general case; it also confirms the standard practice of including unbound discrete states in the lower continuum region. (In fact, using the results of ref. [82] where the resonances in the continuum were included and unique plateau values could be found in the Strutinsky energy  $\bar{E}$ , its agreement with  $E_{\text{ETF}}$  is within 0.25 MeV when  $E_{\text{ETF}}$  is evaluated to that accuracy.)

We finally mention very shortly a new averaging technique developed recently by Ivanyuk and Strutinsky [104,105] which makes use only of bound states and is derived directly from a least-square fit of the single-particle energy sum in powers of  $N^{1/3}$  (similar to eq. (3.20)). In the newest version of this method [105], perfect plateaux are found for the shell-corrections as functions of the number of (bound) levels included. This is illustrated in Figure 9. The method is discussed in the review paper by Strutinsky [67], to which we refer for details. It is important to note that this new method leads to some systematic differences in  $\delta E$  to the standard energy averaging results (see the arrows in Fig. 9). For deformed Woods-Saxon potentials, the difference in  $\delta E$  is roughly constant,  $\sim 1-2$  MeV,

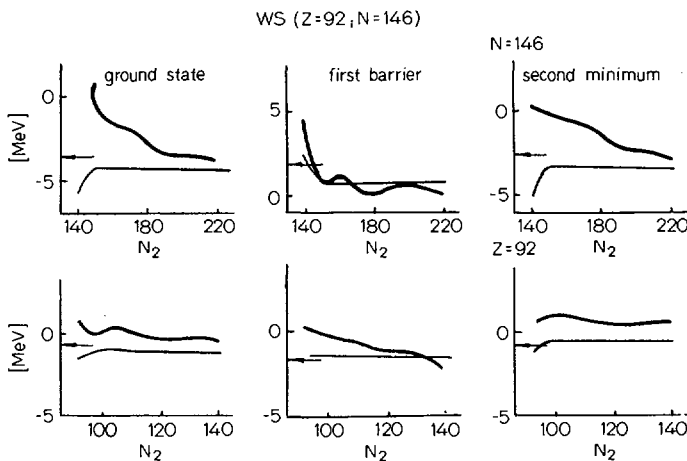


**FIG. 9.** Shell-corrections obtained for deformed Woods-Saxon potentials with the new number-averaging method of Ivanyuk and Strutinsky [105], shown by the thin lines versus twice the number  $N_2$  of the highest level included (see details in Ref. [105]). Fat lines are results from an earlier version [104]; arrows mark the values obtained with the standard energy-averaging technique. Note that in the caption of the original figure (Fig. 3 of Ref. [105]), the role of thin and fat lines was interchanged by mistake (private communication by F.A. Ivanyuk).

and affects relative barrier heights of actinides by less than  $\sim 1$  MeV. For spherical nuclei, however, the difference amounts to several MeV, which has consequences for the so-called Pb-anomaly. (See ref. [67] for a detailed discussion.)

### 3.4 Summary of uncertainties in the SCM

Before turning to a comparison with experiments, let us now briefly recollect the sources and magnitudes of the main uncertainties in the shell-correction method, as discussed in this section.

#### a) Due to the numerical energy averaging:

- in infinite potentials (Nilsson etc.):  $|\Delta \tilde{E}| \lesssim 0.5$  MeV.
- in finite depth potentials (Woods-Saxon, folded Yukawa):  
 $|\Delta \tilde{E}| \lesssim 1 - 1.5$  MeV for  $A \gtrsim 100$ .  
However, larger uncertainties may arise in light nuclei or when the separation energy is small compared to  $\hbar\omega$  (e.g. in nuclei far off the  $\beta$ -stability line).

#### b) From the shell-correction expansion of the HF-energy:

- missing higher order terms:  $|\Delta E| \lesssim 1$  MeV for  $A \gtrsim 100$ .  
This error depends on the selfconsistency of the potential and the LD (droplet) model used; it may easily be several MeV in light nuclei.

- "quality" of commonly used potentials:  $|\Delta\delta E| \lesssim 1 - 2$  MeV.  
This is merely an estimate, taken from comparisons of different calculations with both phenomenological and selfconsistent (HF) potentials.
- "quality" of liquid drop(let) models:  
an error of up to several MeV may be present, in particular in spherical cases. (Pb-anomaly! - see sect. 3.1c above and the discussion in ref. [67].) In contrast to the other uncertainties, this error should show up as a smooth function of N,Z and deformation!

(Note that in the last two items, the word "quality" is to be understood relative to the application in SCM calculations, as judged from the HF point of view. Nothing is said here against the merits and suitability of the phenomenological models in reproducing single-particle properties or average nuclear binding energies.)

Since it appears that most of the above errors or uncertainties are uncorrelated and rather random, one should not expect them to add up. As a rule, we may thus expect an overall uncertainty in SCM results of not much more than  $\sim 1 - 2$  MeV. We emphasize that this should account for the realistic calculations as they were performed in particular for fission barriers, and neither for possible idealized cases where the errors could be somewhat smaller, nor for applications to extreme situations where much larger errors may occur (like e.g. in superheavy predictions [8,9] or heavy ion calculations [106]).

### 3.5 Comparison with experiment

It would lead beyond the scope of this paper to give an extended review of SCM calculations, which are well covered up to 1973 in refs. [38,47]. In the mean time, not many extended compilations were done. One new feature in the results of fission barrier calculations is the appearance of a "second second" saddle which is mass symmetric, but  $\gamma$ -deformed and lies some  $\sim 1 - 2$  MeV higher than the usual mass asymmetric but axially symmetric outer saddle. It was reported in one case by Gavron et al. [107] and, independently, studied systematically over the whole actinide region by Junker and Hadermann [108]. The schematic picture of a typical mid-actinide fission barrier and the role of symmetries is now that shown in Figure 10. The structure at the mass-asymmetric outer saddle, reported for the first time by Möller and Nix at Rochester [47], is now confirmed by other results [109, 67]. It develops to a real third minimum especially for the lighter actinides and may have interesting consequences for the Th-anomaly (see below).

Besides fission barriers, the SCM can, of course, also be applied to (and tested against experimental) ground-state masses [47], moments [110], fission life times [111], fission fragment distributions [112] and other properties, most of which are dealt with at this conference. For a review of fission isomer properties, see especially the paper by Metag [113]. We shall content ourselves here with a short discussion of the two chief applications, where also the two chief discrepancies with experiment have been found, and try to find out whether we can attribute these discrepancies to any of the uncertainties of the SCM discussed above.

#### a) Fission barrier heights and the "Th-anomaly"

The most recent experimental fission barriers have been compiled and compared to shell-correction calculations in the review by Britt [114]. The overall agreement between experiment and theory is essentially unchanged

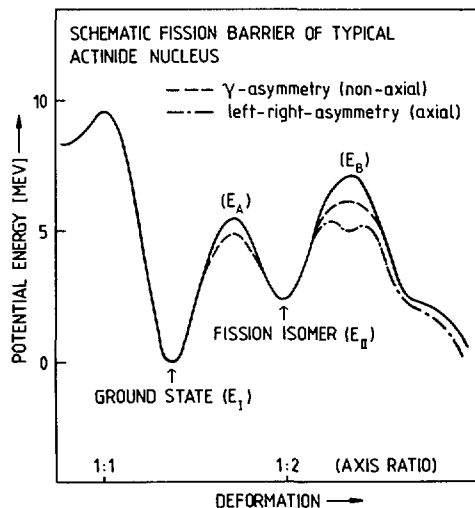


FIG.10. Systematic fission barrier of a typical even-even mid-actinide nucleus.

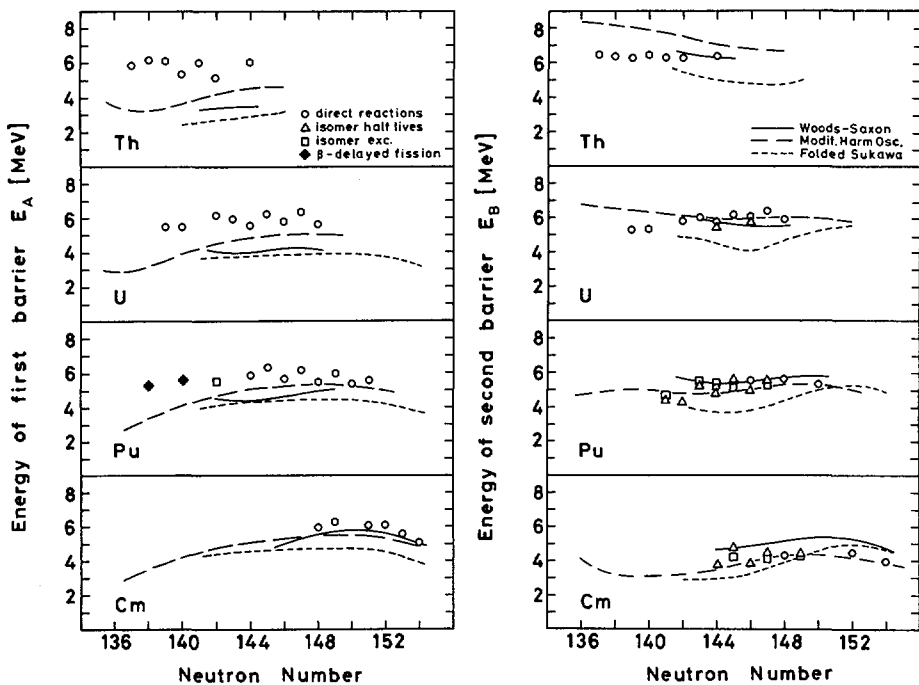


FIG.11. Heights of the inner ( $E_A$ ) and outer ( $E_B$ ) fission barriers of actinide nuclei, compiled by Habs et al. [115]. Circles, triangles and squares show experimental results obtained with different techniques. Solid, long dashed and short dashed lines show theoretical results obtained with the shell-correction method using a Woods-Saxon (Pauli, [47]), a modified harmonic oscillator and a folded Yukawa potential (both by Möller and Nix, [47]), respectively.

since Rochester (see, e.g., Möller and Nix [47]). In Figure 11, we show a comparison of fission barriers, taken from a recent article by Habs et al. [115]. For the outer barriers ( $E_B$ ), the agreement between experimental and three different sets of theoretical results is in all cases within  $\sim 1\text{-}2$  MeV. The same holds for the inner Barriers ( $E_A$ ) of actinides with neutron numbers  $N \geq 140$ . However, there is a clear tendency of the theoretical inner barriers to be too low. This trend gets stronger for the lighter actinides with  $N < 140$ . In the lightest Th-isotopes, the discrepancy reaches up to  $\sim 4$  MeV, which gave rise to the name "Th-anomaly" [38,47]. We see, however, clearly from Fig. 11, that this anomaly is not restricted to Thorium; there is a clear trend for all theoretical barriers  $E_A$  with  $N \leq 144$  to decrease with decreasing  $N$ , whereas all measured values stay constant around  $\sim 5 - 6.5$  MeV. This was emphasized in ref. [115] with the newly measured barriers of  $^{232}\text{Pu}$  and  $^{234}\text{Pu}$ . The former "Th-anomaly" is thus now a clear systematic discrepancy for all actinides (at least up to Pu) with neutron numbers  $N \leq 140$ .

For all the other cases, the agreement within  $\sim 1\text{-}2$  MeV is very satisfactory. As we have summarized in sect. 3.4, the total of uncertainties in the SCM can hardly be expected to be smaller than  $\sim 1\text{-}2$  MeV; the general agreement with experiment is thus the optimal one.

There have been proposed several explanations for the Th-anomaly (see, e.g., Möller and Nix [47], Pauli and Leddergerber [111], Larsson et al. [116]). The most popular is the one using the third minimum found by Möller and Nix [47] and will be much discussed at this conference. We do not want to comment on the possible experimental evidence for this third minimum, which is discussed extensively in several papers [117]. We note, however, that some care should be taken on the theoretical side with the quantitative interpretation of a (third) well with a depth of  $\sim 1$  MeV, in view of the above uncertainty limits of the SCM itself. This is not meant to doubt the qualitative existence of a third minimum, which now seems well established [109,67]. On the other hand, when considering experimental consequences of the existence of this third well, one should not only think of  $^{230}\text{Th}$  and  $^{232}\text{Th}$ , where the original "Th-anomaly" was found, but one should look seriously at all those actinides where a third well is predicted (although this might not be easy experimentally).

In turn, from our point of view taken in this paper, we do not exclude an explanation of the systematic discrepancy in  $E_A$  of the actinides with  $N \leq 140$  due to the uncertainty in the SCM alone (and thus compatible with the old double-humped picture also for the Th-isotopes!). As we stated in sect. 3.4 above, systematic smooth errors larger than  $\sim 1\text{-}2$  MeV may arise in the SCM from a lack of selfconsistency of the shell-model potentials and liquid drop(-let) models employed. In fact, we shall see instantly that this explains the so-called "Pb-anomaly". And indeed, what started out as the Th-anomaly is an error in  $E_A$  which systematically increases as one approaches the Pb-region. To further substantiate - or disprove - this suspicion, it is therefore of great importance to investigate barrier heights of pre-actinide nuclei all the way down to  $^{208}\text{Pb}$  (or even below), both theoretically and experimentally [118].

#### b) Ground state masses and the "Pb-anomaly"

We have now already several times touched upon the other - and largest - discrepancy between experimental data and results calculated with the SCM: a total binding energy of  $^{208}\text{Pb}$  too low by  $\sim 4\text{-}7$  MeV as found with the shell-correction  $\delta E$  in finite depth potentials. Nothing has changed in this

since 8 years (see the details in the reviews [38,47]), and no satisfactory explanation has been given. Our conclusions reached in sect. 3.3 clearly rule out an error of 4-7 MeV in  $\delta E$  due to the Strutinsky averaging method (also in finite depth potentials), as it was sometimes suspected.

We claim (see also ref. [119]) that the material presented in sect. 3.1 above gives a clear (not necessarily unique!) explanation of the Pb-anomaly: namely the fact that no such anomaly exists in the selfconsistent results of ref. [62] using the Strutinsky-smoothed HF-calculations. The "Pb-anomaly" appears thus as due to a lack of selfconsistency in the corresponding SCM calculations. Since the Skyrme-HF results support the value  $\delta E \approx - (18-20)$  MeV of the shell-correction in  $^{208}\text{Pb}$ , found with a Woods-Saxon potential [38], the lack of selfconsistency must be sought in the LD model parameters used in ref. [38].

We note that Strutinsky [67] arrives essentially at the same result; we refer to his review for a further discussion of the LD model. A seemingly different explanation of the Pb-anomaly is given in the paper by Werner et al. [120] using Migdal theory. However, in as far as a large part of their effect is equivalent to the rearrangement in HF, their conclusions agree at least qualitatively with ours.

With the above explanation we have of course not yet given any remedy of the Pb-anomaly. Clearly, better selfconsistent sets of shell model and LD or droplet model parameters should be constructed. For that, more self-consistent (and preferentially semiclassical) calculations with realistic effective forces are needed. Since we argued above, that the old "Th-anomaly" also might be connected with the same effect, more than one problem might be cured in the event of a positive outcome, so that renewed efforts in these directions are certainly justified.

Apart from the region around  $^{208}\text{Pb}$ , the theoretical binding energies obtained with the SCM agree generally with the experimental ones within  $\sim 1-2$  MeV; we thus have here the same satisfactory result as for most of the actinide fission barriers.

#### 4. SUMMARY, CONCLUSIONS AND OUTLOOK

We have examined several methods of calculating nuclear deformation energies, with emphasis on fission barriers of actinides, and compared their results to experiment. We first discussed the constrained Hartree-Fock (CHF) method which makes use of effective nucleon-nucleon interactions fitted to nuclear ground-state properties. Without changing or adding any parameter, the total binding energy is then calculated at large deformations using a constraining external field. That double-humped fission barriers are obtained even qualitatively, is rather remarkable, since they represent only a permille effect in the total binding energy. With the results of HFB calculations by Berger et al. [16], confirming that the average pairing gap  $\Delta$  is roughly constant up to the second barrier, three independent groups now have consistently obtained too high barriers  $E_B$  of  $^{240}\text{Pu}$  or  $^{236}\text{U}$  by roughly a factor of two. This need not be alarming. On one hand, we saw that the freedom in fitting the force parameters (in particular for the case of the Skyrme interaction) leaves enough room for quite appreciable variations in the barrier heights. Especially the spin-orbit force is too little known and leads to large uncertainties. On the other hand it is quite possible that an essential feature of the effective forces in use is generally missing and shows up only at large deformations. This problem in any case presents an interesting challenge for the next future. Clearly, in forthcoming

improvements of the effective interactions, the barrier heights should be carefully watched and incorporated in any adjustment of parameters. It may turn out that the long-range part of the forces needs to be essentially improved. Qualitatively, the inclusion of a second order tensor force should lower the binding energy; whether it brings the desired effect on the fission barriers remains to be investigated.

We have seen that the lengthy HF iterations are not always needed if one only relaxes the required accuracy by a couple of MeV. If carefully deformed realistic potentials are used, one can already in the first step (i.e. by solving the Schrödinger equation once only) obtain deformation energies which locally deviate from the exact CHF results only by a few MeV. This approximate ("expectation value" EV) method should be useful for large scale investigations and rough first-order determinations of force parameters to be used in CHF calculations.

We next discussed several aspects of the shell-correction method (SCM). We have seen that numerical investigations have given an excellent overall verification of the basic assumptions of the SCM within the HF framework. But we also saw that the selfconsistency of nuclear potentials, densities and average (LD) deformation energies play an essential role for the Strutinsky theorem to be accurately fulfilled. Future improvements of the SCM should thus aim at selfconsistent determinations of shell model and droplet model parameters. We showed that this should remove the old Pb-anomaly and argued that it might also improve the inner barriers of the lighter actinides (Th-anomaly). Whether the overall uncertainties of the SCM ever can be brought significantly below a  $\sim 1$  MeV limit, is doubtful even if the ingredients are determined more consistently. When it comes to investigating the "fine structures" of fission barriers [114], we may thus definitely have reached the limits of this method.

One of our conclusions reached in Sect. 3.1 was that shell effects may be treated in perturbation (like in the EVM or the SCM), and that selfconsistency is important mainly for the average potentials and deformation energies. To obtain the latter, semiclassical methods can be applied. Let us briefly outline some recent progress and some plans for the near future along these lines. We have already mentioned in Sect. 3.3 the refinements made in the extended Thomas-Fermi (ETF) method, which was seen to be completely equivalent to the Strutinsky energy averaging and allowed a quantitative confirmation of the latter method also in finite depth potentials. The ETF method cannot be used directly to determine selfconsistent deformation energies, because it leads to densities  $\rho(r)$  which diverge at the classical turning point and are not defined outside. It yields, however, a kinetic energy density functional  $\tau[\rho]$  [122] which has been used quite successfully together with the Skyrme force in variational calculations of average binding energies for spherical nuclei [39,40,123]. The first application of this formalism to calculate average fission barriers will be presented by Bengtsson [124] at this conference.

An important step was reached when it was realized [125] that a partial resummation of the  $\hbar$ -power series (used to derive the ETF expressions, see eq. 3.21) solves the turning point problem, leading to semiclassical densities which are smooth everywhere and fall off exponentially in the tail. With this method, which is still being further developed and tested [126], it is now possible to obtain average densities  $\tilde{\rho}(r)$  and  $\tilde{\tau}(r)$  directly from a given potential  $V(r)$  without the need to evaluate any wavefunctions. This is, however, the most "expensive" step in a HF iteration. The step from  $\rho$  and  $\tau$  to a new (and more selfconsistent) potential is usually done by a simple integration;

in the case of the Skyrme force even by a few algebraic manipulations (including derivatives of  $\rho$ ). Thus, it will shortly be possible to do "short cut" HF iterations semiclassically, which should lead to selfconsistent average potentials and deformation energies at a rather low cost. It remains to be seen numerically to which accuracy this method can be pushed. But we express here the definite hope that most of the calculated fission barriers presented at the next IAEA fission symposium will be evaluated using this method to obtain the average part of the deformation energy.

#### ACKNOWLEDGEMENT

The author is indebted to Ph. Quentin for some enlightening discussions, in particular concerning sect. 2.2.

#### REFERENCES

- [1] BOHR, N., WHEELER, J.A., Phys. Rev. 56 (1939) 426
- [2] FRENKEL, J.A., Zhur. Eksptl. i. Teor. Fyz. 9 (1939) 641
- [3] STRUTINSKY, V.M., Yad. Fiz. 3 (1966) 614 [Sovj. J. Nucl. Phys. 3 (1969) 449]; Nucl. Phys. A 95 (1967) 420; ibid. A 122 (1968) 1
- [4] QUENTIN, P., FLOCARD, H., Ann. Rev. Nucl. Part. Sci. 28 (1978) 523
- [5] SKYRME, T.H.R., Phil. Mag. 1 (1956) 1043; Nucl. Phys. 9 (1959) 615; VAUTHERIN, D., Thèse d'Etat, Orsay (1969), VAUTHERIN, D., BRINK, D., Phys. Rev. C 5 (1972) 626; VAUTHERIN, D., Phys. Rev. C 7 (1973) 296
- [6] FLOCARD, H., QUENTIN, P., KERMAN, A.K., VAUTHERIN, D., Nucl. Phys. A 203 (1973) 433; FLOCARD, H., QUENTIN, P., VAUTHERIN, D., Phys. Lett. 46 B (1973) 304; BEINER, M., FLOCARD, H., GIAI, N. V., QUENTIN, P., Nucl. Phys. A 238 (1975) 29
- [7] FLOCARD, M., QUENTIN, P., VAUTHERIN, D., VENERONI, M., KERMAN, A.K., "Physics and Chemistry of Fission 1973", Rochester, (IAEA Vienna, 1974), Vol. I, p. 221; Nucl. Phys. A 231 (1974) 176; FLOCARD, H., Thèse d'Etat, Orsay (1975)
- [8] BEINER, M., FLOCARD, H., VENERONI, M., QUENTIN, P. "Nobel Symposium on Super-Heavy Elements", Ronneby, 1974 [Physica Scripta 10 A(1974)84]
- [9] BRACK, M., QUENTIN, P., VAUTHERIN, D., "Int. Symp. on Super-Heavy Elements", Lubbock, 1978 (Pergamon, New York, in press)
- [10] KOLB, D., CUSSON, R. Y., HARVEY, M., Nucl. Phys. A 215 (1973) 1
- [11] MEIDNER, H., Phys. Rev. 178 (1969) 1815
- [12] KOLB, D., CUSSON, R.Y., SCHMITT, H.W., Phys. Rev. C 10 (1974) 1529
- [13] FLOCARD, H., private communication
- [14] GOGNY, D., Intern. Conf. Nucl. Phys., Munich 1973, Eds. J. De Boer and H.J. Mang (North-Holland, Amsterdam, 1973) Vol. 1, p. 48
- [15] GOGNY, D., "Nuclear Self-Consistent Fields", I.C.T.P. Conf. Trieste, 1975, Eds. G. Ripka and M. Porneuf (North-Holland, Amsterdam, 1975) p. 333
- [16] BERGER, J.F., GIROD, M., Paper IAEA-SM/241-C2, these proceedings
- [17] KO, C.M., PAULI, H.C., BRACK, M., BROWN, G.E., Phys. Lett. B 45 (1973) 45; Nucl. Phys. A 236 (1974) 236
- [18] BRACK, M., Phys. Lett. B 71 (1977) 239

- [19] QUENTIN, P., Thèse d'Etat, Orsay (1975)
- [20] KELSON, I., SHOSHANI, Y., Phys. Lett. 40 B (1972) 58
- [21] ROSS, C.K., WARKE, C.S., Phys. Rev. Lett. 30 (1973) 55
- [22] GOMBÁS, P., Ann. Phys. (Leipzig) 10 (1952) 253
- [23] NEGELE, J.W., VAUTHERIN, D., Phys. Rev. C 5 (1972) 1472; *ibid.* C 11 (1975) 1031
- [24] TITIN-SCHNAIDER, C., QUENTIN, P., Phys. Lett. 39 B (1974) 397
- [25] QUENTIN, P., to be published
- [26] QUENTIN, P., see ref. [15], p. 297
- [27] CUSSON, R.Y., TRIVEDI, H.P., MELDNER, H.W., WEISS, M.S. WRIGHT, R.E., Phys. Rev. C 14 (1976) 1615
- [28] HAMAMOTO, I., see ref. [15], p. 171
- [29] BROCKMANN, R., Phys. Rev. C 18 (1978) 1510
- [30] BENGTSSON, R., SCHUCK, P., paper IAEA-SM/241-H10, these Proceedings
- [31] DAMGAARD, J., PAULI, H.C., PASHKEVICH, V.V., STRUTINSKY, V.M., Nucl. Phys. A 135 (1969) 432
- [32] HOODBOY, P., NEGELE, J.W., Nucl. Phys. A 288 (1977) 23
- [33] FLOCARD, H., Phys. Lett. B 49 (1974) 129
- [34] ZINT, P.G., MOSEL, U., Phys. Lett. 58 B (1975) 269
- [35] GRAMMATICOS, B., see ref. [15], p. 331; and Thèse d'Etat, Orsay (1977)
- [36] see the review paper by FLOCARD, H., IAEA-SM/241-H1 and the succeeding contributions in these Proceedings.
- [37] BRITT, H.C., BOLSTERLI, M., NIX, H.R., NORTON, J.L., Phys. Rev. C 7 (1973) 801
- [38] BRACK, M., DAMGAARD, J., JENSEN, A.S., PAULI, H.C., STRUTINSKY, V.M., WONG, C.Y., Rev. Mod. Phys. 44 (1972) 320
- [39] BOHIGAS, O., CAMPI, X., KRIVINE, H., TREINER, J., Phys. Lett. 64 B (1976) 381
- [40] CHU, Y.H., JENNINGS, B.K., BRACK, M., Phys. Lett. 68 B (1977) 407
- [41] SWIATECKI, W.J., Sec. Int. Conf. on Nuclidic Masses, Vienna 1963, Ed. W.H. Johnston Jr. (Springer, 1963) p. 58
- [42] MYERS, W.D., SWIATECKI, W.J., Nucl. Phys. 81 (1966) 1
- [43] NILSSON, S.G., Kgl. Dan. Vid. Selsk., Mat.-Fys. Medd. 29 (1955) No.16
- [44] POLIKANOV, S. et al., JETP (Sov. Phys.) 15 (1962) 1016
- [45] STRUTINSKY, V.M., PAULI, H.C., "Physics and Chemistry of Fission 1969", Vienna (I.A.E.A. Vienna, 1969) p. 155
- [46] NILSSON, S.G. et al., Nucl. Phys. A 131 (1969) 1;
- BJØRNHØLM, S., STRUTINSKY, V.M., Nucl. Phys. A 136 (1969) 1
- [47] JOHANSSON, T., NILSSON, S.G., SZYMANSKY, Z., Ann. Phys. (Paris) 5 (1970) 377;
- NIX, J.R., Ann. Rev. Nucl. Sci. 22 (1972) 65;
- PAULI, H.C., Phys. Rep. C 7 (1973) 35;
- MÜLLER, P., NIX, J.R., Rochester 1973, see ref. [7], p. 103;
- Nucl. Phys. A 229 (1974) 269
- [48] BETHE, H.A., Ann. Rev. Nucl. Sci. 21 (1971) 93
- [49] DIETRICH, K., "The Structure of Nuclei", Trieste Lectures 1971 (I.A.E.A. Vienna, 1972) p. 373
- [50] BASSICHIS, W.H., KERMAN, A.K., TSANG, C.F., TUERPE, D.R. WILETS, L., "Magic Without Magic: J.A. Wheeler Festschrift" (Freeman, San Francisco, 1972) p. 15
- [51] BUNATIAN, G.G., KOLOMIETZ, V.M., STRUTINSKY, V.M., Nucl. Phys. A 188 (1972) 225
- [52] STRUTINSKY, V.M., Nucl. Phys. A 218 (1974) 169; *ibid.* A 254 (1975) 197
- [53] BRACK, M. Lectures held at Int. School on Nucl. Physics, Predeal, 1974 (unpublished)
- [54] BASSICHIS, W.H., WILETS, L., Phys. Rev. Lett. 22 (1969) 799;
- WILETS, L., see ref. [45], p. 179

- [55] BRACK, M., QUENTIN, P., Rochester 1973, see ref. [7], p. 231
- [56] BASSICHIS, W.H., TUERPE, D.R. Phys. Rev. C 8 (1973) 541
- [57] KOLOMIETS, V.M. Yad. Fiz. 18 (1973) 288 [Sov. J. Nucl. Phys. 18 (1974) 147]
- [58] MIGDAL, A.B., Theory of finite Fermi systems and properties (Moscow 1965)
- [59] BASSICHIS, W.H., TUERPE, D.R., TSANG, C.F., WILETS, L., Phys. Rev. Lett. 30 (1973) 294
- [60] TABAKIN, F., Ann. of Phys. 30 (1964) 51
- [61] BRACK, M., QUENTIN, P., Intern. Workshop II on gross properties of nuclei and nuclear excitations Hirschegg, 1974 (TH Darmstadt) p. 14; see also in "Atomic Masses and Fundamental Constants", Paris, 1975, Eds. J.H. Sanders and A.H. Wapstra (Plenum, New York 1976) p. 257
- [62] BRACK, M., QUENTIN, P., Trieste 1975, see ref. [15] p. 353; Phys. Lett. 56 B (1975) p. 421
- [63] BRACK, M., Habilitationsschrift, Grenoble 1977; (unpublished); I.L.L. preprint no. 77 BR - 346 S
- [64] KRIEGER, S.J., WONG, C.Y., Phys. Rev. Lett. 28 (1972) 690
- [65] BASSICHIS, W.H., KERMAN, A.K., TUERPE, D.R., Phys. Rev. C 8 (1973) 2140
- [66] TYAPIN, A.S. Yad. Fiz. 19 (1974) 263 [Sov. J. Nucl. Phys. 19 (1974) 129]
- [67] STRUTINSKY, V.M., these Proceedings, review paper IAEA-SM/241-C12
- [68] JENSEN, A.S., DAMGAARD, J., Nucl. Phys. A 203 (1973) 578
- [69] BOHR, A., MOTTELSON, B., Nuclear Structure, Vol. 2 (Reading, 1975)
- [70] see, e.g. HUIZENGA, J.K., MORETTO, L.G., Ann. Rev. Nucl. Sci. 22 (1972) 427; MORETTO, L.G., Rochester, 1973; see ref. [7], p. 329  
DØSSING, T., JENSEN, A.S., Nucl. Phys. A 222 (1974) 493;  
PRAKASH, M., RAMAMURTHY, V.S., KAPOOR, S.S., paper IAEA-SM/241-G2, these proceedings; and further references quoted in these papers
- [71] HASSE, R.W., STOCKER, W., Phys. Lett. 44 B (1973) 26; STOCKER, W., BURZLAFF, J., Nucl. Phys. A 202 (1973) 265
- [72] BRACK, M., QUENTIN, P., Phys. Lett. 52 B (1974) 159; Phys. Scripta 10 A (1974) 163; Trieste 1975, see ref. [15], p. 399
- [73] MOSEL, U., ZINT, P.G., PASSLER, K.H., Nucl. Phys. A 236 (1974) 252; SAUER, G., CHANDRA, H., MOSEL, U., Nucl. Phys. A 264 (1976) 221
- [74] GOTTSCHALK, P.A., Phys. Lett. 64 B (1976) 399; GOTTSCHALK, P.A., LEDERGERBER, T., Nucl. Phys. A 278 (1977) 16
- [75] MØLLER, P., NILSSON, S.G., RAGNARSSON, I., ABERG, S., paper IAEA-SM/241-C4, these Proceedings
- [76] PASSLER, K.H., MOSEL, U., Nucl. Phys. A 257 (1976) 242
- [77] DIETRICH, K., Rochester 1973, see ref. [7], Vol. II. p. 461
- [78] TSANG, C.F., Ph. D. Thesis, Berkeley 1969 (unpublished)
- [79] BOLSTERLI, M., FISET, E.O., NIX, J.R., NORTON, J.L., Phys. Rev. C 5 (1972) 1050
- [80] BRACK, M., PAULI, H.C., Nucl. Phys. A 207 (1973) 401
- [81] LIN, W.-F., Phys. Rev. C 2 (1970) 871; HILLMAN, M., Phys. Rev. C 7 (1973) 2037; CHASMAN, R.R., Phys. Rev. Lett. 33 (1974) 544; RAMAMURTHY, V.S., PRAKASH, M., KAPOOR, S.S., Phys. Lett. 62 B (1976) 124
- [82] ROSS, C.K., BHADURI, R.K., Nucl. Phys. A 188 (1972) 566
- [83] SOBICZEWSKI, A., GYURKOVICH, A., BRACK, M., Nucl. Phys. A 289 (1977) 346
- [84] NERUD, P., HASSE, R.W., University of München Preprint (1977); STRUTINSKY, V.M., private communication

- [85] RAMAMURTHY, V.S., KAPOOR, S.S., KATARIA, S.K., Phys. Rev. Lett. 25 (1970) 386; Phys. Rev. C 5 (1972) 1124;  
RAMAMURTHY, V.S., KAPOOR, S.S., Phys. Lett. 42 B (1972) 399
- [86] KAHN, P.B., ROSENZWEIG, R., Phys. Rev. 187 (1969) 1193
- [87] BENGTSSON, R., Nucl. Phys. A 198 (1972) 591
- [88] DASGUPTA, S., RADHAKANT, S., Phys. Rev. C 9 (1974) 1775
- [89] JUNKER, K., HADERMANN, J., MUKHOPADHYAY, N.C., paper IAEA-SM/241-C10, these Proceedings
- [90] BHADURI, R.K., DASGUPTA, S., Phys. Lett. 47 B (1973) 129
- [91] RAMAMURTHY, V.S., private communication (1978)
- [92] OFENGENDEN, S.R., ZAVARZIN, V.F., KOLOMIETZ, V.M., Phys. Lett. 69 B (1977) 264
- [93] WEYL, H., Nachr. Kgl. Ges. Wiss. Göttingen, Math.-Phys. Klasse (1911) 110
- [94] HILL, D.L., WHEELER, J.A., Phys. Rev. 89 (1953) 1102;  
BALIAN, R., BLOCH, C., Ann. Phys. (N.Y.) 60 (1970) 401; 64 (1971) 271;  
63 (1971) 592; 69 (1972) 76;  
BALTES, H.P., HITL, E.R., Preprint TH Darmstadt (1974)
- [95] GAUDIN, M., SAJOT, A.M., Vienna 1969, see ref. [45], p. 229
- [96] SUGIYAMA, A., INOUE, T., J. Phys. Soc. Japan 17 (1962) 759;  
SIEMENS, P.J., SOBICZEWSKI, A., Phys. Lett. 41 B (1972) 16
- [97] BHADURI, R.K., ROSS, C.K., Phys. Rev. Lett. 27 (1971) 606
- [98] JENNINGS, B.K., Nucl. Phys. A 207 (1973) 538
- [99] JENNINGS, B.K., Ann. Phys. (N.Y.) 84 (1974) 1; Ph. D. thesis, McMaster University, 1976 (unpublished);  
JENNINGS, B.K., BHADURI, R.K., Nucl. Phys. A 237 (1975) 149;
- [100] WIGNER, E., Phys. Rev. 40 (1932) 749;  
KIRKWOOD, J.G., Phys. Rev. 44 (1933) 31;  
UHLENBECK, G.E., BETH, E., Physica 3 (1936) 729
- [101] JENNINGS, B.K., BHADURI, R.K., BRACK, M., Phys. Rev. Lett. 34 (1975) 228; Nucl. Phys. A 253 (1975) 29
- [102] KIRZHNIKS, D.A., Sovj. Phys. JETP 5 (1957) 64; "Field Theoretical Methods in Many-Body Systems", Pergamon Press, 1967
- [103] TYAPIN, A.S., Sov. J. Nucl. Phys. 11 (1970) 401; 14 (1972) 50;  
GROSS, D.H.E., Phys. Lett. 42 B (1972) 41
- [104] STRUTINSKY, V.M., IVANJUK, F.A., Nucl. Phys. A 255 (1975) 405;  
IVANYUK, F.A., STRUTINSKY, V.M., Z. Physik A 286 (1978) 291
- [105] IVANYUK, F.A., STRUTINSKY, V.M., Z. Physik A 290 (1979) 107
- [106] MÖLLER, P., NIX, J.R., Nucl. Phys. A 281 (1977) 354;  
GICK, H. et al., Z. Physik A 282 (1977) 417
- [107] GAVRON, A., BRITT, H.C., GOLDSTONE, P.D., WILHELMY, J.B., LARSSON, S.E., Phys. Rev. Lett. 38 (1977) 1457
- [108] JUNKER, K., HADERMANN, J., Z. Physik A 282 (1977) 391;  
JUNKER, K., Habilitationsschrift, T.U. Wien
- [109] MÖLLER, P., paper IAEA-SM/241-C3, these Proceedings
- [110] BRACK, M., LEDERGERBER, T., PAULI, H.C., JENSEN, A.S., Nucl. Phys. A 234 (1974) 185
- [111] BARAN, A. et al., paper IAEA-SM/241-B2, these Proceedings;  
PAULI, H.C., LEDERGERBER, T., Rochester 1973, see ref. [7], p. 463;  
RANDRUP, J. et al., Phys. Rev. C 13 (1976) 229
- [112] WILKINS, B.D., STEINBERG, E.P., CHASMAN, R.R., Phys. Rev. C 14 (1976) 1832;  
PRAKASH, M., RAMAMURTHY, V.S., KAPOOR, S.S., paper IAEA-SM/241-G2, these Proceedings
- [113] METAG, V., review paper IAEA-SM/241-B3, these Proceedings
- [114] BRITT, H.C., review paper IAEA-SM/241-A1, these Proceedings

- [115] HABS, D., KLEWE-NEBENIUS, H., METAG, V., NEUMANN, B., SPECHT, H., Z. Physik A 285 (1978) 53
- [116] LARSSON, S.E., LEANDER, G., RAGNARSSON, I., RANDRUP, J., Ronneby 1974, see ref. [8], p. 65
- [117] see papers IAEA-SM/241-B5, B6, B8-B11, B 13 in these Proceedings
- [118] see in this respect the papers IAEA-SM/241-A7, C8, C9, C 14 in these Proceedings
- [119] BRACK, M., "Fundamentals of the double-humped fission barrier", lectures presented at the "Winter Courses on Nuclear Physics and Reactors" (Part I), ICTP, Trieste, 1978 (IAEA Vienna), in print
- [120] WERNER, E., DIETRICH, K., MÜLLER, P., NIX, J.R., paper IAEA-SM/241-C26, these Proceedings
- [121] see, e.g., LOMBARD, R.J., Ann. Phys. (N.Y.) 77 (1973) 380 and papers quoted therein
- [122] BRACK, M., JENNINGS, B.K., CHU, Y.H., Phys. Lett. 65 B (1976) 1; GRAMMATICOS, B., VOROS, A., Saclay Preprint 1979
- [123] KRIVINE, H., TREINER, J., Orsay Preprint 1979
- [124] GUET, C., BENGTSSON, R., BRACK, M., paper IAEA-SM/241-H3, these Proceedings
- [125] BHADURI, R.K., Phys. Rev. Lett. 39 (1977) 329;
- [126] DURAND, M., BRACK, M., SCHUCK, P., Z. Physik A 286 (1978) 381
- [126] BARTEL, J., BHADURI, R., BRACK, M., DURAND, M., SCHUCK, P., to be published

## DISCUSSION

K.W. GOEKE: At the beginning of your paper you discuss some of the shortcomings of the Hartree-Fock and constrained Hartree-Fock (CHF) methods at the present time. I would like to add two further problems which, in my view, have prevented CHF from being applied to heavy nuclei on a large scale. One of these shortcomings is conceptual in nature. In CHF one uses a given constraining operator, usually the quadrupole moment, which, although correct near the Hartree-Fock minimum, is not necessarily so, for example, at the second barrier. Another shortcoming is the fact that the Hartree-Fock method is basically an iterative one. Each point on the potential energy surface has to be evaluated separately on the basis of a large number of iterations. P.G. Reinhard and I have tried to find methods of evaluating the potential energy surface 'in one go'. Indeed, within the framework of time-dependent Hartree-Fock, and in particular the adiabatic time-dependent Hartree-Fock method, one can derive a differential equation for the potential energy surface that can be solved by simple step-by-step methods. It determines, in addition, the collective mass parameters. These techniques are currently under investigation and although not yet fully studied, they certainly seem likely to be able to evaluate potential energy surfaces and masses under fully microscopic conditions, and are also much faster than the Hartree-Fock method.

M. BRACK: I completely agree with your comments. As far as the quadrupole constraint is concerned, there is a great deal of support from Strutinsky's calculations showing that Q is certainly a reasonably good fission mode up to the second barrier.

A. FAESSLER: You have told us that by using the Hartree-Fock method one gets a value for the second barrier that is too high on account of the finite basis (1–2 MeV) and also because of spurious effects from rotations (2–3 MeV). You also showed that the second barriers agree, within the limits of this error, if the pairing is taken as proportional to the surface. But I heard recently from Kneissl at Giessen that photofission in the rare-earth nuclei indicates that the data can be explained in this way only if G is constant. In such a case there is a discrepancy of 15 MeV for the second barrier. How do you explain this large difference?

I would also like to make a comment. You have mentioned the dependence of the shell correction plateau on the order of the correction polynomial. At high angular momenta it is no longer possible to obtain such a good plateau. The value of  $\gamma$  depends, further, on the angular momentum. In addition, we have to distinguish between the optimal values for the protons and neutrons, as calculations made here in Jülich have shown.

M. BRACK: In reply to your question, if  $G \approx \text{const.}$  is confirmed by the Hartree-Fock-Bogolyubov results, then I can only say there is something basically wrong with these effective forces (Skyrme forces and K-matrix model) at large deformations. It is even more contradictory in view of the fact that the surface energy coefficient  $a_s^{(0)}$  determined for the force Skyrme III in spherical nuclei is *not* too large, as I have shown.



# CALCULS DE SURFACES D'ENERGIE POTENTIELLE PAR LA METHODE HARTREE-FOCK-BOGOLYUBOV

J.F. BERGER, M. GIROD

Service de physique nucléaire,  
CEA, Centre d'études de Bruyères-le-Châtel,  
Montrouge,  
France

## Abstract—Résumé

### CALCULATION OF POTENTIAL ENERGY SURFACES BY THE HARTREE-FOCK-BOGOLYUBOV METHOD.

The fission barrier of  $^{240}\text{Pu}$  was calculated by the Hartree-Fock-Bogolyubov method with constrained mass quadrupole moment. The interaction used was the density-dependent finite-range interaction D1. The quasiparticle states are developed on the basis of an axially symmetric deformed oscillator including 13 major shells. One-centre and two-centre bases were used for small and large deformations respectively. To begin with, right-left symmetry is imposed on the system. A double-humped potential energy surface is obtained. The zero-point energies associated with rotational, vibrational and centre-of-mass spurious motion were subtracted from this potential energy. The fission barrier of  $^{240}\text{Pu}$  thus obtained is compared with the experimental results and with the results of other theoretical studies. The variation of the pairing correlations as a function of deformation and their influence on the inertial parameters are also shown. Finally, the preliminary result of a calculation in which right-left symmetry is no longer imposed is presented. The height of the second hump is reduced by  $\sim 4$  MeV.

### CALCULS DE SURFACES D'ENERGIE POTENTIELLE PAR LA METHODE HARTREE-FOCK-BOGOLYUBOV.

La barrière de fission de  $^{240}\text{Pu}$  a été calculée par la méthode Hartree-Fock-Bogolyubov avec contrainte sur le moment quadrupolaire de masse. L'interaction utilisée est l'interaction de portée finie D1 dépendante de la densité. Les états de quasi-particules sont développés sur la base de l'oscillateur déformé à symétrie axiale incluant 13 couches majeures. Des bases à un centre et à deux centres ont été utilisées respectivement pour les petites et les grandes déformations. Dans un premier temps, on impose la symétrie droite-gauche au système. On obtient une surface d'énergie potentielle à deux bosses. On a extrait de cette énergie potentielle les énergies de point zéro associées aux mouvements parasites rotationnel et vibrationnel et du centre de masse. On obtient ainsi la barrière de fission de  $^{240}\text{Pu}$  que l'on compare aux résultats expérimentaux et aux résultats d'autres études théoriques. On donne aussi la variation des corrélations d'appariement en fonction de la déformation et leur influence sur les paramètres d'inertie. Enfin, on présente le résultat préliminaire d'un calcul où la symétrie droite-gauche n'est plus imposée. La hauteur de la deuxième bosse est abaissée d'environ 4 MeV.

L'extension à la fission des modèles collectifs fondés sur les approches microscopiques "self-consistantes" du type Hartree-Fock semble constituer l'une des voies pouvant conduire à une description fondamentale de ce phénomène. En effet, la fission d'un noyau apparaît essentiellement comme un mouvement collectif de grande amplitude que l'on peut caractériser par un nombre restreint de paramètres collectifs  $\{q\}$ , le plus important étant la déformation totale du système. Il semble donc naturel d'appliquer à ce phénomène le formalisme développé pour la description des oscillations collectives des noyaux mous [1]. Le principe consiste à reproduire toutes les configurations possibles du système en cours de fission à l'aide d'un calcul Hartree-Fock-Bogolyubov sous contraintes (HFBC). L'ensemble des états de quasiparticules indépendantes  $|\phi(q)\rangle$  ainsi obtenus peut être alors considéré comme une base d'états servant à développer les états stationnaires des voies de fission sous la forme  $|\psi\rangle = \int \chi(\{q\}) |\phi(q)\rangle d\{q\}$ . Les fonctions poids  $\chi(\{q\})$  déterminent le chemin collectif et peuvent être calculées en appliquant un principe variationnel à la fonction d'onde  $|\psi\rangle$ . Elles sont alors solutions d'une équation intégrale du type de GRIFFIN-HILL-WHEELER [2]. Sous certaines conditions équivalant à l'hypothèse adiabatique, cette équation peut être transformée en une équation différentielle du type de BOHR [3, 4]. Celle-ci dépend de deux paramètres : le tenseur des masses collectives  $M_{ij}(\{q\})$  et le potentiel collectif  $U(\{q\})$  qui sont tous deux calculables à partir des états  $|\phi(q)\rangle$ . L'approche ainsi décrite est donc, dans son principe, complètement microscopique.

Nous présentons dans ce travail les résultats d'un calcul représentant la première étape du programme esquisonné ci-dessus, c'est-à-dire la détermination des états  $|\phi(q)\rangle$  et des paramètres collectifs  $M_{ij}(\{q\})$  et  $U(\{q\})$ . Le noyau choisi est le  $^{240}\text{Pu}$  qui est bien connu expérimentalement et qui a déjà donné lieu à de nombreux calculs phénoménologiques [5] et microscopique [6]. Nous avons utilisé la méthode HFBC décrite dans le premier paragraphe avec l'interaction de portée finie, dépendant de la densité appelée D1 [7]. Cette interaction a permis de reproduire correctement non seulement les propriétés globales de la plupart des noyaux stables mais également leurs propriétés de déformation et d'appariement [8]. Elle apparaît donc bien adaptée à un calcul HFBC du type de celui présenté ici. Dans notre approche, le champ d'appariement est, en effet, déterminé d'une façon complètement consistante à partir de l'interaction à deux corps elle-même. Pour des raisons liées à la taille du calcul, nous n'avons contraint

qu'une seule variable collective : le moment quadrupolaire de masse  $q = \langle Q_2^0 \rangle$ , et nous avons imposé la symétrie axiale et l'invariance par renversement du temps. De même nous n'avons pas calculé la contribution de l'interaction coulombienne au terme d'échange du champ moyen et au champ d'appariement. La majeure partie du calcul a été effectuée en imposant une parité donnée aux états de quasiparticules, c'est-à-dire en supposant la symétrie droite - gauche. Nous donnerons cependant dans le troisième paragraphe les résultats préliminaires d'un calcul où cette symétrie a été abandonnée.

Nous avons déterminé la masse  $M(q)$  au moyen du modèle "du cranking" [9]. Quant au potentiel collectif  $U(q)$ , il s'obtient en soustrayant à l'énergie potentielle  $V(q) = \langle H \rangle$  du système la contribution des énergies de point zéro associées aux mouvements parasites contenus dans les états intrinsèques  $|\phi\{q\}\rangle$  [3]. L'évaluation et la discussion de ces quantités seront développées dans le second paragraphe. Le troisième paragraphe sera consacré à la discussion des courbes d'énergie potentielles et à la comparaison du potentiel collectif avec l'expérience.

### I. LE CALCUL "SELF-CONSISTANT"

Conformément à la méthode HFBC, nous avons pris pour états intrinsèques du système à chaque déformation les vides de quasiparticules  $|\phi_q\rangle = \prod_j |\eta_j(q)\rangle^{\hat{0}}$  solutions du problème variationnel :

$$\delta \langle \phi_q | \hat{H} - \frac{\hat{P}^2}{2Am} - \lambda \hat{Q}_2^0 - \mu_N \hat{N} - \mu_Z \hat{Z} | \phi_q \rangle = 0 \quad (1)$$

Dans cette expression  $\hat{H} = \sum_{i=1}^A \hat{t}_i + \frac{1}{2} \sum_{i+j=1}^A \hat{v}_{ij}$  est l'hamiltonien effectif des A nucléons et  $\hat{P}^2/2Am$  est l'énergie cinétique du centre de masse du système (nous avons tenu compte des termes à un et à deux corps). La contrainte  $-\lambda \hat{Q}_2^0$  permet d'imposer la déformation  $\langle Q_2^0 \rangle = q$  au noyau. Les deux autres contraintes assurent simplement la conservation en moyenne des nombres de neutrons et de protons.

Partant de l'expression (1), on obtient les équations non linéaires que doivent vérifier les états individuels  $\eta^+(q)$ . Ces équations ont été résolues par itérations, les  $\eta^+(q)$  étant développés sur des bases fines. Dans le calcul présenté ici, deux types de base ont été employés. Pour des déformations inférieures à  $q = 140$  barns nous avons utilisé le développement

$$\eta_{i\Omega\pi}^+ = \sum_{(a)} \left( U_{i(a)}^{\Omega\pi} C_{(a)}^+ + V_{i(a)}^{\Omega\pi} C_{(a)} \right) \quad (2)$$

sur les états  $C_{(a)}^+$  de l'oscillateur harmonique déformé axialement (OHDA). Les indices  $(a) \in (m, n_1, n_z)$  repèrent les états de l'oscillateur,  $\Omega$  est la projection du moment angulaire individuel sur l'axe Oz et  $\pi$  la parité de l'état. La sommation est étendue à tous les états de l'oscillateur tels que

$$(2n_\perp + |m| + 1) \hbar\omega_\perp + (n_z + 1/2) \hbar\omega_z \leq (N + 2) \hbar\omega_0 \quad (3)$$

avec  $N = 12$ . Dans (3) les paramètres  $\omega_\perp$  et  $\omega_z$  sont les fréquences radiale et longitudinale de l'oscillateur et  $\omega_0 = \omega_\perp^{2/3} \omega_z^{1/3}$ .

Pour les déformations plus grandes que  $q = 140$  barns nous avons utilisé un développement sur une base à deux centres. Ceci est nécessaire pour obtenir une description convenable de la deuxième barrière de fission et une fragmentation possible du système. Cette base à deux centres est constituée de deux ensembles d'états de l'OHDA, centrés respectivement en  $-d/2$  et  $+d/2$  sur l'axe Oz. Les états de quasiparticules sont alors exprimés sous la forme :

$$\begin{aligned} \eta_{i\Omega\pi}^+ = & \sum_{(a)} \left( U_{i(a)}^{(1)\Omega\pi} C_{(a)}^+(-d/2) + V_{i(a)}^{(1)\Omega\pi} C_{(a)}(-d/2) \right) \\ & + \sum_{(a)} \left( U_{i(a)}^{(2)\Omega\pi} C_{(a)}^+ (+d/2) + V_{i(a)}^{(2)\Omega\pi} C_{(a)} (+d/2) \right) \quad (4) \end{aligned}$$

Dans les sommes, le nombre de termes est ajusté de façon à obtenir une base équivalente à la base  $N = 12$  de l'expression (3). Ceci conduit à prendre  $N = 9$  dans l'expression (3) pour chacune des deux bases décentrées. (Nous avons, par ailleurs, constaté que nous obtenions des résultats semblables avec les deux types de base entre 125 et 140 barns). Cette valeur de  $N$  montre que la représentation à deux centres réduit la taille des bases de l'oscillateur à manipuler tout en rendant possible la description d'états ayant un grand nombre de noeuds sur l'axe Oz. Ceci explique en partie la faisabilité de nos calculs aux très grandes déformations. Pour obtenir ces avantages nous avons cependant dû introduire dans l'expression (4) des états de l'oscillateur qui ne sont pas tous orthogonaux entre eux. Afin d'éviter des difficultés numériques, nous procédons, avant tout calcul HFB, à l'orthogonalisation de la base à deux centres. Nous utilisons

pour cela une méthode rapide et précise qui permet d'éliminer correctement les états redondants éventuels [10]. Il est à noter que les deux types de base envisagés sont compatibles avec l'emploi de la méthode de séparation des variables dans les potentiels à deux corps [11]. Ce point est essentiel car, sans cette méthode, l'utilisation de l'interaction de portée finie DI dans le présent calcul serait techniquement inaccessible.

Les paramètres de LAGRANGE correspondant aux trois contraintes sont, dans nos calculs, réajustés à chaque itération au moyen d'une méthode de perturbation [7, 8]. Après convergence, l'énergie potentielle du système est définie par :

$$V(q) = \langle \phi_q | H - \frac{P^2}{2 Am} | \phi_q \rangle \quad (5)$$

Les paramètres de l'oscillateur intervenant dans les bases utilisées ont été déterminés en minimisant à chaque déformation l'énergie totale (5) du système. Dans le cas de la base à deux centres nous avons effectué le calcul en prenant à chaque déformation différentes valeurs de la distance  $d$ . Puis nous avons tracé la courbe de contrainte  $V(q)$  en prenant l'enveloppe des courbes de déformation calculées à distance  $d$  constante. Le résultat obtenu est la courbe en trait plein de la figure 1.

## 2. CORRECTIONS A LA COURBE D'ENERGIE POTENTIELLE

### 2.1. Energie cinétique relative du système scissioné

Ainsi que nous l'avons mentionné dans l'introduction, la courbe d'énergie potentielle  $V(q)$  n'est pas assimilable au potentiel collectif  $U(q)$ . Ceci est particulièrement net lorsque l'on examine l'énergie totale du système complètement scissioné. En effet, le calcul HFB défini par l'éq.(1) ne permet pas de retrouver asymptotiquement la quantité

$$E(q) = Z \times E_0(^{120}\text{Ag}) + (Ze)^2/R \quad (6)$$

obtenue en ajoutant à l'énergie de deux noyaux  $^{120}\text{Ag}$ , dans leur fondamental, leur énergie d'interaction coulombienne. La différence  $V(q) - E(q)$  qui vaut 6,80 MeV pour une déformation  $q = 385$  barns, représente en fait l'énergie cinétique du mouvement relatif des fragments contenu dans les états de quasiparticules indépendantes  $|\phi_q\rangle$ .

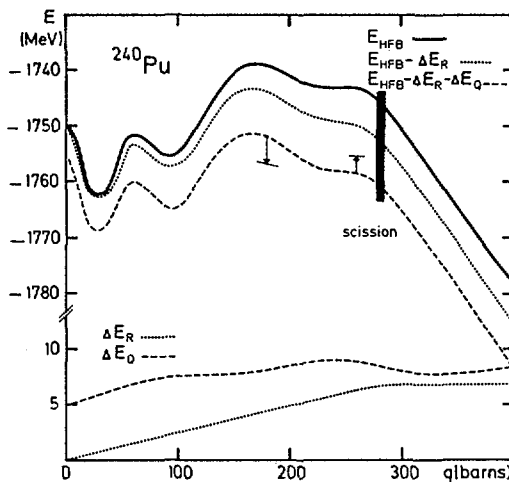


*FIG.1. Courbes d'énergie potentielle et corrections effectuées. La courbe en trait plein ( $E_{HFB}$ ) est le résultat du calcul Hartree-Fock-Bogolyubov avec contrainte sur le moment quadrupolaire de masse. Les deux autres courbes ont été obtenues en ôtant l'énergie cinétique du mouvement relatif des préfragments ( $\Delta E_R$ ) puis les énergies parasites de rotation-vibration ( $\Delta E_Q$ ) représentées au bas de la figure. Les deux flèches indiquent les corrections apportées par un calcul préliminaire permettant l'asymétrie de masse. La bande foncée verticale indique la position du point de scission.*

Pour le vérifier nous avons répété le calcul HFBC dans cette région de déformation en remplaçant l'hamiltonien intrinsèque du noyau  $^{240}\text{Pu}$

$$H_1 = H - \frac{P^2}{2 A m} \quad (7)$$

intervenant dans l'éq.(4), par l'hamiltonien

$$H_2 = H - \frac{P_1^2}{2 A_1 m} - \frac{P_2^2}{2 A_2 m} \quad (8)$$

représentant la somme des hamiltoniens intrinsèques des deux noyaux  $^{120}\text{Ag}$ . Dans l'éq.(8),  $A_1 = A_2 = A/2$ ,  $\vec{P}_1 = \sum_{i=1}^{A_1} \vec{P}_i$  et  $\vec{P}_2 = \sum_{i=A_1+1}^{A_2} \vec{P}_i$ . L'énergie potentielle  $V_2(q) = \langle \phi_q^{(2)} | H_2 | \phi_q^{(2)} \rangle$  correspondante a été trouvée égale à  $E(q)$  à moins de 600 keV près. Par ailleurs, il est facile de montrer que

$$H_2 - H_1 = \frac{(\vec{P}_R)^2}{2\mu} \quad (9)$$

où  $\mu$  est la masse réduite ( $A/4$ ) du système et  $\vec{P}_R = \frac{\vec{P}_1 - \vec{P}_2}{2}$  l'impulsion relative des fragments. Il en résulte que la différence  $\Delta E_R = V(q) - E(q)$  est bien égale à l'énergie cinétique relative des deux noyaux  $^{120}\text{Ag}$ .

Il est clair que l'énergie cinétique  $\Delta E_R$  doit être ôtée de l'énergie potentielle  $V(q)$  lorsque le système est constitué de fragments séparés. Par ailleurs, il apparaît que l'extraction d'une telle quantité lorsque le noyau  $^{240}\text{Pu}$  est sphérique n'a pas de sens. En fait, il semble que la correction à effectuer doit être nulle pour  $q = 0$ , puis augmente avec la déformation suivant une loi qui dépend du degré de préfragmentation du système. Lorsque la fragmentation complète est réalisée, la correction atteint la valeur  $\Delta E_R = V(q) - E(q)$ . Il est aisément de montrer que cette correction devient ensuite indépendante de la déformation.

Nous n'avons pas trouvé de méthode praticable permettant de calculer la correction  $\Delta E_R(q)$  dans la région précédant la scission. Aussi avons nous fait l'hypothèse d'une correction linéaire depuis le point sphérique jusqu'au point de scission. Cette prescription empirique qu'il serait difficile de justifier, donne cependant une idée du type de barrière que fournirait la vraie correction. Nous avons représenté en pointillé sur la figure 1 la correction  $\Delta E_R(q)$  et la courbe d'énergie potentielle corrigée  $E_{HFB} - \Delta E_R$ .

## 2.2. Energie de rotation-vibration

Les états de quasiparticule indépendantes  $|\phi_q\rangle$  ne sont pas des états propres de l'opérateur  $\hat{Q}_2^0$ . Ils ne sont pas non plus invariants par rotation. Ils contiennent donc une énergie de point zéro associée aux mouvements parasites de vibration et de rotation qu'il est nécessaire d'ôter. En fait, ces deux types de mouvements ne sont indépendants que pour les grandes déformations du noyau. Afin de disposer d'une méthode de calcul valable quelle que soit la déformation, il s'avère préférable de traiter globalement les cinq degrés de liberté de rotation-vibration. Pour cela nous considérons les cinq opérateurs quadrupolaires  $\hat{Q}_2^\mu$  et nous extrayons les énergies de point zéro associées aux cinq modes engendrés par les opérateurs

$$\overline{\hat{Q}_2^0} = \hat{Q}_2, \quad \overline{\hat{Q}_2^{\pm 1}} = \hat{Q}_2^1 \pm \hat{Q}_2^{-1} \quad \text{et} \quad \overline{\hat{Q}_2^{\pm 2}} = \hat{Q}_2^2 \pm \hat{Q}_2^{-2}$$

Une expression donnant la valeur de l'énergie de point zéro relative à un degré de liberté  $\overline{q_2^\mu} = \langle \overline{Q_2^\mu} \rangle$  peut être obtenue à partir de la théorie générale du mouvement collectif [3]. Elle s'écrit dans le cas de la symétrie axiale :

$$\Delta E(\overline{q_2^\mu}) = \frac{\hbar^2}{2} (2 \sigma_\mu^2 M_\mu)^{-1} \quad (10)$$

où  $\sigma_\mu$  est la largeur, dans la direction de la variable  $\overline{q_2^\mu} = \langle \overline{Q_2^\mu} \rangle$ , du paquet d'onde supposé gaussien qui représente l'état  $|\phi_q\rangle$  dans l'espace collectif, et  $M_\mu$  est la masse diagonale associée. Pour calculer les masses  $M_\mu$  nous nous sommes servis de l'expression dite "du cranking" [9].

$$M_\mu = \frac{\hbar^2}{2} \frac{S_{3\mu}}{(S_{1\mu})^2} \quad (11)$$

où les quantités  $S_{\eta\mu}$  sont données par

$$S_{\eta\mu} = \sum_{\alpha < \beta} \frac{|\langle \alpha\beta | \overline{Q_2^\mu} | \phi_q \rangle|^2}{(E_\alpha + E_\beta)^\eta} \quad (12)$$

les états  $|\alpha\beta\rangle$  sont les états à deux quasiparticules construits sur les vides  $|\phi_q\rangle$  et  $E_\alpha$  est l'énergie de quasiparticule associée à  $\eta_\alpha^+$ . L'expression (11) de la masse n'étant pas exacte (elle ne contient pas les termes de réarrangement du champ self-consistant en présence d'une vitesse collective), nous avons calculé la largeur  $\sigma_\mu$  également à l'approximation "du cranking" au moyen de la formule [12]

$$(\sigma_\mu)^{-2} = \frac{S_{2\mu}}{4(S_{1\mu})^2} \quad (13)$$

L'énergie de point zéro (10) s'exprime donc simplement par

$$\Delta E(\overline{q_2^\mu}) = \frac{1}{4} \frac{S_{2\mu}}{S_{3\mu}} \quad (14)$$

c'est-à-dire comme le rapport de deux quantités du type (12). Cette particularité permet de penser que l'influence de l'omission des termes de réarrangement est moins importante dans (14) que dans (12). En effet, la

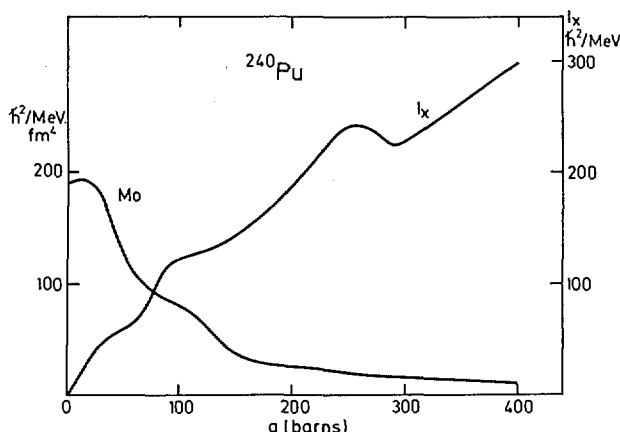


*FIG.2. Variations de la masse collective  $M_0$  et du moment d'inertie  $I_x$  avec la déformation. La masse collective est associée au moment quadrupolaire total  $Q_2^0$  qui a été mis en contrainte. Les deux quantités ont été calculées à l'approximation du cranking.*

sous-estimation de la valeur du numérateur de (14) est approximativement compensée par une sous-estimation de celle du dénominateur.

Avant de discuter de la correction (14), il est intéressant d'examiner les valeurs obtenues pour les masses collectives avec l'expression (11). A titre d'exemple, nous avons représenté sur la figure 2, la masse collective  $M_0$  associée à la déformation totale  $q_2^0$  du système. Sa variation apparaît très régulière, les effets de couche ne se manifestant que sous forme de légers changements de courbure. Une telle régularité est essentiellement due à la prise en compte des corrélations d'appariement. En effet, celles-ci interviennent à la façon d'un terme résiduel prévenant l'apparition de valeurs petites dans les dénominateurs de l'expression (11) et, donc, de valeurs excessivement grandes pour la masse. Ceci montre, en particulier, que les paramètres d'inertie calculés à partir d'une expression du type (11) sont dans certaines régions de déformation très sensibles à la valeur de l'énergie de quasiparticule la plus faible, c'est-à-dire, en première approximation au "gap" d'appariement.

Les mêmes remarques s'appliquent au moment d'inertie  $I_x$  représenté également sur la figure 2. Nous l'avons calculé par la formule "du cranking" [9] qui s'écrit, avec les mêmes notations que l'éq.(12)

$$I_x = 2 \hbar^2 \sum_{\alpha\beta} \frac{|\langle \alpha\beta | J_x | \phi_q \rangle|^2}{E_\alpha + E_\beta} \quad (15)$$

La descente observée entre  $q = 260$  et  $q = 290$  barns correspond à la région de scission. En ce qui concerne les valeurs trouvées au niveau du premier et du deuxième puits elles apparaissent plus faibles que celles dérivées des spectres rotationnels expérimentaux [13]. On obtient, en effet, les valeurs  $42,9 \text{ h}^2$  et  $119,1 \text{ h}^2$  au lieu de  $69,87 \text{ h}^2$  et  $150,06 \text{ h}^2$  respectivement. Ce désaccord est sans doute dû à l'omission des termes de réarrangement dans l'expression (15).

Il est à noter que l'influence de cette omission est probablement plus faible dans le cas des masses collectives. En effet, celles-ci sont calculées comme le rapport de deux quantités du type (12). La remarque faite à propos de la formule (14) s'applique donc aussi à l'expression (11).

La correction totale  $\Delta E_Q = \sum_{\mu=1}^5 \overline{\Delta E(q_2^\mu)}$  a été tracée dans le bas de la figure 1. On constate qu'elle augmente régulièrement de 5 à 9 MeV jusqu'au point de scission, puis subit une légère diminution avant de croître de nouveau lorsque les fragments sont séparés. La courbe semble tendre asymptotiquement vers 10 MeV, valeur égale au double de la correction de point zéro rotationnelle-vibrationnelle relative à un noyau  $^{120}\text{Ag}$ . La courbe d'énergie potentielle obtenue après soustraction de la contribution  $\Delta E_Q$  est notée  $E_{HFB} - \Delta E_R - \Delta E_Q$  sur la figure 1.

### 3. DISCUSSION

Nous commencerons par analyser les trois courbes d'énergie potentielle de la figure 1. La première de ces courbes (courbe  $E_{HFB}$ ) est comparable aux résultats obtenus par FLOCARD et coll. avec l'interaction de SKYRME S III [6]. Le fondamental du noyau a un moment quadrupolaire de charge  $q_c = 11,08$  barns et un moment hexadécapolaire  $h = 1,02 (\text{barns})^2$ . Ces chiffres sont à la fois très proches des valeurs trouvées par ces auteurs et des valeurs expérimentales ( $q_c = 11,58 \pm 0,06$  barns,  $h = 1,15 \pm 0,28 (\text{barns})^2$ ). La hauteur de la barrière sphérique est également comparable au calcul de la réf. [6] effectué avec une constante  $G$  d'appariement proportionnelle à la surface. Au-delà de la première barrière de fission, cependant la courbe  $E_{HFB}$  se rapproche du résultat obtenu en réf. [6], avec un "gap" d'appariement constant. Au niveau de la première barrière de fission, nos résultats se situent de façon intermédiaire entre les deux prescriptions adoptées par FLOCARD et coll. Au voisinage du second minimum, la

forme du noyau s'apparente à un ellipsoïde dont les axes sont dans un rapport 1,90. Cette valeur est en bon accord avec les estimations tirées de l'expérience [14]. Ces observations semblent montrer (i) que les interactions S III et D1 décrivent correctement la déformation du noyau dans son fondamental et dans l'état isomérique; (ii) que la prescription G proportionnelle à la surface reproduit bien les corrélations d'appariement aux faibles déformations mais que l'approximation d'un "gap" constant est plus réaliste aux grandes déformations; (iii) que la hauteur excessive de la première et de la seconde barrière dans la courbe d'énergie potentielle  $E_{HFB}$  n'a pas pour origine une mésestimation des corrélations d'appariement.

On peut voir sur la figure 1 que la seconde barrière de fission subit un ressaut au voisinage de  $q = 260$  barns. L'examen des densités de particules montre que cette région de déformation correspond à la formation des fragments de scission. La forme extérieure du noyau varie peu, tandis qu'une masse de plus en plus importante de matière se regroupe de part et d'autre du centre de masse du noyau.

Nous avons représenté sur la figure 3 les variations de l'énergie d'appariement et celles de l'énergie de quasiparticule la plus basse pour les protons et les neutrons. Alors que l'énergie d'appariement des protons varie peu autour de 15 MeV, celle des neutrons oscille fortement, en étroite corrélation avec l'énergie de déformation du système. Ce comportement met particulièrement bien en lumière la variation des effets de couche avec la déformation, leur influence sur la formation des minima de l'énergie potentielle et leur origine essentiellement neutronique dans le cas du  $^{240}\text{Pu}$ . Les énergies de quasiparticule tracées sur la même figure peuvent être assimilées, en première approximation, aux "gaps" d'appariement neutron  $\Delta_n$  et proton  $\Delta_p$ . Les valeurs obtenues aux faibles déformations sont proches de celles trouvées par FLOCARD et coll. [6]. Au-delà de  $q = 150$  barns, les résultats de la réf. [6] montrent une augmentation régulière de  $\Delta_n$  et  $\Delta_p$ . Les valeurs que nous trouvons restent au contraire toujours inférieures à 1,7 MeV avant de rejoindre celles correspondant à un noyau  $^{120}\text{Ag}$ . Ces résultats confirment les remarques faites plus haut concernant le type de prescription reproduisant le mieux l'appariement aux grandes déformations.

On voit sur la figure 1 que la position des deux premiers minima de la courbe  $E_{HFB}$  n'est pratiquement pas affectée par l'extraction des corrections  $\Delta E_R$  et  $\Delta E_Q$ . Les principales modifications concernent, en fait,

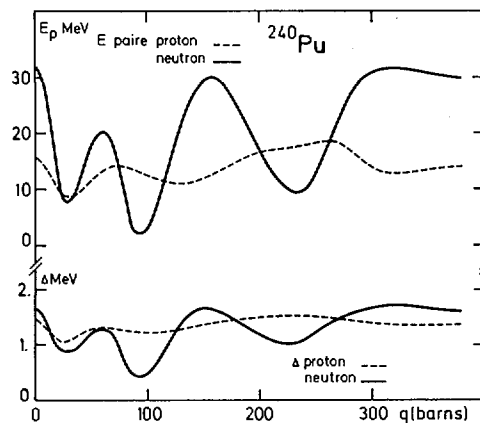


FIG.3. Variations en fonction de la déformation de l'énergie d'appariement  $E_p$  et de la plus petite énergie de quasiparticule  $\Delta$  pour les protons (tirets) et les neutrons (trait plein).

TABLEAU I. HAUTEURS DE LA BARRIERE SPHERIQUE ( $E_0$ ), DE LA PREMIERE ( $E_A$ ), DE LA DEUXIEME ( $E_B$ ) BARRIERE DE FISSION ET DU PUITS ISOMERIQUE ( $E_{II}$ ) PAR RAPPORT AU PREMIER PUITS ( $E_I$ )

	$E_0 - E_I$	$E_A - E_I$	$E_B - E_I$	$E_{II} - E_I$
$E_{HFB}$	11,8	10,7	23,2	6,9
$E_{HFB} - \Delta E_R$	11,3	9,2	18,8	4,6
$E_{HFB} - \Delta E_R - \Delta E_Q$	13,5	9	17,2	3,7
Calcul asymétrique préliminaire			$\sim 13$	
Expérience [13]		6	5,4	2

Les quatre premiers jeux de valeurs correspondent aux trois courbes de la figure 1 et à l'estimation donnée par le calcul asymétrique. Les valeurs expérimentales de la dernière ligne ont été tirées de la Réf. [13].

les hauteurs relatives des différents extrema. Ces quantités sont regroupées dans le tableau I. Lorsqu'on passe de la courbe  $E_{HFB}$  à la courbe complètement corrigée, on remarque que (i) la barrière sphérique augmente de 1,7 MeV; (ii) les deux maxima s'abaissent; (iii) la différence de hauteurs entre les deux premiers puits diminue; (iv) le ressaut situé au voisinage du point de scission s'estompe. Les corrections s'effectuent donc dans un sens favorisant la réduction des structures de la courbe de déformation; le tableau I montre cependant que les chiffres correspondant à la courbe corrigée sont nettement plus grands que les estimations tirées des résultats expérimentaux [12]. La première barrière apparaît trop haute de 3 MeV, la seconde de 11,8 MeV et le puits isomérique est situé 1,7 MeV au-dessus de la valeur attendue.

Il semble que l'origine de ces différences soit d'abord à rechercher dans les approximations effectuées dans notre calcul. En effet celles-ci ont souvent pour conséquence une surestimation de l'énergie intrinsèque du système le long du chemin de fission. Ce sont essentiellement :

### 3.1. La symétrie axiale

Il semble que cette approximation soit assez bien justifiée excepté au voisinage de la première barrière, on estime généralement que l'inclusion de déformations triaxiales abaisse cette barrière de près de 1 MeV [15].

### 3.2. La symétrie droite-gauche

Cette hypothèse conduit à une fragmentation symétrique du  $^{240}\text{Pu}$  que l'on sait être moins probable que la fragmentation asymétrique. Elle n'est donc certainement pas justifiée au moins pour les grandes déformations. Des calculs utilisant la prescription de STRUTINSKI ont montré que la prise en compte de l'asymétrie de masse abaissait la seconde barrière d'environ 3 MeV dans le cas du noyau  $^{240}\text{Pu}$  et produisait l'apparition d'un minimum supplémentaire peu profond [16, 17]. Afin de voir si notre approche prévoyait un effet analogue, nous avons effectué un calcul préliminaire dans lequel nous cessons d'imposer une parité donnée aux états de quasi-particules  $n_{i\Omega}$  de l'expression (4). Etant donné la taille du calcul, nous n'avons pas introduit de contrainte sur l'asymétrie de masse. Notre but a été de rechercher un éventuel minimum dans la direction asymétrique. Afin de simplifier ce premier calcul, nous avons utilisé une base d'états plus

réduite ( $N = 8$  au lieu de  $N = 9$  dans l'expression (3) pour chacune des bases de l'oscillateur décentrées) et nous avons tenu compte des corrélations d'appariement à l'approximation de "gaps" proton et neutron constants. Les résultats obtenus ont ensuite été comparés avec ceux d'un calcul symétrique réalisé exactement dans les mêmes conditions (même taille de la base, même approximation pour l'appariement et mêmes valeurs pour les "gaps" proton et neutron). Pour les "gaps" proton et neutron nous avons repris les valeurs obtenues par le calcul HFBC complet aux déformations correspondantes. Les deux déformations  $q = 180$  barns (peu après le sommet de la seconde barrière) et  $q = 260$  barns ont été envisagées. Les modifications en énergie obtenues sont celles indiquées par des flèches sur la figure 1. On constate que l'énergie du point  $q = 180$  barns descend de 4,7 MeV. Par contre le point à  $q = 260$  barns subit une remontée de 2,8 MeV. Ce comportement peut s'expliquer de la façon suivante: pour les deux déformations, nous avons initialisé le calcul itératif en prenant une asymétrie de départ correspondant à des fragments de fission  $(Z_1, N_1) = (40,60)$  et  $(Z_2, N_2) = (54,86)$  expérimentalement observés. Il semble que dans le cas  $q = 260$  barns, cette asymétrie de départ conduise, après convergence, vers un minimum relatif dans la direction asymétrique qui se trouve à une énergie plus élevée que le point symétrique. Le système symétrique devrait donc être localement stable dans la direction asymétrique à cette déformation. Il est à noter qu'un tel comportement a été observé dans les résultats de calculs "macroscopique-microscopique" [5]. Les asymétries obtenues après convergence apparaissent cependant plus faibles que celles attendues; elles correspondent à des rapports de masses  $\chi = A_2/A_1$  valant 1,16 et 1,12 à  $q = 180$  et 260 barns respectivement, au lieu de 1,30 à 1,40 [16]. Ce désaccord semble s'expliquer par le fait que notre calcul favorise l'apparition d'un nombre  $Z_2 = 50$  pour le nombre de protons du préfragment lourd. Il est également possible qu'il existe un (ou plusieurs) autre minimum relatif dans la direction asymétrique. Cette question ne pourra être tranchée que par un calcul complet avec contrainte sur l'asymétrie de masse.

En tenant compte des pentes obtenues aux deux déformations envisagées il est possible d'avoir une idée de la seconde barrière déduite d'un calcul asymétrique. La hauteur de barrière qui en résulte est alors ramenée à environ 13 MeV.

### 3.3. L'omission des énergies de point zéro

Associées à des observables non conservés à l'approximation HFB, telles que les nombres de protons et de neutrons, les corrections correspondantes, qu'il est difficile de chiffrer, pourraient aller dans le sens d'une réduction de la hauteur du maxima dans les courbes d'énergie potentielle. De même, les états  $|\phi_q\rangle$  ne sont pas états propres de l'isospin total T du noyau (même en l'absence d'interaction coulombienne). Une énergie de point zéro associée à la violation de T par les états de quasiparticules indépendantes est donc incluse dans nos énergies potentielles. A elles seules ces trois types de correction ne suffisent pas à réduire la hauteur excessive de nos barrières de fission de même que les incertitudes propres à nos calculs (comme par exemple l'erreur due à la troncation de la base ou les approximations faites dans l'évaluation des énergies de point zéro prises en compte).

En conclusion cette étude du  $^{240}\text{Pu}$  montre qu'il est actuellement possible d'effectuer des calculs self-consistants relativement sophistiqués même pour des noyaux très lourds. Rappelons en effet ce qui fait l'originalité de ce travail :

- i) l'interaction DI utilisée est de portée finie,
- ii) le champ moyen et le champ d'appariement sont calculés de façon consistante avec la même interaction,
- iii) une base d'état à deux centres est utilisée pour les grandes déformations.

L'extension de ce type de calcul à des formes de noyau asymétriques apparaît également réalisable. Ces nouvelles possibilités des calculs microscopiques permettent de mieux situer l'origine des désaccords observés entre les prédictions théoriques et l'expérience. A notre avis, notre traitement des effets d'appariement nous semble suffisamment réaliste pour ne pas être mis en cause. En particulier nos calculs ne confirment pas l'hypothèse d'une force d'appariement proportionnelle à la surface. Par contre il semblerait que l'origine des désaccords provienne d'une estimation incomplète des corrélations de longue portée. Le recensement des différents modes d'excitation et l'évaluation complète des énergies de point zéro associées demeurent un problème très délicat.

## REFERENCES

- [1] KUMAR, K., BARANGER, M., Nucl. Phys. **A110** (1968) 529;  
GIROD, M., KUMAR, K., GRAMMATICOS, B., AGUER, P., Phys. Rev. Lett. **41** (1978) 1765.
- [2] HILL, D.L., WHEELER, J.A., Phys. Rev. **89** (1953) 1102; GRIFFIN, J.J., WHEELER, J.A., Phys. Rev. **108** (1957) 311.
- [3] GIRAUD, B., GRAMMATICOS, B., Nucl. Phys. **A233** (1974) 373; et **A255** (1975) 141;  
ONISHI, N., UNE, T., Prog. Theor. Phys. **53** (1975) 504.
- [4] VILLARS, F., in Nuclear Self-Consistent Fields (RIPKA, G., PORNEUF, M., éd.), North-Holland (1965); VILLARS, F., Nucl. Phys. **A285** (1977) 269.
- [5] MÖLLER, P., NIX, J.R., «Calculation of fission barriers», Physics and Chemistry of Fission (C.R. Coll. Rochester, 1973) I, AIEA, Vienne (1974) 103; voir également les références citées dans ce rapport.
- [6] FLOCARD, H., QUENTIN, P., VAUTHERIN, D., KERMAN, A.K., «Hartree-Fock calculations of the fission barriers of plutonium isotopes», Physics and Chemistry of Fission (C.R. Coll. Rochester, 1973) I, AIEA, Vienne (1974) 221.  
FLOCARD, H., QUENTIN, P., VAUTHERIN, D., VENERONI, M., KERMAN, A.K., Nucl. Phys. **A231** (1974) 176.
- [7] GOGNY, D., in Nuclear Self-Consistent Fields (RIPKA, G., PORNEUF, M., éd.), North-Holland (1975).
- [8] DECHARGE, J., GIROD, M., GOGNY, D., Phys. Lett. **55B** (1975) 361; GIROD, M., GOGNY, D., Phys. Lett. **64B** (1976) 5.
- [9] INGLIS, D.R., Phys. Rev. **103** (1956) 1786; BELYAEV, S.T., Mat. Fys. Medd. Dan. Vid. Selsk. **31** (1959) 11.
- [10] BERGER, J.F., Soumis à Nucl. Phys.
- [11] GOGNY, D., Nucl. Phys. **A237** (1975) 399.
- [12] GIROD, M., GRAMMATICOS, B., Soumis à Nucl. Phys.
- [13] BJORNHOLM, S., LYNN, E., Cités en [5]; BRITT, H.C., BOLSTERLI, M., NIX, J.R., NORTON, J.L., Phys. Rev. C7 (1973) 801; WEIGMANN, H., THEOBALD, J.P., Nucl. Phys. **A187** (1972) 305.
- [14] LEDERER, C.M., HOLLANDER, J.M., PERLMAN, I., Table of Isotopes, Wiley, New York (1978); SPECHT, H.J., WEBER, J., KONECNY, E., HEUNEMANN, D., Phys. Lett. **41B** (1972) 43.
- [15] PASHKEVICH, V.V., Nucl. Phys. **A133** (1969) 400; LARSON, S.E., RAGNARSSON, I., NILSSON, S.G., Phys. Lett. **38B** (1972) 269; GOTZ, U., PAULI, H.C., JUNKER, K., Phys. Lett. **39B** (1972) 436.
- [16] PAULI, H.C., LEDERBERGER, I., BRACK, M., Phys. Lett. **34B** (1971) 264.
- [17] BOLSTERLI, M., FISSET, E.O., NIX, J.R., NORTON, J.L., Phys. Rev. C5 (1972) 1050;  
JUNKER, K., HADERMANN, J., Z. Phys. **A282** (1977) 391.

## DISCUSSION

P. SCHUK: How large are your uncertainties in the barrier heights deriving from truncation of the basis?

J.F. BERGER: Tests have indicated that they could not exceed 1 or 2 MeV. The error seems to be maximum in the region of the scission point.

P. SCHUK: Thank you. Have I also understood correctly that you consider the unduly high barriers to result from the fact that you did not project to a satisfactory particle number, or to satisfactory angular momentum?

J.F. BERGER: As far as the angular momentum is concerned, we believe the correction that we made is satisfactory. But I agree that we should project to better particle numbers.

M. BRACK: Do you think the inclusion of a tensor force or a deformation-dependent spin orbit force might improve the situation?

J.F. BERGER: The main point for the moment is to extract all spurious contributions. When we have done that, we may have to improve the two-body interaction in order to obtain agreement with the experimental barriers.



# MACROSCOPIC-MICROSCOPIC CALCULATION OF FISSION BARRIERS AND MASSES FOR HEAVY ELEMENTS WITH A YUKAWA-PLUS-EXPONENTIAL MODEL FOR THE MACROSCOPIC ENERGY

P. MÖLLER

Department of Mathematical Physics,  
Lund University,  
Lund,  
Sweden

## Abstract

### MACROSCOPIC-MICROSCOPIC CALCULATION OF FISSION BARRIERS AND MASSES FOR HEAVY ELEMENTS WITH A YUKAWA-PLUS-EXPONENTIAL MODEL FOR THE MACROSCOPIC ENERGY.

For elements with  $Z$  in the range 90 to 104 fission barriers, nuclear ground-state masses and, for a few nuclei, ground-state  $Q_2$  and  $Q_4$  moments are calculated by the use of the macroscopic-microscopic method. The macroscopic energy includes a recently proposed generalized surface-energy term, calculated in terms of a double volume integral of a Yukawa-plus-exponential folding function. The microscopic shell and pairing corrections are calculated by use of Strutinsky's method from the single-particle levels of a modified-oscillator single-particle potential. The calculated energy quantities agree with experimental quantities to within the expected accuracy of about 1 MeV of the macroscopic-microscopic method. In the discussion of the results it is pointed out that some of the deviations between calculated and experimental quantities may be removed by an improved adjustment of the constants of the Yukawa-plus-exponential term, by an improved shape parametrization and by an improved treatment of the microscopic term.

## 1. INTRODUCTION

At the last IAEA meeting six years ago in Rochester, we were able to explain many experimental properties of fissioning nuclei in terms of potential-energy surfaces calculated as functions of various deformation parameters. In most calculations the potential energy was calculated as the sum of a macroscopic term and a microscopic term. The macroscopic term is usually a few MeV in magnitude and fluctuates rapidly as a function of deformation and particle number. For a highly bound nucleus

the magnitude of the microscopic correction may be as large as 10 MeV or even slightly larger. The remainder of the total potential energy, which for instance varies by about 200 MeV during fission of a heavy nucleus, is described by the macroscopic term.

The microscopic term arises because nuclei consist of a relatively small number of individual particles. It is calculated by use of the Strutinsky prescription [1] on single-particle energies generated by single-particle potentials such as a modified oscillator potential or a Woods-Saxon type of potential [2-4]. The macroscopic term is usually calculated by use of the liquid-drop model [5] or the droplet model [6, 7]. At the last IAEA meeting it was shown that macroscopic-microscopic calculations employing the droplet model were particularly successful in reproducing experimentally determined fission barrier heights [8].

It has been pointed out [9-11], however, that the liquid-drop and droplet model expressions for the nuclear macroscopic energy, which are asymptotic expansions in powers of  $A^{-1/3}$ , become invalid for shapes with curvature radii comparable to the surface thickness. The models also fail to describe the interaction energy of two nuclear surfaces at distances smaller than the surface thickness.

To avoid the above difficulties Krappe and Nix, at the last IAEA-meeting, suggested a modification of the liquid-drop model. The modification consists in doubly folding a short-range single-Yukawa function over a sharp-surface density distribution [8]. This model has been used in the study of heavy-ion reactions [12-14] and to calculate fission barriers [15] and nuclear ground state masses [15, 16].

However, the interaction energy per unit area  $e(\xi)$  between two parallel semi-infinite slabs of nuclear matter, where  $\xi$  is the separation between their equivalent sharp surfaces, should have a minimum at  $\xi=0$ . The model above, containing a single-Yukawa function, does not fulfill this condition. A generalization to correct for this deficiency is to use a folding function that contains two Yukawa functions [17, 18]. Such a generalization has been investigated by Krappe, Nix and Sierk [10, 11]. They have also determined a preliminary set of model parameters. We use this model for the macroscopic term in the macroscopic-microscopic model and calculate ground state masses and fission barriers for elements in the actinide region.

## 2. DETAILS OF THE CALCULATIONS

By varying the ranges of the two Yukawa functions and imposing the saturation condition, while keeping fixed the effective surface energy, Krappe, Nix and Sierk [10] found that the two ranges should be approximatively equal. In the limit that the two ranges are equal the two strengths of the Yukawa functions go to infinity while their difference remains finite. This leads to the following expression for the generalized nuclear surface energy

$$E_n = - \frac{c_s}{8\pi^2 a^6} \left( \frac{a}{r_o} \right)^2 \iint \left( \frac{\rho}{a} - 2 \right) \frac{\exp(-\rho/a)}{\rho/a} d^3 r d^3 r'$$

where  $\rho = |\vec{r} - \vec{r}'|$  and  $c_s = a_s \{1 - \kappa_s |(N-Z)/A|\}$ . The determination of the four constants of the above expression is discussed in refs. [10,11]. One determined from this preliminary study, that

$$\begin{aligned} r_o &= 1.18 \text{ fm}, \\ a &= 0.65 \text{ fm}, \\ a_s &= 21.7 \text{ MeV} \quad \text{and} \\ \kappa_s &= 3.00. \end{aligned}$$

The complete expression for the macroscopic contribution to the mass excess of a nucleus is [11]

$$\begin{aligned} M_{\text{macro}}(\text{def}) &= M_N N + M_H Z - a_v (1 - \kappa_v I^2) A + E_n(\text{def}) \\ &+ \frac{3}{5} \frac{e^2}{r_o} \frac{Z^2}{A^{1/3}} \cdot g(\text{def}) - \frac{3}{5} \frac{e^2}{r_o} \left[ \frac{5}{2} \left( \frac{b}{r_o} \right)^2 \frac{Z^2}{A} - \frac{5}{4} \left( \frac{3}{2\pi} \right)^{2/3} \frac{Z^{4/3}}{A^{1/3}} \right] \\ &+ w(|I| + d) - a_{\text{el}} Z^{2.39} \\ &+ \left\{ \begin{array}{l} \Delta - \frac{1}{2} \delta, \text{ N and Z odd} \\ \frac{1}{2} \delta, \text{ N or Z odd} \\ -(\Delta - \frac{1}{2} \delta), \text{ N and Z even} \end{array} \right. \end{aligned}$$

The additional constants in this expression are discussed in ref. [11], which gives

$$\begin{aligned}
 M_n &= 8.071431 \text{ MeV}, \\
 M_H &= 7.289034 \text{ MeV}, \\
 a_v &= 16.012 \text{ MeV}, \\
 \kappa_v &= 2.04 \\
 e^2 &= 1.4399764 \text{ MeV fm}, \\
 b &= 0.99 \text{ fm}, \\
 W &= 30 \text{ MeV}, \\
 a_{el} &= 1.433 \times 10^{-5} \text{ MeV}, \\
 \Delta &= 12 \text{ MeV}/\sqrt{\text{A}}, \\
 \delta &= 20 \text{ MeV/A}, \\
 d &= \begin{cases} 1/\text{A}, & \text{N and Z odd and equal} \\ 0 & \text{otherwise.} \end{cases}
 \end{aligned}$$

In the above expression  $g(\text{def})$  is the ratio between the Coulomb energy for the deformed nucleus and the spherical nucleus. The Coulomb energy is calculated as the electrostatic energy for a homogeneously charged sharp-surface body. The expression for the macroscopic contribution to the mass excess includes surface-diffuseness and exchange corrections to the Coulomb energy and a Wigner term.

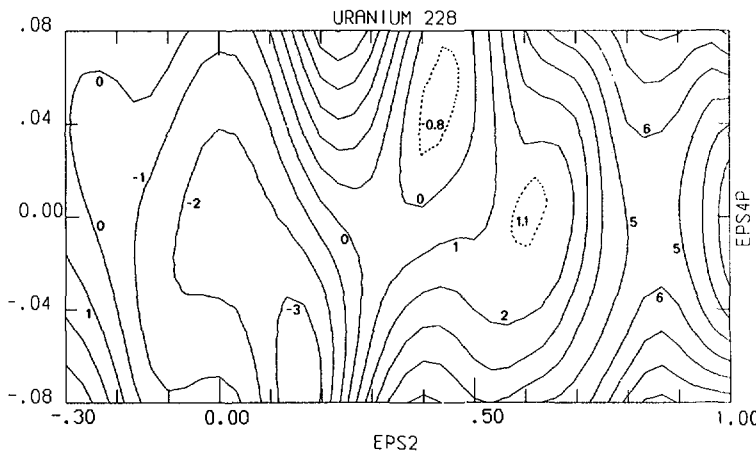


*FIG.1a. Potential energy surface for  $^{228}\text{U}$  as a function of the elongation co-ordinate  $\epsilon_2$  and the necking co-ordinate  $\epsilon'_4$ . The value  $\epsilon'_4 = 0$  gives approximatively the locus of liquid-drop-model saddle-point shapes. The energy is the sum of a Yukawa-plus-exponential macroscopic energy (relative to the sphere) and a modified-oscillator single-particle microscopic energy. This sum is sometimes called "single-particle correction", see Section 2. The presence of two "second" minima is indicated by dashed contours. The distance between solid contour lines is 1 MeV.*

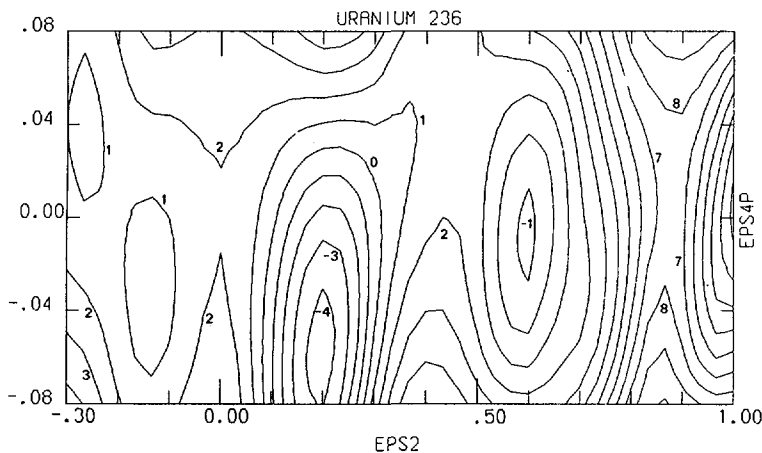


FIG.1b. Same as Fig. 1a but for  $^{236}\text{U}$ . Note change in location of second minimum.

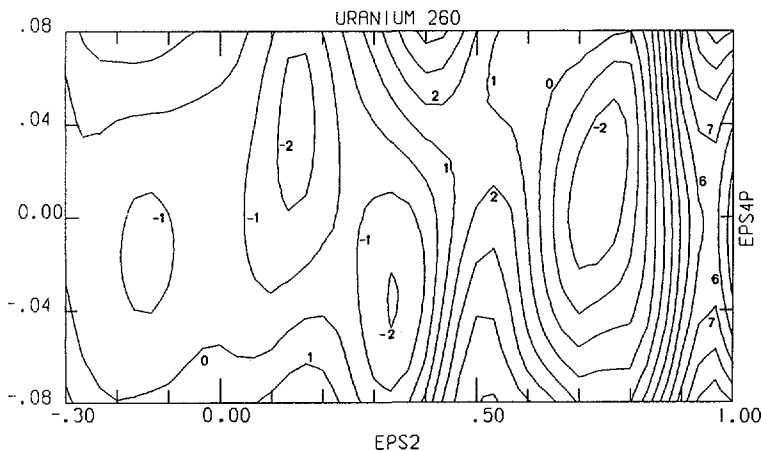


FIG.1c. Same as Fig. 1a but for  $^{260}\text{U}$ . This surface has three minima of approximatively equal depth. The deepest is at  $\epsilon_2 = 0.75$ . Also note the very low inner barriers. The outer barrier is reduced by 5.5 MeV if mass-asymmetric distortions are included.

We obtain the total mass excess by adding a microscopic correction due to single particle effects to the macroscopic mass excess. Thus

$$E_{\text{total}}(\text{def}) = E_{\text{macr}}(\text{def}) + E_{\text{micr}}(\text{def})$$

By the expression "single-particle correction" one means, for deformed shapes the sum of  $E_{\text{micr}}(\text{def})$  and the changes of the Coulomb and

TABLE I. GROUND-STATE DEFORMATION PARAMETERS FOR  $^{228}\text{U}$  AND  $^{236}\text{U}$ . EXPERIMENTAL VALUES ARE TAKEN FROM Ref. [23]

$^{228}\text{U}$						
Model	EPS2	EPS4	$Q_2^{\text{micr}}$ (b)	$Q_4^{\text{micr}}$ ( $b^2$ )	$Q_2^{\text{macr}}$ (b)	$Q_4^{\text{macr}}$ ( $b^2$ )
Mod. Osc. and Yukawa-plus-exp.	0.155	-0.076	7.77	2.92	7.62	2.52
Mod. Osc. and single-Yukawa	0.150	-0.079	7.61	2.95	7.41	2.55
Mod. Osc. and Droplet	0.153	-0.034	6.93	1.67	6.90	1.33
$^{236}\text{U}$						
Model	EPS2	EPS4	$Q_2^{\text{micr}}$ (b)	$Q_4^{\text{micr}}$ ( $b^2$ )	$Q_2^{\text{macr}}$ (b)	$Q_4^{\text{macr}}$ ( $b^2$ )
Mod. Osc. and Yukawa-plus-exp.	0.198	-0.056	9.40	2.98	9.78	2.60
Mod. Osc. and single-Yukawa	0.200	-0.062	9.59	3.20	10.01	2.84
Mod. Osc. and Droplet	0.197	-0.034	9.00	2.27	9.35	1.89

generalized surface energies from their spherical values. Thus,

$$E_{s.p.}^{(def)} = E_{\text{macr}}^{(def)} - E_{\text{macr}}^{(\text{sphere})} + E_{\text{micr}}^{(def)}$$

We now determine ground state masses and fission barrier heights by calculating total potential-energy surfaces as discussed in ref. [19] with the difference that we here for the macroscopic energy mostly use the Yukawa-plus-exponential model and that we only consider the case of a constant surface-independent pairing strength  $G = \text{const.}$

### 3. RESULTS OF THE CALCULATIONS

We calculate two sets of potential-energy surfaces.

The first set is calculated by considering the elongation coordinate  $\epsilon_2$  and the necking coordinate  $\epsilon_4$ . Positive values of  $\epsilon_4$  generate shapes with a small neck radius, negative values of  $\epsilon_4$  result in "diamond-like" shapes with a large neck radius [2]. In figs. 1a-1c we display a few representative potential-energy surfaces. The figures are contour plots of the energy as a function of  $\epsilon_2$  and  $\epsilon_4$  for the nuclei  $^{228}\text{U}$ ,  $^{236}\text{U}$  and  $^{260}\text{U}$ . For  $\epsilon_2 \leq 0.25$  we have the relation

$$\epsilon_4 = \epsilon'_4$$

and for  $\epsilon_2 \geq 0.25$  the relation

$$\epsilon_4 = \epsilon'_4 + \epsilon_2/5 - 0.05$$

This choice of coordinates for the grid is convenient, because for heavy nuclei liquid-drop model saddle-point shapes correspond approximatively to  $\epsilon'_4 = 0$ .

The contour plots of the three actinide nuclei display several minima and saddle points. For the two nuclei  $^{228}\text{U}$  and  $^{236}\text{U}$  we tabulate, in table 1, the values of  $\epsilon_2$ ,  $\epsilon_4$ ,  $Q_2^{\text{micr}}$ ,  $Q_4^{\text{micr}}$ ,  $Q_2^{\text{macr}}$  and  $Q_4^{\text{macr}}$  at the ground state obtained in three different calculations. The quantities  $Q_v^{\text{micr}}$  and  $Q_v^{\text{macr}}$  are the expectation values of  $2r^v P_v(\cos\theta)$  calculated from the proton single particle wave-functions (with inclusion of

pairing) and from a homogeneous charge distribution, respectively [20]. More extensive discussions of calculated ground state deformations and experimental data in the actinide region are found in refs. [21-23]. Here we will only point out a few characteristics of the finite-range models for the nuclear macroscopic energy.

We note that the Yukawa-plus-exponential and the single-Yukawa results for the ground state deformations are equal to within the accuracy in the determination of  $\epsilon_2$  ( $\pm 0.005$ ) and  $\epsilon_4$  ( $\pm 0.005$ ). The results from these two models are, on the other hand, significantly different from the calculation with the droplet model. This is due to the smaller stiffness of the finite-range models with respect to higher multipole distortions as compared to the droplet or liquid-drop model [9,11]. The experimental values of  $Q_2$  and  $Q_4$  for the ground state of  $^{236}\text{U}$  are [23]:

$$Q_2 = 10.80 \text{ b} \quad \text{and}$$

$$Q_4 = 3.07 \text{ b}^2.$$

Thus, as also noted previously [22], a finite-range model for the macroscopic energy may give better agreement between calculated and experimental ground state  $Q_4$  moments in the light actinide region. The reason that the calculated value of  $Q_2$  is somewhat lower (although the calculated value is larger with the finite-range models than in the calculation with the droplet model) than the experimental value may be, according to ref. [21], that the Coulomb field is not explicitly included in the modified oscillator single-particle potential.

In the limit  $a \rightarrow 0$  the finite-range models yield exactly the surface energy of the liquid drop model. One might therefore have expected the Yukawa-plus-exponential model with its range  $a = 0.65 \text{ fm}$  to yield ground state distortions somewhat intermediate between the single-Yukawa model with a range  $a = 1.4 \text{ fm}$  and the droplet model results. As we have seen this is not the case; the folding function and the range of the Yukawa-plus-exponential model combine to give results, for the nuclear ground state deformations, similar to those of the single-Yukawa model, with its different folding function and different range.

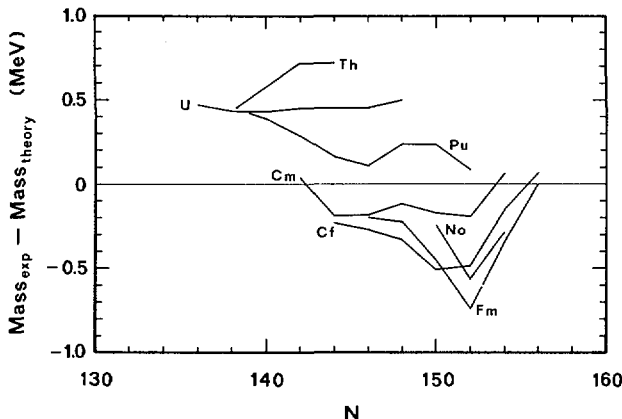


FIG.2. Difference between experimental and calculated ground-state masses.

We note from figures 1a-1c that the appearance of the nuclear potential energy surface varies considerably from nucleus to nucleus. Actually, it is only for actinide elements close to the line of  $\beta$ -stability that the potential energy surface corresponds to the conventional picture, with a nuclear ground state at around  $\epsilon_2 = 0.2$ , a second isomeric minimum and a first and a second barrier peak. From figs. 1a and 1b we see a shift in  $\epsilon_2$  of the second minimum from a smaller value of around 0.4 for  $^{228}\text{U}$ , which nucleus actually has two "secondary" minima, to a larger value of around 0.6 for  $^{236}\text{U}$ . This shift in deformation is associated with the shift in deformation of the nuclear ground state from a spherical shape to a deformed shape which in the calculations occurs around  $^{224}\text{U}$ .

For the very neutron rich nucleus  $^{260}\text{U}$  the potential energy surface looks quite different, with three pronounced minima of approximatively equal depth. The two inner barriers are very low and the outer barrier is lowered by 5.5 MeV by mass-asymmetric distortions. The consequence is a very short fission half-life for this nucleus. The potential energy surfaces for other neutron-rich actinide nuclei look very similar. The low fission barriers and short fission half-lives of these nuclei are of consequence for the synthesis of new elements in the r-process. More detailed studies of these neutron rich nuclei, with somewhat different macroscopic-microscopic models, are found in refs. [24,25], for example.

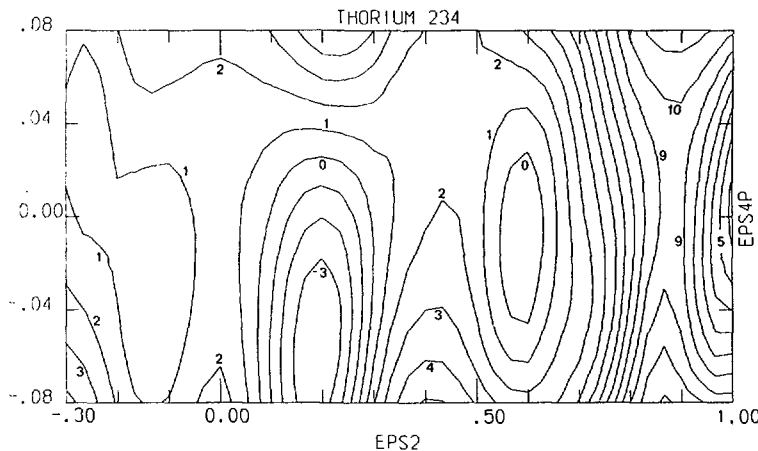


FIG. 3a. Same as Fig. 1a but for  $^{234}\text{Th}$ .

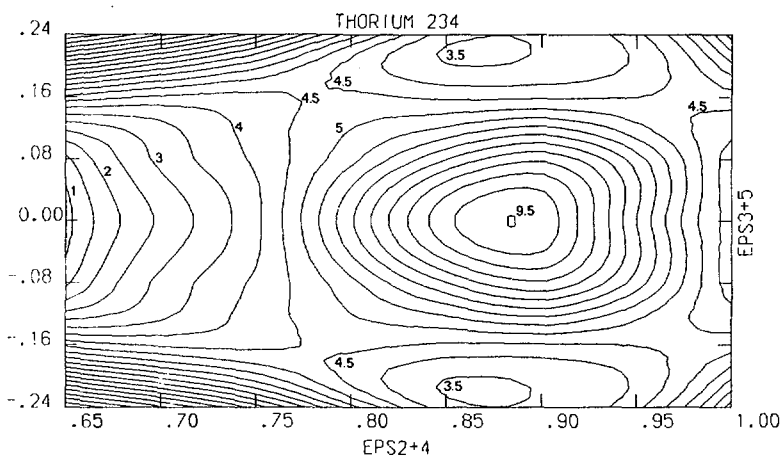


FIG. 3b. Potential energy surface for  $^{234}\text{Th}$  as a function of symmetric shapes ( $\epsilon_2$  and  $\epsilon_4$ ) and asymmetric shapes ( $\epsilon_3$  and  $\epsilon_5$ ). The line  $\text{EPS}3+5 = 0$  corresponds approximatively to the line  $\text{EPS}4\text{P} = 0$  in Fig. 3a. The precise definition of the shape co-ordinates is found in Ref. [19]. The distance between contour lines is here 0.5 MeV. As in Fig. 1a we have plotted the energy relative to the spherical Yukawa-plus-exponential model. Note that the symmetric saddle point at 9.5 MeV is lowered by 4 MeV by mass-asymmetric shape distortions. The symmetric saddle is actually split up into two asymmetric saddle points separated by a shallow "third" minimum.

Fig. 2 displays a comparison of calculated and experimental [26] nuclear ground state masses. A 0.5 MeV zero point energy was added to the calculated ground state potential energy in the mass calculation. The discrepancy is much smaller than could be expected in a comparison over a wider range of nuclei, for which one usually has a root-mean-square deviation in excess of 1 MeV [11]. The discrepancy at  $N = 152$  for nuclei in the vicinity of Fm would be decreased by the consideration of  $P_6$  distortions at the nuclear ground state [22].

Figs. 3a and 3b show calculated potential-energy surfaces for  $^{234}\text{Th}$ . In fig. 3a, which like figs. 1a-1c represents the first set of potential-energy surfaces, we have calculated the energy as a function of the symmetric shape coordinates discussed above. The second set of surfaces we have calculated is represented by fig. 3b. Here the energy in the region of the second saddle point is displayed as a function of symmetric shape coordinates (along the horizontal axis) and mass-asymmetric shape coordinates (along the vertical axis). The parametrisation is identical to the parametrisation used for the similar surfaces in ref. [19]. From fig. 3b we see that the introduction of mass-asymmetric shape degrees of freedom lowers the height of the second saddle considerably, a fact known earlier [27,19]. Actually, for this nucleus, the introduction of mass-asymmetric shape degrees of freedom splits the second symmetric saddle into two asymmetric saddles, separated by a shallow minimum. It was suggested at the last IAEA meeting [8] that some experimental data on light actinides indicated such a structure, namely two asymmetric saddle points, separated by a shallow "third minimum". Later, new experimental data gave some additional support to this interpretation [28,29]. It is of interest to note that with the Yukawa-plus-exponential model the third minimum is deeper than in calculations employing the droplet model. For example, we find for  $^{234}\text{Th}$  that with the Yukawa-plus-exponential model the third minimum is some 1.2 MeV deep relative the lower of the two asymmetric saddle points. With the droplet model the depth is only 0.6 MeV relative the lower of the asymmetric saddle points [30]. In these numbers no zero-point energies were included.

From the two sets of potential energy surfaces we determine the heights of saddle points and minima relative to the ground state. A 0.5 MeV zero-point energy has been added at the ground state and at the second minimum. The results are displayed and compared to experimental data [31] in figs. 4a-4c. We see that there is rough agreement between

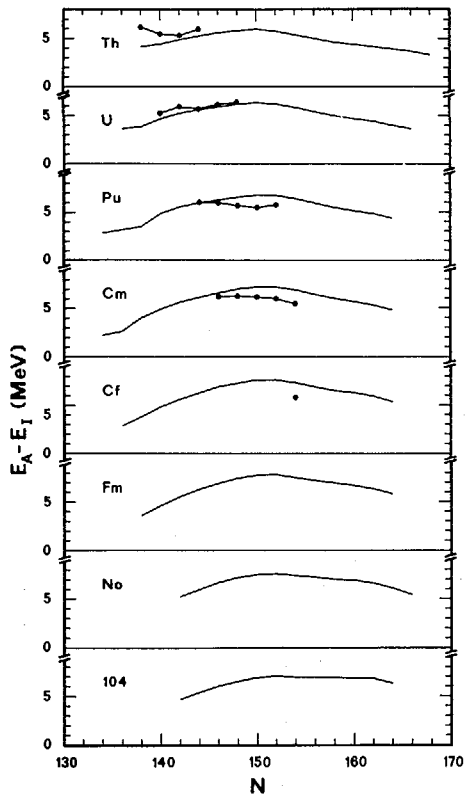


FIG. 4a. Calculated and experimental (dots) [31] first-barrier heights.

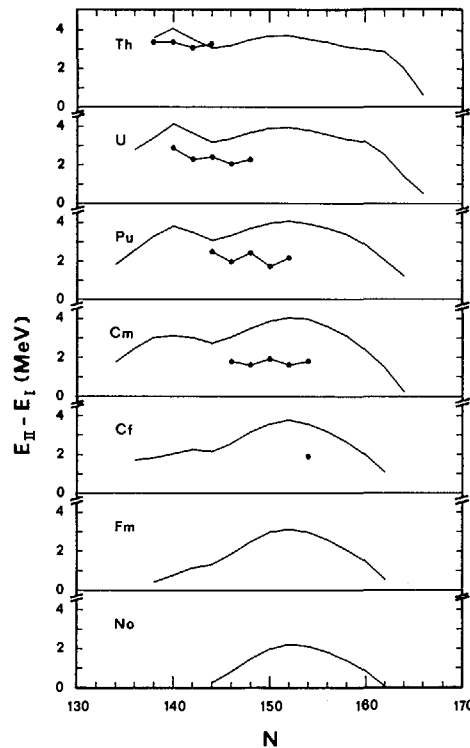


FIG. 4b. Calculated and experimental (dots) [31] second-minimum heights.

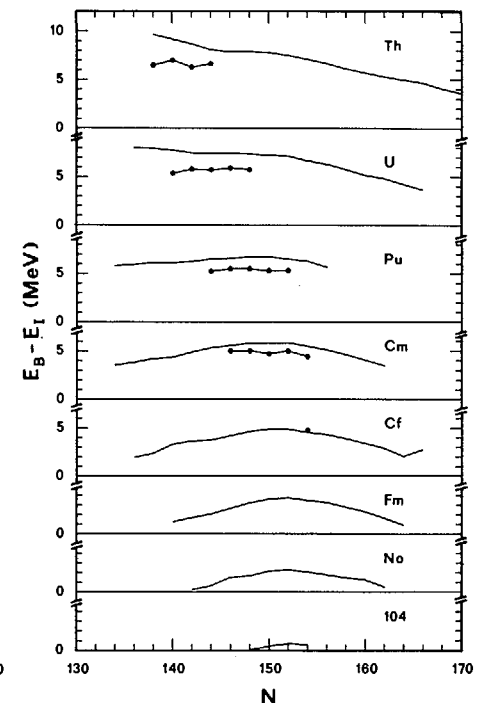


FIG. 4c. Calculated (with inclusion of mass asymmetry) and experimental (dots) [31] second-barrier heights.

calculated values and experimental data to within the estimated accuracy of 1 MeV [32] of the macroscopic-microscopic method.

The largest difference between the calculated values and experimental data occurs for the second minimum, for neutron numbers around 152. To improve the agreement here may require changes in the single-particle potential. Also, for the lighter actinides the calculated second barrier height is a little higher than the experimental data. The reason for the latter discrepancy is probably that, in the determination [11] of  $a_s$  and  $\kappa_s$ , the ground state shell correction for light actinide nuclei was assumed to be larger (that is, the ground state was assumed to be somewhat less deep) than is actually the result in a full minimization of the sum of the macroscopic Yukawa-plus-exponential term and the microscopic term. In the determination of  $a_s$  and  $\kappa_s$ , it was assumed that the ground state shape was that which is obtained in a calculation with a droplet model macroscopic term. This leads to a ground state that is higher than obtained with a Yukawa-plus-exponential term.

At the first peak we have not considered axially asymmetric  $\gamma$ -deformations. With a droplet model macroscopic term, the first peak is lowered by a maximum amount of 2.2 MeV at  $Z = 100$  and  $N = 152$  due to  $\gamma$ -distortions [33]. At  $N < 140$  the first peak is unaffected by  $\gamma$ -distortions. As the magnitude of the effect of  $\gamma$ -distortions on a Yukawa-plus-exponential term would be similar to the effect on a droplet model term, an inclusion of  $\gamma$ -distortions in the calculation of the barrier heights displayed in fig. 4a would still yield results in good agreement with the experimental data.

In figs. 5a and 5b we compare, for uranium isotopes, the results of macroscopic-microscopic calculations of the heights of the first and second barrier peaks and experimental barrier data. The calculations were done with four different models for the macroscopic energy, namely the Yukawa-plus-exponential model [11], the single-Yukawa model [9], the droplet model [7] and the liquid-drop model [5].

Figure 5a shows a comparison of first barrier heights. The results fall into two distinct groups, one group is the two finite-range model results, the other is the droplet and liquid-drop model results. The differences between the models arise mainly because of their different behaviour at the ground state. The smaller stiffness, with respect to higher multipole distortions, of the finite-range models, as compared to the liquid-drop model and the droplet model, will result in lower

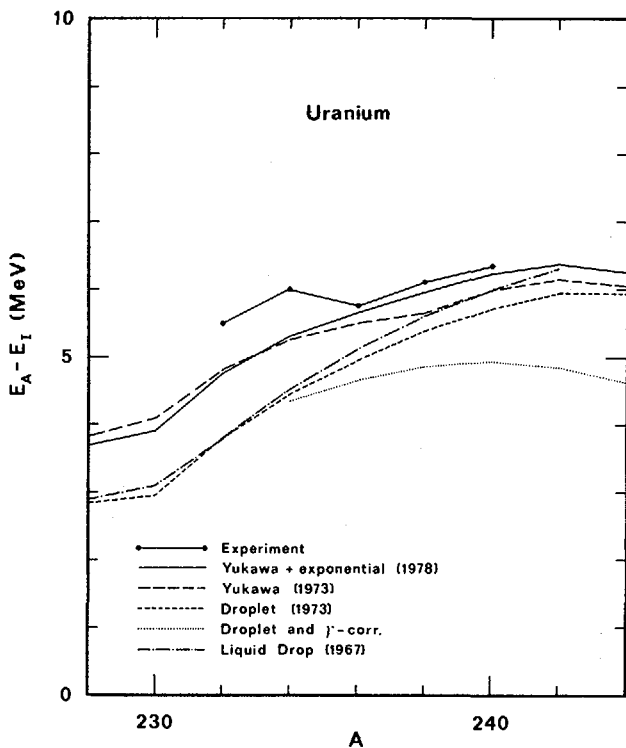


*FIG. 5a.* Comparison between calculated and experimental [31] first-barrier heights. The calculations were done without the inclusion of axially asymmetric  $\gamma$ -distortions. However, for one case, the droplet model, we give the result also with the reduction of the barrier height, due to  $\gamma$ -distortions, included. This result is given by the dotted line. The decrease in barrier height due to  $\gamma$ -distortions is taken from Ref. [33].

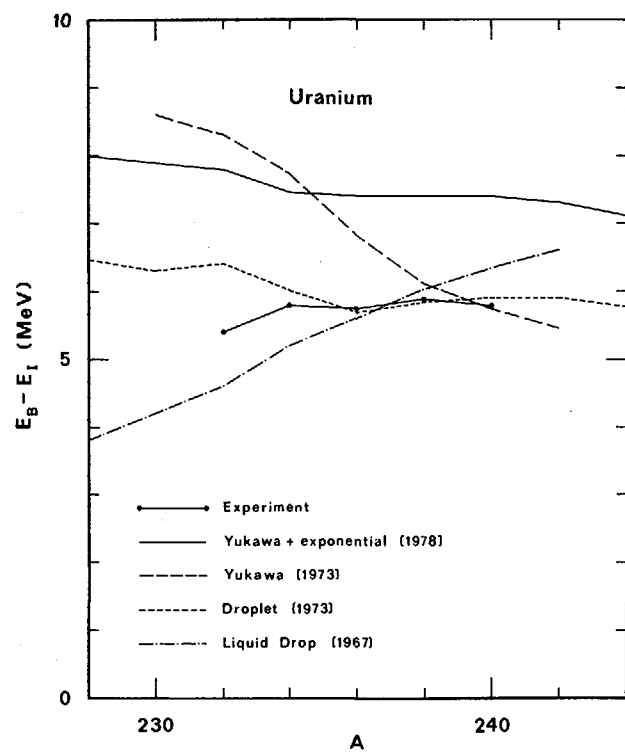


*FIG. 5b.* Comparison between calculated and experimental [31] second-barrier heights. The calculations were done with the inclusion of mass-asymmetric distortions.

ground state energies and, consequently, higher first barriers in finite-range model calculations, for elements where the microscopic correction is unstable with respect to higher multipole distortions. The lighter uranium isotopes have large negative values of  $\epsilon_4$  at the ground state. Therefore the difference between the models is large for the lighter uranium isotopes. For the heavier uranium isotopes where the ground state value of  $\epsilon_4$  is close to zero there are only minor differences between the models.

In the calculation of the barrier heights displayed in fig. 5a, the macroscopic contribution is given by the difference of the macroscopic energy at the first saddle point and at the ground state. Since the shape change is rather small between the ground state and the first saddle point and, consequently, the change in macroscopic energy is rather small, the differences between the macroscopic models do not manifest themselves very clearly in fig. 5a, except as the ground state effect discussed previously. In the comparison of second barrier heights in fig. 5b the differences stand out very clearly, however. We see that the calculation with the droplet model agrees very well with the experimental data. The liquid-drop model results increase too quickly when the neutron number increases, the single-Yukawa results decrease too quickly. This behaviour may be understood in terms of the magnitude of the surface asymmetry constant. We have for the liquid drop model [5]  $\kappa_s = 1.7826$  and for the single-Yukawa model [9]  $\kappa_s = 4.0$ . The Yukawa-plus-exponential result is, as is also the case for the experimental results, fairly constant as a function of neutron number. For this model the value of  $\kappa_s$  is 3.0 [11]. The droplet model effective  $\kappa_s$  is also close to 3.0 [34]. The fact that the Yukawa-plus-exponential results were a little too high was discussed earlier.

Comparisons as those in figs. 5a and 5b, but for other actinide nuclei, would lead to very similar results and conclusions.

#### 4. SUMMARY

We have studied the new Yukawa-plus-exponential model in the actinide region. An earlier study and presentation [11] of this unified nuclear potential has shown that it reproduces experimental data for heavy-ion elastic scattering, fusion, fission and ground state masses. Here we performed a more elaborate calculation of potential energy

surfaces in the actinide region, than in the previous study. We calculated two sets of potential energy surfaces. One set was calculated in terms of an elongation and a necking shape coordinate, the other in terms of symmetric and mass-asymmetric shape coordinates. From these surfaces we determined ground state masses and deformations and fission barriers.

We found very good agreement between calculated and experimental ground state masses in the actinide region. The agreement between calculated and experimental  $Q_2$  and  $Q_4$  values for light actinides was probably improved somewhat by the use of the Yukawa-plus-exponential model relative to a calculation with a droplet model macroscopic energy. The deviation between calculated and experimental fission barriers in the actinide region was less than about 1 MeV, the expected accuracy of the macroscopic-microscopic method. A calculation with a droplet model macroscopic energy agreed still better with experimental fission barrier data. We discussed above, however, that some of the deviations between experimental fission barrier data and the results calculated with the Yukawa-plus-exponential macroscopic energy should improve if the effect of the Yukawa-plus-exponential model on the ground state single particle correction were more accurately included in the determination of the model constants. Other deviations might improve by use of an improved single-particle potential.

The author has profited from discussions with G. Leander, S.G. Nilsson, J.R. Nix and A.J. Sierk. The author is also grateful to A.J. Sierk for calculating the Yukawa-plus-exponential energy with the Los Alamos computer code for a few shapes that are also described with the Lund code.

#### REFERENCES

- [1] STRUTINSKY, V.M., Nucl. Phys. A95 (1967) 420; A122 (1968) 1.
- [2] NILSSON, S.G., TSANG, C.F., SOBICZEWSKI, A., SZYMAŃSKI, Z., WYCECH, S., GUSTAFSSON, C., LAMM, I.L., MÖLLER, P., NILSSON, B., Nucl. Phys. A131 (1969) 1.
- [3] BRACK, M., DAMGAARD, J., JENSEN, A.S., PAULI, H.C., STRUTINSKY, V.M., WONG, C.Y., Rev. Mod. Phys. 44 (1972) 320.
- [4] BOLSTERLI, M., FISSET, E.O., NIX, J.R., NORTON, J.L., Phys. Rev. C5 (1972) 1050.

- [5] MYERS, W.D., SWIATECKI, W.J., *Ark. Fys.* 36 (1967) 343.
- [6] MYERS, W.D., SWIATECKI, W.J., *Ann. Phys. (New York)* 55 (1969) 395.
- [7] MYERS, W.D., SWIATECKI, W.J., *Berkeley Preprint LBL-1957* (1973).
- [8] MÖLLER, P., NIX, J.R., *Proc. Third IAEA Symp. on Physics and Chemistry of Fission, Rochester 1973*, (IAEA, Vienna, 1974) Vol. 1, p. 103.
- [9] KRAPPE, H.J., NIX, J.R., *Proc. Third IAEA Symp. on Physics and Chemistry of Fission, Rochester 1973*, (IAEA, Vienna, 1974) Vol. 1, p. 159.
- [10] KRAPPE, H.J., NIX, J.R., SIERK, A.J., *Phys. Rev. Lett.* 42 (1978) 215.
- [11] KRAPPE, H.J., NIX, J.R., SIERK, A.J., Los Alamos preprint LA-UR-79-885, subm. to *Phys. Rev. C*.
- [12] NIX, J.R., SIERK, A.J., *Phys. Scr.* 10A (1974) 94.
- [13] MÖLLER, P., NIX, J.R., *Nucl. Phys.* A272 (1976) 502.
- [14] MÖLLER, P., NIX, J.R., *Nucl. Phys.* A281 (1977) 354.
- [15] MÖLLER, P., *Proc. International Workshop om Gross Properties of Nuclei and Nuclear Excitations III, Hirschegg, Kleinwalsertal, Austria, Jan. 13-18, 1975, AED-Conf-75-009-000*, p. 207.
- [16] ANDERSSON, G., Lund Universtiy Department of Mathematical Physics report (1975).
- [17] GREINER, W., in *Proceedings of the International Conference on Nuclear Reactions Induced by Heavy Ions, Heidelberg, Germany, 1969* (North-Holland, Amsterdam, 1970), p. 748.
- [18] SATCHLER, G.R., LOVE, W.G., *Phys. Lett.* 65B (1976) 415.
- [19] MÖLLER, P., *Nucl. Phys.* A192 (1972) 529.
- [20] EKSTRÖM, C., RUBINSZTEIN, H., MÖLLER, P., *Phys. Scripta* 14 (1976) 199.
- [21] BRACK, M., LEDERGERBER, T., PAULI, H.C., *Nucl. Phys.* A234 (1974) 185.
- [22] MÖLLER, P., NILSSON, S.G., NIX, J.R., *Nucl. Phys.* A229 (1974) 292.
- [23] BEMIS, C.E. Jr., McGOWAN, F.K., FORD, J.L.C. Jr., MILNER, W.T., STELSON, P.H., ROBINSON, R.L., *Phys. Rev. C8* (1973) 1466.
- [24] HOWARD, W.M., NIX, J.R., *Nature* 247 (1974) 17.
- [25] BENGTSSON, R., BOLEU, R., LARSSON, S.E., *Phys. Scr.* 10A (1974) 142.
- [26] WAPSTRA, A.H., BOS, K., *At. Data Nucl. Data Tables* 19 (1977) 175.
- [27] MÖLLER, P., NILSSON, S.G., *Phys. Lett.* 31B (1970) 283.

- [28] BLONS, J., MAZUR, C., PAYA, D., Phys. Rev. Lett. 35 (1975) 1749.
- [29] CARUANA, J., BOLDEMAN, J.W., WALSH, R.L., Nucl. Phys. A285 (1977) 205.
- [30] ÅBERG, S., LARSSON, S.E., MÖLLER, P., NILSSON, S.G., RAGNARSSON, I., Paper IAEA-SM/241-C4 these proceedings.
- [31] BRITT, H.C., WILHELMY, J.B., Priv. comm. (1978).
- [32] BRACK, M., QUENTIN, P., Proc. Third IAEA Symp. on Physics and Chemistry of Fission, Rochester 1973, (IAEA, Vienna, 1974) Vol. 1, p. 231.
- [33] RANDRUP, J., LARSSON, S.E., MÖLLER, P., NILSSON, S.G., POMORSKI, K., SOBICZEWSKI, A., Phys. Rev. C5 (1976) 229.
- [34] HOWARD, W.M., NIX, J.R., Proc. Third IAEA Symp. on Physics and Chemistry of Fission, Rochester 1973, (IAEA, Vienna, 1974) vol. 1, p. 145.

## DISCUSSION

S.S. KAPOOR: In your calculations do you ensure that the plateau condition is satisfied individually for each shape for which the shell correction is made? I ask this because in some of the work published by our group we drew attention to the difficulty created by not obtaining a stationary value for the correction for the mass-symmetric outer barrier shape.

P. MÖLLER: A long time ago I checked the plateau condition in the modified oscillator model for quite a few shapes and particle numbers. As far as I recollect, the second, symmetric saddle point was also included in the study. The plateau condition was always satisfied for this potential, with a correction polynomial of the order of 6 and a smearing range of  $1.2 \hbar\omega$ .

M. BRACK: I must agree with Dr. Kapoor that it is somewhat risky to go too high up with the order of the correction polynomials. Confidence in the results stems mainly from confirmation using the extended Thomas-Fermi model.

But I want to ask you the following question. One of the essential components of the droplet model is the inclusion of a curvature term proportional to  $A^{\frac{1}{3}}$  in the mass fits. For the sake of consistency this term should also be included in the deformation energy. Did you do this and, if so, how was it done?

P. MÖLLER: The droplet model contains higher-order terms for  $A^{-\frac{1}{3}}$  and  $(N-Z)^2/A$  than the liquid-drop model. However, the coefficient of the  $A^{\frac{1}{3}}$  curvature term, which was determined by Myers and Swiatecki (see Ref. [7]) from a fit to experimental data, was found to be approximately zero. This expansion will break down for shapes with small necks and two nearly contiguous nuclei. To overcome these limitations, it has been suggested (Ref. [11]) on more or less phenomenological

grounds that there should be use of the Yukawa-plus-exponential model for the smooth macroscopic energy. This is discussed in the second section of my paper. The integral may be evaluated exactly for a sphere. An expansion for small distortions around a sphere is given in Ref. [11]. Since the Yukawa-plus-exponential model is not a power series expansion of  $A^{-\frac{1}{3}}$  and  $(N-Z)^2/A$ , the behaviour of the above expressions in terms of  $A^{\frac{1}{3}}$  is complicated.

H.-G. CLERC: I notice that you consider the fission barrier for neutron-deficient isotopes of elements such as thorium to increase with neutron deficiency, while the experimental fission barriers tend to decrease. How do you explain this barrier behaviour?

P. MÖLLER: From Fig. 5b we see that the behaviour of the calculated second barrier heights depends appreciably on the macroscopic model employed. The microscopic corrections will cause major deviations from a pure macroscopic model in the calculated barrier heights. The differences between the calculated and experimental barriers in Fig. 4c indicate that a somewhat better set of parameters for the Yukawa-plus-exponential model might be found. For  $N \leq 142$  it is possible to lower the second thorium and uranium barrier to some extent by simultaneously varying the  $\epsilon_2, \epsilon_3, \epsilon_4, \epsilon_5$  and  $\epsilon_6$  shape co-ordinates.

R. SCHULTHEIS: The third minima you have shown seem rather shallow. Could you comment on your confidence level for the existence of a third minimum in view of the large inaccuracies involved in a calculation of this kind, as discussed by Professor Brack in his paper. (See SM-241/C1 in these Proceedings).

P. MÖLLER: I cannot say for certain that a third minimum of specific depth exists for a particular nucleus since the calculations are not sufficiently accurate. But since third minima seem to occur in calculations for thorium and uranium nuclei with  $N \approx 140$  both for calculations with a modified oscillator potential and those with a folded Yukawa single-particle potential (employing a different shape parametrization than in the modified oscillator potential calculations) it could be said that calculations indicate the possibility of third minima existing in the potential energy surface for nuclei in this region.



# SHELL STRUCTURE AT HIGH SPINS

S. ÅBERG, S.E. LARSSON, P. MÖLLER, S.G. NILSSON

Department of Mathematical Physics,  
Lund Institute of Technology,  
Lund, Sweden

G. LEANDER\*

Nordita, Copenhagen, Denmark

I. RAGNARSSON\*

CERN, Geneva, Switzerland

## Abstract

### SHELL STRUCTURE AT HIGH SPINS.

Theoretical predictions for the evolution of nuclear deformation, under the influence of rotations up to the critical angular momentum for fission, are discussed. The emphasis lies on recent advances in an overall understanding of the role of shell structure. In heavy nuclei at the large deformations relevant for fission, the intrinsic shell structure that in many ways significantly modifies the liquid-drop behaviour is predicted to be changed rather little by rotational frequencies up to the limit set by instability toward fission. It is in general necessary to consider deformations with low symmetry, and in this context a section is devoted to the analysis of recent  $^{238}\text{U}$  ( $\gamma$ , f) data. As regards those manifestations of high-spin shell structure that are presently being studied experimentally, an account is given of the current status of theoretical understanding. A few more detailed predictions are presented. For the superheavy compound nuclei that might be formed in heavy-ion reactions, quantitative estimates are given concerning the yrast decay modes.

### 1. INTRODUCTION

In their lowest energy states even-even nuclei may have a deformed shape. This is then said to be an effect due to shell structure. With increasing angular momentum the energetically most favourable shape may be seen as the result of a competition between the macroscopic terms in the nuclear energy and the microscopic ones. The former consist of the surface and Coulomb terms, to which a rigid-body rotational energy is

---

\* On leave of absence from the Department of Mathematical Physics, Lund, Sweden.

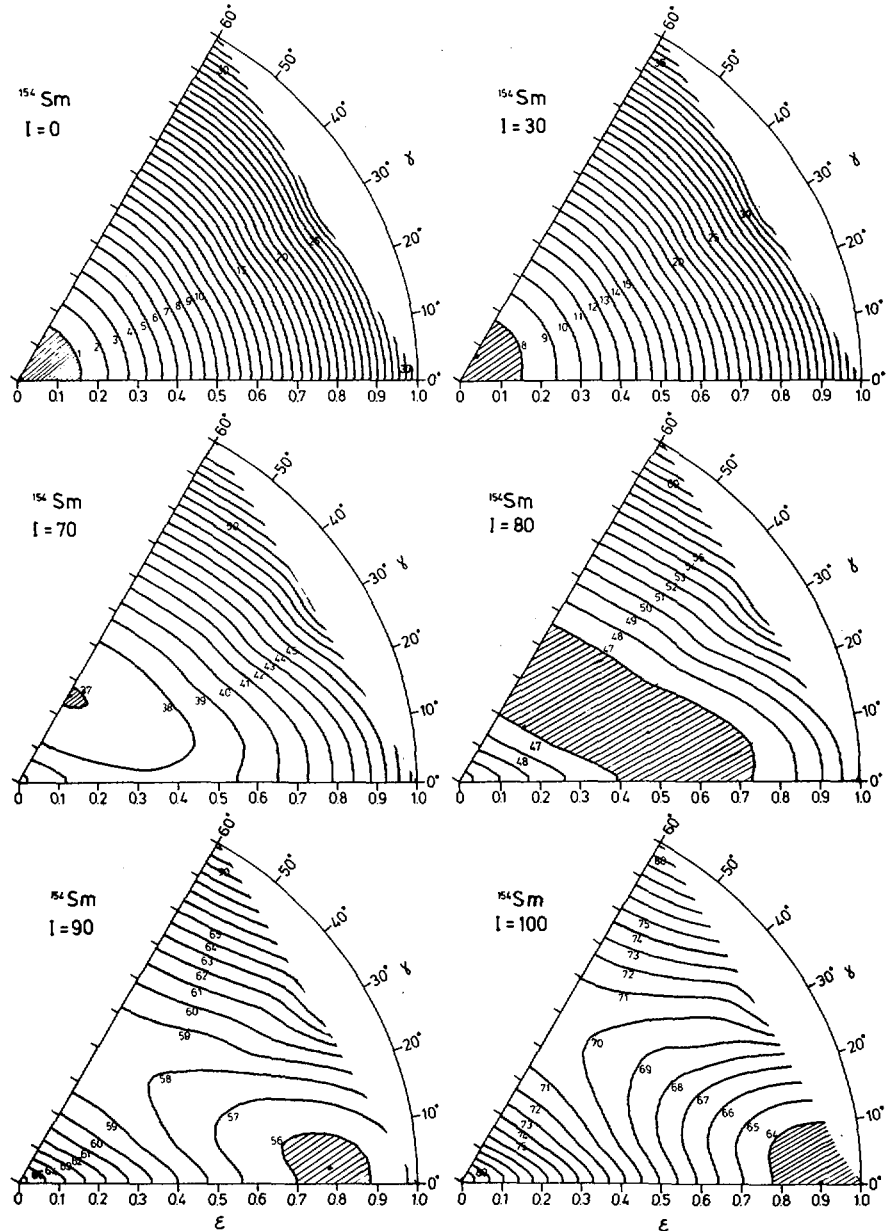


**FIG.1.** Energy of rotating liquid drop at different angular momenta  $I$  in terms of  $\epsilon$  (elongation) and  $\gamma$  (axial asymmetry), valid for the nucleus  $^{154}\text{Sm}$ . At each grid point a minimization with respect to  $\epsilon_4$  is applied. The axis  $\gamma = 60^\circ$  corresponds to rotation around the oblate symmetry axis while  $\gamma = 0^\circ$  corresponds to prolate shapes with rotation around an axis perpendicular to the symmetry axis. Note the drastic change from moderate oblate deformation at  $I = 70$  to large triaxial deformation at  $I = 80$ . The spectral manifestation of this is a 'superbackbend'. For still larger spin-values the fission barrier has almost completely vanished. However, the fission barrier of  $^{154}\text{Sm}$  is not very accurately described within the  $(\epsilon, \epsilon_4, \gamma)$  parametrization (from Ref. [5]).

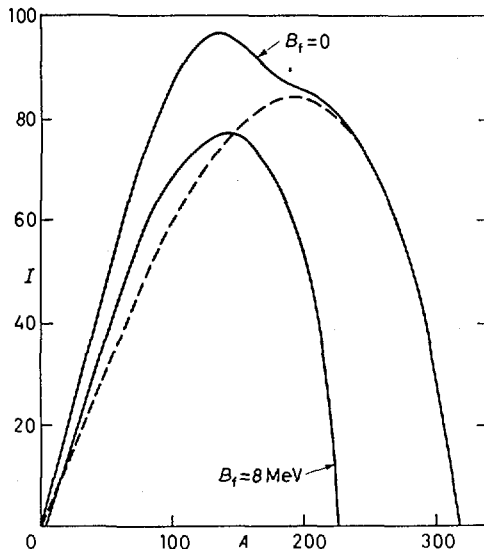


*FIG.2. Stability limits in the rotating liquid-drop model. The figure shows, for nuclei along the  $\beta$ -stability line, the angular momentum  $I$  for which the fission barrier vanishes ( $B_f = 0$ ), and also the angular momentum for which  $B_f$  assumes the value 8 MeV. The latter value is chosen equal to the average neutron separation energy. The dashed line marks the angular momenta where the rotating liquid drop changes shape from oblate to triaxial (compare Fig. 1; from Ref. [1]).*

added. These terms favour an increasingly oblate shape (up to a critical spin, see below). The shell energy terms (among which also pairing is usually included) may favour different shapes. This is due both to the fact that the nuclear orbitals change with rotational frequency and to the fact that a different set of orbitals are filled under the additional requirement of a given angular momentum.

Considering separately the macroscopic part, made up of the macroscopic surface, Coulomb and rotational energies, one reaches the conclusions obtained in 1972 by Cohen, Plasil and Swiatecki [1] in their now classical paper. Both the ground state and barrier energies are affected by rotation. Generally the barrier is reduced by rotation and vanishes entirely for a certain critical angular momentum. The main reason is that the inertia is larger for the deformed barrier shape than for the usually near-spherical ground state shape and the rotational energy varies as  $\sim \frac{1}{J} I^2$ . Thus, the rotational energy is larger in the

case of a near-spherical shape. The nucleus in part adjusts to this by acquiring first an oblate and for higher spins a triaxial or prolate deformation (fig. 1). The resulting barrier as a function of  $I$  and  $A$  is given in fig. 2.

The conclusions are somewhat - but only somewhat - modified by the inclusion of shell structure as anticipated by Bohr and Mottelson [2]. The trend is generally in the direction of slightly higher barriers. In particular the barriers are very much extended towards larger mass and spin. It is tempting to add that in general the trend is also to make the barriers somewhat "thinner" although obviously the latter concept does not have a well-defined meaning without a detailed discussion of the metric.

Furthermore, the change in the deformation of the yrast state with increasing angular momentum is often more sudden in a system with shell structure. For example, angular momentum can be obtained from the particles in the near-spherical valence shell, or alternatively by a strong coupling between the rotation and higher-lying shells leading to a large deformation. The transition from the former to the latter mode of rotation at some critical angular momentum may be quite abrupt.

## 2. SHELL STRUCTURE AT HIGH SPIN. GENERAL CONSIDERATIONS.

The new term relative to the Cohen, Plasil and Swiatecki work, introduced [3, 4] by the Warsaw-Lund investigation and that of the Moscow, Copenhagen and Jülich groups, is the shell structure term. The first problem to be solved is thus the calculation of single-particle orbitals in a potential characterized by  $\epsilon$ ,  $\epsilon_q$  and  $\gamma$  (or some other parametrization), subject to the auxiliary condition of given angular momentum:

$$h^\omega = h^0 - \hbar\omega j_x \quad (1)$$

where  $\omega$ , a Lagrangian multiplier, can be interpreted as the rotational frequency. Furthermore,  $h^0$  is the static single-particle Hamiltonian and  $j_x$  is the  $x$ -component of the angular momentum operator. The single-particle wave-functions  $\chi_i^\omega$  are now obtained from the solution of

$$h^\omega \chi_i^\omega = e_i^\omega \chi_i^\omega \quad (2)$$

where the eigenvalues  $e_i^\omega$  are the single-particle energies in the rotating system. The energies in the laboratory system,  $e_i$ , are obtained as expectation values,  $e_i = \langle \chi_i^\omega | h^0 | \chi_i^\omega \rangle = e_i^\omega + \hbar\omega m_i$ , where  $m_i$  is the expectation value of  $j_x$ . The single-particle sum is given by  $E_{sp} = \sum e_i$  and the total spin by  $I = \sum m_i$ . The corresponding smeared quantities are then calculated from a generalised Strutinsky procedure [3, 5] and subsequently the shell energy is obtained as

$$E_{shell}(I) = E_{sp}(I) - \langle E_{sp}(I) \rangle \quad (3)$$

In this equation, the discrete and smeared sums should be evaluated for the same value of the spin  $I$ , since this is the physically relevant variable, and the  $\omega$ -values are therefore generally different. In addition, the proton and neutron degrees of freedom are coupled through the fact that the same auxiliary  $\omega$  is used for neutrons and protons. These complications have as an effect that there is no simple explicit relation between the single-particle level densities and the shell energies.

On the other hand, one may employ an intermediate concept, the quasi-shell-energy, as a measure of the level density around the Fermi surface (cf. ref. [6])

$$E_{quasi-shell}(\omega) = \sum e_i^\omega(\omega) - \langle \sum e_i^\omega(\omega) \rangle \quad (4)$$

This quantity is defined separately for protons and neutrons and the discrete and smeared quantities are evaluated for the same  $\omega$ -value. It can then be shown that  $E_{quasi-shell}(\omega)$  is numerically very similar to  $E_{shell}(I)$  of eq. (3) [7]. This is especially true for heavy nuclei, since the difference goes as  $A^{-1}$ . In this subsection, where we study more general trends, we will thus use the expression  $E_{quasi-shell}(\omega)$  for the shell energy, whereas in later sections, with explicit calculations for specific nuclei, we will use the more accurate expression  $E_{shell}(I)$ .

In the case of a non-rotating single-particle potential, it is well-known that the orbitals are two-fold degenerate due to the time-reversal symmetry. When the rotational degree of freedom is added, this degeneracy is removed and a priori one would thus expect smaller shell

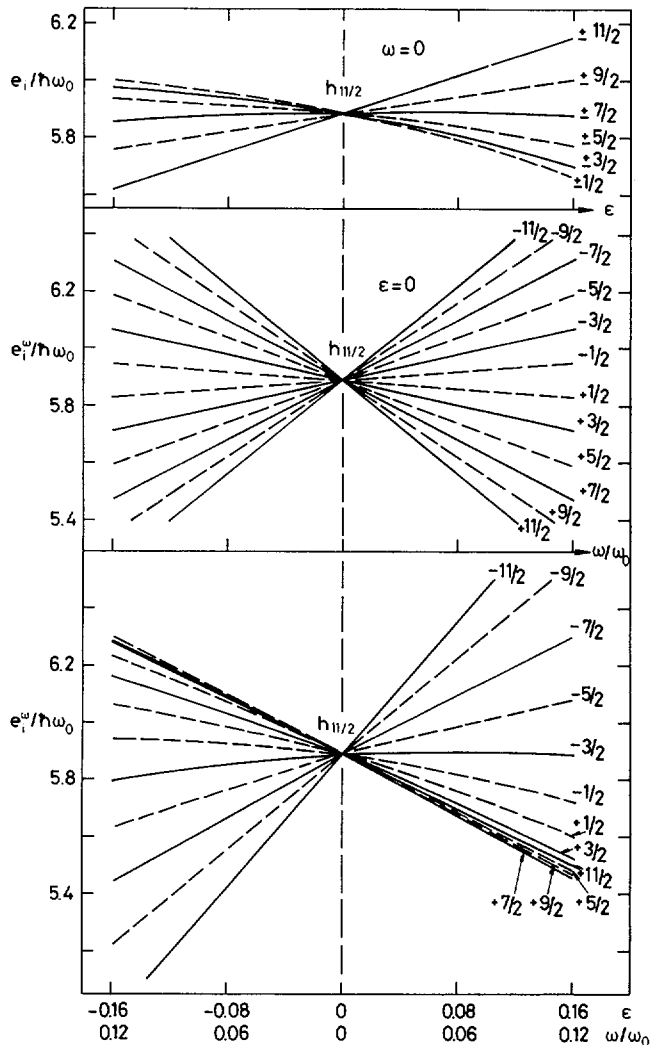


**FIG. 3.** The influence of quadrupole deformation and rotation on an  $h_{11/2}$  subshell. The different orbitals are labelled by the spin component,  $m$  ( $= \Omega$ ), along the symmetry axis. The upper and middle plots illustrate the pure deformation splitting and rotation splitting respectively. In the lower plot, deformation and rotation are turned on simultaneously with  $\omega/\omega_0$ :  $\epsilon = 0.75$ . Note that, in this case, the positive- $m$  orbitals are almost degenerate for all values of  $\epsilon$  (or  $\omega$ ).

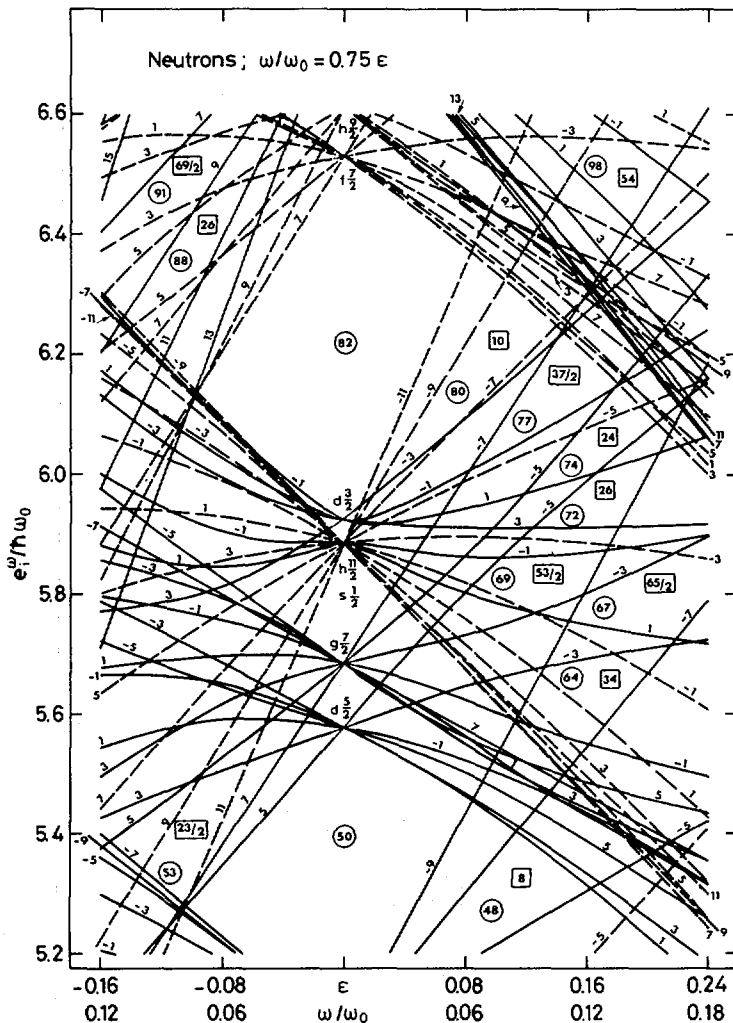


*FIG.4. Neutron single-particle levels calculated as functions of  $\epsilon$  ( $\omega/\omega_0$ ) for a deformed potential cranked around its symmetry axis. The rotational frequency is related to the quadrupole deformation through  $\omega/\omega_0 = 0.75 \epsilon$  (the sign of the rotational frequency is of no physical significance and has been chosen positive). The number on each orbital refers to  $2m$  where  $m$  is the projection on the symmetry axis of the single particle angular momentum. The numbers within rings refer to the total neutron number and those within rectangles to the total spin (from Ref. [8]).*

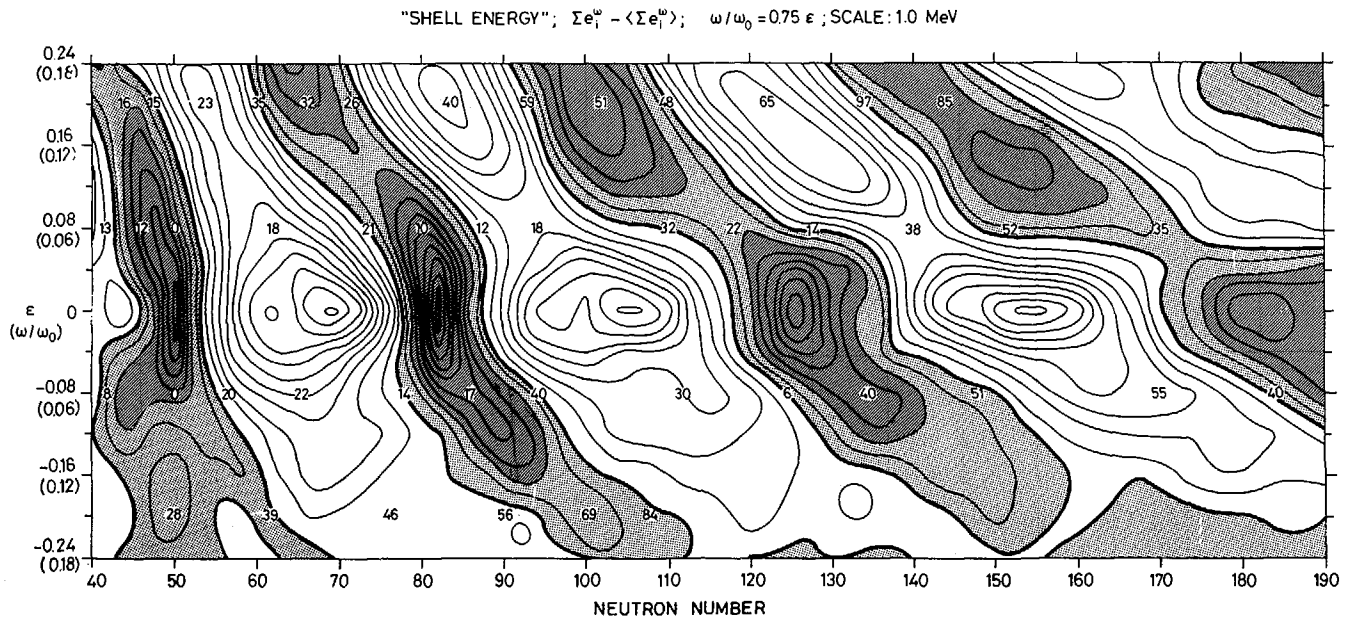


**FIG. 5.** Shell energy landscape for neutrons calculated for the same ratio of  $(\omega/\omega_0):\epsilon$  as in Fig. 4. The thick lines separate regions of positive and negative shell energy, and in the shaded regions the shell energy is below  $-2$  MeV. The numbers within the contour map refer to the total spin for the corresponding deformation (rotational frequency) and particle number. In this figure, as in Fig. 4, the  $\kappa$ - and  $\mu$ -values are chosen different for the different  $N$ -shells to make the potential applicable all over the nuclear periodic table. Note the pronounced ridges and valleys and the very strong effects for large deformations (from Ref. [8]).

effects in the rotating than in the non-rotating case. This also seems to be what comes out from the calculations in most cases. There are however exceptions from the general rule and in this section we will discuss some cases where strong shell effects are expected at high spins.

### 2.1. Shell structure for nuclei rotating around a symmetry axis

It is well-known that the strongest nuclear shell effects are observed for spherical shape and that these shell effects gradually disappear when the nucleus is deformed. However, if also rotation around the symmetry axis is included together with deformation, it turns out that a large fraction of the spherical shell effects can be preserved up to quite large deformations and spins [8]. The fact that the nucleus rotates around a symmetry axis implies that the high spins are built from pure single-particle excitations. Regions of large negative shell energy might then give rise to yrast isomers or long-lived states, so-called traps [2], which could be studied experimentally.

The influence on a single  $j$ -shell from quadrupole deformation and rotation respectively is illustrated in the upper and middle parts of fig. 3. From these two figures, it is easy to understand that with an appropriate ratio of  $\omega$  to  $\epsilon$ , the orbitals with a positive  $m$ -value can be made almost degenerate. This is illustrated in the lower part of the figure where we have chosen  $\omega/\omega_0 : \epsilon = 0.75$ . In addition, it can be shown that this strong degeneracy is obtained, independently of particle number, at about the same ratio of  $\omega/\omega_0$  to  $\epsilon$  for all high- $j$  subshells [8]. Observe also that on the prolate side, the coupling to other shells, leading to a general depression of the low- $m$  orbitals, helps to further improve the degeneracy. On the oblate side, on the other hand, these couplings between different shells have a dispersive effect.

A complete single-particle diagram for the same ratio of  $\omega$  to  $\epsilon$  as in fig. 3 is exhibited in fig. 4. One observes that not only do the positive  $m$  orbitals of the high- $j$  subshells stick together almost independently of deformation, but also that the bunches of levels originating from the different subshells have a tendency to intersect at a finite deformation. This is, for example, the case for the levels

from  $h_{11/2}$ ,  $g_{7/2}$  and  $d_{5/2}$  which come close together at  $\epsilon$ -values around 0.20.

The shell energy landscape corresponding to the single-particle levels of fig. 4 is shown in fig. 5. The very regular structure of this whole plot is at once apparent. The valleys of low shell energy having their minima at the spherical closed shells  $N = 50, 82, 126$  and  $184$  extend on the prolate side towards smaller particle numbers. In the region of  $\epsilon \approx 0.20$  we observe local minima with particle numbers more or less corresponding to maximum shell energy for spherical shape and no rotation. These local minima are obviously related to the intersection of the different groups of orbitals as seen in fig. 4. It is interesting to observe that the shell structure in this case appears to be stronger than for any clearly deformed shape without rotation. On the oblate side, the valleys of fig. 5 are not as pronounced but it is evident that with increasing oblate deformation they tend to be displaced towards larger particle numbers.

As the proton shell energy landscape is very similar to that for neutrons, the implications of fig. 5 are evident. To get maximum shell effects at high spins, we should combine proton and neutron numbers both being alternatively somewhat above or somewhat below closed shells. Prolate shapes are then expected for the former nuclei and oblate shapes for the latter ones [9,10]. Even if the liquid drop effects, favouring rotations around the oblate symmetry axis, will somewhat alter these general considerations, it appears that the long-lived high spin states which have been observed to date can be roughly classified into this general scheme. Thus for the yrast isomers in the lead region, weakly oblate shapes are calculated e.g. for  $^{212}\text{Rn}$  and weakly prolate shapes for  $^{204}\text{Pb}$  [10]. The yrast isomers for nuclei with  $N \geq 82$  and  $Z \geq 64$  [11,12] are apparently oblate [5,9,10]. Here the newly proposed strong shell closure at  $Z = 64$  might be of importance [13]. The prolate high-spin yrast isomers in the Hf region, with a maximum observed spin of 22 [14], clearly represent a realisation of the prolate coupling scheme in fig. 5. For these nuclei, however, much stronger shell effects are expected at higher spins. In addition, from fig. 5, it is easy to find other regions where strong and observable shell effects should be present (cf. also fig. 15 below). Due to the fact that the macroscopic terms disfavour rotation around a prolate symmetry axis, these states

are expected to sometimes lie above the yrast line at high spin values. Nevertheless, they may still be observable experimentally.

As already mentioned, with increasing angular momentum the liquid-drop energy minimum comes rather far out on the oblate side (with rotation around the symmetry axis). It is then interesting to look for strong shell effects at such deformations. Indeed, according to the calculations of Døssing et al. [9] (see also ref. [15]) the shell effects at the axis ratio 3:3:2 ( $\epsilon = -0.429$ ) should be observable at finite  $\omega$ -values. For some nuclei with neutron number  $N = 82, 84$  these authors calculate, with a Woods-Saxon potential, yrast traps around this deformation and at spin values  $I \approx 50$ . In the modified-oscillator calculations, the 3:2 oblate minimum does not become the lowest one. On the other hand, for nuclei with neutron and proton numbers around 36, yrast traps are predicted at  $\epsilon \approx -0.4$  (see below).

The single-particle structure at  $\epsilon = -0.429$ , in this case plotted in an  $e_i$  vs.  $m_i$  diagram, is shown in fig. 6. In such a diagram, the angular frequency  $\omega$  is given by the slope of the Fermi surface. The different deformed shell gaps are clearly seen and they are mainly disturbed by some high- $m$  orbitals originating from higher shells. In fig. 6, a sloping Fermi surface roughly corresponding to the yrast isomers calculated by Døssing et al. [9] is drawn. In addition, some suggested Fermi surfaces, in connection with other deformed shells where yrast isomers might be expected, have been drawn. They all correspond to  $\omega/\omega_0 \approx 0.075$ , and in the lower part of the figure the shell energy for this rotational frequency has been plotted as a function of neutron number. It is obvious that all these Fermi surfaces roughly correspond to minima in the shell energy. Note also that for  $\omega/\omega_0 = 0.075$ , the negative- $m$  orbitals from the high- $j$  shells are to a large extent degenerate. The shell effects at this large oblate deformation are thus formed in a way similar to that discussed above for near-spherical shapes.

## 2.2. Shell effects for fission barrier shapes

The shell effects discussed so far should mainly be of importance for the lowest energy states at a specific spin. They determine the

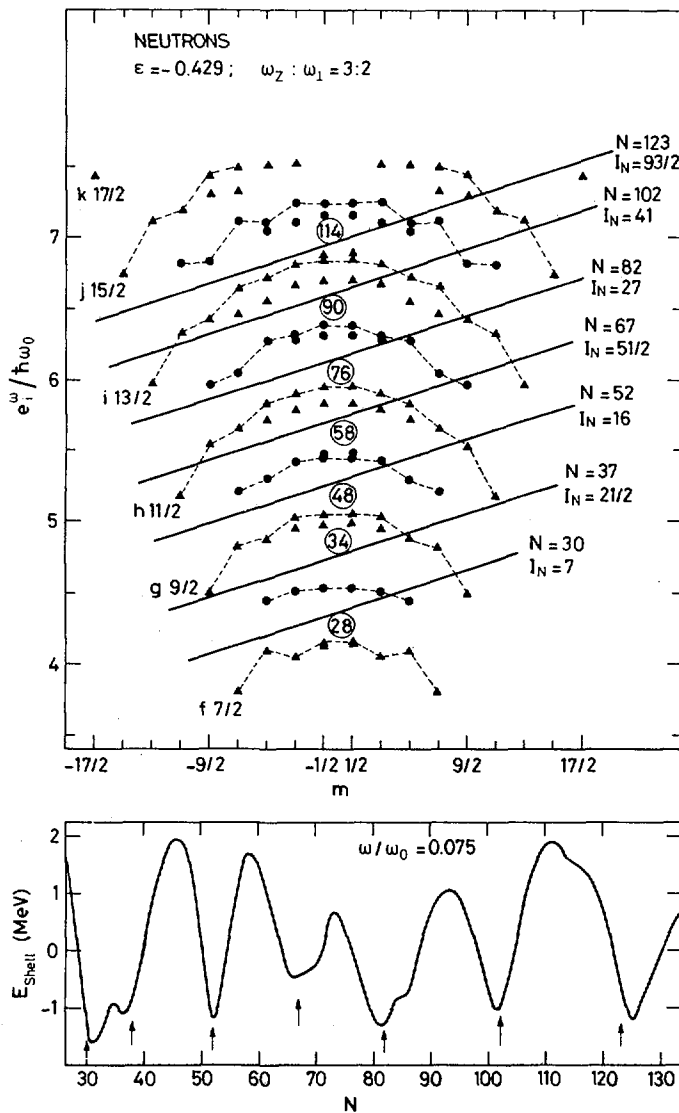


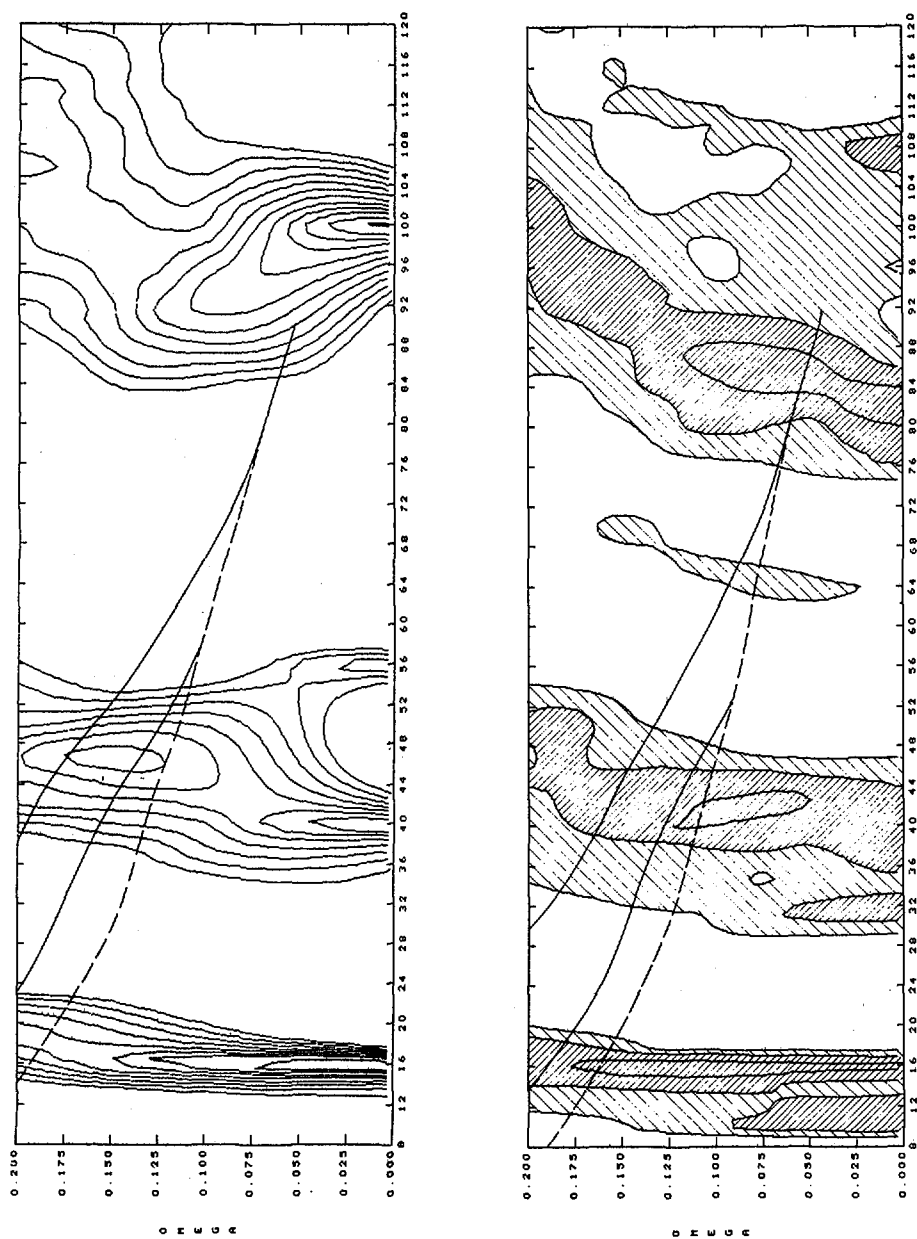
*FIG. 6. Illustration of the shell structure in an oblate potential with  $\omega_z : \omega_\perp = 3:2$ . In the upper plot, the single-neutron energies are plotted versus the angular momentum projection  $m$  along the symmetry axis. The different deformed shells of the pure oscillator are easily identified and, for the sake of illustration, every second is plotted with triangles and every second with points. The magic numbers of the pure oscillator are also given, and in connection with each of these a Fermi surface corresponding to  $\omega/\omega_0 \approx 0.075$ . These Fermi surfaces are labelled by neutron number  $N$  and neutron spin  $I_N$ . In the lower plot, the shell energy at  $\omega/\omega_0 = 0.075$  is exhibited. The arrows indicate the neutron numbers for the Fermi surfaces in the upper plot. Note that these neutron numbers in all cases approximately correspond to a shell-energy minimum.*

starting point for a fissioning nucleus and in this way influence the fission probability and the height of the fission barrier.

In this section we will look for structure in the fission barriers themselves. It is well-known that at spin zero the actinides with neutron numbers 140-150 have a second minimum, and it has been shown that this second minimum can be explained as being due to the strong shell structure at the axis ratio 2:1 [16, 7]. Similar shell effects are expected for lighter nuclei but because of the macroscopic energy, with a high fission barrier at  $I = 0$ , these effects should be very difficult to observe. However, as the fission barriers are decreasing with increasing spin, the interesting suggestion presents itself that the 2:1 structure could be observed for lighter nuclei at high spin values.

The first problem to investigate is then if the 2:1 shell structure survives at finite spin values [17]. To answer this question, figs. 7 and 8 were constructed. In three different more or less realistic nuclear models, the proton shell energy is shown as a function of particle number and rotational frequency in fig. 7. The upper part of fig. 7 corresponds to the rotation of two sticking spheres where the field of each sphere is taken as unperturbed by the presence of the other sphere. Thus, for  $I = 0$ , the magic numbers are twice the magic numbers of a single sphere. The lowest plot is calculated for a 2:1 spheroidal harmonic oscillator potential (i.e. with no  $\vec{k} \cdot \vec{s}$ - and  $\vec{k}^2$ -terms) while the middle one should be most realistic as it corresponds to the rotation of a 2:1 modified oscillator (i.e.  $\epsilon = 0.6$ ) and with  $\epsilon_4$  chosen at the realistic value of 0.08. In this case, also the couplings between the different oscillator shells are fully taken into account. It is at once evident that in all three models strong shell effects survive up to quite high rotational frequencies.

Let us concentrate on the modified oscillator plots, shown also for neutrons in fig. 8, where the most apparent feature is that the negative shell energies at or just above particle numbers 40, 60, 80, 110 and 140 are shifted to somewhat higher particle numbers with increasing angular frequency. The shell effects are certainly not destroyed, and in some cases the minima are deepest at non-zero  $\omega$ -values.



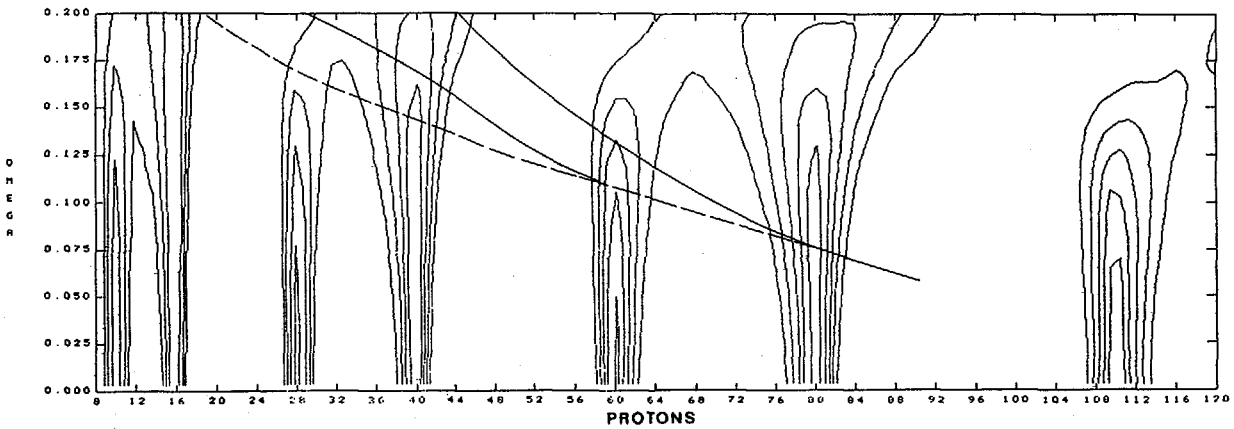


**FIG. 7.** Proton shell energy as a function of particle number and rotational frequency for three rotating systems with a 2:1 prolate deformation. From the upper part of the figure, the plots are for two sticking spheres, the modified oscillator with  $\epsilon_4 = 0.08$  and the harmonic oscillator, respectively. The contour line separation is one MeV, and the lines of positive shell energy are not drawn. Curves also indicate the regions where the rotating liquid drop favours large deformations. Thus, the dashed curves show the rotational frequency where the oblate regime becomes unstable, the upper thick curve corresponds to instability to fission and the lower thick curve indicates a liquid-drop fission barrier of 4 MeV (from Ref. [17]).

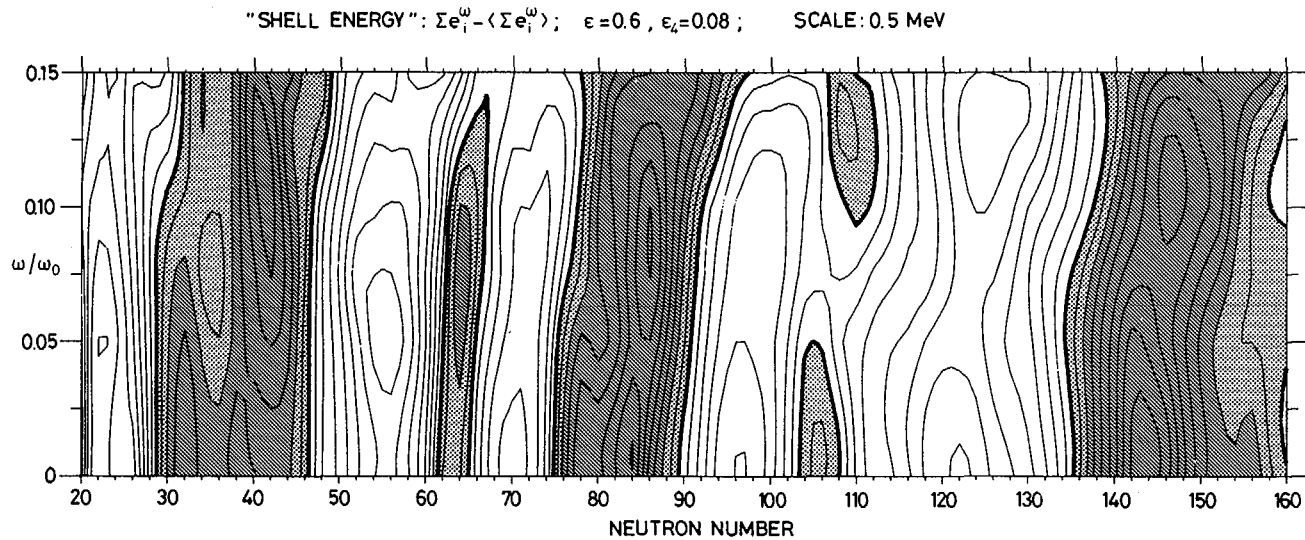


*FIG. 8.* The neutron shell energy calculated in the modified oscillator model and with  $\epsilon = 0.6$  and  $\epsilon_4 = 0.08$  as was also shown for protons in the middle plot of Fig. 7. The contour line separation is 0.5 MeV, and the thick lines demarcate regions of positive and negative shell energies. Thus, in the dotted regions the shell energy lies between 0 and -1 MeV while it is below -1 MeV in shaded regions (from Ref. [17]).

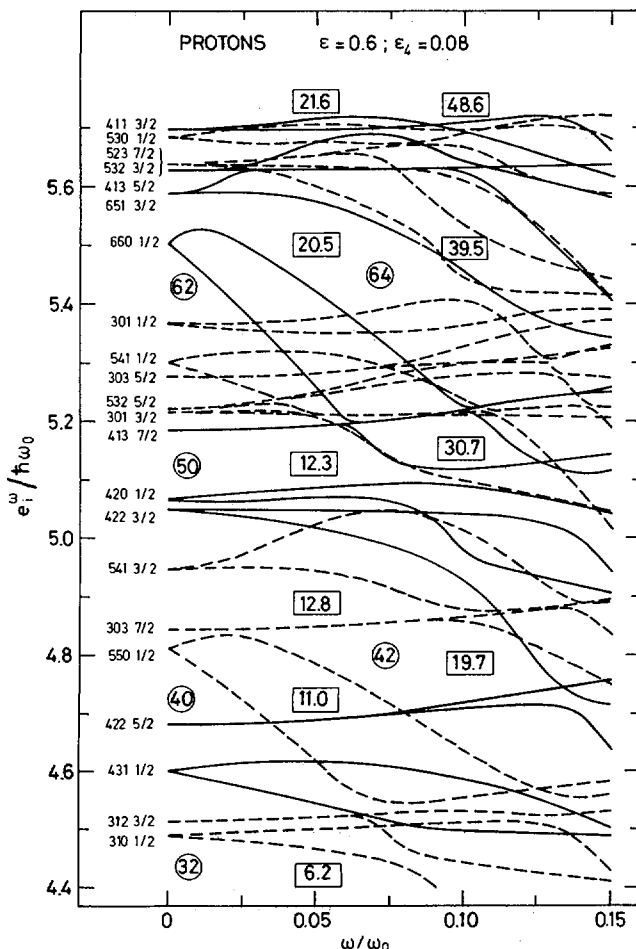


**FIG.9.** Single-proton levels at  $\epsilon = 0.6$  and  $\epsilon_4 = 0.08$ , drawn as functions of the rotational frequency  $\omega$ . At  $\omega = 0$  the orbitals are labelled by the asymptotic quantum numbers  $[Nn_z\Lambda\Omega]$ . The numbers within rings refer to particle number and those within rectangles to total neutron spin. Note the strong alignment of the  $[550 \frac{1}{2}]$  and  $[660 \frac{1}{2}]$  orbitals, which makes these orbitals bend away from the 'deformed shell gaps' at  $N \approx 40-42$  and  $N \approx 62-64$  (from Ref. [17]).

The proton single-particle levels, corresponding to the M.O. plot of fig. 7 in the region  $Z = 32-70$ , are drawn in fig. 9 and it is now rather easy to get a qualitative understanding of figs. 7 and 8. As was discussed in ref. [7], the orbitals with low  $n_z$  values are regularly bunched together at  $\omega = 0$  and they are thus mainly responsible for the strong shell structure. However, these orbitals are very little affected by the rotation and the general shell structure is thus preserved also for  $\omega \neq 0$ . On the other hand, the orbitals with large  $n_z$ , especially those labelled by  $n_z = N$  as  $[550\frac{1}{2}]$  and  $[660\frac{1}{2}]$ , are strongly affected by the rotation. However, these orbitals are quite few and in addition they are generally within or close to the shell gaps at  $\omega = 0$ . Thus, when they are bent down by an increasing  $\omega$ , they disappear from the gaps and the shell structure might even increase, with the minima occurring at somewhat higher particle numbers than for  $\omega = 0$ .

The single-particle diagram of fig. 9 also allows us to draw more general conclusions. It was shown in ref. [7] that strong shell effects are observed not only at  $\epsilon = 0.6$ , but in a region of quadrupole deformation centered around  $\epsilon = 0.6$ . Furthermore, with increasing deformation the shell energy minima will correspond to increasing particle numbers. This change in particle numbers is due to some strongly down-sloping orbitals, i.e. orbitals with large  $n_z$ -values, which cross the shell gaps around  $\epsilon = 0.6$ . Thus, based on arguments similar to those employed above, we conclude that also for  $\omega \neq 0$  strong shell effects should be observed not only at  $\epsilon = 0.6$  but in a region around this deformation, and that with increasing deformation the shell energy minima will be somewhat shifted towards larger particle numbers.

We end this subsection with a remark concerning the mass-asymmetric deformation ( $\epsilon_3$ ). It is well-known that the  $\epsilon_3$ -deformations in the fission barriers are mainly due to couplings between  $n_z = 0$  and  $n_z = 1$  'waistline' orbitals [18, 7]. These orbitals are however exactly those which are least affected by rotation. Thus, the  $\epsilon_3$  and  $\omega$  degrees of freedom are almost completely uncoupled. The fission barriers for specific particle numbers should then be strongly unstable to  $\epsilon_3$ -deformations also for  $\omega > 0$ , and the effect of the rotation should only be to somewhat increase the particle numbers where the largest shell effects are present.

## 3. THE PROPERTIES OF NUCLEI AT HIGH SPIN

3.1. Energy surfaces

The total angular momentum vector of a nucleus at high angular momentum is the sum of the mutually aligned contributions from the constituent nucleons, but its distribution over the nucleons in an yrast state is interwoven with the nature of the average field. There is a large variety, governed by the specific shell structure of each nucleus, and a first step in the theoretical study of an individual nucleus must be to chart the symmetries and size of the deformation that minimizes the energy for given spin. Such detailed investigations were initiated in Lund and Dubna [3, 4]. Potential-energy surfaces were calculated using the techniques that had been developed for the study of for example ground-state deformations [19,20], but now the motion of the individual nucleons was studied under the additional constraint of a cranked rotational motion for the deformed average field. Then the potential energy is written as

$$E_{\text{tot}}(\bar{\epsilon}, I) = E_{\text{shell}}(\bar{\epsilon}, I) + E_{\text{RLD}}(\bar{\epsilon}, I)$$

where  $\bar{\epsilon}$  stands for the deformation coordinates,  $I$  is the angular momentum,  $E_{\text{shell}}$  is the shell energy as described in section 2 above and  $E_{\text{RLD}}$  is the rotating liquid drop energy

$$E_{\text{RLD}}(\bar{\epsilon}, I) = E_{\text{surf}}(\bar{\epsilon}) + E_{\text{coul}}(\bar{\epsilon}) + \frac{I^2}{2J_{\text{rig}}(\bar{\epsilon})} I^2$$

Potential-energy surfaces are constructed for a given value of the total spin, and a unified picture emerges in which the energy cost of different ways to obtain angular momentum is compared. Primary possibilities are

- (i) Collective rotation of an axially symmetric shape around an axis perpendicular to the symmetry axis, whereby all the nucleons may contribute to the total spin. With the conventions of ref. [5], the intrinsic quadrupole angular deformation  $\gamma$  is then  $0^\circ$  in the prolate case and  $-60^\circ$  in the oblate case. Alternatively collective rotation may take place around one of the principal axes of a triaxial shape, with the sector  $0^\circ < \gamma < 60^\circ$  corresponding to the largest moment of inertia.

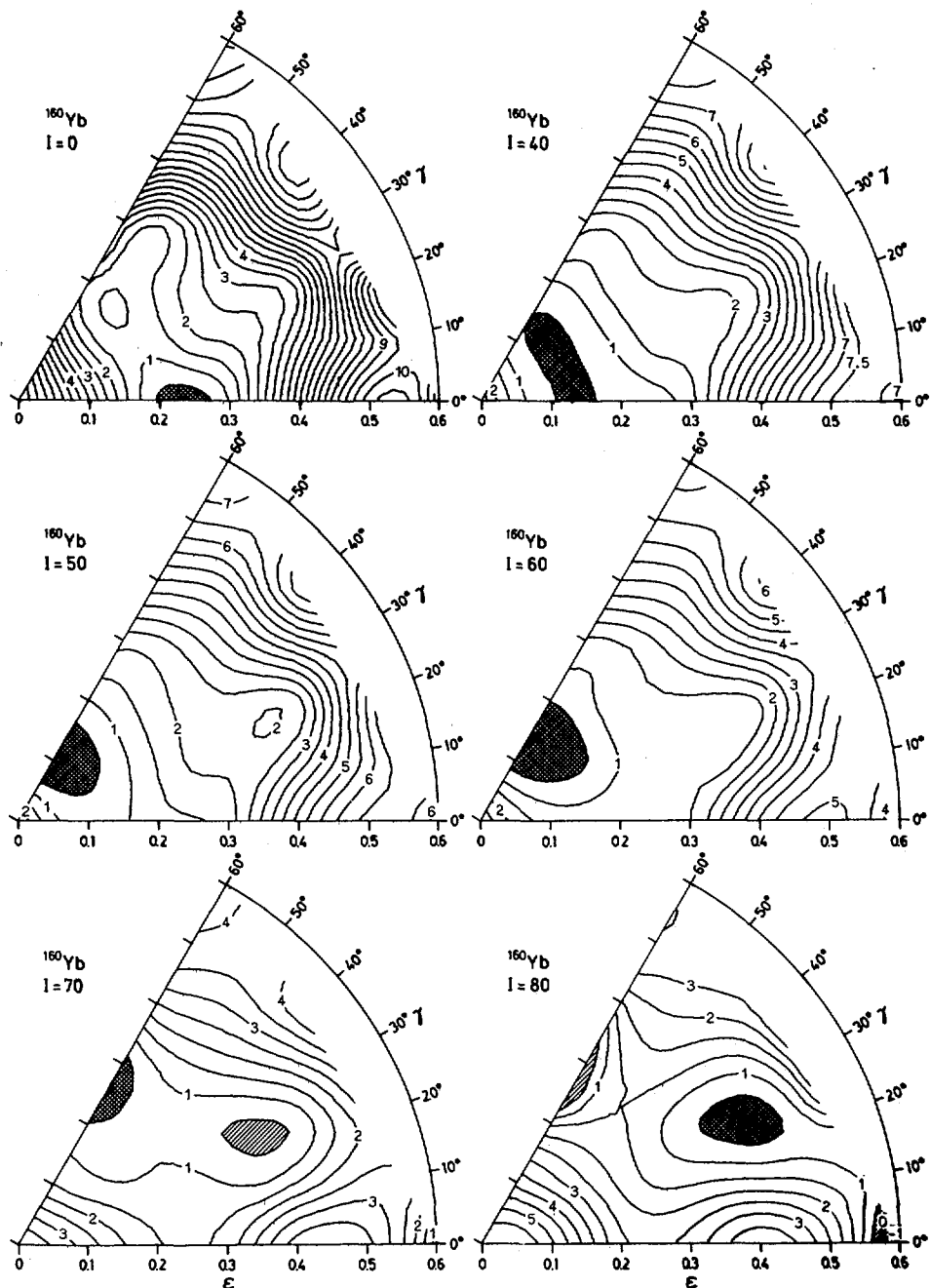
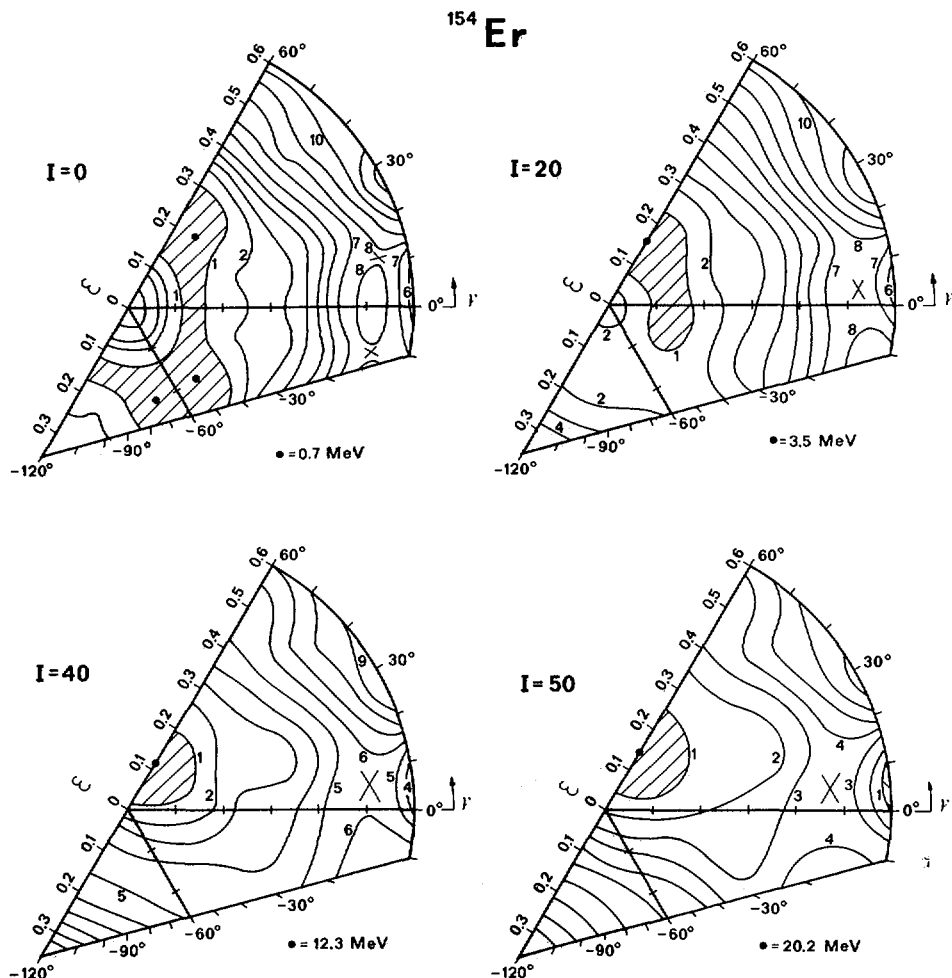


FIG. 10. Potential-energy surfaces in the  $(\epsilon, \gamma)$  plane, with inclusion of the shell energy for  $^{160}\text{Yb}$  as a function of angular momentum. For the surface, Coulomb and macroscopic-rotation energy terms, a minimization is performed with respect to  $\epsilon_4$  (from Ref. [5]).



**FIG.11.** Same as fig. 10 but for  $^{154}\text{Er}$ . Here also the possibility of rotation around other axes than that with the largest moment of inertia is investigated ( $-120^\circ \leq \gamma < 0^\circ$ ). Outside the figure at  $\epsilon \gtrsim 0.6$ , a second minimum develops, which for a spin value somewhat below 50 becomes lower than the minimum on the oblate axis. As for all other energy surfaces in this section, pairing has been neglected and the results for  $I = 0$  are therefore not realistic. The number below each  $(\epsilon, \gamma)$  triangle corresponds to the minimum of the energy surface relative to the liquid-drop energy at spherical shape for  $I = 0$ .

(ii) Rotation around a symmetry axis. Then the rotation of the intrinsic system does not perturb the wave functions of the single-particle orbits, and the rotating state can be viewed to arise through the excitation of a few particles or quasiparticles relative to the non-rotating intrinsic state at the same deformation ( $\gamma = 60^\circ$  oblate,  $\gamma = -120^\circ$  prolate).

Such a preliminary theoretical analysis of the nuclides available to experiment is actually a massive task. The calculations carried out up to now [3-6,9,10,21-32] cover only some of the relevant degrees of freedom. Let us however proceed to review these first results, starting with the example of energy surfaces for different angular momenta shown in fig. 10. There the quadrupole deformation coordinates are varied over the domain  $\epsilon < 0.6$ ,  $0^\circ \leq \gamma \leq 60^\circ$ , and also the liquid drop contribution  $E_{RLD}$  is minimized with respect to a hexadecapole coordinate  $\epsilon_4$ . Pairing correlations are not taken into account. Then the nucleus  $^{160}\text{Yb}$  is calculated to have a prolate deformation at  $I = 0$ . When it is set to rotate, it rotates around an axis perpendicular to the symmetry axis (collective rotation). Then time reversal symmetry is broken and the nucleons begin to align their spins along the axis of rotation, starting with those having a high  $j$ -value and  $\Omega = 1/2$  (see fig. 7 of ref. [5]). This affects the matter distribution around the axis of rotation and the potential accordingly assumes a non-axial deformation. At  $I = 50$  it has traversed to an oblate shape rotating around the symmetry axis. This means that the total spin is now supplied by a few unpaired particles. At higher spin values a triaxial minimum develops, which for  $I = 80$  becomes lower than the minimum at  $\gamma = 60^\circ$ .

The behaviour of the nucleus  $^{160}\text{Yb}$ , as described so far, roughly coincides with the overall features predicted by Bohr and Mottelson from general considerations [2]. As another example, fig. 11 shows potential-energy surfaces for the nucleus  $^{154}\text{Er}$ , where recent experiments [33,34] indicate rotation around a symmetry axis from  $I \sim 11$  up to at least  $I \sim 36$  in agreement with the calculations. However, the range of deformations studied may in fact be irrelevant at the still higher spins. In the energy surfaces of figs. 10 and 11 there are indications of an additional minimum at large prolate deformation, which certainly becomes the lowest at some spin below 80. Within the axially symmetric  $\beta$ - $r$  parametrisation of the Jülich group, there exists even for high spins a substantial barrier against fission beyond the superdeformed minimum

at  $\beta \approx 0.6$  [32]. The stability of this minimum seems to be a manifestation of the superdeformed shell structure obtained in ref. [17] and displayed in figs. 7 and 8 above.

The role of neutron shell structure at smaller spins and deformations is illustrated in fig. 12, which shows the calculated behaviour of the doubly even isotopes  $^{158-164}\text{Yb}$ . In this figure, part of the information from the potential-energy surfaces has been concentrated by marking the deformation of the lowest minimum at each spin and connecting these points. For  $I = 0$  the Yb isotopes with neutron number 90-94 have their minima at about the same prolate deformation, at any rate in the present approximation where pairing is ignored. However, it is only the lighter isotopes with  $N \leq 92$  that change to oblate deformation at higher spin and rotate around the symmetry axis. This occurs for lower spin values the closer the neutron number comes to the  $N = 82$  closed shell. Such behaviour in nuclei with a few particles outside a closed shell was explained in sect. 2.1 above (see fig. 5).

Other non-classical behaviour can also be observed in fig. 12. Thus for example the deformation is generally seen to shrink for increasing spin. This occurs because some orbitals, that carry a great deal of aligned angular momentum and are also deformation driving, are located below the non-rotating Fermi level. Furthermore, it is seen that the minimum may lie at a negative  $\gamma$ , corresponding to rotation around an axis other than the one with maximal moment of inertia for rigid shape. The small negative  $\gamma$ 's shown in fig. 12 were first noticed in the calculations of the Dubna group, and the underlying shell effect is examined in ref. [5].

The figures 10-12 describe results obtained with the cranked modified oscillator potential, but analogous calculations have been made with a cranked Woods-Saxon potential [25] and a quadrupole-quadrupole force [35,30]. A direct comparison with the modified oscillator model, made in ref. [25] and partly reproduced in fig. 13, shows that the overall features of the shell structure are quite similar in the different models. This result is not immediately obvious since the models differ not only by the details of the spacing between the  $I = 0$  single-particle levels, but also by the average energy of rotation under the constraint of fixed deformation. The average moment of inertia in the Woods-Saxon potential is close to the rigid-body value, while the average moment of

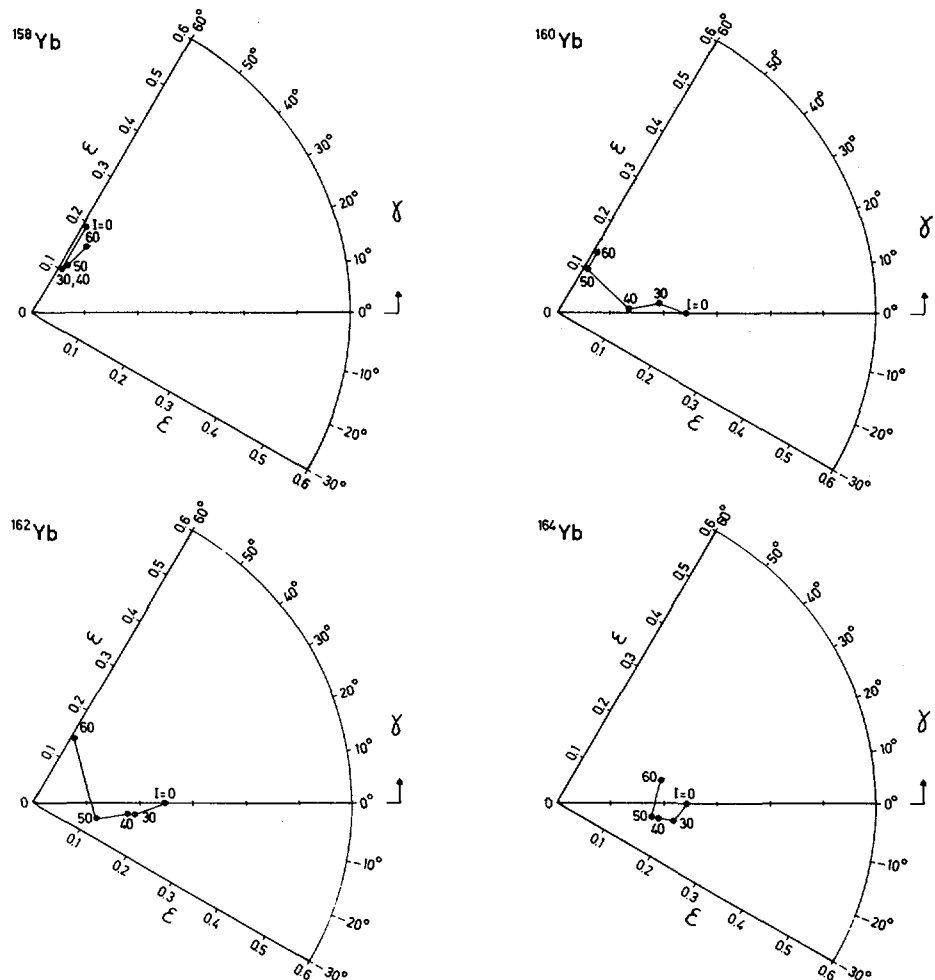
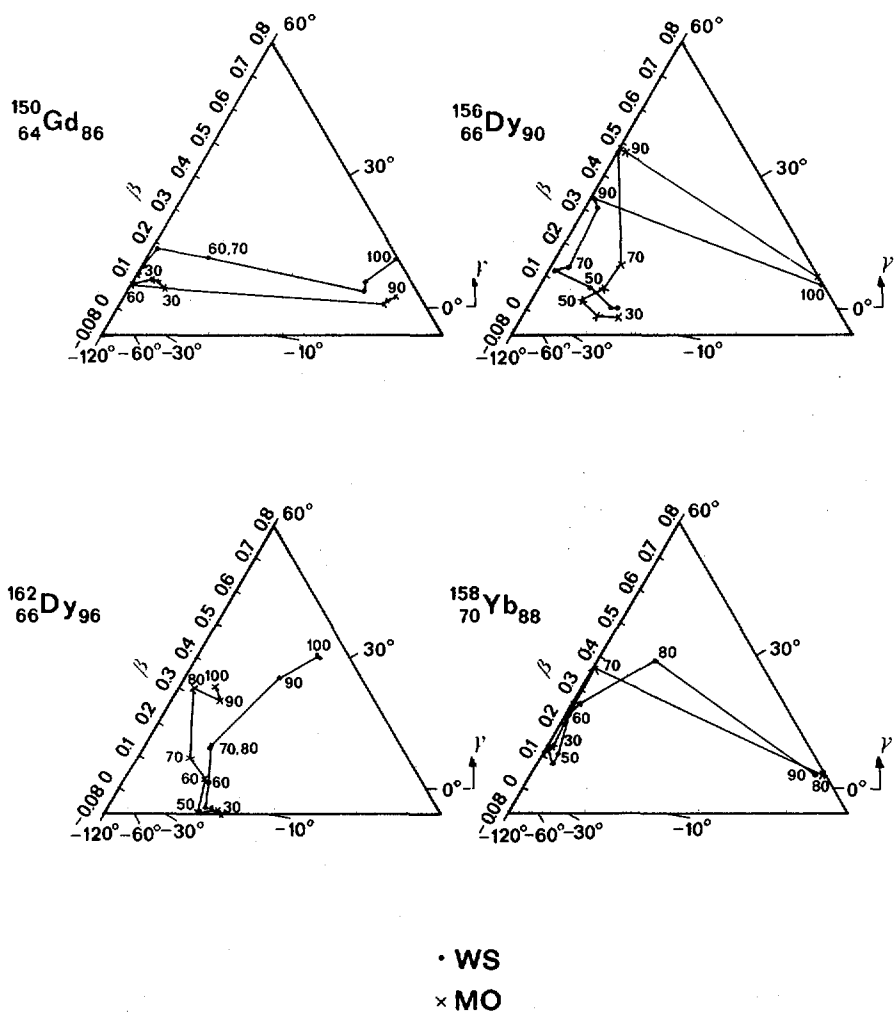


FIG. 12. For isotopes of  $\gamma_0\text{Yb}$ , the locus of the lowest minimum in the  $(\epsilon, \gamma)$  plane is shown as a function of total angular momentum  $I$  (from Ref. [5]).



*FIG.13.* Spin trajectories analogous to those in Fig. 12 for some rare-earth nuclei, calculated both with the modified oscillator potential (M.O.) and Woods-Saxon potential (WS). For the axial asymmetry parameter  $\gamma$ , the convention of Ref. [5] is used (from Ref. [25]).

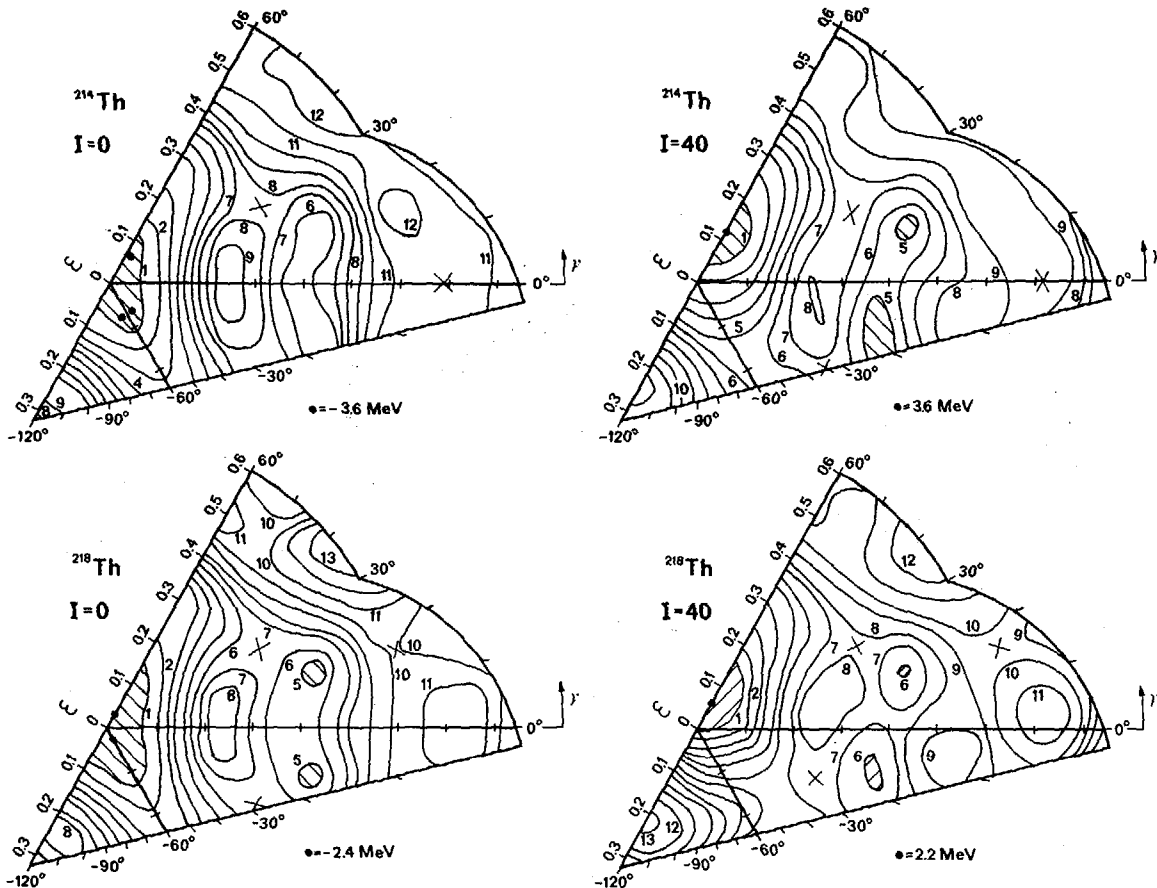


FIG.14. Same as Fig. 11 but for  $^{214},^{218}\text{Th}$ . Here the shell energy includes  $\epsilon_4$  in addition to  $\epsilon$  and  $\gamma$ . The  $\epsilon_4$  values are chosen so as to minimize the liquid-drop part of the energy (the  $^{214}\text{Th}$  surfaces are from Ref. [10]).

inertia in the modified oscillator potential is about 1.3 times larger due to the presence of the  $\tilde{\chi}^2$ -term. It is an open question to what extent the nuclear moment of inertia should conform to the rigid-body value, but there is no reason to attach significance to the systematic deviation caused by the  $\tilde{\chi}^2$ -term. On the contrary, in calculations with the modified oscillator model the Strutinsky procedure is used to renormalize the gross properties to those of the rotating liquid drop.

A mass region similar to the light rare earth region with  $N > 82$  is the light "actinide" region with  $Z > 82$ . There, neutron-deficient isotopes far from the stability line are experimentally available at high angular momenta through heavy-ion collisions. Calculated potential-energy surfaces for the two isotopes  $^{214,218}_{90}\text{Th}$  are shown in fig. 14. Both these nuclei build up their yrast states with single-particle excitations for all angular momenta studied. At  $I = 0$  the second minimum for both nuclei is found at a triaxial deformation, and there the rotation will take place preferentially around one of the two smallest axes, corresponding to  $\gamma \approx \pm 15^\circ$ . These two secondary minima persist up to very high spin. The second saddle point appears for  $^{218}\text{Th}$  at a triaxial deformation ( $\gamma \approx 15^\circ$ ) while it is found close to the prolate axis for  $^{214}\text{Th}$ . This example illustrates how, in general, the triaxial shape degree of freedom cannot a priori be neglected in a quantitative study of large deformations and fission (c.f. also section 3.3 below).

### 3.2. High-spin yrast isomers

#### 3.2.1. Rotation around a symmetry axis

A necessary condition for yrast isomers to occur is that the rotation, for some region in spin, takes place around a symmetry axis. Then only a few nucleons participate in the rotation and the total angular momentum is taken as the sum of the single-particle contributions along the symmetry axis. The rest of the nucleons, which do not participate in the rotation, respond to the rotation through polarisation effects as the deformation varies self-consistently. Without any collectivity the yrast line will be irregular and the electromagnetic transitions will be of single particle type, which implies favourable conditions for the

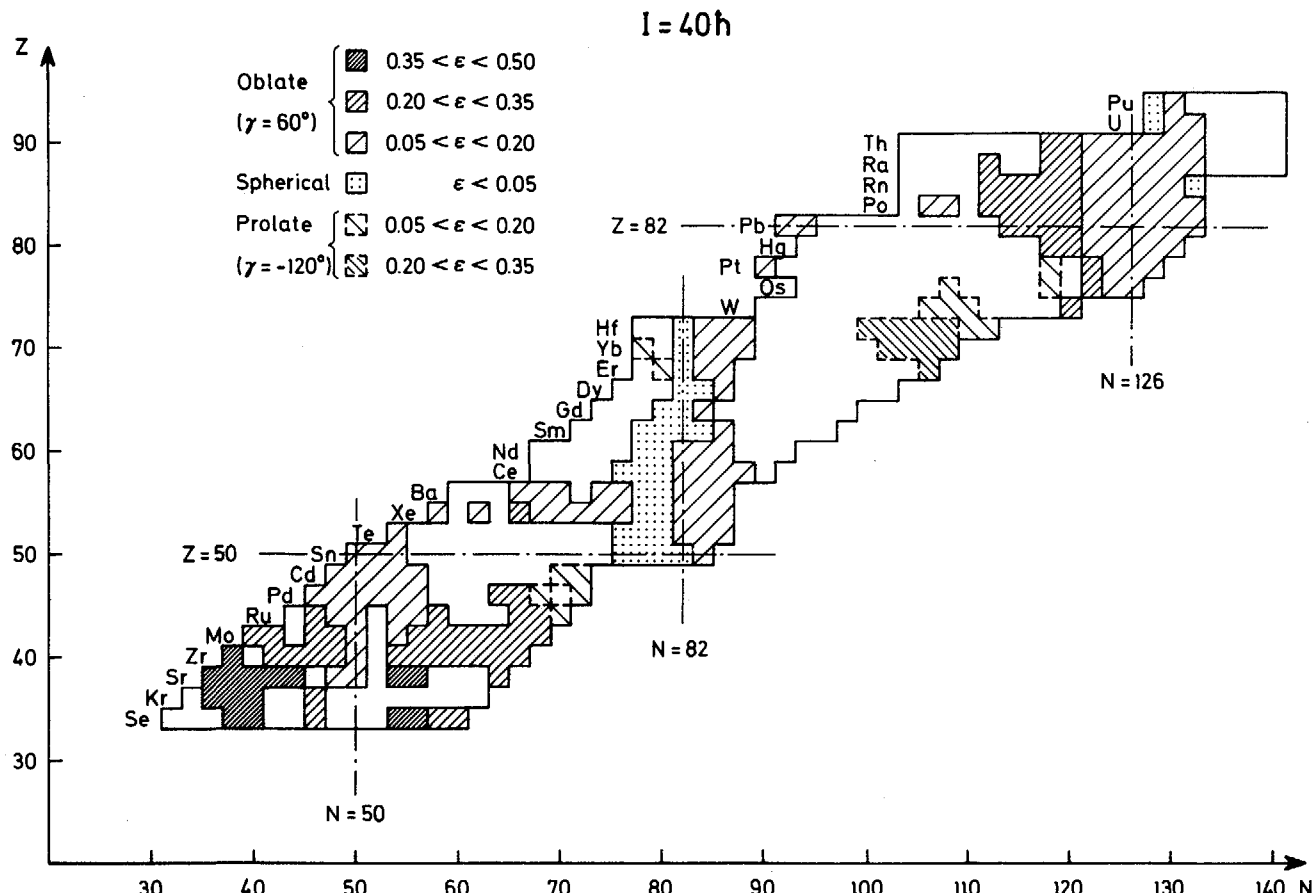


*FIG. 15. Mass regions in  $N$  and  $Z$  over which calculations were performed in Ref. [10]. Nuclei, which for a spin value of  $I = 40$  are found to rotate around a symmetry axis, oblate, spherical or prolate, are indicated by shaded or dotted squares. These are regions where "yrast traps" might a priori be expected. The absolute value of  $\epsilon$  is smaller than 0.05 in the dotted regions while it is larger than 0.05 in all the shaded regions. As shown in the figure, different densities of the shading are used to distinguish different magnitudes of deformations. Furthermore nuclei with prolate and oblate energy minima, respectively, are shaded with lines sloping left or right. Finally, for those nuclei which are left blank, the energetically most favourable rotation is found to take place around an axis which is not a symmetry axis. Spin traps are there highly unlikely. (from Ref. [10])*

occurrence of high spin yrast isomers. The necessary condition has been investigated theoretically for nuclei over almost all the periodic system. In fig. 15 the nuclei are marked out that, according to the predictions, rotate around a symmetry axis at spin 40. Depending on whether the rotation takes place around a spherical, oblate or prolate symmetry axis the marking consists of dots or hatching with the lines sloping right or left. The denser the lines, the larger is the calculated deformation. For those nuclei that are left blank in fig. 15, the energetically most favourable rotation is found to take place around an axis that is not a symmetry axis. In that case spin traps are unlikely.

Several of the regions marked in fig. 15 have been investigated experimentally and high-spin yrast isomers have been found. One is the region around  $^{208}\text{Pb}$ , where the yrast states often seem to be aligned single-particle configurations (rotation around a symmetry axis). The yrast line is for example for  $^{212}\text{Rn}$  known up to spin 30, which is found to be a 154 ns isomeric state [36]. The very long-lived  $K'' = 16^+$  state in  $^{178}\text{Hf}$  ( $\tau_{1/2} = 31\text{y}$ ) is a clear-cut example of an yrast trap where the rotation takes place around the prolate symmetry axis (fig. 15). Khoo et al were the first to consider the high-K isomers as states with rotation around a prolate symmetry axis [14]. In the region of Hf-W isotopes near the stability line, the highest measured spin is 22 (in  $^{176}\text{Hf}$ ) and the deformation is fairly large ( $\epsilon \approx 0.25$ ). Experimental evidence for high-spin isomers became available in the light rare-earth region [11] only a couple of years after the first theoretical predictions of the Lund group [3, 5]. Furthermore, this experiment confirmed the predicted absence of isomers in the surrounding regions (fig. 15). Currently, a broad experimental effort is being made to establish the details of the excitation spectra and the yrast cascades in the light rare earths [12]. Spins up to  $I \sim 37$  have been reached in a couple of nuclei with  $N = 86$ , and for the near future we eagerly anticipate relatively complete information. Shell model analyses by Blomqvist [37], based on the  $^{146}_{64}\text{Gd}_{82}$  core, provide a valuable complement to the experimental information.

Two other regions where the rotation is calculated to take place around a symmetry axis, and that can be reached in heavy-ion reactions, are the light "actinide" region discussed in section 3.1 above and the light krypton region. Nuclei in the latter region with proton and neutron

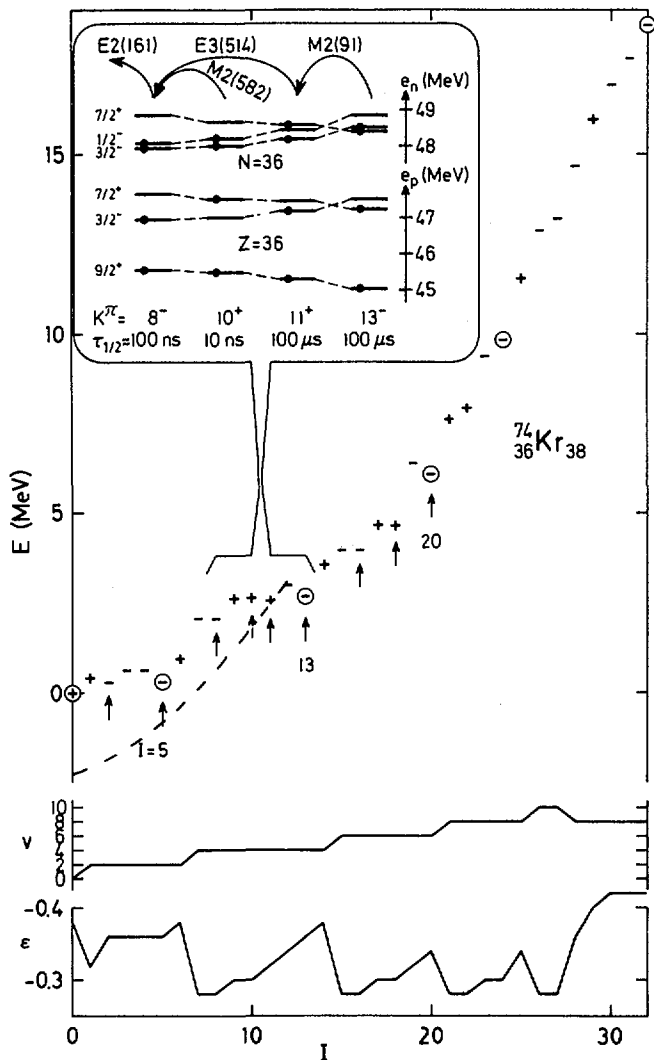


**FIG.16.** The calculated yrast line for  $^{74}\text{Kr}$ . Pairing is neglected in the calculation. In addition the experimentally known collective yrast band of  $^{76}\text{Kr}$  is indicated by the dashed line, whose position on the energy scale relative to the calculated levels is based on a determination of the SPBCS pairing energy [10] in the  $I = 0$  ground state with standard parameters. The present theoretical description may become meaningful above the point where the dashed line crosses the calculated yrast line. States with estimated life-times longer than 10 ps are indicated with an arrow, and optimal states [5] are encircled.

The lower part of the figure shows the seniority  $v$  and the (oblate) deformation  $\epsilon$  for each spin. The inserted figure describes the nature of the yrast states with  $K^\pi = 8^-, 10^+, 11^+$  and  $13^-$ , and in particular which orbitals are occupied by the unpaired particles. Note the deformation energy gained from  $K^\pi = 8^-$  to  $13^-$  (from Ref. [38]).

numbers close to 36, are predicted to have a large oblate deformation ( $\epsilon \approx -0.43$ ) resulting from strong shell structure at an axis ratio 3:3:2 (fig. 6). As yet there is no experimental evidence for a non-collective yrast cascade or for yrast traps.

The calculations presented in fig. 15 are continued in ref. [38] to regions of lower mass, down to  $^{36}_{18}\text{Ar}_{18}$ . Almost all the nuclei in the  $A \sim 40-80$  region are calculated to rotate around a symmetry axis for some range of spins.

### 3.2.2. Calculations for yrast states built from single-particle excitations

When the potential-energy surfaces imply that the rotation for a certain spin region takes place around a symmetry axis, a further investigation of possible yrast isomers requires a detailed description of the complete yrast cascade. The methods presently available in nuclear theory do not give predictive results of sufficient accuracy for this purpose, but in ref. [5] an approximative scheme was developed that is hoped to reproduce the essential features in a representative if not quantitative way. For each spin the energy is calculated for the relevant many particle-many hole configurations. These are selected on the basis of the sloping-Fermi-surface picture by a technique that is refined in ref. [10]. The total spin is simply taken as the sum of single-particle contributions along the symmetry axis. The energy is given by the sum of the shell energy and the liquid drop energy. The shell energy is calculated as the difference between the sum of the single-particle energies and a Strutinsky-smeared energy. The total energy is then for each spin and for each many particle-many hole configuration minimized with respect to axially symmetric deformations. This method was later employed also in refs. [39,9,27,40] to search for 'energy traps' that do not have any possible decays of multipolarity less than or equal to two.

An example of an yrast spectrum calculated in this way without the inclusion of pairing is shown in fig. 16, valid for  $^{36}_{38}\text{Kr}_{38}$ . In the modified oscillator level scheme  $N = Z = 36$  is magic at an oblate deformation corresponding to a ratio between the axes of 3:3:2 ( $\epsilon \approx -0.43$ ) (see fig. 6 above). For comparison the experimental

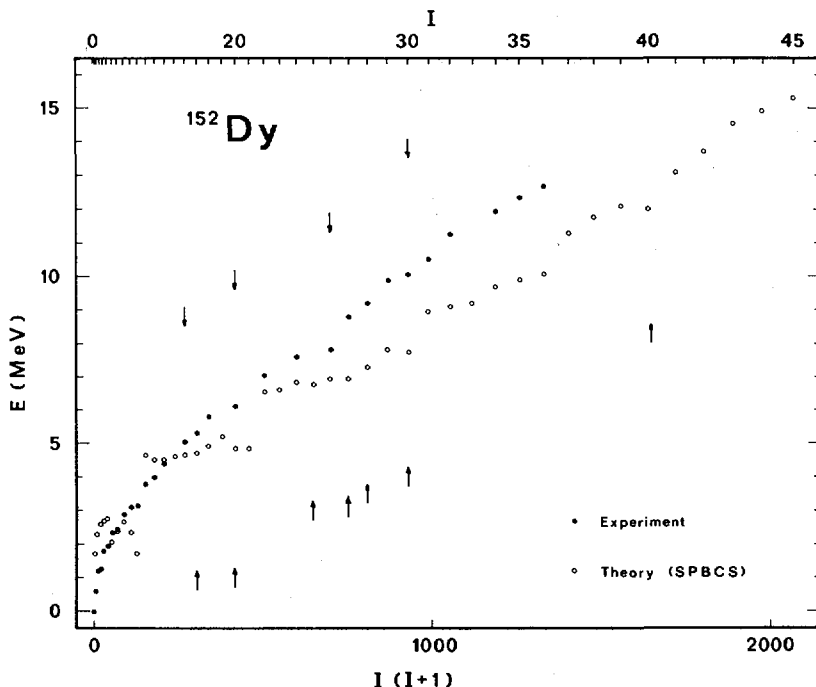


*FIG. 17. The experimental and calculated yrast energies in  $^{152}\text{Dy}$ , plotted versus  $I(I+1)$ . The observed isomers and the calculated states with life-times longer than one nanosecond are indicated by arrows pointing down and up, respectively (from Ref. [41]).*

collective yrast line of  $^{76}\text{Kr}$  is plotted as a dashed line in fig. 16. It is above the crossing between the two lines, that the calculated yrast line may be valid. The inserted section in fig. 16 shows the importance of varying the deformation for each configuration. The saw-tooth variation in deformation shown in the lower part of the figure comes from the promotion of unpaired particles into deformation driving high- $\Omega$  orbitals in order to increase the spin.

In the theoretical calculations referred to above, mainly energy traps were considered. With this limitation very few traps were found in general, and for the nucleus in fig. 16 the highest calculated energy trap has  $I = 11$ . Rotation around a symmetry axis does not necessarily give rise to energy traps, especially not in spin regions where the yrast line becomes too steep. In ref. [38] the search for yrast

traps was put on a new footing, in that a crude way to actually estimate the lifetimes of the yrast states was adopted. For a particle-hole transition the transition rate is taken as the Weisskopf single-particle rate and for each additional particle-hole rearrangement an ad hoc hindrance factor of 1000 is applied. With this simple estimate, a certain possibility also for higher spin traps is found. For example the  $34^+$  state in  $^{74}\text{Kr}$  is calculated to have a half-life of 10 ps and in the neutron-deficient rare earths a few states above  $I \sim 40$  are predicted to have lifetimes in the nanosecond range (fig. 19) [41,42].

The particle alignment scheme described above gives good agreement with experimental level schemes in the lead region [10,43]. In other regions, such as the light or heavy rare earths, pairing is calculated to persist up to high spins and in refs. [10, 41 - 49] a corresponding quasiparticle alignment scheme is introduced. However, an adequate algorithm for selecting the configurations that may participate in an yrast cascade has not yet been developed. The ordering between the states of a given spin can be altered substantially due to the presence of a relatively strong pairing in some configurations, which subsequently come down in energy. The pairing energy for each configuration can be found by a blocked BCS calculation, and particle-number projection is easiest taken into account by the saddle-point method (SPBCS) [50].

In fig. 17 the experimental yrast spectrum for  $^{152}\text{Dy}$ , recognized up to spin  $I \sim 36$  [51,52], is compared with a calculation that includes pairing as described above. The proton pairing is found to persist up to  $I \sim 40$  in some configurations, which can become yrast precisely due to the energy gain entailed by pairing. Yrast states estimated to have longer lifetimes than 1 ns are marked with arrows pointing up, while the experimental isomers are marked with arrows pointing down. The theoretical spectrum, both in fig. 17 and in general, resembles a staircase where the steps correspond to the number of quasiparticles and the high-spin end of each step is an optimal state. This conspicuous feature of the theoretical spectra does not seem to be present in the experimental spectra. Let us here suggest an assorted medley of some more or less different mechanisms, each of which could give a smoothing of the staircase structure and furthermore is reasonably straightforward to investigate within the standard formalism:

- i) a state-dependent pairing interaction strength, rather than the constant value employed in BCS theory
- ii) further steps toward making the residual interaction more closely resemble the empirical interaction
- iii) collective rotation around a non-symmetry axis superimposed on the intrinsic rotation around the symmetry axis
- iv) even when the potential-energy surfaces indicate a stable axial shape for the optimal states, it is conceivable that the nucleus in other configurations could gain energy by assuming a triaxial shape and rotating collectively
- v) the coupling of the yrast states to collective vibrational degrees of freedom such as gamma vibrations may lower several of the non-optimal states [45]
- vi) angular-momentum projection significantly affects the energies of particularly the non-aligned configurations [53].

Averaged dynamical moments of inertia may be extracted from plots such as fig. 17 to the extent that the yrast states fall around a straight line. This is roughly the case in fig. 17 for spins 16-36, which in the following will be the spin range considered. Calculations [41] for all the neutron-deficient rare-earth nuclei give neither any systematic dependence on the proton number nor any systematic odd or odd-odd effect, so the moment of inertia for  $I \sim 16-36$  can be roughly plotted as a function only of the neutron number  $N$ . The plots in fig. 18 show moments of inertia  $B_J$ , normalized to give unity for the spherical rigid-body value, calculated with and without pairing. The conclusion is that both shell effects around the  $N = 82$  gap and proton pairing are important. The geometrical rigid-body moment of inertia, corrected for deformation, is about 1.0-1.1 in the relevant range of spins and nuclei. However, the fact that the experimental moments of inertia come close to this value seems to stem from a cancellation between the large shell and pairing effects. Indeed, a reasonable phenomenological adjustment of the pairing strength can give quantitative agreement between theory and experiment for both  $N = 82$  and  $N = 86$  [49]. The coupling between the moment of inertia and the deformation is comparatively weak, and thus deformations should not be deduced from the experimental slopes.

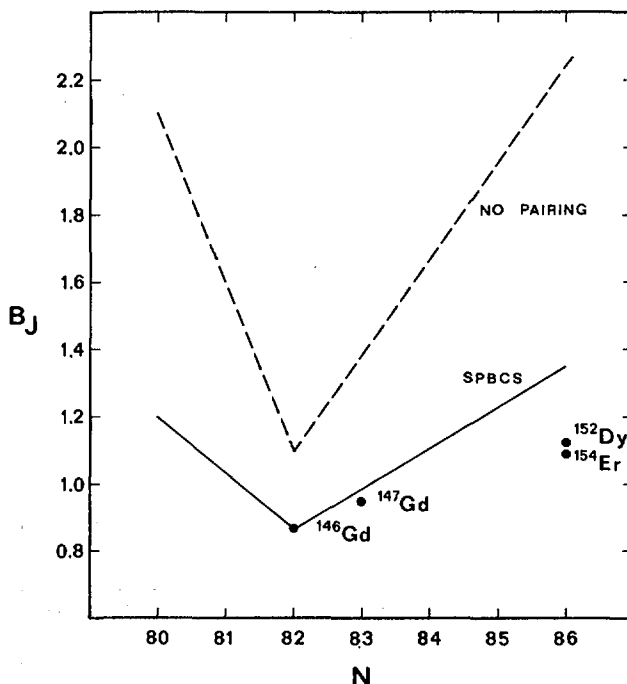


FIG.18. The straight lines indicate roughly the reduced moments of inertia  $B_J$ , calculated with and without pairing for rare-earth nuclei with neutron numbers around 82 and at spins in the range 16–36. The points are from experiment (from Ref. [41]).

### 3.2.3. Alpha-emitting isomers

The alpha-decay from high-spin states has been considered in refs. [38,54]. In the first reference the life-time was estimated within the WKB approximation for penetration of a Coulomb plus centrifugal barrier. The energy was taken from calculated yrast states in the mother and daughter nuclei. No formation factors or additional hindrance factors are considered so the estimate is very crude. However, in fig. 19 the calculated alpha lifetimes for the yrast states in  $^{74}\text{Kr}$  are compared with the likewise crudely estimated gamma lifetimes, calculated as described above. According to the calculations the yrast cascade can be described as follows: If the compound nucleus reaches the yrast line above spin 40–45 it decays by the emission of an alpha particle. Below this spin gamma transitions are the dominant decay mode down to the isomeric state

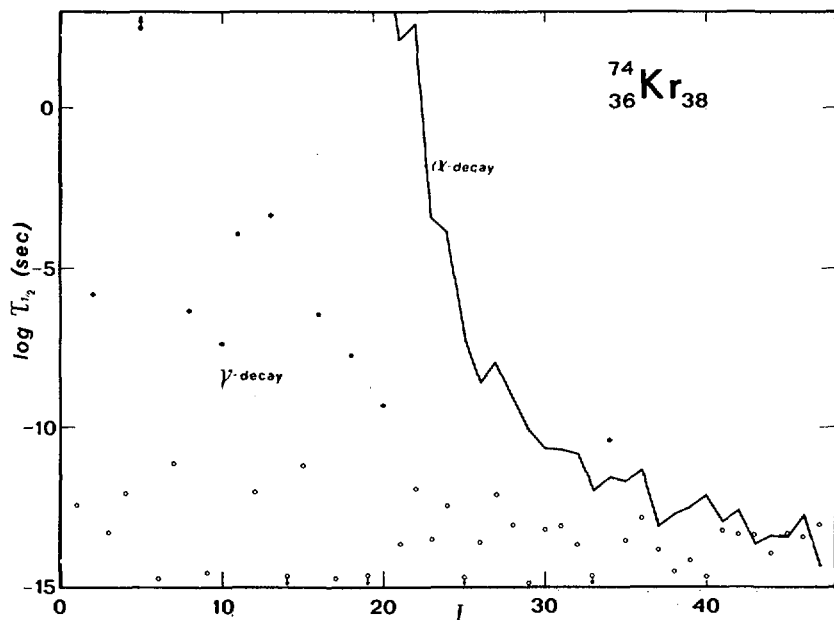


FIG. 19. The estimated life-times of calculated yrast states in  $^{74}\text{Kr}$  for  $\gamma$ -decay (circles) and  $\alpha$ -decay (jagged line) (from Ref. [38]).

at spin 34. From this state a delayed alpha particle would be expected with an energy of about 10 MeV and carrying about 14 units of spin. Such alpha-emitting isomeric states are to be expected also in other mass regions.

### 3.3. Fission barriers at high spin

It has been mentioned above that in the liquid drop model the height of the fission barrier is a continuously decreasing function of the angular momentum. Then, as shown in fig. 2, there is a certain critical spin  $I_{\text{crit}}$  where the barrier has disappeared completely. In recent calculations with shell structure included [5, 55, 10, 32], it has been found that even if the main features of the liquid drop calculations persist, important deviations from fig. 2 are present.

The most important deformation degrees of freedom in the fission process are elongation, necking, axial asymmetry and mass asymmetry,

i.e.  $\epsilon$ ,  $\epsilon_4$ ,  $\gamma$  and  $\epsilon_3$  in the modified oscillator parametrization. However, a full variation of all these parameters has not been carried out even at angular momentum zero, (see section 4 below) and at non-zero angular momenta it has been necessary to impose even more restrictions. Thus, the shell energy variation as a function of the mass asymmetry degree of freedom has still not been investigated at high spin. Furthermore, in ref. [5] where the barriers of superheavy nuclei were calculated,  $\epsilon_4$  was included only in the liquid drop part. In ref. [10], where translead nuclei were considered,  $\epsilon_4$  was included also in the shell energy part but not allowed to vary freely. In refs. [55,32] on the other hand, where different nuclei with  $A \geq 150$  were investigated, the elongation and necking degrees of freedom were allowed to vary independently, but the  $\gamma$  degree of freedom was neglected in the barrier calculations.

The potential-energy surfaces of the nuclei  $^{214,218}\text{Th}$ , presented in fig. 14 above, were drawn in the  $(\epsilon, \gamma)$ -plane with  $\epsilon_4$  implicitly included. It is seen that for  $^{218}\text{Th}$  and for spin values  $I = 0-80$ , the outer barrier is lowered around 2 MeV by the inclusion of the  $\gamma$  degree of freedom. For  $^{214}\text{Th}$  on the other hand, the fission proceeds at  $\gamma \approx 0$ . Thus, for this latter nucleus, we show in fig. 20 the outer part of the fission barrier in the  $(\epsilon, \epsilon_4)$ -plane calculated for  $\gamma = 0$ . In addition, in this figure the full coupling between the different  $N_t$ -shells has been included, which is not the case in fig. 14. In fig. 20 also the liquid drop barrier is shown, and at least in the region  $\epsilon = 0.5-1.0$  it is a very good approximation to fix  $\epsilon_4$  at the value given by the liquid drop. It is also the general conclusion from calculations at  $I = 0$  that a full variation of  $\epsilon_4$  is important only at the ground state, while the liquid drop energy for the outer parts of the barrier is so stiff in the  $\epsilon_4$  direction that the shell energy variation as a function of  $\epsilon_4$  is of minor importance.

It is now possible to construct the path to fission for  $^{214}\text{Th}$  and in fig. 21 the heights of the first and the second barriers are exhibited. These barriers are calculated with respect to the first minimum, which remains lowest up to angular momentum  $I = 80$ . For the nucleus  $^{214}\text{Th}$  the neutron separation energy is 9.4 MeV (at  $I = 0$ ). In fig. 21 the higher of the two fission barriers has about this height at  $I = 40-50$ , which

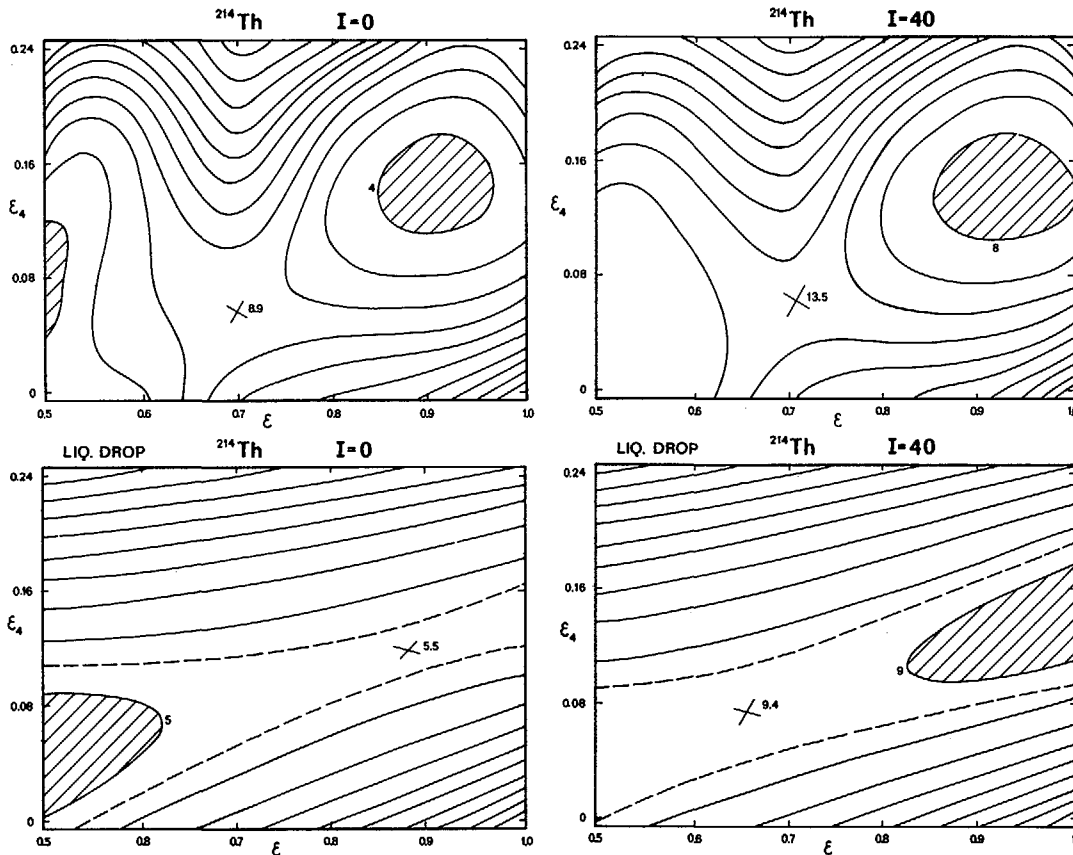


FIG.20. Total potential energy in the M.O. model and liquid-drop energy surfaces for  $^{214}\text{Th}$  at  $I = 0$  and  $I = 40$ . The outer part of the fission barrier is exhibited in the  $(\epsilon, \epsilon_4)$ -plane at  $\gamma = 0$ . The separation between the full lines is 2 MeV and the numbers refer to the excitation above the energy of the spherical liquid drop at  $I = 0$ .

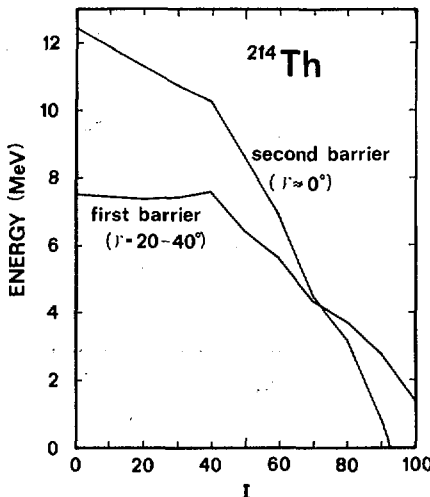


FIG.21. The calculated heights of the first and second barriers of  $^{214}\text{Th}$  as functions of angular momentum (see Figs 14 and 20). The heights refer to the first minimum, which remains lowest up to  $I = 80$ .

is thus expected to be the maximum angular momentum of yrast states populated in heavy ion reactions.

For nuclei in the translead region, the average neutron separation energy is around 8 MeV. The spin value corresponding to this height of the fission barrier is exhibited for an extended region of nuclei in fig. 22. Note that in view of the criterion above, it seems impossible to study high spin states in heavy ion reactions for nuclei beyond thorium, as the fission barrier shows a sudden drop around proton number 90.

The fission barrier of nuclei with  $x$ -values much smaller than that for  $^{214}\text{Th}$  cannot be very accurately calculated in the  $(\varepsilon, \varepsilon_4)$  parametrisation of the modified oscillator model. However, the parametrisation used by Faber, Ploszajczak and Faessler [32] is applicable also for somewhat lighter nuclei. Their results for  $^{194}\text{Pb}$ , calculated in the  $(\beta, r)$ -plane, are shown in fig. 23. Here  $\beta$  corresponds to elongation and  $r$  to necking. In this parametrisation, the shape is spherical at  $\beta = 0$  and  $r = 1.0$  while  $\beta > 0$  and  $r < 1$  corresponds to a necked-in prolate shape. A Woods-Saxon potential is employed and  $\gamma$  is set equal to zero. We see that the barrier decreases monotonically with

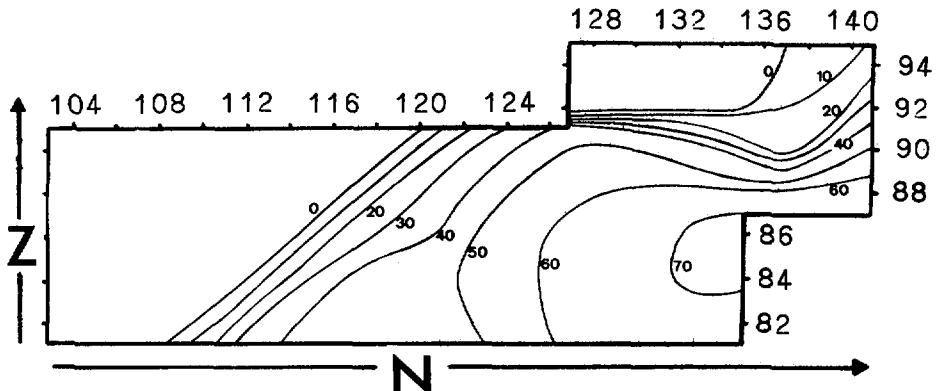


FIG.22. Contour diagram indicating at which spin value the calculated fission barrier is 8 MeV high (from Ref. [10]).

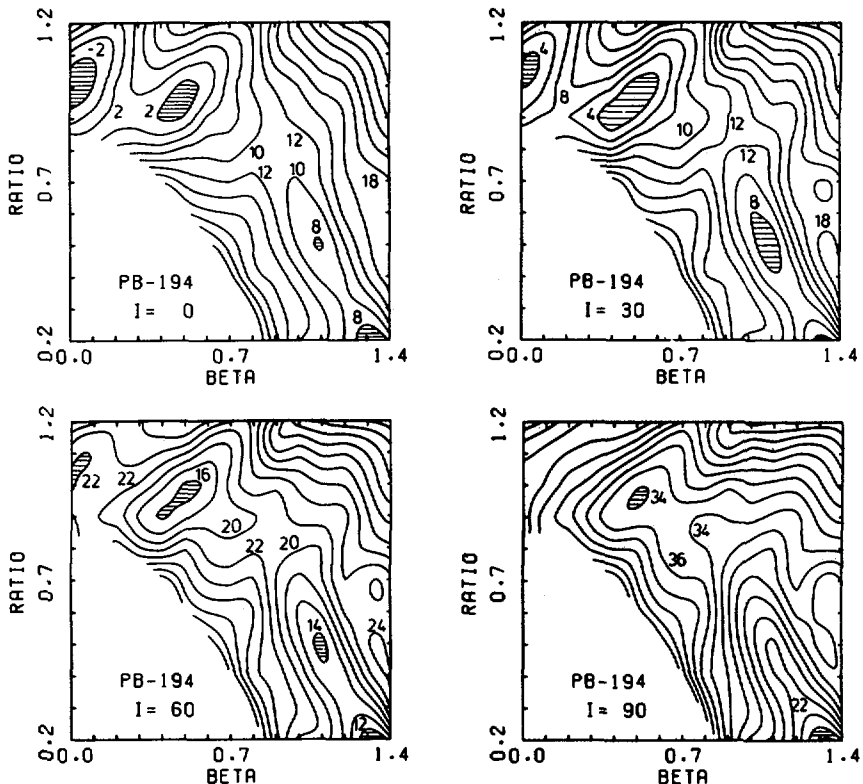


FIG.23. Potential-energy surface for  $^{194}_{\text{Pb}} \text{Pb}_{112}$ , obtained in the  $\beta, r$  ( $\gamma = 0^\circ$ ) plane with a Woods-Saxon potential for angular momenta  $I = 0, 30, 60$  and  $90$ . A shaded area indicates a local minimum. The contour lines are separated by 2 MeV. They are labelled in MeV relative to the energy of the spherical liquid drop at  $I = 0$  (from Ref. [32]).

spin and has the approximate set of values 14, 9, 6 and 1 MeV for spin values 0, 30, 60 and 90. In addition, at angular momentum around 20, there is a change to a new lowest minimum at  $\beta \approx 0.4$ . The shell structure of this deformed minimum was (in the case of  $I = 0$ ) first discussed by Tsang and Nilsson [56].

A general observation is that with shell structure included, a shell energy pocket is usually formed somewhere in the deformation plane, and the fission barrier disappears at a much higher spin value than is the case for the pure liquid drop model. Another general observation, exemplified in figs. 7 and 8 and in shell energy plots of ref. [32], is that the shell energy does not vary strongly with spin for heavy nuclei. This can be understood as a consequence of the fact that the rotational frequency at a given angular momentum is proportional to  $A^{-5/3}$ , while the strongest individual response to the rotation from any orbital is related to the maximum  $l$ -values which go roughly as  $A^{1/3}$ . In addition, the moment of inertia is augmented at large deformations, which further reduces the frequency at given spin. The variation with spin of the fission barriers in heavy nuclei is thus mainly determined by the rotating liquid drop.

### 3.4. Superheavy elements at high angular momenta

After a fusion reaction leading to the superheavy region, the compound system that might be formed would be highly excited above the yrast line and would carry a fairly high angular momentum. The deexcitation to the yrast region takes place under competition between fission, particle evaporation and gamma decay. If the nucleus reaches the yrast line, there is still competition between the different decay modes.

Fig. 24 shows the potential energy surfaces for  $^{298}114$  at some different spins. The  $I = 0$  ground state shape is found to be spherical. At all spin values the rotation is calculated to take place around the oblate symmetry axis. The fission barrier decreases with increasing spin, but at  $I = 60$  it is still almost 4 MeV. Fig. 25 shows the calculated yrast spectrum of this hypothetical nucleus and spin isomeric states, marked by arrows, are calculated to occur at remarkably high spins. The lower part of the figure shows the equilibrium deformation at each spin.

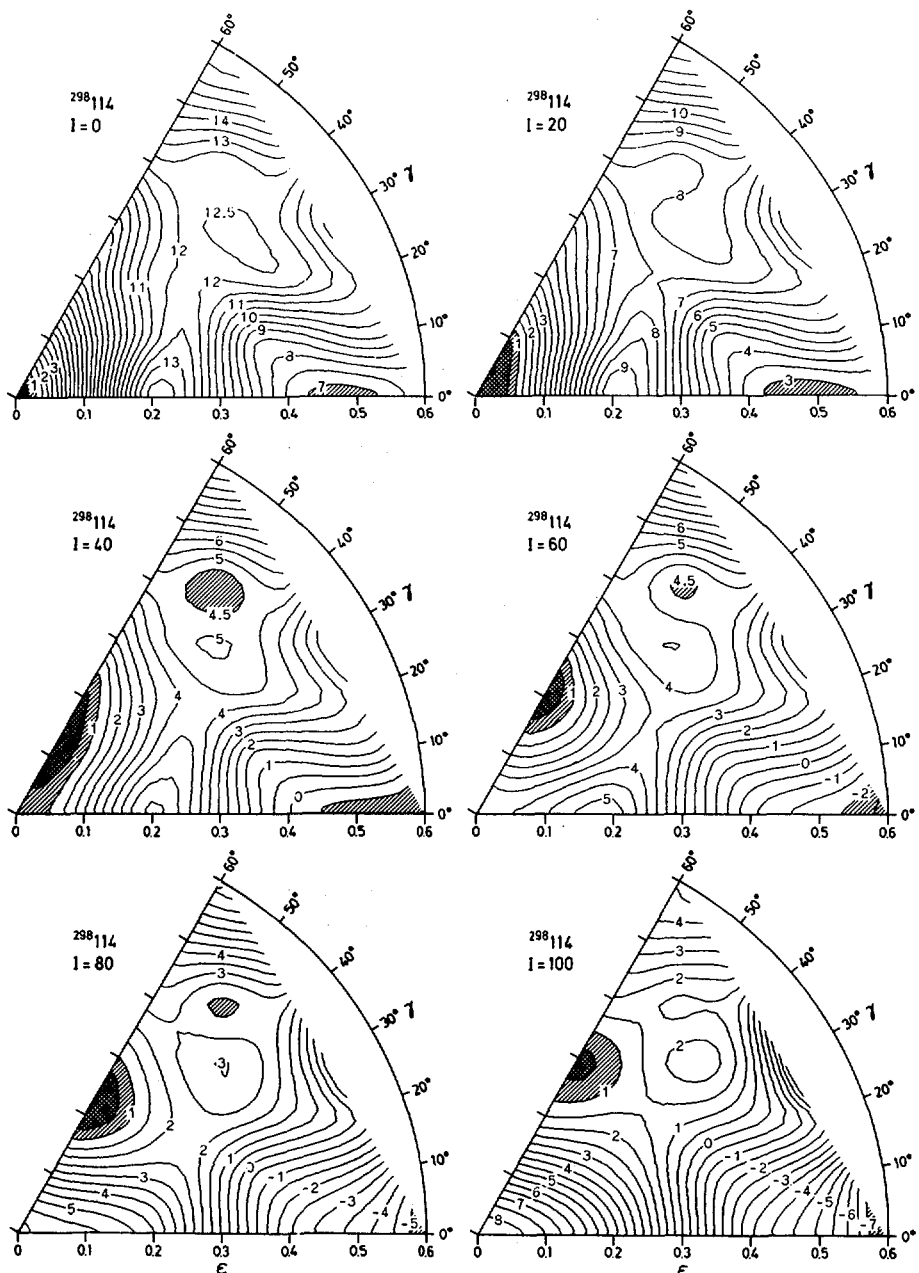
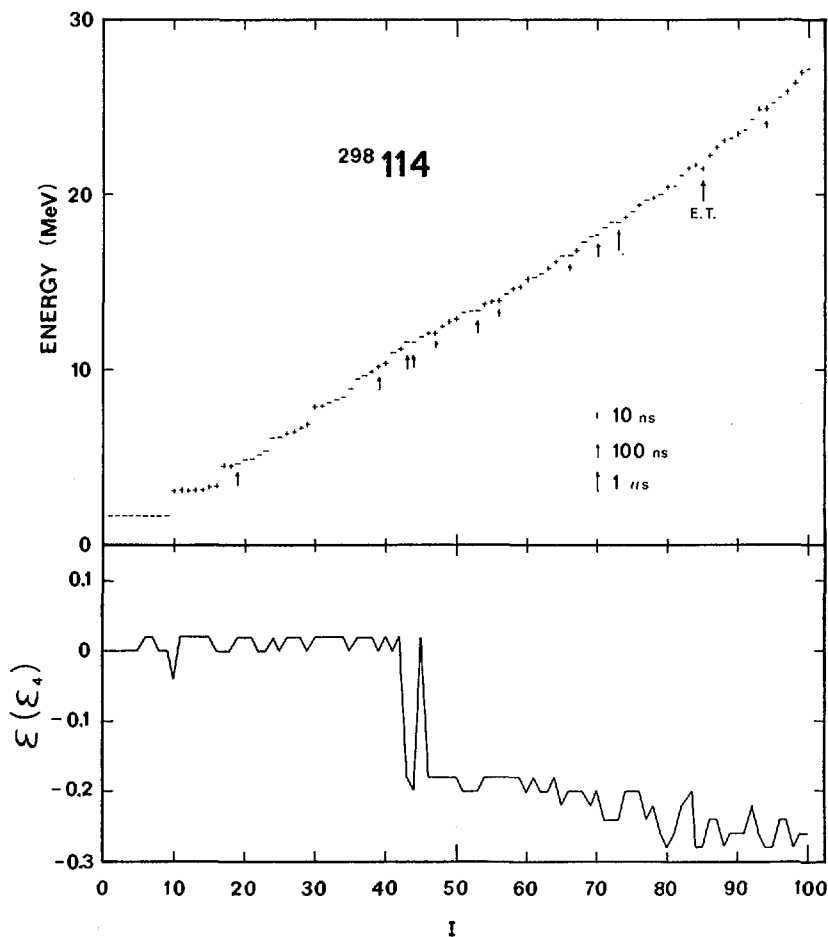


FIG. 24. The potential energy surface in the  $(\epsilon, \gamma)$ -plane for the super-heavy nucleus  $^{298}114$ . With increasing spin, the lowest minimum moves out on the oblate and thus there is barrier towards fission even at very high spins (from Ref. [5]).



**FIG.25.** Similar to Fig. 16, but for  $^{298}114$ . States with relatively long estimated  $\gamma$  decay times are marked by arrows, whose lengths differentiate between orders of magnitude in the estimates as indicated in the figure. The abbreviation E.T. stands for energy trap (from Ref. [58]).

Note the shape transition at spin 43-46 from sphericity to an oblate deformation with  $\epsilon = -0.2$ . This change in deformation gives rise to some traps since the spherical intrinsic configurations are very different from the intrinsic configurations of the lowest deformed states.

In the  $I = 0$  ground state the nucleus  $^{298}114$  is calculated to have a long fission half-life ( $\tau_{1/2} \approx 10^8$  y) and to decay primarily by alpha-emission with a half-life of about 0.1 years [57]. But as the fission

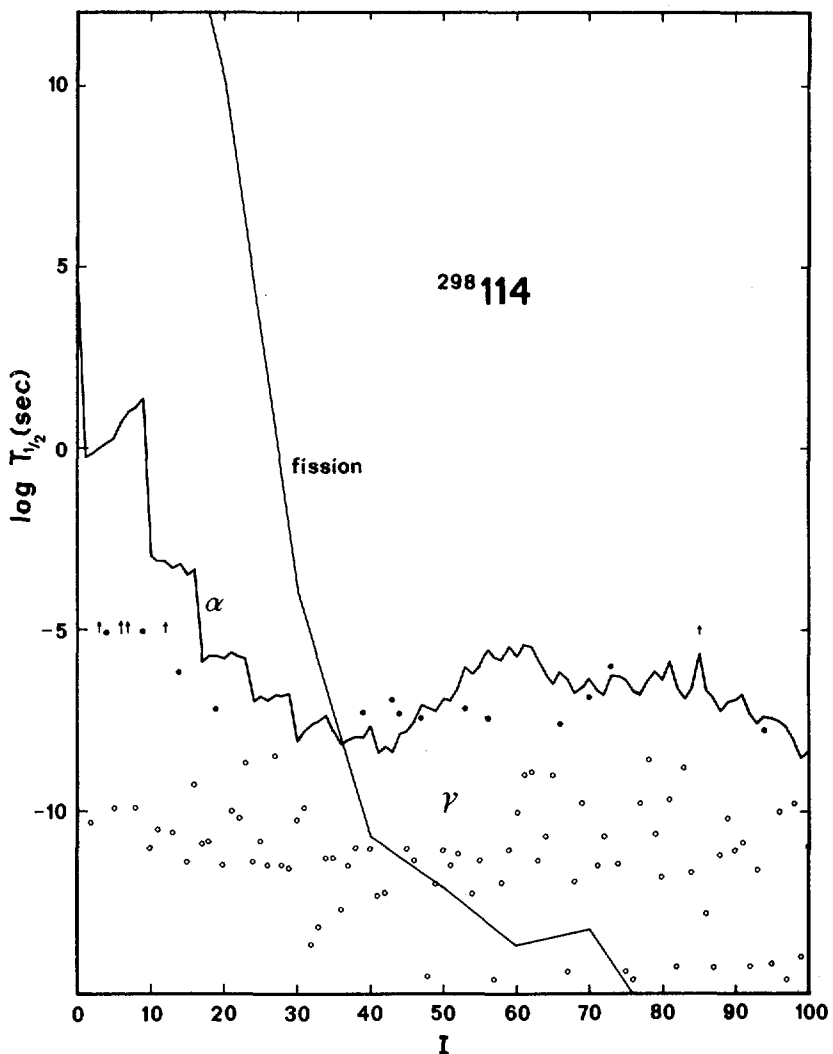


FIG. 26. Similar to Fig. 19, but for  $^{298}\text{114}$ . In addition, the arrows signify energy traps with respect to  $\gamma$  decay, and the steeply down-sloping line shows the estimated half-life for penetration of the calculated fission barrier (from Ref. [58]).

barrier decreases with increasing angular momentum, the nucleus rather goes to fission than to the ground state through electromagnetic transitions. There is also a competition from alpha decay in the high-spin states. Fig. 26 shows crudely calculated [58] half-lives of fission, alpha decay and gamma decay along the yrast line for  $^{298}\text{114}$ . Gamma decay is seen to be the fastest decay mode along the yrast line up to  $I \approx 40$ . If the compound nucleus reaches the yrast line with an angular momentum above 40, it would fission with a very short half-life. It is only in the  $I = 0$  state that alpha decay is calculated to be the fastest decay mode. Finally, let us recall that the discussion above is applicable only after the compound system has reached the yrast line.

#### 4. THE STRUCTURE OF THE SECOND PEAK IN THE FISSION BARRIER

We have seen above how the nuclear potential-energy surface behaves as a function of shape variables such as elongation, axially asymmetric distortions and necking coordinates. We have also seen that the surfaces depend strongly on the spin of the nucleus. From such potential-energy surfaces "fission barriers" can be determined.

At the last IAEA meeting in Rochester it was seen that without rotation the calculated heights of the first and second barrier peaks and the second minimum are in good agreement with experimental values for these quantities, except perhaps for the so called "thorium anomaly" in the light actinide elements (c.f. the review of ref. [59]). The experimental barriers are mostly determined by use of statistical models, which will be discussed in more detail in other contributions to this meeting [60-62]. Here we shall examine some new results on the second barrier obtained from such statistical models and macroscopic-microscopic calculations.

At the last meeting in Rochester it was suggested by Nix [59] that the resolution of the thorium anomaly was perhaps an interpretation of the experimental results in terms of a shallow third minimum splitting the asymmetric saddle into two asymmetric saddle points. Such structures had been observed in some calculations [59,63,64]. Since then, this interpretation has received new support from additional experimental results [65,66].

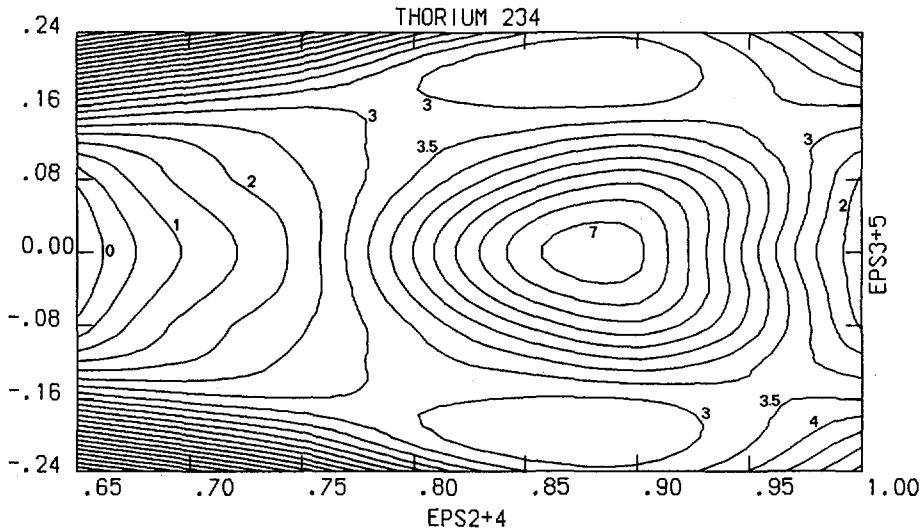


*FIG. 27. The mass-asymmetric second fission barrier for  $^{234}\text{Th}$  calculated at zero angular momentum in the M.O. model. The potential energy surface is shown as a function of  $\epsilon$  with  $\epsilon_4$  implicitly included and  $\epsilon_3$  with  $\epsilon_5$  implicitly included. The droplet model is used for the macroscopic energy.*

Fig. 27 exhibits a potential-energy surface for  $^{234}\text{Th}$  in the region of second saddle point. The potential energy is calculated by the macroscopic-microscopic method as a function of elongation-necking and mass-asymmetric shape coordinates. The line  $\text{EPS}3+5 = 0.00$  corresponds to symmetric shapes. We see that the mass-asymmetric shape degree of freedom lowers the height of the second saddle considerably. Furthermore, for each of the two equivalent cases  $\epsilon_3 > 0$  and  $\epsilon_3 < 0$  the second symmetric saddle is split into two asymmetric saddles, separated by a shallow minimum which lies about 0.6 MeV lower than the lowest of these two asymmetric saddle points. A modified oscillator potential underlies the microscopic energy in fig. 27, and the macroscopic energy is evaluated with the droplet model. The details of the calculation are discussed in ref. [59]. In a calculation that is similar, but employs the Yukawa-plus-exponential model for the macroscopic energy, it is found [67] that the minimum lies 1.2 MeV deeper than the lowest of the two asymmetric saddle points. In comparisons with experiment, a zero-point energy should be added to these two theoretical values for the depth. Ref. [66] gives the

experimental barrier parameters for  $^{233}\text{Th}$  as follows. Relative to the ground-state the height of the first barrier  $E_A = 4.0 \text{ MeV}$ , the energy at the second minimum  $E_{II} = 2.0 \text{ MeV}$ , the two mass-asymmetric saddle-points lie at  $E_B = 6.2 \text{ MeV}$  and  $E_C = 7.0 \text{ MeV}$  and at the intermediate minimum  $E_{III} = 5.7 \text{ MeV}$ . The calculations with the Yukawa-plus-exponential model for the macroscopic energy give, for  $^{232}\text{Th}$ , the values  $E_A = 4.9 \text{ MeV}$ ,  $E_{II} = 3.6 \text{ MeV}$ ,  $E_B = 8.1 \text{ MeV}$ ,  $E_{III} = 7.7 \text{ MeV}$  and  $E_C = 8.7 \text{ MeV}$ . These values include a zero-point energy of 0.5 MeV at the minimum. The shallow third minimum obtained with the droplet model for the macroscopic energy cannot hold a zero-point energy of this commonly adopted magnitude. Therefore we now give the results for  $^{232}\text{Th}$ , obtained with the droplet model and without the addition of a zero-point energy at the minima. The results are  $E_A = 4.6 \text{ MeV}$ ,  $E_{II} = 2.3 \text{ MeV}$ ,  $E_B = 6.9 \text{ MeV}$ ,  $E_{III} = 6.6 \text{ MeV}$  and  $E_C = 7.9 \text{ MeV}$ . Both sets of calculated values are a little high but the general structure in the barrier is compatible with the experimental data. In particular we note that the third minimum is more strongly developed with the Yukawa-plus-exponential model, in agreement with the experimental data.

Recently additional facts have been learned, which suggest a further complexity of the potential-energy surface around the second saddle. Namely, it has been possible to fit  $^{238}\text{U}(\gamma, f)$  data [68,69], to give fission probability distributions  $P_f(E_{\text{exc}})$  in the 7-11 MeV region, when the theoretically derived enhancements [70,71] of the level density due to low-lying collective rotations are accounted for. The role of the symmetry of the nuclear shape for rotational contributions to the level density was discussed [70] at the last IAEA meeting in Rochester. At that time preliminary results showed that the empirical values of  $\Gamma_f/\Gamma_n$  were considerably larger than the theoretical estimates. It was speculated that this might be due to axial asymmetry at the second saddle point and a corresponding increase in the level density.

Let us now follow the line of ref. [69] from which we have taken fig. 28. The lower part of the figure shows fits to resonance data for  $^{238}\text{U}$  using the resonant statistical model described in ref. [72]. This fit determines  $E_A$  and  $E_B$  for the  $K^\pi = 0^-$  and  $0^+$  bands. The character of the parity splitting is consistent with a mass-symmetric first barrier and a mass-asymmetric second barrier. After this fit no free parameters are

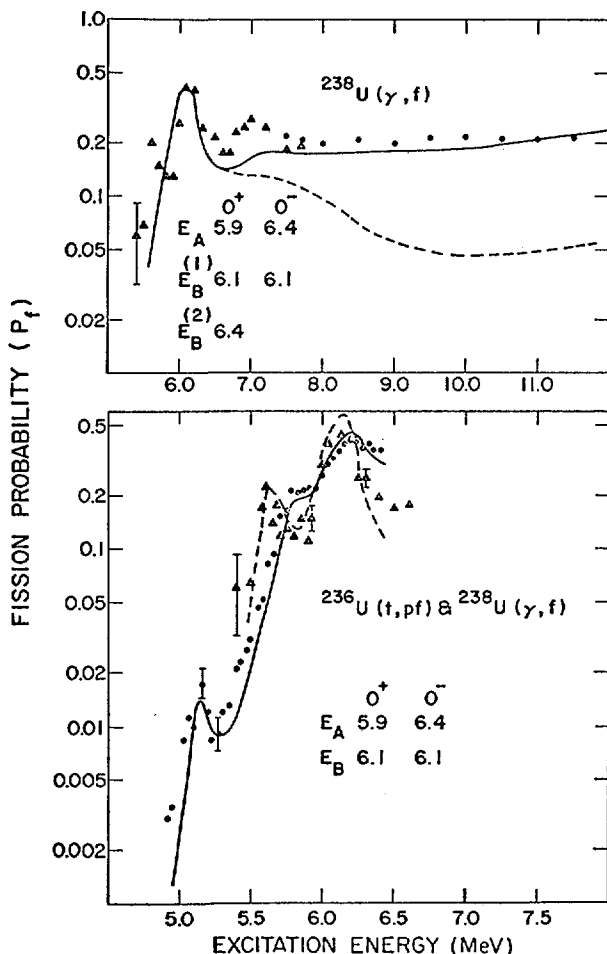


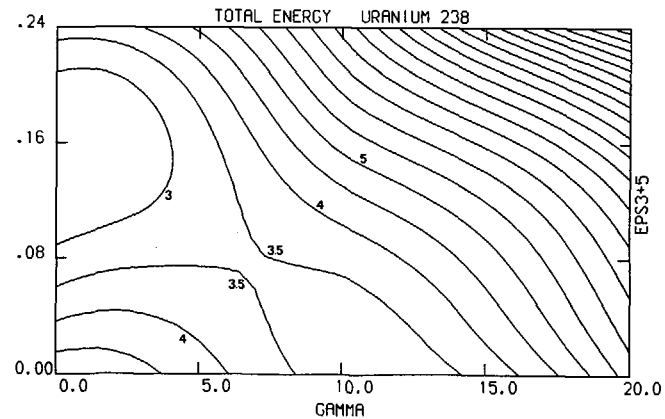
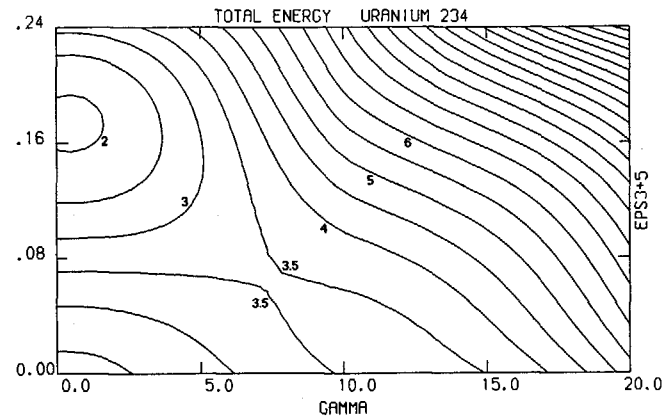
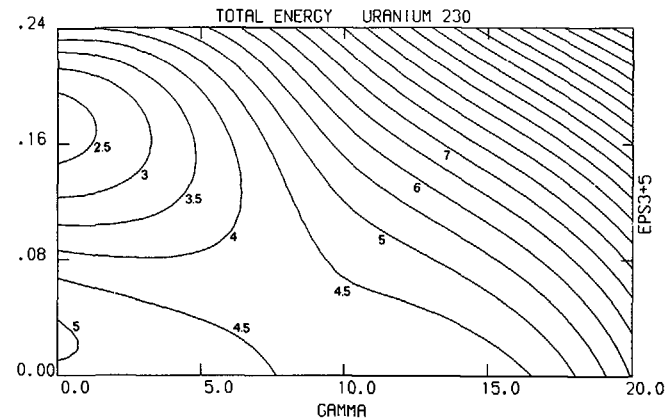
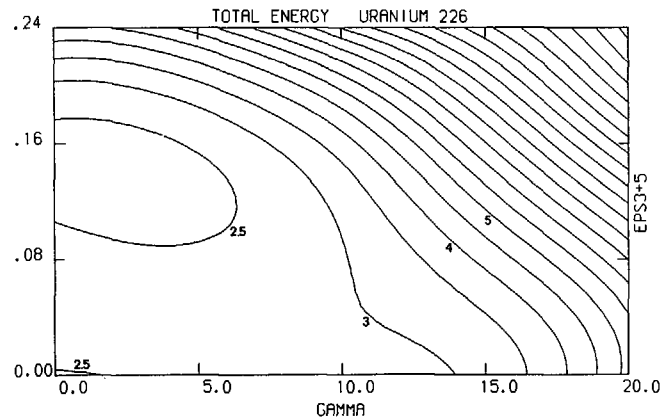
FIG. 28. Fits to  $^{238}\text{U}$  fission-probability data with microscopic statistical models. The lower figure exhibits resonant fits to low-energy ( $t, \text{pf}$ ) (solid circles, solid line) and ( $\gamma, \text{f}$ ) (solid triangles, dashed line) data. The upper figure shows non-resonant fits to the photofission data assuming only a mass-asymmetric second barrier,  $E_B^{(1)}$ , dashed curve, and assuming an additional parallel fission path over an additional axial asymmetric barrier,  $E_B^{(2)}$ , solid curve. Barrier heights (in MeV) are listed for the lowest  $K^\pi = 0^+$  and  $0^-$  channels in each case (from Ref. [69]).

available to fit the data in the higher-energy region 7-11 MeV. The results at these energies are shown in the upper part of the figure. The nonresonant statistical model [68], with the barrier parameters determined in the lower part of the figure and the assumption of axial symmetry, leads to the dashed curve for  $P_f$  in the upper part figure. The resulting theoretical fission probabilities  $P_f$  are about 4 times lower than the experimental data. The solid line in the upper figure results if it is assumed that there exists an additional axially asymmetric saddle  $E_B^{(2)}$  whose height is adjusted to obtain an optimum fit in the region 7-11 MeV. One then finds that  $E_B^{(2)}$  is higher than the mass-asymmetric saddle by 0.3 MeV. The existence of the axially asymmetric saddle would increase the level density substantially at high energies.

In fig. 29 we show some calculations of the potential energy, in the vicinity of the second saddle, where both  $\epsilon_3$  (octupole) and  $\gamma$ -deformations are included simultaneously. The results for  $^{238}\text{U}$  fit nicely into the picture suggested by the analysis above of the experimental data. The minimum on the  $\gamma$ -axis would correspond to the saddle point whose energy has been denoted  $E_B^{(2)}$ , and the minimum on the  $\epsilon_3$  axis is the usual mass-asymmetric saddle point ( $E_B$ ) in the  $\epsilon_2-\epsilon_3$  plane.

The  $\epsilon_3$ - and  $\gamma$ -instabilities of the second barrier reflect the distribution of the single-particle orbitals and their quantum numbers. Fundamentally, the positive shell energy at the second barrier is due to the high level density caused by the crossing of the  $N = 4, n_z = 0$  orbitals with those having  $N = 5, n_z = 1$ . This crossing occurs at  $\epsilon = 0.8 - 0.9$  and for neutron numbers in the region of  $N = 150$ , see fig. 16 of ref. [7]. The  $\epsilon_3$ -instability is then caused by the strong  $Y_{30}^-$  coupling between these groups of orbitals as was first discussed in refs. [73, 18]. As a consequence of this coupling, the orbitals are split away from the region of high level density and the shell energy becomes lower at  $\epsilon_3 \neq 0$ . In a similar way, the strong matrix elements of  $Y_{22}$  within the groups of orbitals with  $N = 4, n_z = 0$  and  $N = 5, n_z = 1$  respectively give rise to the  $\gamma$ -instability. Thus, from the single-particle diagram referenced above it is possible to get a rough estimate of the neutron numbers where the different instabilities are to be expected.

## SECOND SADDLE EPS2= 0.85 EPS4= 0.12



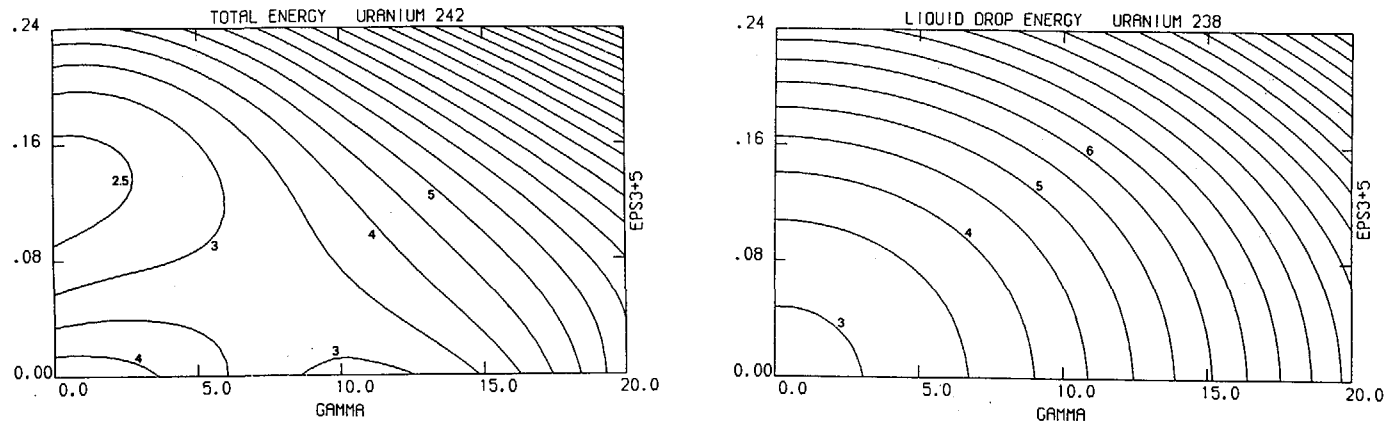


*FIG.29. Potential energy surfaces for a series of uranium isotopes, calculated with fixed values of  $\epsilon$  and  $\epsilon_4$  that correspond to the second barrier. The variables along the axes are mass asymmetry ( $\epsilon_3/\epsilon_5$ ) and axial asymmetry ( $\gamma$ ). In the lower right figure, the corresponding liquid-drop energy for one of the isotopes ( $^{238}\text{U}$ ) is shown. The contour line separation is 0.5 MeV.*

The systematics in the structure of the calculated potential energy as the neutron number varies through some uranium isotopes is shown in fig. 29. The surface for  $^{226}\text{U}$  is essentially stable but very soft with respect to both mass-asymmetric and axially asymmetric distortions. The surface for  $^{230}\text{U}$  is unstable with respect to both types of shape distortions, as are also the remaining total-energy surfaces. The liquid-drop model energy-surface, on the other hand, is stable with respect to both types of distortions. From the total energy surfaces we see that the decrease in energy is larger in the  $\epsilon_3$  direction than in the  $\gamma$  direction for all the neutron numbers studied. In the analysis of the experimental data for  $^{238}\text{U}$ , a difference of 0.3 MeV was found between the axially asymmetric saddle point and the mass-asymmetric saddle point [69] which roughly agrees with the calculated difference of 0.7 MeV. From this figure we also see that for the lighter isotope  $^{234}\text{U}$  the calculated difference between the two saddle points is almost 1.5 MeV. Therefore a more decisive test of the interpretation of the data in terms of asymmetries favoured by the potential energy around the second barrier would be obtained if the experiments discussed in ref. [69] were to be extended to for example this nucleus.

## REFERENCES

- [ 1 ] COHEN, S., PLASIL, F., SWIATECKI, W.J., Ann. of Phys. 82 (1974) 557.
- [ 2 ] BOHR, A., MOTTELSON, B.R., Phys. Scripta 10A (1974) 13.
- [ 3 ] BENGTSSON, R., LARSSON, S.E., LEANDER, G., MÖLLER, P., NILSSON, S.G., ÅBERG, S., SZYMAŃSKI, Z., Phys. Lett. 57B (1975) 301.
- [ 4 ] NEERGÅRD, K., PASHKEVICH, V.V., Phys. Lett. 59B (1975) 218.
- [ 5 ] ANDERSSON, C.G., LARSSON, S.E., LEANDER, G., MÖLLER, P., NILSSON, S.G., RAGNARSSON, I., ÅBERG, S., BENGTSSON, R., DUDEK, J., NERŁO-POMORSKA, B., POMORSKI, K., SZYMAŃSKI, Z., Nucl. Phys. A268 (1976) 205.
- [ 6 ] NEERGÅRD, K., PASHKEVICH, V.V., FRAUENDORF, S., Nucl. Phys. A262 (1976) 61.
- [ 7 ] RAGNARSSON, I., NILSSON, S.G., SHELINE, R.K., Phys. Rep. 45 (1978) 1.

- [ 8] RAGNARSSON, I., Phys. Lett. 80B (1978) 4.
- [ 9] DÖSSING, T., NEERGÅRD, K., MATSUYANAGI, K., HSI-CHEN CHANG, Phys. Rev. Lett. 39 (1977) 1395.
- [10] ANDERSSON, C.G., HELLSTRÖM, G., LEANDER, G., RAGNARSSON, I., ÅBERG, S., KRUMLINDE, J., NILSSON, S.G., SZYMANSKI, Z., Nucl. Phys. A309 (1978) 141.
- [11] PEDERSEN, J., BACK, B.B., BERNTHAL, F.M., BJØRNHOLM, S., BORGREEN, J., CHRISTENSEN, O., FOLKMANN, F., HERSKIND, B., KHOO, T.L., NEIMAN, M., PÜHLHOFER, F., SLETTEN, G., Phys. Rev. Lett. 39 (1977) 990.
- [12] Proc. Conf. on High Spin Phenomena in Nuclei, Argonne, 1979.
- [13] KLEINHEINZ, P., Proc. Hirschegg workshop 1979.
- [14] KHOO, T.L., BERNTHAL, F.M., ROBERTSSON, R.G.H., WARNER, R.A., Phys. Rev. Lett. 37 (1976) 823.
- [15] BOHR, A., MOTTELSON, B.R., Proc. Conf. on Nuclear Structure, Tokyo 1977, p. 157.
- [16] BOHR, A., MOTTELSON, B.R., Nuclear Structure, vol. 2 (Benjamin, New York, 1975).
- [17] FABER, M., LEANDER, G., PŁOSZAJCZAK, M., RAGNARSSON, I., to be published.
- [18] GUSTAFSSON, C., MÖLLER, P., NILSSON, S.G., Phys. Lett. 34B (1971) 349.
- [19] STRUTINSKY, V.M., Nucl. Phys. A95 (1967) 420.
- [20] NILSSON, S.G., TSANG, C.F., SOBICZEWSKI, A., SZYMAŃSKI, Z., WYCECH, S., GUSTAFSSON, C., LAMM, I.-L., MÖLLER, P., NILSSON, B., Nucl. Phys. A131 (1969) 1.
- [21] FAESSLER, A., HILTON, R.R., SANDHYA DEVI, K.R., Phys. Lett. 61B (1976) 133.
- [22] PŁOSZAJCZAK, M., SANDHYA DEVI, K.R., FAESSLER, A., Z. Physik A282 (1977) 267.
- [23] POMORSKI, K., NERŁO-POMORSKA, B., Z. Physik A283 (1977) 383.
- [24] ÅBERG, S., Proc. Varenna Summer School, 1976 (North-Holland, Amsterdam 1977) p. 473.
- [25] NEERGÅRD, K., TOKI, H., PŁOSZAJCZAK, M., FAESSLER, A., Nucl. Phys. A287 (1977) 48.

- [26] FAESSLER, A., PLOSZAJCZAK, M., SANDHYA DEVI, K.R., WAKAI, M., Proc. Int. Conf. Nucl. Struct., Contributed Papers, Tokyo, September 5-10, 1977, J. Phys. Soc. Japan 44 (1978) Suppl. p. 613.
- [27] PLOSZAJCZAK, M., FAESSLER, A., LEANDER, G., NILSSON, S.G., Nucl. Phys. A301 (1978) 477.
- [28] GLAS, D., MOSEL, U., Phys. Lett. 78B (1978) 9.  
CHANDRA, H., MOSEL, D., Nucl. Phys. A298 (1978) 151.
- [29] PLOSZAJCZAK, M., TOKI, H., FAESSLER, A., J. of Phys. G, Nucl. Phys. Vol. 4 (1978) 743.
- [30] PLOSZAJCZAK, M., TOKI, H., FAESSLER, A., Z. Physik A287 (1978) 103.
- [31] FLECKNER, J., MOSEL, U., ZINT, P.G., preprint 1979.
- [32] FABER, M., PLOSZAJCZAK, M., FAESSLER, A., Nucl. Phys., to be published.
- [33] BAKTASH, C., DER MATEOSIAN, E., KISTNER, O.C., SUNYAR, A.W., Proc. Conf. on Nuclear Interactions, Canberra, 1978.
- [34] AGUER, P. et al., Z. Physik A285 (1978) 59.
- [35] FAESSLER, A., SANDHYA DEVI, K.R., GRÜMMER, F., SCHMID, K.W., HILTON, R.R., Nucl. Phys. A256 (1976) 106.
- [36] HORN, D., HÄUSSER, O., FAESTERMANN, T., MCDONALD, A.B., ALEXANDER, T.K., BEENE, J.R., HERRLANDER, C.J., Phys. Lett. 39 (1977) 389.
- [37] BLOMQVIST, J., at the Conf. on High-Spin Phenomena in Nuclei, Argonne 1979.
- [38] ÅBERG, S., LEANDER, G., to be published.
- [39] CERKASKI, M., DUDEK, J., SZYMAŃSKI, Z., ANDERSSON, C.G., LEANDER, G., ÅBERG, S., NILSSON, S.G., RAGNARSSON, I., Phys. Lett. 70B (1977) 9.
- [40] CERKASKI, M., DUDEK, J., ROZMEJ, P., SZYMAŃSKI, Z., NILSSON, S.G., Nucl. Phys. A315 (1979) 269.
- [41] ANDERSSON, C.G., ÅBERG, S., LEANDER, G., NEERGÅRD, K., current work.
- [42] LEANDER, G., ANDERSSON, C.G., NILSSON, S.G., RAGNARSSON, I., ÅBERG, S., ALMBERGER, J., DØSSING, T., NEERGÅRD, K., Proc. Conf. on High Spin Phenomena in Nuclei, Argonne 1979.
- [43] MATSUYANAGI, K., DØSSING, T., NEERGÅRD, K., Nucl. Phys. A307 (1978) 253.
- [44] DUDEK, J., Proc. Varenna Summer School, 1976 (North-Holland, Amsterdam 1977) p. 465.

- [45] ANDERSSON, C.G., KRUMLINDE, J., Nucl. Phys. A291 (1977) 21.
- [46] FAESSLER, A., PLOSZAJCZAK, M.. Phys. Rev. C16 (1977) 2032.
- [47] ÅBERG, S., Nucl. Phys. A306 (1978) 89.
- [48] FAESSLER, A., PLOSZAJCZAK, M., preprint 1978.
- [49] NEERGÅRD, K., DØSSING, T., MATSUYANAGI, K., Proc. Conf. on High Spin Phenomena in Nuclei, Argonne 1979.
- [50] BANG, J., KRUMLINDE, J., NILSSON, S.G., Phys. Lett. 15 (1965) 55.
- [51] KHOO, T.D., SMITHÉR, R.K., HAAS, B., HÄUSSER, O., ANDREWS, H.R., HORN, D., WARD, D., Phys. Rev. Lett. 41 (1978) 1027.
- [52] MERDINGER, J.C., BECK, F.A., BYRSKI, T., GEHRINGER, C., VIVIEN, J.P., BOZEK, E., STYCZEN, J., Phys. Rev. Lett. 42 (1978) 23.
- [53] HÄKANSSON, H.-B., ÅBERG, S., current work.
- [54] PLOSZAJCZAK, M., FABER, M., preprint 1979.
- [55] FABER, M., FAESSLER, A., PLOSZAJCZAK, M., TOKI, H., Phys. Lett. 70B (1977) 399.
- [56] TSANG, C.F., NILSSON, S.G., Nucl. Phys. A140 (1970) 275.
- [57] RANDRUP, J., LARSSON, S.E., MÖLLER, P., SOBICZEWSKI, A., ŻUKASIAK, A., Physica Scripta 10A (1974) 60.
- [58] MÖLLER, P., ÅBERG, S., to be published.
- [59] MÖLLER, P., NIX, J.R., Proc. Third IAEA Symp. on Physics and Chemistry of Fission, Rochester 1973, (IAEA, Vienna, 1974) Vol. 1, p. 103.
- [60] BRITT, H.C., Paper IAEA-SM/241-A1 these proceedings.
- [61] IGNATYUK, A.V., ISTEKOV, K.K., OKOLOVICH, V.N., SMIRENKO, G.N., Paper IAEA-SM/241-C9 these proceedings.
- [62] JUNKER, K., HABERMANN, J., MUKHODADHYAY, N.C., Paper IAEA-SM/241-C10 these proceedings.
- [63] PASHKEVICH, V.V., Nucl. Phys. A169 (1971) 275.
- [64] MÖLLER, P., Nucl. Phys. A192 (1972) 529.
- [65] BLONS, J., MAZUR, C., PAYA, D., Phys. Rev. Lett. 35 (1975) 1749.
- [66] CARUANA, J., BOLDEMAN, J.W., WALSH, R.L., Nucl. Phys. A285 (1977) 205.
- [67] MÖLLER, P., Paper IAEA-SM/241-C3 these proceedings.
- [68] GAVRON, A., BRITT, H.C., KONECNY, E., WEBER, J., WILHELMY, J.B., Phys. Rev. C13 (1976) 2374.
- [69] GAVRON, A., BRITT, H.C., GOLDSTONE, P.D., WILHELMY, J.B., LARSSON, S.E., Phys. Rev. Lett. 38 (1977) 1457.

- [70] BJØRNHOLM, S., BOHR, A., MOTTELSON, B.R., Proc. Third IAEA Symp. on Physics and Chemistry of Fission, Rochester 1973 (IAEA, Vienna, 1974) Vol. I, p. 367.
- [71] BOHR, A., MOTTELSON, B.R., Nuclear Structure, vol. 2 (Benjamin, New York, 1975) pp. 36, 127, 622.
- [72] BACK, B.B., HANSEN, O., BRITT, H.C., GARETT, J.D., Phys. Rev. C9 (1974) 1924.
- [73] JOHANSSON, S.A.E., Nucl. Phys. 22 (1961) 529.

## DISCUSSION

K.W. GOEKE: You base many of your conclusions on the potential energy surfaces at various angular momenta and as a function of  $\beta$ ,  $\gamma$ ,  $\epsilon_4$ , etc. Do you have any idea how the corresponding collective mass tensor behaves as a function of  $J$  and  $\beta$ ,  $\gamma$ ? I ask this as it is very difficult to predict the behaviour of the nucleus from the potential energy surface if the masses vary with  $\beta$ ,  $\gamma$ , ... and  $J$ , comparable with those of the potential energy surface. In such a case static considerations are not adequate and we have to take into account the dynamics of the process by solving collective Schrödinger equations.

S. ÅBERG: Most of my conclusions based on potential energy surfaces relate to the ground-state deformation at various angular momenta. In this case the mass parameters seem to be of less importance. This also applies to evaluation of the spin that may survive fission in a heavy-ion reaction, for which we made a rough comparison of the neutron separation energy and the calculated fission barrier. The only conclusion I drew, assuming that the mass parameters have a direct effect, relates to the fission half-lives for  $^{298}114$  at various spins. The  $B_r$  used in the calculation are not microscopically calculated, but obtained from fits to half-lives for actinide nuclei.

A. FAESSLER: You described the shrinking of the deformation of rare earth nuclei with increasing angular momentum, an effect which we have also found in our calculations if we disregard pairing correlations. We have recently developed a method of calculating the Strutinsky shell energy also for non-time-reversed states, as in the case of very high spin. The method is based on the Hartree-Fock-Bogolyubov approach and the calculations show that the pairing correlations prevent this anti-stretching effect.

M.E. FABER: Dr. Åberg, the staircase behaviour of the yrast levels obtained in your calculations stems from disregarding the residual part of the two-body interaction. By including these residual interactions we can increase the slope of the yrast line and ensure better agreement with the experimental data.

S. ÅBERG: Yes, there are certainly residual interactions present that are not accounted for in my calculations of the yrast spectra. But several other effects, as I discussed, may also alter the calculated spectrum for  $^{152}\text{Dy}$ . For example, states created by a non-aligned spin configuration are not very accurately described by this model. After projection of the desired angular momentum, these states are found in certain cases to have a wave function in which the original component is only represented by 40%.

K.M. DIETRICH (*Chairman*): I think we should keep in mind that so far all Hartree-Fock calculations, with  $\delta$  interactions as well as Gogny's finite range effective interaction, have produced secondary barriers that are too high. It does not seem likely that projections onto conserved quantities, such as the angular momentum, would lower the theoretical barrier heights enough to make them comparable with experimental barrier heights. So we are presumably faced with a theoretical problem to which we will just have to give more attention.



# THE FISSION BARRIER OF NUCLEI AT VERY HIGH ANGULAR MOMENTA

M.E. FABER\*

Institut für Kernphysik der TU Wien,  
Vienna, Austria

A. FAESSLER\*\*

Institut für Kernphysik, KFA Jülich,  
Jülich, Federal Republic of Germany

M. PLOSZAJCZAK

Institute of Nuclear Physics,  
Cracow, Poland

## Abstract

### THE FISSION BARRIER OF NUCLEI AT VERY HIGH ANGULAR MOMENTA.

The deformation energy surfaces of rotating nuclei are investigated within the Strutinsky shell correction approach extended to non-zero angular momenta. A cranked Woods-Saxon potential is used to calculate the shell corrections. The heights of the fission barriers of nuclei in the actinide region are studied as a function of the total angular momentum. The critical angular momenta at which the fission barriers vanish are found to be higher than those predicted by the rotating-liquid-drop model. Then, the shell effects are investigated for excited compound nuclei. It is shown that, by statistical excitation of particle-hole states, the shell effects decrease. Finally, the effect of finite angular momenta and finite temperatures on the mass distribution of fission fragments is discussed.

By heavy-ion reactions it is possible to bring high angular momenta into a compound nucleus. These high angular momenta cause strong Coriolis and centrifugal forces changing the behaviour of nuclei considerably. Cohen, Plasil and Swiatecki [1] investigated the equilibrium configurations of rotating liquid drops and predicted the limiting angular momenta for fission. For non-rotating nuclei it is very well known [2] that the shell

---

\* Present address: Institut für Kernphysik, KFA Jülich, D-5170 Jülich, Federal Republic of Germany.

\*\* Also: Physikalisches Institut, Universität Bonn, D-5300 Bonn, Federal Republic of Germany.

structure gives rise to the double-humped shape of the fission barrier. The aim of this work is: (i) to show the existence of strong shell effects for very high spins and to discuss their influence on the fission process, (ii) to study the effect of statistical excitations of the compound system on the fission barriers for high angular momenta, (iii) to discuss the effects of finite angular momenta and finite temperatures on the mass distributions of fission fragments.

We investigate the deformation energy surfaces of rotating nuclei within the Strutinsky shell correction method [2] extended for finite angular momenta [3,4]. The shell model Hamiltonian in the rotating system

$$H = T_{\text{kin}} + V_c^{\text{SW}}(\vec{r}) + V_{\text{so}}(\vec{r}) + \frac{1}{2} (1+\tau_3) V_{\text{Coul}}(\vec{r}) - \omega j_x$$

contains the kinetic energy  $T_{\text{kin}}$ , the Woods-Saxon shaped central potential  $V_c^{\text{SW}}(\vec{r}) = V_0 / \{1 + \exp[\ell(\vec{r})/a]\}$ , the spin-orbit potential  $V_{\text{so}}(\vec{r}) = -i\vec{\sigma}[\vec{\nabla}V_{\text{so}}^{\text{SW}}(\vec{r}) \times \vec{v}]$  and the Coulomb potential approximated by the uniformly charged drop with  $Z-1$  protons. The cranking term  $-\omega j_x$  takes into account the Coriolis and centrifugal forces. The zeros of the length function  $\ell(\vec{r}) = 0$  define the nuclear surface.

In dimensionless coordinates we describe the surface of necked nuclei by

$$u^2 p + v^2 / p = (1-w^2)(A+\alpha w+Bw^2)$$

and the bulged diamond-like [5] shapes by

$$u^2 p + v^2 / p = (1-w^2) \left[ A - (B - \alpha w) e^{-Qw^2} \right]$$

To show potential energy surfaces we are using instead of the unillustrative internal parameters  $A, B, P, Q$  the ellipsoidal parameters  $\beta$  and  $\gamma$  of Bohr and a neck parameter  $r$  [6]. The parameter  $r$  is defined as the ratio of the

cross-section of the necked (bulged) nucleus to the cross-section of the ellipsoid with same volume and same length of symmetry axis. The parameter  $\alpha$  allows for mass asymmetries.

Solving the Schrödinger equation for each set of deformation parameters  $q = \{\beta, \gamma, r, \alpha\}$  one gets the single particle energies  $\epsilon_i^\omega$  in the rotating coordinate system. The total energy  $R$  in the rotating frame and the total angular momentum  $I$  are splitted according to Strutinsky's prescription in a part  $\tilde{R}$  (resp.  $\tilde{I}$ ) varying smoothly with Fermi energy and mass number  $A$  and a part  $\delta R$  (resp.  $\delta I$ ) including the influences of the shell structure:

$$R(\omega) = \sum_{i=1}^A \epsilon_i^\omega = \tilde{R} + \delta R, \quad I(\omega) = \sum_{i=1}^A \langle j_x \rangle_{ii} = \tilde{I} + \delta I$$

Substituting the smooth quantities by the corresponding quantities of the rotating liquid drop model (RLDM) one gets the correct deformation and angular momentum dependence of the total energy in the laboratory system:

$$E = R + \omega I = \tilde{R} + \omega \tilde{I} + \delta R + \omega \delta I = \tilde{E} + \delta E \rightarrow E_{LD} + \omega \theta_{rig} \omega^2 / 2 + \delta E$$

$$I = \tilde{I} + \delta I \rightarrow I_{rig} + \delta I = \omega \theta_{rig} + \delta I$$

To investigate the influence of the shell effects on the fission process at high angular momenta we confine ourselves to the  $\beta$ - $r$  parameter space, thus to axially symmetric ( $\gamma=0$ ) and mass symmetric ( $\alpha=0$ ) nuclei rotating normal to the symmetry axis. In fig. 1a we show for  $^{232}\text{Th}$  the RLDM energy surface for the angular momentum  $I_{rig} = 60\hbar$ . As in all other parts of fig. 1, the equi-energy lines have distances of 2 MeV. For  $I_{rig} = 0$  the RLDM energy shows a minimum for the spherical shape ( $\beta=0$ ,  $r=1$ ). Increasing the prolate deformation ( $\beta>0$ ) the liquid drop model valley runs to necked nuclei ( $r<1$ ). The saddle at  $\beta=0.8$  and  $r=0.8$  is

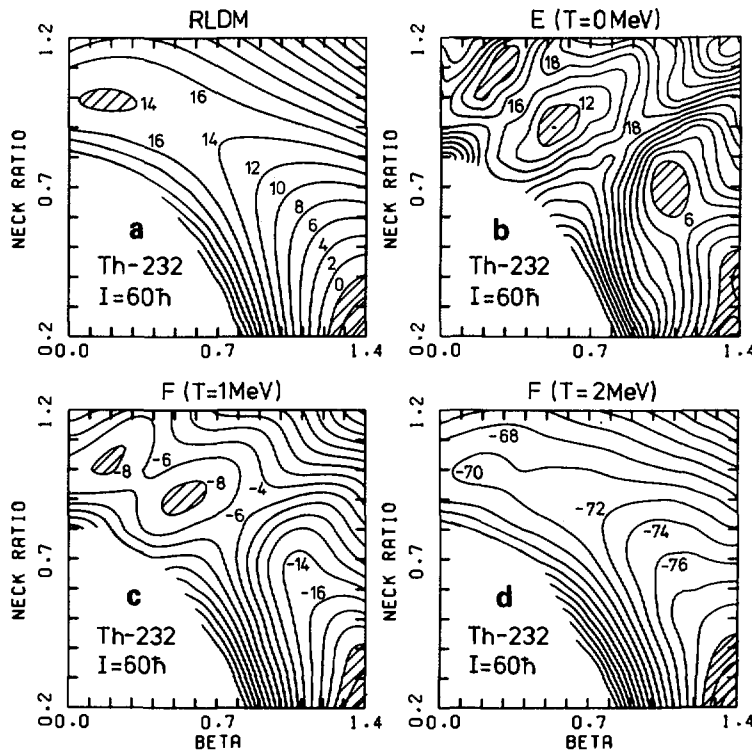


*FIG.1. Deformation energy surfaces of  $^{232}\text{Th}$  at  $I = 60\text{ h}$  for mass-symmetric and axially symmetric shapes in  $\beta$ - $r$  space:*

- a) total energy as given by the rotating-liquid-drop model;
- b) total energy with inclusion of shell corrections;
- c) free energy for  $T = 1 \text{ MeV}$ ;
- d) free energy for  $T = 2 \text{ MeV}$ .

5.5 MeV higher than the minimum. Increasing the angular momentum  $I_{\text{rig}}$  the liquid drop model saddle moves toward the spherical nucleus and the minimum moves to prolate deformations. The height of the fission barrier decreases. In fig. 1a one can clearly see the shallow shadowed minimum of  $\sim 0.5$  MeV at  $I_{\text{rig}} = 60\text{h}$ . Slightly above  $60\text{h}$  minimum and saddle point meet at  $\beta \approx 0.4$  and the fission barrier vanishes.

In the Strutinsky approach the total energy  $E$  is the sum of the RLDM energy,  $E_{\text{LD}} + \Theta_{\text{rig}} \omega^2/2$ , and the shell corrections  $\delta E = \delta R + \omega \delta I$ . The total

energy surface of  $^{232}\text{Th}$  is shown in fig. 1b for  $I = I_{\text{rig}} + \delta I = 60\hbar$ . For  $I=0$  the shell corrections have large positive values of 13.7 MeV for the spherical shape, show three parallel valleys of negative shell corrections (-2 to -6 MeV) and two parallel ridges of hills of positive shell corrections (3 to 5 MeV), leading with increasing prolate deformation  $\beta$  to larger neck cross-sections  $r$ . The negative shell corrections determine the positions of the minima in the deformation energy surface, the hills the first and second fission barrier. With increasing angular momentum the shell corrections for a given deformation point may change, the gross structure of shell corrections remains, however, constant. Even for angular momenta of the order of  $100\hbar$  this gross structure is unchanged. The most significant changes of shell corrections with angular momentum are close to the spherical shape. For  $I=0$ , the strong positive shell corrections press the first minimum against diamond-like shapes. These strong positive shell corrections vanish with increasing angular momentum and change sign at around  $70\hbar$ . At  $\sim 90\hbar$  the first minimum becomes spherical. Since the liquid drop model fission barrier decreases with increasing angular momentum, the height of the double-humped fission barrier is also decreasing. However, only far above  $100\hbar$  the descent of the liquid drop model is strong enough to compensate for the oscillations of the shell corrections and to get rid of the fission barriers. The minima of the total energy and the beginning of the fission valley in fig. 1b are again shadowed. For the angular momentum of  $60\hbar$  because of the centrifugal forces the second minimum is already slightly deeper than the first minimum. The total height of the barrier for symmetric fission is 9 MeV, higher than the liquid drop barrier for  $I=0$  of 5.5 MeV, whereas the liquid drop barrier for  $I=60\hbar$  is already vanishing.

We can conclude that the shell effects preserve the fission barriers up to very high angular momenta ( $>100\hbar$ ). If in some fusion reactions

critical angular momenta for fission are measured and are found to be comparable to the liquid drop values, there must be an additional influence. The reason is that these experiments produce highly excited compound nuclei containing a large number of particle hole excitations.

To investigate the influence of excitations of the compound nucleus one has to extend the shell correction approach to finite temperatures. In the framework of the grand canonical ensemble one describes the distribution of nuclear states by the statistical operator

$$\Psi = e^{-\beta(H-\mu N)}, \quad \beta = 1/T$$

The occupation numbers of the eigenvalues  $\epsilon_i^\omega$  of the Hamiltonian  $H = \sum_i \epsilon_i^\omega a_i^+ a_i$  in the rotating frame are given by

$$n_i = 1/\{1+\exp(\epsilon_i^\omega - \mu)\}$$

The formulae of the independent particle model can be used to calculate the energy E and the entropy S:

$$E = \sum_{i=1}^{\infty} (\epsilon_i^\omega + \omega \langle j_x \rangle_{ii}) n_i$$

$$S = - \sum_{i=1}^{\infty} [n_i \ln n_i + (1-n_i) \ln(1-n_i)]$$

Crucial for the stability of a certain nuclear shape is the driving force p tending to change the set of deformation parameters q. From the differentials of the energy E and the free energy F=E-TS,

$$dE = TdS - pdq + \mu dN$$

$$dF = -SdT - pdq + \mu dN$$

one obtains the Maxwell relations

$$p = -\partial E / \partial q|_{S,N} = -\partial F / \partial q|_{T,N}$$

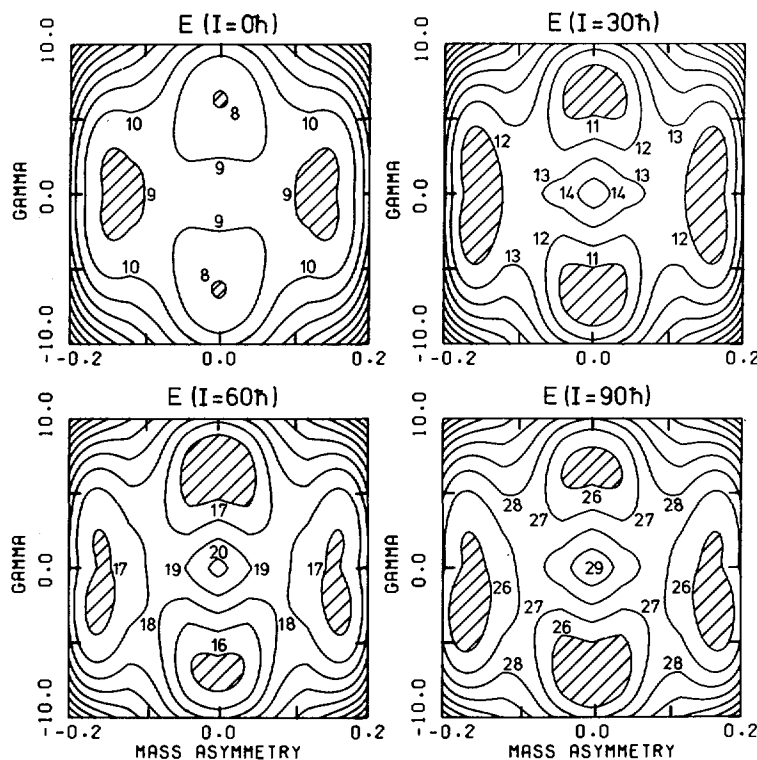


FIG.2. Total energy of  $^{232}\text{Th}$  for prolate deformation  $\beta = 0.8$  and neck parameter  $r = 0.8$  as function of the mass asymmetry parameter  $a$  and the axial asymmetry parameter  $\gamma$  for  $I = 0, 30, 60$  and  $90 \text{ h}$ .

Therefore, the free energy surface for constant temperature  $T$  determines the driving force  $p$  and the stationary points with vanishing driving force.

In fig. 1c the free energy surface  $F$  is drawn for angular momentum  $I = 60\text{h}$  and temperature  $T = 1 \text{ MeV}$  corresponding to a thermal excitation energy of 20 MeV and to a total energy at the second saddle of 39 MeV. The two minima are shadowed. They are only separated by a small saddle of 1.5 MeV. The height of the second barrier is 4 MeV. For this temperature already a large part of the shell effects of fig. 1b is washed out by the statistical excitations of particle hole states. The values of the free

energy for the investigated temperatures become negative because of the additional term  $-TS$  in the definition. However, only the variations of the free energy influence the driving force. To the temperature  $T = 2$  MeV and the same angular momentum  $I = 60\hbar$  corresponds a thermal energy of 80 MeV and a total energy of 100 MeV at the second saddle point. For this temperature - fig. 1d - the shell corrections have already almost vanished. The deformation energy surfaces show only the slope of the liquid drop model valley. The nucleus has lost its stability against fission already for the angular momentum of  $60\hbar$ .

For comparison of experimental fission barriers at high angular momenta and critical angular momenta for fission with theoretical calculations one has to take into account both: the influence of the shell structure and the statistical excitations of the compound nuclei. In some experiments the critical angular momenta are found in good agreement with the liquid drop values. This does not mean that for these angular momenta the shell effects are vanishing, but the thermal excitation of the nucleus is so high that the large number of statistical particle hole excitations hides the shell structure.

In the last part of this work we study the influence of angular momentum and temperature on the ratio between symmetric and asymmetric fission. As suggested by Weber et al. [7] and shown theoretically for the first time by Gavron et al. [8] with a modified harmonic oscillator potential the symmetric and asymmetric fission yields can be explained by assuming two different fission paths leading over two second saddle points. One of them corresponds to mass-asymmetric and the other one to axially asymmetric shapes. In fig. 2a the total energy  $E$  of  $^{232}\text{Th}$  close to the second saddle ( $\beta=0.8$  and  $r=0.8$ ) is shown varying with the mass asymmetry parameter  $\alpha$  and the axial asymmetry parameter  $\gamma$  independently. In all

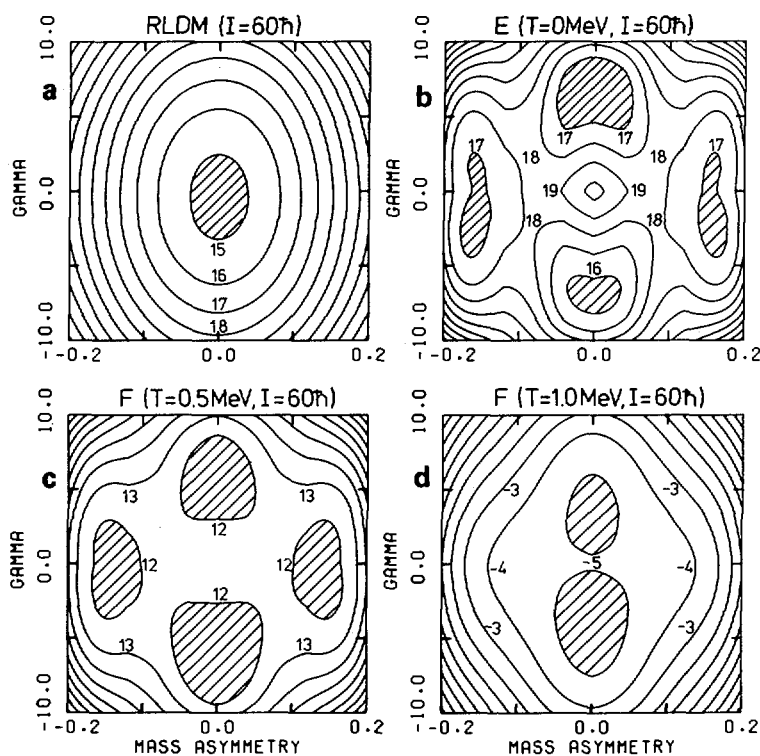


*FIG.3. Deformation energy surfaces of  $^{232}\text{Th}$  at  $I = 60 \hbar$  for  $\beta = 0.8$  and  $r = 0.8$  as function of  $\alpha$  and  $\gamma$ :*

- a) total energy as given by the rotating-liquid-drop model;
- b) total energy with the inclusion of shell corrections;
- c) free energy for  $T = 0.5 \text{ MeV}$ ;
- d) free energy for  $T = 1 \text{ MeV}$ .

following figures the equi-energy lines differ by 1 MeV. The minima are again shadowed. As one can clearly see, there exist two pairs of distinct minima, one for mass asymmetric shapes ( $\alpha = \pm 0.15$ ) and another one for axially asymmetric shapes ( $\gamma = \pm 8^\circ$ ). The two pairs of minima are separated by a barrier and correspond to two different saddle points lying not one after the other but one beside the other in the liquid drop model valley. Since

the two saddles are separated by a barrier, there exist two distinct fission channels, a mass asymmetric ( $\alpha \neq 0, \gamma = 0$ ) channel and a mass symmetric ( $\alpha = 0, \gamma \neq 0$ ) but axially asymmetric channel. In fig. 2a the mass symmetric saddle is the deeper one. This does not mean that this fission channel is preferred, since the depth of the minima depends on the  $\beta$ -r point. In fig. 2b-2d one can see the influence of the rotation on the saddle points for  $I = 30, 60$  and  $90\hbar$ . The influence is threefold: i) The barrier between the fission channels is for high spins larger than for the non rotating nucleus. ii) The negative  $\gamma$ -deformations become favoured in comparison to the positive  $\gamma$ -deformations. iii) There is a slight trend toward mass-asymmetric fission.

A still more drastic effect on the mass distribution is due to the increase of the nuclear temperature than due to the increase of the angular momentum. To show this, in fig. 3 four different deformation energy surfaces of  $^{232}\text{Th}$  for angular momentum  $I = 60\hbar$  are drawn. The rotating liquid drop energy surface in fig. 3a has a flat symmetric minimum and yields therefore a broad symmetric mass distribution. In fig. 3b the total energy surface for  $T=0$  is shown. The two fission channels are limited to a small region of the mass asymmetry parameter and give rise to small peaks in the fission yields. The temperature  $T = 0.5$  MeV (fig. 3c) corresponds to a thermal excitation energy of 5 MeV and to a total energy of 24 MeV at  $\alpha=\gamma=0$ . The shell effects in the free energy surface are already much smaller than in fig. 3b. The depths of the symmetric and the asymmetric fission minimum are roughly equal. A temperature of 1 MeV (fig. 3d) corresponding to a total energy of 39 MeV is already sufficient to get rid of the asymmetric mass component and to get a broad mass distribution as for the liquid drop model. For a temperature of 2 MeV the free energy surface would look like a liquid drop surface.

## REFERENCES

- [1] S. Cohen, F. Plasil, W.J. Swiatecki, Ann.Phys. 82 (1974) 557.
- [2] M. Brack, J. Damgaard, A.S. Jensen, H.C. Pauli, V.M. Strutinsky, C.Y. Wong, Rev.Mod.Phys. 44 (1972) 320.
- [3] K. Neergård, V.V. Pashkevich, S. Frauendorf, Nucl.Phys. A262 (1976) 61.
- [4] G. Andersson, S.E. Larsson, G. Leander, P. Möller, S.G. Nilsson, I. Ragnarsson, S. Åberg, R. Bengtsson, J. Dudek, B. Nerlo-Pomorska, K. Pomorski, Z. Szymański, Nucl.Phys. A268 (1976) 205.
- [5] H.C. Pauli, Phys.Rep. 7 (1973) 35.
- [6] M. Faber, M. Ploszajczak, A. Faessler, to be published.
- [7] J. Weber, H.C. Britt, A. Gavron, E. Konecny, J.B. Wilhelmy, Phys.Rev. C13 (1976) 2413.
- [8] A. Gavron, H.C. Britt, P.D. Goldstone, J.B. Wilhelmy, S.E. Larsson, Phys.Rev.Lett. 38 (1977) 1457.

## DISCUSSION

H.J. SPECHT: Did you make a systematic survey of the dependence of the shell-corrected barriers on angular momentum and temperature for very heavy nuclei, let us say from  $Z = 100$  to  $Z = 115$ , where the liquid-drop barriers vanish even in the case of zero angular momentum? The fission properties of these elements are now being investigated in heavy-ion reactions and any stabilization of the barrier by angular momentum, as seems to be visible in your calculations for  $Z < 100$ , would therefore be very relevant.

M.E. FABER: The decreasing heights of the fission barriers with increasing angular momentum are mainly affected by the decreasing heights of the fission barriers in the rotating-liquid-drop model and not by decreasing shell corrections. There are some nuclei in the Th-U region where the first barrier even shows a tendency to increase with angular momentum on account of fluctuations in the shell corrections. We have not yet investigated the influence of angular momentum on the heights of the fission barriers in the region  $Z > 100$ .

P. MÖLLER: I imagine you must have had major computational problems in breaking so many symmetries for your calculations. So how large are the matrices you diagonalize?

M.E. FABER: The dimensions of the matrices are in the region 250–300.



# NUCLEAR FRICTION AND GIANT RESONANCE CHARACTERISTICS OBSERVED IN FISSION OF HEAVY NUCLEI

P. DAVID, J. DEBRUS, J. SCHULZE

Institut für Strahlen- und Kernphysik,  
Universität Bonn,  
Bonn, Federal Republic of Germany

J. VAN DER PLICHT, M.N. HARAKEH, A. VAN DER WOUDE

Kernfysisch Versneller Instituut, Rijksuniversiteit Groningen,  
Groningen Paddepoel,  
The Netherlands

## Abstract

NUCLEAR FRICTION AND GIANT RESONANCE CHARACTERISTICS OBSERVED IN FISSION OF HEAVY NUCLEI.

The total kinetic energy (TKE) release in the fission processes  $^{236}\text{U}$  ( $^4\text{He}, ^4\text{He}'\text{f}$ ) at  $E(^4\text{He}) = 50 \text{ MeV}$ ,  $^{235}\text{U}(\text{d}, \text{pf})$  at  $E(\text{d}) = 23 \text{ MeV}$  and  $^{238}\text{U}$ ,  $^{232}\text{Th}$  ( $^4\text{He}, ^4\text{He}'\text{f}$ ) at  $E(^4\text{He}) = 120 \text{ MeV}$  is investigated as a function of the excitation energy of the fissioning systems. For  $^{232}\text{Th}$ , the slope ( $\delta \text{TKE}/\delta E_x$ ) is positive in the energy region from the fission threshold  $B_f$  up to about ( $B_f + 1.5 \text{ MeV}$ ) and remains approximately constant in the region above. The fission probability of the isoscalar giant quadrupole resonance, excited by the inelastic scattering of 120 MeV  $^4\text{He}$ -particles is, at most, 20% of the fission probability of the underlying continuum and the giant dipole resonance in  $^{232}\text{Th}$  and  $^{238}\text{U}$ .

## I. INTRODUCTION

The study of the TKE released in the fission process as a function of the excitation energy of the fissioning nucleus can contribute to a better insight into the nature of the dissipative process involved in fission.

Previous studies have been performed on U - [1], Pu - [2] and Am-isotopes [3]. We have, by means of the ( $^4\text{He}, ^4\text{He}'\text{f}$ ) reaction, investigated the TKE release for the nucleus  $^{232}\text{Th}$ , where in the model of the double humped barrier the outer barrier is higher than the inner, in contrast to the heavier nuclei mentioned above. Contrary to heavy ion reactions the fission processes under consideration allow a study of

TABLE I. LIST OF REACTIONS INVESTIGATED AND DISCUSSED IN THIS PAPER

Reaction	Energy MeV	Detection System	Cyclotron Beam
$^{232}\text{Th}(\text{He}^4, \text{He}'^4)$	120	Telescope, Q3D-Spectrograph	Groningen
$^{235}\text{U}(\text{d}, \text{pf})$	23	Telescope	Bonn
$^{236}\text{U}(\text{He}^4, \text{He}'^4)$	50	Telescope	Bonn
$^{238}\text{U}(\text{He}^4, \text{He}'^4)$	50	Telescope	Bonn
$^{238}\text{U}(\text{He}^4, \text{He}'^4)$	120	Q3D-Spectrograph	Groningen

the deformation and energy dissipation phenomena from the state of a cold nucleus at the barriers, where mainly collective degrees of freedom are involved, over the two quasi-particle threshold up to high excitation energies, where many degrees of freedom contribute.

The study of isoscalar giant resonances in heavy nuclei has been mainly concentrated [4] on systematics of excitation energies, widths and percentages of energy weighted sum rules exhausted by the giant resonances of various multipolarities. Except for the total width, very little is known experimentally about the partial decay modes of the giant quadrupole resonance (GQR) in heavy nuclei. For nuclei in the actinide region, where fission can compete with neutron decay the giant dipole resonance (GDR) [5] is already known to have a fission probability that is similar to the one of the compound nucleus, as expected [6].

In this paper we report on a measurement of the fission probability of the GQR in  $^{232}\text{Th}$  and  $^{238}\text{U}$ .

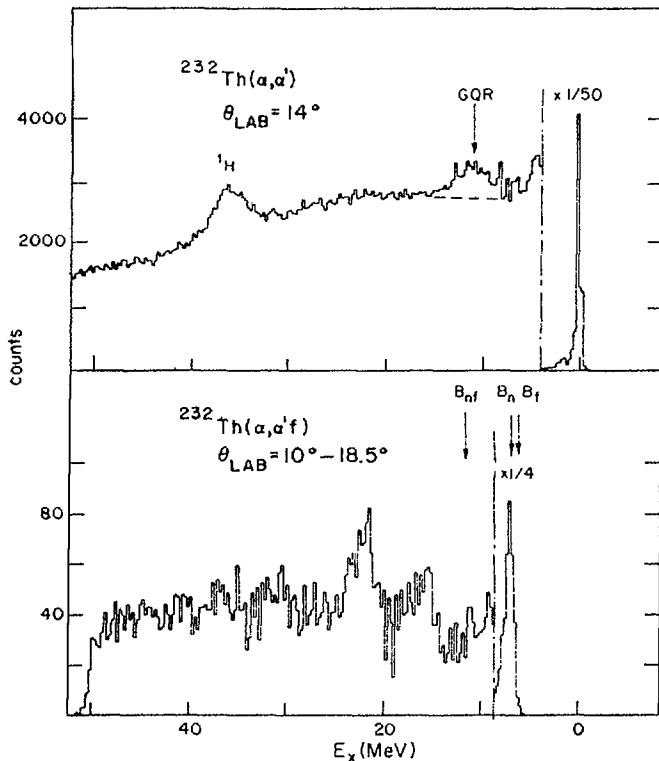


FIG.1. Upper part: Single spectrum of 120-MeV inelastically scattered  $^4\text{He}$ -particles. Lower part: coincidence ( $^4\text{He}, ^4\text{He}'\text{f}$ )-spectrum summed for  $\Theta_{\text{lab}} = 10 - 18.5^\circ$ .

## 2. EXPERIMENTAL SET-UP

The triple coincidence experiments, detecting the ejectile and two fission fragments were performed at the University of Bonn and the University of Groningen isochronous cyclotrons. We have studied the reactions summarized in table I. The ejectiles were detected in  $\Delta E - E$  telescope systems and in a Q 3 D magnetic spectrograph. For the TKE-measurements the fission fragment detectors were collinear in the recoil axis as defined by the detection system for the ejectile. The GQR decay measurements on  $^{232}\text{Th}$  and  $^{238}\text{U}$  were performed for the fission fragments along the recoil axis and in addition at 10, 20,

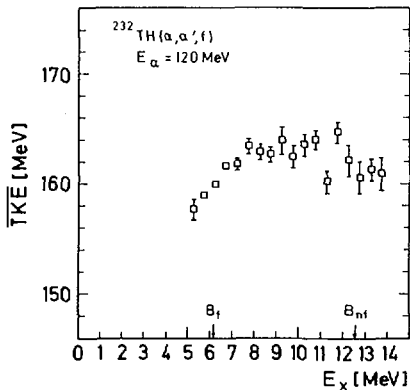


FIG.2. Average  $\overline{TKE}$  ( $E_x$ ) for 0.5-MeV intervals of excitation energy.

30, 40, 50, 75 and  $90^\circ$  with respect to the recoil axis. More details of the experiments are given in references [1, 7, 8].

### 3. RESULTS AND DISCUSSION

#### 3.1 The Total Kinetic Energy

Figure 1 shows a single spectrum of 120 MeV inelastically scattered  $^4\text{He}$ -particles at  $\theta_{\text{lab}} = 14^\circ$  taken with a telescope system. The bump characteristic for the isoscalar giant resonance [4] is located at  $E_x = (11.0 \pm 0.3) of excitation, with a width of  $(4.0 \pm 0.5). The coincidence  $(^4\text{He}, ^4\text{He}'f)$  spectrum summed for  $\theta_{\text{lab}}$  from  $10^\circ$  to  $18.5^\circ$  is shown in the second part of the figure. The bump around 6 MeV results from the fact that the fission threshold ( $B_f = 6.15$  MeV [9]) is lower than the neutron binding energy ( $B_n = 6.4$  MeV). Beyond this bump the spectrum is flat and decreases slightly up to the second chance fission threshold ( $B_{nf} = 12.6$  MeV), after which it rises to about double its value. After again decreasing slightly towards the third chance fission threshold ( $B_{2nf} = 18.1$  MeV) it rises again. The apparent bump at  $E_x \sim 21$  MeV is presumably due to two-neutron evaporation to the excitation energy range  $B_f \leq E_x \leq B_n$  in  $^{230}\text{Th}$ .$$

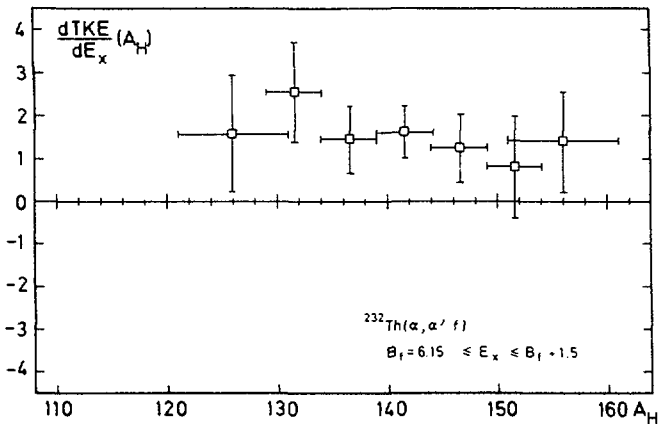


FIG.3. Slopes  $\delta TKE (E_x, \bar{A}_H) / \delta E_x$  of linear least-square fits to  $TKE (E_x, \bar{A}_H)$ ,  $E (^4\text{He}) = 120 \text{ MeV}$ .

For  $^{232}\text{Th}$  a detailed study of the TKE was made for excitation energies  $B_f \leq E_x \leq B_{nf}$ , where for  $B_f$  particle induced fission data [9] indicate a much higher value for the outer barrier ( $E_B = B_f = 6.15 \pm 0.2 \text{ MeV}$ ) than for the inner one ( $E_A \approx 5.5 \text{ MeV}$ ). The threshold for second chance fission is given by  $B_{nf} = B_n (A) + B_f (A-1)$ , where  $B_n (A)$  is the neutron binding energy in the nucleus  $A$ ,  $B_f (A-1)$  is the fission threshold in the nucleus  $(A-1)$ . Fig. 2 shows  $\overline{TKE} (E_x)$ , where the data were summed over 0.5 MeV intervals and are averaged over all different masses of the fission fragments.

The preneutron TKE release was determined according to the procedure outlined in [10], with the prompt neutron distributions taken from [11]. In the analyses it is assumed that the number of neutrons evaporated from the fragments and the energy carried away by this process remains constant as a function of excitation energy and that the neutrons are emitted isotropically. Corrections were made for the energy loss of the fragments in the target.

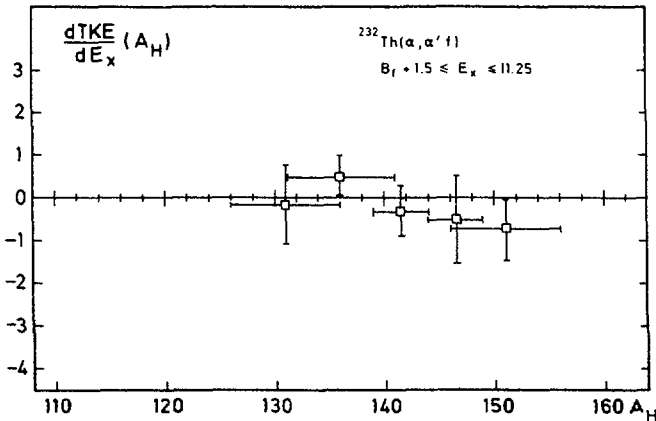


FIG.4. Slopes  $\delta \overline{\text{TKE}} (E_x, \bar{A}_H) / \delta E_x$  of linear least-square fits to  $\text{TKE} (E_x, \bar{A}_H)$ ,  $E (^4\text{He}) = 120 \text{ MeV}$ .

The data show that  $\delta \overline{\text{TKE}} / \delta E_x$  behaves very differently for excitation energies below and above about 7.75 MeV. Figure 3 shows  $\delta \overline{\text{TKE}} (E_x, \bar{A}_H) / \delta E_x$  for  $B_f \leq E_x \leq B_f + 1.5 \text{ MeV}$ , where the averaging is now performed over different mass groups as indicated. Figure 4 displays the slopes  $\delta \overline{\text{TKE}} (E_x, \bar{A}_H) / \delta E_x$  for  $B_f + 1.5 \leq E_x \leq B_{nf}$ , which are consistent with zero or slightly negative values. In the interval  $B_f \leq E_x \leq B_f + 1.5 \text{ MeV}$  the value of the linear least square fit slope is  $\delta \overline{\text{TKE}} (E_x, \bar{A}_H) / \delta E_x = 1.5 \pm 0.4$ .

It is interesting to compare the observed behaviour of  $\delta \overline{\text{TKE}} / \delta E_x$  of  $^{232}\text{Th}$  with similar data for other nuclei. Recently a Russian group [12] has studied the reaction  $^{232}\text{Th}(n, f)$ ; they observe a similar increase in  $\overline{\text{TKE}}$  as function of  $E_x$  for  $^{233}\text{Th}$  in the region up to about 1.5 MeV above the barrier as we have observed for  $^{232}\text{Th}$ . However these  $^{233}\text{Th}$  data have not been confirmed in a recent study of the same nucleus  $^{233}\text{Th}$  by Trochon et al. [13]. For the uranium isotopes there are some indications that the situation is different. In figure 5 we display the behaviour of  $\overline{\text{TKE}}$  vs.  $E_x$  for  $^{238}\text{U}$  and

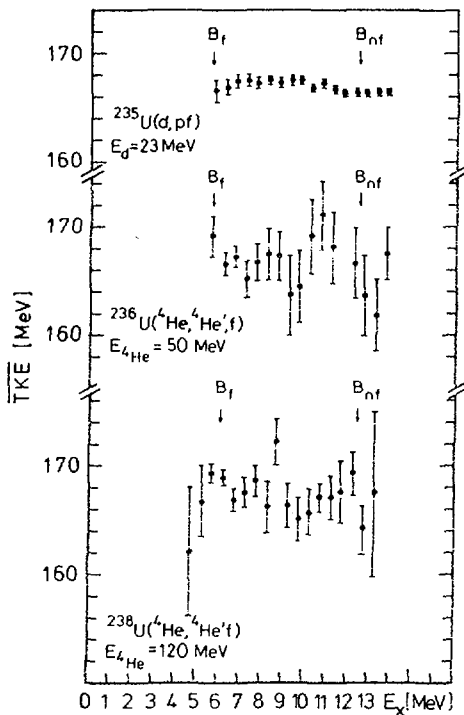


FIG. 5. Average  $\overline{TKE}$  ( $E_x$ ) for  $^{236}U$  and  $^{238}U$  as measured in the reactions  $^{235}U(d, pf)$  at  $E(d) = 23$  MeV,  $^{236}U(^4\text{He}, ^4\text{He}'f)$  at  $E(^4\text{He}) = 50$  MeV and  $^{238}U(^4\text{He}, ^4\text{He}'f)$  at  $E(^4\text{He}) = 120$  MeV.

$^{236}\text{U}$  as measured in the reactions  $^{238}\text{U}(^4\text{He}, ^4\text{He}'f)$  at  $E(^4\text{He}) = 120$  MeV,  $^{236}\text{U}(^4\text{He}, ^4\text{He}'f)$  at  $E(^4\text{He}) = 50$  MeV and  $^{235}\text{U}(d, pf)$  at  $E_d = 23$  MeV respectively. Although the statistical accuracy of these data is not as good as for  $^{232}\text{Th}$  the data suggest that the slope

$\delta \overline{TKE} / \delta E_x \approx 0$  (averaged over all mass divisions) for the whole excitation range  $B_f \leq E_x \leq B_{nf}$ . For  $^{242}\text{Am}$  [3] and  $^{240}\text{Pu}$

[2] the data seem to indicate still a different behaviour:

$\delta \overline{TKE} / \delta E_x \approx 0$  up to  $B_f + 1.5$  MeV and  $\delta \overline{TKE} / \delta E_x < 0$  for  $(B_f + 1.5 \text{ MeV}) \leq E_x \leq B_{nf}$ . This situation has been schematically summarized in figure 6. It is tempting to correlate this different behaviour of  $\delta \overline{TKE} / \delta E_x$  with the different double humped barrier structure as is also indicated.

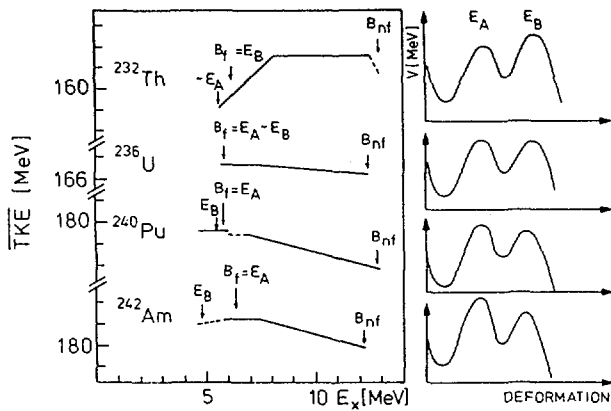
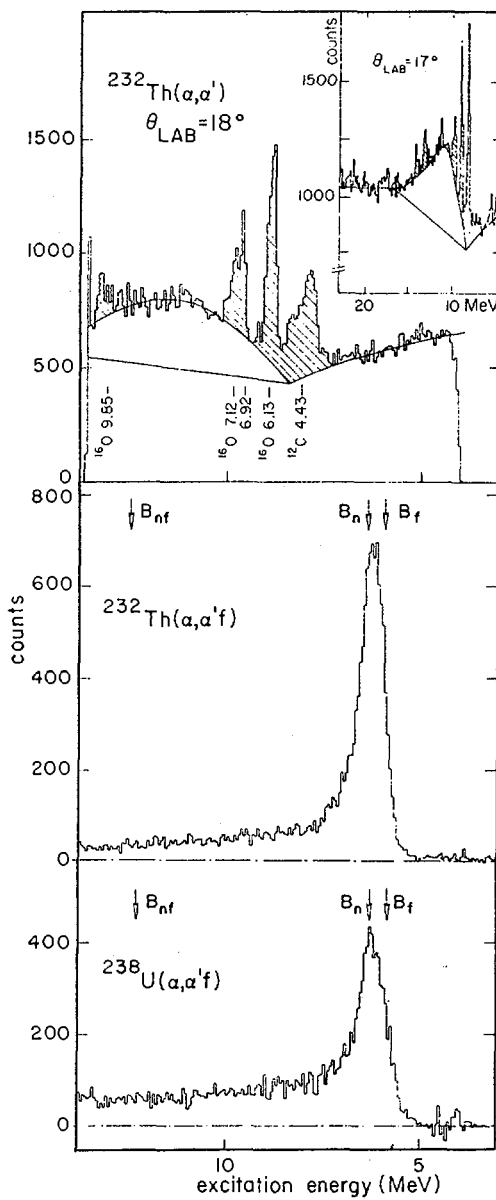


FIG. 6. Schematical presentation of average  $\overline{TKE}(E_x)$  for  $^{232}\text{Th}$  (this work),  $^{236}\text{U}$  [1],  $^{240}\text{Pu}$  [2] and  $^{242}\text{Am}$  [3] for  $B_f \leq E_x \leq B_f + 1.5 \text{ MeV}$  and  $B_f + 1.5 \leq E_x \leq B_{nf}$ ; on the right side the double-humped barrier structure is indicated [9].

### 3.2 The Giant Quadrupole Resonance

The top of figure 7 displays a spectrum of  $^4\text{He}$ -particles scattered inelastically on  $^{232}\text{Th}$  at 120 MeV. This spectrum was taken with the Q3D magnetic spectrograph. The peaks due to  $^{12}\text{C}$  and  $^{16}\text{O}$  contaminants are indicated. The background was drawn corresponding to the way it was done in the insert spectrum, which was taken with a  $\Delta E - E$  counter telescope. In the middle and at the bottom of fig. 7  $^4\text{He}$ -spectra from  $^{232}\text{Th}$  and  $^{238}\text{U}$  in coincidence with fission are shown. Beyond the peak above the fission threshold the spectra are structureless and the absence of a bump corresponding to the decay of the GQR into the fission channel is obvious.

$^4\text{He}$ -fission angular correlation data were measured for  $^{232}\text{Th}$ . The fission fragments were detected at 10, 20, 30, 40, 50, 75 and  $90^\circ$  with respect to the recoil axis. These data were used for obtaining fission probabilities, assuming the  $^4\text{He}$ -fission angular correlation pattern to be cylindrically symmetric around the recoil axis. For  $^{232}\text{Th}$  resulted a fission probability of  $P_f = 0.27 \pm 0.05$  for the interval  $6.0 \leq E_x \leq 6.4 \text{ MeV}$  and  $P_f = 0.055 \pm 0.015$  for the continuum



**FIG. 7.** Upper part: Single spectrum of  ${}^4\text{He}$ -particles scattered inelastically on  ${}^{232}\text{Th}$  at  $E({}^4\text{He}) = 120 \text{ MeV}$  taken with a Q3D magnetic spectrograph. Insert:  $\Delta E - E$  counter telescope single spectrum.

Middle and bottom:  ${}^4\text{He}$ -spectra from  ${}^{232}\text{Th}$  and  ${}^{238}\text{U}$  in coincidence with fission at  $E({}^4\text{He}) = 120 \text{ MeV}$ .

between 9 and 13 MeV. The former value agrees with the fission probability found by Back et al. [9], the latter value agrees with data obtained from photofission and fast neutron induced fission [6]. To obtain an upper limit for the fission decay probability of the GQR in  $^{232}\text{Th}$  a smooth line is drawn through the continuum in the coincident  $^4\text{He}$ -fission spectra. This results in an upper limit of 0.01 for the fission probability of the GQR in  $^{232}\text{Th}$ . For  $^{238}\text{U}$  the fission probability of the GQR is found to be at most 20 % of that of the underlying continuum. These surprising results imply that the two components of the total damping width

$$\Gamma = \Gamma^\uparrow + \Gamma^\downarrow$$

are different for the GQR compared to the GDR. Here  $\Gamma^\uparrow$  is the direct component describing the escape width of a simple state, and  $\Gamma^\downarrow$  is the spreading width due to mixing with states of complicated structure.

For the GDR Dover, Lemmer and Hahne [14] assume the direct component  $\Gamma^\uparrow$  in heavy nuclei to be small : 10 - 15 %. The coupling of the collective 1p - 1h states of the  $1\hbar\omega$  mode GDR to 2p2h and further more complicated configurations,  $\Gamma^\downarrow$ , is the main damping mechanism. A compound nucleus results and fission would be the result of a complete statistical equilibrium. This explains why the fission probability for the GDR and the continuum are equal and agree with the systematic trend. A similar damping mechanism was predicted for the GQR in  $^{208}\text{Pb}$  by Bertsch et al. [15]. However, since the GQR mode is found to be inhibited to fission it suggests that the direct component  $\Gamma^\uparrow$  may not be small as for the GDR and/or that the 1p-1h, 2p-2h, ... chain is not developed to a statistical equilibrium. More detailed information about the decay mechanism can be obtained only by measuring the neutron decay spectrum.

#### 4. SUMMARY AND CONCLUSION

In the results outlined we have shown properties in the collective motion of excited heavy nuclei in an extremely deformed state. The overall behaviour of the slopes of the TKE for  $B_f \leq E_x \leq B_{nf}$  is possibly due to more than one effect: pairbreaking and deformation.

We have further found that the decay of the isoscalar giant quadrupole resonance into the fission channel in  $^{232}\text{Th}$  and  $^{238}\text{U}$  is much smaller than one would predict from systematics and than what is observed for the underlying continuum. This is difficult to understand on the basis of the usual models for giant resonance decay in heavy nuclei.

#### REFERENCES

- 1 David, P., Debrus, J., Lübke,F., Schoenmackers,R., Schulze, J., Phys.Lett. 77 B(1978)178
- 2 Lachkhar, S., Patin, Y., Sigaud, J., J.de Physique 36(1975) L -79  
Kuz'minov,B.D., Sergachev,A.I., Sov.J.Nucl.Phys.25(1977)23
- 3 Weber, J., Erdal,B.R., Gavron,A., Wilhelmy, J.B., Phys.Rev. C 13 (1976) 189
- 4 Bertrand, F.E., Ann.Rev.Nucl.Sci.26 (1976)457  
Harakeh, M.N. et al., to be published
- 5 Veyssiére, A., Beil, H., Bergere, R., Carlos, P., Lepretre,A., Kernbath, K., Nucl.Phys. A 199 (1973) 45
- 6 Vandebosch, R., Huizinga,J.R., Nucl.Fission (Academic Press, 1973) and references therein.
- 7 David, P., Debrus,J., Lübke,F., Mommsen,H., Schmitt,E., Schoenmackers, R., Simons,H., Phys.Lett. 61 B (1976) 158
- 8 Plicht, v.d. J., Harakeh, M.N., Woude, v.d.A., David,P., Debrus, J., Phys. Rev.Lett. 42 (1979)
- 9 Back, B.B., Hansen, O., Britt, H.C., Garrett, J.D., Phys. Rev. C 9 (1974) 1924
- 10 Schmitt, H.W., Neiler, J.H., Walter, F.J., Phys. Rev.141 (1966) 1146  
Plasil, F., Ferguson, R.L., Pleasonton,F., Schmitt,H.W., Phys. Rev. C 7 (1973) 1186

- 11 Terell, J., Phys. Rev. 127 (1962) 880
- 12 D'yachenko, N.P., Kuzminov, B.D., Mitrofanov, V.F., Sergachev, A.I., Sov. J. Nucl. Phys. 26 (4) (1977) 365
- 13 Tronchon, J., Abon Yehia, H., Brisard, F., Pranal, Y., Nucl. Phys. A 318 (1979) 63
- 14 Dover, C.B., Lemmer, R.H., Hahne, F.J.W., Ann. Phys. 70 (1972) 458
- 15 Bertsch, G. F., Bortignon, P.F., Broglia, R.A., Dasso, C.H., Phys. Lett. 80 B (1979) 161

## DISCUSSION

J.W. BOLDEMAN: First a question. Have you compared your experimental  $\bar{E}_{TKE}$  data with the  $\bar{\nu}$  ( $E_n$ ) data that should show an inverse effect? The two nuclei in the  $^{232}\text{Th}(n, f)$  and  $^{232}\text{Th}(\alpha, \alpha'f)$  reactions are, of course, different.

The comment I wish to make is as follows: you have related the change in the sign of the slope of the total kinetic energy with excitation energy to the change in the relative heights of the two humps of the fission barrier. We have found evidence of a similar effect for low-energy neutron-induced fission between 0 and 2 MeV. In other words, strong channel effects appear in the  $\bar{\nu}(E_n)$  dependence for  $^{233}\text{U}$  and, possibly, for  $^{235}\text{U}$ . For neutron fission of  $^{239}\text{Pu}$ , however, channel effects have been reduced by  $\sim 50\%$ .

P. DAVID: Yes, I know about the exact  $\bar{\nu}_p$  data you have obtained for  $^{233}\text{U}$  and  $^{235}\text{U}$ . In your case inverse behaviour with excitation energy, as compared to TKE, occurs over a very small energy range 150–200 keV. As far as I know, there have not been any data published on a dramatic decrease in  $\bar{\nu}_p$  over the range 1.5–2 MeV in the case of  $^{232}\text{Th}$ .

A. FAESSLER: I would just like to make a comment on the basic idea of measuring the giant quadrupole resonance (GQR) in coincidence with fission. One might have expected the quadrupole vibrational states to couple to fission as strongly as the low-lying quadrupole ( $\beta$ ) vibrations. But the GQR is characterized by  $2\hbar\omega$  excitation and is orthogonal to the  $\beta$ -vibrations. It is therefore not a doorway state to fission. Fission is mainly a  $0\hbar\omega$  particle-hole excitation phenomenon, like the  $\beta$ -vibrations. In addition, the E2 resonance should be more coherent and more stable against damping than the E1 resonance. Hence it should decay mainly by neutron emission before damping.

H.C. BRITT: Professor Faessler's suggestion that the quadrupole resonance has a very low fission probability because of its poor overlap with the fission mode implies very low mixing into the underlying compound states for the quadrupole resonance. Does that possibility seem reasonable?

P. DAVID: Yes, I think it does. That is why stated that for the GQR the direct component  $\Gamma^\dagger$  of the damping width is probably large and that  $\Gamma^\dagger$  is small, meaning that there is little mixing into complicated states.

H.J. SPECHT: First a question and then a comment. A slope  $d\langle E_k \rangle / dE_x > 1$  for the kinetic energy variation in  $^{232}\text{Th}(\alpha, \alpha'f)$  is not easily understandable. How sure are you regarding possible systematic errors?

My comment is that I seem to remember data on  $\bar{\nu}$  in  $^{232}\text{Th}(n, f)$ , though admittedly not for the same nucleus, which show fairly constant behaviour over an energy interval close to the barrier. So I think that for simple energy conversation, variations in  $\langle E_k \rangle$  and  $\bar{\nu}$  have to be strongly correlated.

P. DAVID: A decrease in  $\bar{\nu}_p$  would lower the slope  $S = \delta \text{TKE}(E_x, \bar{A}_H) / \delta E_x$  from  $\sim 1.5$  for the excitation energy interval  $(B_f, B_f + 1.5)$  in the case of  $^{232}\text{Th}$ . No such sharp decrease is known to me.

S.S. KAPOOR: How do you explain the decrease in kinetic energy with excitation energy that you observed?

P. DAVID: The decrease in  $\overline{\text{TKE}}$  with excitation energy is most probably due to quasi-particle excitation. This again may increase with  $Z^2/A^{1/3}$  as the  $\overline{\text{TKE}}$  data indicate, for increasing distance, i.e. deformation, between saddle and scission points. Hence quasi-particle excitation and deformation effects may work together.

H.M.A. THIERENS: You may be interested to hear that some new results have been obtained by Caldwell and co-workers on the variation in  $\bar{\nu}$  with excitation energy during photofission of  $^{232}\text{Th}$ . I believe they have observed that the behaviour of  $\bar{\nu}$  in this case shows a discontinuity. Its value decreases in the energy region around 7 MeV, while at higher energies there is an increase.

P. DAVID: This is encouraging news.

A.F. MICHAUDON: In your presentation you made a reference to differences in the total kinetic energy ( $\overline{\text{TKE}}$ ) data from the  $^{232}\text{Th}(n, f)$  reaction obtained by Trochon and co-workers, as compared with those of Dyachenko and co-workers. I should like to say that Trochon's data, which have just been published in Nuclear Physics, are consistent with  $\bar{\nu}$  data, whereas Dyachenko's values do not seem to be.

As far as the variation in  $\bar{\nu}$  with energy is concerned, I have no recollection of data showing a constant  $\bar{\nu}$  value over a few-MeV energy range. Rather, the available data are consistent with an increase in  $\bar{\nu}$ , with perhaps a local plateau of at most a few hundred keV at low energy.

Lastly, the  $^{232}\text{Th}(\alpha, \alpha'f)$   $\overline{\text{TKE}}$  data you have presented, with a strong increase in the  $\overline{\text{TKE}}$  versus excitation energy over several MeV, are not consistent with  $\bar{\nu}$  data. Nevertheless, it should also be noted that in such a case the  $\bar{\nu}$  and  $\overline{\text{TKE}}$  data have not been obtained for the same fissioning nucleus — it was  $^{232}\text{Th}$  for  $\overline{\text{TKE}}$  and  $^{233}\text{Th}$  for  $\bar{\nu}$  — and that these two different nuclei are also formed with different angular momenta.

P. DAVID: Thank you for your comments. It was our intention to measure the  $^{232}\text{Th}(\alpha, \alpha'\text{f})$  reaction at 120 and 50 MeV, and to look for different angular momentum effects. With regard to  $\bar{\nu}_p$ , I think the availability of exact  $\bar{\nu}$  data would be very useful.

H:G. CLERC: I notice that for thorium you observed an increase in the total kinetic energy with increasing excitation energy, while the total kinetic energy remained constant for heavier nuclei or even decreased. This result fits in with the behaviour of the proton odd-even effect, which decreases when moving from thorium through uranium to plutonium and californium. It indicates that the effect of damping increases with the  $Z^2/A$  of the fissioning nucleus.

# THE ROLE OF BLOCKING LIFE-TIME MEASUREMENTS IN THE STUDY OF HEAVY-ION-INDUCED FISSION

J.U. ANDERSEN, A.S. JENSEN,  
E. LAEGSGAARD, K.O. NIELSEN

Institute of Physics,  
University of Aarhus,  
Denmark

J.S. FORSTER, I.V. MITCHELL, D. WARD  
Chalk River Nuclear Laboratories, AECL,  
Chalk River,  
Ontario, Canada

W.M. GIBSON  
ISAACS, SUNY, Albany, New York,  
United States of America

## Abstract

### THE ROLE OF BLOCKING LIFE-TIME MEASUREMENTS IN THE STUDY OF HEAVY-ION-INDUCED FISSION.

The crystal-blocking technique has been used to study the time development of fission of highly excited Hg nuclei produced by bombarding a thin W crystal with  $^{12}\text{C}$  ions in the energy range of 80–87 MeV. Life-times are extracted by comparing the fission-blocking patterns with those for backscattering of low-energy  $^{12}\text{C}$  ions. The large differences are attributed to fission components with intermediate life-time ( $\tau \sim 10^{-17}$  s) and with long life-time ( $\tau \gtrsim 10^{-16}$  s). These results have been supplemented with measurements of fission cross-sections and fission angular distributions for  $^{12}\text{C}$  bombardment of the four W isotopes ( $^{182, 3, 4, 6}\text{W}$ ) for the energies used in the blocking measurements. The results are analysed with the aid of statistical model calculations, which follow the spin and energy distribution of compound nuclei through the neutron evaporation cascade. The three sets of measurements supplement each other and together determine a set of model parameters, with which all the experimental data are reproduced by the calculations. The role of the life-time measurements is to provide the information on the average number of neutrons evaporated before fission, which is needed in particular for the interpretation of fission angular distributions. With barrier deformations from the liquid-drop model and rigid-body moments of inertia, cross-sections for complete fusion are obtained which agree with the semi-empirical estimates from the Bass model.

### 1. INTRODUCTION

By the crystal-blocking technique, very short nuclear lifetimes,  $\tau \sim 10^{-15} - 10^{-18}$  s, have been measured for compound nuclei decaying by charged-particle emission [1]. One of the first applications for this technique was to the fission process [2,3], and the study of lifetimes of fissioning nuclei has since been one of the major applications of the technique [1]. For heavy-ion induced fission, the interpretation of crystal-blocking results presents special problems due to the high excitation energy of the fissioning compound nuclei and the consequent possibility of higher-chance fission. However, we recently demonstrated [4,5] that one may obtain useful information with the crystal-blocking technique about the relative contribution to the fission yield from fission after evaporation of several neutrons.

In Ref. 5, hereinafter referred to as I, we studied fission of Pb compound nuclei created by  $^{16}\text{O}$  bombardment of W. The main result was the establishment of a method of analysis and interpretation of the blocking data. In addition, it was shown that these blocking measurements play an important role in the investigation of heavy-ion-induced fission since the information obtained about the distribution of the fission yield over stages in the neutron-evaporation chain is crucial for the unambiguous interpretation of other types of measurements such as total fission cross sections and fission-fragment angular distributions. This is particularly so for analysis and interpretation of fission-fragment angular distributions. In the formalism first developed by Halpern and Strutinsky [6], the anisotropy depends on three parameters: the square of the angular momentum  $I^2$ , the temperature  $T$ , and the effective moment of inertia  $J_e$  at the fission barrier, given by  $1/J_e = 1/J_{\parallel} - 1/J_{\perp}$ , where  $J_{\parallel}$  and  $J_{\perp}$  correspond to rotations about the axis of deformation and about an axis perpendicular to this direction, respectively. In early studies of fission-fragment angular distributions for heavy-ion-induced fission [7], none of these quantities was known accurately and the conclusions were at best tentative. Today our knowledge of spin distributions of compound nuclei is considerably improved, and reliable estimates are available [8]. The main uncertainty in the temperature of fissioning nuclei is associated with the distribution of fission over several stages, and we obtain information on this distribution from the lifetime measurements. If the effective moment of inertia at the fission barrier can be calculated, we should then be able to estimate the anisotropy of the fragment angular distribution and compare with experiment.

This application of blocking measurements is the main theme of the present paper. The particular case we have studied is the fission of Hg isotopes formed by bombardment of W with  $^{12}\text{C}$  projectiles. The blocking measurements were performed as part of the work reported in I, and a preliminary analysis was presented there. These measurements have been supplemented with fission cross sections and fission-fragment angular distributions. The analysis of the results relies on statistical-model calculations which have been developed in parallel to the experimental work. An early version of the model was presented in Ref. 9, and improvements were described in I. There it was shown that the model

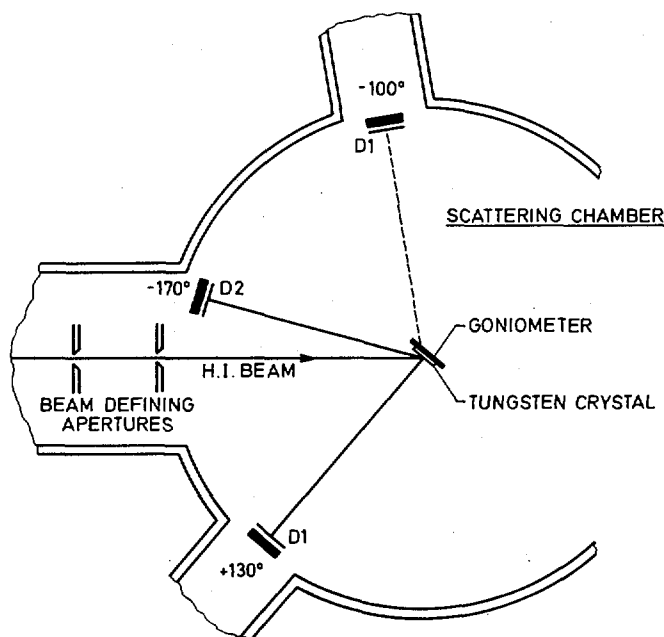


*FIG.1. Set-up for the blocking experiment. The detector systems D1 and D2 are thin position-sensitive silicon detectors, backed by a veto counter. The position of D1 at -100° was not used in this experiment. The exact position of the centre of D2 was at -165° or -168° (see Fig. 2).*

was able to reproduce all the experimental data for fission induced by  $^{16}\text{O}$  bombardment of W isotopes. Due to the strong correlation of many of the model parameters, the individual values are not unique, but we believe that the distribution in excitation energy of fissioning nuclei is well represented by the model when the calculations reproduce the experimental lifetime distribution and its dependence on bombarding energy.

Fission of one of the compound nuclei formed by C bombardment of W,  $^{198}\text{Hg}$ , has been studied earlier [10] through the reaction  $^{197}\text{Au}(\text{p},\text{f})$ . The fission cross section was measured over a wide region of bombarding energies, and the results have been used to determine the fission barrier for  $^{198}\text{Hg}$  [11]. The requirement that our statistical model should reproduce also these results turns out to be difficult to meet, and we shall discuss the possible implications of this difficulty.

## 2. EXPERIMENTAL

### 2.1. Blocking lifetime measurements

The experimental and analysis techniques have been described in considerable detail in I and will only be described briefly here. All measurements were made using a 3350-Å thick crystal of

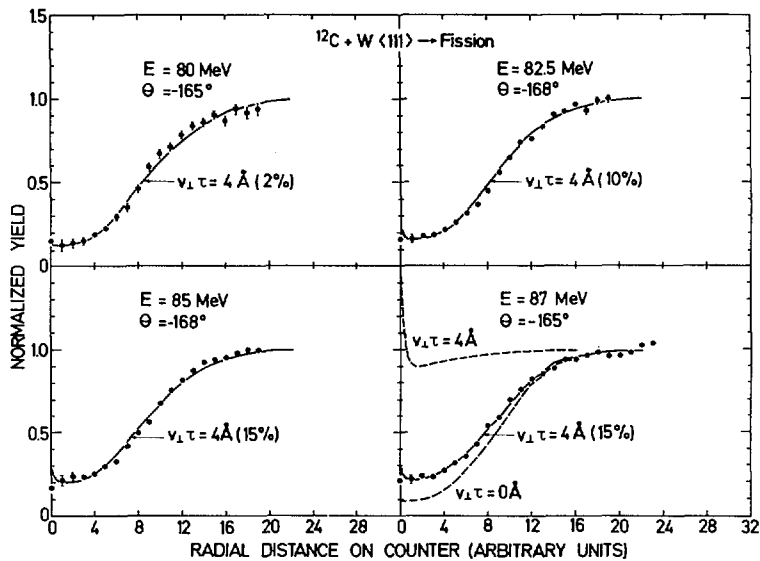


*FIG. 2. Fission-fragment blocking dips measured with the back detector (D2 in Fig. 1). The solid lines through the points are fits, discussed in the text, obtained as superpositions of a calculated dip for a long-recoil component and a dip for  $v_{\perp}\tau = 0$  obtained by scaling in angle a measured blocking dip for elastic scattering. The two components are shown by dashed curves for  $E = 87 \text{ MeV}$ , and the relative amount of the long-recoil component is given in parentheses for the different fits. The uncertainty of these numbers, as obtained from the variation of  $\chi^2$  for the fits, is 1–2%.*

natural W grown epitaxially on  $\text{Al}_2\text{O}_3$  with a  $\langle 111 \rangle$  axis normal to the surface. Beams of 80, 82.5, 85, and 87 MeV  $^{12}\text{C}$  ions from the Chalk River MP tandem were used to bombard the target crystal, which was oriented with the  $\langle 111 \rangle$  axis directed towards either detector 1 or detector 2, as shown in Fig. 1. Fission fragments were detected in two-dimensional position-sensitive counters, 14 mm by 14 mm by  $\sim 20 \mu\text{m}$  thick. The output of these counters were the products  $(1-x)\text{E}$ ,  $x\text{E}$ , and  $y\text{E}$  which, after electronic processing, gave the position coordinates  $(x,y)$  and the energy  $\text{E}$ . Behind each of these detectors was a large-area veto counter, which allowed discrimination between fission fragments, which stopped in the front detector, and light, energetic particles, e.g., elastically and inelastically scattered  $^{12}\text{C}$  ions, passing through the front detector and giving a signal in the veto counter.

The  $x$ ,  $y$ , and  $\text{E}$  signals were encoded by ADC's with a conversion range of 256 channels, and the data were written event by event on magnetic tape for later analysis. The data were played back by setting windows on the fission energy spectra and accumulating two-dimensional position spectra. The windows were chosen to be symmetric about the fission peak in the energy spectrum so that a symmetric average over fission-fragment charge and mass, about the mean value, would be taken.

The two-dimensional position spectra were corrected for detector non-linearities which arise due to non-uniformities in sheet resistivity over the implantation region of the detector and from compromises required in electronic shaping time constants, as described in Ref. 12 and in I. The experimental blocking dips were generated by making circular averages about the minimum in the blocking pattern. The dip center was determined by a search for the minimum number of counts in a small area.

Blocking patterns obtained for the back detector, D2, are shown in Fig. 2 for 80, 82.5, 85, and 87 MeV  $^{12}\text{C}$  bombarding energies; the error bars are due to statistical errors only. Included on the plot of the 87-MeV data is a curve obtained for 25-MeV  $^{12}\text{C}$  elastic scattering ( $v_{\perp\tau} = 0\text{\AA}$ ). This elastic-scattering dip has been scaled in angle by a factor  $(Z_{\text{ff}}/Z_C \times E_C/\text{Eff})^{\frac{1}{2}}$ , where  $Z$  and  $E$  denote atomic number and energy of fission fragments and scattered C. The average fission-fragment energy,  $\text{Eff}$ , was calculated from published values of energy released in fission [13]. Also shown in Fig. 2 is a calculated curve for a long lifetime  $\tau$ , corresponding to an average recoil distance  $v_{\perp\tau} = 4\text{\AA}$  perpendicular to the axis. The line through the data points was obtained by a superposition of these two (short- and long-lifetime) dips and, as discussed in I, we believe this interpretation to be the only one consistent with our data.

The calculation of blocking dips for different average recoils perpendicular to the axis,  $v_{\perp\tau}$ , is discussed in detail in I. The results may roughly be divided into three categories. For  $v_{\perp\tau} \lesssim 0.05\text{\AA}$ , the recoil has very little effect on the blocking dip. In an intermediate range,  $0.05\text{\AA} \lesssim v_{\perp\tau} \lesssim 0.5\text{\AA}$ , the dip is very sensitive to the magnitude of  $v_{\perp\tau}$ . There is a small increase in the minimum yield, but the main modification is a narrowing of the width of the dip. Finally, for long recoils,  $v_{\perp\tau} \gtrsim 0.5\text{\AA}$ , there is only a weak dependence on the magnitude of  $v_{\perp\tau}$  since the blocking dip has almost disappeared. In the fits shown in Fig. 2, the component corresponding to  $v_{\perp\tau} = 4\text{\AA}$  thus represents lifetimes in this third region.

The calculations of dips do not take into account effects of multiple scattering and crystal imperfections. These effects are most important for zero recoil [1], and since they are expected to be similar for the fission fragments and the elastically scattered ions, the scaled elastic dip is used for  $v_{\perp\tau} = 0$  in the fitting procedure. An approximate correction of calculations for finite average recoils  $v_{\perp\tau}$  is obtained by replacing the calculated yield function  $Y_C$  by  $Y_C(1 - \chi_{\text{el}}) + \chi_{\text{el}}$ , where  $\chi_{\text{el}}$  is the measured minimum yield for the elastic blocking dip.

The blocking dips for the forward counter D1 are shown in Fig. 3 for 80, 82.5, and 85 MeV  $^{12}\text{C}$  bombarding energy. Also shown for 82.6 MeV are the blocking dip for scaled  $^{12}\text{C}$  elastic scattering ( $v_{\perp\tau} = 0\text{\AA}$ ), the calculation for a large recoil displacement ( $v_{\perp\tau} = 4\text{\AA}$ ), and the calculated dip for an intermediate recoil displacement,  $v_{\perp\tau} = 0.1\text{\AA}$ . Initial attempts to fit these data were made using only two recoil distances,  $v_{\perp\tau} = 0\text{\AA}$  and  $v_{\perp\tau} = 4\text{\AA}$ , as for the back-counter data. However, we were unable to obtain good fits to both the minimum yield and width of the fission-fragment blocking dips with only two components. Inclusion of a third recoil distance ( $v_{\perp\tau} = 0.1\text{\AA}$ ) greatly improved the fits, which are shown as solid lines through the data points in

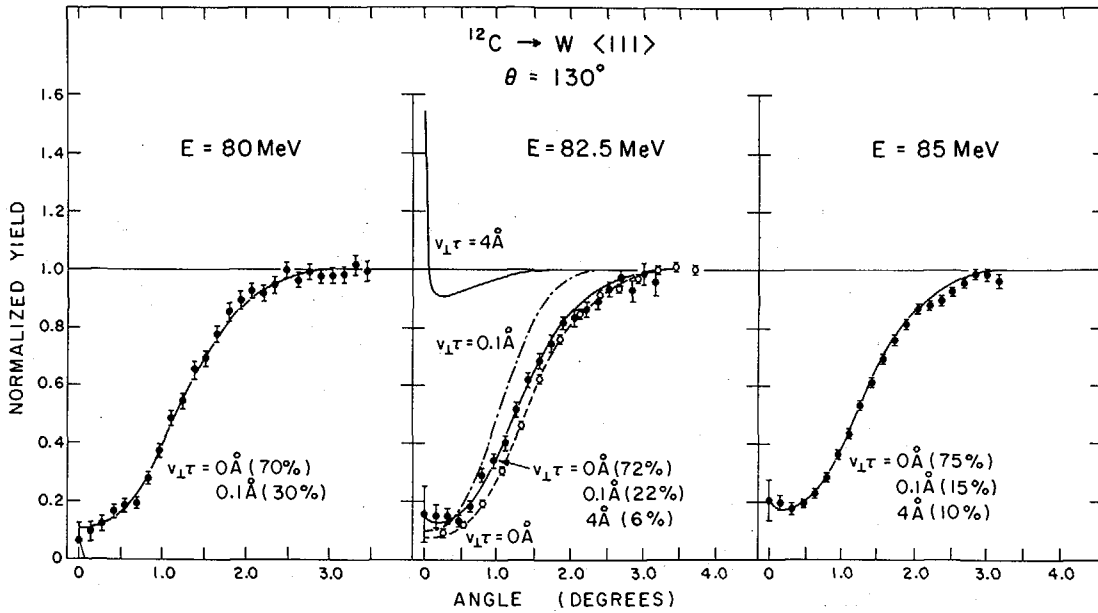


**FIG.3.** Blocking dips for fission fragments, measured with the forward detector (D1 in Fig. 1). The dips are fitted with a superposition of three components, two calculated for finite average recoil distances ( $v_{\perp}\tau = 4 \text{ \AA}$  and  $v_{\perp}\tau = 0.10 \text{ \AA}$ ), and one scaled in angle from a measured blocking dip for elastically scattered C ions ( $v_{\perp}\tau = 0$ ). The three components are shown separately for  $E = 82.5 \text{ MeV}$ , and the relative amounts are indicated for the individual fits. The uncertainty of the amount of the long-recoil component is about 1–2% (see Fig. 2) but much larger for the intermediate recoil component, for which an estimate from the variation of  $\chi^2$  is rather meaningless (see text).

Fig. 3. This result is not inconsistent with the back-counter data as the recoil distance  $v_{\perp T}$  for two different angles of observation is related by the ratio of the sines of the angles. Therefore, 0.1 Å at 130° corresponds to a recoil distance  $v_{\perp T} = 0.1 \sin 165^\circ / \sin 130^\circ = 0.03 \text{ Å}$  at 165° and this value is below our lower limit of sensitivity.

It should be noted, however, that the extraction of an intermediate-lifetime component is much more uncertain than the determination of the long-lifetime component. The reason is partly that the width of the measured blocking dips is much more sensitive than the minimum yield to detector non-linearity and deficiencies in our correction procedure. Furthermore, use of the detailed shape of the dip for lifetime extraction is critically dependent on the accuracy of the scaling of the dip measured for elastic scattering of low-energy ions. We may again refer to I for a detailed discussion. There we did not use an intermediate-lifetime component in the fits, but the large discrepancy observed in Fig. 3 between the data and the two-component fits seems to justify an attempt to extract information about intermediate lifetimes from the present data.

## 2.2. Angular distribution and total fission

### Cross section measurements

A separate experiment to measure fission-fragment angular distributions and cross sections was made using targets of the four separated isotopes of W. The targets were in the form  $\text{WO}_3$  of thickness  $\sim 100 \mu\text{g/cm}^2$  (for  $^{182}\text{W}$ ) to  $\sim 250 \mu\text{g/cm}^2$  (for  $^{186}\text{W}$ ) on thin ( $\sim 30 \mu\text{g/cm}^2$ ) Al backing foils.  $^{12}\text{C}$ -ion beams of the same energies as those for the blocking measurements were used.

To completely separate fission events from other scattering events, an array of five small proportional counters was used. Each counter had a rectangular aperture, 3 mm wide by 8 mm high, covered by a 2  $\mu\text{m}$  thick Al-mylar foil supported by a grid. The counters were operated at atmospheric pressure, and a continuous flow of P-10 gas (90% Ar + 10%  $\text{CH}_4$ ) was maintained through the counters. Each anode consisted of a 10  $\mu\text{m}$  diameter W wire connected to a charge-sensitive preamplifier. It was found that the fission events were best separated from other events with an anode bias of  $\sim +350 \text{ V}$ . The five counters were mounted on a turntable with 18° spacing between aperture centers at a distance of 7 cm from the target; the turntable could be rotated 360° about the target position.

A 500- $\mu\text{m}$  thick Si surface-barrier detector was mounted at 40° to the beam direction and was used to normalize the yields in the proportional counters for different target and beam-energy combinations. The solid angle ratio of each of the proportional counters to the monitor detector was determined by elastic scattering of 30-MeV  $^{12}\text{C}$  ions with the counter array at forward angles. This test confirmed that the solid angles of the five counters were identical (to within  $\sim 2\%$ ). Absolute fission cross sections were determined by using the experimentally known solid-angle ratios and by assuming that the elastic-scattering cross section in the monitor counter was given by the Rutherford expression for all energies used in the experiment.

During the fission measurements, the turntable was positioned with the five counters at laboratory angles of 98°, 116°, 134°,

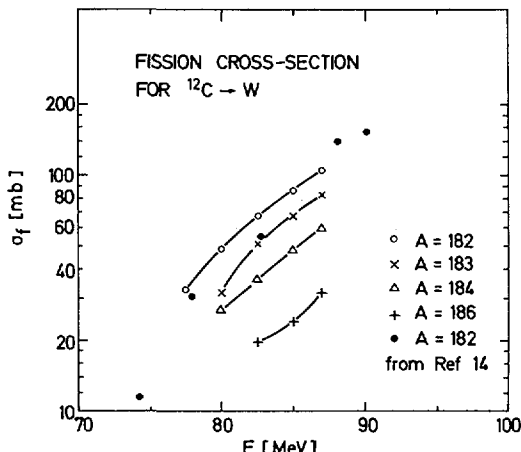


FIG. 4. Measured fission cross-sections (see also Table II). The lines are to guide the eye only.

152°, and 170°. For each target and beam-energy combination, the laboratory differential cross sections were converted to center-of-mass angles and cross sections; the angular distributions closely follow a  $(\sin\theta)^{-1}$  distribution for angles from 90° to  $\sim 150^\circ$  with deviations to lower values at larger angles. The angular-distribution data, multiplied by  $\sin\theta$ , were least-squares-fitted by the function  $A[(1+B)\sin\theta/(1+B\sin\theta)]$ . In this expression,  $A$  is a normalization constant and  $B$  takes account of the deviation from a  $(\sin\theta)^{-1}$  dependence at large values of  $\theta$ . This function has the advantage that it can be integrated analytically to give an expression, in terms of the parameters  $A$  and  $B$ , for the total-fission cross section. The results are plotted in Fig. 4, where the data from  $^{12}\text{C}$  bombardment of  $^{182}\text{W}$  of Sikkeland et al.[14] are also shown.

The differential cross sections are shown in Fig. 5. These data were normalized to a  $(\sin\theta)^{-1}$  distribution for the three points nearest to 90°. Inspection of Fig. 5 shows that this normalization procedure is valid and, in general, only the point at the largest angle of observation shows a large deviation from the  $(\sin\theta)^{-1}$  dependence.

### 3. CALCULATIONS

The statistical model used in the calculations is in the main described in Ref. 9, and the modifications are specified in detail in the appendix of I. Here, we shall partly give a broad outline of the model, partly specify the special parameter values, which have been used to fit the data.

The fission process is assumed to proceed via formation of a compound nucleus with well-defined excitation energy and a spin distribution characterized by a sharp cut-off at a maximum angular momentum  $I_{\max}$ . Three modes of decay are included, i.e.,

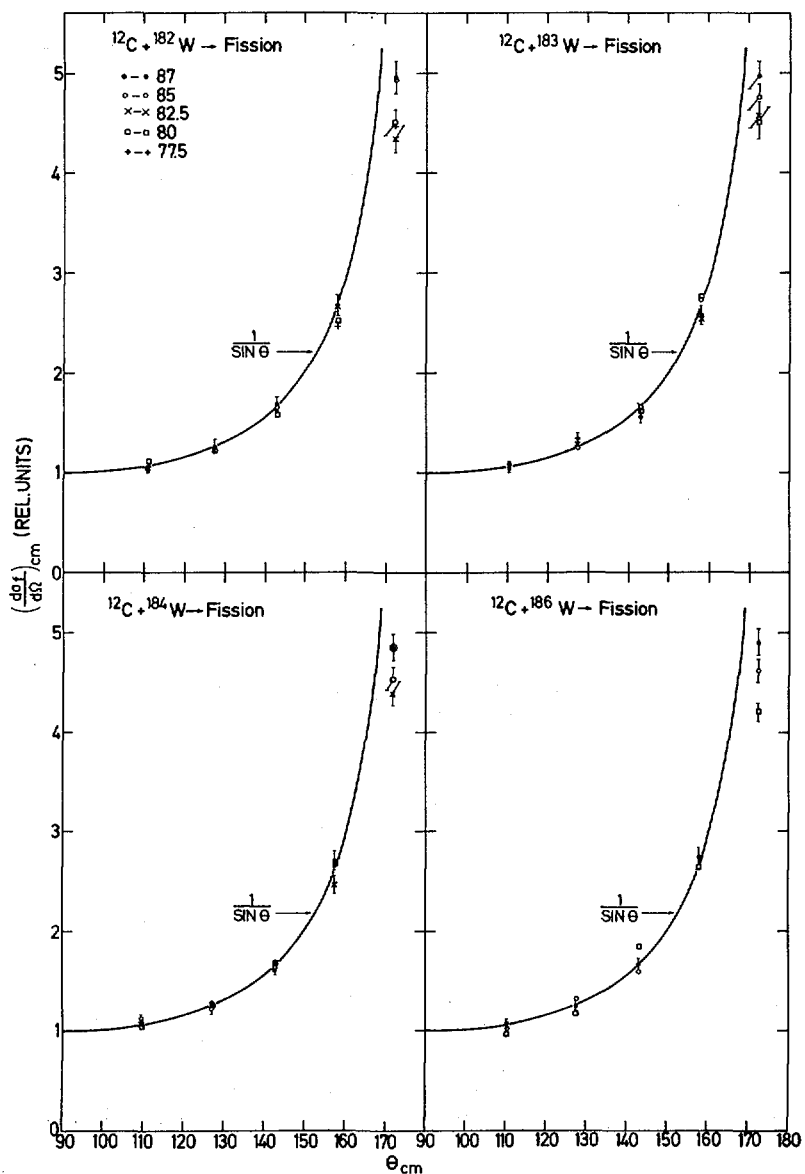


FIG. 5. Measured angular distributions, normalized as described in the text. The error bars are statistical, and do not include a contribution from the normalization.

fission, neutron emission, and  $\gamma$  emission, and the development of the distribution in excitation energy and spin of the nucleus is followed through the neutron-evaporation cascade. Radiative decay is only competitive in the last stage of the cascade.

### 3.1. Widths

The partial widths for the three decay modes are calculated from the standard formulas for a statistical model, which express the widths in terms of level densities and appropriate constants and weighting functions. The neutron width may be expressed as a sum of contributions from final nuclear states with spin  $I'$  and excitation energy  $E - \epsilon$ ,

$$\Gamma_n(E, I) = \sum_{I'} \int_0^{E-B_n} \rho_n(E, I, \epsilon, I') d\epsilon \quad (3)$$

where

$$\begin{aligned} \Gamma_n(E, I, \epsilon, I') &= \\ \frac{1}{2\pi\rho(E, I)} \sum_{j=|I-I'|}^{I+I'} \sum_{l=j-\frac{1}{2}}^{j+\frac{1}{2}} \rho_D(E-B_n - \epsilon, I') T_{lj}(\epsilon) \end{aligned} \quad (3')$$

Here  $\rho$  and  $\rho_D$  are the level densities for the nucleus before and after the neutron emission. The transmission coefficients  $T_{lj}(\epsilon)$  for a neutron with orbital angular momentum  $l$ , total spin  $j$ , and kinetic energy  $\epsilon$  are calculated from an optical model with an average parameter set given in Ref. 15. The neutron-binding energies  $B_n$  are specified in Table I.

The fission width is given by

$$\Gamma_f(E, I) = \frac{1}{2\pi\rho(E, I)} \int_0^E \frac{\rho_B(\epsilon, I) d\epsilon}{1 + \exp(-\frac{2\pi}{\hbar\omega}(E - B_f - \epsilon))} \quad (4)$$

which for  $E > B_f$  reduces to

$$\Gamma_f(E, I) \approx \frac{1}{2\pi\rho(E, I)} \int_0^{E-B_f} \rho_B(\epsilon, I) d\epsilon \quad (4')$$

Here  $\rho_B$  is the level density at the saddle point for fission. Note that the dependence of the effective fission barrier on angular momentum is implicitly included through this level density (cf. Eq. (6)). The main parameter in formula (4) is the fission barrier  $B_f$ . It may be expressed as a smooth contribution  $B_f$  corrected for barrier- and ground-state shell and pairing corrections,

$$B_f = \tilde{B}_f - \delta U_{gs} - \delta P_{gs} + \delta U_B + \delta P_B \quad (5)$$

The values of the individual parameters are specified in Table I for all the relevant isotopes of Hg.

The  $\gamma$  width is determined from a giant dipole expression with the parameters given in I.  $\gamma$  emission is competitive only for the lowest excitation energies, but the magnitude of  $\Gamma_\gamma$  is important for the contribution to the fission yield from

TABLE I. PARAMETER VALUES USED TO OBTAIN THE RESULTS PRESENTED IN TABLE II FOR MULTIPLE-STAGE FISSION OF Hg ISOTOPES. All energies are in units of MeV. The fitting procedure is described in the text, and the symbols are defined in Section 3.1.

A	$\tilde{B}_f$	$\delta U_{g.s.}$	$\delta U_B$	$\delta P_{g.s.}$	$\delta P_B$	$B_f$	$B_n$
198	13.8	-4.21	-1.0	-2.48	-3.29	16.2	8.30
7	13.7	-3.56	-1.0	-1.66	-2.48	15.4	6.96
6	13.6	-3.00	-1.0	-2.45	-3.26	14.8	8.87
5	13.5	-2.49	-1.0	-1.63	-2.44	14.2	6.92
4	13.4	-2.08	-1.0	-2.41	-3.23	13.7	9.26
3	13.3	-1.78	-1.0	-1.60	-2.41	13.3	7.12
2	13.2	-1.66	-1.0	-2.38	-3.19	13.0	9.56
1	13.1	-1.56	-1.0	-1.56	-2.38	12.8	7.59
0	13.0	-1.49	-1.0	-2.35	-3.16	12.7	9.82
189	12.9	-1.42	-1.0	-1.53	-2.34	12.5	7.40

very long lifetimes, i.e. for the magnitude of the long-lifetime component.

From the partial widths, the energy- and spin-dependent fission probability may be calculated. This quantity is used as a weighting function for calculations of averages over the energy and spin distribution in the cascade to obtain the total fission cross section, the total angular distribution of fission fragments, and the total lifetime distribution. The lifetime  $\tau$  corresponding to fission at a given stage in the cascade and for given values of  $E$  and  $I$  is calculated directly from the total width, i.e., the contribution from the preceding neutron evaporation is neglected. This is justified by the fact that neutron emission increases  $\tau$  by about an order of magnitude.

### 3.2. Level density

The level density enters crucially in the calculation of decay widths. The intrinsic level density is taken from Ref. 16 with a small modification for low excitation energies, which is described in I, where also the relevant parameter values are specified. The expression takes account of the influence of shell effects and its dependence on nuclear temperature. For both the ground state and the fission barrier, rotational contributions for an axially- and R-symmetric system are then included, and one obtains

$$\rho(E, I) = \frac{1}{2\sqrt{2\pi J_1 T}} \sum_{K=-I}^I \rho(E - \frac{I(I+1)}{2J_1} - \frac{K^2}{2J_e}) \quad (6)$$

which, when the rotational energies are small relative to  $E$ , simplifies to

$$\rho(E, I) \approx \frac{\rho(E)}{2\sqrt{2\pi J_1 T}} \exp(-\frac{I(I+1)}{2J_1 T}) \sum_{K=-I}^I \exp(-\frac{K^2}{2J_e T}) \quad (6')$$

Here,  $\mathcal{J}_{\parallel}$  and  $\mathcal{J}_{\perp}$  denote the moments of inertia parallel and perpendicular to the symmetry axis, and  $\mathcal{J}_e$  is the effective moment of inertia,  $1/\mathcal{J}_e = 1/\mathcal{J}_{\parallel} - 1/\mathcal{J}_{\perp}$ . The intrinsic level density is  $\rho(E)$  and  $T$  is the temperature,

$$1/T = \frac{\partial}{\partial E} \ln \rho(E)$$

It should be noted that apart from the shell corrections, the level density does not include any adjustable parameters, i.e., the parameters have been chosen independently of the present data. In particular, the  $a$  parameter is the same in the ground state and at the barrier,  $a = A/9.5$ , where  $A$  is the number of nucleons.

The moments of inertia have been taken as rigid-body values. The parameterization of shapes of deformed nuclei defined in Ref. 17 has been used, with values  $(c,h) = (1,0)$  for the ground state and  $(c,h) = (1.87,0)$  for the barrier. The latter value of  $c$  is determined from the liquid-drop barrier for fission. With a radius parameter  $r_0 = 1.2f$ , the values  $\mathcal{J}_{gs} = 93.4$ ,  $\mathcal{J}_{\parallel} = 46.0$ ,  $\mathcal{J}_{\perp} = 292.4$ , and  $\mathcal{J}_e = 54.6$  are obtained for Hg. All values are given in units of  $\text{h}^{-\frac{1}{2}} \text{ MeV}^{-1}$ ; the first quantity corresponds to the spherical ground state and the last three quantities to the barrier deformation. For the other isotopes involved, the values may be obtained by scaling with  $A^{5/3}$  since the deformation is taken to be independent of  $A$ . The moments of inertia enter into the expression (6) for the level density. For the anisotropy of the fission-fragment angular distribution, the important quantity is  $\mathcal{J}_e$  at the barrier (cf. below).

### 3.3. Angular distribution of fission fragments

For a nucleus of spin  $I$  and energy  $E$ , the distribution in angle  $\theta$  of the emitted fission fragments with the beam axis is approximately [18]

$$W_{I,E}(\theta) = \sqrt{\frac{2p}{\pi}} \frac{J_0(p \sin^2 \theta) \exp(-p \sin^2 \theta)}{\operatorname{erf}(\sqrt{2p})} \quad (7)$$

where

$$p = \frac{(I + \frac{1}{2})^2}{4K_o^2} \quad , \quad K_o^2 = T_B \mathcal{J}_e \quad (7')$$

Here  $\operatorname{erf}$  is the error function and  $J_0$  the zero-order Bessel function. The temperature  $T_B$  corresponds to the intrinsic excitation energy at the barrier and therefore depends on spin,

$$\frac{1}{T_B} = \frac{\partial}{\partial E} \ln \rho_B(E - B_f, I) \quad (8)$$

Expression (7) corresponds to the relative probabilities of different projections  $K$  of the spin on the symmetry axis, which are implicitly given in Eq. (6'). However, to arrive at Eq. (7), only the expansion in the last parameter in Eq. (6),  $K^2/2\mathcal{J}_e$ , is necessary. The total angular distribution is obtained by summing and integrating Eq. (7) over the spin and energy distribution of all stages in the evaporation cascade, weighted, of course, with the fission probability.

TABLE II. COMPARISON OF EXPERIMENTAL AND CALCULATED FISSION PROBABILITIES FOR  $^{12}\text{C}$ -BOMBARDMENT OF W-ISOTOPES

The first column gives the nucleon number of the compound Hg nucleus, and the second and third columns the laboratory  $^{12}\text{C}$ -energy and the Hg-excitation energy, respectively. The latter is calculated from the Q-values 16.0, 15.3, 13.8, and 11.5 for the four reactions. All energies are in MeV. From the measured fission cross-section,  $\sigma_f$ , and the complete-fusion cross-section,  $\sigma_{CF}$ , corresponding to the spin cut-off  $I_m$ , the experimental fission probability is derived. It is compared to the calculated total fission probability  $P_f^{\text{CAL}}$ .

A	E	E*	$\sigma_f$ [mb]	$I_m$	$\sigma_{CF}$ [mb]	$P_f^{\text{EXP}}$	$P_f^{\text{CAL}}$
194	77.5	56.7	32.1	35	1033	0.031	0.030
	80.0	59.0	48.2	37	1112	0.043	0.044
	82.5	61.4	67.5	38	1140	0.059	0.056
	85.0	63.7	86.3	39	1162	0.074	0.071
	87.0	65.6	106	40	1190	0.089	0.089
195	80	59.8	31.7	37	1113	0.029	0.038
	82.5	62.1	50.9	38	1134	0.045	0.049
	85.0	64.5	67.0	39	1156	0.058	0.061
	87.0	66.4	83.4	40	1191	0.070	0.076
196	80	61.3	26.9	37	1107	0.024	0.024
	82.5	63.6	36.2	38	1135	0.032	0.032
	85.0	66.0	48.4	39	1157	0.042	0.043
	87.0	67.8	59.8	40	1186	0.050	0.054
198	80	63.6		37	1109		0.012
	82.5	66.0	19.3	38	1135	0.017	0.016
	85.0	68.3	23.9	39	1158	0.021	0.022
	87.0	70.2	31.8	40	1188	0.027	0.027

### 3.4. Fitting procedure

The parameters which are varied to fit the data are the maximum angular momentum  $I_m$ , the smooth part of the fission barriers  $B_f$ , and the shell corrections. The three quantities are rather selective in the sense that the anisotropy of the fragment angular distribution is very sensitive to  $I_m$ , the fission cross sections to  $B_f$ , and the relative contributions from different stages to the fission yield is very sensitive to the magnitude of the shell corrections. It is therefore possible by successive approximations to obtain a good fit to the data. The value of  $I_m$  depends on bombarding energy and is specified in the following section (cf. Table II), while the other parameters are given in Table I. The smooth part of the barrier,  $B_f$ , was first assumed constant (as in I), but a weak linear dependence on A turns out to be necessary for a good fit to the data. For the shell corrections, only small constant adjustments are considered, and for the ground state, the A dependence is consistent with that used for Pb isotopes in I, while the values are

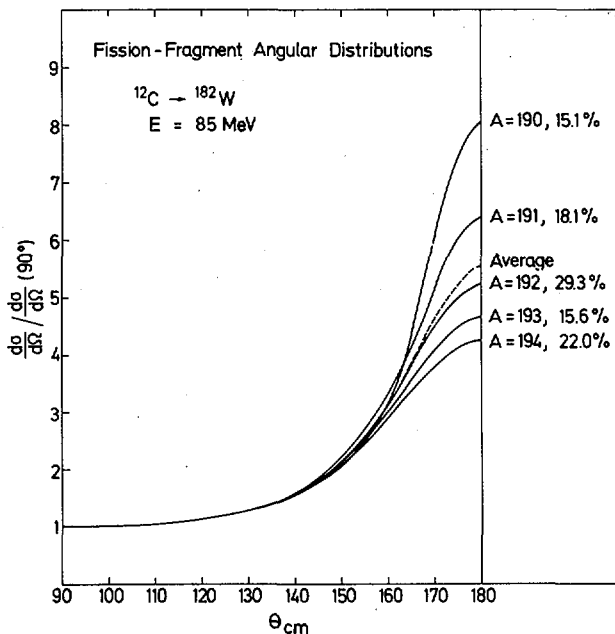


*FIG. 6. Calculated angular distributions of fragments from fission at different stages of neutron evaporation from the compound Hg nucleus. The individual curves are labelled with the corresponding mass number, and the relative contributions from the different stages to the total fission yield are indicated. The average angular distribution is given by the dashed curve. The curves are drawn smoothly through calculated points at the angles  $90^\circ$ ,  $130^\circ$ ,  $160^\circ$ ,  $165^\circ$ ,  $170^\circ$ , and  $180^\circ$ .*

lower than expected by about 1 MeV. The pairing corrections are calculated as in I and, finally, the neutron-binding energies are taken from Ref. 19.

#### 4. COMPARISON WITH EXPERIMENTS

##### 4.1. Fission cross sections

With the model parameters specified in Table I all the measured quantities may be calculated, provided that the initial spin distribution of the compound nucleus is known. A comparison with the measured fission cross sections is given in Table II. The maximum spin  $I_m$  is determined from the angular distribution, as discussed below. It determines the total cross section for fusion,

$$\sigma_{\text{CF}} = \pi \lambda^2 (I_m + 1)^2 \quad (9)$$

TABLE III. COMPARISON OF MEASURED AND CALCULATED ANISOTROPIES. The experimental values are for  $\theta = 172^\circ$  and the calculated for  $\theta = 170^\circ$ . Both are normalized to W(90) and the errors on the experimental numbers include a contribution from the normalization (see Section 2.2). The difference in angle corresponds to an expected difference of  $(W(172) - W(170))/W(90) \approx 0.20$ . A is the mass number of the compound Hg nucleus and E the  $^{12}\text{C}$  energy in MeV.

E	A=194		A=195		A=196		A=198	
	W(172)	W(170)	W(172)	W(170)	W(172)	W(170)	W(172)	W(170)
77.5	4.49±.14	4.07						
80.0	4.49±.16	4.35	4.51±.19	4.49	4.53±.16	4.28		4.08
82.5	4.34±.17	4.48	4.57±.16	4.58	4.40±.16	4.44	4.22±.12	4.20
85.0	4.97±.15	4.62	4.77±.17	4.66	4.84±.17	4.60	4.61±.13	4.37
87.0	4.96±.20	4.74	4.98±.19	4.76	4.85±.18	4.73	4.91±.16	4.50

where  $\lambda$  is the De Broglie wavelength of the relative motion of the projectile and target nuclei. Calculations and experiments may then be compared in terms of the total fission probability. They are seen to agree within ~10% for all isotopes and energies, except for the lowest energy for  $^{183}\text{W}$ . The experimental cross section would appear to be too low for this case, however (cf. Fig. 4). Note also, that fluctuations of a few percent should be expected from the choice of integer values for  $I_m$ , alone.

#### 4.2. Angular distributions of fission fragments

If we assume the moments of inertia to be known, the angular distributions depend mainly on the spin and temperature distribution of fissioning nuclei. The average temperature, related to the average number of neutrons evaporated prior to fission, is mainly determined by the lifetime measurements, discussed below. The importance of this parameter is indicated by the results shown in Fig. 6. The anisotropy is changing rapidly as the nucleus is cooling off by neutron emission.

The spin distribution may be changed by varying the maximum spin of the compound nucleus. With the values of  $I_m$  given in Table II the calculated enhancement of the fragment yield at  $170^\circ$ ,  $W(170)/W(90)$ , given in Table III are obtained. The experimental anisotropy is measured at a CM-angle of  $172^\circ$ , and as may be seen from Fig. 6 the enhancement,  $W(172)/W(90)$ , at this angle should be larger by about 0.20. Within the experimental uncertainty this relation is generally fulfilled. The expected increase of the anisotropy with increasing bombarding energy is clearly established by the measurements, while the decrease with increasing mass number, which is indicated by the calculation, is barely significant experimentally.

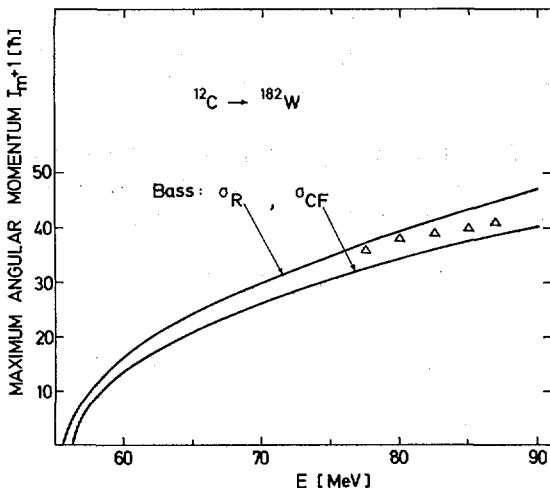


*FIG. 7. Comparison of the maximum angular momentum derived from the measurements of angular distributions of fission fragments with the prediction of Ref. [8]. The triangles correspond to the numbers given in Table II, and the curves labelled  $\sigma_R$  and  $\sigma_{CF}$  correspond to the total reaction cross-section and the cross-section from complete fusion, respectively.  $I_{m+1}$  is plotted because, in a sharp cut-off model,  $\sigma \propto (I_{m+1})^2$ .*

The values of the maximum spin,  $I_m$ , may be compared to the semiempirical estimates by Bass [8] of the total cross section,  $\sigma_R$ , and the cross section for complete fusion,  $\sigma_{CF}$ . Through the relation in Eq.(9) these may be converted to estimates of  $I_{m+1}$ . As seen from Fig. 7 the agreement with the curve labelled  $\sigma_{CF}$  is reasonable, and the discrepancy is probably within the uncertainty of the estimate. It may be noted that a change in the value of the effective moment of inertia would be directly reflected in a change in spin, since the angular distribution determines the value of the parameter  $p$  given by Eq.(7'). If the discrepancy in Fig. 7 is taken seriously, it would suggest that our value of  $J$  is too high by 10-20%, and this would be consistent with experimental results for He induced fission [20].

#### 4.3. Lifetime distributions

In I it was shown that for fission induced by oxygen bombardment the statistical model calculations were able to reproduce the main features of the results obtained with the crystal blocking technique. As shown in Fig. 8 this appears also to be the case for the present measurements. In the figure are shown the contributions from different lifetime intervals, obtained partly from calculations for  $^{12}\text{C}$  bombardment of  $^{182}\text{W}$ , partly as an average over calculations for all four isotopes. The most significant information obtained from the blocking results is the relative contribution of fission after

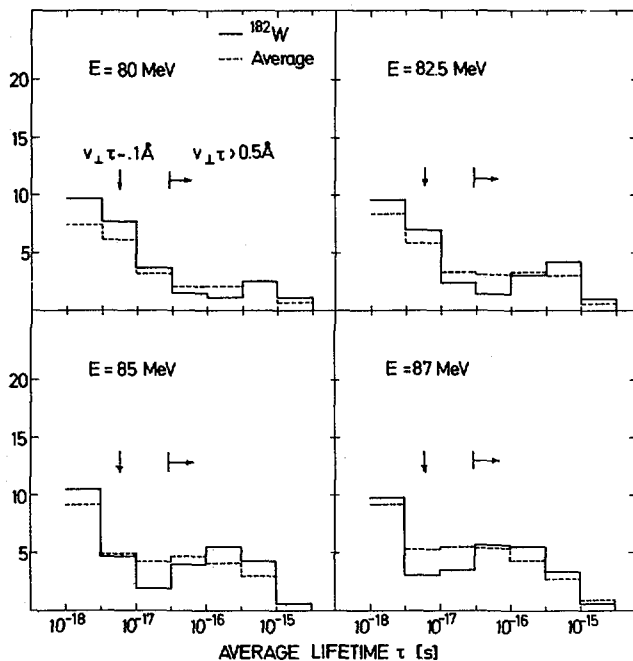


*FIG. 8. Calculated relative contributions [%] of different average-life-time intervals to the total fission yield. Only life-times  $\tau > 10^{-18}$  s are included. The distribution indicated by a solid line is for  $^{12}\text{C} \rightarrow ^{182}\text{W}$ , while the dashed lines indicate the average distribution for a target of natural composition. The relative weights of the different isotopes are determined from the measured fission cross-sections and the natural abundancies. They depend slightly on beam energy, but are approximately 42% (182), 17% (183), 27% (184), and 14% (186). The life-times corresponding to intermediate and long recoils for the forward detector at  $\theta = 130^\circ$  are indicated by arrows (see Fig. 3).*

long average recoils of the compound nucleus ( $v_1\tau \gtrsim 0.5\text{\AA}$ ). Dips for such long recoils were in Figs. 2 and 3 represented by the calculation for  $v_1\tau = 4\text{\AA}$ . For the forward detector ( $\theta = 130^\circ$ ) the limit  $v_1\tau \gtrsim 0.5\text{\AA}$  corresponds approximately to  $\tau \gtrsim 3 \times 10^{-17}$  sec. The calculations then indicate an increase of this component from ~7% at  $E = 80$  MeV to ~15% at  $E = 87$  MeV, in reasonable agreement with the experiment.

For the back counter, at  $\theta \approx 165^\circ$ , the recoil is for fixed lifetime shorter by about a factor of 3 due to the projection factor  $v_1/v = \sin\theta$ . The long-recoil region therefore corresponds approximately to  $\tau \gtrsim 10^{-16}$  sec. and we should expect to find a smaller long-recoil component than for the measurements at  $\theta = 130^\circ$ . As discussed in I, however, this difference may be cancelled by an effect of the anisotropy of the fragment angular distribution. For low temperature and corresponding long lifetime the anisotropy is much larger than the average

(cf. Fig. 6) and this will enhance the contribution of long-lifetime fission at backward angles. It may also be noted that the inclusion of an intermediate-lifetime component in the analysis shown in Fig. 3 reduces the amount ascribed to long lifetimes.

Finally, we may ask whether the experimental results for the intermediate lifetime component are consistent with the calculations. The lifetime corresponding to an average recoil  $v\tau = 0.1\text{Å}$  for the forward detector ( $\theta=130^\circ$ ) is indicated by an arrow in Fig. 8. Clearly there is an appreciable contribution from lifetimes around this value but the very large numbers obtained from the analysis shown in Fig. 3 are not reproduced. Neither is the strong variation of the intermediate lifetime component reproduced by the calculations. Although this discrepancy appears to be significant the large uncertainty in the extraction of an intermediate component must be born in mind (cf. sec. 2.1.). One qualitative feature does seem to be reproduced. In the analysis shown in Fig. 2 of the results obtained with the back detector it was not necessary to introduce a third component in order to obtain acceptable fits. This is in qualitative agreement with the fact that in the region  $\tau \sim 10^{-17}$  sec. the distribution is decreasing with increasing  $\tau$  (for  $\theta=-165^\circ$  an average recoil of  $v\tau = 0.1\text{Å}$  corresponds to  $\tau \sim 2 \times 10^{-17}$  sec.). Let us end this section, however, by emphasizing that concerning the energy dependence of the contribution from long lifetimes the calculations agree with experiments. This is of special importance because in the fitting procedure only the magnitude and not the energy dependence of this contribution is adjusted by parameter variation.

##### 5. DISCUSSIONS AND CONCLUSIONS

The aim of this work has been to analyze the role of blocking lifetime measurements in the study of heavy ion induced fission, and we have mainly concentrated on the analysis of angular distributions of fission fragments. Without information on the average number of neutrons emitted prior to fission such an analysis is ambiguous and rather meaningless (see e.g. the discussions in Ref. 21). In contrast it appears that with the additional lifetime information it is possible to extract useful information from the measurements.

The analysis has relied on model calculations with a parameter set adjusted to fit the data. In connection with the analysis of angular distributions the role of these calculations has been to extract the distribution in spin and temperature from an assumed initial spin distribution, characterized by the maximum value  $I_m$ , and the measured long-lifetime fission component. The selected set of parameters is clearly not unique, and should be interpreted with some caution. One of the compound nuclei created by  $^{12}\text{C}$  bombardment of tungsten,  $^{198}\text{Hg}$ , has been studied also through proton induced fission of gold, and the results have been used [11] to extract the magnitude of the fission barrier for  $^{198}\text{Hg}$ . The value obtained for  $B_f$  is about 5 MeV higher than the value given in Table I. A calculation of fission probabilities for  $^{197}\text{Au}(p,f)$  with the parameter set in Table I confirmed the discrepancy since the calculated fission probability, while reasonable at high energies, was too large by several orders of magnitude for low proton

energies. We have fitted the proton data with parameters and a procedure similar to that of Ref. 11), i.e. with similar ground-state shell corrections, with  $\delta U_B = 0$ , and with a variation of  $B_f$  and the ratio  $a_f/a_n$  of the level density parameters  $a$  for the barrier and for the ground state. A good fit is obtained for  $B_f \approx 21$  MeV for  $^{198}\text{Hg}$  and  $a_f/a_n = 1.05$ , i.e. for values not very different from those obtained in Ref. 11) (cf. also Ref. 22)).

The crucial question is now whether it is possible to reproduce the proton data and the heavy-ion data with a common set of parameters. Preliminary investigations indicate that this is difficult. In particular, with the higher barriers necessary to reproduce the proton data the fission yield will be more dominated by early-stage fission, and the long-lifetime component will be much smaller than that derived from the blocking experiments. In order to reproduce the observed long-lifetime component the effective fission barrier at low excitation energy must for the heavy-ion induced fission be much smaller than the barrier deduced from the proton data. One possibility is that the large negative ground-state shell corrections are strongly reduced for the high-spin states populated by heavy ion bombardment. It should also be noted that the shell corrections at the barrier deformation are rather uncertain. The simple choice of a constant  $\delta U_B$ , independent of neutron number  $N$ , is probably not realistic for the large variation of  $N$  involved. If the value of  $\delta U_B$  is correlated with the shell corrections for the fragments [23] the approach with decreasing mass number  $A$  for the compound nucleus to the magic number  $N = 50$  for the fragments may conceivably lead to a strong variation in  $\delta U_B$ .

It would be very gratifying if the lifetime measurements could help shed some light on such difficult questions. It should be noted that the blocking measurements in principle could give much more detailed information, e.g. through measurements for target crystals of separated tungsten isotopes. Also the detection technique may be improved, and thereby more reliable information about the intermediate lifetime region,  $\tau \sim 10^{-17}$  sec., should be obtainable. Work along these lines is in progress.

#### REFERENCES

- [1] W.M.Gibson, Ann.Rev.Nucl.Sci. 25 (1975) 465
- [2] W.M.Gibson and K.O.Nielsen, Proc. II Int.Conf. on the Physics and Chemistry of Fission (1969 IAEA, Vienna 861 pp.); Phys.Rev.Lett. 24 (1970) 114
- [3] Yu.V.Melikov, Yu.D.Otstavnov, and A.F.Tulinov, Zh.Eksp.Teor. Fiz. 56 (1969); Sov.Phys. JETP 29 (1969) 968; Yad.Fiz. 12 (1970) 50; Sov.J.Nucl.Phys. 12 (1971) 27
- [4] J.U.Andersen, E.Lægsgaard, K.O.Nielsen, W.M.Gibson, J.S.Forster, I.V.Mitchell, and D.Ward, Phys.Rev.Lett. 36 (1976) 1539

- [5] J.U.Andersen, A.S.Jensen, K.Jørgensen, E.Lægsgaard, K.O. Nielsen, J.S.Forster, I.V.Mitchell, D.Ward, W.M.Gibson, and J.J.Cuomo, to be published
- [6] I.Halpern and V.M.Strutinsky, Int.Conf. on Peaceful Uses of Atomic Energy, Geneva, Vol. 15 (U.N., N.Y., 1958) 408
- [7] H.C.Britt and A.R.Quinton, Phys.Rev. 124 (1961) 877
- [8] R.Bass, Nucl.Phys. A231 (1974) 45
- [9] H.Hagelund and A.S.Jensen, Physica Scripta 15 (1977) 225
- [10] A.Kodai-Joopari, Ph.D. Thesis, University of California, Lawrence Radiation Laboratory Report UCRL-16489 (1966)
- [11] L.G.Moretto, S.G.Thompson, J.Routti, and R.C.Gatti, Phys.Letters 38B (1972) 471
- [12] E.Lægsgaard, to be published in Nucl.Inst. and Meth. (1979)
- [13] V.E.Viola, Jr., Nucl.Data Tables A1 (1965) 391
- [14] T.Sikkeland, J.E.Clarkson, N.H.Steiger-Shafir, and V.E. Viola, Phys.Rev. C3 (1971) 329
- [15] C.M.Perey and F.G.Perey, Atomic Data and Nuclear Data Tables 17 (1976) 1
- [16] A.S.Jensen and J.Sandberg, Phys.Scrip. 15 (1977) 225
- [17] M.Brack, J.Damgaard, A.S.Jensen, H.C.Pauli, V.M.Strutinsky, and C.Y.Wong, Rev.Mod.Phys. 44 (1972) 320
- [18] R.Vandenbosch and J.R.Huizenga, "Nuclear Fission", Acad. Press. N.Y. and London 1973, p. 184
- [19] A.H.Wapstra and K.Bos, Atomic Data and Nuclear Data Tables 19 (1977) 215
- [20] R.F. Reising, G.L.Bate, and J.R.Huizenga, Phys.Rev. 141 (1966) 1161
- [21] R.Chaudry, R.Vandenbosch, and J.R.Huizenga, Phys.Rev. 126 (1962) 220
- [22] A.V.Ignatyuk, M.G.Itkis, V.N.Okolovich, G.N.Smirenkin, and A.S.Tishin, Sov.J.Nucl.Phys. 21 (1976) 612 (Yad.Fiz. 21 (1975) 1185)
- [23] U.Mosel and H.W.Schmitt, Phys.Rev. C4 (1971) 2185  
U.Mosel, Phys.Rev. C6 (1972) 971

## DISCUSSION

J.B. WILHELMY: Should we conclude from your results that shell effects are washed out at high angular momenta?

J.U. ANDERSEN: Our results suggest that the dependence on excitation energy of the effective fission barrier is different for proton-induced fission and fission induced by heavy-ion bombardment. For high excitation energy the barriers are similar, while for low excitation energy they are much lower for

the heavy-ion-induced fission. The simplest explanation seems to be that the large negative shell corrections for the ground state are reduced in the case of high angular momentum, since shell correction contributes to the effective fission barriers mainly at low excitation energies. I do not think that this explanation is incompatible with the results reported earlier at this meeting by M.E. Faber (see paper SM-241/C5 in these Proceedings).

M.E. FABER: Further to Dr. Wilhelmy's question, we should recall that with increasing spin the degeneracy of the levels close to spherical shapes is eliminated. So the strong shell corrections in this region decrease with increasing angular momentum. But this does not hold for strongly deformed nuclei, where the gross structure of the shell corrections remains more or less unchanged with increasing spin.

J. PETER: Dr. Andersen, in your calculations do you take into account competition from alpha evaporation and gamma emission? These can significantly compete with fission at high angular momentum, especially after the evaporation of a few neutrons.

J.U. ANDERSEN: Competition from gamma emission was taken into account and does play an important part in the last stages of the evaporation cascade. On the other hand, we did not include alpha emission. Partly on the basis of published experimental data for much higher bombarding energies, we estimated the contribution by alpha emission to be small for the energies at which we bombarded.

H.H. DUHM: I do not quite see why you say that there are particular spin-dependent shell effects that lower the fission barrier. Do you not think the usual reduction in the fission barrier due to angular momentum is enough to explain the long-lived components in the fission yield? Further, what is the extent of the barrier reduction you mentioned, as compared to the barrier observed in the proton-induced reaction?

J.U. ANDERSEN: The usual reduction in the fission barrier at high angular momentum does not depend on the excitation energy, provided the moments of inertia are assumed to be constant, i.e. rigid-body values.

To explain the results of life-time measurements, we need a further reduction in the fission barrier at low excitation energy relative to the barriers deduced from the proton experiment. The extent of the reduction is a few MeV relative to proton barriers of  $\sim 20$  MeV for particle-induced fission.

H.C. PAULI (*Chairman*): Did you also consider pre-compound fission in the analysis of your data?

J.U. ANDERSEN: No, we did not.

S.S. KAPOOR: One of the parameters included in your analysis is the effective moment of inertia, which is saddle-shaped and is taken from the liquid-drop model calculations. Did you estimate the effect of uncertainties in this parameter on your conclusions regarding fission barrier heights?

J.U. ANDERSEN: A change in the effective moment of inertia requires a corresponding adjustment of the maximum angular momentum so as to reproduce the angular distribution, and hence also a change in the average fission probability to fit the fission cross-section. For a small change in  $J_{\text{eff}}$  ( $\sim 10\%$ ) the necessary adjustment of the barriers turns out to be small, and so our qualitative conclusions remain unchanged.

# EXPERIMENTAL DETERMINATION OF FISSION PROBABILITIES FOR PROTON-RICH NUCLEI NEAR THE N = 126 SHELL

K.-H. SCHMIDT, W. FAUST, G. MÜNZENBERG, W. REISDORF  
 Gesellschaft für Schwerionenforschung, GSI, Darmstadt

H.-G. CLERC, D. VERMEULEN, W. LANG  
 Institut für Kernphysik, Technische Hochschule Darmstadt,  
 Darmstadt,  
 Federal Republic of Germany

## Abstract

### EXPERIMENTAL DETERMINATION OF FISSION PROBABILITIES FOR PROTON-RICH NUCLEI NEAR THE N=126 SHELL.

In a study of Ar-induced fusion reactions, production cross-sections and  $Q_\alpha$  values for proton-rich evaporation residues in the region  $84 \leq Z \leq 91$  and  $N \leq 127$  were determined. Particularly by use of the  $^{176}, \dots, ^{180}\text{Hf}$  isotope chain as target nuclei different Th isotopes across the 126 neutron shell could be produced as evaporation residues. Though there is a pronounced shell effect of about 5 MeV observed in the ground-state masses, no enhancement in the measured cross-sections of evaporation residues around  $N = 126$  is observed. The lack of influence of the ground-state shell effect on the evaporation residue cross-sections is discussed in terms of the collective enhancement of the level density of deformed nuclei. Moreover, surprisingly small cross-sections of very-neutron-deficient evaporation residues indicate that for these nuclei far from stability the fission barriers are overestimated by the droplet model.

## 1. INTRODUCTION

Our knowledge of fission barriers is confined to a rather limited region of the nuclide chart, see fig. 1. Nuclei with measured fission barriers are situated in a rather narrow range of the asymmetry parameter  $I = (N - Z) / A$ . Therefore the dependence of the fission barriers on this parameter could not yet be studied comprehensively. In the present work, a systematic study of proton rich nuclei has been performed. These nuclei were produced by heavy ion fusion reactions with Ar projectiles and the target nuclei  $^{164}\text{Dy}$ ,  $^{165}\text{Ho}$ ,  $^{169}\text{Tm}$ ,  $^{171}\text{Yb}$ ,  $^{174}\text{Yb}$ ,  $^{176}, \dots, ^{180}\text{Hf}$  and  $^{181}\text{Ta}$ .

For the nuclei which are studied in this work two characteristics coincide:

a pronounced shell correction energy of a major shell and a high fission probability in the deexcitation process.

Thus the proton-rich nuclei around the 126 neutron shell offer the unique possibility for a first systematic test of the common assumption that an increased fission barrier due to a

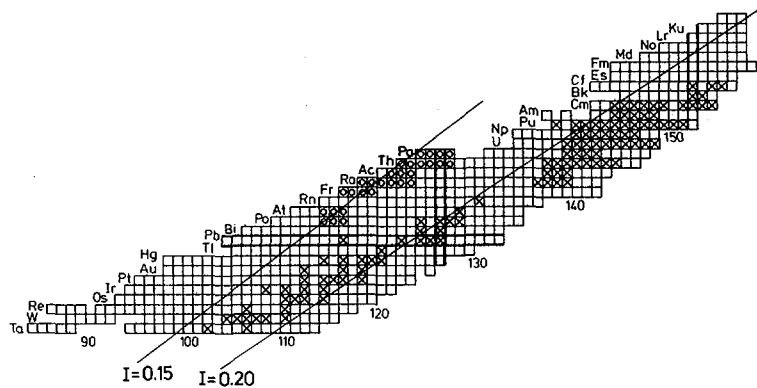


*FIG. 1. Part of the nuclide chart. The known nuclei are represented by boxes. Crosses indicate nuclei with measured fission barriers. The neutron-deficient evaporation residues investigated in this work are characterized by open points. The two lines connect nuclei with constant asymmetry parameter  $I = (N-Z)/A$ .*

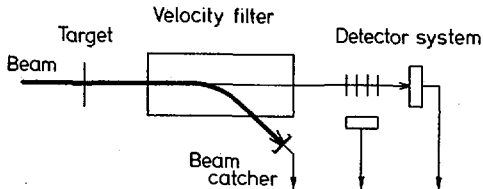


*FIG. 2. Schematic diagram of experimental set-up for the investigation of alpha-active evaporation residues.*

major shell favours the production cross section for nuclei in the presence of high fission competition (see, e.g. ref. [1]). This assumption is crucial for the possibility of producing superheavy elements in heavy ion reactions.

## 2. EXPERIMENTAL PROCEDURE

The measurements were performed at GSI in Darmstadt. As indicated by fig. 2, the velocity filter SHIP was used to suppress the primary beam of the UNILAC accelerator and to transport the fusion products to a detector system. The evaporation residues were implanted into a surface barrier detector where they were identified by their subsequent alpha decay. A secondary-electron detector was used as a transmission detector to discriminate against counts from incoming reaction products and scattered projectiles. The experimental technique is described in detail in ref. [2].

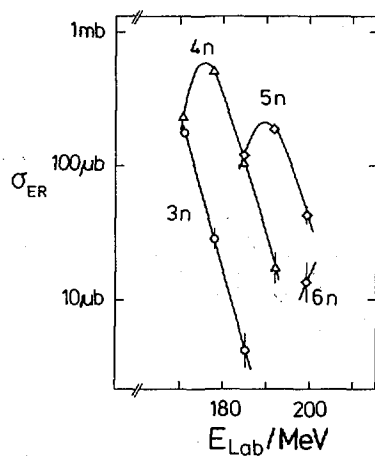


FIG.3. Cross-sections of evaporation residues, formed by the reaction  $^{169}\text{Tm}(^{40}\text{Ar}, xn)^{209-x}\text{Fr}$ . The statistical errors are indicated.

The observed alpha activity allowed us to determine the cross sections for the formation of different evaporation residues. As an example fig. 3 shows excitation functions of evaporation residues which were formed by the reaction  $^{169}\text{Tm}(^{40}\text{Ar}, xn)^{209-x}\text{Fr}$ .

The transport efficiency of the velocity filter was estimated by ion optical calculations [3] and checked by catcher foil measurements [4]. Cross sections could be determined within an accuracy of  $\pm 40\%$ .

### 3. SYSTEMATIC COMPARISON OF FISSION PROBABILITIES

A considerable number of evaporation residue cross sections after fusion reactions have been measured in the actinide region near the valley of beta stability. In order to compare these data with the cross sections of this work, a reduced quantity is deduced, which eliminates the influence of the different projectiles used in these measurements. As a suitable quantity, the average ratio of neutron to fission width  $\langle \Gamma_n/\Gamma_f \rangle$ , reduced to zero angular momentum, has been chosen. The excitation energy has been fixed at a nearly constant value by taking the maxima of the cross sections of evaporation residues formed by the evaporation of four neutrons.

The reduction to zero angular momentum has been performed by using the rotating liquid drop model [5]. It will be shown by simple considerations, that only a limited part of the angular momentum distribution which is populated by the fusion process contributes appreciably to the evaporation residue cross section. The moments of inertia of the nucleus in the ground

state  $\theta_g$  and at the saddle point  $\theta_s$  define the behaviour of the fission barrier  $B_f$  as a function of the angular momentum  $l$ :

$$\begin{aligned} B_f(l) &= B_f(l=0) + l(l+1) \frac{\hbar^2}{(2\theta_s)} - l(l+1) \frac{\hbar^2}{(2\theta_g)} \\ &= B_f(l=0) - \delta B_f(l) \end{aligned}$$

The part of the fission barrier which is due to shell effects is assumed to vary in a similar way as the liquid drop part as a function of the angular momentum.

The fission probability is approximately given by the following expression:

$$\Gamma_n/\Gamma_f \approx \text{const. } \exp(B_f - B_n)/T$$

The temperature  $T$  is related to the excitation energy  $E^*$  and the level density parameter  $a$  by:

$$E^* = a T^2$$

The angular momentum dependency can be separated:

$$\begin{aligned} \Gamma_n/\Gamma_f &\approx \text{const. } \exp(B_f(l=0) - B_n)/T \exp(-\delta B_f(l)/T) \\ &\approx (\Gamma_n/\Gamma_f)_{l=0} \exp(-l^2/l_{\lim}^2) \end{aligned}$$

with

$$l_{\lim} = \sqrt{\frac{T}{\frac{\hbar^2}{(2\theta_g)} - \frac{\hbar^2}{(2\theta_s)}}}$$

Thus, the ratio of the neutron to fission width is cut off at higher angular momenta by a gaussian-like factor. The width of this cutoff is smallest in the last evaporation step. As an example the effective limiting angular momentum  $l_{\lim}$  for  $^{235}\text{U}$  can be estimated from the rotating liquid drop model [5] as follows:

$$\frac{\hbar^2}{(2\theta_g)} \approx 4 \text{ keV}, \quad \frac{\hbar^2}{(2\theta_s)} \approx 1.5 \text{ keV}$$

$$l_{\lim} \approx 15 \quad \text{at an excitation energy } E^* = 10 \text{ MeV.}$$

If we assume that only a small amount of angular momentum is removed by the evaporated neutrons, the evaporation residue cross section  $\sigma_{ER}$  can be calculated by pretending that only the lower  $l$ -range below  $l_{\lim}$  is populated by the fusion process followed by the fission competition for zero angular momentum. Thus only the partial fusion cross section  $\sigma_{lim}$  below  $l_{\lim}$  will be considered.

$$\begin{aligned} (\Gamma_n/\Gamma_{tot})_{l=0} &= (\Gamma_n / (\Gamma_n + \Gamma_p + \Gamma_\alpha + \Gamma_f + \Gamma_\gamma))_{l=0} \\ &= \sigma_{ER}/\sigma_{lim} \end{aligned}$$

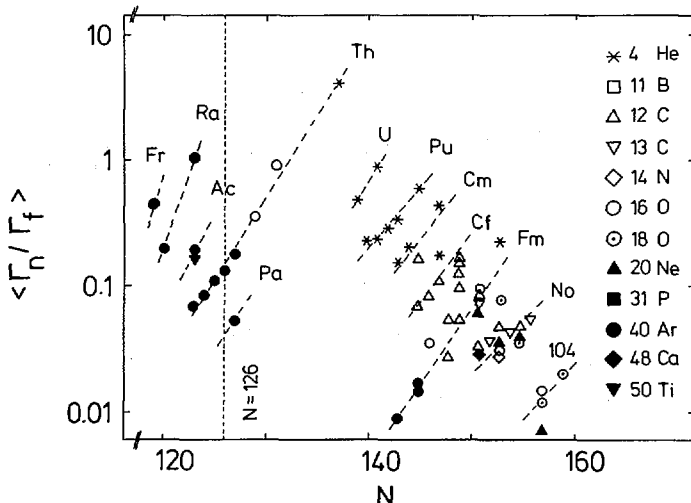


FIG.4.  $\langle \Gamma_f / \Gamma_n \rangle$  values, averaged over the evaporation of four neutrons and reduced to zero angular momentum as a function of the neutron number  $N$  of the last evaporating nucleus. The data with  $N \leq 127$  are measured in this work. The other data points are derived from evaporation residue cross-sections published previously ([6–16] and References cited therein).

The validity of this relation is demonstrated by the following. In case of a high fission probability we get:

$$\Gamma_n / \Gamma_{\text{tot}} \approx \Gamma_n / \Gamma_f$$

It has been checked by evaporation calculations that the evaporation of charged particles can be neglected in all cases considered here. For the evaporation of one neutron we get:

$$\sigma_{\text{ER}} \approx \int_0^{l_{\text{crit}}} \pi \lambda^2 (2l + 1) \exp\left(-\frac{l^2}{l_{\text{lim}}^2}\right) \left(\frac{\Gamma_n}{\Gamma_f}\right)_{l=0} dl$$

with  $l_{\text{crit}}$  being the critical angular momentum, which determines the fusion cross section.

If  $l_{\text{crit}} > l_{\text{lim}}$ , which is assumed to be the case for nearly all heavy ion fusion reactions above the fusion barrier leading to actinide compound nuclei:

$$\sigma_{\text{ER}} \approx \pi \lambda^2 l_{\text{lim}}^2 \left(\frac{\Gamma_n}{\Gamma_f}\right)_{l=0} = \sigma_{\text{lim}} \left(\frac{\Gamma_n}{\Gamma_f}\right)_{l=0}$$

Additionally evaporated neutrons do not change the angular momentum cutoff very much, because the limiting angular momentum  $l_{\text{lim}}$  is smallest in the last evaporation step.

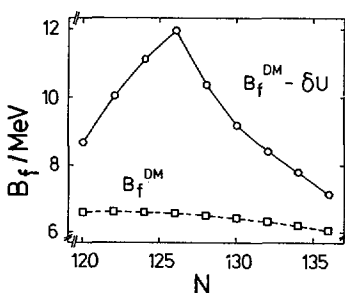


FIG. 5. Droplet fission barriers  $B_f^{DM}$  according to Ref. [19] and the differences of droplet fission barriers and ground-state shell corrections  $\delta U$  for Ac isotopes.  $\delta U$  has been determined as the difference of experimental [18] and droplet [19] masses.

In fig. 4 the values of  $\langle \Gamma_n / \Gamma_f \rangle = (\sigma_{ER} / \sigma_{lim})^{1/4}$ , defined as the average ratio of neutron to fission width reduced to zero angular momentum, are shown for all available measured  $4n$  cross sections as a function of the neutron number  $N$  of the last evaporating nucleus. By the reduction to zero angular momentum, the fission probabilities should become independent of the projectile-target combination having formed the compound nucleus.

The data points can be approximated by straight lines for each element. For the neutron rich nuclei these values agree with the  $\Gamma_n / \Gamma_f$ -systematics of Vandenbosch and Huizenga [17] which refers to small angular momenta.

#### 4. CROSS SECTIONS OF EVAPORATION RESIDUES NEAR $N = 126$

The ground state masses of proton rich nuclei near the 126 neutron shell have recently been determined by M. Epherre et al. [18]. In fig. 5 the estimated heights of the fission barriers of Ac-isotopes are shown. If shell effects at the saddle point are disregarded, the expected fission barrier of the magic  $^{215}\text{Ac}$  amounts to 12 MeV, consisting of a droplet contribution [19] of 6.5 MeV and a considerable ground state shell correction of about 5.5 MeV. The latter has been deduced from the difference of the experimental [18] and the droplet [19] mass.

In spite of this pronounced shell effect (for Th about the same shell effect as for the neighboured Ac isotopes is expected) no structure is seen near  $N = 126$  for the fission competition of Th isotopes in fig. 4.

In fig. 6 the measured  $\langle \Gamma_n / \Gamma_f \rangle$  values are compared with model calculations. Besides the rotating liquid drop model for the determination of the fission barrier as a function of the angular momentum, the energy dependence of the level density as proposed by Ignatyuk et al. [20] has been used. In qualitative agreement with calculations of Moretto [1] and Gottschalk and Lederman [21], Ignatyuk assumes that for nuclei with a negative shell correction  $\delta U$  the level density is lowered near the ground state. For energies higher than about 30 MeV only a

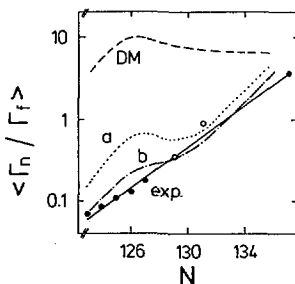


FIG. 6. Average  $\langle \Gamma_n / \Gamma_f \rangle$  values as in Fig. 4 for Th isotopes. exp: experimental values as given in Fig. 4; DM: calculated values using droplet fission barriers and the level density description of Ignatyuk et al. [20] (damping constant = 18.5 MeV). a: calculated values using liquid-drop fission barriers with the parameters  $\kappa = 1.11$ ,  $a_2 = 17.944$  and  $2a_2/c_3 = 48.04$ . (For definition of these parameters, see Ref. [26].) b: calculated values using the same liquid-drop fission barriers as in case a, but a reduced damping constant of 10 MeV.

backshift to the fictive ground state of a liquid drop nucleus remains. Between these two extrema, Ignatyuk assumes an exponential transition with a damping constant of 18.5 MeV:

$$a E^* = \tilde{a} (E^* + \delta U) - \tilde{a} \delta U \exp(-E^*/18.5 \text{ MeV})$$

Here  $\tilde{a}$  is the asymptotic level density parameter for high excitation energy  $E^*$ .

The calculated  $\langle \Gamma_n / \Gamma_f \rangle$  values, using droplet fission barriers [19] and shell effects deduced from semiempirical binding energies [22,23] are shown in fig. 6 (dashed line). They are much higher than the experimental values and show a structure near  $N = 126$  which is missing in the measured data. If the fission barriers are lowered by using ad hoc liquid drop barriers with modified parameters (see caption of fig. 6), the peak in the calculated  $\langle \Gamma_n / \Gamma_f \rangle$  values around  $N = 126$  remains (dotted line). Only with a damping constant as low as 10 MeV the discrepancies between calculated and measured  $\langle \Gamma_n / \Gamma_f \rangle$  values are reduced considerably (dot-dashed line).

Possible explanations of the lack of structure in the dependency of the  $\langle \Gamma_n / \Gamma_f \rangle$  values on the neutron number near the  $N = 126$  shell are a strong sensitivity of the ground state shell effect to angular momentum or an enhancement of the fission probability of spherical nuclei when compared with deformed nuclei due to rotational contributions to the level density [24].

At an angular momentum of  $10 \hbar$ , which is estimated to be the most probable angular momentum of the evaporation residues before emission of  $\gamma$  rays, the ground state shell correction of  $^{210}\text{Po}$  is calculated without regarding pairing correlations to be reduced by only about 25% [25]. Thus, the angular momentum dependency of the fission barriers would not explain the observed smooth behaviour of the  $\langle \Gamma_n / \Gamma_f \rangle$  values across the  $N = 126$  shell.

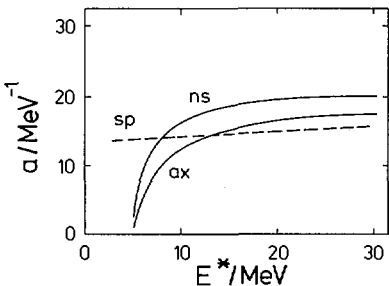


FIG. 7. Level-density parameter  $\alpha$  of a spherical magic nucleus ( $A = 220$ ) with a deformed isomeric state at 5 MeV excitation energy. The level density of the nucleus in the spherical shape is exceeded by the level density in the deformed shape at rather low excitation energy if the collective enhancement of the level density is taken into account. sp: spherical shape, ax: axial-symmetric shape, ns: no rotational symmetry.

Moretto estimated the deformation probability of a nucleus by single particle calculations and statistical arguments [11]. Let us consider the effect of rotational contributions to the level density on these considerations. In a spherical magic nucleus a deformed state may be situated at an excitation energy of about the ground state shell correction. In Fig. 7 the level density parameters of the nucleus in its spherical ground state shape and its isomeric state which is assumed to have either an axial symmetric or a non-symmetric shape are compared. The level density parameter has been calculated as the theoretically expected value [20] of a Fermi gas in a Woods-Saxon potential:

$$\tilde{\alpha} = (A / 13.7 + .056 A^{2/3}) \text{ MeV}^{-1}$$

The mass number 220 has been chosen as an example. For the level density in the spherical shape the influence of the ground state shell correction was taken into account according to the procedure as proposed by Ignatyuk et al. [20]. For this qualitative estimate, the level density parameters in the other states were obtained by multiplying the asymptotic level density by 25 for the axial symmetric shape and by 625 for the shape without rotational symmetry [24].

Though it is necessary to exceed the shell correction energy in order to populate the deformed states, those grow so quickly that they soon surmount the level density of the spherical ground state. That would mean that above a rather low excitation energy (in our example about 10 MeV)

a) the level densities of a magic spherical nucleus and a deformed nucleus without shell effects are about equal if taken at the same excitation energy above a fictive liquid drop ground state,

b) the most probable shape of this nucleus would switch to deformation.

Thus the rotational contributions to the level density may make the influence of a spherical shell effect on the level density vanish at a rather low excitation energy and hence on the evaporation residue cross sections.

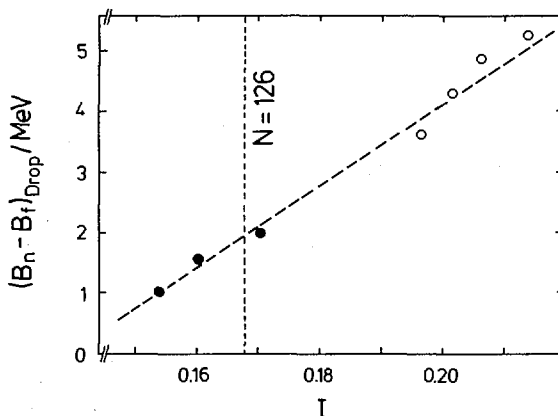


FIG. 8. Difference  $(B_n - B_f)_\text{Drop}$  of the neutron binding energy and the fission barrier according to the droplet model [19] for some nuclei which show a constant measured value of  $\langle \Gamma_n / \Gamma_f \rangle = 0.2$  in Fig. 4 as a function of the asymmetry parameter  $I = (N - Z)/A$  of the last evaporating nucleus.

## 5. DROPLET FISSION BARRIERS

The calculations shown in fig. 6 indicated already that the fission barriers of very neutron deficient Th isotopes may be overestimated by the droplet model [19]. This conclusion is corroborated by the following considerations.

If in fig. 4 nuclei with the same  $\langle \Gamma_n / \Gamma_f \rangle$  value are selected, they are expected to have the same difference  $B_n - B_f$  of neutron binding energy and fission barrier. E. g. for nuclei with  $\langle \Gamma_n / \Gamma_f \rangle = 0.2$  a value of  $B_n - B_f \approx 3$  MeV is expected. There might be some deviation due to shell effects but fig. 6 does not suggest any strong influence of the  $N = 126$  shell.

Therefore, in fig. 8 the difference of the droplet values  $B_n - B_f$  according to the droplet model [19] is shown for those nuclei which have a constant  $\langle \Gamma_n / \Gamma_f \rangle$  value of 0.2. The parameter  $B_n - B_f$  obviously is not constant but varies by more than 4 MeV in a smooth way across the  $N = 126$  shell. As the selection of these nuclei does not seem to reveal any influence of the 126 neutron shell which would account for the variation in fig. 8, this discrepancy may be caused by the droplet barriers. If the influence of ground state shell corrections of spherical nuclei on the fission competition is neglected as suggested by section 4, the measured evaporation residue cross sections of the present work can be reproduced if we assume that the fission barriers of these very neutron deficient isotopes, about 20 neutrons away from the valley of beta stability, are about 2 MeV smaller than estimated by the droplet model [19]. Probably this deviation is related to surprisingly low fission barriers of very neutron deficient Hg isotopes [27] and to very low fission barriers which are deduced from the analysis of the fusion- and evaporation residue cross sections of even lighter neutron deficient nuclei [28]. It seems that this tendency already shows up in the deduced Z-dependent liquid drop parameters of heavy actinides [26].

## 6. CONCLUSION

The analysis of the evaporation residue cross sections suggests that the droplet barriers of very neutron deficient isotopes near thorium are smaller than predicted by the Myers droplet model [19]. This seems to be a general trend which shows up more and more for lighter nuclei. Therefore it may be suspected that the low fission barriers of light neutron deficient nuclei reveal some isospin dependent characteristic of nuclei which is not included in the droplet model.

The absence of any observed enhancement of the evaporation residue cross sections near the  $N = 126$  shell indicates that the influence of the ground state shell effect on the fission probability is rather weak in this case. If this is a general effect, the production of superheavy elements by fusion reactions will be extremely difficult, even if they are stabilized by a considerable ground state shell correction.

## ACKNOWLEDGMENTS

We are very much obliged to P. Armbruster for the encouraging interest in this work and the many fruitful discussions. Furthermore we are indebted to the UNILAC crew for providing a stable beam as well as to the data processing crew for helping to utilize the EDAS data acquisition system. We wish to thank W. D. Myers for the possibility of using the computer codes for the calculation of droplet properties of nuclei.

## REFERENCES

- [1] MORETTO, L. G., Proc. 3rd IAEA Symp. on physics and chemistry of fission, Rochester 1973, vol. 1 (IAEA, Vienna, 1974) p. 329
- [2] SCHMIDT, K.-H., FAUST, W., MÜNZENBERG, G., CLERC, H.-G., LANG, W., PIELENZ, K., VERMEULEN, D., WOHLFARTH, H., EWALD, H., GÜTTNER, K., Nucl. Phys., A318 (1979) 253
- [3] FAUST, W., thesis, Universität Giessen, 1978
- [4] VERMEULEN, D., CLERC, H.-G., SCHMIDT, K.-H., in annual report GSI J-79-1, 1979, in print
- [5] COHEN, S., PLASIL, F., SWIATECKI, W. J., Ann. Phys. (N.Y.) 82 (1974) 557
- [6] VANDENBOSCH, R., HUIZENGA, J. R., Peaceful Uses of Atomic Energy (Proc. Int. Conf. Geneva, 1958) 15, UN, New York (1958) 284
- [7] NEUBERT, W., Nuclear Data Tables 11, (1973) 531
- [8] ALONSO, J. R., "Gmelin Handbuch der anorg. Chemie", 7b part A1,II, (KOCH, G., Ed.), Springer (1974) 28
- [9] DELAGRANGE, H., et al., Phys. Rev. C17 (1978) 1706
- [10] HÄUSSER, O., et al., Phys. Rev. Lett. 31 (1973) 323
- [11] MARINOV, A., private communication
- [12] DRUIN, V. A., et al., Sov. J. Nucl. Phys. 24 (1976) 131
- [13] OGANESIAN, Yu. Ts., et al., Nucl. Phys. A239 (1975) 353
- [14] TER-AKOPYAN, G. M., et al., Nucl. Phys. A255 (1975) 509

- [15] NITSCHKE, J. M., et al., Nucl. Phys. A313 (1979) 236
- [16] FLEROV, G. N., et al., Nucl. Phys. A267 (1976) 359
- [17] VANDENBOSCH, R., HUIZENGA, J. R., "Nuclear Fission", (Academic Press, New York, 1973)
- [18] EPHERRÉ, M., et al., to be published
- [19] MYERS, W. D., "Droplet model of atomic nuclei" (IFI/Plenum New York, 1977)
- [20] IGNATYUK, A. V., ITKIS, M. G., OKOLOVICH, V. N., SMIRENKIN, G. N., TISHIN, A. S., Sov. J. Nucl. Phys. 21 (1975) 612
- [21] GOTTSCHALK, P. A., LEDERGERBER, T., Nucl. Phys. A278 (1977) 16
- [22] WAPSTRA, A. H., BOS, K., Atomic Data and Nucl. Data Tables 19 (1977) 185
- [23] LIRAN, S., ZELDES, N., Atomic Data and Nucl. Data Tables 17 (1976) 431
- [24] BJØRNHOLM, S., BOHR, A., MOTTELSON, B. R., Proc. 3rd IAEA Symp. on physics and chemistry of fission, Rochester 1973, vol. 1 (IAEA, Vienna, 1974) 367
- [25] FABER, M., private communication
- [26] PAULI, H. C., LEDERGERBER, T., Proc. 3rd IAEA Symp. on physics and chemistry of fission, Rochester 1973, vol. 1 (IAEA, Vienna, 1974) 463
- [27] REISDORF, W., GOWDY, G., HUBER, G., KIRCHNER, R., KLEPPER, O., RÖCKL, E., TIDEMAND-PETERSSON, P., ALQUIST, L., in annual report GSI J-79-1, 1979, in print
- [28] BECKERMAN, M., BLANN, M., Phys. Rev. Lett. 38 (1977) 272

## DISCUSSION

K.M. DIETRICH: I assume that at excitation energies  $E^* \lesssim (5-7)$  MeV the specific nature of the excitation spectrum is of great importance for the level density. In other words, the usual approximations such as the Thomas-Fermi model, or uniformly-spaced single-particle levels, are not expected to yield reliable level densities. At the Rochester meeting, Huizenga reported on level densities calculated on the basis of the Nilsson model. Perhaps we ought to use this code for analysis of the experimental data, as it could modify the resulting fission barrier heights.

K.H. SCHMIDT: We did not actually carry out calculations of that kind, though I agree with you that the absolute determination of fission barrier heights does depend on the level density used in the analysis.

I doubt, however, whether single-particle level densities would solve the problem, since it is still unclear how one should include the energy dependence of rotational contributions to the level density.

We base our arguments in determining fission barrier parameters on trends in the neutron-to-fission widths as a function of the neutron number (see my Fig.6), which can hardly be interpreted as variation in the level density parameters.

H.C. BRITT: The absence of a shell effect in your data at  $N = 126$  is well demonstrated and highly significant. I would only comment that the detailed extraction of fission barrier heights is very sensitive to the details of the level density functions used, especially in the near-barrier region. This question needs further investigation before it will be possible to draw conclusions regarding the accuracy of the fission barriers from the droplet model.

K.H. SCHMIDT: It seems rather hard to explain the smooth variation in the predicted droplet values  $(B_n - B_f)_{\text{drop}}$  for nuclei with the same measured ratio of neutron-to-fission width  $\langle \Gamma_n/\Gamma_f \rangle = 0.2$ , shown in Fig.8, in any other way than by the shortcomings of the droplet model.

Any other explanation, such as the effect of the 126 neutron shell or the influence of nuclear shape on the level densities, could be expected to result in deviations nearly symmetrical to  $N = 126$ . This is clearly not observed experimentally.

V.J. ROBINSON: Since your  $\Gamma_n/\Gamma_f$  values are weighted averages over the nuclei leading to the evaporation residues, don't you think that the shell effects would disappear? After all, when you approach the shell, you involve both pre-shell (high binding energy) and post-shell (low binding energy) neutrons.

K.H. SCHMIDT: It is not only the neutron binding energies but also the fission barriers that are affected by the ground-state shell corrections. In the calculations shown in my Fig.6 we average over four evaporation steps, but we still expect a large bump in the  $\langle \Gamma_n/\Gamma_f \rangle$  values.

# ПЛОТНОСТЬ УРОВНЕЙ И ВЕРОЯТНОСТЬ ДЕЛЕНИЯ СФЕРИЧЕСКИХ И ДЕФОРМИРОВАННЫХ ЯДЕР

А. В. ИГНАТЮК, К. К. ИСТЕКОВ, В. Н. ОКОЛОВИЧ,

Г. Н. СМИРЕНКИН

Институт ядерной физики

Академии наук Казахской ССР,

Алма-Ата,

Союз Советских Социалистических Республик

## Abstract—Аннотация

### LEVEL DENSITY AND FISSION PROBABILITY IN SPHERICAL AND DEFORMED NUCLEI

The important role of rotational increase in the level density of nuclei in a description of the observed fission probability of sub-actinide nuclei is demonstrated. From an analysis of the experimental data available the authors find for the corresponding coefficient an energy dependence, which exhibits deviations from the adiabatic estimate of rotational effects in highly excited nuclei. By allowing for collective effects in fission and neutron decay channels of compound nuclei it is possible to obtain a consistent description of the fissionability observed both in the near-threshold region and in the high-energy region, where fission by means of emission is dominant. The dependence of fission barriers on mass number, as determined from an analysis of the fissionability of sub-actinide nuclei, differs considerably from what was found in previous work.

### ПЛОТНОСТЬ УРОВНЕЙ И ВЕРОЯТНОСТЬ ДЕЛЕНИЯ СФЕРИЧЕСКИХ И ДЕФОРМИРОВАННЫХ ЯДЕР.

Показана важная роль ротационного увеличения плотности уровней ядер при описании наблюдаемой вероятности деления доактинидных ядер. Из анализа имеющихся экспериментальных данных найдена энергетическая зависимость соответствующего коэффициента, демонстрирующая отклонения от адиабатической оценки ротационных эффектов в высоковозбужденных ядрах. Учет коллективных эффектов в делительном и нейтронном каналах распада составных ядер позволяет получить взаимосогласованное описание наблюдаемой делимости как на околовороговом участке, так и в высокоэнергетической области, где доминирующим является эмиссионный способ деления. Найденная из анализа делимости доактинидных ядер зависимость барьеров деления от массового числа заметно отличается от результатов прежних работ.

## 1. ВВЕДЕНИЕ

Экспериментальные данные об энергетической зависимости сечений деления  $\sigma_f(E)$  являются основным источником информации о высоте барьеров деления  $E_f$ . В последние годы в тесной связи с прогрессом теории, достигнутым на основе метода оболочечной поправки [1], эта важная характеристика процесса деления при-

обрела значение и в более широком аспекте — для описания целой совокупности свойств ядер: масс, энергий, деформации, границ стабильности, потенциалов взаимодействия тяжелых ионов и др. Не менее важной является информация о статистических свойствах возбужденных ядер, которую можно извлечь из анализа сечений деления.

Повышенный интерес к анализу экспериментальных данных о делимости доактинидных ядер обусловлен целым рядом их специфических преимуществ в сравнении с более сильно делящимися соседями — актинидами:

- 1) значительная разница между высотой барьеров и энергией связи нейтронов, уменьшающая делимость и создавая определенные трудности для эксперимента, очень благоприятна для анализа энергетической зависимости плотности уровней;
- 2) благодаря большой седловой деформации, практически предельно возможной для ядер, переходное состояние доактинидов, по-видимому, в наибольшей степени избавлено от влияния оболочечных эффектов, что существенно упрощает анализ делительных ширин;
- 3) область доактинидов содержит островок сферических ядер в окрестности  $Z = 82$ ,  $N = 126$ , слева и справа от которого ядра в равновесном состоянии деформированы. Это обстоятельство представляет уникальную возможность для изучения влияния деформации ядер на коллективные свойства плотности уровней в нейтронном канале.

Малая вероятность исследуемых событий в недалеком прошлом сильно ограничивала возможности изучения этой области ядер, но в настоящее время трудности успешно разрешаются с помощью трековых детекторов [2-4]. Интенсивные исследования вероятности деления доактинидных ядер протонами,  $\alpha$ -частицами и ионами  ${}^3\text{He}$  проводились в последние годы на Алма-Атинском изохронном циклотроне. Полученные экспериментальные данные достаточно полно представлены в работах [4-6], и мы не будем останавливаться на их рассмотрении. Совместно с результатами более ранних исследований [2, 3] накопленные данные могут служить основой для систематического анализа делимости всей совокупности доактинидных ядер в широком диапазоне энергий возбуждения.

В прошлом неоднократно предпринимались попытки анализа вероятности деления доактинидных ядер, главным образом, с целью получения информации о барьерах деления. В настоящей работе в центре внимания находится другой аспект данной проблемы — энергетическая зависимость плотности уровней. Как будет показано ниже, результаты анализа обеих величин теснейшим образом связаны между собой. В большинстве предыдущих работ по данному вопросу анализ делимости проводился на основе соотношения модели ферми-газа с феноменологическим учетом оболочечных эффектов и эффектов спаривания нуклидов. Однако, развитие микроскопических методов теоретического описания плотности уровней отчетливо демонстрирует примитивность такой модели и существенную ограниченность области ее применимости [7, 8]. В частности, для интерпретации многих статистических свойств возбужденных ядер важную роль играют коллективные степени свободы [9]. Только

совместный учет всех трех эффектов – оболочечных неоднородностей одночастичного спектра, парных корреляций нуклонов сверхпроводящего типа и коллективных возбуждений ядер – приводит ко взаимосогласованному описанию наблюдаемой плотности нейтронных резонансов сферических и деформированных ядер [7, 8]. Эквивалентное описание экспериментальных данных можно получить также в рамках достаточно простой феноменологической модели, включающей в себя все перечисленные выше эффекты [10]. Значительный интерес представляет проверка его в более широкой области энергий возбуждения. В последующих разделах будет показано, что применение этого описания к анализу вероятности деления доактинидов позволяет уточнить как представление о самой плотности уровней, так и извлекаемые из анализа сведения о свойствах переходных состояний делящихся ядер.

## 2. ОСНОВНЫЕ СООТНОШЕНИЯ ДЛЯ АНАЛИЗА ДЕЛИМОСТИ

Вероятность деления (или делимость) определяется конкуренцией двух доминирующих ширин распада составного ядра: делительной  $\Gamma_f$  и нейтронной  $\Gamma_n$ , и может быть записана в виде

$$P_f(E) = \frac{\sigma_f(E)}{\sigma_c(E)} = \left( \sum_J (2J+1) T_J \right)^{-1} \sum_J (2J+1) T_J \frac{\Gamma_f^J(E)}{\Gamma_f^J(E) + \Gamma_n^J(E)} \quad (1)$$

где  $\sigma_f$  – сечение деления,  $\sigma_c$  – сечение образования составного ядра,  $E$  и  $J$  – его энергия и угловой момент и  $T_J$  – коэффициенты прилипания для налетающей частицы. Число параметров, характеризующих ширину  $\Gamma_f$  и  $\Gamma_n$ , значительно уменьшается в области энергий возбуждения, где к их описанию применим статистический подход. В этом случае отношение ширин можно представить в виде

$$\frac{\Gamma_f^J(E)}{\Gamma_n^J(E)} = \frac{\kappa}{2A^{2/3}} \frac{\int_0^E \rho_f(U, J) T_f(U) dU}{\int_0^{E-B_n} \rho_n(U, J) (E - B_n - U) dU} \quad (2)$$

где  $T_f(U)$  – проницаемость барьера деления,  $B_n$  – энергия связи нейтрона,

$\kappa = \frac{\hbar^2}{2m r_0^2} \approx 10$  МэВ. Отношение (2) в силу экспоненциального характера энергетической зависимости  $P(U, J)$  с точностью до возникающих при интегрировании

предэкспоненциальных множителей является отношением плотности уровней в делительном и нейтронном каналах распада составного ядра  $\rho_f(E - E_f, J)/\rho_n(E - B_n, J)$ .

При учете вклада ротационных степеней свободы плотность уровней деформированных аксиально-симметричных ядер должна быть записана как [9]:

$$\rho_{\text{деф}}(U, J) = \frac{\omega(U)}{2\sqrt{2\pi}\sigma_{\parallel}} \sum_{K=-J}^J \exp \left\{ -\frac{J(J+1)}{2\sigma_1^2} - \left( \frac{1}{\sigma_{\parallel}^2} - \frac{1}{\sigma_1^2} \right) \frac{K^2}{2} \right\} \quad (3)$$

где  $\omega(U)$  – полная плотность неротационных возбужденных состояний ядра,  $\sigma_1^2 = F_1 t/\hbar^2$  и  $\sigma_{\parallel}^2 = F_{\parallel} t/\hbar^2$  – параметры спиновой зависимости, связанные с перпендикулярным  $F_1$  и, соответственно, параллельным  $F_{\parallel}$  моментом инерции деформированного ядра,  $K$  – проекция углового момента на ось симметрии и  $t$  – температура возбужденного ядра. Для сферически-симметричных ядер соотношение, аналогичное (3), имеет более простой вид

$$\rho_{\text{сф}}(U, J) = \frac{2J+1}{2\sqrt{2\pi}\sigma^3} \omega(U) \exp \left\{ -\frac{J(J+1)}{2\sigma^2} \right\} \quad (4)$$

Удобно переписать соотношение (3) в несколько ином виде, выделяя в нем сомножитель, эквивалентный (4),

$$\rho_{\text{деф}}(U, J) = K_{\text{rot}} \rho_{\text{внутр}}(U, J) \quad (5)$$

$$\rho_{\text{внутр}}(U, J) = \frac{2J+1}{2\sqrt{2\pi}\sigma_{\perp}^2\sigma_{\parallel}^2} \omega(U) \exp \left\{ -\frac{J(J+1)}{2\sigma_1^2} \right\} \quad (6)$$

$$K_{\text{rot}}(U, J) = \frac{\sigma_1^2}{2J+1} \sum_{K=-J}^J \exp \left( -\frac{K^2}{2K_0^2} \right) \quad (7)$$

В последнем соотношении использовано традиционное для физики деления определение параметра  $K_0^2 = \sigma_{\parallel}^2 \sigma_{\perp}^2 (\sigma_{\parallel}^2 - \sigma_{\perp}^2)^{-1}$ . При характерных для рассматриваемых реакций значениях углового момента для равновесной деформации ядер редкоземельной области показатель экспоненты в (7) достаточно мал, и можно принять  $K_{\text{rot}} \approx \sigma_1^2$ . Поэтому при описании плотности уровней в нейтронном канале можно использо-

вать соотношение (5) как для деформированных, так и для сферических ядер, принимая

$$K_{\text{rot}}^n = \begin{cases} \sigma_{\perp n}^2 & \text{для деформированных ядер,} \\ 1 & \text{для сферических ядер} \end{cases} \quad (8)$$

В переходном состоянии ядро деформировано гораздо сильнее, чем в равновесном. Вследствие неравенства  $\sigma_{\perp f}^2 > \sigma_{\parallel f}^2$ , особенно сильного при низких энергиях возбуждения  $U_f = E - E_f$  в делительном канале, нельзя игнорировать J-зависящий фактор соотношения (7). В этом случае удобно воспользоваться более строгим выражением

$$K_{\text{rot}}^f (U, J) \simeq \sigma_{\perp f}^2 \frac{\sqrt{2\pi} K_0}{2J+1} \operatorname{erf} \left( \frac{J+1/2}{\sqrt{2} K_0} \right) \quad (9)$$

В соотношениях для плотности уровней можно было бы также учесть вибрационные степени свободы введением коэффициентов  $K_{\text{vibr}}$  [7-9]. Однако в данном анализе мы не будем их рассматривать, так как этот коэффициент входит в виде примерно одинакового множителя в числитель и знаменатель соотношения (2), и, ввиду неравенства  $K_{\text{vibr}} \ll K_{\text{rot}}$ , в рамках феноменологического подхода роль вибрационных эффектов нецелесообразно выделять на фоне существующих погрешностей описания  $K_{\text{rot}}$ . С учетом изложенного перепишем соотношение (2) в виде

$$\frac{\Gamma_f^J(E)}{\Gamma_n^J(E)} = \frac{K_{\text{rot}}^f}{K_{\text{rot}}^n} \frac{\kappa}{2A^{2/3}} \gamma(J) \frac{\int_0^E \rho_{\text{внутр}}^f(U, 0) T_f(U) dU}{\int_0^{E-B_n} \rho_{\text{внутр}}^n(U, 0) (E - B_n - U) dU} \quad (10)$$

где все J- зависящие факторы выделены в сомножитель

$$\gamma(J) = \frac{\sqrt{2\pi} K_0}{2J+1} \operatorname{erf} \left( \frac{J+1/2}{\sqrt{2} K_0} \right) \exp \left\{ \frac{J(J+1)}{2} \left( \frac{1}{\sigma_{\perp n}^2} - \frac{1}{\sigma_{\perp f}^2} \right) \right\} \quad (11)$$

и в соответствии с этим везде в дальнейшем мы будем применять по аналогии с нейтронным каналом (8) определение  $K_{\text{rot}}^f = \sigma_{\perp f}^2$ . Величины  $\sigma_{\perp}^2$  и  $\sigma_{\parallel}^2$ , входящие в  $K_{\text{rot}}$  и  $\gamma(J)$ , зависят от энергии примерно как  $\sqrt{U}$ , т.е. слабо в сравнении с экспоненциальной зависимостью  $\rho_{\text{внутр}}(U, 0)$ , чем мы воспользовались, вынеся их из-под интегров по теореме о среднем. В результате, с достаточной точностью их можно считать функциями верхних пределов  $E - E_f$  и  $E - B_n$ , соответственно.

Соотношение (10) отличается от использованного ранее [4, 5] только множителем  $K_{\text{rot}}^f / K_{\text{rot}}^n$ . Однако, влияние этого множителя на величину отношения делительной и нейтронной ширин весьма значительно, поскольку  $K_{\text{rot}}^n$  с переходом от дефор-

мированных ядер к сферическим меняется в десятки раз. В то же время, выделение такого сомножителя не затрагивает вопросов, которые связаны с описанием J-зависимости интегральных и дифференциальных сечений деления.

Наблюдаемую делимость в этой области энергий, где пренебрежим вклад реакций с предварительным испусканием нейтронов, можно выразить используя (10), как

$$P_f(E) \simeq \frac{1}{J_{\max}^2} \int_0^{J_{\max}} \gamma(J) dJ^2 \frac{\Gamma_f^0(E)}{\Gamma_n^0(E)} \quad (12)$$

где  $J_{\max}$  – эффективная граница квазиклассического распределения угловых моментов  $\frac{2 J dJ}{J_{\max}^2}$ , соответствующая реальному распределению  $\sigma_c^J$ ,  $\Gamma_f^0(E)/\Gamma_n^0(E)$  – отношение ширин (10) для нулевого углового момента.

### 3. ОПИСАНИЕ ПЛОТНОСТИ УРОВНЕЙ

Для вычисления плотности внутренних возбуждений ядра  $\rho_{\text{внутр}}(U, J)$  в данной работе использовались соотношения сверхтекущей модели ядра, детальное описание которых приведено в работе [10]. Для последующего обсуждения важно отметить следующие основные особенности модели.

1. В описании различных термодинамических характеристик ядер важную роль играет величина критической энергии фазового перехода из сверхтекущего состояния в нормальное (ферми-газовое)

$$U_{kp} = 0,47a \Delta_0^2 \sim 7 \div 8 \text{ МэВ} \quad (13)$$

где  $a$  – параметр плотности уровней и  $\Delta_0$  – корреляционная функция ядра в основном состоянии. Выше критической энергии парные корреляции нуклидов можно учесть, введя в соотношения модели ферми-газа соответствующее определение эффективной энергии возбуждения  $U^* = U - E_{\text{конд}}$ , где энергия конденсации  $E_{\text{конд}} \simeq 0,15a \Delta^2$ . Как правило, величина  $E_{\text{конд}}$  заметно выше, чем поправка на четно-нечетные различия в традиционном ферми-газовом описании [12]. Ниже критической энергии корреляционные эффекты не сводятся к какой-либо простой модификации энергии возбуждения и для описания поведения плотности уровней, моментов инерции и т.п. необходимо привлекать более громоздкие соотношения сверхтекущей модели ядра [7, 10].

2. Оболочечные эффекты были включены в рассмотрение на основе феноменологически подобранной энергетической зависимости параметра плотности уровней

$$a(U, Z, A) = \begin{cases} \tilde{a}(A) \left\{ 1 + \delta W(Z, A) \frac{f(U - E_{\text{конд}})}{U - E_{\text{конд}}} \right\} & \text{для } U \geq U_{kp} \\ a(U_{kp}, Z, A) & \text{для } U < U_{kp} \end{cases} \quad (14)$$

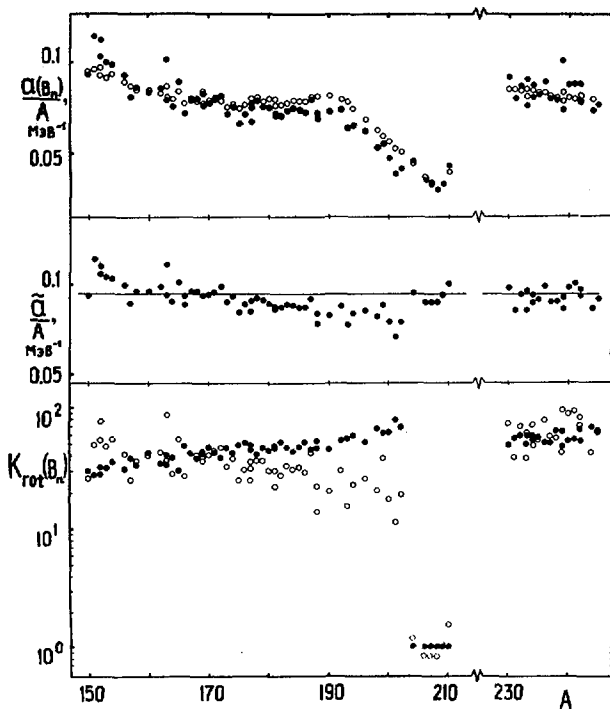


Рис. 1. Систематика параметра плотности уровней  $a(B_n)$  (вверху) и асимптотических значений этого параметра  $\tilde{a}$  (в средней части), полученная из анализа плотности нейтронных резонансов ( $\bullet$ ) и на основе соотношений (14) ( $\circ$ ). В нижней части рисунка показана величина коэффициентов  $K_{\text{rot}}(B_n)$ , соответствующих экспериментальным значениям  $\tilde{a}/A$  ( $\bullet$ ) и значениям  $\tilde{a}/A = 0,094 \text{ MeV}^{-1}$  ( $\circ$ ).

где  $\tilde{a}(A)$  – асимптотическая величина параметра плотности уровней при больших энергиях возбуждения ядра,  $\delta W$  – оболочечная поправка к энергии связи ядер,  $f(x) = 1 - e^{-\lambda x}$  – безразмерная функция, определяющая энергетическое изменение параметра плотности уровней.

3. Вклад коллективных возбуждений учитывался с помощью коэффициентов ротационного  $K_{\text{rot}}$  и аналогичного вибрационного  $K_{\text{vibr}}$  увеличения плотности уровней. Для оценки энергии вибрационных возбуждений использовались соотношения модели жидкой капли [10]. Так как величина  $K_{\text{vibr}} \sim 3 \div 5$  оказывается значительно ниже величины  $K_{\text{rot}}$ , то влияние коэффициента вибрационного увеличения учитывалось при систематике экспериментальных данных по плотности нейтронных резонансов, но им, как отмечено выше, пренебрегалось при описании делимости. Ротационное увеличение плотности уровней описывалось на основе соотношения (8), но чтобы учсть возможные отступления от адиабатической оценки для деформированных ядер в определение  $K_{\text{rot}} = \sigma_1^2 q(U)$  вводилась "универсальная" функция  $q(U)$ ,

поведение которой было найдено из анализа делимости. Определение этой функции будет обсуждено ниже.

4. Величина параметров  $\tilde{a}/A = 0,094 \text{ МэВ}^{-1}$  и  $\lambda = 0,064 \text{ МэВ}^{-1}$  была найдена из систематики в рамках данной модели экспериментальных данных по плотности нейтронных резонансов в области ядер с  $A \geq 150$ . При этом в качестве  $\delta W_n$  использовались экспериментальные значения оболочечных поправок к энергии связи ядер [11] и корреляционная функция ядра с равновесной деформацией (нейтронный канал) принималась равной  $\Delta_0^n = 12/\sqrt{A} \text{ МэВ}$ .

Полученные в данном анализе параметры плотности уровней  $a(B_n)$ , так же как соответствующие асимптотические значения параметров  $\tilde{a}/A$ , представлены на рис. 1. Отметим, что найденные величины параметров отличаются очень слабо от значений, полученных ранее в работе [10], где использовалась адиабатическая оценка коэффициента  $K_{\text{rot}}$ . Поэтому отклонения от адиабатической оценки  $K_{\text{rot}}$ , которые, как будет показано ниже, важны для последовательного описания делимости высоковозбужденных ядер, практически не чувствуются при энергиях возбуждения, близких к энергии связи нейтрона.

На первый взгляд может показаться, что построенная систематика параметров плотности уровней не сильно отличается от традиционной систематики плотности нейтронных резонансов, основанной на соотношениях модели ферми-газа [12]. Но существенным различием между обеими систематиками являются более низкие значения параметров плотности уровней, полученные при учете коллективных эффектов. Эти значения хорошо согласуются как с результатами теоретических расчетов параметров  $a$ , выполненных для схемы уровней потенциала Вудса-Саксона, так и с экспериментальными данными, извлекаемыми из спектров неупруго-рассеянных нейтронов с энергиями до 7 МэВ [7]. Такое согласие данных представляется очень важным, так как испарительные спектры чувствительны именно к величине параметра плотности уровней, а не к абсолютному значению плотности уровней. В рамках традиционной модели ферми-газа, не учитывающей коллективных эффектов, невозможно объяснить расхождение значений параметра  $a$ , извлекаемых из резонансных данных и испарительных спектров [13].

Сегодня необходимость использования при анализе и систематике экспериментальных данных более строгих, но неизбежно и более сложных моделей, кажется почти очевидной. Это могут быть последовательные микроскопические модели, учитывающие рассмотренные выше эффекты на базисе реалистических схем одночастичных уровней [7, 8], но, по-видимому, в большинстве случаев почти эквивалентное описание можно достичь и в рамках рассмотренного выше полифеноменологического подхода [10]. Такой подход представляется особо оправданным в применении к описанию статистических свойств переходных конфигураций делящихся ядер, где более строгие микроскопические методы сталкиваются со значительными трудностями однозначного выбора схем одночастичных уровней и параметров эффективных сил, ответственных за когерентные корреляционные и коллективные эффекты. В последующих разделах будет продемонстрировано, каким образом рассмотренные

выше особенности поведения плотности уровней проявляются в наблюдаемой делимости доактинидных ядер.

#### 4. АНАЛИЗ ВЕРОЯТНОСТИ ДЕЛЕНИЯ СФЕРИЧЕСКИХ И ДЕФОРМИРОВАННЫХ ЯДЕР

##### 4.1. Делимость доактинидов вблизи порога

Исходя из соотношения (8), предсказывающего резкую зависимость коэффициента ротационного усиления плотности уровней от равновесной деформации ядра, можно сделать очень важные качественные заключения о существенном различии в поведении делимости сферических и деформированных ядер. Это различие практически всецело связано с величиной и энергетической зависимостью  $K_{\text{rot}}^n$  в нейтронном канале. Делимость сферических ядер ( $K_{\text{rot}}^n = 1$ ) в сравнении с деформированными ( $K_{\text{rot}}^n \approx \sigma_{1n}^2$ ) будет характеризоваться более высокой и быстро растущей величиной. Этот эффект, кроме того, будет усилен оболочечными эффектами в поведении  $\rho_{\text{внутр}}^n(U)$ , возникающими из-за меньших, чем у деформированных ядер, значений параметра  $a_n(U)$  (14).

Вытекающая из этого рассмотрения разница между сферическими и деформированными ядрами отчетливо проявляется в экспериментальных данных. На рис.2 представлены низкоэнергетические участки наблюдаемой делимости ряда доактинидных ядер ( $E - E_f \leq 15$  МэВ). Из большой совокупности известных данных были выбраны лишь наиболее типичные представители сферических и деформированных ядер [3-7, 14, 15]. Для каждого из ядер приведено по две расчетные кривые, одна из которых соответствует предположению  $K_{\text{rot}}^n = \sigma_{1n}^2$  (нижняя), другая –  $K_{\text{rot}}^n = 1$ . Вычисление  $\rho_f(E)$  производилось на основе описанных выше соотношений с барьерами деления  $E_f^{\text{MS}}$  и оболочечными поправками в нейтронном канале  $\delta W_n$  Майерса и Святецкого [11]. Для делительного канала принимались  $\delta W_f = 0$ ,  $\tilde{a}_f = \tilde{a}_n$  и  $\Delta_0^f = 14/\sqrt{A}$  МэВ. Принятая величина  $\Delta_0^f$  достаточно надежно определяется из анализа критической энергии фазового перехода, отчетливо проявляющегося в энергетической зависимости эффективных моментов инерции переходных конфигураций изотопов ртути и полония [4, 5]. Для расчета  $\sigma_{1f}^2$  и  $K_0^2$  использовались значения твердотельных моментов инерции переходных конфигураций делящихся ядер, найденные в рамках модели жидккой капли для  $(Z^2/A)_{\text{kp}} \approx 45$  [17]. В случае радия использовано значение  $E_f = 8,3$  МэВ [14] и  $K_{\text{rot}}^f = 2\sigma_{1f}^2$  для остальных, более легких доактинидов. Формула (2) учитывает дополнительное увеличение плотности уровней в делительном канале, обусловленное грушевидной ассиметрией седловой конфигурации для преобладающего асимметричного способа деления  $^{226}\text{Ra}(n, f)$ .

Рис.2 представляет собой яркую демонстрацию влияния коллективных эффектов на плотность уровней  $\rho_n(U)$ , проявляющуюся в перемещении экспериментальных точек с верхней кривой для сферических ядер, наиболее близких к замкнутой

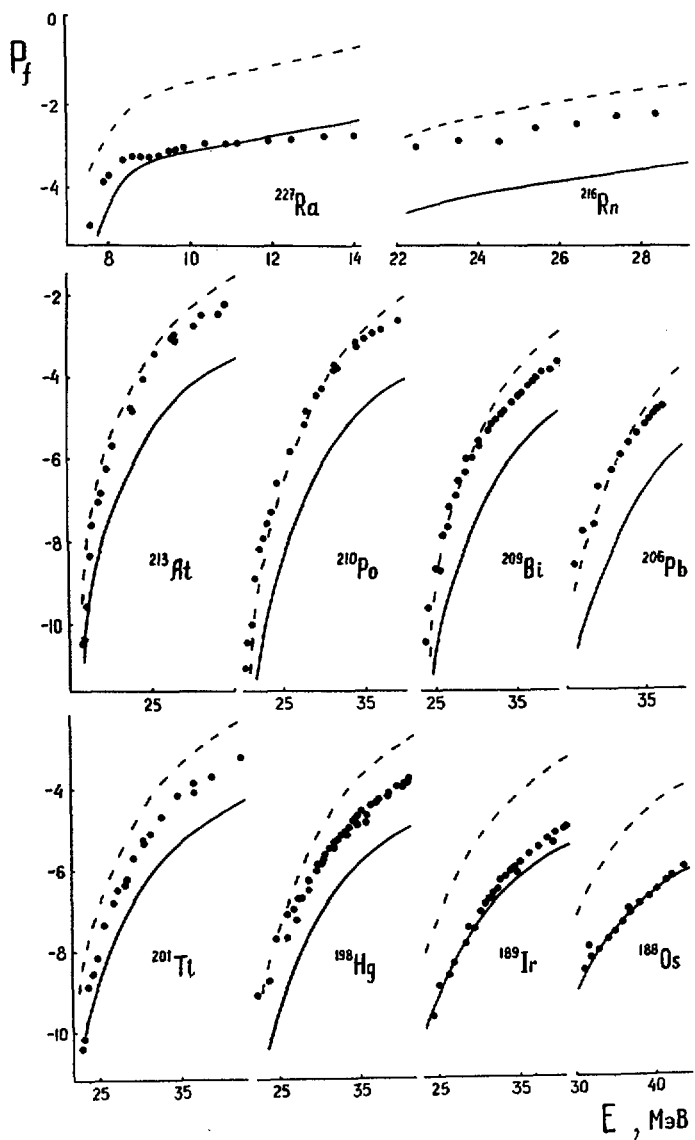


Рис. 2. Делимость  $P_f(E)$  некоторых доактинидных ядер при энергиях возбуждения, близких к порогу деления  $E-E_f \lesssim 15$  МэВ. ● — экспериментальные значения, полученные в реакциях  $(\alpha, f) - ^{213}\text{At}$ ,  $^{210}\text{Po}$ ,  $^{209}\text{Bi}$ ,  $^{201}\text{Tl}$ ,  $^{198}\text{Hg}$ ,  $^{189}\text{Ir}$ ,  $^{188}\text{Os}$  [3, 4],  $(p, f) - ^{209}\text{Bi}$ ,  $^{206}\text{Pb}$ ,  $^{196}\text{Hg}$  [3, 5],  $(n, f) - ^{227}\text{Ra}$  [14],  $(^7\text{Li}, f) - ^{216}\text{Rn}$  [15]. Кривыми показаны результаты расчета: пунктирными — при  $K_{tot}^n = \sigma_{ln}^2$

оболочке  $Z = 82$ ,  $N = 126$  ( $^{206}\text{Pb}$ ,  $^{209}\text{Bi}$ ,  $^{210}\text{Po}$ ,  $^{213}\text{At}$ ), на нижнюю при переходе к деформированным ( $^{188}\text{Os}$ ,  $^{189}\text{Ir}$ ,  $^{227}\text{Ra}$ ), расположенным по обе стороны от области  $A \sim 208$ . Ядра  $^{196}\text{Hg}$ ,  $^{201}\text{Tl}$ ,  $^{216}\text{Rn}$  по своему поведению соответствуют промежуточному случаю. Таким образом, наблюдаемое поведение делимости доактинидных ядер подтверждает рассмотренную выше качественную картину ожидаемого проявления колективных эффектов в плотности уровней и, в целом, согласуется с принятой при феноменологическом описании  $\rho(U, J)$  [10] классификацией ядер: для сферических ядер  $204 \leq A \leq 210$ , для деформированных ядер  $A \leq 190$ ,  $A \geq 225$ .

#### 4.2. Трудности описания делимости доактинидов в широкой области энергий возбуждения

Для нескольких типичных сферических и деформированных ядер экспериментальные данные и результаты расчета по делимости  $\rho_f(E)$  представлены на рис.3 в более широком диапазоне энергий. В случае сферических ядер делимость изучена вплоть до порога деления, положение которого определяется участком наиболее резкого уменьшения  $P_f(E)$ , обусловленного падением проницаемости барьера  $T_f(U)$ . В такой ситуации определение  $E_f$  мало зависит от модели, которая используется для описания плотности уровней  $\rho_f(U)$  и, тем более,  $\rho_n(U)$ . Это очень благоприятное для анализа обстоятельство, существенно уменьшающее неопределенность извлекаемых параметров модели. Расчетным кривым для сферических ядер на рис.3, подогнанным под экспериментальные данные в околоворотовой области энергий, соответствуют значения  $E_f$ , которые отличаются от барьеров Майерса-Святецкого [11] не более, чем на 0,3 МэВ.

Можно видеть, что при учете коэффициента ротационного увеличения плотности уровней  $K_{\text{rot}}^f = \sigma_{1f}^2$  в делительном канале соотношения сверхтекущей модели ядра дают достаточно хорошее описание наблюдаемой делимости вплоть до энергии  $\sim 10$  МэВ над барьером, но при более высоких энергиях расчетная кривая для всех сферических ядер отклоняется вверх от экспериментальных точек. Этот эффект проявился уже на границе более узкой области энергий, представленной на рис. 2.

В случае деформированных ядер нет таких факторов, благоприятствующих делению сферических ядер, как оболочки в основном состоянии и отсутствие ротационных возбуждений, которые уменьшают конкурирующую нейтронную ширину. Поэтому для деформированных ядер в непосредственной близости к порогу отсутствуют экспериментальные данные о сечении деления, которое, по-видимому, настолько мало, что его не удается измерить при существующей чувствительности методик. В этом случае извлекаемая величина  $E_f$  существенно сильнее зависит от модели, используемой при статистическом описании экспериментальных данных. На рис.3 расчетные кривые для деформированных ядер подогнаны так, чтобы в предположении  $K_{\text{tot}}^f = \sigma_{1f}^2$  и  $K_{\text{tot}}^n = \sigma_{1n}^2$  достигалось описание участка  $P_f(E)$  при наиболее низких энергиях. Обращает на себя внимание, что при этом для деформированных ядер отклонения рас-

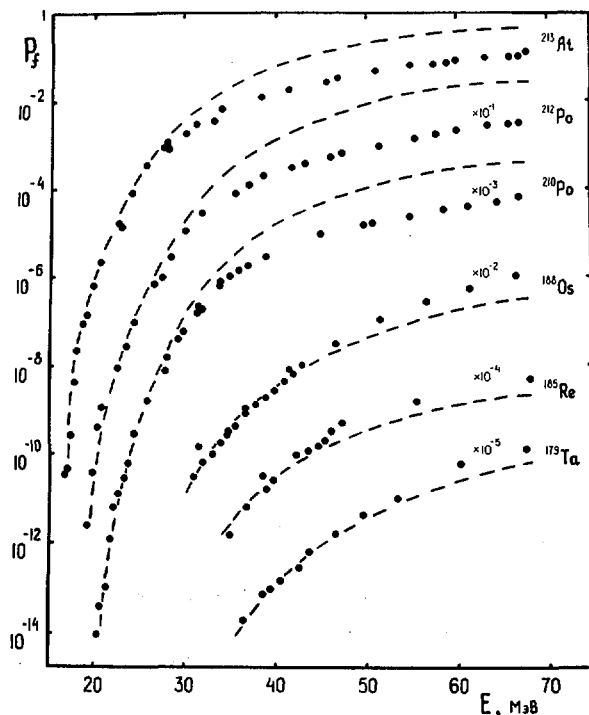


Рис. 3. Делимость некоторых сферических ( $^{213}\text{At}$ ,  $^{212}\text{Po}$ ,  $^{210}\text{Po}$ ) и деформированных ( $^{188}\text{Os}$ ,  $^{185}\text{Re}$ ,  $^{179}\text{Ta}$ ) ядер в широкой области энергий возбуждения. ● – данные работ [2, 3, 16], пунктирные кривые – расчет  $P_f$  для значений  $K_{\text{tot}}(U)$ , соответствующих адабатической оценке.

четных кривых от наблюдаемой зависимости, как и для сферических ядер, имеют систематический характер, но они существенно меньше и направлены в противоположную сторону.

В связи с рассматриваемыми расхождениями расчетов  $P_f(E)$  с экспериментальными данными в существенно надпороговой области энергий  $E - E_f \geq 15$  МэВ необходимо подчеркнуть, что удовлетворительное описание вероятности деления сферических ядер в широком диапазоне энергий до сих пор не было достигнуто ни в одном из проводившихся различными авторами анализов [3, 4, 18-21]. Недостатки традиционной модели ферми-газа с постоянным значением параметров плотности уровней  $a_f$  и  $a_n$  демонстрировались во многих работах [3, 4, 18]. При этом сложилось впечатление, что основные трудности описания делимости можно устраниć в области энергий  $E - E_f > U_{kp}$ , если учесть оболочечные эффекты в нейтронном канале [4]. Однако, выполненный в соответствии с этим подходом анализ высокоэнергетического участка  $P_f(E)$  дал значения барьеров деления  $E_f$  сферических ядер, которое примерно на 2-3 МэВ ниже непосредственно наблюдаемых в делимости. В ра-

ботах [18] авторы попытались достичь в первую очередь удовлетворительного описания околопорогового участка делимости, включив в рассмотрение наряду с оболочечными эффектами также парные корреляции нуклонов. При этом в сферических ядрах с известными порогами  $E_f$  для объяснения наблюдаемой скорости роста  $P_f(E)$  в надпороговой области потребовались неоправданно низкие значения корреляционных функций делительного канала  $\Delta_f^f \sim 0,1$  МэВ.

Проведенный выше анализ (рис.1) показал, что непротиворечивой интерпретации низкоэнергетических участков наблюдаемой делимости удается достичь только при включении в описание плотности уровней коллективных эффектов. Аналогичный вывод был сделан также в работах [19, 20], где использовался несколько иной подход к моделированию плотности уровней нейтронного и делительного каналов. Важно отметить, что в области более высоких энергий  $E - E_f \geq 15$  МэВ согласия с экспериментом в рамках рассмотренного теоретического описания достичь не удалось. Расхождения носили такой же характер, как и представленные на рис.3.

#### 4.3. Феноменологическое описание энергетической зависимости $K_{\text{rot}}$

Нам представляется естественным предположение, что ответственность за возникающие расхождения расчета с экспериментом несет неточность описания именно фактора  $K_{\text{rot}}(U)$ , а не каких-либо иных компонент плотности уровней в делительном или нейтронном канале. Данное предположение мотивируется тем, что использованное выше выражение (8) для  $K_{\text{rot}}$  основано на адиабатической оценке влияния ротационных мод на статистические характеристики ядер, которая должна быть справедливой лишь при небольших энергиях возбуждения [9]. Так как с увеличением энергии возбуждения практически всегда имеет место смешивание элементарных мод, то с ростом энергии мы должны в первую очередь ожидать отклонения  $K_{\text{rot}}$  от адиабатической оценки. Такие отклонения должны иметь единый для всех ядер характер, и их можно надеяться определить экспериментально из сравнения извлекаемой делимости  $P_f(E)$  сферических ядер с делимостью  $P_f^{\text{ад}}(E)$ , рассчитанной в предположении  $K_{\text{rot}}^f = \sigma_{1f}^2$ . Для этой цели мы введем в рассмотрение "универсальную" функцию ослабления ротационных эффектов в плотности уровней

$$q(E - E_f) = P_f(E)/P_f^{\text{ад}}(E) \leq 1 \quad (15)$$

с помощью которой можно будет феноменологически учесть отклонение  $K_{\text{rot}}$  от адиабатической оценки.

При построении функции  $q(U)$  из экспериментальных данных о делимости необходимо учитывать, что в рассматриваемом на рис.3 диапазоне энергий становится заметным вклад процессов деления с предварительным испусканием нейtronов. При их учете наблюдаемая делимость  $P_f^{\text{набл}}(A, E)$  должна быть представлена в виде суммы вероятностей деления цепочки ядер  $A - \nu$ , образующихся после испускания  $\nu$  нейtronов. При этом для расчета парциальных делимостей необходимо задать поведение функции  $q(E - E^{A-\nu})$ , которая сама подлежит определению. Итерационный процесс,

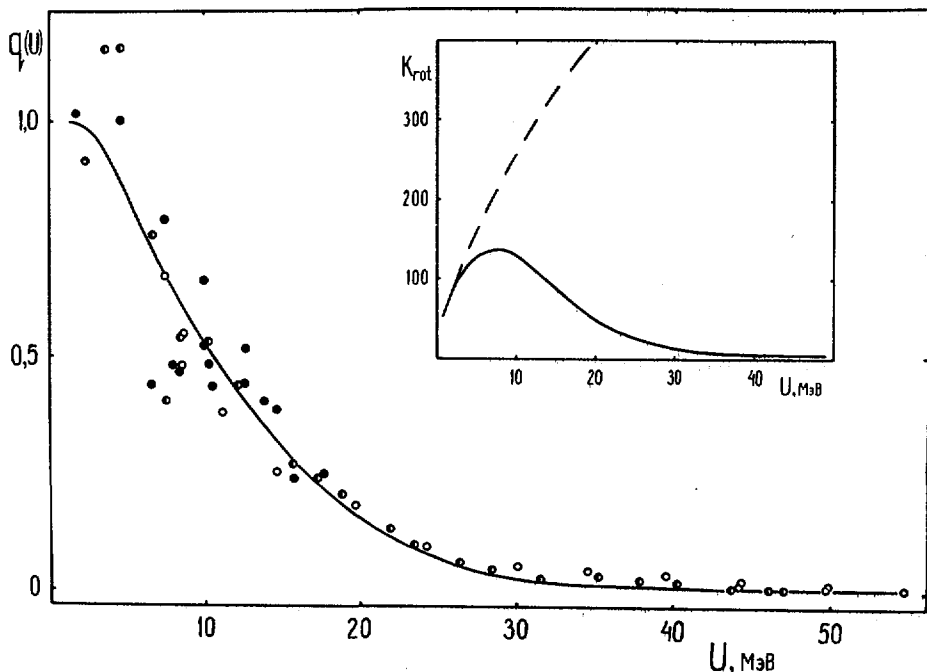


Рис. 4. Энергетическая зависимость функции  $q(U)$ , описывающей отступления  $K_{\text{rot}}(U)$  от адиабатической оценки. Экспериментальные значения:  $\bullet - {}^{210}\text{Po}$ ,  $\circ - {}^{212}\text{Po}$ . Сплошная кривая получена итерационным способом. На вставке: сплошная кривая соответствует  $K_{\text{rot}} = \sigma_1^2(U)$ , пунктирная – адиабатической оценке  $K_{\text{rot}} = \sigma_1^2$ .

в котором в качестве начального приближения для делимости исходного ядра  $P_f(A, E)$  рассматривалась наблюдаемая делимость  $P_f^{\text{набл.}}(A, E)$  изотопов  ${}^{210}\text{Po}$ ,  ${}^{211}\text{Po}$ ,  ${}^{212}\text{Po}$ , дал кривую, показанную на рис. 4 сплошной линией [21]. Требуемую для сравнения с расчетом делимость исходного ядра можно также определить непосредственно из наблюденных делимостей соседних изотопов, не прибегая к итерационному процессу. С точностью до незначительных поправок в  $J$ -зависимости

$$P_f(A, E) = \frac{P_f^{\text{набл.}}(A, E) - P_f^{\text{набл.}}(A - 1, E_1)}{1 - P_f^{\text{набл.}}(A - 1, E_1)} \approx P_f^{\text{набл.}}(A, E) - P_f^{\text{набл.}}(A - 1, E_1) \quad (16)$$

По этой формуле из наблюдаемых делимостей ядер  ${}^{210}\text{Po}$ ,  ${}^{211}\text{Po}$ ,  ${}^{212}\text{Po}$ , была восстановлена делимость, так называемого, первого шанса  $P_f(A, E)$  для ядер  ${}^{211}\text{Po}$  и  ${}^{212}\text{Po}$ . Аналогичная процедура была проделана в работе [16] для изотопов осмия, и результаты такого анализа для ядер  ${}^{212}\text{Po}$  и  ${}^{188}\text{Os}$  показаны на рис. 5. Можно видеть, что при энергиях, близких к порогу, а именно  $E - E_f \leq 15$  МэВ наблюдаемая делимость в поправках не нуждается и совпадает с искомой величиной  $P_f(A, E)$ . Для этого участка

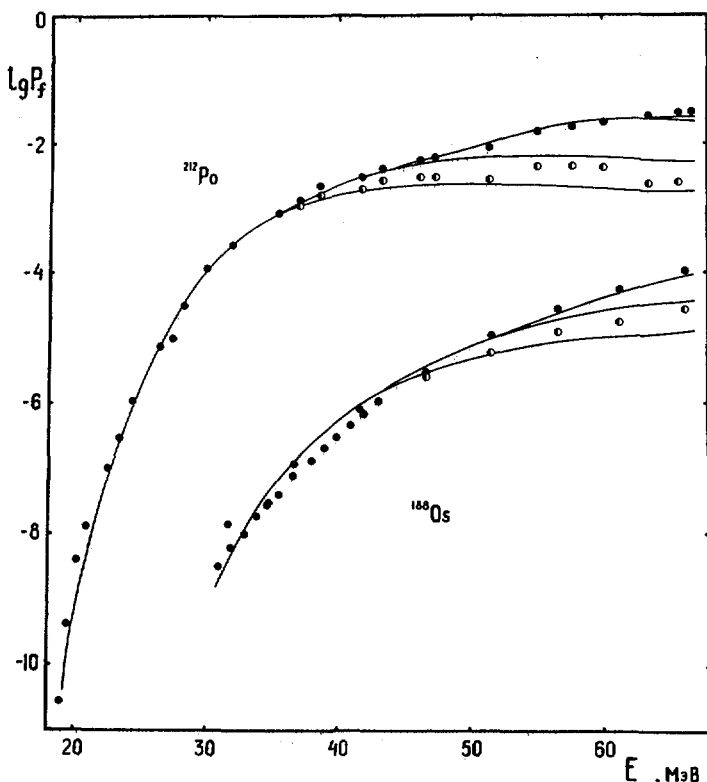


Рис. 5. Энергетическая зависимость наблюдаемой делимости  $P_f^{\text{набл}}(E)$  (●) и делимости исходного ядра (○) для ядер  $^{212}\text{Po}$  [3] и  $^{188}\text{Os}$  [16]. Кривые соответствуют расчетам делимости исходного ядра, делимости с испусканием одного нейтрона и т.д.

энергий экспериментальные точки  $q(U)$ , определенные в соответствии с соотношением (15), приведены на рис. 4 для всех трех изотопов полония, при более высоких энергиях — для изотопов  $^{211}\text{Po}$  и  $^{212}\text{Po}$ . Рассмотренный способ экспериментального определения  $q(U)$  является более прямым, чем итерационный метод, однако, ему свойственна значительная, быстро возрастающая с энергией погрешность. Она обусловлена трудностью корректного определения разности двух больших величин в (16), усугубленной немногочисленностью дискретного набора экспериментальных значений  $P_f^{\text{набл}}(A, E)$  и  $F_f^{\text{набл}}(A - I, E_1)$ . Поэтому в дальнейшем анализе мы будем пользоваться функцией  $q(U)$ , восстановленной итерационным методом. Результаты соответствующих такой функции расчетов делимостей изотопов  $^{212}\text{Po}$  и  $^{188}\text{Os}$  при различном числе испущенных нейtronов показаны на рис. 5.

Если данная выше интерпретация функции  $q(U)$  верна, то она должна обладать универсальностью, т.е. распространение ее на другие ядра, а также на нейтронный

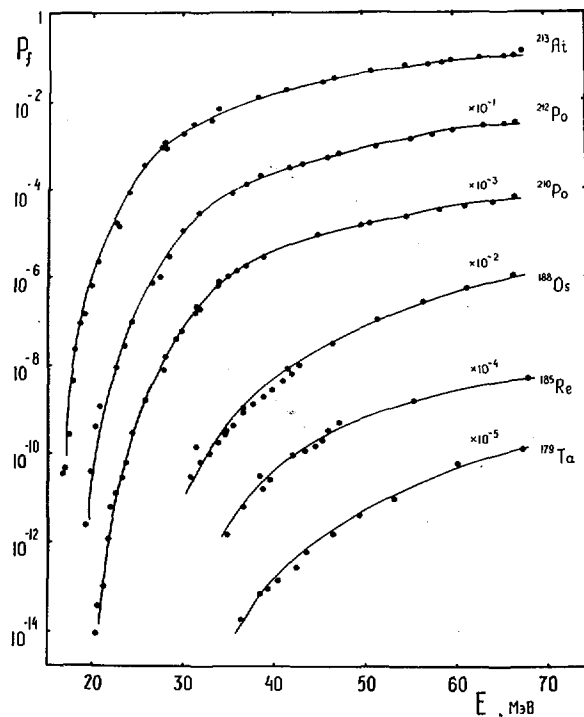


Рис. 6. Энергетическая зависимость наблюдаемой делимости ряда сферических и деформированных ядер. Рассчитанные кривые, в отличие от изображенных на рис. 3, учитывают отступления  $K_{\text{rot}}$  от адабатической оценки с помощью эмпирически определенной функции  $q(U)$  и вклад делений после предварительного испускания нейтрона.

канал деформированных ядер должно обеспечить описание наблюдаемой делимости во всем диапазоне энергий. Напомним, что без учета установленной зависимости  $q(U)$ , т.е. в предположении  $K_{\text{rot}} = \sigma_{\perp}^2$ , существовало расхождение расчета с экспериментом, имевшее разный знак для сферических и деформированных ядер. Этот факт можно интерпретировать как прямое следствие убывания с энергией функции  $q(U)$ , так как в соответствии с определением последней должно иметь место соотношение:

$$\frac{P_f(A, E)}{P_f^{\text{ан}}(A, E)} \sim q(E - E_f) < 1 \quad \text{для сферических ядер}$$

$$\frac{q(E - E_f)}{q(E - B_n)} > 1 \quad \text{для деформированных ядер} \quad (17)$$

Более строгие расчеты делимости, учитывающие зависимость  $q(U)$  в нейтронном канале, подтверждают это предположение. Расчет производился с учетом испускания

нейтронов для всей цепочки ядер, дающих вклад в наблюдаемую делимость. Полученное в этом случае описание рассматривавшихся ранее (рис.3) экспериментальных данных показано на рис.6. Отметим, что при уточнении энергетической зависимости  $K_{\text{rot}} = \sigma_{\perp}^2 \cdot q(U)$  новая подгонка расчетных кривых к экспериментальным данным по делимости деформированных ядер приводит к изменению барьера, в сравнении со значениями, полученными ранее (рис.3) для адиабатической оценки  $K_{\text{rot}}$ .

Рассмотренные выше новые черты описания делимости ядер вносят ряд важных уточнений в существующие представления о характере деления доактинидных ядер. До сих пор обычно предполагалось, что в широкой области энергий (например, в работах [16, 18] – до 100 МэВ) вклад делений с предварительным испусканием нейтронов невелик, и его влияние при анализе делимости доактинидов можно не учитывать. Это оправдывалось тем, что неточность, связанная с данным допущением, компенсируется другой неточностью – отождествлением сечения всех неупругих взаимодействий с сечением образования составного ядра [3, 16]. Из проведенного анализа следует, что реальная ситуация не соответствует этому грубому предположению – слишком велика разница  $P_f^{\text{набл}}(A, E)$  и  $P_f(A, E)$ . Таким образом, в традиционной области исследования доактинидных ядер деление при энергиях возбуждения выше 50-60 МэВ оказывается существенно эмиссионным, при котором с делимостью исходного составного ядра связана лишь небольшая часть происходящих процессов. Этот весьма важный вывод требует переоценки многих результатов предыдущих работ, в которых анализ экспериментальных данных при значительных энергиях возбуждения проводился без учета эмиссионного характера деления доактинидных ядер.

#### 4.4. Ядра переходной области

Область доактинидных ядер  $Z \leq 88$ ,  $A < 225-230$  замечательна тем, что в ней с изменением числа нуклидов происходит глубокая перестройка структуры ядра, как следствие его коллективных свойств. Экспериментальные данные о плотности нейтронных резонансов как для островка сферических ядер в окрестности  $^{208}\text{Pb}$ , так и для более обширных областей деформированных ядер  $150 \leq A \leq 190$  и  $A > 230$  получают в рамках рассмотренной в разделе 2 систематики вполне удовлетворительное единобразное описание (рис.1). Однако, в переходной области  $190 \leq A \leq 200$  проявляются систематические отступления от данного описания. Для более выразительной демонстрации таких отступлений в нижней части рис.1 показано сравнение "теоретической" оценки  $K_{\text{rot}}(B_n) = \sigma_{\perp n}^2 \cdot q(B_n)$  с теми значениями этого параметра, которые потребовались бы для получения наблюдаемой плотности уровней в предположении гладкой зависимости  $\tilde{a} = 0,094 A \text{ МэВ}^{-1}$ . В переходной области ядер требуемые значения коэффициента  $K_{\text{rot}}$  являются промежуточными по отношению к оценке (8), т.е. они в 2-3 раза меньше  $\sigma_{\perp}^2 \cdot q(B_n)$ , но значительно больше единицы.

Мы задержались на классификации ядер в зависимости от деформации, так как этот вопрос имеет большое значение при анализе большинства доактинидных ядер, для

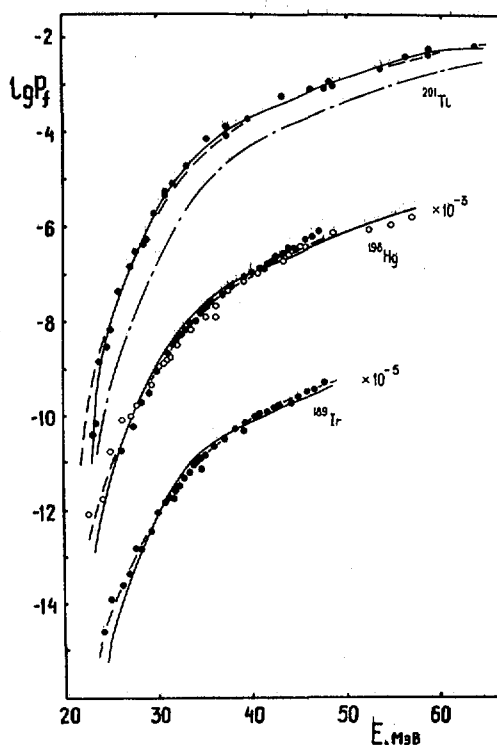


Рис. 7. Энергетическая зависимость наблюдаемой делимости  $^{201}\text{Tl}$  [3],  $^{196}\text{Hg}$  [3, 5],  $^{189}\text{Ir}$  [3, 5].  
 ● — из  $(a, f)$ -реакций, ○ — из  $(p, f)$ -реакций, сплошные кривые — расчет в предположении  $K_{\text{rot}}^f = 1$ ,  
 пунктирные —  $K_{\text{rot}}^n = \sigma_{\ln}^2 q(U)$ .

которых область порога в измерениях  $P_f(E)$  не достигнута. При описании делимости ядер коэффициенты коллективного увеличения плотности уровней входят в числитель ( $K_{\text{rot}}^f$ ) и знаменатель ( $K_{\text{rot}}^n$ ) соотношения (10), однако роль их в исследуемой области ядер неодинакова. Если  $K_{\text{rot}}^f$  варьируется от ядра к ядру незначительно, то  $K_{\text{rot}}^n$  при переходе через островок сферических ядер увеличивается более чем на порядок, и это существенно сказывается на результатах анализа делимости  $P_f(E)$ . На рис. 7 продемонстрировано несколько примеров, показывающих масштаб неопределенности  $\Delta E_f$ , которые могут возникнуть в этом случае из-за сильной зависимости  $K_{\text{rot}}$  от деформации ядер при ошибочной идентификации их коллективных свойств.

Ядро  $^{201}\text{Tl}$  по формальным признакам обычно относят к переходной группе ядер. Это самое легкое из ядер, для которого имеются результаты измерений делимости в непосредственной окрестности порога деления [3]. Как и для упомянутых выше более тяжелых ядер от Pb до At, по "излому" энергетической зависимости делимости  $^{201}\text{Tl}$  легко оценить положение "порога", не прибегая к какому-либо теоретическому анализу:  $dP_f/dE$  ниже и выше точки 23,8 MeV отличаются не менее чем на порядок.

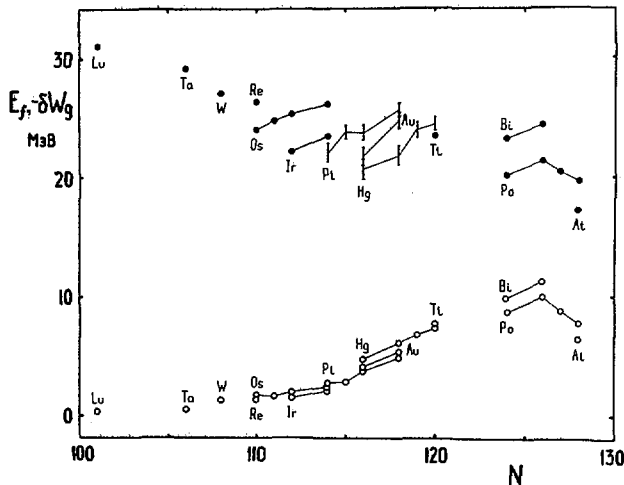


Рис. 8. Зависимость высот барьеров деления  $E_f$  и взятых с обратным знаком оболочечных поправок ( $-\delta W_d$ ) [11] от числа нейтронов, о – данные работы [18].

Можно видеть, что кривая  $P_f(E)$ , рассчитанная в предположении  $K_{\text{rot}}^n = 1$  и  $E_f = 23,6$  МэВ, хорошо согласуется с экспериментальными данными вплоть до 50 МэВ, тогда как кривая, соответствующая альтернативной возможности  $K_{\text{rot}}^n = \sigma_{\ln}^2 q(U)$  и тому же значению порога (штрихпунктир), проходит значительно ниже точек. Это позволяет заключить, что ядро  $^{201}\text{Tl}$  следует относить к группе сферических ядер. Для  $^{201}\text{Tl}$  на рис. 7 показана кривая (пунктир), рассчитанная как для деформированного ядра, но подогнанная так, чтобы "наилучшим" образом описывался надпороговый участок наблюдаемой делимости. Эта кривая лишь немного хуже согласуется с экспериментом в указанной области энергий, но ей соответствует значение  $E_f$  на 1,4 МэВ ниже истинного (непосредственно наблюдаемого порога).

Ядро  $^{189}\text{Ir}$  по принятой выше классификации находится на границе с переходной областью со стороны деформированных ядер. Благодаря хорошо изученному низкоэнергетическому участку  $P_f(E)$  [16] можно сделать вывод, что  $^{189}\text{Ir}$  весьма близок по своим коллективным свойствам к деформированным ядрам, и соответствующая теоретическая кривая (пунктир) на рис. 7 хорошо описывает наблюдаемую делимость во всем диапазоне энергий возбуждения.

Ядро  $^{198}\text{Hg}$  представляет собой характерный пример неопределенностей в извлекаемой при анализе величине  $E_f$ , связанных с отсутствием достоверных сведений о коллективных свойствах и с разбросом разнородной экспериментальной информации [3, 4, 22], не позволяющей составить представление о положении порога. Разница в значениях  $E_f$ , соответствующих альтернативным предположениям о  $K_{\text{rot}}^n$ , составляет 1,5–2,0 МэВ. Этую цифру мы и должны принимать в качестве реалистической оценки погрешности барьеров деления, извлекаемых для большинства ядер переходной области.

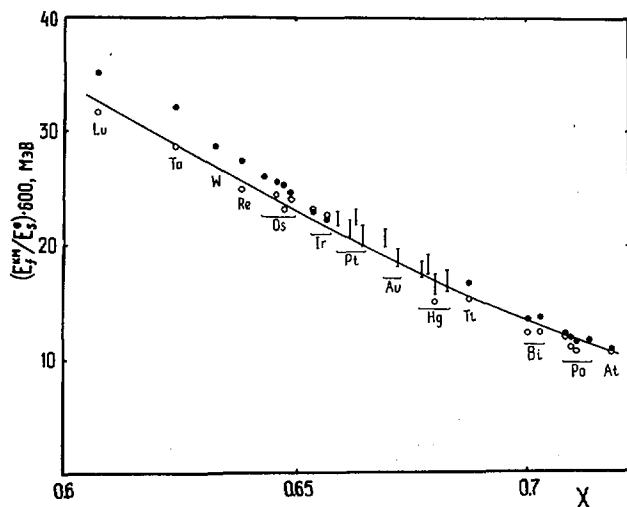


Рис. 9. Зависимость высоты жидкокапельного барьера деления  $E_f^{KM}$  (в единицах поверхностной энергии сферической капли  $E_s^0$ ) от параметра  $x$ .

## 5. БАРЬЕРЫ ДЕЛЕНИЯ ДОАКТИНИДЫХ ЯДЕР

Барьеры деления, полученные в рамках описанного выше подхода из анализа имеющейся совокупности экспериментальных данных [2, 4, 16], показаны на рис.8. Для ядер от  $^{201}\text{Tl}$  до  $^{213}\text{At}$ , у которых либо  $Z$ , либо  $N$  удовлетворяет условию  $Z=82 \pm 1$ ,  $N=126 \pm 2$ , обработка экспериментальных данных производилась в предположении  $K_{\text{rot}}^n = 1$ . Для деформированных ядер  $Z \leq 77$ ,  $A \leq 200$  мы принимали  $K_{\text{rot}}^n = \sigma_{\text{Lip}}^2 q(U)$ . Для ядер Pt, Au, Hg, попадающих в переходную область, анализ производился в двух крайних предположениях, и представленные на рис.8 линии соединяют оба полученных значения  $E_f$ . Из результатов других авторов мы привели на рис.8 лишь наиболее полную систематику значений  $E_f$ , полученных в [18] при анализе экспериментальных данных [2, 3, 16], большая часть которых использовалась и в настоящей работе. В нижней части рис.8 показана оболочечная составляющая барьера деления, определяемая величиной оболочечной поправки к основным состояниям делящихся ядер [11].

На рис.9 показаны данные о жидкокапельной компоненте барьеров деления доактинидных ядер  $\tilde{E}_f = E_f - SW_d$ , полученные из результатов проведенного анализа. На этом же рисунке приведена соответствующая кривая модели жидкой капли [23]

$$\xi(x) = \tilde{E}_f / E_s^0 \quad (18)$$

при построении которой мы использовали параметры Майерса-Святецкого [11]:

$$C_3 = 0,705 \text{ МэВ}, a_2 = 17,94 \text{ МэВ}, K = 1,78.$$

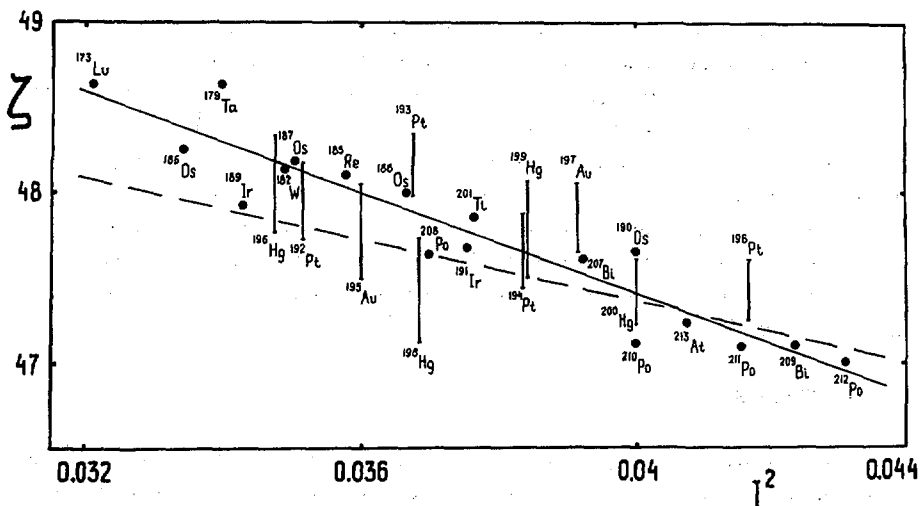


Рис. 10. Изоспиновая зависимость параметра  $\xi(I^2)$ . —  $53.3(1 - 2.79I^2)$ , ---  $51(1 - 1.78I^2)$ .

Основное отличие анализа делимости в настоящей работе и работах [18] связано с различием в описании плотности уровней: наши коллективные эффекты учитываются, а в работах [18] — нет. Тем не менее, полученные значения барьеров деления сферических ядер, несмотря на отличие подходов, между собой согласуются вполне удовлетворительно. В этом нет ничего удивительного, поскольку как мы уже подчеркивали, результаты анализа низкоэнергетического участка делимости, включающего область наблюдаемого порога практически нечувствительны к описанию плотности уровней в нейтронном и делительном каналах. Напротив, сравниваемые величины для деформированных ядер, которые экспериментально изучены только в существенно надпороговой области энергий, отличаются заметно: учет коллективных эффектов приводит к увеличению  $E_f$ , причем разница в порогах возрастает с уменьшением  $x$ . Как хорошо видно на рис. 8, этот эффект проявляется систематически по отношению к жидкокапельной кривой  $\xi(x)$ .

Чтобы проследить, каких изменений параметров модели жидкой капли требуют полученные барьеры деления, можно рассмотреть величину эффективного критического параметра делимости

$$\xi(I^2) = \frac{2a_2}{C_3} (1 - KI^2) = \frac{Z^2/A}{x} \quad (19)$$

где  $I = (N - Z)/A$  — изоспиновый фактор. Параметр  $x$  при этом определяется из трансцендентного уравнения

$$\tilde{E}_f = E_c^0 \xi(x)/2x \quad (20)$$

в левую часть которого входят найденные значения  $\tilde{E}_f$ . Экспериментальные данные в таком представлении показаны на рис. 10. Наилучшему описанию эксперименталь-

ных точек соответствуют значения параметров:  $2a_2/C_3 = 53,3$ ,  $K = 2,79$ . Пунктиром на рис. 10 показана величина (19) для параметров Майерса-Святецкого ( $2a_2/C_3 = 51,0$ ,  $K = 1,78$ ) [11]. Отметим, что найденное значение параметра изоспиновой поверхностной энергии оказывается весьма близким к величине  $K = 2,78$ , полученной при анализе жидкокапельной компоненты барьеров деления трансурановых ядер [24]. Однако, результаты приведенного анализа едва ли следует трактовать как простое переопределение рассмотренных выше параметров модели жидкокапельной капли. Для решения вопроса необходим более полный анализ жидкокапельных и оболочечных компонент барьеров деления совместно с экспериментальными данными о массах ядер.

## 6. ЗАКЛЮЧЕНИЕ

Проведенный учет коллективных эффектов в плотности уровней нейтронного и делительного каналов позволяет устраниТЬ существовавшие ранее трудности описания вероятности деления доактинидных ядер в широком диапазоне энергий. При этом удается получить непротиворечивую интерпретацию долгое время игнорировавшихся фактов, свидетельствующих о существенной роли деления с предварительным испусканием нейтронов уже при энергиях возбуждения  $\sim 20\text{-}30\text{МэВ}$  над порогом.

В настоящее время сделаны конечно только первые шаги в понимании тех изменений в представлении о делении ядер, которые должны повлечь за собой учет коллективных свойств при значительных возбуждениях. Мы отдаём себе отчет в том, что в предпринятом в данной работе анализе, содержится целый ряд упрощений, которые, однако, по нашему мнению, вполне оправданы на данном этапе исследований. При оценке полученных результатов необходимо считаться также с отсутствием последовательных теоретических разработок в описании указанных свойств, вследствие чего анализ их имел преимущественно феноменологический характер. Тем не менее мы надеемся, что прогресс в этой интересной области существенно не изменит основных выводов данной работы о барьерах деления и статистических характеристиках переходных состояний доактинидных ядер.

## ЛИТЕРАТУРА

- [1] STRUTINSKY, V.M., Phys. Chem. Fission, v. I (Proc. Symp. Vienna, 1968) IAEA, Vienna (1969) 352.  
BRACK, M., et al., Rev. Mod. Phys. 44 (1972) 320.
- [2] REISBECK, G.M., COBBLE, I.W., Phys. Rev. 153 (1967) 1270.
- [3] MORETTO, L.G., GATTI, R.C., THOMPSON, S.G., Ark. Fys. 36 (1967) 142.  
Reports UCRL-17987, Berkley (1969).  
KHADAI, A., Joopari Ph. D. Thesis Reports UCRL-16489, Berkley (1969).
- [4] ИГНАТОК, А.В., ИТКИС, М.Г., ОКОЛОВИЧ, В.Н., СМИРЕНКИН, Г.Н., ТИШИН, А.С.,  
Ядерная физика 21 (1975) 1185; 25 (1977) 25.
- [5] ЖУКОВА, О.А., ИГНАТОК, А.В., ИТКИС, М.Г., МУЛЬГИН, С.И., ОКОЛОВИЧ, В.Н.,  
СМИРЕНКИН, Г.Н., ТИШИН, А.С., Ядерная физика 26 (1977) 473.

- [6] БЕЙЗИН, С.Д., ИГНАТОК, А.В., ИТКИС, М.Г., МУЛЬГИН, С.И., ОКОЛОВИЧ, В.Н., СМИРЕНКИН, Г.Н., Изв. АН КазССР, сер. физ.-мат., 2 (1977) 1.
- [7] IGNATYUK, A.V., Nuclear Theory in Neutron Data Evaluation, v.I (Proc. Meetings in Trieste, 1975) IAEA, Vienna (1976) 211.
- [8] ВДОВИН, А.И., ВОРОНОВ, В.В., МАЛОВ, Л.А., СОЛОВЬЕВ, В.Г., СТОЯНОВ, Ч., ЭЧАЯ 7 (1976) 952.
- [9] БОР, О., МОТТЕЛЬСОН, Б., Структура Атомного Ядра, М., Мир, том II (1977).
- [10] ИГНАТОК, А.В., ИСТЕКОВ, К.К., СМИРЕНКИН, Г.Н., Ядерная физика 29 (1979) 875.
- [11] MYERS, W.D., SWIATECKI, W.S., Ark. Fys. 36 (1967) 593.
- [12] LYNN, J.E., The Theory of Neutron Resonance Reactions, Oxford, Clarendon Press (1968).
- МАЛЫШЕВ, А.В., Плотности Уровней и Структура Атомных Ядер, М., Атомиздат (1969).
- GILBERT, A., CAMERON, A., Can. J. Phys. 43 (1965) 1446.
- [13] BATCHELOV, R., et al., Nucl. Phys. 65 (1965) 236.
- OWENS, R.O., TOWLE, J.H., Nucl. Phys. A 112 (1968) 337.
- [14] СЕЛИЦКИЙ, Ю.А., Нейтронная физика [Материалы 3-й Всесоюзной конференции по нейтронной физике, Киев (1975)] М., ЦНИИатоминформ, 5 (1976) 216.
- [15] FREIESLEBEN, H., BRITT, H.C., HUIZENGA, J.R., Phys. Chem. Fission, v.I (Proc. Symp. New York, 1975) IAEA, Vienna (1974) 447.
- [16] MORETTO, L.G., et al., Report UCRL-17989, Berkley (1970).
- [17] СТРУТИНСКИЙ, В.М., Ядерная физика 1 (1965) 821.
- [18] MORETTO, L.G., et al., Phys. Letters, 38 (1972) 471.
- MORETTO, L.G., Phys. Chem. Fission, v. I (Proc. Symp. New York, 1975) IAEA, Vienna (1974) 447.
- [19] HAPELUNG' H., JENSEN, A.S., Phys. Scripta 15 (1977) 225.
- [20] GOTTSCHALK, P.A., LEDERGERBER, T., Nucl. Phys. A 278 (1977) 16.
- [21] ИГНАТОК, А.В., ИСТЕКОВ, К.К., СМИРЕНКИН, Г.Н., Нейтронная физика [Материалы 4-й Всесоюзной конференции по нейтронной физике, Киев (1977)], М., ЦНИИатоминформ (1977) 72; Ядерная физика 30 (1979) в печати.
- [22] NATOWITZ, J.B., CHULICK, E.I., Nucl. Phys. A 172 (1971) 185.
- [23] COHEN, S.D., SWIATECKI, W.S., Ann. Phys. 22 (1963) 406.
- [24] PAULI, H.C., LEDERGERBER, T., Nucl. Phys. A 175 (1971) 545.

## DISCUSSION

J.P. THEOBALD: Mathematical fits to experimental fission cross-section data with the fission barrier and one or two level density parameters as variables are not necessarily either significant or satisfactory. Photo-fission cross-sections of  $^{209}\text{Bi}$  obtained with mono-energetic gamma radiation between 40 and 65 MeV (see paper SM-241/A7 in these Proceedings) could be reproduced with the experimental fission barrier height and level densities of a microscopic model (CARJAN, N., et al., Phys. Rev. C (1979)) without corrections for collective degrees of freedom.

J.B. WILHELMY: Dr. Okolovich, is there any evidence from your analysis that collective effects in level density enhancements vary as a function of the nuclear excitation energy? In other words, if we interpret the collective motion

as a coherent superposition of higher-lying single-particle states, will we, at some excitation energy, exhaust the available single-particle strength, with a subsequent decrease of the collective enhancements to the level density?

V.N. OKOLOVICH: It is not possible to describe  $\Gamma_f/\Gamma_n(E)$  over a broad range of excitation energies without taking into account the dependence of rotational enhancement of the levels on energy. At fairly high excitation energies we should expect mixing of the elementary modes and reduction in the influence of collective effects on the level density. In such a case an adiabatic evaluation of the collective enhancement is invalid. Or at least this assumption is confirmed by experiment.

# THEORY OF INTRINSIC STATE DENSITY CALCULATIONS IN THE SHELL-CORRECTION APPROACH

K. JUNKER, J. HADERMANN

Swiss Federal Institute for Reactor Research (EIR),

Würenlingen

and

N.C. MUKHOPADHYAY

Swiss Institute for Nuclear Research (SIN),

Villigen,

Switzerland

## Abstract

### THEORY OF INTRINSIC STATE DENSITY CALCULATIONS IN THE SHELL-CORRECTION APPROACH.

The theory of intrinsic state density calculations is reviewed in the framework of a recently proposed renormalization of the logarithm of the grand partition function. The entropy is written in a form similar to the back-shifted Fermi gas model, and its asymptotic behaviour at higher temperatures is discussed. The vanishing of the shell corrections at such temperatures is investigated in making the Fourier analysis of the fluctuating part of the single-particle level density.

## 1. INTRODUCTION

Analytic level density expressions in common use are based on the exponential form given by the equidistant model. It was first shown by Kahn and Rosenzweig [1], using a model system with periodically bunched levels, that the asymptotic form of the entropy is similar to that of the equidistant model with an effective energy, however, that is related to the true excitation energy by a shift parameter. Several authors [2-4] tried to relate this shift parameter to the ground-state shell correction. Moretto [5] has, however, pointed out that for arbitrary level schemes there is no simple relationship between them, the shift parameter showing a smooth energy dependence even in the asymptotic region, where the shell corrections have already disappeared. In this paper we re-investigate this problem in the framework of a recently proposed [6] renormalization of the thermodynamic potential. For the sake of simplicity, the calculation of all relevant thermodynamic functions is performed in a pure single-particle model, neglecting pairing corrections. Since we can always write the entropy in its 'asymptotic' form, it is possible to give a description of the shift parameter in

terms of the thermodynamic functions. The temperature dependence of the shell terms is studied by Fourier analysing the oscillating part of the intrinsic single-particle density. Since we do not require the chemical potential to be constant, our result deviates from that of Ref. [4], and, at the same time, becomes more complex. It is shown that the description of the oscillating part of the intrinsic single-particle density by a simple Fourier series is, in principle, incompatible with the simultaneously required variation of the chemical potential with temperature and the vanishing of the shell corrections at higher excitation energies.

## 2. THERMODYNAMIC FUNCTIONS

In the statistical theory of level density calculations one starts from the grand partition function. Its Laplace transform is usually performed in the saddle-point approximation. This well-known procedure [7] then leads to the intrinsic state density in the form

$$\rho = \frac{e^S}{2\pi|D|^{1/2}} \quad (1)$$

where the entropy  $S$  is given by

$$S = \phi + \beta E - \alpha A \quad (2)$$

$\phi$  is the logarithm of the grand partition function and  $D$  is, in our case, a  $2 \times 2$  determinant of the second derivatives of  $S$  with respect to  $\alpha$  and  $\beta$ . For convenience, we confine ourselves to one kind of particles only. The thermodynamic potential  $\phi$  is given by

$$\phi(\alpha, \beta) = \int_0^\infty g(\epsilon) \lg(1 + e^{\alpha - \beta\epsilon}) d\epsilon \quad (3)$$

and the Lagrangian multipliers  $\alpha$  and  $\beta$  are determined by the saddle point condition

$$\frac{\partial \phi(\alpha, \beta)}{\partial \alpha} = A, \quad \frac{\partial \phi(\alpha, \beta)}{\partial \beta} = -E \quad (4)$$

$\beta^{-1}$  can be identified with the temperature T. In the spirit of Strutinsky's energy renormalization procedure, one may decompose the potential  $\phi$  into a smooth and an oscillating part [6]:

$$\phi = \tilde{\phi} + \delta\phi \quad (5)$$

where finally  $\tilde{\phi}$  is replaced by a phenomenological (liquid-drop) potential  $\bar{\phi}$  and  $\delta\phi$  is entirely given by the shell-model single-particle levels:

$$\phi \rightarrow \phi_R = \bar{\phi}(\alpha, \beta) + \delta\phi(\alpha, \beta) \quad (6)$$

This corresponds to a replacement of the smooth component  $\tilde{g}(\epsilon)$  in

$$g(\epsilon) = \sum_i \delta(\epsilon - \epsilon_i) = \tilde{g}(\epsilon) + \delta g(\epsilon) \quad (7)$$

by a phenomenological smooth level density  $\bar{g}(\epsilon)$ :

$$g \rightarrow g_R(\epsilon) = \bar{g}(\epsilon) + \delta g(\epsilon) \quad (8)$$

The details of the renormalization procedure for  $\phi$  have been worked out by Gottschalk and Ledergerber [6].  $\phi_R$  is still defined by Eq.(3), with  $g$ , however, replaced by  $g_R$ . Also the saddle-point equations are still valid. Since the smooth 'liquid-drop nucleus' should, however, have the same particle number A, we are forced to distinguish between its chemical potential  $\bar{\mu} = \bar{\alpha}/\beta$  and that of the real nucleus  $\mu = \alpha/\beta$ . We require

$$\frac{\partial \bar{\phi}(\bar{\alpha}, \beta)}{\partial \bar{\alpha}} = A \quad \text{and} \quad \frac{\partial \bar{\phi}(\alpha, \beta)}{\partial \beta} = -\bar{E} \quad (9)$$

where  $\bar{E}$  is the liquid-drop energy at the given temperature  $T = \beta^{-1}$ . To obtain a relation between  $\bar{\phi}(\bar{\alpha}, \beta)$  and  $\bar{\phi}(\alpha, \beta)$ , we may expand  $\bar{\phi}(\bar{\alpha}, \beta)$  into a Taylor series:

$$\bar{\phi}(\bar{\alpha}, \beta) = \bar{\phi}(\alpha, \beta) + \frac{\delta\alpha}{1!} \left. \frac{\partial \bar{\phi}}{\partial \bar{\alpha}} \right|_{\bar{\alpha}=\alpha} + \frac{\delta\alpha^2}{2!} \left. \frac{\partial^2 \bar{\phi}}{\partial \bar{\alpha}^2} \right|_{\bar{\alpha}=\alpha} + \dots \quad (10)$$

where

$$\delta\alpha = \bar{\alpha} - \alpha \quad (11)$$

The renormalized thermodynamic potential then becomes

$$\phi_R = \bar{\phi}(\bar{\alpha}, \beta) + \delta\phi_{sh}(\alpha, \beta) \quad (12)$$

where

$$\delta\phi_{sh} = \delta\phi - \delta\alpha \left. \frac{\partial\bar{\phi}}{\partial\bar{\alpha}} \right|_{\bar{\alpha}=\alpha} - \frac{\delta\alpha^2}{2!} \left. \frac{\partial^2\bar{\phi}}{\partial\bar{\alpha}^2} \right|_{\bar{\alpha}=\alpha} - \dots \quad (13)$$

defines the shell corrections. From Eqs (9) and (10), we find

$$A = \left. \frac{\partial\bar{\phi}}{\partial\bar{\alpha}} \right|_{\bar{\alpha}=\alpha} + \delta\alpha \left. \frac{\partial^2\bar{\phi}}{\partial\bar{\alpha}^2} \right|_{\bar{\alpha}=\alpha} + \dots = \left. \frac{\partial\bar{\phi}(\alpha, \beta)}{\partial\alpha} \right|_{\bar{\alpha}=\alpha} + \delta\alpha \left. \frac{\partial^2\bar{\phi}}{\partial\bar{\alpha}^2} \right|_{\bar{\alpha}=\alpha} + \dots \quad (14)$$

With the definition

$$\delta A \equiv \frac{\partial\delta\phi(\alpha, \beta)}{\partial\alpha} = A - \left. \frac{\partial\bar{\phi}(\alpha, \beta)}{\partial\alpha} \right|_{\bar{\alpha}=\alpha} = \int_0^\infty \frac{\delta g(\epsilon) d\epsilon}{1 + e^{\beta\epsilon - \alpha}} \quad (15)$$

we obtain a relation between  $\delta A$  and  $\delta\alpha$  from Eq.(14), neglecting terms of higher order in  $\delta\alpha$ :

$$\delta\alpha = \frac{\beta}{g(\mu)} \delta A \quad (16)$$

This is equivalent to

$$\mu = \bar{\mu} - \frac{1}{g(\mu)} \delta A \quad (17)$$

which for zero temperature goes over into a relation given in Ref.[8]:

$$\epsilon_f = \bar{\epsilon}_f - \frac{1}{g(\epsilon_f)} \int_0^{\epsilon_f} \delta g d\epsilon \quad (18)$$

We note that in the evaluation of the integrals defining the second derivatives of  $\bar{\phi}$  we have set  $\bar{g}$  equal to  $\bar{g}(\mu)$  and neglected contributions from the lower limits. Therefore, the relations (16) and (17) are strictly valid only in the range of temperatures where  $\alpha$  is sufficiently large<sup>1</sup>. Using Eq.(16) gives us, up to first order in  $\delta\alpha$ , the following result for the temperature-dependent liquid-drop energy:

$$\bar{E} \cong - \frac{\partial \bar{\phi}(\alpha, \beta)}{\partial \beta} + \frac{\alpha}{\beta} \delta A \quad (19)$$

For zero temperature, we have

$$\bar{E}(0) \cong \int_0^{\epsilon_f} \bar{g}(\epsilon) \epsilon d\epsilon + \epsilon_f \int_0^{\epsilon_f} \delta g d\epsilon = \int_0^{\bar{\epsilon}_f} \bar{g}(\epsilon) \epsilon d\epsilon \quad (20)$$

Proceeding as above also for the shell corrections, we obtain up to first order in  $\delta\alpha$ :

$$\frac{\partial \delta\phi_{sh}(\alpha, \beta)}{\partial \alpha} = 0 \quad (21)$$

and

$$\delta E_{sh}(T) = - \frac{\partial \delta\phi_{sh}(\alpha, \beta)}{\partial \beta} = - \frac{\partial \delta\phi(\alpha, \beta)}{\partial \beta} - \frac{\alpha}{\beta} \delta A \quad (22)$$

The corresponding zero-temperature result quoted in Ref. [8] is:

$$\delta E_{sh}(0) = \int_0^{\epsilon_f} \delta g \epsilon d\epsilon - \epsilon_f \int_0^{\epsilon_f} \delta g d\epsilon \quad (23)$$

---

<sup>1</sup> The approximate results are:  $\left. \frac{\partial^2 \bar{\phi}}{\partial \bar{\alpha}^2} \right|_{\bar{\alpha}=\alpha} \approx \frac{\bar{g}(\mu)}{\beta}$  and  $\left. \frac{\partial^2 \bar{\phi}}{\partial \beta \partial \bar{\alpha}} \right|_{\bar{\alpha}=\alpha} \approx - \frac{\alpha}{\beta^2} \bar{g}(\mu)$

Equations (19) to (23) are, up to first order in  $\delta\alpha$ , equivalent to the original saddle-point condition. This result enables a unique separation of all the thermodynamic quantities into smoothly behaving liquid-drop parts and oscillating shell corrections. In the following, the smooth quantities themselves will be split up into two parts, one of which is explicitly dependent on temperature and the other one implicitly through the chemical potential. As usual, in evaluating thermodynamic integrals, this can be done by splitting up the range of integration into two parts, one extending from 0 to  $\bar{\mu}$ , and the other one extending from  $\bar{\mu}$  to  $\infty$  (see, e.g. Ref. [7]). The results are:

$$\bar{\phi}(\bar{\alpha}, \beta) = \beta \left[ \int_0^{\bar{\mu}} (\bar{\mu} - \epsilon) \bar{g}(\epsilon) d\epsilon + \frac{1}{\beta} \Delta \bar{\phi}(\bar{\alpha}, \beta) \right] \quad (24)$$

where  $\Delta \bar{\phi}$  is given by a series expansion in  $\beta^{-1}$ :

$$\Delta \bar{\phi}(\bar{\alpha}, \beta) = \frac{1}{\beta} \sum_{\ell \geq 0} \frac{1+(-1)^\ell}{\beta^\ell} \left( 1 - \frac{1}{2^{\ell+1}} \right) \xi(\ell+2) \bar{g}^{(\ell)}(\bar{\mu}) + R_{\Delta \bar{\phi}} \quad (25)$$

Here  $\xi(\ell+2)$  is Riemann's zeta function and  $R_{\Delta \bar{\phi}}$  is a residual term of the order  $e^{-\alpha}$  and expected to be small as long as  $\alpha$  remains large enough.  $R_{\Delta \bar{\phi}}$  can be calculated by means of a series expansion. The liquid-drop energy calculated according to Eq.(9) is

$$\bar{E} = \bar{E}(0) + \bar{E}_x(T) \quad (26)$$

where the smooth excitation energy is determined as

$$\bar{E}_x(T) = -\Delta_x + \Delta \bar{E} \quad (27)$$

with

$$\Delta_x = \int_{\bar{\mu}}^{\bar{\epsilon}_f} \bar{g}(\epsilon) (\epsilon - \bar{\mu}) d\epsilon \quad (28)$$

The other term is again given by its asymptotic series expansion:

$$\Delta \bar{E} = \frac{1}{\beta^2} \sum_{\ell \geq 0} \frac{1+(-1)^\ell}{\beta^\ell} (\ell+1) \left( 1 - \frac{1}{2^{\ell+1}} \right) \xi(\ell+2) \bar{g}^{(\ell)}(\mu) + R_{\Delta \bar{E}} \quad (29)$$

The residual term  $R_{\Delta\bar{e}}$  is also expected to be small. Usually, the dependence of  $\bar{\mu}$  on T is ignored, i.e.  $\Delta_x = 0$  is assumed. This leads to the well-known equidistant-model behaviour of the excitation energy as a function of energy. As was first pointed out by Moretto [5],  $\Delta_x = 0$ , is, however, not even true for the Fermi gas model.

Using Eqs (3), (12), (13) and (15), we obtain for the entropy:

$$S_R = \beta(\bar{E} + \delta E_{sh}(T)) - \alpha A + \bar{\phi}(\bar{\alpha}, \beta) + \delta \phi(\alpha, \beta) - (\bar{\alpha} - \alpha) A + O(\delta \alpha^2) \quad (30)$$

or

$$S_R = \bar{S}(\bar{\alpha}, \beta) + \delta S_{sh}(\alpha, \beta) \quad (31)$$

where the smooth component is given by

$$\bar{S}(\bar{\alpha}, \beta) = \beta \left( \bar{E} - \frac{\bar{\alpha}}{\beta} A + \frac{1}{\beta} \bar{\phi}(\bar{\alpha}, \beta) \right) = \beta \left( \Delta \bar{E} + \frac{1}{\beta} \Delta \bar{\phi} \right) \quad (32)$$

and the shell correction to the entropy, up to first order in  $\delta \alpha$ , is given by

$$\delta S_{sh}(\alpha, \beta) = \beta \delta E_{sh}(T) + \delta \phi(\alpha, \beta) + O(\delta \alpha^2) \quad (33)$$

The free energy

$$F = E - TS \quad (34)$$

may as well be split up into a smooth term

$$\bar{F} = \bar{E}(0) - \Delta_x - \frac{1}{\beta} \Delta \bar{\phi} \quad (35)$$

and a shell correction

$$\delta F_{sh}(T) = -\frac{1}{\beta} \delta \phi(\alpha, \beta) + O(\delta \alpha^2) \quad (36)$$

Finally, we quote the trivial relation between smooth and real excitation energies:

$$E_x(T) = \bar{E}_x(T) + \delta E_{sh}(T) - \delta E_{sh}(0) \quad (37)$$

### 3. THE ASYMPTOTIC FORM OF THE ENTROPY AND THE BACK-SHIFTED FERMI GAS MODEL

In principle, the asymptotic behaviour of the entropy is best discussed by using Eqs (31) to (33). Since numerical calculations show that both  $\delta E_{sh}$  and  $\delta\phi$  vanish for higher temperatures, we have in this case

$$S_R(T \gg 0) \approx \bar{S}(\bar{\alpha}, \beta) = \beta \left( \Delta \bar{E} + \frac{1}{\beta} \Delta \bar{\phi} \right) \quad (38)$$

and

$$E_x(T \gg 0) \approx \bar{E}_x(T) - \delta E_{sh}(0) = -\Delta_x + \Delta \bar{E} - \delta E_{sh}(0) \quad (39)$$

which is very different from the usual relationship between entropy and excitation energy in the equidistant model. Since a large body of experimental data has been analysed in terms of the back-shifted Fermi gas model, we would like to express the entropy in a similar form. This is always possible, the price we have to pay is, however, a rather complicated expression for the shift parameter. We start with the definition of free energy, Eq.(34), and solve for the entropy:

$$S_R = \frac{E - F}{T} = 2\beta \left( E - \frac{E + F}{2} \right) = 2\beta \left( E_x + \frac{2E(0) - E - F}{2} \right) = 2\beta(\bar{E}_x + \tilde{\Delta}) \quad (40)$$

where the newly introduced quantity  $\tilde{\Delta}$  will be given explicitly below. To remove the reciprocal temperature  $\beta$ , we introduce a completely arbitrary constant (or function of excitation energy)  $a$  in the following way:

$$\bar{E}_x = \bar{E}_x - \frac{a}{\beta^2} + \frac{a}{\beta^2} \equiv -\tilde{\Delta}_1 + \frac{a}{\beta^2} \quad (41a)$$

or

$$\beta = \sqrt{\frac{a}{\bar{E}_x + \tilde{\Delta}_1}} \quad (41b)$$

This allows the elimination of  $\beta$  from Eq.(40) and gives, at the same time, the entropy in the desired form:

$$S_R = 2\sqrt{a(\bar{E}_x + \tilde{\Delta}_{shift}(T))} \quad (42)$$

The shift parameter is defined through a set of equations:

$$\tilde{\Delta}_{shift}(T) = \frac{2\tilde{\Delta} - \tilde{\Delta}_1 + \tilde{\Delta}^2/\bar{E}_x}{1 + \tilde{\Delta}_1/\bar{E}_x} \quad (43)$$

$$2\tilde{\Delta} = \frac{1}{\beta} \Delta\bar{\phi} - \Delta\bar{E} + 2\Delta_x + \delta E_{sh}(T) - \delta F_{sh}(T) \quad (44)$$

$$\tilde{\Delta}_1 = \Delta_x - \Delta\bar{E} + \frac{a}{\beta^2} = -\bar{E}_x + \frac{a}{\beta^2} \quad (45)$$

$$2\tilde{\Delta} - \tilde{\Delta}_1 = \Delta_x + \frac{1}{\beta} \Delta\bar{\phi} - \frac{a}{\beta^2} + \delta E_{sh}(T) - \delta F_{sh}(T) \quad (46)$$

This set of equations is completely equivalent to the original form of the entropy. A re-definition of the shift parameter as follows:

$$\Delta_{shift}(T) = -\delta E_{sh}(T) + \delta E_{sh}(0) + \tilde{\Delta}_{shift}(T) \quad (47)$$

then gives the well-known expression for the back-shifted Fermi gas model:

$$S_R = 2\sqrt{a(E_x + \Delta_{shift}(T))} \quad (48)$$

Since this expression is exact, it is valid over the whole range of excitation energies. Note that the level density parameter  $a$  is a quantity which can be chosen freely. The choice

$$a = \frac{\pi^2}{6} \bar{g}(\bar{\mu}) \quad (49)$$

is particularly useful since in this case the first terms of the series expansion for  $(1/\beta)\Delta\bar{\phi}$  and  $\Delta\bar{E}$  will be cancelled. Since the chemical potential is a slowly varying function of temperature, also  $a$  will depend on  $T$ .

As the simplest example, we may consider the equidistant model. In this special case,  $\bar{g}$  and  $\bar{\mu} = \bar{\epsilon}_f$  are constants. Therefore, all smooth contributions to  $\Delta_{\text{shift}}$  vanish, and in the high-temperature limit, we obtain:

$$\Delta_{\text{shift}}^{\text{equ}}(T \gg 0) = \delta E_{\text{sh}}(0)$$

and

$$S^{\text{equ}}(T \gg 0) = 2\sqrt{a(E_x + \delta E_{\text{sh}}(0))}$$

This is the well-known result of Kahn and Rosenzweig [1].

In the general case there is, however, always a component present in  $\Delta_{\text{shift}}$  which varies smoothly with the energy and persists even at high energies where the shell corrections have been washed out completely. Detailed numerical calculations performed by Moretto [5] attest to this fact. Experimental data fitted with the back-shifted Fermi gas model exhibit the same trend [3, 9].

#### 4. SHELL CORRECTIONS AT HIGHER TEMPERATURES TREATED IN A SIMPLE MODEL

The behaviour of shell corrections for a realistic nucleus as a function of temperature can only be studied by means of microscopic calculations [2, 10]. However, for the following model case, in which the fluctuating part of the single-particle level density is represented by a strictly periodic function, we can give analytic expressions for all relevant thermodynamic quantities [4, 11]. As we shall see, such model calculations are, in principle, restricted to cases where the chemical potential is a constant. We assume that  $\delta g$  can be represented by a Fourier expansion of the form:

$$\delta g(\epsilon) = \sum_k \gamma_k e^{i\omega_k \epsilon} = \sum_k |\gamma_k| e^{i\omega_k (\epsilon - \epsilon_0)}, \quad k = \pm 1, \pm 2, \dots \quad (50)$$

with  $\omega_k = 2\pi k/\hbar\omega_{\text{sh}}$  and  $\hbar\omega_{\text{sh}} \sim 41.A^{-1/3}$  being the distance between major shells. This gives the previously defined shell quantities in the following form:

$$\delta\phi(T) = \beta \left[ \Gamma(\mu) + \sum_k \frac{\gamma_k}{\omega_k^2} e^{i\omega_k \mu} \phi\left(\frac{\pi\omega_k}{\beta}\right) \right] + R_{\delta\phi} \quad (51)$$

$$\delta A(T) = \sum_k \frac{i\gamma_k}{\omega_k} + \sum_k \frac{i\gamma_k}{\omega_k} e^{i\omega_k \mu} (\phi - 1) + R_{\delta A} \quad (52)$$

$$\delta E_{sh}(T) = -\Gamma(\mu) - \sum_k \frac{\gamma_k}{\omega_k^2} e^{i\omega_k \mu} \psi\left(\frac{\pi\omega_k}{\beta}\right) + R_{\delta E} \quad (53)$$

with  $\Gamma(\mu)$  defined as

$$\Gamma(\mu) = \int_0^\mu \delta g(\mu - \epsilon) d\epsilon = \sum_k \frac{\gamma_k}{\omega_k^2} (1 + i\mu\omega_k) - \sum_k \frac{\gamma_k}{\omega_k^2} e^{i\omega_k \mu} \quad (54)$$

and, for  $T = 0$ ,

$$\Gamma(\mu(0) = \epsilon_f) = -\delta E_{sh}(0) \quad (55)$$

The terms  $R_{\delta\phi}$ , etc. are contributions from the lower limits of the thermodynamic integrals and small of the order  $e^{-\alpha}$ . The functions  $\phi$  and  $\psi$  which contain the essential temperature dependence of the shell quantities are given by

$$\phi(\tau) = 1 - \frac{\tau}{\sin h\tau} \quad (56)$$

and

$$\psi(\tau) = 1 - \frac{\tau^2 \cosh \tau}{\sin^2 \tau} \quad (57)$$

with the property

$$\phi(0) = \psi(0) = 0 \quad (58a)$$

$$\phi(\infty) = \psi(\infty) = 1 \quad (58b)$$

In the limit of high temperatures, the shell corrections approach the values

$$\delta\phi(T \gg 0) \sim \beta \left( \Gamma(\mu) + \sum_k \frac{\gamma_k}{\omega_k^2} e^{i\omega_k \mu} \right) + R_{\delta\phi} = \beta \sum_k \frac{\gamma_k}{\omega_k^2} (1 + i\mu\omega_k) + R_{\delta\phi} \quad (59)$$

$$\delta A(T \gg 0) \sim \sum_k \frac{i\gamma_k}{\omega_k} + R_{\delta A} \quad (60)$$

$$\delta E_{sh}(T \gg 0) \sim - \sum_k \frac{\gamma_k}{\omega_k^2} (1 + i\mu\omega_k) + R_{\delta E} \quad (61)$$

This shows that, with our ansatz (50), the shell corrections will in general not vanish for higher temperatures, which contradicts the results of microscopic calculations. We may, however, adjust the phase  $\epsilon_0$  in Eq.(50) such as to make either  $\delta A(T \gg 0)$  or  $\delta\phi(T \gg 0)$  and  $\delta E_{sh}(T \gg 0)$  vanish. In practice, we would expect this phase to be determined by the shell model potential. Setting  $\text{Im } \gamma_k = 0$  would make  $\delta A$  vanish and, therefore, the chemical potentials of smooth and real nuclei would coincide at higher temperatures. The shell correction to the energy would asymptotically approach a constant value  $-\sum_k \gamma_k / \omega_k^2$ , which is of the order of the ground-state shell correction itself. The condition leading to vanishing shell corrections is

$$\delta E_{sh}(T \gg 0) = - \sum_{k>0} \frac{2|\gamma_k|}{\omega_k^2} (\cos \omega_k \epsilon_0 + \omega_k \mu \sin \omega_k \epsilon_0) \rightarrow 0 \quad (62)$$

or, equivalently,

$$\tan \omega_k \epsilon_0 = - \frac{1}{\omega_k \mu} \quad (63)$$

with the solution

$$\omega_k \epsilon_0 = n\pi - \arctan \frac{1}{\omega_k \mu} \quad n = 0, 1, 2, \dots \quad (64)$$

Since this equation depends on the chemical potential, its use would introduce a temperature dependence in the original Fourier expansion of  $\delta g$ , which was assumed to be a temperature-independent quantity. We then conclude that this model is only applicable to the case of a constant chemical potential. We then adjust the phase  $\epsilon_0$  for zero temperature ( $\mu = \epsilon_f$ ). Since  $\text{arctg}(1/\omega_k\mu)$  is a small quantity for reasonable values of  $\mu$ ,  $\omega_k\epsilon_0$  will be close to  $n\pi$  and therefore  $\text{Im } \gamma_k = -|\gamma_k| \sin(\dots)$  will be a small quantity. We then see that this phase condition ensures that all shell quantities will become small at higher temperatures. Adapting this condition results in the following expressions for the shell corrections:

$$\Gamma(\mu) \equiv \sum_{k>0} \Gamma_k(\mu) = -2 \sum_{k>0} \frac{|\gamma_k|}{\omega_k^2} \cos \omega_k(\mu - \epsilon_0) \quad (65)$$

$$\delta\phi(T) \approx \beta \sum_{k>0} \Gamma_k(\mu) \left(1 - \phi\left(\frac{\pi\omega_k}{\beta}\right)\right) \quad (66)$$

$$\delta A(T) \approx \sum_{k>0} \frac{d\Gamma_k}{d\mu} (1 - \phi) \quad (67)$$

$$\delta E_{sh}(T) \approx - \sum_{k>0} \Gamma_k(\mu) (1 - \psi) \quad (68)$$

$$\delta S_{sh}(T) \approx -\beta \sum_{k>0} \Gamma_k(\mu) (\psi - \phi) \quad (69)$$

Since the phase condition, Eq.(64), depends only very weakly on T, we may, as an approximation, apply these results also to cases where the chemical potential is a function of temperature. We then have the following form for the entropy and the excitation energy:

$$S_R(T) \sim \beta \left( \Delta \bar{E} + \frac{1}{\beta} \Delta \bar{\phi} + \sum_{k>0} \Gamma_k(\mu) (\psi - \phi) \right) \quad (70)$$

$$E_x(T) \sim -\Delta_x + \Delta \bar{E} + \sum_{k>0} \Gamma_k(\mu) (\psi - 1) - \delta E_{sh}(0) \quad (71)$$

which generalizes that given by Kataria et al. [4]. The authors of Ref. [4] very successfully applied this set of formulas, assuming a constant smooth level density and a constant Fermi energy, to a large body of experimental data, using only the first harmonic of  $\delta g$ .

## CONCLUSIONS

In the framework of the recently proposed renormalization of the thermodynamic potential, we have derived a mathematical expression for the entropy which consists of a smooth term that can be related unambiguously to the liquid-drop model, and an oscillating shell term. In the range of high temperatures only the liquid-drop term remains, differing from the result of a model with constant average single-particle level density. Since self-consistent calculations [2, 10] do not show such a behaviour, this places severe constraints on the shape of  $\bar{g}(\epsilon)$ . The question of level densities at relatively high excitation energies is, of course, not entirely academic and is particularly relevant for reactions studied at meson factories, where compound nuclear excitation energies in the range of 40–100 MeV are reached in many reactions. Thus, the absorption of stopped pions in heavy nuclei can be shown to result in such high excitation energies, as indicated by the decay products, such as neutrons as well as fission products. In pion-induced fission, for example, use of the asymptotic form of the entropy given by the equidistant model with periodic level bunching leads to a good description of the data, provided the ratio of fission-to-neutron level density parameters  $a_f/a_n$  is taken to be about 1.1 [12]. Nix et al. [13] claim that this indicates a need for a lowering of the liquid-drop barriers, as at high temperatures one expects this ratio to be equal to one. Thus, the question of the true form of the entropy at intermediate energies should be settled in the near future.

## REFERENCES

- [1] KAHN, P.B., ROSENZWEIG, R., Phys. Rev. **187** (1969) 1193.
- [2] BRACK, M., QUENTIN, P., Physica Scripta **10A** (1974) 163.
- [3] WILLIAMS, F.C., CHAN, G., HUIZENGA, J.R., Nucl. Phys. **A187** (1972) 163.
- [4] KATARIA, S.K., RAMAMURTHY, V.S., KAPOOR, S.S., Phys. Rev. **C18** (1978) 549.
- [5] MORETTO, L.G., Phys. Lett. **38B** (1972) 393.
- [6] GOTTSCHALK, P.A., LEDERGERBER, T., Nucl. Phys. **A278** (1977) 16.
- [7] BOHR, A., MOTTELSON, B.R., Nucl. Structure, Vol.1, Benjamin, New York (1969).
- [8] BRACK, M., et al., Rev. Mod. Phys. **44** (1972) 320.
- [9] VONACH, H.K., KATSANOS, A.A., HUIZENGA, R., Nucl. Phys. **A122** (1968) 465.
- [10] BRACK, M., Habilitationsschrift (1977) unpublished.
- [11] BOHR, A., MOTTELSON, B.R., Nucl. Structure, Vol.2, Benjamin, New York (1975).
- [12] MUKHOPADHYAY, N.C., HADERMANN, J., JUNKER, K., Nucl. Phys. **A** (1979) to be published.
- [13] KRAPPE, H.J., NIX, J.R., SIERK, A.J., preprint (1979).

**DISCUSSION**

M. BRACK: I think that here we should try to use the expression for the extended Thomas-Fermi model, which makes it possible to calculate  $\bar{g}(\epsilon)$  by simple integration in terms of a given analytical potential  $V(r)$ .

K. JUNKER: Yes, I agree. It would be useful to do so to see whether the higher derivatives of  $g(\epsilon)$  really give, at least in the energy range of interest, a small contribution as compared with the leading terms in the expansions of entropy and excitation energy.

M.E. FABER: In calculations of shell corrections to total energy and free energy surfaces one finds that the total energy shell corrections decrease slowly, while the free energy corrections decrease very suddenly. Does this fit in with your equation?

K. JUNKER: The mathematical expressions for the simple model given in Eqs (51) and (53) show the same trend as you observed in your own numerical calculations.



# A MANY-BODY MODEL STUDY OF FRAGMENT FORMATION IN FISSION\*

W. BAUHOFF, H. SCHULTHEIS, R. SCHULTHEIS, K. WILDERMUTH

Institut für Theoretische Physik,  
Universität Tübingen,  
Tübingen,  
Federal Republic of Germany

## Abstract

### A MANY-BODY MODEL STUDY OF FRAGMENT FORMATION IN FISSION.

The mechanism of fragment formation in fission has been studied in  $^{32}\text{S}$  as calculable many-body model for similar effects in the fission of actinides. The calculations have been performed for soft-core two-body forces with alpha cluster model (ACM) states, and these wave functions have been compared with two-centre shell-model (TCSM) states. The results show that, already at a small deformation, a correlation of the nucleons into two closed-shell clusters ( $^{16}\text{O} + ^{16}\text{O}$ ) is energetically favoured over the many-body states without such clustering. No cluster structure of that kind is found in the ACM ground-state of the compound nucleus. The ( $^{16}\text{O} + ^{16}\text{O}$ ) clustering sets in at the barrier between the first and the second minimum. In fact, the gain in correlation energy associated with the clustering turns out to be the very reason behind the occurrence of a shape isomeric state. This explains the paradox of 'fragment pre-formation', as these fragment-like correlations are noticeable long before the actual break-up into fragments. A comparison of the minimum energy ACM states with the lowest TCSM  $1\text{p} - 1\text{h}$  states yield very high overlaps at any deformation. This demonstrates that the description of fission in terms of cluster formation results in the same consequences as those from the usual shell-model picture of fission.

## 1. INTRODUCTION

For a long time, effects from fragment shells have been observed in many data from low-energy actinide fission. Examples are the kinetic energies, the neutron emission, and  $\gamma$ -radiation associated with the fragment de-excitation. When plot-

---

\* Supported by the Bundesministerium für Forschung und Technologie of the FRG and the Deutsche Forschungsgemeinschaft.

ted against the fragment mass, these data show peculiarities in the vicinity of the closed-shell ( $Z \approx 50$ ,  $N \approx 82$ ) mass (see, e.g. ref. [1]).

The existence of large clusters in fission consisting of roughly one half of the total number of nucleons has early been advocated [2]. This has been substantiated by shell-model calculations following the Strutinsky method [3] which have demonstrated [4,5] that the single-particle level scheme of the compound nucleus approaches that of the separated fragments already at remarkably small deformations. Thus, fragment shells are more decisive in many respects than the shell structure of the fissioning nucleus itself. Fragment shells tend to dominate already in the moderately deformed compound nucleus, much prior to the actual fragment formation.

It is the aim of the present paper to study the mechanism of fragment formation in the many-body wave function of the fissioning nucleus. We are especially interested in the possible existence of long-range many-nucleon correlations that may precede, and finally lead to, the actual formation of fission fragments. As the gain in correlation energy should be particularly large in clusters containing magic numbers of nucleons, the fragment shell closures ( $Z = 50$ ,  $N = 50$ ,  $N = 82$ ) are expected to play an important role in actinide fission [2,6,7]. Therefore, our treatment will focus on the following aspects:

- (i) the many-body mechanism of fragment formation,
- (ii) the deformation at which conceivable clustering sets in,
- (iii) the sudden or adiabatic nature of this process,
- (iv) the correlation energy and particular effects from closed-shell clusters,
- (v) the overlaps between cluster and two-center shell-model wave functions.

A quantitative study of large clusters in a microscopic many-body calculation for actinides, however, is beyond present-day's computational facilities. In the actinide region, so far only constrained Hartree-Fock calculations [8,9] with zero-range forces have been carried out. Apart from these, no other than relatively light systems like  $^8\text{Be}$ ,  $^{20}\text{Ne}$ ,  $^{24}\text{Mg}$  and  $^{32}\text{S}$  have been considered as many-body models for certain aspects of the fission problem [10,11]. We shall restrict our calculations to the study of deformed states in  $^{32}\text{S}$ , a system which is light enough for completely microscopic calculations to be performed, but which already exhibits the essential shell and substructure properties that are characteristic for actinide fission: Although not fissile in its ground state,  $^{32}\text{S}$  has a shape isomer (according to the Strutinsky method [12] and certain Hartree-Fock [13] calculations) and can be divided into two closed-shell fragments (like  $^{26,4}\text{Fm}$ ).

In order to facilitate the comparison with actinide fission, the calculations have been performed in two different representations, namely, Brink's alpha-cluster model [14], which is particularly efficient for the treatment of many-body correlations, and the two-center shell model [15], the conventional method of actinide fission studies. It is in the spirit of a model calculation for nuclear fission phenomena that no efforts have been made in the present paper to achieve close agreement with experimental  $^{32}\text{S}$  data (e.g.  $^{16}\text{O} - ^{16}\text{O}$  heavy-ion interaction potentials). Therefore, no parity or angular momentum projection has been included. The computational methods, which have previously been described in two separate papers [16,17] are outlined in section 2. The resulting potential energy surfaces and overlaps are given in section 3, and the conclusions for the many-body picture underlying actinide fission are summarized in section 4.

## 2. METHOD

In the present work, the formation of fragments in fission has been described in the conventional shell-model approach and in a many-body model. Correspondingly, two types of Hamiltonians and wave functions have been used: the two-center shell model and its single-particle states, and a two-body soft-core Hamiltonian together with alpha-cluster states. Both methods are briefly described in the following subsections.

### 2.1. Alpha-cluster model (ACM)

We make use of the alpha-cluster model<sup>1</sup> as developed by Brink [14] for the study of nuclei like  $^4\text{He}$ ,  $^8\text{Be}$ ,  $^{12}\text{C}$ ,  $^{16}\text{O}$ , ... which can be considered to be composed of  $\alpha$ -particles. A detailed description of the model is given in refs. [14,18].

The nucleons of  $^{32}\text{S}$  are distributed in eight alpha-clusters which are centered at the positions  $\vec{R}_1, \dots, \vec{R}_8$ . The spatial part of the single-nucleon states is given by

$$\langle \vec{x} | \vec{R}_i, b \rangle = (b \sqrt{\pi})^{-\frac{3}{2}} \exp(-(\vec{x} - \vec{R}_i)^2 / 2b^2) \quad (i = 1, \dots, 8) \quad (1)$$

Here, the four nucleons of each alpha cluster (i) share (with anti-aligned spins and isospins) a 1s orbit around the center  $\vec{R}_i$  with an oscillator width  $b = (\hbar/m\omega)^{1/2}$ . The width  $b$  is taken to be the same in all clusters. The antisymmetrized ( $A$ ) state of the whole system is then given by the Slater determinant  $|\phi\rangle$  of the (non-orthogonal) single-nucleon states (1)

$$|\phi\rangle = N_\phi A |\vec{R}_1, b\rangle |\vec{R}_2, b\rangle \dots |\vec{R}_8, b\rangle \quad (2)$$

---

<sup>1</sup> We refer to alpha-clusters rather than alpha-particles, in order to stress the full antisymmetry of the many-body state.

As usual in this model, admixtures of p-shell or higher states are not taken into account. It has been shown [19,20] that these states can be neglected. Even without such an admixture, ACM states in light nuclei require up to 4p - 4h components in a harmonic oscillator particle-hole expansion [14].

The Hamiltonian of the  $A = 32$  particle system

$$H = T + V - T_{CM} \quad (3)$$

consists of the kinetic energy

$$T = \frac{1}{2m} \sum_{i=1}^A \vec{p}_i^2 \quad (4)$$

the potential energy

$$V = \sum_{i < j}^A v_{ij} \quad (5)$$

and a center-of-mass term  $T_{CM}$ . For the two-body interaction  $v_{ij}$ , soft-core potentials with Wigner and Majorana ( $P_X$ ) terms and Gaussian form factors have been used

$$v_{ij} = \sum_{n=1}^2 S_n (1 - M_n + M_n P_X) \exp(-r_{ij}^2 / \beta_n^2) \quad (6)$$

The parameter sets  $(S_n, M_n, \beta_n)$  are taken to be those of the Volkov force [21] no.1,  $V_1$ , and alternatively the Brink-Boeker force [22],  $B_1$ . The matrix elements of the spin-orbit and tensor potential vanish because the wave function (2) has  $S=0$ . The spurious center-of-mass motion can be separated, and has been accounted for by subtracting the expectation value of

$$T_{CM} = \frac{1}{2Am} \left( \sum_{i=1}^A \vec{p}_i \right)^2 = \frac{1}{A} T + \frac{1}{mA} \sum_{i < j}^A \vec{p}_i \cdot \vec{p}_j \quad (7)$$

In contrast to actinide fission, the effect of the Coulomb energy in  $^{32}S$  is rather small; it lowers the binding energy but leaves the minimum energy state essentially unchanged. Therefore, the Coulomb energy will be neglected in the following sections.

The norm factor  $N_\phi$  of eq. (2) and the expectation values of one-body and two-body operators are determined by the single-nucleon matrix elements and the elements of the inverse overlap matrix

$$\langle \phi | \phi \rangle = N_\phi^2 \det^4 \langle i | j \rangle / A! \quad (8)$$

$$\langle \phi | T | \phi \rangle = 4 \langle \phi | \phi \rangle \sum_{i,j} \langle i | \frac{\vec{p}^2}{2m} | j \rangle B_{ji} \quad (9)$$

$$\langle \phi | V | \phi \rangle = \frac{1}{2} \langle \phi | \phi \rangle \sum_{i,j,k,\ell} \langle ij | v_{12} | k\ell \rangle [(8-10M) B_{ki} B_{\ell j} + (10M-2) B_{kj} B_{\ell i}] \quad (10)$$

Here,  $|i\rangle = |\vec{R}_i, b\rangle$  denotes the single-nucleon state,  $B = (\langle i | j \rangle)^{-1}$  is the inverse of the overlap matrix, and  $M$  the Majorana exchange parameter of the nucleon-nucleon interaction. The matrix elements  $\langle i | j \rangle$ ,  $\langle i | p^2/2m | j \rangle$  and  $\langle ij | v_{12} | kl \rangle$  can be determined analytically [18]. The results of subsection 3.1. are obtained by minimizing the energy

$$\langle \phi | H | \phi \rangle / \langle \phi | \phi \rangle = f(\vec{R}_1, \dots, \vec{R}_8, b) \quad (11)$$

as a function of the variational parameters  $\vec{R}_1, \dots, \vec{R}_8, b$  (under constraints as discussed below).

## 2.2. Two-center shell model (TCSM)

The two-center shell model has been applied to the description of actinide fission in numerous papers (see e.g. refs. [23, 24]). Therefore, it is instructive to compare the  $^{32}\text{S}$  wave functions obtained in the ACM calculation with those of the TCSM. We will use the TCSM in its most simple version, allowing only for symmetric fission and neglecting angular momentum dependent terms in the potential. The restriction to symmetric fission is motivated by the ACM results (see section 3.1.). Since a spin-orbit or  $i^2$  term does not contribute in the ACM, we have discarded these terms also in the TCSM.

The TCSM wave functions we have adopted are therefore Slater determinants of one-particle states which are generated by the potential:

$$V(x, y, z) = \begin{cases} (\hbar^2/2mb^4)[x^2 + y^2 + (z+z_0)^2] & z < 0 \\ (\hbar^2/2mb^4)[x^2 + y^2 + (z-z_0)^2] & z > 0 \end{cases} \quad (12)$$

In the limit  $z_0 \rightarrow 0$ , it reduces to the usual oscillator potential, whereas for  $z_0 \rightarrow \infty$ , it leads to two separated identical oscillators (for a figure of this potential see e.g. ref. [15]). By increasing the parameter  $z_0$  of this potential, one can describe the process of symmetric fission.

The one-particle Schrödinger equation with the potential (12) can be separated in Cartesian coordinates. For our purposes, this separation is more suitable than in cylindrical coordinates, because it facilitates the calculation of the overlaps with the ACM wave functions. The eigenfunctions can be written in the form

$$\langle \vec{x} | n_x n_y n_z \rangle = \psi_{n_x}(x) \psi_{n_y}(y) \psi_{n_z}(z) \quad (13)$$

where  $\psi_{n_x}(x)$  and  $\psi_{n_y}(y)$  are oscillator functions with  $n_x$  and  $n_y$  quanta, respectively. The functions  $\psi_{n_z}(z)$  can be given explicitly in terms of hypergeometric functions [15], and  $n_z = 0, 1, 2, \dots$  labels the various excited states. The one-particle energy of the state (13) is given by

$$E(n_x, n_y, n_z) = \hbar \omega (n_x + n_y + \epsilon_{n_z}(z_0) + \frac{3}{2}) \quad (14)$$

where  $\hbar \omega = \hbar^2/m b^2$  with  $b$  being the oscillator width parameter. The eigenvalues  $\epsilon_{n_z}(z_0)$  have to be calculated numerically. In general, they are non-integers with the following limiting cases:

$$\begin{aligned} \epsilon_{n_z}(0) &= n_z \\ \epsilon_{2n_z}(\infty) &= \epsilon_{2n_z+1}(\infty) = n_z \end{aligned} \quad (15)$$

The various states of  $^{32}\text{S}$  have been constructed by filling eight orbitals with four nucleons each that have different spin and isospin. In the oscillator limit  $z_0 \rightarrow 0$ , the ground state is 15-fold degenerate with the 1s and 1p shells filled and four states in the (2s,1d) shell occupied. These states will be denoted as  $|I_i\rangle$  with  $i=1, \dots, 15$ . For  $z_0 \neq 0$ , they are no longer degenerate but split into 5 groups of states. All of them are, however, lower in oscillator energy than any other state for  $z_0 < 0.4 b$ .

The one-particle, one-hole state of  $^{32}\text{S}$  with one quantum of excitation is 218-fold degenerate in the oscillator limit; these states will be called  $|II_i\rangle$ ,  $i=1, \dots, 218$ . The most interesting state among them is the state

$$|II_1\rangle = |(0,0,0)^4 (1,0,0)^4 (0,1,0)^4 (0,0,1)^4 (0,0,2)^4 (1,0,1)^4 (0,1,1)^4 (0,0,3)^4\rangle \quad (16)$$

which, for  $z_0 \rightarrow \infty$ , is the ground state of two separated  $^{16}\text{O}$  nuclei as can be seen from the asymptotic value of the oscillator energy expressed by eq. (15). Since  $^{16}\text{O}$  is a closed-shell nucleus, the ground state of two separated  $^{16}\text{O}$  nuclei is non-degenerate.

### 3. RESULTS

#### 3.1. Energy

Previous ACM calculations have shown that the ground-state wave functions of the 4N nuclei lighter than  $^{32}\text{S}$  are associated with certain geometrical structures of the  $\alpha$  cluster positions  $\vec{R}_i$ . In the ACM ground state of  $^{12}\text{C}$ , for instance, the  $\alpha$  clusters form an equilateral triangle, in  $^{16}\text{O}$  a regular tetrahedron (for figures see, e.g. ref. [25]). In order to study the fragmentation of the  $^{32}\text{S}$  system, we restrict the eight cluster positions  $\vec{R}_i$  in (2) to configurations of the type shown in Fig. 1, where the two tetrahedrons can be shifted together, blown up and distorted. This allows for possible clustering and fragmentation into  $^{16}\text{O} - ^{16}\text{O}$  or  $\alpha - ^{12}\text{C} - ^{16}\text{O}$  or  $\alpha - ^{12}\text{C} - ^{12}\text{C} - \alpha$  or  $^{16}\text{O} - \alpha - ^{12}\text{C}$  or  $^{20}\text{Ne} - ^{12}\text{C}$  as well as shell model states  $(\vec{R}_1 = \vec{R}_2 = \dots = \vec{R}_8)$  or alpha clustering only.

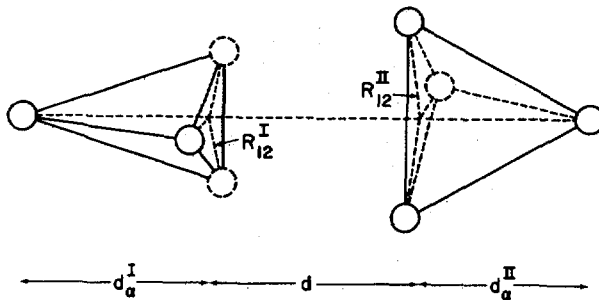


FIG.1. Alpha-cluster positions and variational parameters. The positions  $R_1, \dots, R_8$  in Eq.(2) are restricted to alphas in the corners of two tetrahedrons. The variational parameters  $R_{12}^I, R_{12}^{II}, d_\alpha^I, d_\alpha^{II}$  and  $d$  are indicated.

Fig. 2 shows the energy (11) of the ACM states of Fig. 1 as a function of the deformation parameter  $d$ , the distance between the nascent fragments. The energy is calculated for Volkov's soft-core interaction No. 1 [21]. At each given  $d$ , the other parameters in Fig. 1 and the oscillator constant  $b$  have been varied independently.

We find two separate valleys in the potential energy landscape extending along increasing separation  $d$ . The ground state of  $^{32}\text{S}$  (at  $d=0$ ) lies in one valley, the separated fragments  $^{16}\text{O} + ^{16}\text{O}$  lie in the other. The valleys are associated with different types of correlations in the many-body wave functions. For small separations  $d$ , the  $^{32}\text{S}$  valley is lower in energy. With the approach to the ground-state minimum, all the position parameters ( $R_{12}, d_\alpha, d$ ) in Fig. 1 go to zero; i.e. the ACM state of minimum energy goes over into a ( $b = 1.4$  fm) shell model state of  $^{32}\text{S}$ . With increasing  $d$ , the triangular  $^{12}\text{C}$  structure in  $\alpha - ^{12}\text{C} - ^{16}\text{O}$  blows up, whereas the nucleons of the  $^{16}\text{O}$  structure remain clustered together.

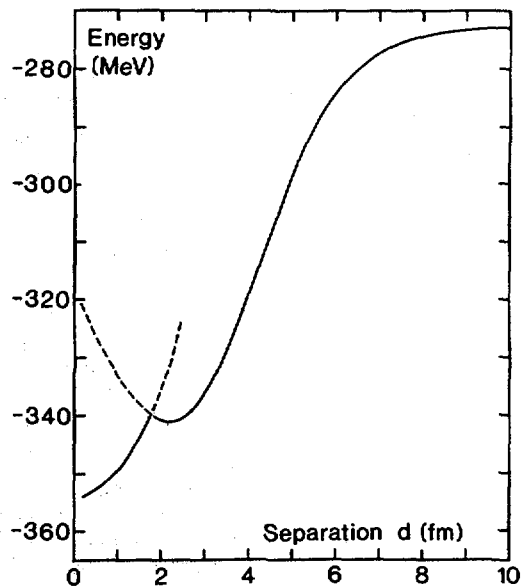
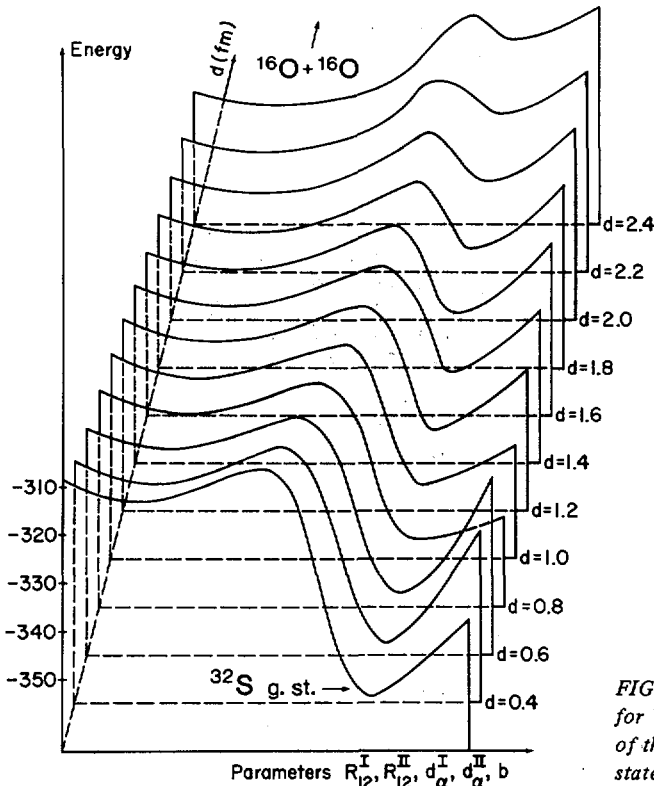


FIG.2. The energy valleys in  $^{32}\text{S}$  as a function of the separation parameter  $d$ .

At  $d = 1.8$  fm, both valleys are equal in energy (but separate in the parameter space). The transition from the  $^{32}\text{S}$  ground state to the separated fragments  $^{16}\text{O} + ^{16}\text{O}$  requires that the system passes over to the other valley. This is associated with a drastic rearrangement in the correlation of the wave function: In the  $^{16}\text{O} - ^{16}\text{O}$  valley, there is noticeable clustering into two  $^{16}\text{O}$  substructures, whereas there is no such substructure correlation in the  $^{32}\text{S}$  valley.

The corresponding energy surface, similar to contour plots in actinide fission, is given in Fig. 3.



The energies have been computed by linearly interpolating the parameters  $R_{12}$ ,  $d_a$  and  $b$  for a given  $d$  between their values in the two valleys. The interpolated values serve as generator coordinates for a sequence of Slater determinants, and plotted are the energies of the diagonalized Hill-Wheeler equation. Details of this procedure as well as more results for configuration mixing are given in ref. [16].

FIG. 3. The energy  $\langle\phi|H|\phi\rangle/\langle\phi|\phi\rangle$  for  $V_1$  interaction as a function of the parameters of the ACM state given in Fig. 1.

The ACM ground state of  $^{32}\text{S}$  has not previously been determined. As the configurations of Fig. 1 may not well describe the ground state of  $^{32}\text{S}$ , an unconstrained variation of all parameters has also been performed in this case and for the second minimum. It turns out that the shape isomeric state resulting from the constrained variation is locally stable against the full variation. The constrained ground state of the model, however, is found to lie 12 MeV above the absolute ACM minimum (resulting from the full variation).

The calculations have been repeated for Brink-Boeker interaction  $B_1$ . The results for substructure correlations are similar to the above  $V_1$  results [16].

### 3.2. Overlaps

When we have obtained the state of minimum energy for each separation  $d$ , we can expand it in terms of TCSM states. The expansion coefficients are given by the overlaps of the ACM states with the various TCSM states specified in section 2.2. For definiteness, we have chosen  $z_0 = d/2$ . It has been checked that other reasonable choices do not alter the results appreciably. The oscillator width  $b$  is taken to be the same in the ACM and the TCSM.

Explicitly, we have calculated the following quantities:

$$P_1 = \sum_{i=1}^{15} |\langle I_i | \text{ACM} \rangle|^2 \quad (17)$$

$$P_2 = P_1 + \sum_{i=1}^{218} |\langle II_i | \text{ACM} \rangle|^2 \quad (18)$$

$$P_3 = |\langle III_1 | \text{ACM} \rangle|^2 \quad (19)$$

Here, for a given ACM state  $|\text{ACM}\rangle$ ,  $P_1$  is the probability for the 15 TCSM states which are degenerate in the ground state of  ${}^{32}\text{S}$ ,  $P_2$  is the probability for the ground state or any  $1p - 1h$  state with one additional oscillator quantum, and  $P_3$  is the probability for the state which asymptotically goes over into the two  ${}^{16}\text{O}$  ground states. These quantities are plotted in Fig. 4 as functions of the separation  $d$ . As is seen, there is a drastic change in the probabilities around  $d = 1.8$  fm. At this point,  $P_3$  increases sharply from nearly zero to 90 %, whereas  $P_1$  drops down to almost zero. This is due to a rapid change in the parameters of the ACM states of minimum energy at this separation (compare Fig. 2 and ref. [16]). Beyond  $d = 1.8$  fm, the two tetrahedrons of Fig. 1 are congruent but elongated in the state of minimum energy. For large separations, they approach the ground state of two separated  ${}^{16}\text{O}$  nuclei consisting of two identical regular tetrahedrons. The probability  $P_1$  is zero in this region, since one cannot reach the ground state of  ${}^{32}\text{S}$  by bringing together two  ${}^{16}\text{O}$  nuclei in their ground state [11].

For smaller separations, the probability  $P_1$  increases from 60 % at  $d = 1.8$  fm to 100 % in the  ${}^{32}\text{S}$  shell model limit ( $d = 0$ ). Hence, also in this limit, the two models yield almost identical wave functions. The probability  $P_2$  of the TCSM ground state and the lowest  $1p - 1h$  excitations together, is nearly independent of the separation and varies between 90 % and almost 100 %. This shows that the wave functions of the deformed  ${}^{32}\text{S}$  nucleus calculated in the ACM can be represented by a small number of the lowest TCSM wave functions.

The same calculation has been performed using the minimum energy ACM states calculated with the  $B_1$  force. The results are qualitatively similar to those obtained for the  $V_1$  force.

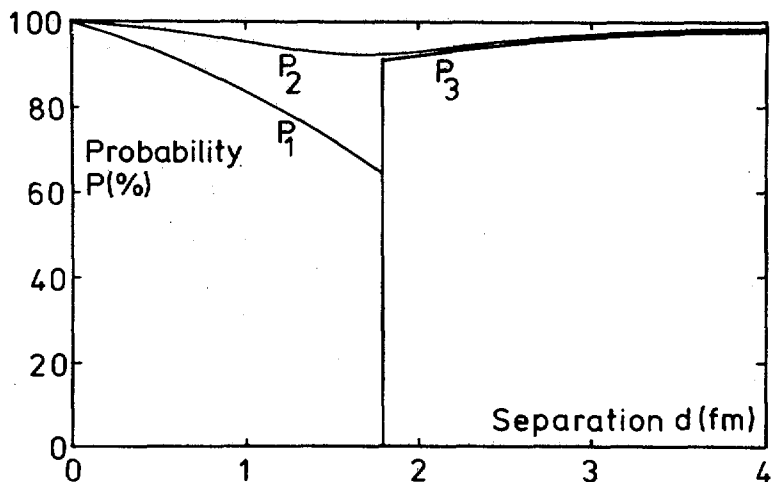


*FIG. 4. Probabilities of finding the various TCSM states in the ACM states of minimum energy. For the definition of  $P_1, \dots, P_3$ , see Eqs (17)–(18).*

#### 4. CONCLUSIONS

From the fission point of view, the following results are interesting to note: Like in actinides, the energy of our model system  $^{32}\text{S}$  has two minima when plotted versus deformation. In the first minimum, the ACM state is almost identical with the 15-fold degenerate  $^{32}\text{S}$  spherical shell-model state. With increasing deformation  $d$ , the probability for these 15 TCSM states decreases to about 60 % at the barrier. The energy gain in the second minimum in  $^{32}\text{S}$  is due to the formation of the magic substructure correlation  $^{16}\text{O} + ^{16}\text{O}$  in the many-body state. The strong correlation is associated with a spectacular increase in the overlap (up to 95 %) between the minimum energy ACM state and the TCSM state which goes over into  $^{16}\text{O} + ^{16}\text{O}$  for  $d \rightarrow \infty$ . We note that the formation of such large clusters is favoured already at a rather small deformation ( $d = 1.8$  fm associated with a quadrupole moment of  $Q_0 = 0.5$  barn), but no such correlations occur in the ground state. The complete rearrangement in structure between the states of the first and second well occurs rather suddenly within a small interval of the parameter  $d$ . It is connected with an abrupt change in quadrupole moment and rms radius. Beyond the barrier, closed shell clusters ( $^{16}\text{O} + ^{16}\text{O}$ ) are lower in energy than non-magic ones.

The ACM and the TCSM approach lead to rather similar wave functions. At any deformation, the minimum energy ACM state is almost completely (> 90 %) contained in the lowest part of the TCSM one-particle one-hole space.

The paradox of "fragment pre-formation" in fission can be explained as follows: Already in the second minimum, there is

an enhanced probability for closed-shell clusters. Although the antisymmetrization tends to diminish the effect of such sub-structures, some correlations of many nucleons remain. These have to some extent the properties which fragments of the same charge and mass would have. Thus, fragments are "pre-formed" and experimentally noticeable much prior to scission.

Actinide fission differs from our model in one minor respect: The relative neutron excess in most actinides is larger than that of the closed shell fragment ( $Z = 50$ ,  $N = 82$ ,  $A = 132$ ). Accordingly, in actinide fission maximum yield is observed for fragment masses that are slightly larger than the closed shell mass. Only the hypothetical fission of  $^{264}\text{Fm}$  is analogous to our model: Here, two magic  $^{132}\text{Sn}$  clusters can be formed simultaneously. This is in accord with the observed tendency towards symmetric fission in neighbouring Fermium isotopes.

## REFERENCES

- [1] VANDENBOSCH, R., HUIZENGA, J.R., Nuclear Fission, Academic Press, New York-London (1973).
- [2] FAISSNER, H., WILDERMUTH, K., Phys. Lett. 2 (1962) 212; Nucl. Phys. 58 (1964) 177.
- [3] STRUTINSKY, V.M., Nucl. Phys. A95 (1967) 420; Nucl. Phys. A122 (1968) 1.
- [4] MOSEL, U., MARUHN, J., GREINER, W., Phys. Lett. 34B (1971) 587.
- [5] MOSEL, U., SCHMITT, H.W., Nucl. Phys. A165 (1971) 73.
- [6] SCHULTHEIS, H., SCHULTHEIS, R., WILDERMUTH, K., Phys. Lett. 53B (1974) 325; Nukleonika 20 (1975) 423.
- [7] GÖNNENWEIN, F., SCHULTHEIS, H., SCHULTHEIS, R., WILDERMUTH, K., Z. Physik A278 (1976) 15.
- [8] FLOCARD, H., QUENTIN, P., VAUTHERIN, D., KERMAN, A.K., Physics and Chemistry of Fission (Proc. Int. Conf. Rochester, 1973) 1, IAEA, Vienna (1974) 221.
- [9] FLOCARD, H., QUENTIN, P., VAUTHERIN, D., VENERONI, M., KERMAN, A.K., Nucl. Phys. A231 (1974) 176.
- [10] KOLB, D., CUSSON, R.Y., HARVEY, M., Nucl. Phys. A215 (1973) 1.
- [11] HARVEY, M., Clustering Phenomena in Nuclei (Proc. 2nd Int. Conf. College Park, Maryland, 1975; GOLDBERG, D.A., MARION, J.B., WALLACE, S.J., Eds.), National Technical Information Service Rep. ORO-4856-26 (1975) 549.
- [12] SHELINE, R.K., RAGNARSSON, I., NILSSON, S.G., Phys. Lett. 41B (1972) 115.
- [13] ZINT, P.G., MOSEL, U., Phys. Lett. 58B (1975) 269; Phys. Rev. C14 (1976) 1488.
- [14] BRINK, D.M., Proc. of the International School of Physics "Enrico Fermi", Course XXXVI, 1965 (BLOCH, C., Ed.), Academic Press, New York-London (1966) 247.
- [15] SCHARNWEBER, D., GREINER, W., MOSEL, U., Nucl. Phys. A164 (1971) 257.
- [16] SCHULTHEIS, H., SCHULTHEIS, R., WILDERMUTH, K., FAESSLER, A., GRÜMMER, F., Z. Physik A286 (1978) 65.
- [17] BAUHOFF, W., WILDERMUTH, K., Z. Physik A289 (1979) 261.

- [18] ARIMA,A., HORIUCHI,H., KUBODERA,K., TAKIGAWA,N., Advances in Nuclear Physics (BARANGER,M., VOGT,E., Eds.) 5, Plenum Press, New York-London (1972) 345.
- [19] GRÜMMER,F., FAESSLER,A., Z. Physik 255 (1972) 112.
- [20] ABE,Y., Clustering Phenomena in Nuclei (Proc. 2nd Int. Conf. College Park, Maryland, 1975; GOLDBERG,D.A., MARION,J.B., WALLACE,S.J., Eds.), National Technical Information Service Rep. ORO-4856-26 (1975) 500.
- [21] VOLKOV,A.B., Nucl. Phys. 74 (1965) 33.
- [22] BRINK,D.M., BOEKER,E., Nucl. Phys. A91 (1967) 1.
- [23] HOLZER,P., MOSEL,U., GREINER,W., Nucl. Phys. A138 (1969) 241.
- [24] MUSTAFA,M.G., MOSEL,U., SCHMITT,H.W., Phys. Rev. C7 (1973) 1519.
- [25] FRIEDRICH,H., HÜSKEN,H., WEIGUNY,A., Phys. Lett. 38B (1972) 199.

## DISCUSSION

K.M. DIETRICH: In a shell model with two centres and a barrier  $V_0$  between them there arises preferential localization of nuclear matter on the left and right of this potential barrier if the latter becomes larger than the zero point energy in the direction of axial symmetry (Z axis). In this case the wave function for the lowest mode along the Z axis shows a minimum at the position of the barrier, i.e. a localization. The effect of this on the total localization of the nuclear matter is appreciable since the weight of the single-particle states with no modes along the Z axis is large. So I wonder whether you agree that your findings for light nuclei could be extrapolated to heavy nuclei in this manner?

R. SCHULTHEIS: Yes, I do agree. Different representations of the same process may lead to different pictures of the same phenomenon. As we have seen in our model, the results for the two-body Hamiltonian can be approximated quite satisfactorily by the states of a suitably selected one-body Hamiltonian. This can then be interpreted in the manner you have suggested.

D. HOFFMAN: In a paper originally submitted for possible presentation at this Symposium, M.G. Mustafa reported that he had found from calculation for a rapid descent from saddle to scission for nuclei from  $^{208}\text{Pb}$  to  $^{264}\text{Fm}$  that all the nuclei studied showed a preference for asymmetric mass division. He concludes that a rapid descent from saddle to scission is therefore inconsistent with the data showing a transition to symmetry at  $^{258}\text{Fm}$ , and that a slowly moving potential energy surface near scission, where fragment shell effects are dominant, reproduces the data more satisfactorily. Your cluster model seems to indicate formation of the cluster already in the second minimum. I wonder whether we have a contradiction here.

The second question is, on the basis of your calculations for elements with  $Z > 100$ , would you predict that the mass division will again become asymmetric

as one moves away from the possibility of division into two fragments, with almost the doubly magic  $^{132}\text{Sn}$  configuration?

R. SCHULTHEIS: According to our results, clustering sets in suddenly at low deformation and the remaining increase in clustering between the second minimum and scission is slow, as a function of elongation. Whether the elongation, in turn, is a rapid or slow function of time cannot be decided on the basis of our calculation.

As regards the mass asymmetry in actinides, our model has  $N = Z$ , and the magic fragmentation coincides with symmetric fission, similar to  $^{264}\text{Fm}$ . In lighter actinides the formation of the ( $Z = 50$ ;  $N = 82$ ) sub-structure requires an asymmetric mass split. For elements beyond ( $Z = 100$ ;  $N = 164$ ) fission should again be symmetric, since two simultaneous ( $Z = 50$ ;  $N = 82$ ) shell closures can be achieved in the symmetric fragmentation.

H.H. DUHM: We are presently studying the binary fragmentation of  $^{32}\text{S}$  at 30–50 MeV excitation energy. Do you think one could perform a fission type calculation to obtain the cross-section, and could barrier heights be obtained from your calculation?

R. SCHULTHEIS: Calculations of a more sophisticated nature than the present model have been performed, with Coulomb energy and angular momentum projection included, for a possible isomeric band and gamma transitions in  $^{32}\text{S}$ . Similar calculations can be made, although this has not yet been done, for the barrier heights and for estimates of the fission cross-section.

J.J. GRIFFIN: I have two related questions: first, what can you say about the barrier between the two valleys in your  $^{32}\text{S}$  potential surface? And second, is the onset of the  $^{16}\text{O}$ - $^{16}\text{O}$  shell structure in the single-particle level sensitive to the higher-order distortion parameters?

R. SCHULTHEIS: To take your second question first, the  $^{16}\text{O}$ - $^{16}\text{O}$  structure in the second minimum is resistant to an unconstrained variation. Apart from this, our results may, of course, depend on the choice of the constraint and we do not know to what extent a higher-order constraint could affect the variational results.

As regards your first question, the exact barrier between the valleys in our potential energy surface is difficult to determine in a multi-parameter space. The plot in Fig.3 shows the energies of the diagonalized Hill-Wheeler equation with the generator co-ordinate taken to be a straight path from one valley to the other. The barrier height along this cut in the parameter space is about 10 MeV. The exact barrier between the valleys may be lower than that.

G. SCHÜTTE: Does the early  $^{16}\text{O}$  clustering depend largely on the excitation energy? In an experimental application such as that mentioned by Dr. Duhm, occupation probability is brought to the higher-lying states during the passage from the saddle to the scission point on account of the dynamics. In contrast to this, you consider the configuration lowest from the energy

standpoint. The single-particle energies you have shown would then suggest that the pre-formation of clusters occurs at higher deformations.

R. SCHULTHEIS: Our variational calculation is designed as a model for spontaneous or low-energy fission such as occurs in the actinide region. Unfortunately, there is no spontaneously fissioning medium-mass nucleus that would be accessible for such a calculation. Generally speaking, the correlation energy associated with clustering phenomena should increase in importance as the total excitation of the system decreases. Hence little, if any, clustering would remain at the high excitation energies you refer to.

# SHELL STRUCTURE IN FISSION

V.M. STRUTINSKY

Institute for Nuclear Research,

Kiev, Union of Soviet Socialist Republics

*Presented by M. Brack*

## Abstract

### SHELL STRUCTURE IN FISSION.

Some new aspects in the theory of heavy nuclei emerging from studies of nuclear shell structure in the nuclear-fission process are described. Specific subjects cover general understanding of shell structure, the significance of macroscopic modes and the droplet model, together with developments in more technical aspects of shell calculations.

As was expected at the time of the second fission symposium ten years ago, the process of nuclear fission, indeed, proved to be a very firm testing ground for checking our basic understanding of nuclear processes involving significant variations of nuclear shape, finite velocity of deformation and, in general, a significant redistribution of the nuclear constituents. The current process of formation of a theory of heavy-ion collisions is in many respects based upon experimental and theoretical fission studies. It is the author's firm belief that fission will again be in the centre of attention for nuclear physicists when the predictions of the new theory are checked, since it is difficult to find another process that has been studied so thoroughly and yet is so demanding as nuclear fission. The quiet period between the active studies of fission resulting from the Vienna Symposium (1969) and the meeting at Rochester, USA (1973) was the expected period when fission studies started to bring notable gains to nuclear physics.

This paper reviews some points which have arisen from a study of various shell phenomena in fission and from numerous attempts to improve or disprove a theoretical approach known as the shell correction method. It may demonstrate the variety of problems arising in the theory of the fission process. The somewhat arbitrary selection of topics reflects the author's intention to summarize those aspects of nuclear theory where the study of shell structure effects in fission has contributed most significantly and, at the same time, to describe the developments of more technical aspects of the shell correction calculations. It turned, however, out that the progress made in solving these problems was also closely related to a better understanding of the *first principles* of the combined macroscopic-microscopic approach, thus showing that these subjects are closely interwoven.

The first general question resulting from the many numerical investigations [1-3] of the shell structure in strongly deformed nuclei was: Why is the shell structure so widely applicable? or:

### 1. WHAT IS SHELL STRUCTURE?

The calculations with a variety of single-particle potentials — realistic and not quite so realistic — have disclosed that the characteristic feature of nuclear shell structure — the relatively regular structure of single-particle level bunching — was a property common to all single-particle spectra. Only by way of exceptions were relatively smooth distributions of single-particle energies obtained, and it was then suspected that one was dealing with some general feature of the eigenvalue distributions whose description was, however, missing in the textbook references.

Phenomenologically, the nucleon shell structure in heavy nuclei plays a role which, in very many respects, is analogous to that of the zone structure of electron spectra in solid-state physics: as in crystals, zones of allowed and forbidden energies exist. The unfilled zone — or shell — leads to an increase in susceptibility and, therefore, to decreased stability of the nucleus in the given state. In contrast, the filled zone — or the magic nucleus — is characterized by an increased stability. The appearance of the nuclear zone structure is even more dramatic because, as it has turned out, the specific distribution of the nucleon shells — or the zones — depends significantly on the shape of the nuclear surface, which is the least stiff one among all nuclear collective degrees of freedom. The distortion of the nuclear shape redistributes the shells, and the stability conditions vary in the process of deformation. The result is the appearance of stable deformed shapes of some nuclei and the double-, or, possibly, even more often humped fission barriers.

After these computer-based findings we are naturally inclined to look for a general theory to explain the origin of such phenomena in nuclei from some *first principles* of quantum mechanics and hence provide the true explanation of why nuclei are deformed; furthermore, to give qualitative estimates for various nuclear-shell-structure effects as well as to enable a solid understanding of what is the role of shell structure in extreme conditions of nuclear dynamics at larger deformations, higher excitations and in super-heavy nuclides. Balian and Bloch were the first to recognize the connection between nuclear shell structure and the semi-classical quantization of motion in a three-dimensional well which they have formulated [4a]. The general expansion, however, for the single-particle Green function in terms of classical paths of increasing complexity as discussed in Ref. [4a] did not converge in the limit  $\hbar \rightarrow 0$ , and the Balian-Bloch theory was actually valid only for the special case of the spherical square well [4b]. It

could not, therefore, answer the intriguing questions related to deformed nuclei. Another technique — Feynman's path-integral method — has provided a more general solution. The earlier calculations by Gutzwiller along this line [5a, b] were extended [6–8] to the case of Hamiltonians with certain degrees of symmetry, where continuous families of classical periodical orbits appear. This extension made it possible to analyse the shell structure in deformed potentials and to find closed solutions for such important particular cases as the general spherical potential [6, 7], the deformed harmonic oscillator [7, 8], and the ellipsoidal square well [9].

In accordance with Balian and Bloch's conclusions, the distance between the shells is determined by a condition which is similar to the familiar Bohr-Sommerfeld quantization rule, i.e.

$$\Delta e (\equiv \hbar\Omega) = \frac{2\pi\hbar}{d S_\beta(e)/de} = \frac{2\pi\hbar}{T_\beta} \quad (1)$$

Here,  $S_\beta(e)$  is the action integral for the  $\beta$ -th family of, in general, degenerate periodical classical paths in the three-dimensional well, and

$$T_\beta = d S_\beta(e)/de \quad (2)$$

is the period of rotation. In contrast to the Bohr-Sommerfeld rule, condition (1) does not determine positions of specific eigenenergies. It gives, instead, the distribution of the shells, i.e. of the zones of allowed energies in the particle's phase space. The two rules are identical only in the exceptional cases of completely degenerate classical Hamiltonians, such as the one-dimensional well, the hydrogen-like atom or the harmonic oscillator with all partial frequencies related as ratios of integer numbers. Equation (1) is the true extension of the one-dimensional Bohr-Sommerfeld quantization to three-dimensional problems which could not be found in treatises dealing with the subject: The traditional extension of the semi-classical quantization to many dimensions is not relevant since it ignores any special feature due to the appearance of *periodical* paths in the many-dimensional space. (Note, for example, that the textbook theory does not, at all, consider the apparent condition of periodicity, i.e. that the partial frequencies should be related as ratios of integer numbers.) In contrast to the textbook case, condition (1) characterizes the properties of the averaged eigenvalue distribution and is related neither to properties of specific energy levels nor to the corresponding wave functions and quantum-mechanical quantities such as parity, orbital momentum or spatial distributions related to these. This is so because the very notion of classical paths requires a consideration of wave packets that extend over many quantal states. As an example, no solution for the spherical square well potential can be given [4b, 5]. The major contributions

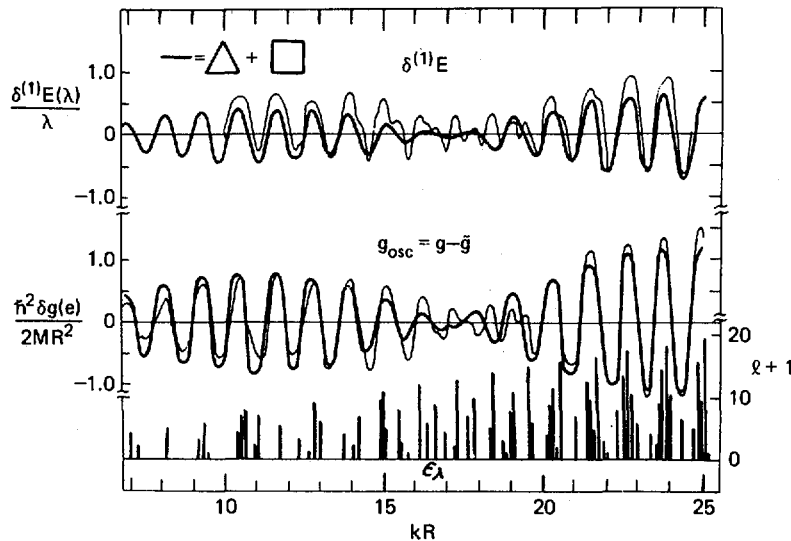


*FIG. 1.* Eigenvalues for spherical, infinitely deep potential and their quantal degeneracy (bottom). Oscillating component of level density calculated by numerical averaging and — bold lines — by quasi-classical approximation (centre). Shell energy  $\delta E$  found numerically and in semi-classical approximation (bold line) in accordance with expression (4).

to the shell structure are made by the orbits in the form of triangle- and square-shaped polygons which by no means resemble the density distributions or the  $\ell$ -values of the familiar wave functions in the quantal problem. The shell-spacing parameter  $\hbar\Omega$  obtained from relation (2) for such orbits is in good agreement with the value known for the semi-empirical nuclear potentials. On the other hand, the shell energies as well as the shell component of the level density derived from the general theory are in close agreement with the values obtained for the spherical square well by the traditional numerical technique (Fig. 1).

It should be mentioned that it is just this feature of the new theory, i.e. considering properties averaged over quantal states, that led to relatively simple solutions in the semi-classical limit. This is the case since classical properties manifest themselves only in such averaged quantities. One should therefore distinguish between such calculations and the attempts to approximate specific quantal eigenstates.

The quantity important for the analysis of nuclear shell structure is the oscillating component of the single-particle energy distribution, which is the sum of contributions from all families of periodic paths:

$$g_{\text{osc}}(e) = \sum_{\beta} g_{\text{osc}}^{(\beta)}(e) \quad (3)$$

In each component, the main period is as in relation (1), and the amplitude is determined by such properties of the classical problem as the number of the degrees of freedom (the classical degeneracy D), which specifies a single path in the continuous family of classical periodical orbits with the same action integral  $S_\beta$ , the stability of the orbit, and the volume in the phase space occupied by the family of the orbits. The integer number D is restricted by the degree of phase-space symmetry of the Hamiltonian, and it also cannot exceed a maximum of  $2n - 2$ , where n is the number of dimensions. In the case of maximum symmetry, all classical trajectories are periodical orbits, and families of orbits may exist in three-dimensional space with D up to four. In the one-dimensional well,  $D_{\max} = 0$ , which puts this case among other examples of completely degenerate classical motion.

For the energy derivations the quantity of interest is not  $g_{\text{osc}}$  itself but, rather, the related component of the single-particle energy which turns out to be given by [6, 7]

$$\delta E = \sum_{\beta} \left( \frac{\hbar}{T_{\beta}} \right)^2 g_{\text{osc}}^{(\beta)}(\mu_N) = \sum_{\beta} \left( \frac{\hbar \Omega_{\beta}}{2\pi} \right)^2 g_{\text{osc}}^{(\beta)}(\mu_N) \quad (4)$$

$$\cong \sum_{\beta} \left( \frac{\hbar v_{\beta}(\mu_N)}{L_{\beta}} \right)^2 g_{\text{osc}}^{(\beta)}(\mu_N) \quad (5)$$

Here,  $\mu_N$  is the Fermi energy for the given number N of particles, and  $L_{\beta}$  is the mean length of the  $\beta$ -th periodical paths. Through formulas (4) and (5), the shell energy  $\delta E$  is expressed in terms of classical quantities. The quantity  $\delta E$  plotted in Fig. 1 was derived from formula (4) with  $g_{\text{osc}}^{(\beta)}(e)$  and  $\Omega_{\beta}$  corresponding to the triangle- and square-shaped orbits in the spherical well.

The shell energy is approximately proportional to

$$\hbar^{-D/2} \propto (k_F R)^{D/2} \approx 2^D A^{D/6} \quad (6)$$

where A is the atomic number. This explains why more pronounced shell structure can be found in Hamiltonians of higher symmetry. No less important is, however, the fact that, according to relations (4) and (5), contributions to the shell energy decrease abruptly with increasing length of the orbits (also because of the diminished stability of the lengthier orbits) and with decreasing

volume occupied by the orbits. Hence, only the shortest stationary orbits not too close to the perimeter of the well are of importance for the analysis of the shell structure. This, of course, simplifies the problem essentially, at the same time making the conclusions more reliable.

The general theory sets the following conditions for a certain shape to be in equilibrium, such as the ground state or a shape isomer:

- (a) The shell distribution should correspond to the condition of minimum level density at the Fermi level (closed shell or the magic nucleus!): According to relations (4) and (5), the shell structure reduces the total energy in this case;
- (b) the intensity of the shell structure must be maximum. The most important condition for this to hold true is the presence of simple, short, periodical orbits of reasonably high degeneracy.

The second condition should be clarified. Although  $\delta E$  increases exponentially with  $D$ , as in relation (6), in real nuclei with  $k_F R \approx 10$  degeneracy and simplicity of the orbits play comparable roles and often less degenerate, but simpler orbits determine the shell structure [9]. This is true for the not too strongly deformed, axially symmetric harmonic oscillator. In realistic potentials, the shell structure leading to stable deformed shapes of nuclei in their ground states — the *first well* in the deformation energy — is due to the presence of periodical, rhomboid-shaped paths in the axis-of-symmetry plane with  $D = 2$ . No analogous families of classical paths exist in the deformed harmonic oscillator. There, the main contributions to the shell energy are made by the Lissajous figures in the plane perpendicular to the symmetry axis.

The difference is reflected in the positions of the shell minima in the familiar contour diagrams showing the distribution of the shell energies (Fig. 2). For not too strong distortions, the slopes of the minima valleys in the ellipsoidal square well and also in the Woods-Saxon potential are opposite to that derived for the deformed harmonic oscillator. This can be explained now as due to the fact that the rhomboids are stretched and elongated, and that the action integral increases with deformation. In contrast, the abovementioned Lissajous trajectories in the harmonic oscillator shrink and the action integral decreases under the same conditions. The theory gives, however, somewhat more than just a qualitative consideration. Indeed, as long as only one type of orbits contributes to the shell energy in expression (4), it can be expected that the positions of the extrema of the shell energies as shown in Fig. 2 will follow the lines of constant action-integral value:

$$S_\beta(\mu_N, \eta) = \text{const} \quad (7)$$

(equal to an integer multiple of  $2\pi$ ), where  $g_{osc}$  is extremal. Here and in Fig. 2,  $\eta$  is the deformation parameter and  $\eta = 1$  corresponds to the spherical shape. From expression (7), the slope of the extremum line in  $(\mu, \eta)$ -space is found to be

$$\frac{d\mu}{d\eta} = - \frac{\partial S/\partial\eta}{\partial S/\partial\mu} \quad (8)$$

For contour diagrams showing the shell energies as functions of  $N$  and  $\eta$ , the slope is found as

$$\frac{dN}{d\eta} = \tilde{g}(\mu_N) \frac{d\mu}{d\eta} \quad (9)$$

For the family of rhomboids with  $D = 2$  in the ellipsoidal square well, we obtain (for  $\eta \approx 1$ )

$$\frac{d\mu}{d\eta} = \frac{\mu}{3\eta} < 0 \quad (10)$$

and, correspondingly,

$$\frac{dN}{d\eta} = -\frac{1}{2} N \quad (11)$$

The Lissajous figures in the plane perpendicular to the symmetry axis give for the harmonic oscillator:

$$\frac{d\mu}{d\eta} = \frac{\mu}{3\eta} > 0 \quad (12)$$

and

$$\frac{dN}{d\eta} = \frac{\mu^3}{3(\hbar\omega_0)^3} \eta \quad (13)$$

The fat solid lines in Fig. 2 mark the positions of the minima of the shell energies obtained from relations (8)–(13). The agreement with the numerical calculations is remarkable. From the same simple arguments an estimate for the nuclear ground-state quadrupole deformations follows directly. The broken line in Fig. 3 is drawn with slope (11), and it agrees with the data in the rare-earth region (see also the discussion in Ref.[9]).

This ‘catholic heresy’ in the orthodox traditions on the origin of the nuclear deformations also led to the conclusion that it was not correct to relate the minima in the nuclear energy surface to special degeneracies in the harmonic-oscillator well which appear when the three partial frequencies (which here, at the same

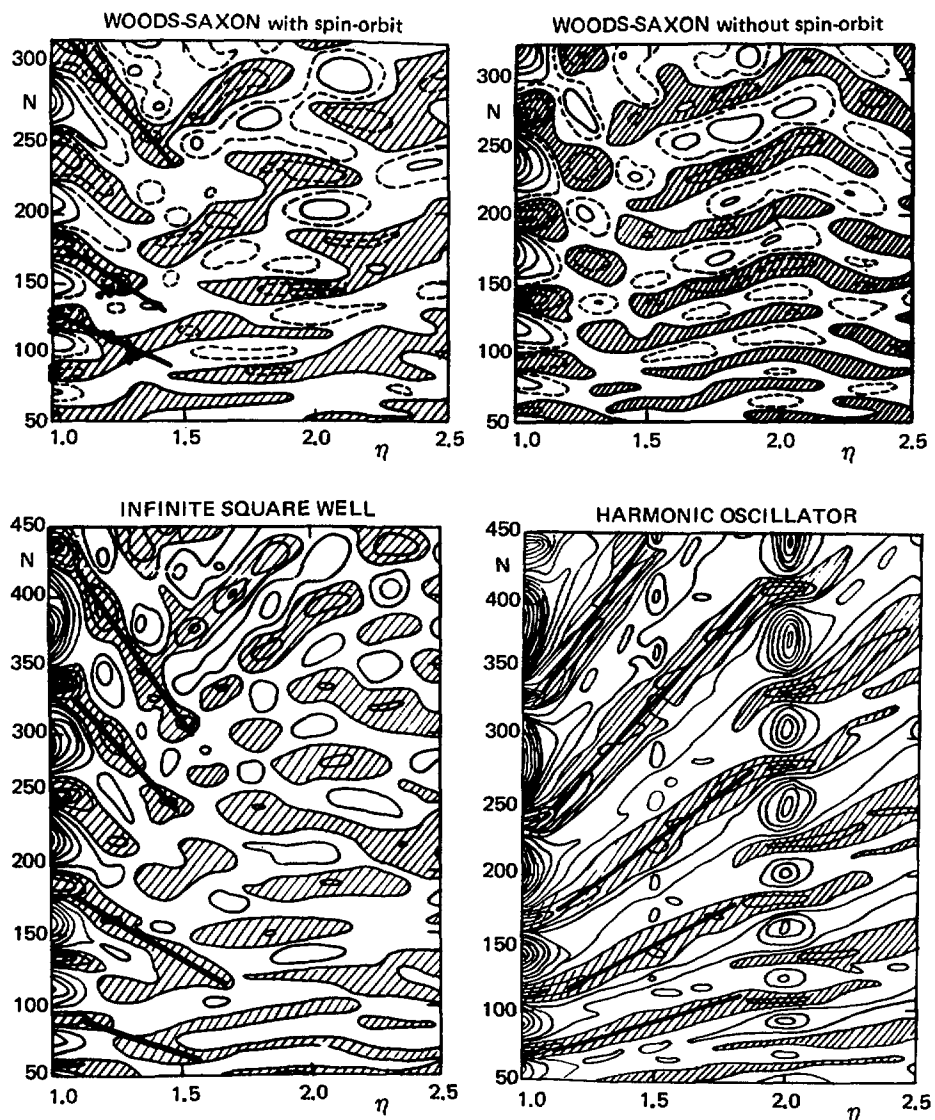


FIG. 2. Shell energies  $\delta E(N, \eta)$  derived numerically with potentials as indicated. Bold solid lines designate positions of minimum valleys obtained for two-fold degenerate ( $D = 2$ ) planar families of classical orbits in the plane of the symmetry axis for the ellipsoidal, infinitely deep well (also plotted in the Woods-Saxon diagram) and in the perpendicular plane for the axially deformed harmonic oscillator. Black dots in the left-hand upper diagram are experimental values of nuclear deformations in the ground states and in the second well (from Ref. [9]).

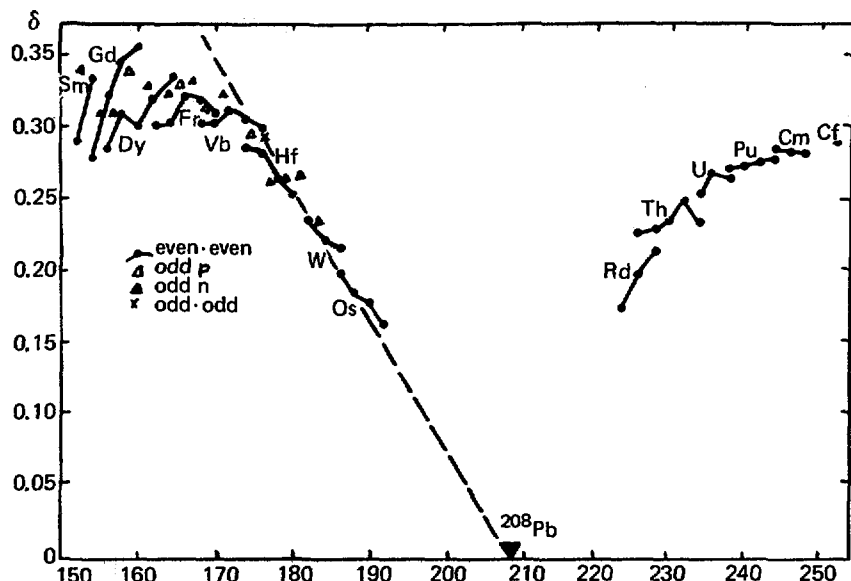


FIG.3. Quadrupole deformations of heavy nuclei. The broken line is drawn with slope given by expression (11) corresponding to rhomboid-shaped orbits in the axis-of-symmetry plane. The actinide region is too narrow for comparison (see also Fig.2).

time, are the deformation parameters) are related as ratios of integer numbers. These special shapes of the harmonic potential do, indeed, provide conditions for the existence of families of orbits of the highest degeneracy with  $D = 4$ . However, for smaller deformations — except for the spherical shape itself — the lengths of such orbits are strongly increased: to adjust two, only slightly differing frequencies, one has to go to higher harmonics, which results in longer periods of rotations and, consequently, smaller contributions to the shell energy (4). (In the harmonic oscillator the periods  $T_\beta$  for such highly degenerate orbits decrease as  $(\eta - 1)^{-1}$  near the spherical shape where  $\eta \rightarrow 1$ .) This can be recognized as a common qualitative feature. Simple periodic non-planar paths appear only at very large distortions of the order of 100%. The simplest of them are the three-dimensional orbits with the partial frequencies (such as  $\omega_\varphi$  and  $\omega_\mu$  in the ellipsoidal square well) related as 2:1. They are considered as making the main contributions to the shell structure, leading to the *second well* in the deformation energy surface and to the double-humped fission barrier. Such orbits appear naturally when the deformation approximately reaches the value of 2:1. This is *not* related to the special harmonic-oscillator degeneracies in the

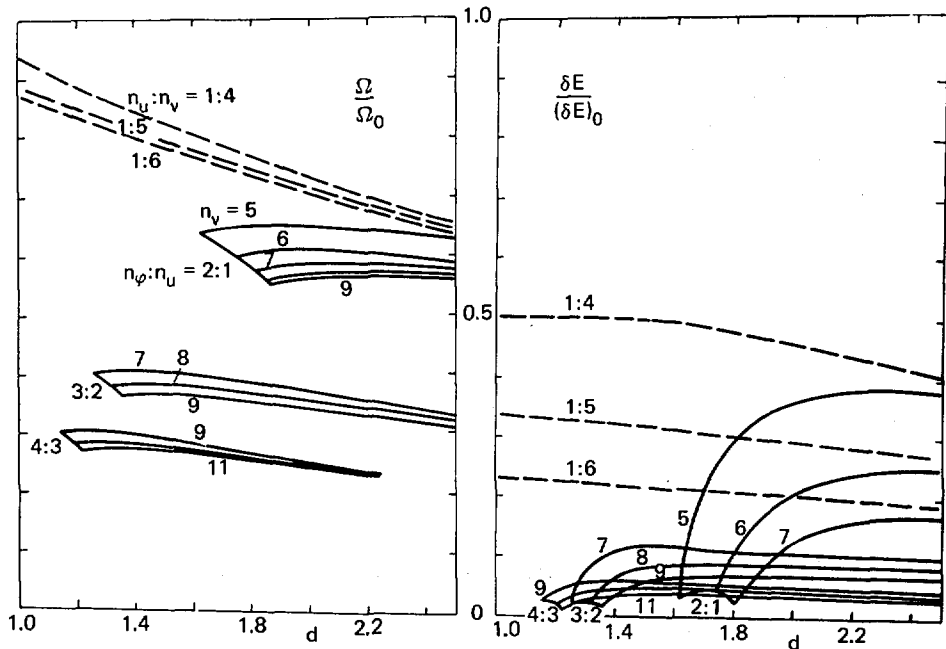


FIG. 4. Rotation frequencies  $\Omega_\beta$  for the shortest periodical orbits in the axially symmetric, infinitely deep ellipsoidal well; solid and broken lines are for the non-planar and planar paths, respectively (left); estimated shell energy contributions (right). With the curves the ratios  $\omega_\varphi : \omega_u$  of the two partial frequencies are shown; this is analogous to the  $\omega_\perp : \omega_\parallel$  ratios (but not as shape parameter!) in the harmonic oscillator.

average nuclear potential. In fact, the realistic shells need not have the same strength as those observed in the harmonic oscillator at a 2:1 axis ratio. A reasonable degeneracy of  $D = 2$ , i.e. that of the rhomboids in the ellipsoidal well, would be sufficient to provide the shell structure which is observed in realistic nuclei in connection with fission. Another difference to the harmonic oscillator is that, in general, the partial frequencies are not uniquely related to the shape parameters. Consequently, the three-dimensional orbits of the required type can be found for all shapes starting at around a deformation of 2:1, in contrast to the harmonic oscillator, where they arise just at this particular axis ratio. Figure 4 illustrates the appearance of the planar and three-dimensional families of periodical orbits in the ellipsoidal square-well potential and also their estimated contributions to the shell energy. The data there show that not only the deformation where the second minimum occurs but also the strength of the shell structure required for the double-humped barrier can be explained in this way..

At the still larger distortions corresponding to the second barrier and close to the scission point, the shell structure is the result of a complex superposition of contributions of stationary paths of rather different kinds and it allows for an easy — but also too ambiguous — qualitative explanation of the *third well*, as well. Such a minimum occurs systematically in the calculations of the fission barrier in the thorium region and in lighter isotopes of uranium and plutonium (see Ref.[10] and Fig.6). A simpler picture may arise *after* the neck has been formed: It can be assumed that at this stage of the fission process the necked shape of the nucleus does not allow the occurrence of any rhomboidal or other simple orbits crossing the nucleus from one end to the other. Instead, periodical paths constrained within either half of the nucleus become important and a transition to the shell structure in the fragments being formed takes place. In contrast to the whole-nucleus shell structure which apparently emphasizes symmetry, asymmetric shapes are now generally preferred. Within the model of two touching spherical wells, this problem has been approached by P. Bonche [11].

The general theory also sheds some new light on other aspects of the shell effects in fission. One of these effects is the transition to the classical droplet model limit at higher excitations. The temperature at which this transition takes place was found to be equal to

$$T_{\text{crit}} = \frac{1}{\pi} \hbar \Omega = 2.0 - 2.5 \text{ MeV} \quad (14)$$

where  $\hbar \Omega$  is given by relation (1). This value is in good agreement with the numerical calculations [12–14]. It turned, however, out that, in the intermediate excitation range, the very notion of potential energy of deformation fails: Instead of a fission barrier, one deals here with the amount of work required to fission the nucleus, and this thermodynamic problem cannot be reduced to a mechanical — or a hydrodynamic — Hamiltonian with characteristic potentials, forces etc. The extreme cases of very low or very high excitation energies are the only exception to this [15]. Some new aspects were also found in the problem of shell structure in the density of neutron resonances [6, 7].

The general theory outlined here was not intended and does not pretend to replace the numerical derivations in obtaining quantitative results on the process of nuclear fission. For this purpose, several more effective numerical methods are available by now. Some of these methods are elaborations of the originally suggested method of energy averaging. Other methods are based on different principles. By now, a new effective technique has been developed for finite-depth potentials, even when the Fermi energy is only a few MeV below the edge of the well (see Section 3). But this development has required clarification of some points in the theory of heavy nuclei treated as nearly macroscopic systems (see Section 4).

An important development in fission barrier calculations has been taking place since the breakthrough in the Hartree-Fock calculations had occurred. It has also contributed significantly to establishing the questioned accuracy of the shell correction expansion. This subject is partly dealt with in the review paper by Brack [33]. What is described in the rest of this paper refers to the traditional approach and, in particular, to those of its aspects that are most closely related to the question:

## 2. WHAT ARE THE SHELL MODEL POTENTIAL AND THE NUCLEAR SHAPE?

Apparently, the accuracy of the energy expansion depends on the quality of the shell model potential used in the calculations. Convergence requires what may be called the *statistical self-consistency* between the shell model potential and the spatial density distribution [23]: The statistically averaged shell model density distribution  $\rho_s$  should be the same as the original (not self-consistent) smoothed distribution  $\bar{\rho}$  which presumably generates the shell model potential  $\bar{V}$ :

$$\bar{V}(r_1) = \text{tr}_2(t(1,2)\bar{\rho}(1,2)) = \text{tr}_2(t(1,2)\tilde{\rho}_s(1,2)) \quad (15)$$

Here,  $t(1,2)$  is the effective nucleon-nucleon interaction. The second-order term in the energy expansion is given by [15]

$$\delta^{(2)}E = \frac{1}{2} \delta\rho_s \tilde{\Gamma} \delta\rho_s + \delta\rho_s \tilde{\Gamma} (\tilde{\rho}_s - \bar{\rho}) \quad (16)$$

Here,

$$\delta\rho_s = \rho_s - \tilde{\rho}_s \quad (17)$$

and  $\rho_s$  is the density matrix corresponding to the shell model problem with the potential of the given shape. In expression (16),  $\tilde{\Gamma}$  is the statistically averaged self-consistent effective scattering amplitude. The condition (15) of the relaxed statistical consistency makes the second term in expression (16) for all nuclear shapes. The second-order energy term, so far neglected in most of the calculations, is then determined entirely by the nucleon forces and the magnitude of the difference between the actual and the statistically averaged shell model density matrices (17). The consistency requirement (15) is a very natural condition, namely, that the density distribution in the deformed potential should follow the shape of the potential. It is, however, quite clear that this condition is met with different degrees of accuracy in different phenomenological shell model potentials which

were designed irrespective of this criterion. Quantitatively, the role of condition (15) is described in M. Brack's paper [33] within the framework of the Hartree-Fock theory.

To satisfy the *statistical* self-consistency condition might be much easier than to go through the original Hartree-Fock routine, and the combined semi-classical development might prove to be rather fruitful. The shell correction approach suggests, however, yet another way of handling the problem. Instead of the total rejection of the phenomenological shell model potential (as the popular Hartree-Fock way of thinking goes) one might try to exploit it as some valuable initial approximation and to correct it in such a way that condition (15) is met with sufficient accuracy. In the first order, the statistically self-consistent potential is

$$\tilde{V}_c = \bar{V} + \text{tr}_2 (\tilde{\Gamma} (\tilde{\rho}_s - \bar{\rho})) \quad (18)$$

where  $\bar{V}$  is anyone of the commonly used shell model potentials. Other forms of this equation can be found in Ref.[16]. The corrected potential has the following remarkable feature: It is stationary with respect to the selection of the original potential, i.e. Eq.(18) would give approximately the same quantity no matter whether the Woods-Saxon or the Nilsson potential were in the input. Also, the nucleon force in expression (18) need not be as sophisticated as the one used in the Hartree-Fock calculations because the whole self-consistency routine need not be carried through. Instead, a simpler interaction can be used more suitably in reproducing the features essential for the shell corrections such as, for example, the structure at the diffuse nuclear surface. Unfortunately, little has been done along this line, as yet.

The effort undertaken to clarify the higher-order terms in the shell correction expansion has emphasized the fact that, among statistically averaged quantities, not only the smoothed energy, but also all other quantities appearing in the theory, such as shell correction energy, single-particle potential as well as the very notion of nuclear shape are important. They should rather be interpreted as macroscopic quantities averaged over many intrinsic quantal states. Approximation of the independent motion involves averaging over the distribution of particle and hole states near the Fermi energy and the single-particle part of the deformation energy is the quantity averaged over a number of subsequent level crossings or particle-hole distributions. For example, the driving force due to the shell structure was found equal to

$$F_\eta = -\frac{\partial \delta E}{\partial \eta} = \text{tr} \left( \tilde{\Gamma} \frac{\partial \rho_0}{\partial \eta} \right) \quad (19)$$

where  $\partial \rho_0 / \partial \eta$  is the derivative of the averaged diagonal part of the density matrix due to the variation of the occupation numbers under deformation. No such

effects are accounted for in the perturbation-based microscopic theories dealing with the so-called particle-hole interactions which assume that the given particle-hole distribution does not change. The characteristic deformation which causes the re-distribution of the particle and hole states can be estimated rather easily because both the mean slopes of the levels in the Nilsson diagram and the distance between the levels are well known. Up to the sign, the first item is of the order of the Fermi energy per unit of the quadrupole deformation, and the second one is the Fermi energy divided by A. Thus, the mean level crossing deformation is given by

$$\eta^* \approx \frac{1}{A} = 0.01 - 0.03 \quad (20)$$

It is easy to check that expression (20) agrees with what is actually seen in the Nilsson diagrams in strongly deformed nuclei. The quantity (20) is, however, so small that hardly any significance can be assigned to what happens within such a range of quadrupole deformation. On the other hand, quantities derived by the shell correction method become only significant as averages over a sufficient number of such re-distributions, which makes them appropriate to be used in the theory of processes where the amplitudes significantly exceed the characteristic deformation (20). Fission is one example of such large-amplitude macroscopic collective modes, which are the general feature of heavy nuclei, particularly at higher excitation energies. Dipole resonances on neutron shape resonances in heavy nuclei may also be recalled as examples of such modes. In all such cases, transition to the classical regime takes place, and collective states can only be seen in properly averaged quantities like the densities of certain states or strength functions.

The phenomenon of particle-hole re-distribution is a very special feature of finite-size quantal systems. Here, in contrast to the plane waves of infinite matter, each of the wave functions — which are real — carries information on certain density distributions, which do not, in general, correspond to the mean shape of the body. The particle-hole re-distribution takes place when two levels crossing at the Fermi energy correspond to opposing density distributions. (This is the reason why the slopes are different!). Providing that the lower-energy state is predominantly inhibited, the re-distribution helps to restore the consistency between the mean shape of the density distribution and that in the specific quantal state. Redistribution of particle and hole states is also caused by the finite velocity of the deformation process. It corresponds to a transition to a dynamical ground state and should be considered in the dynamical theory of large-amplitude processes [17].

Alongside the somewhat abstract arguments of this section, the averaging process involved discussions of some more practical problems, one of which was

the use of single-particle energies in calculations with realistic finite-depth potentials. So:

### 3. WAS THERE A CONTINUUM PROBLEM?

The criticism with which the original prescription was met seemed to be partly supported by some ambiguities in the results of calculations with realistic finite-depth potentials. To avoid these difficulties (which were often exaggerated), several alternative approaches were suggested, such as a) obtaining [18–21] the smoothed single-particle energy by extrapolation to the temperature  $T = 0$  of the asymptotic quantity for  $T > T_{crit}$  (see expression (14)); considering the asymptotic limit for a very large number of particles [19, 22]; refined calculations within the so-called improved Thomas-Fermi theory [32]. These apparently different approaches are, in fact, closely related to each other, and in each of them the problem of averaging — though implicitly — is posed. The original method is advantageous in this respect, as it deals with the problem directly. Since we think that the difficulties were brought about by ignoring some *first principles* of the shell correction approach, or, in some cases, by a misuse of the original prescription, the rest of this paper will be devoted to a further development of the original method rather than to a review of these alternative suggestions.

In the shell correction averaging, the specific form of the smoothing function  $\xi_M(x, x')$  is determined by the condition that the smoothing should restore the function which is already a smooth function of the original arguments, such as the Fermi energy or the particle number  $N$ , or a simple function of such, as, e.g.  $N^{1/3}$ . The smoothed quantity is

$$\bar{E}(x) \equiv \langle E(x') \rangle_{x' \approx x} = \int_{x_1}^{x_2} \xi_M(x, x') E(x') dx' \quad (21)$$

and if we denote the already smooth function as  $\tilde{E}(x)$ , the condition can be formulated as

$$\tilde{E}(x) = \bar{E}(x) \quad (22)$$

If  $\tilde{E}(x)$  is defined as a polynomial of low degree, say,  $M$ , conditions (21) and (22) determine  $\xi_M(x, x')$  in a unique way, and it can be shown that the prescription (21) is equivalent to finding the least-square-deviation (LSD) fit to  $E(x)$  among the

polynomials of a degree smaller than or equal to  $M$ . The weight function  $w(x, x')$  can be introduced and is interpreted as an error's price in the LSD-fit. The function  $w(x, x')$  involves a parameter  $\Delta$  which determines its width. The  $\gamma$ -parameter of the original prescription is relevant to the specific case of energy averaging in expression (21) and to the choice of  $w(x, x')$  as a Gaussian of  $(e - e')$ . The function  $\xi_M(x, x')$  is expressed in terms of the system of the polynomials  $p_k(x')$ , orthogonal and normalized with weight  $w(x, x')$  in the interval  $(x_1, x_2)$ :

$$\xi_M(x, x') = \sum_{k=0}^M p_k(x) p_k(x') w(x, x') \quad (23)$$

$\xi_M(x, x')$  is the kernel in the formal theory of orthogonal polynomials [24]. These arguments solve the problem in the general form. Specific prescriptions are obtained for given averaging range  $(x_1, x_2)$  and  $w(x, x')$ . For the smooth quantity, prescription (21) should give a result independent of these and the other arbitrary parameters involved in the numerical calculations, such as  $M$ ,  $\Delta$ .

When applied to calculations of shell energy corrections, this — apparently very general — formulation involves, however, a very important physical assumption, i.e. that the so-called phenomenological droplet part ( $E_{DM}$ ) is, indeed, the smooth function in the above sense. In other words, the smoothed quantity determined as in (21) should correspond to the phenomenological definition of the DM-energy. Otherwise, with the shell energy determined as

$$\delta E = E_s - \bar{E}_s \quad (24)$$

the total energy

$$E = E_{DM} + \delta E \quad (25)$$

contains some uncontrolled smooth component, and the whole idea of using the expression for the semi-empirical droplet-model energy is no longer meaningful.

A check of this (yet another) consistency condition is that a certain smooth part was, indeed, lost in the calculations using the Myers-Swiatecki fit [24]: Their shell-correction modelling function  $S(N, Z, \eta)$  contains a smooth energy component proportional to  $A^{1/3}$ , in contradiction to definitions (21)–(24), according to which the average of  $\delta E$  should be equal to zero. This component should, correspondingly, be subtracted from the so-called empirical values of  $\delta E(N, Z)$ . It would reduce the value of  $\delta E$  in  $^{208}\text{Pb}$  to  $-17$  to  $-18$  MeV instead of the value of  $-13$  MeV accepted at present.

Nearly all calculations exploit the original prescription which was developed specifically for the case of the *infinite* averaging range ( $x_1 = -\infty$ ,  $x_2 = +\infty$ ) and the Gaussian  $w(x, x')$ . The uncritical use of this prescription with finite-depth potentials leads to misunderstandings: since the actual level distribution is, in this case, determined within the finite range of the argument only, the smoothing (21) yields an interpolation between the region of negative energies where the quantity is actually defined and the zero value outside. This accounts for the unstable results which, however, in no way provide an evidence for the failure of the prescription as such. The number of levels within the well is large enough to determine the smooth quantity, should the smoothing be adequately defined, i.e. for a finite range of the argument ( $e_2 < 0$ ). It seemed [26] that a better prescription could immediately be obtained from relations (21) to (23). The calculations have shown that the stability required was not reached although the quality of the plateau was significantly better than in any other calculation with the bound spectrum. The origin of this new and unexpected difficulty has become clear only recently [27]. It is related to the fact that in the total single-particle energy the irregular component due to the shell structure is present on the background of a curved polynomial part ( $M = 3-8$ ) and the averaging (21) involves the smoothing function  $\xi_M(x, x')$ , sharply peaked at  $x = x'$  even if the weight  $w(x, x')$  is constant. It increases the uncertainty of the LSD-fit near the edge of the averaging interval, for  $x$  close to  $x_2$ . The difficulty was removed by adding an auto-correction to the smoothing procedure. According to this improved prescription, the corrected value for the first-order shell energy is found as

$$\delta E = E_s - \bar{E}_s + \bar{S} \quad (26)$$

where  $E_s$  is the single-particle energy sum, and the smoothed quantities  $\bar{E}_s$  and  $\bar{S}$  are both determined as in expression (21). In relation (26),  $S(N, Z, \eta)$  is some function of the arguments shown which approximates the shell energy. It has been found that a convenient choice of  $S(N, Z, \eta)$  is the expression which follows from the general theory described in Section 1, i.e.

$$S(N, Z, \eta) = a \delta g(\mu) \quad (27)$$

except that the level density variation  $\delta g$  in expression (27) is determined directly by the numerical method rather than from the theory. This quantity is easy to find for any nuclear shape and given single-particle potential as the difference

$$\delta g(e) = g_0(e) - \tilde{g}(e) \quad (28)$$

as soon as the single-particle spectrum is available. The first term in expression (28) is obtained by numerical averaging with a smaller  $\gamma = 2-3$  MeV, and the second

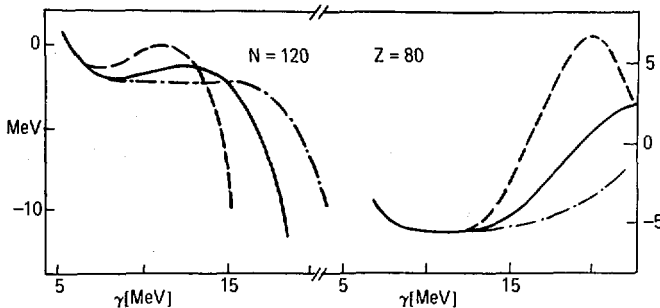


*FIG. 5. Examples of plateaus in calculations with the Woods-Saxon potential and discrete spectrum extended into the continuum by means of diagonalization. The basis parameter was, in units of  $A^{-1/3}$  MeV, equal to 41 (broken line), 55 (solid line) and 69 (dot-dashed line).*

one is the inverse of the second derivative of the polynomial-smoothed energy  $\bar{E}_s(N)$ ,

$$\tilde{g}(N) = (\partial^2 \bar{E}(N, \eta) / \partial N^2)^{-1} \quad (29)$$

Let us note that the calculation of  $\bar{S}$  through (27) to (29) requires only a moderate accuracy in determining the quantities involved there and can be obtained without difficulty by using only the energies of the bound states. The numerical coefficient  $a$  in expression (27) is found from the condition of maximum stability of the shell energy, as derived through expression (26), with respect to the position of the upper limit of the averaging interval,  $N_2$ .

It has turned out that in this way excellent plateaus in  $\delta E$  as functions of all arbitrary parameters ( $M, N_2, \gamma$ ) and by using the unambiguous bound energies only are obtained. Moreover, the value of  $\delta E$  can be determined even when the cut-off energy is only 2–3 MeV above the Fermi level. In Fig.6, the new values of the deformation energies of some heavy nuclei are compared with those obtained in the traditional manner with the spectrum extended into the positive energies by diagonalization in a restricted basis [28–29]. The basis size parameter  $\hbar\omega_0$  in these calculations was equal to the traditional Nilsson value,

$$\hbar\omega_0 = 41 A^{-1/3} \text{ MeV} \quad (30)$$

Constrained shape variations explain the – not too good – absolute values of the fission barriers in Fig.6. However, the data demonstrate quite clearly that the traditional and the new results agree well, except for some shift which is, however, nearly constant for the deformed shapes and, therefore, does not

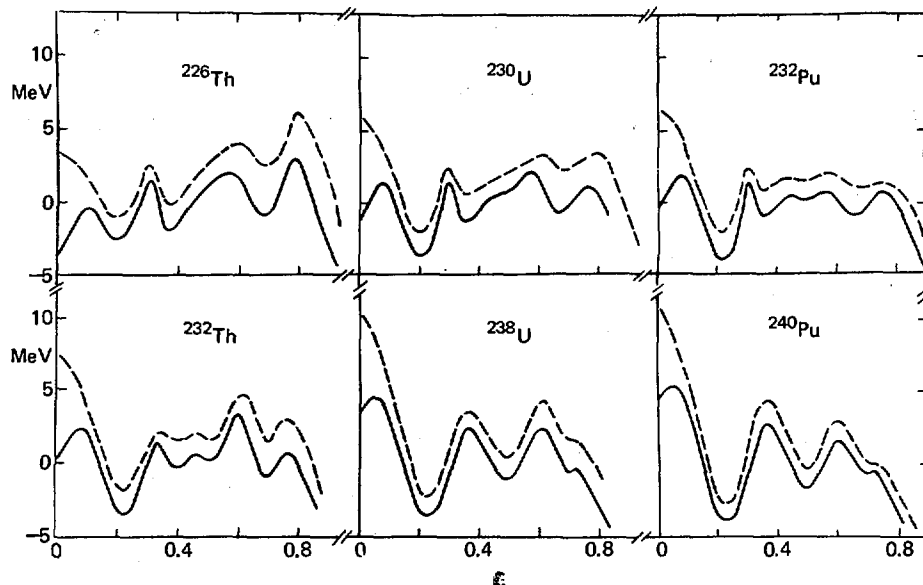


**FIG.6.** Deformation energies (in MeV) of some actinide nuclei, obtained by means of traditional method with extended spectrum (broken lines) and by N-averaging for deformed Woods-Saxon potential. The deformation parameter  $\epsilon$  is the same as that used in Ref. [12].

affect the deformation energies in the actinide nuclei. In particular, the formation of the *third well* at very large deformations is quite pronounced in thorium and the lighter isotopes of uranium and plutonium, such as was found in earlier calculations by Nix and co-workers [10]. In heavier nuclides, this well merges into the *second well*. The shift between the two sets of data was found as a common feature in all calculations involving N-averaging. Larger shifts were found for the spherical shapes and, in general, in cases of a particularly pronounced shell structure. The origin of this effect proved to be rather deeply rooted and, because of its possible implications, we shall deal with this topic again in the next section. The use of the discrete single-particle spectrum extended to the positive-energy region was one of the causae belli in the discussions around the shell correction prescription. In this connection, it should be noted that using the positive-energy spectrum has nothing to do with the foundation or the *first principles* of the shell correction calculations, because the definition of the average quantities involves neither the unbound nuclear states nor the scattering properties. Moreover, only states below the Fermi energy would be required if the change of the potential well volume with  $N$  had been taken into account. The need for higher states arises only because the averaging of the true single-particle

energies is replaced by averaging the single-particle states in a fixed well. The argument may run as follows:

Assuming that the energy  $\epsilon_\nu(N)$  of the  $\nu$ -th single-particle state in a nucleus of  $N$  nucleons depends smoothly on  $N$ , we can approximately write the  $N$ -average of the total single-particle energy as

$$\begin{aligned} \langle E_s(N') \rangle_{N' \approx N} &= \left\langle \sum_{\nu=1}^{N'} \epsilon_\nu(N') \right\rangle_{N' \approx N} \\ &= \left\langle \sum_{\nu=1}^{N'} \epsilon_\nu(N) + (N' - N) \sum_{\nu=1}^{N'} \frac{\partial \epsilon_\nu(N)}{\partial N'} + \dots \right\rangle_{N' \approx N} \end{aligned} \quad (31)$$

The first term in the sum on the right-hand side of Eq.(31) is just the smooth single-particle energy in a fixed well such as that considered in the shell correction calculations. Should the slope  $\partial \epsilon_\nu(N)/\partial N$  be a smooth function of the level number  $\nu$ , all terms in Eq.(31), except for the first, would turn into zero, owing to the properties of LSD-averaging which restores the value of the smooth function at the central point  $N' = N$ . Therefore, in each of the sums in Eq.(31), except for the first, only the fluctuating parts of the level slopes contribute and, assuming that there is no correlation among them, we conclude that these sums are, by order of magnitude, equal to the mean value of the single item in the sum. The latter is estimated to be given by

$$\frac{\partial \epsilon_\nu}{\partial N} \approx 2 \mu/3 N \quad (32)$$

and is of the order of the mean spacing between the single-particle energies. Neglecting such relatively small contributions we may state that averaging within a fixed well corresponds to  $N$ -averaging of the total single-particle energies, i.e.

$$\left\langle \sum_{\nu=1}^{N'} \epsilon_\nu(N') \right\rangle_{N' \approx N} \approx \left\langle \sum_{\nu=1}^N \epsilon_\nu(N) \right\rangle_{N' \approx N} \quad (33)$$

It is clear now that the single-particle spectrum used in the shell correction calculations should be a smooth extrapolation of the energies in the average nuclear potentials of the nuclei around. In particular, the positive energy levels — if they are needed — are the extrapolations of the bound states in heavier nuclei. Such a spectrum need not represent the positive energy resonances. The spectrum extended by diagonalization with the constrained basis turns out as a simple and also very reasonable way of obtaining the required spectrum. From the practical viewpoint, this method has the advantage that such an extended spectrum is obtained in the computer simultaneously with the discrete energies. The significance of the extended spectrum was explained in Ref.[29]. It is merely a smooth extrapolation of the discrete-level distribution and significantly improves the quality of the plateau, in particular, if the parameter  $\hbar\omega_0$  and the total number of harmonic-oscillator shells are fitted to the radius of the real nuclei. The best plateau is obtained with

$$\hbar\omega_0 = (55-70)A^{-1/3} \text{ MeV} \quad (34)$$

This value corresponds to the basis size normalized at the Fermi energy to the radius of the Woods-Saxon well. In contrast, the smaller Nilsson value (30) adjusts the radii averaged over *all* occupied states in the harmonic potential. Figure 5 shows the quality of plateaus obtained with different values of the parameter  $\hbar\omega_0$  (Pashkevich 1978). Larger  $\hbar\omega_0$  also improves the moments of inertia evaluated with the Nilsson model [1]. In spite of all these advantages, the value (30) for  $\hbar\omega_0$  was, by tradition, used in all earlier calculations. Anyway, finding a plateau was never really a problem.

Since the significance of the positive energy levels was doubted, the widely spread opinion was that the density in the extended spectrum should correspond to the real density of states in the continuum due to the presence of the potential well,

$$g^+(e) = \frac{1}{\pi} \sum_j \frac{\partial \delta_j(e)}{\partial e} \quad (35)$$

or, at least, represent the positions of the true resonances in the phase shifts,  $\delta_j(e)$ . Calculations along this line were performed in Refs [30, 31]. It has been demonstrated [31] that the plateau is, indeed, improved in comparison with the standard results if energies up to  $\gtrsim 60$  MeV and angular momenta up to 10 are included. This alone makes such calculations quite impracticable. (Furthermore, the derivation of the phase shifts for deformed potentials is not only much more

complicated, but also ambiguous because of their dependence on the orientation of the nucleus with respect to the beam).

The use of the true continuum spectrum in the shell correction calculations is also erroneous simply because the density of the continuum states (35) is not a continuation from the bound-state region. This point can be illustrated by using the semi-classical expressions for the partial phase shifts in the spherical well  $V(r)$ . A simple derivation gives for such an analogue of the Thomas-Fermi level density in the continuum:

$$\tilde{g}^+(e) = \frac{4m}{\pi \hbar^3} \int_0^\infty r^2 dr \left( \sqrt{2m(e - V(r))} - \sqrt{2me} \right) \quad (36)$$

(Magner, 1979). There is a singularity at  $e = 0$ , and the behaviour at large values of  $e$  is also quite different from the polynomial approximation. In expression (36), it has been assumed that the potential  $V(r) = 0$  for  $r > R$ ; the conclusion is, however, true in the general case. Moreover, for smooth potentials such a singularity appears also in the Thomas-Fermi density of the *bound* states, i.e. at  $e = -0$ . Both these singularities hinder the use of the smoothing routine (21) whenever the edge of the potential well gets close to the Fermi energy, within the range essential for the averaging.

The conclusion is that, should the use of the extended diagonalization spectrum be considered insufficient, the only way to do the averaging is to use the modified prescription not referring to any continuum states. This involves, however, an answer to the question:

#### 4. WHAT IS THE DROPLET ENERGY?

Qualitatively, the droplet model is understood as one or more relationships between the exact (quantal) quantities, statistically averaged in the particle phase-space in a Thomas-Fermi-like manner. However, as the preceding discussion shows, there could exist at least as many specific definitions of the smoothed quantities as different definitions of the shell energy have been suggested. These definitions are essentially equivalent, except for the systematic shift of the newly found values of  $\bar{E}_s$ . These  $N$ -averaged exact quantities differ from the Thomas-Fermi energy-averaged values because the shell structure in the single-particle spectrum introduces some irregularity in the relationship between the energy and the particle number. Quantitatively, the effect can be described in the

following way. For a given total nucleon number  $N$ , the energy-averaged quantity is

$$\bar{E}^{(e)}(N) = \langle E(\mu') \rangle_{\mu' \approx \bar{\mu}_N} \quad (37)$$

which is equivalent to the other, more familiar expressions, such as

$$\bar{E}^{(e)}(N) = \int_{-\bar{\mu}_N}^{\bar{\mu}_N} e' \tilde{g}(e') de' \quad (38)$$

or

$$\bar{E}^{(e)}(N) = \int_{-\infty}^{\infty} e' g(e') \tilde{n}(e', \bar{\mu}_N) de' \quad (39)$$

where  $\tilde{g}$  and  $\tilde{n}$  are the smoothed level density and the nucleon occupation distributions. In expressions (37) to (39),  $\bar{\mu}(N)$  is found from the conservation of the partial number:

$$N = \int_{-\infty}^{\infty} g(e') \tilde{n}(e', \bar{\mu}_N) de' \quad (40)$$

and  $\mu_N$  was defined earlier. On the other hand, the  $N$ -averaged energy is

$$\bar{E}^{(N)}(N) = \langle E(N') \rangle_{N' \approx N} = \int E(N') \xi_M(N, N') dN' \quad (41)$$

In both cases, the same quantity — the quantal energy  $E(N)$  — is being smoothed, but in the first instance it is regarded as a function of the argument  $\mu_N$ , which in itself is not a smooth function of  $N$ , because of the shell structure. The two averaged energies, (37)–(39) and (41), are related as

$$\bar{E}^{(N)} = \bar{E}^{(e)} + \Xi \quad (42)$$

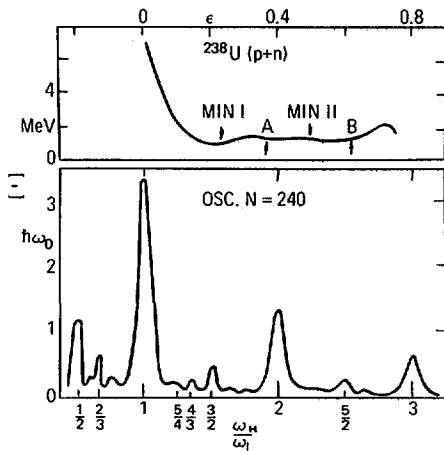


FIG. 7. Symmetry corrections to the droplet-model  $\Xi$  as determined according to expressions (43) and (44) and calculated for deformed Woods-Saxon potential of  $^{238}\text{U}$  (top) and for deformed harmonic oscillator ( $N = 240$ ) (bottom). In the top part of the figure, the deformations at first and second minima (I and II) and at the two barriers, A and B, are shown.

where

$$\Xi = \frac{1}{2} \tilde{g}_N \langle (\mu - \bar{\mu})^2 \rangle_{av} \quad (43)$$

(Ivanyuk, 1979). In expression (43),  $\tilde{g}_N$  is the mean level density at the Fermi energy. According to expression (43), the difference between the two smoothed energies is proportional to the mean squared fluctuation of the actual Fermi energy around the mean Thomas-Fermi-type value. We note that the shift of the Fermi energy  $\mu - \bar{\mu}$  is proportional to the local deviation from the mean value of the level density. Thus, it can be concluded that the correction  $\Xi$  is proportional to the amplitude of the shell energy  $\delta E$  for the given shape and approximately equals one third of it. (There is a numerical coefficient of the type of  $\langle \sin^2 x \rangle_{av}$  which depends on the form of  $\delta g(\epsilon)$ . The specific definition of averaging is of no importance for this correction.) Now, we explained in Section 1 that the amplitude of  $\delta E$  increases with the degree of the degeneracy of classical motion and sharply decreases with the length of the orbits. Because of the last factor, nuclear shell structure is usually related to simpler orbits whose lengths are of the order of the perimeter of the well and change little with deformation. Now an important conclusion can be drawn: The variation of  $\Xi$  with deformation mainly reflects the change in degeneracy  $D$  of the families of orbits responsible for shell structure. This agrees with the calculated results (Fig. 7). In the

Woods-Saxon case,  $\Xi$  drops sharply around the spherical shape ( $D = 3$ ) and then remains nearly constant ( $D = 2$  in the deformed well). In the harmonic oscillator,  $\Xi$  jumps at deformations where higher-symmetry ( $D = 4$ ), three-dimensional Lissajous orbits occur. It is, therefore, natural to call  $\Xi$  the symmetry correction to the smoothed energy. It gives the difference between the Thomas-Fermi-type energy and the LSD-fit to the nuclear mass (for a given shape) in N-space. In realistic potentials,  $\Xi$  varies rather smoothly as a function of  $N$ , but changes rapidly around the spherical shape. It may be noted that  $\Xi$  assumes the asymptotic value characteristic of the deformed well at a deformation significantly slighter than that for the shape of the ground state. This is one further evidence for nuclear ground state deformations being due to a special shell structure developed in the deformed nucleus, analogous to that in the ellipsoidal square well, and not constituting a secondary effect of spherical symmetry, as was argued in Ref.[19].

Since  $\Xi$  varies so little in the deformed nucleus, the symmetry correction does not affect the shape of the fission barriers in deformed nuclei, but may be of importance if spherical nuclear shapes are concerned. This argument could have repercussions on the practice of fitting the droplet-model-based semi-empirical mass formulas to the nuclear masses, which corresponds to a LSD-fit in N-space as employed in the new shell correction prescription. A better approximation to the nuclear masses should include the symmetry correction  $\Xi$  to the smooth energy term:

$$M(N, Z, \eta) = E_{DM} + \Xi(\eta) + S(N, Z, \eta) \quad (44)$$

Here,  $M$  is the nuclear mass,  $E_{DM}$  the classical droplet-model energy, and  $S(N, Z, \eta)$  is the shell correction. According to expression (44), the correction  $\Xi$  should be subtracted from the mass values before fitting the Thomas-Fermi theory to them (including the shell energy obtained by energy averaging). For a rough estimate, the symmetry correction can be neglected in deformed nuclei, and the empirical values of  $S$  found in this way for spherical nuclei are then to be decreased according to the value of  $\Xi(0)$ , i.e. by several MeV. This would further diminish the so-called lead anomaly. The inclusion of the symmetry correction into the mass fit may also affect the values of the parameters of the droplet model, in particular the surface energy term.

## REFERENCES

- [1] BRACK, M., DAMGAARD, J., JENSEN, A.S., PAULI, H.C., STRUTINSKY, V.M., WONG, C.Y., *Rev. Mod. Phys.* **44** (1972) 320.
- [2] NILSSON, S.G., TSANG, C.F., SOBICZEWSKI, A., SZYMANSKI, Z., *Nucl. Phys.* **A131** (1969) 1.
- [3] NIX, J.R., *Annu. Rev. Nucl. Sci.* **22** (1972) 65.

- [4] BALIAN, R., BLOCH, C., Ann. Phys. (a) **69** (1972) 76; (b) **60** (1970) 401.
- [5] GUTZWILLER, M., J. Math. Phys. (a) **8** (1967) 1979; (b) **12** (1971) 343.
- [6] STRUTINSKY, V.M., Nukleonika **20** (1975) 679.
- [7] STRUTINSKY, V.M., MAGNER, A.G., Sov. J. Part. Nucl. **7** 2 (1976) 138.
- [8] MAGNER, A.G., Yad. Fiz. **28** (1978) 1477.
- [9] STRUTINSKY, V.M., MAGNER, A.G., OFENGENDEN, S.R., DØSSING, T., Z. Phys. **A283** (1977) 269.
- [10] MÖLLER, P., NIX, J.R., in Physics and Chemistry of Fission (Proc. Symp. Rochester, 1973), Vol.1, IAEA, Vienna (1974) 103.
- [11] BONCHE, P., Nucl. Phys. **A191** (1972) 609.
- [12] MORETTO, L.G., Nucl. Phys. (a) **A180** (1972) 337; (b) **A182** (1972) 641.
- [13] RAMAMURTHY, V.S., KAPOOR, S.S., KATARIA, S.K., Phys. Rev. Lett. **25** (1970) 386.
- [14] BRACK, M., QUENTIN, Ph., Phys. Scripta **10A** (1974) 163.
- [15] STRUTINSKY, V.M., KOLOMIETZ, V.M., Shell Structure and Fission (Proc. 8th Winter School on Nuclear Physics) Vol.2 483–594.
- [16] STRUTINSKY, V.M., Nucl. Phys. **A254** (1975) 197.
- [17] STRUTINSKY, V.M., Z. Phys. A **280** (1977) 99.
- [18] RAMAMURTHY, V.S., KAPOOR, S.S., Phys. Lett. **69B** (1974) 96.
- [19] BOHR, Aa., MOTTELSON, B.R., Nuclear Structure, Vol.2, Benjamin (1975).
- [20] KOLOMIETZ, V.M., Sov. J. Nucl. Phys. **18** (1974) 147.
- [21] OFENGENDEN, S.R., ZAVARZIN, V.F., KOLOMIETZ, V.M., Phys. Lett. **69B** (1977) 264.
- [22] SOBICZEWSKI, A., GYURKOVICH, A., BRACK, M., Nucl. Phys. **A289** (1977) 346.
- [23] BRACK, M., QUENTIN, P., Phys. Lett. **56B** (1975) 421.
- [24] SZÖGÖ, G., Orthogonal Polynomials, Am. Math. Soc., New York (1959).
- [25] MYERS, W.D., SWIATECKI, W., Nucl. Phys. **81** (1966) 1.
- [26] STRUTINSKY, V.M., INVANYUK, F.A., Nucl. Phys. **A255** (1975) 405.
- [27] IVANYUK, F.A., STRUTINSKY, V.M., (a) Z. f. Phys. **A286** (1978) 291; (b) Z. Phys. **A290** (1979) 107.
- [28] PASHKEVICH, V.V., Nucl. Phys. **A169** (1971) 275.
- [29] DAMGAARD, J., PAULI, H.C., PASHKEVICH, V.V., STRUTINSKY, V.M., Nucl. Phys. **A135** (1969) 432.
- [30] LIN, W.F., Phys. Rev. **C2** (1970) 871.
- [31] ROSS, C.K., BHADURI, R.K., Nucl. Phys. **A188** (1972) 566.
- [32] BHADURI, R.K., ROSS, C.K., Phys. Rev. Lett. **27** (1971) 606; see also JENNINGS, B.K., BHADURI, R.K., BRACK, M., Nucl. Phys. **A253** (1975) 29.
- [33] BRACK, M., paper IAEA-SM-241/C1, these Proceedings.

# ON THE SHELL CORRECTION ENERGY AT DOUBLY MAGIC NUCLEI

E. WERNER

Universität Hannover,  
Hannover,  
Federal Republic of Germany

K.M. DIETRICH

Technische Universität München,  
Munich

and

GSI Darmstadt,  
Darmstadt,  
Federal Republic of Germany

P. MÖLLER

University of Lund,  
Lund,  
Sweden

R. NIX

Los Alamos Scientific Laboratory,  
New Mexico,  
United States of America

## Abstract

### ON THE SHELL CORRECTION ENERGY AT DOUBLY MAGIC NUCLEI.

The close relation between the Landau expansion and Strutinsky's energy theorem is used to evaluate the shell correction energy for  $^{208}\text{Pb}$ . Using the Landau-Migdal theory, the authors find that the energies  $\epsilon_\nu^0$  to be used in the shell correction term for  $^{208}\text{Pb}$  differ from the excitation energies of the neighbouring odd nuclei by shifts which describe polarization effects due to the addition or subtraction of a particle. It is the distribution of single-particle strength typical for the region of shell closures which then implies that all the shifts have the *same* sign and are directed towards the Fermi energy. This reduces the shell correction for  $^{208}\text{Pb}$  by some 5 MeV in agreement with the empirical data. A similar renormalization is expected to be important for superheavy nuclei and may lead to appreciable changes in the expected life-times.

If the excitation energies  $\Delta E_\mu$  of the neighbouring odd nuclei of  $^{208}_{82}\text{Pb}_{126}$  are interpreted as 'single-particle energies' of  $^{208}_{82}\text{Pb}_{126}$  and the phenomenological shell correction energy in the form

$$E_{sc} = \sum_{\mu} \Delta E_{\mu} \delta \tilde{n}_{\mu} \quad (1)$$

$$\delta \tilde{n}_{\mu} = \overset{\circ}{n}_{\mu} - \bar{n}_{\mu} \quad (1')$$

where

$$\overset{\circ}{n}_{\mu} = \begin{cases} 1 & \text{for occupied single-particle states} \\ 0 & \text{for unoccupied single-particle states} \end{cases}$$

and  $\bar{n}_{\mu}$  is the smooth occupation pattern following Strutinsky's prescription, a value  $E_{sc} \approx -20$  MeV is obtained. The empirical binding energy of  $^{208}_{82}\text{Pb}_{126}$  would require a shell correction

$$E_{sc} = -13 (\pm 2) \text{ MeV}$$

where the uncertainty of  $\pm 2$  MeV reflects the uncertainty of the average liquid-drop energy one refers to. This discrepancy is known as the 'lead anomaly' and was extensively discussed in the famous 'funny hill' paper [1]. It is substantially larger than the typical errors obtained if the Strutinsky method is applied to calculate the ground-state energies of deformed nuclei on the basis of phenomenological deformed shell-model potentials fitted to excitation energies of odd nuclei.

The striking analogy between Strutinsky's energy theorem and the Landau expansion was noted quite early [2], and it is the close relation between the two expansions which we shall use to calculate an improved shell correction energy starting from the experimental levels of the neighbouring odd nuclei of  $^{208}_{82}\text{Pb}_{126}$ .

We assume that the energy of the system can be represented as a functional of the one-body density in a unique way, a hypothesis which, according to Kohn-Hohenberg [3], is valid under very general premises. We choose the single-particle representation in such a way that the one-body density is diagonal:

$$\rho_{\mu\nu} := \langle A; 0 | a_{\mu}^{\dagger} a_{\nu} | A; 0 \rangle = : \delta_{\mu\nu} n_{\nu}(A) : \quad (2)$$

where  $|A; 0\rangle$  is the ground state of the (even-even) nucleus of A nucleons. If the occupation numbers  $n_{\nu}$  are infinitesimally modified, the resulting change of the energy of the system can be represented by a Taylor expansion of the

energy functional around the 'unperturbed' value of the energy. This 'Landau expansion' has the general form:

$$\delta E = \sum_{\nu} \hat{\epsilon}_{\nu} \delta n_{\nu} + \frac{1}{2} \sum_{\nu \nu'} F_{\nu \nu'} \delta n_{\nu} \delta n_{\nu'} + \dots \quad (3)$$

We refer to the energies  $\hat{\epsilon}_{\nu}$  as 'Landau energies' and to the matrix-elements  $F_{\nu \nu'}$  as the (reducible) interaction between the quasi-particles. In the Landau-Migdal theory, the matrix  $F_{\nu \nu'}$  can be obtained by starting from an effective density-dependent phenomenological interaction ('Migdal interaction') which is adjusted to a large body of experimental data [4] (energies, transition probabilities, magnetic moments, etc.).

Strutinsky's expansion of the ground-state energy  $E_0$  of a system is in terms of the deviations  $\delta \tilde{n}_{\nu}$  of the actual occupation numbers  $n_{\nu}$  from the occupation numbers of an artificial smooth level distribution which is determined in such a way that the value of the energy functional for this smooth density can be represented by the liquid-drop model. The 'Strutinsky expansion' has, thus, the general form

$$E_0(A) = E_0[\bar{\rho}] + \sum_{\nu} \left( \frac{\delta E_0}{\delta n_{\nu}} \right)_{\bar{n}_{\nu}} \delta \tilde{n}_{\nu} + \dots \quad (4)$$

$$= E_{LD} + E_{sc} \quad (5)$$

The energy  $E_0[\bar{\rho}]$  is the energy of a (hypothetical) A-particle system which is characterized by the smooth occupation pattern  $\bar{n}_{\nu}$ . Thus, in contrast to the changes  $\delta n_{\nu}$  of the Landau expansion, the  $\delta \tilde{n}_{\nu}$  add up to zero:

$$\sum_{\nu} \delta \tilde{n}_{\nu} = 0 \quad (6)$$

If the functional is taken to be the Hartree-Fock (HF) expression, the 'true' occupation numbers  $n_{\nu}$  are one up to the Fermi energy  $\lambda$  and zero above. It is in this HF-case that the term of  $O[\delta \tilde{n}_{\nu}, \delta \tilde{n}_{\nu}]$  in expression (4) was calculated and

generally found to be small ( $\lesssim 0.2$  MeV in the absolute value). This is largely due to the cancellation between terms of different signs (note that  $\delta\tilde{n}_\nu > 0$  for  $\dot{\epsilon}_\nu < \lambda$  and  $\delta\tilde{n}_\nu < 0$  for  $\dot{\epsilon}_\nu > \lambda$ ). Neglecting terms of second order in  $\delta\tilde{n}_\nu$ , we may identify the energies  $(\delta E_0 / \delta n_\nu) \bar{n}_\nu$  of the Strutinsky expansion (4) with the Landau energies  $\dot{\epsilon}_\nu$  of expansion (3):

$$\left( \frac{\delta E_0}{\delta n_\nu} \right)_{\{\bar{n}_1, \dots\}} \approx \left( \frac{\delta E_0}{\delta n_\nu} \right)_{\{n_1, \dots\}} \equiv \dot{\epsilon}_\nu \quad (7)$$

We now use the Landau-Migdal theory to calculate the energies  $\dot{\epsilon}_\nu$  from the experimental excitation energies of neighbouring odd nuclei and use them to evaluate the shell correction term  $E_{sc}$  in Eq. (5):

$$E_{sc} = \sum_\nu \left( \frac{\delta E_0}{\delta n_\nu} \right)_{\{\bar{n}_1, \dots\}} \delta\tilde{n}_\nu \approx \sum_\nu \dot{\epsilon}_\nu \delta\tilde{n}_\nu \quad (8)$$

In the following, we first describe the calculation of the energies  $\dot{\epsilon}_\nu$  and then present the results.

We consider an odd nucleus in which the last odd particle (hole) is assumed to be in the 'quasi-particle state  $\mu$ '. The quasi-particle energy is defined as

$$\epsilon_\mu := E_\mu(A+1) - E_0(A)$$

where  $E_0(A)$  and  $E_\mu(A+1)$  are the ground-state energy of the even-even and the excitation energies of the odd nucleus, respectively. The occupation number distribution in the excited states  $|\mu; A+1\rangle$  of the  $(A+1)-$  particle nucleus differs from the distribution in the  $A$ -particle nucleus by the presence of an additional particle which is predominantly added in the single-particle state  $\mu$ , and to a small extent also in all the other single-particle states:

$$n_\nu(A+1) = n_\nu(A) + \Delta n_\nu \quad (9)$$

with  $\Delta n_\mu \approx 1$  and  $|\Delta n_{\nu \neq \mu}| \ll 1$ .

In the Landau-Migdal quasi-particle picture [4, 5], the quasi-particles form independent excitations of the system (for states close to the Fermi surface). Therefore, the quasi-particle distribution is that of an ideal gas:

$$N_\mu = \begin{cases} 1 & \text{if quasi-particle state } \mu \text{ is occupied} \\ 0 & \text{otherwise} \end{cases}$$

(We denote quasi-particle (q.p.) occupation numbers by capital letters in order to distinguish them from single-particle occupation numbers.)

Performing an infinitesimal change of the q.p. occupation number  $N_\mu \rightarrow N_\mu + \delta N_\mu$ , we, evidently, have to change the occupation numbers  $n_\nu$  of all the single-particle states  $\nu$  which are associated with the 1p-, 2p1h-, 3p2h-components, etc. of the quasi-particle state  $|\mu; A+1\rangle$ . The resulting change of the occupation number of the single-particle state  $\nu$  is denoted by  $\delta n_\nu^{(\mu)}$ , where the superscript  $\mu$  keeps track of the q.p. state which we want to modify. We evidently have thus:

$$\delta N_\mu : = \sum_{\nu} \delta n_\nu^{(\mu)} \quad (10)$$

To be able to calculate the energy change  $\delta E_\mu$  induced by the variation  $\delta N_\mu$ , we have to consider the q.p. energy  $\epsilon_\mu$  as a function of  $N_\mu$ :

$$\epsilon_\mu = \epsilon_\mu(N_\mu)$$

where

$$\epsilon_\mu(N_\mu = 1) := E_\mu(A+1) - E_0(A)$$

We may imagine that the energies  $\epsilon_\mu(N_\mu)$  can be calculated, also for  $N_\mu \neq 1$ , from the many-body theory, for instance on the basis of the Landau expansion. We now define energies  $\mathcal{E}_\mu(N_\mu)$ :

$$\epsilon_\mu(N_\mu) = : N_\mu \mathcal{E}_\mu(N_\mu) \quad (11)$$

and the energy change  $\delta \epsilon_\mu$  induced by the variation  $N_\mu = 1 \rightarrow N_\mu = 1 + \delta N_\mu$  becomes

$$\begin{aligned} \delta \epsilon_\mu &= \frac{\partial}{\partial N_\mu} \left[ N_\mu \mathcal{E}_\mu(N_\mu) \right]_{N_\mu=1} \delta N_\mu \\ &= \left[ \mathcal{E}_\mu(N_\mu=1) + \left( \frac{\partial \mathcal{E}_\mu}{\partial N_\mu} \right)_{N_\mu=1} \right] \delta N_\mu \\ \delta \epsilon_\mu &= \left[ E_\mu(A+1) - E_0(A) + \left( \frac{\partial \mathcal{E}_\mu}{\partial N_\mu} \right)_{N_\mu=1} \right] \delta N_\mu \quad (12) \end{aligned}$$

The derivative  $\partial\mathcal{E}_\mu/\partial N_\mu$  can be further evaluated by making use of the identity

$$\mathcal{E}_\mu(N_\mu) = e_\mu(N_\mu) + M_\mu(\epsilon_\mu, N_\mu) \quad (13)$$

which results from the Dyson equation (see, e.g. Ref. [4]). Here  $e_\mu$  is an approximate q.p. energy which is obtained if the nuclear field acting on the q.p. is replaced by a self-consistent, generally non-local, but energy-independent potential field. A possible choice for  $e_\mu(N_\mu)$  could be a Hartree-Fock energy. By the requirement of self-consistency this potential field depends on the occupation number  $N_\mu$ . The quantity  $M$  is the energy-dependent self-energy of the q.p., which takes account of the interaction processes not yet contained in  $e_\mu(N_\mu)$ . The principal contributions to this quantity originate from the coupling of the single-particle degrees of freedom to the low-lying collective states of the  $A$ -particle nucleus.

Thus, we obtain from Eqs (12) and (13):

$$\delta\epsilon_\mu = \left[ E_\mu(A+1) - E_0(A) + \frac{\partial e_\mu}{\partial N_\mu} + \frac{\partial M_\mu}{\partial N_\mu} (\epsilon_\mu; N_\mu = 1) \right] \delta N_\mu \quad (14)$$

We assume that  $\delta N_\mu$  is sufficiently small so that in the Landau expansion (3) we may safely neglect second-order terms; we then have

$$\delta\epsilon_\mu = \sum_\nu \overset{\circ}{\epsilon}_\nu \delta n_\nu^{(\mu)} \quad (15)$$

with the additional restriction (10). It is important to note that the quantities  $\overset{\circ}{\epsilon}_\nu = \partial E / \partial n_\nu$  have to be evaluated at the occupation numbers  $n_\nu^{(\mu)}$  corresponding to one q.p. in the state  $\mu$ , i.e.  $n_\mu^{(\mu)} \approx 1$  and  $n_{\nu \neq \mu}^{(\mu)} \ll 1$ .

Since  $|\delta N_\mu| \ll 1$ , we define the infinitesimal changes  $\delta n_\nu^{(\mu)}$  to be proportional to the changes  $\Delta n_\nu^{(\mu)}$  of the occupation numbers which are obtained from the addition of a q.p. in the state  $\mu$ :

$$\Delta n_\nu^{(\mu)} := n_\nu(\mu; A+1) - n_\nu(0; A) \quad (16)$$

Therefore, we have

$$\delta n_\nu^{(\mu)} = \Delta n_\nu^{(\mu)} \delta N_\mu \quad (16')$$

Combining Eqs (14), (15) and (16'), we obtain

$$E_\mu(A+1) - E_0(A) + \frac{\partial e_\mu}{\partial N_\mu} + \frac{\partial M_\mu}{\partial N_\mu} = \sum_{\nu} \overset{\circ}{e}_\nu(n_\nu^{(\mu)}) \Delta n_\nu^{(\mu)} \quad (17)$$

$$= \overset{\circ}{e}_\mu(n_\mu^{(\mu)}) + \sum_{\nu \neq \mu} \left[ \overset{\circ}{e}_\nu(n_\nu^{(\mu)}) - \overset{\circ}{e}_\mu(n_\mu^{(\mu)}) \right] \Delta n_\nu^{(\mu)} \quad (17')$$

where we have used the sum rule

$$\sum_{\nu} \Delta n_\nu^{(\mu)} = 1$$

Eq. (17') serves to determine the quantities  $\overset{\circ}{e}_\nu = \delta E / \delta n_\nu$  which should be used in Strutinsky's expansion (4). The occupation numbers  $n_\nu^{(\mu)}$  which occur as arguments of the Landau energies in Eq.(17) are approximately equal to the quantities  $\bar{n}_\nu$  of Eq.(4) for  $\nu \neq \mu$  whereas for  $\nu = \mu$  this is not the case, since  $\Delta n_\mu^{(\mu)} \approx 1$ . We can remedy this defect taking the term  $\partial e_\mu / \partial N_\mu$  from the left-hand side to the right-hand side of Eq.(17) and making use of

$$\overset{\circ}{e}_\mu(n_\mu^{(\mu)}) - \frac{\partial e_\mu}{\partial N_\mu} \cdot 1 \approx \overset{\circ}{e}_\mu(n_\mu \approx 0) \approx \overset{\circ}{e}_\mu(n_\mu = \bar{n}_\mu) \quad (18)$$

This has the following reason: The quantity  $\partial e_\mu / \partial N_\mu$  is approximately equal to the rearrangement energy of the self-consistent field eigenvalue  $e_\mu$  which results from the addition of a particle. Now, whereas  $e_\mu$  and  $\overset{\circ}{e}_\mu$  are certainly not equal, their rearrangement energies are indeed approximately equal, because they are both determined by the change of the self-consistent nuclear field resulting from the addition of a particle. This is the physical meaning of Eq.(18). We further simplify Eq.(17) by neglecting the quantity  $\partial M_\mu / \partial N_\mu$  on the left-hand side for the following reason: The dependence of  $M_\mu$  on  $N_\mu$  through the external lines which brings about a factor  $N_\mu$  is already taken into account by the definition of Eq.(11). Therefore, the derivative  $\partial M_\mu / \partial N_\mu$  in Eqs (14) and (17) receives non-zero contributions only through the dependence of the single-particle energies and wavefunctions on  $N_\mu$ . Since for these contributions  $|\partial M_\mu / \partial N_\mu| \ll |E_\mu(A+1) - E_0(A)|$ , we can neglect the derivative of  $M_\mu$ . Equation (17') now becomes

$$E_\mu(A+1) - E_0(A) = \overset{\circ}{e}_\mu(\bar{n}_\mu) + \sum_{\nu \neq \mu} \left[ \overset{\circ}{e}_\nu(n_\nu^{(\mu)}) - \overset{\circ}{e}_\mu(n_\mu^{(\mu)}) \right] \Delta n_\nu^{(\mu)} \quad (18')$$

We rewrite this equation in a form which is more appropriate to later use. To simplify the reasoning we think of a situation where the single-particle state couples to  $2p-1h$  configurations only. The inclusion of more complicated configurations is then straightforward. If a  $2p-1h$  configuration with particles in the states  $\kappa_1$  and  $\kappa_2$  and a hole in the state  $\lambda_1$  couples with the amplitude  $\alpha_{\kappa_1 \kappa_2 \lambda_1}^{(\mu)}$  to the single-particle state  $\mu$ , the change in the occupation number  $\Delta n_{\nu; \kappa_1 \kappa_2 \lambda_1}^{(\mu)}$  corresponding to this configuration is given by

$$\Delta n_{\nu; \kappa_1 \kappa_2 \lambda_1}^{(\mu)} = |\alpha_{\kappa_1 \kappa_2 \lambda_1}^{(\mu)}|^2 [\delta_{\nu \kappa_1} + \delta_{\nu \kappa_2} - \delta_{\nu \lambda_1}]$$

Substituting this into the right-hand side of Eq.(18') and summing over  $\kappa_1, \kappa_2, \lambda_1$ , we obtain

$$\sum_{\nu} (\dot{\epsilon}_{\nu} - \dot{\epsilon}_{\mu}) \Delta n_{\nu}^{(\mu)} = \sum_{\kappa_1 \kappa_2 \lambda_1} |\alpha_{\kappa_1 \kappa_2 \lambda_1}^{(\mu)}|^2 (\dot{\epsilon}_{\kappa_1} + \dot{\epsilon}_{\kappa_2} - \dot{\epsilon}_{\lambda_1} - \dot{\epsilon}_{\mu}) + \dot{\epsilon}_{\mu} (\bar{n}_{\nu})$$

or

$$E_{\mu}(A+1) - E_0(A) = \dot{\epsilon}_{\mu} + \sum_{\kappa_1 \kappa_2 \lambda_1} |\alpha_{\kappa_1 \kappa_2 \lambda_1}^{(\mu)}|^2 \Delta E_{\kappa_1 \kappa_2 \lambda_1}^{(\mu)} \quad (18'')$$

where we have introduced the excitation energy

$$\Delta E_{\kappa_1 \kappa_2 \lambda_1}^{(\mu)} := (\dot{\epsilon}_{\kappa_1} + \dot{\epsilon}_{\kappa_2} - \dot{\epsilon}_{\lambda_1}) - \dot{\epsilon}_{\mu}$$

of the configuration  $\kappa_1, \kappa_2, \lambda_1$  relative to the single-particle configuration  $\mu$ . The generalization of Eq.(18'') to the inclusion of more complicated configurations is obvious.

As it stands, the set of Eq.(18'') cannot yet be solved for  $\dot{\epsilon}_{\mu}$ , since it contains too many unknowns: The sum over  $\nu$  on the right-hand side extends over all the states which couple to the state  $\mu$ . On the other hand, the number of equations of the set (18'') is equal to the number of empirically known q.p. energies in the four odd neighbours of the  $A$ -particle nucleus. Even for  $^{208}\text{Pb}$ , this number is considerably smaller than the number of states which contribute to the sum over  $\nu$  in Eq.(18''). We can circumvent this difficulty in the following way: The coupling of the single-particle state  $\mu$  and each individual competing configuration

is weak and can be treated by perturbation theory. The amplitudes  $\alpha_{\kappa_1 \kappa_2 \lambda_1}^{(\mu)}$  depend on the energy spectrum through energy denominators which contain only energy differences (see the later Eq.(19)), just as the energy-weighting factor does. Therefore, we commit only a small error if we evaluate the sum over  $\nu$  by using shell-model energies instead of the energies  $\hat{\epsilon}_\nu$ . This has been checked numerically.

For the numerical treatment we introduced a further simplification: For the odd neighbours of  $^{208}\text{Pb}$ , the coupling of the single-particle degrees of freedom to more complicated configurations is governed by particle-phonon coupling. We, therefore, want to replace Eq.(18'') by the equation

$$E_\mu(A+1) - E_0(A) = \hat{\epsilon}_\mu + \sum_{\kappa, s} |\beta_{\kappa, s}^{(\mu)}|^2 (\hat{\epsilon}_\kappa + \omega_s - \hat{\epsilon}_\mu) \quad (18''')$$

where  $\beta_{\kappa, s}^{(\mu)}$  is the amplitude for the coupling of the particle-phonon state  $\kappa, s$  to the single particle configuration  $\mu$  ( $\omega_s$  denotes the energy of the phonon state  $s$ ). The justification for this replacement is as follows:

The coupling of each individual 2p-1h or particle-phonon configuration to the state  $\mu$  is weak and can, therefore, be treated in perturbation theory. The difference between the second terms of Eqs (18'') and (18''') is that in the latter case a diagonalization in the space of ph-states of the A-particle nucleus has been performed before the coupling of the odd particle to the degrees of freedom of the core is taken into account. We denote the Hamiltonian by

$$H_{2p, 1h} = H_0; \quad H_{p-ph} = H_0 + V_{ph} = H$$

respectively (for the definitions, see Fig.1). We obtain, by using first-order perturbation theory for  $\alpha_{\kappa_1 \kappa_2 \lambda_1}^{(\mu)}$  and  $\beta_{\kappa s}^{(\mu)}$ :

$$\begin{aligned} & \sum_{\kappa_1 \kappa_2 \lambda_1} |\alpha_{\kappa_1 \kappa_2 \lambda_1}^{(\mu)}|^2 [\hat{\epsilon}_{\kappa_1} + \hat{\epsilon}_{\kappa_2} - \hat{\epsilon}_{\lambda_1} - \hat{\epsilon}_\mu] \\ &= \sum_{\kappa_1 \kappa_2 \lambda_1} \frac{|\langle \mu | V_{1\kappa_1 \kappa_2 \lambda_1} \rangle|^2}{[\hat{\epsilon}_\mu - (\hat{\epsilon}_{\kappa_1} + \hat{\epsilon}_{\kappa_2} - \hat{\epsilon}_{\lambda_1})]^2} (\hat{\epsilon}_{\kappa_1} + \hat{\epsilon}_{\kappa_2} - \hat{\epsilon}_{\lambda_1} - \hat{\epsilon}_\mu) \\ &= - \left\langle \mu | V \frac{1}{\hat{\epsilon}_\mu - H_0} V | \mu \right\rangle \end{aligned} \quad (19)$$

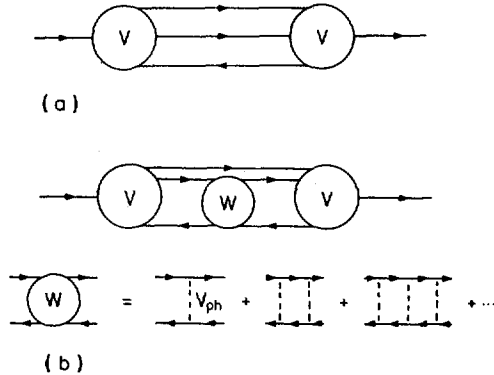


FIG. 1. Graphical representation of particle-core coupling: the box  $V$  is the irreducible  $(p)$ - $(2p\ 1h)$  interaction.

(a) Diagram corresponding to the Hamiltonian  $H_0$ ;

(b) diagram corresponding to the Hamiltonian  $H$ .  $V_{ph}$  represents the irreducible ph-interaction;  $W$  is the reducible ph-interaction.

and, analogously,

$$\sum_{k,s} |\beta_{ks}^{(\mu)}|^2 (\overset{\circ}{\epsilon}_k + \omega_s - \overset{\circ}{\epsilon}_{\mu}) = - \left\langle \mu | V \frac{1}{\overset{\circ}{\epsilon}_{\mu} - H_0 - V_{ph}} | V | \mu \right\rangle \quad (19')$$

The difference  $D$  of the two terms becomes

$$D = \left\langle \mu | V \left[ \frac{1}{\overset{\circ}{\epsilon}_{\mu} - H_0 - V_{ph}} - \frac{1}{\overset{\circ}{\epsilon}_{\mu} - H_0} \right] | V | \mu \right\rangle \quad (20)$$

Making use of the operator identity

$$\frac{1}{z - H_0 - V_{ph}} - \frac{1}{z - H_0} = \frac{1}{z - H_0} V_{ph} \frac{1}{z - H_0 - V_{ph}} \quad (21)$$

and of the expansion

$$\frac{1}{z - H_0 - V_{ph}} = \frac{1}{z - H_0} + \frac{1}{z - H_0} V_{ph} \frac{1}{z - H_0} + \dots \quad (21')$$

TABLE I. EXCITED STATES OF THE  
CORE NUCLEUS  $^{208}\text{Pb}$  TAKEN INTO  
ACCOUNT IN THE CALCULATION

J	$E_{\text{exp.}}$
$3^-$	2.61
$5^-$	3.19
$4^-$	3.47
$5^-$	3.71
$6^-$	3.92
$4^-$	3.96
$2^+$	4.08
$4^+$	4.32
$6^+$	4.61

we obtain

$$\begin{aligned} \frac{1}{z - H_0 - V_{\text{ph}}} - \frac{1}{z - H_0} &= \frac{1}{z - H_0} \left[ V_{\text{ph}} + V_{\text{ph}} \frac{1}{z - H_0} V_{\text{ph}} + \dots \right] \frac{1}{z - H_0} \\ &= \frac{1}{z - H_0} W(z) \frac{1}{z - H_0} \end{aligned} \quad (22)$$

where we have introduced the reducible ph-interaction  $W(z)$  defined by

$$W(z) = V_{\text{ph}} + V_{\text{ph}} \frac{1}{z - H_0} V_{\text{ph}} + \dots \quad (23)$$

We thus can write for Eq.(20):

$$\begin{aligned} D &= \left\langle \mu | V \frac{1}{\hat{\epsilon}_\mu - H_0} W(\hat{\epsilon}_\mu) \frac{1}{\hat{\epsilon}_\mu - H_0} V | \mu \right\rangle \\ &= \sum_{\substack{\kappa_1 \kappa_2 \lambda_1 \\ \kappa'_1 \kappa'_2 \lambda'_1}} \alpha_{\kappa'_1 \kappa'_2 \lambda'_1}^{(\mu)*} \langle \kappa'_1 \kappa'_2 \lambda'_1 | W(\hat{\epsilon}_\mu) | \kappa_1 \kappa_2 \lambda_1 \rangle \alpha_{\kappa_1 \kappa_2 \lambda_1}^{(\mu)} \end{aligned} \quad (24)$$

where

$$\begin{aligned} \langle \kappa'_1 \kappa'_2 \lambda'_1 | W(\overset{\circ}{\epsilon}_\mu) | \kappa_1 \kappa_2 \lambda_1 \rangle &= \delta_{\kappa'_1 \kappa_1} \langle \kappa_2 \lambda'_1 | W(\overset{\circ}{\epsilon}_\mu - \overset{\circ}{\epsilon}_{\kappa_1}) | \kappa_2 \lambda_1 \rangle \\ &+ \delta_{\kappa'_2 \kappa_2} \langle \kappa_1 \lambda'_1 | W(\overset{\circ}{\epsilon}_\mu - \overset{\circ}{\epsilon}_{\kappa_2}) | \kappa_1 \lambda_1 \rangle \end{aligned}$$

The first (second) term on the right-hand side is the contribution where particle  $\kappa_1$  ( $\kappa_2$ ) is the spectator.

Comparing the right-hand side of Eq.(24) with the second term on the right-hand side of Eq.(18'') we can make the following statements:

- (i) Considering at first only the contribution of the sum over diagonal terms ( $\kappa_1 = \kappa'_1$ ,  $\kappa_2 = \kappa'_2$ ,  $\lambda_1 = \lambda'_1$ ) in Eq.(24) we have

$$D_{\text{diagonal terms}} = \sum_{\kappa_1 \kappa_2 \lambda_1} |\alpha_{\kappa_1 \kappa_2 \lambda_1}^{(\mu)}|^2 \Delta E_{\kappa_1 \kappa_2 \lambda_1}^{(\mu)} \left( \frac{\langle \kappa_1 \kappa_2 \lambda_1 | W | \kappa_1 \kappa_2 \lambda_1 \rangle}{\Delta E_{\kappa_1 \kappa_2 \lambda_1}^{(\mu)}} \right) \quad (25)$$

Typical matrix elements of  $W$  are smaller than 0.2 MeV in absolute value and they have varying signs; the excitation energy  $\Delta E_{\kappa_1 \kappa_2 \lambda_1}^{(\mu)}$  is several MeV, on the average. The partial sum  $D$  (diagonal terms) is therefore small compared to

$$-\left\langle \mu | V \frac{1}{\overset{\circ}{\epsilon}_\mu - H_0} V | \mu \right\rangle$$

(see Eq.(19)).

- (ii) The absolute values of the non-diagonal matrix elements are, on the average, still one to two orders of magnitude smaller than the diagonal ones. Because of the summation of the terms of changing signs, we may expect that the contribution of the non-diagonal terms does not qualitatively change the conclusion reached in (i). We have, in addition, checked this statement by a numerical calculation for the following three states:

$3p_{1/2}$  in  $^{207}_{82}\text{Pb}_{125}$

$1j_{1/2}^{15}$  in  $^{209}_{82}\text{Pb}_{127}$

$1h_{1/2}^9$  in  $^{209}_{83}\text{Bi}_{126}$

TABLE II. SHIFTS  $\Delta E_\mu$  OF THE EXPERIMENTAL ENERGY LEVELS OF THE ODD NEIGHBOURS OF  $^{208}\text{Pb}$  ACCORDING TO Eq.(26)

The sign convention is such that  $\Delta E_\mu > 0$  yields a shift *towards* the Fermi energy

$^{207}\text{Pb}$			$^{209}\text{Pb}$			$^{207}\text{Tl}$			$^{209}\text{Bi}$		
		$\Delta E_\mu$									
3p	1/2	0.34	2g	9/2	0.50	3s	1/2	0.40	1h	9/2	0.30
2f	5/2	0.35	1i	11/2	0.13	2d	3/2	0.35	2f	7/2	0.70
3p	3/2	0.42	1j	15/2	0.85	1h	11/2	0.65	1i	13/2	0.80
1i	13/2	0.54	3d	5/2	0.30	2d	5/2	0.80	2f	5/2	0.80
2f	7/2	0.90	4s	1/2	0.30	1g	7/2	0.65	3p	3/2	0.80
1h	9/2	0.30	2g	7/2	0.51				3p	1/2	0.90

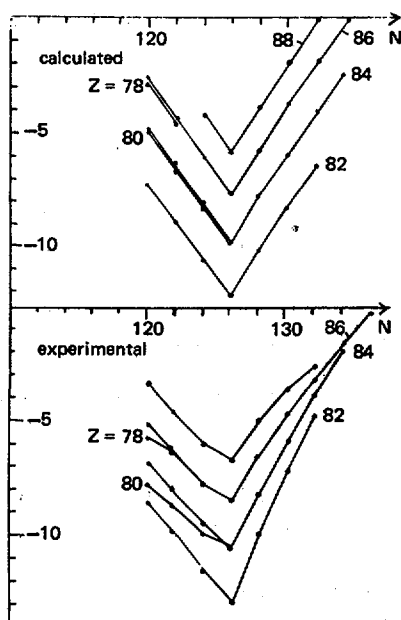


FIG.2. Empirical and calculated shell correction energies (MeV) as a function of neutron number  $N$  for given proton number  $Z$ .

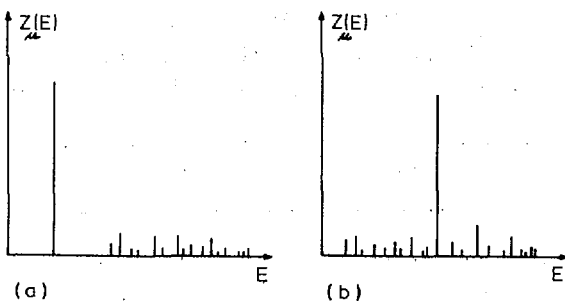


FIG. 3. Typical distribution of spectroscopic factors for  
(a) spherical, closed-shell nuclei plus one particle;  
(b) open-shell or deformed nuclei plus one particle.

$$Z_\mu(E) \equiv |\langle \phi(A+1; E) | a_\mu^\dagger | \phi_0(A) \rangle|^2$$

We have calculated the difference  $D$  directly, obtaining  $-D = 0.06, 0.08, 0.05$  MeV, respectively. These quantities are small compared to the energy corrections of interest of Table I which will be discussed below; the approximation which consists in the replacement of Eq.(18'') by Eq.(18''') is thus justified.

The final form of the equation for  $\hat{e}_\mu(\bar{n}_\mu)$  which is obtained in this way and which was solved numerically is

$$E_\mu(A+1) - E_0(A) = \hat{e}_\mu(\bar{n}_\mu) + \sum_{\kappa s} (\hat{e}_\kappa + \omega_s - \hat{e}_\mu) |\beta_{\kappa s}^{(\mu)}|^2 \quad (26)$$

with the following meaning of the symbols:

$\hat{e}_\kappa$ : shell-model energies of the  $(A+1)$ -particle nucleus (see preceding discussion).  
 $\omega_s$ : phonon energies of the  $A$ -particle nucleus.

$\beta_{\kappa s}^{(\mu)}$ : amplitude for the coupling of the particle-phonon configuration  $\kappa \otimes s$  to the quasi-particle  $\mu$ .

The main contribution to the sum on the right-hand side originates from low-lying collective levels from the following reasons:

- (a) Their coherence properties considerably increase the coupling vertices  $\beta_{\kappa s}^{(\mu)}$  compared to the single particle vertices.
- (b) The product  $(\hat{e}_\kappa + \omega_s - \hat{e}_\mu) |\beta_{\kappa s}^{(\mu)}|^2$  is roughly inversely proportional to  $(\hat{e}_\kappa + \omega_s - \hat{e}_\mu)$ . The small excitation energy of collective states makes this energy denominator particularly small.

The excited states of  $^{208}_{82}\text{Pb}_{126}$  that have been taken into account in the calculations are listed in Table I.

In Table II we show the quasi-particle (hole) states of the four odd neighbours for which the energy  $\hat{\epsilon}_\mu$  has been calculated from Eq.(26). The vertices  $\beta_{\kappa s}^{(\mu)}$  were taken from an earlier publication [6] on particle-phonon coupling in the lead region. For the energies which appear in the sum over  $\kappa$  and  $s$ , experimental values were used. Therefore, no adjustable parameters entered the numerical calculations.

The columns headed by  $\Delta E_\mu$  show the energy shift leading from the experimental energy to  $\hat{\epsilon}_\mu$ . The sign convention is such that  $\Delta e > 0$  means a shift towards the Fermi energy (for particle and hole states equally).

The shell correction obtained from the energies  $\hat{\epsilon}_\mu$  is given by

$$E_{sc} = -12.7 \text{ MeV}$$

in good agreement with the empirical value. The variation of the shell correction energy  $E_{sc}$  as a function of neutron and proton numbers in the vicinity of  $^{208}\text{Pb}$  is shown in Fig.2.

Whereas the actual value of the energy shift  $\Delta E_\mu$  for a given level must be determined by a numerical calculation from Eq.(26), the general trend of the level shifts can be recognized by inspection of the distribution of spectroscopic factors for single-particle transfer (single-particle strength):

For the quasi-particle states of the odd neighbours of  $^{208}\text{Pb}$  lying within one shell above or below the Fermi energy, all core-excited states  $\kappa \otimes s$  lie higher in energy than the q.p. state, i.e.  $\hat{\epsilon}_\kappa + \omega_s > \hat{\epsilon}_\mu$  for all  $\kappa, s, \mu$ . The distribution of single-particle strengths is shown in Fig. 3a, and  $\hat{\epsilon}_\mu$  is shifted towards the Fermi energy (relative to the q.p. energy).

For states in the second shell above or below the Fermi energy, the situation is qualitatively different: the distribution of single-particle strengths is more like in Fig. 4b. This reduces the energy shift  $\Delta E_\mu$  practically to zero, and  $\hat{\epsilon}_\mu$  becomes almost identical with the experimental energy. The same is true for all single-particle states in nuclei far away from closed shells; in particular, this is also the characteristic situation in deformed nuclei where, mainly because of the effect of pairing, the single-particle strengths are distributed as in Fig. 3b. This was checked in a calculation for the deformed nucleus  $^{174}_{79}\text{Yb}$ .

Therefore, for nuclei sufficiently far away from closed shells, the energies to be used in Eq.(1) are practically identical with the quasi-particle energies, whereas in the vicinity of closed shell nuclei they must be determined from Eq.(26) or (18').

A similar calculation would be desirable for the superheavy element. Unfortunately, this is impossible since the excitation energies of neighbouring odd nuclei are not available. If a similar result were obtained, consequences for the stability of the superheavy elements would result. If the binding energy of

the spherical ground state of the superheavy nucleus were similarly reduced, the heights of the fission barrier would be lowered by about this amount. The fission life-times could thus change by orders of magnitude because of the strong dependence of the penetrability on the height of the potential barrier. Similar results concerning the shell correction energy of  $^{208}\text{Pb}$  were obtained by Hamamoto and Siemens within the collective model [7].

#### ACKNOWLEDGEMENTS

We acknowledge valuable discussions with Drs Ring and Zawischa. Travel grants by the DFG have made our collaboration possible, and a travel grant of the BMFT enabled one of us (K.D.) to participate in the Jülich Conference. We are grateful for this support.

#### REFERENCES

- [1] BRACK, M., et al., Rev. Mod. Phys. **44** (1972) 320.
- [2] BUNATIAN, G.G., KOLOMIETZ, V.M., STRUTINSKY, V.M., Nucl. Phys. **A188** (1972) 225.
- [3] HOHENBERG, P.G., KOHN, W., Phys. Rev. **136** (1964) B864.
- [4] MIGDAL, A.B., Theory of Finite Fermi Systems and Application to Atomic Nuclei, J. Wiley, New York (1967); SPETH, J., WERNER, E., WILD, W., Phys. Rep. **33C** (1977) 128.
- [5] LANDAU, L.D., Sov. Phys. – JETP **3** (1957) 920; JETP **5** (1957) 101; JETP **8** (1959) 70.
- [6] RING, P., WERNER, E., Nucl. Phys. **A211** (1973) 198.
- [7] HAMAMOTO, I., in Nuclear Self-consistent Fields (Proc. Int. Conf. Trieste, 1975) 171–188.

#### DISCUSSION

K-H. SCHMIDT: In your comparison of the measured and calculated shell effects around  $^{208}\text{Pb}$  there still seems to be a minor systematic deviation. While the slopes of the experimental shell corrections close to  $N=126$  decrease with increasing distance from the doubly magic  $^{208}\text{Pb}$ , they do not vary for the calculated values. This deviation would probably show up more clearly in the neutron binding energies.

E. WERNER: Yes, that is right. It is hard to say what the exact reason for the deviation is. We ourselves were interested only in the quantitative effect. Hard work will be needed to obtain better agreement.

B. ARMBRUSTER: Does your approach in other mass regions yield data different from the usual Strutinsky procedure? And can you estimate corrections for other doubly magic nuclei such as  $^{132}\text{Sn}$ ?

E. WERNER: Calculations similar to those we made for  $^{208}\text{Pb}$  can be performed for all cases in which there is enough information on the excited states of all neighbouring odd nuclei. Unfortunately, for other doubly magic nuclei these data are not available, or are not available to an adequate extent.

H.C. PAULI (*Chairman*): Comparing the data presented by Dr. Brack (see SM-241/C1 in these Proceedings) on the basis of the Hartree-Fock approach and your own, I conclude that your respective fission barriers will be different by roughly 8 MeV. Is this correct?

M. BRACK: No, not necessarily. In both approaches the total binding energy of  $^{208}\text{Pb}$  is within  $\sim 1$  MeV of the experimental value. So one starts from the same ground state energy, although it is arrived at by different methods. If the effect of correlation vanishes in the case of the deformed nuclei, as Dr. Werner seems to suggest, we arrive at the same fission barrier.

K.M. DIETRICH: I think the answer to Dr. Pauli's question is that, according to our results, the main difference between the experimental excited levels of the neighbouring odd nuclei and the energies  $(\partial E / \partial n_\nu)$  to be used in the shell corrections for  $^{208}\text{Pb}$  is given by the 'static' part ( $\delta\mu$  in our table) of the p-phonon coupling. This 'static' part is precisely the difference between the self-consistent Hartree-Fock levels for  $^{208}\text{Pb}$  on the one hand and for the odd neighbours on the other.



**FISSION AND HEAVY IONS**  
**(Session D)**

**Chairman**

**E. CHEIFETZ**

Israel

# HEAVY-ION-INDUCED FISSION FOLLOWING FUSION\*

F. PLASIL, R.L. FERGUSON

Oak Ridge National Laboratory,  
Oak Ridge, Tennessee,  
United States of America

## Abstract

### HEAVY-ION-INDUCED FISSION FOLLOWING FUSION.

The dramatic lowering of fission barriers with increasing angular momentum has provided a firm bridge between the fields of fission and of heavy-ion-induced reactions. The purpose of this review paper is to explore problems of current interest at the intersection of these two fields. — Theoretical considerations of fission of systems with high angular momenta are usually made in the framework of the rotating-liquid-drop model. The most stringent tests of this theory involve studies of excitation functions for evaporation residue products. At present, there is no evidence for the survival of any rotating system which is predicted not to have a fission barrier. The extent to which the vanishing fission barrier imposes a limit on evaporation residue cross-sections will be discussed with reference to several cases, ranging from very light systems, such as  $^{14}\text{N} + ^{12}\text{C}$ , to medium mass systems, such as  $^{86}\text{Kr} + ^{65}\text{Cu}$ . The prevalence of deeply inelastic processes in heavy-ion reactions poses a problem for arriving at an operational definition of heavy-ion-induced fission. This, in turn, makes it difficult to define fusion of complex nuclei. While some yield at symmetric mass divisions is usually observed and while the products in this region often have fission-like kinetic energies and even angular distributions, indications are that in most cases tails of strongly damped distributions are involved, rather than the fusion-fission process. This point will be illustrated with reference to the  $\text{Ne} + \text{Ni}$  and  $\text{Kr} + \text{Bi}$  reactions. In some cases, there is strong evidence for the existence of a separate and distinct fission component. Reference will be made to the  $\text{Ar} + \text{Au}$  and  $\text{Xe} + \text{Fe}$  cases. — When excitation functions for both evaporation residue products and for well-characterized fission fragments are available, it is possible to carry out a statistical model analysis and extract values of the fission barrier. Beckerman and Blann have carried out such analyses for systems ranging from  $^{35}\text{Cl} + ^{62}\text{Ni}$  to  $^{35}\text{Cl} + ^{116}\text{Sn}$  and concluded that liquid-drop fission barriers must be reduced by  $\approx 40\%$  to reproduce experimental results. A critical appraisal of this conclusion will be given. New results will be introduced for the compound nucleus  $^{153}\text{Tb}^*$  obtained from  $^{20}\text{Ne} + ^{133}\text{Cs}$  and  $^{12}\text{C} + ^{141}\text{Pr}$  reactions. These data allow a very stringent test of the theory of angular-momentum dependence of fission barriers.

---

\* Research sponsored by the Division of Physical Research, US Department of Energy, under contract W-7405-eng-26 with Union Carbide Corporation.

### 1. Introduction

The rapid lowering of the fission barrier  $B_f$  with increasing angular momentum was first discussed more than 15 years ago [1], and detailed calculations in the framework of the liquid drop model were published in 1974 [2]. It was emphasized [2,3] that the fission barrier is predicted to become zero for all nuclei provided that the angular momentum is sufficiently high; thus, at angular momenta greater than about 100  $\hbar$ , no nuclei are expected to have a finite fission barrier. Since angular momenta of 100  $\hbar$  are easily achieved in reactions with heavy ions from present-day facilities, the consequences of the lowering of  $B_f$  with increasing angular momentum have aroused considerable interest in recent years. Among the possible consequences, we may consider the following: First, heavy-ion-induced fission may be observable for nuclei in all mass regions; second, cross sections for evaporation residue (ER) products may be limited by the angular-momentum-dependent fission competition; and third, the vanishing fission barriers may imply a limit on the probability of compound nucleus formation and/or on the probability of fusion of the heavy-ion nuclei with those of the target.

In this review paper we shall discuss some of the above effects with reference to experimental results. We shall also discuss quantitative aspects of the angular-momentum dependence of fission barriers, including the extraction of  $B_f$  values from experimental data on heavy-ion-induced fission. In section 2 fission-imposed limits on evaporation residue products will be considered. In section 3 we shall address the question of characterization of heavy-ion-induced fission, and, finally, fission barriers will be discussed in section 4.

### 2. Cross Section Limits for Evaporation Residue Products

In some sense, comparisons of measured cross sections  $\sigma_{ER}$  for evaporation residue products with theoretical predictions constitute the most stringent tests of the theory of the angular-momentum dependence of fission

barriers. This is due to the fact that such tests are essentially independent of the reaction mechanism giving rise to the ER products. Thus if  $\sigma_{ER}$  for any given case were to be found to exceed substantially the predicted  $B_f = 0$  limit, nuclei predicted to be unstable against fission would have had to deexcite by particle emission rather than by fission. Such a situation would certainly imply a serious quantitative discrepancy between theory and experiment.

Before reviewing experimental results, we wish to comment on quantitative limitations of the rotating liquid drop theory. As was pointed out in Ref. 2, the liquid drop calculations have been made under the assumption of axial symmetry. This approximation, however, is believed not to lead to serious error, since most of the shapes under consideration are either very elongated or are, in fact, predicted to be axially symmetric (see Ref. 2). A more serious problem can be raised by questioning the validity of the liquid drop model in general. The first point we wish to make in this regard is that the lowering of fission barriers with increasing angular momentum is relatively independent of model assumptions. The basic requirement is that the moment of inertia of the saddle-point shape be significantly greater than that of the rotating ground state and that this situation persist with increasing angular momentum. Since rotational energy varies inversely with the moment of inertia, the total energy of the saddle-point shape will increase more slowly with increasing angular momentum than the energy of the rotating ground state. Thus the fission barrier, which is the difference between the energies of the two shapes, will decrease. Since the saddle-point shapes are believed to be very elongated in the case of most nuclei and since there is no reason to believe that this situation changes as the angular momentum is increased, the above condition is very probably satisfied.

The second point to be made regarding the validity of the liquid drop model refers to conditions under which single particle effects may dominate.

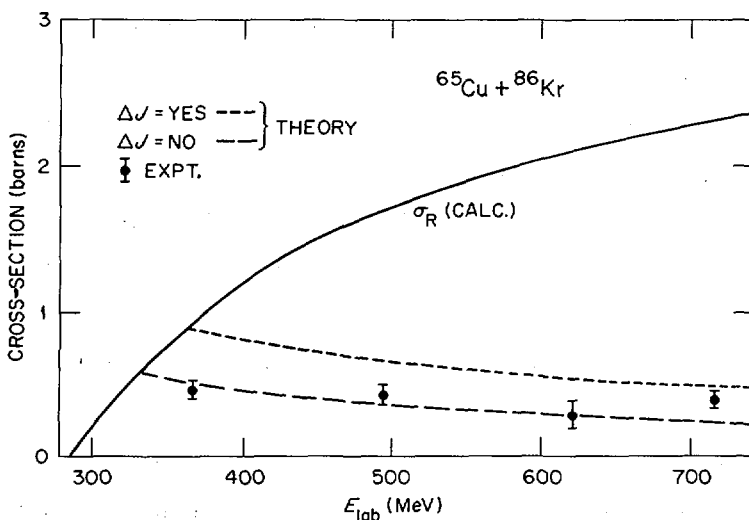


FIG.1. Experimental and theoretical excitation functions for evaporation residue products from the system  $^{65}\text{Cu} + ^{86}\text{Kr}$ . The difference between the two theoretical curves is discussed in the text. An estimate of the total reaction cross-section  $\sigma_R$  is also shown. From Ref.[4].

These conditions may apply in the case of systems with relatively few nucleons, where the description of nuclei in liquid drop terms may be inappropriate, as well as in the case of very heavy systems, where shell effects may strongly influence the value of the fission barrier.

In addition to keeping in mind the points mentioned above, it is necessary that we examine only those cases where  $\sigma_{ER}$  is not limited by entrance channel conditions. All these constraints lead us to the region of medium mass nuclei as being the most favorable for comparison between experiment and theory. In Fig. 1  $\sigma_{ER}$  results are shown for  $^{86}\text{Kr}$  bombardments of  $^{65}\text{Cu}$  [4]. Theoretical curves were obtained by means of statistical model calculations [5-8] in which angular-momentum dependent fission barriers are included [2]. The experimental points are seen to fall between two extreme assumptions of the approximate statistical model calculation. (In one case evaporated particles are assumed not to change the angular momentum distribution, while in the other case each evaporated neutron decreases the angular momentum by 2  $\hbar$ , each proton by 3  $\hbar$ , and each  $^4\text{He}$  by 10  $\hbar$  [8].)

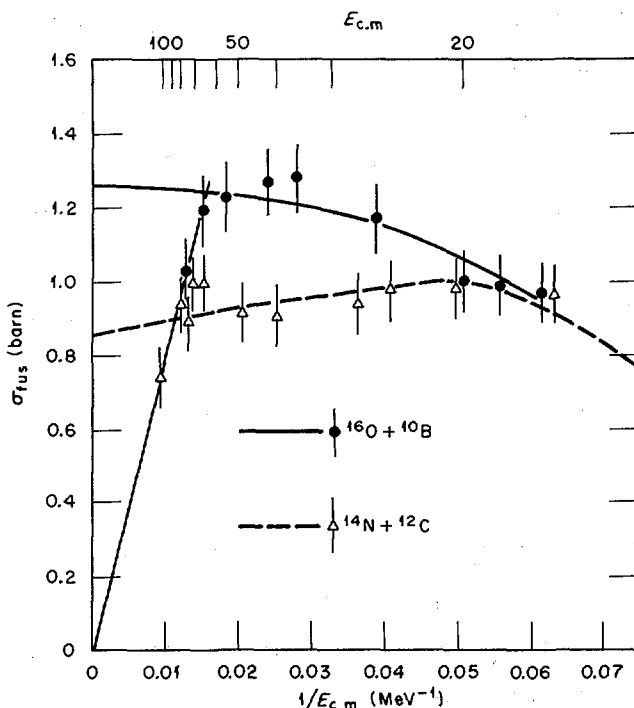


FIG.2. Fusion cross-sections versus  $1/E_{cm}$  for the systems  $^{16}\text{O} + ^{10}\text{B}$  and  $^{14}\text{N} + ^{12}\text{C}$ . The steeply sloping solid line appearing at  $1/E_{cm}$  values of  $<0.02 \text{ MeV}^{-1}$  corresponds to the predicted liquid-drop limit for  $B_f = 0$ . From Ref.[13].

Thus agreement between experiment and theory for this system is good.

Similar good agreement is obtained in a number of other cases, including the  $^{109}\text{Ag} + ^{40}\text{Ar}$  reaction of Britt, et al. [9].

If we consider very light systems in spite of the reservations expressed above, we find that  $\sigma_{ER}$  values often approach the liquid drop limit [10-11]. In a recent study, Stokstad, et al. [12-13] investigated the deexcitation of  $^{26}\text{Al}$  formed in the reactions  $^{10}\text{B} + ^{16}\text{O}$  and  $^{12}\text{C} + ^{14}\text{N}$ . Their results [13] are shown in Fig. 2. While the differences between the two reactions are beyond the scope of this paper, it is interesting to note that both reactions exhibit a remarkable decrease in  $\sigma_{ER}$  as a function of energy at exactly the  $B_f = 0$  limit predicted by the rotating liquid drop model [2].

Given the low mass of the  $^{26}\text{Al}$  compound nucleus, this striking agreement is perhaps better than one might have expected.

Another interesting case involving the relatively light system  $^{16}\text{O} + ^{40}\text{Ca}$  was investigated recently by Vigdor, et al. [14]. The  $\sigma_{\text{ER}}$  values were found to be essentially constant near 1150 mb over an energy range from 40 MeV to 214 MeV. At the highest energy, the ER cross section reached the value calculated to correspond to the  $B_f = 0$  limit. Recently, measurements on this system were extended to 316 MeV by Britt, et al. [15], and from preliminary results it appears that the ER cross section is considerably lower than 1150 mb. The decrease is consistent with the predicted  $B_f = 0$  limit.

We are not aware of any case in which the measured  $\sigma_{\text{ER}}$  values exceed substantially the calculated  $B_f = 0$  limit; nevertheless, caution must be used when calculations with liquid drop fission barriers are used to predict evaporation residue cross sections. Such predictions are reasonably reliable only when the non-rotating barrier,  $B_f^0$ , is considerably larger than typical particle binding energies. This point is illustrated in Table I for the reactions  $^{65}\text{Cu} + ^{86}\text{Kr}$  and  $^{109}\text{Ag} + ^{86}\text{Kr}$  [4]. The compound nucleus  $^{151}\text{Tb}^*$  has a calculated value of  $B_f^0 \approx 33.5$  MeV, while for  $^{195}\text{Bi}^*$ ,  $B_f^0 \approx 11.7$  MeV. It can be seen that in the  $^{65}\text{Cu} + ^{86}\text{Kr}$  case calculated  $\sigma_{\text{ER}}$  values are relatively insensitive to the choice of  $a_f/a_v$ , the ratio of the statistical model level density parameter for fission to that for particle emission. On the other hand, the calculated ER cross sections are very sensitive to the value of the level density parameter ratio in the  $^{109}\text{Ag} + ^{86}\text{Kr}$  case, and since the  $a_f/a_v$  values in the table all fall within a reasonable range, it is not reliable to use calculated fission barriers and the statistical model to predict  $\sigma_{\text{ER}}$  for such a relatively high-Z case.

Thus we may conclude that the liquid drop theory of angular-momentum-dependent fission barriers predicts absolute limits on ER cross sections

TABLE I. EFFECTS OF LEVEL DENSITY  
PARAMETER VARIATION ON CALCULATED  
EVAPORATION RESIDUE CROSS-SECTIONS

$a_f/a_v$	$^{65}\text{Cu} + ^{86}\text{Kr}$ (mb)	$^{109}\text{Ag} + ^{86}\text{Kr}$ (mb)
1.0	245	76.1
1.01	243	59.1
1.05	216	8.70
1.10	173	0.0024

which are not known to have been exceeded. Furthermore, provided that the non-rotating fission barrier is considerably larger than the particle binding energy, and, provided that entrance channel effects do not limit the fusion cross section, the rotating liquid drop theory gives reasonable predictions for total ER cross sections. Finally, the liquid drop model appears to work even for very light systems such as N + C, at least as far as the limit on  $\sigma_{ER}$  is concerned. In these light cases,  $\sigma_{ER}$  is often observed to be close to that corresponding to the calculated  $B_f = 0$  limit.

### 3. Characterization of Heavy-Ion-Induced Fission

In this section, we will attempt to categorize heavy-ion-induced fission and fission-like phenomena. In early studies of heavy-ion-induced fission, the question of definition of the fission process did not pose a problem. In the systems studied, fission was induced with relatively light heavy ions ranging from C to Ne [15-21], and fission products constituted a well-defined and separated peak in the mass and kinetic energy distributions of reaction

products. The peak in the mass-yield distribution was found to be centered at symmetric mass divisions, and the angular distributions of the fission fragments followed a  $1/\sin \theta$  functional form. The kinetic energies were understood in terms of Coulomb repulsion between the elongated nascent fragments at the time of scission, and it was concluded from all indications that fission followed compound nucleus formation. Empirically, the four observable conditions characterizing fission are: (i) a distinct peak in the mass (or charge) yield distribution of products that is centered at symmetric mass divisions; (ii) a  $1/\sin \theta$  angular distribution; (iii) a predictable fragment kinetic energy distribution [22]; and (iv) full momentum transfer from the projectile to the fissioning system (as determined by angular correlation measurements [16,20,23]).

Conceptually, fission following compound nucleus formation is certainly a well-defined process. Target and projectile nuclei fuse with each other, the system equilibrates in all degrees of freedom while undergoing several rotations, and fission finally takes place during the deexcitation process if it has successfully competed with particle emission. In practice, compound nucleus formation may be difficult to achieve in systems with very high excitation energies and angular momenta, since the composite system of target and projectile is likely to have a short lifetime and may begin to deexcite by particle emission even before equilibrium in all degrees of freedom has been achieved. We shall refer to the fission of a fused composite system as fusion-fission (FF). Thus compound nucleus fission, CNF, is a special case of FF; namely, one in which equilibrium in all degrees of freedom has taken place prior to fission. While FF in general may satisfy all of the fission conditions listed above, a statistical model treatment is applicable only to CNF.

Before giving examples of experimental results, we would like to describe one more reaction category which may give rise to fission-like

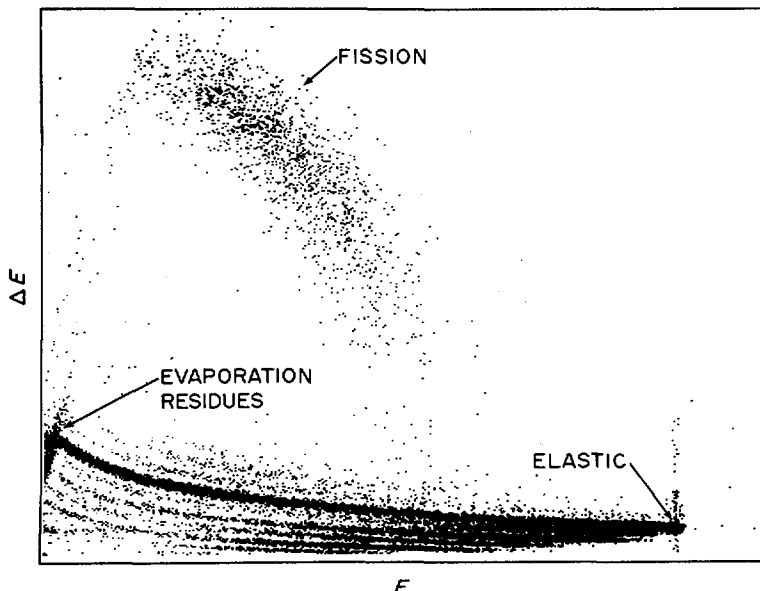


*FIG.3.  $\Delta E$ -versus- $E$  map for the system  $^{150}\text{Nd} + 175\text{-MeV} ^{20}\text{Ne}$ . The principal reaction-product groupings are labelled. From Ref.[24].*

products, namely, deeply inelastic collisions, DIC. These have been very successfully described in terms of diffusion models. In many cases, when the collision time is sufficiently long, diffusion processes may involve sufficient mass and charge transfer so that DIC products can be observed in the same mass region as FF products. Since the time associated with the tail of the DIC distribution may be similar to the time relevant to FF, the distinction between FF and the DIC tail may be only academic. It is unlikely, however, that DIC will result in a peak in the mass distribution centered at symmetric mass divisions (except, of course, in those cases when the target and projectile have nearly equal masses), and thus distributions of products resulting from DIC will in general not satisfy fission condition (i) listed above.

By way of illustrating the above discussion, we shall first consider fission events resulting from reactions with relatively light heavy ions

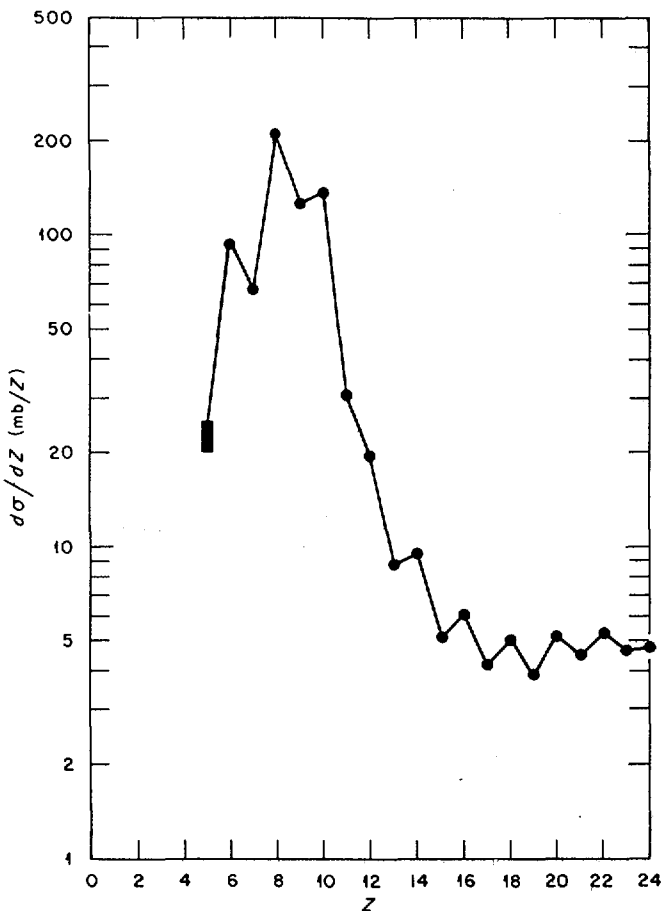


FIG. 4. Production cross-section versus  $Z$  for the system  $\text{Ni} + 164\text{-MeV } ^{20}\text{Ne}$ . From Ref.[25].

such as Ne. An example of raw data in which the fission products stand out clearly is shown in Fig. 3 for the case of  $^{20}\text{Ne} + ^{150}\text{Nd}$  [24]. The fission events form a separate peak at relatively high values of  $\Delta E$  and medium values of  $E$ . From the kinetic energy measurement and from studies of similar systems, it can be concluded that the fission peak shown in Fig. 3 is definitely a result of FF and is very probably due to CNF.

A quite different picture emerges for the case of  $^{20}\text{Ne} + \text{Ni}$  [25]. In Fig. 4 the overall charge distribution of the lighter reaction products is

shown. Since the composite system has  $Z = 38$ , symmetric charge divisions correspond to  $Z = 19$ , or about 2 units of charge less ( $Z = 17$ ) if evaporation from the composite system and/or from the products is taken into account. It is clear that there is no hint of a peak at symmetric charge divisions. On the other hand, other conditions characterizing fission are satisfied. For example, the angular distributions shown in Fig. 5 are given in terms of  $d\sigma/d\theta_{cm}$ , and thus a constant distribution implies a  $1/\sin \theta$  functional form. It can be seen that for products with  $Z \geq 15$  this condition is satisfied. In Fig. 6, the kinetic energy of the observed reaction products is plotted as a function of  $Z$ . Theoretical predictions for kinetic energies of fission fragments, derived from the work of Davies, et al. [22], are indicated by the curve. When the theoretical calculations are corrected for particle emission from the excited fragments, the open circles are obtained. For  $Z \geq 15$ , the calculated fission fragment energies are in excellent agreement with measured values. Thus the case of  $^{20}Ne + Ni$  constitutes a typical example of a system in which the tail of the deeply inelastic products extends to the region of symmetric charge divisions, and in which the characteristic properties of the near-symmetric products, such as angular distributions and kinetic energies, are identical to those expected for FF. As was discussed above, whether or not these events are due to DIC or FF is perhaps a matter of personal preference, since on the one hand the near-symmetric events display fission characteristics, while on the other hand, these characteristics evolve smoothly from the deeply inelastic properties. It is unlikely, however, that compound nucleus formation was involved in this case, and thus the events observed are very probably not due to CNF.

An intermediate case between the CNF of  $Ne + Nd$  and the DIC of  $Ne + Ni$  is the case of  $Ne + Ag$  [26]. The charge distributions at several angles and at two bombarding energies are shown in Fig. 7. At the lower bombarding energy there appears a peak at near-symmetric charge splits, but it is not

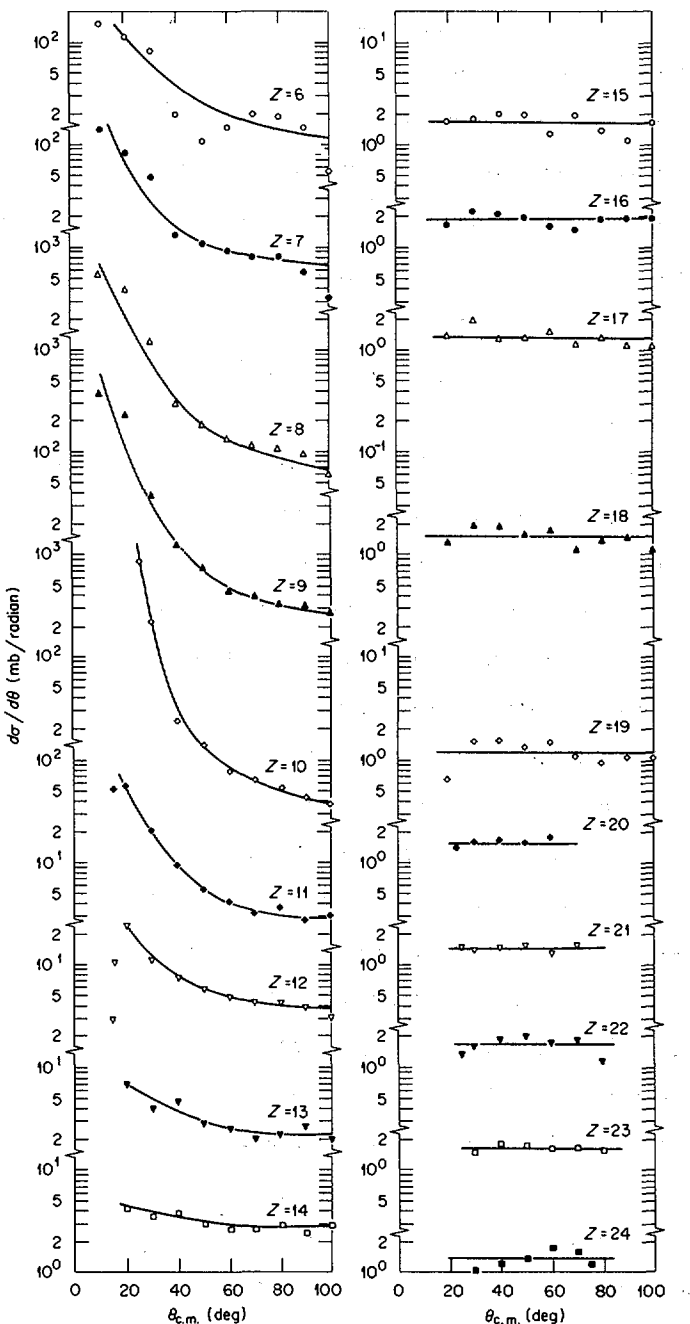


FIG. 5. Production cross-sections versus  $\theta_{\text{c.m.}}$  for various elements from the system  $\text{Ni} + 164\text{-MeV } ^{20}\text{Ne}$ . Flat distributions for  $Z > 15$  in this plot indicate an angle-equilibrated  $1/\sin \theta$  functional form. From Ref.[25].

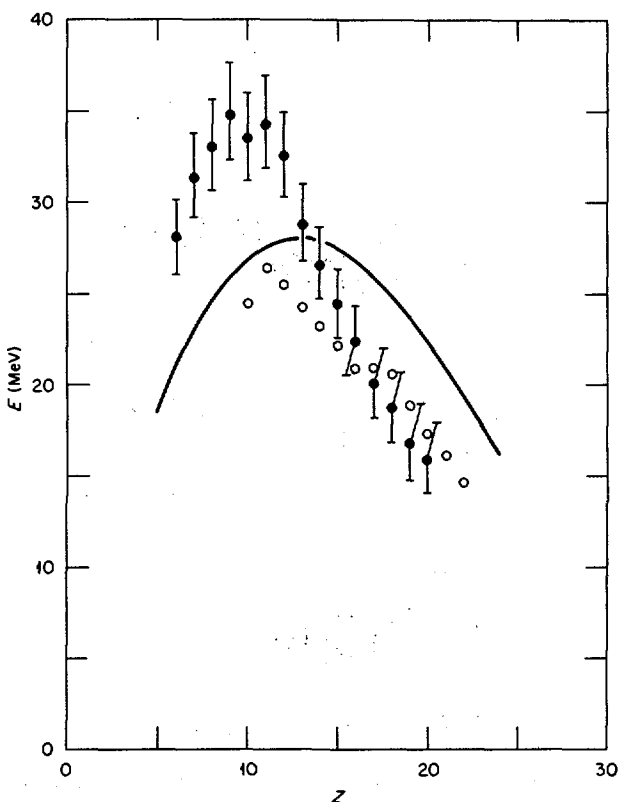


FIG.6. Experimental and theoretical kinetic energies for products from the reaction Ni + 164-MeV  $^{20}\text{Ne}$ . The filled points are the experimental single-fragment kinetic energies in the centre-of-mass system; the theoretical curve is derived from Ref.[22]; the open points are the theoretical results corrected for evaporation. From Ref. [25].

well separated from the deeply inelastic events. At the higher energy, the peak is even less distinct. Babinet, et al. [26] have interpreted the data of Fig. 7, in terms of the diffusion model, but in view of the fact that at near-symmetric charge divisions the kinetic energies and angular distributions of the products satisfy the FF criteria, and since a distinct peak in the charge yield curve does exist, it is possible that products with  $Z \geq 16$  consist of a mixture of DIC and CNF events. The washing out of the peak in the charge distribution with increasing bombarding energy is consistent with this point of view.

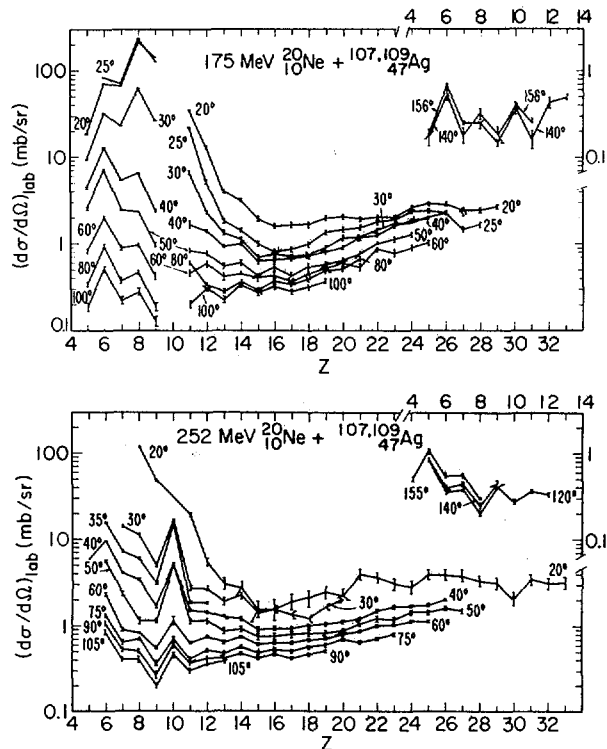
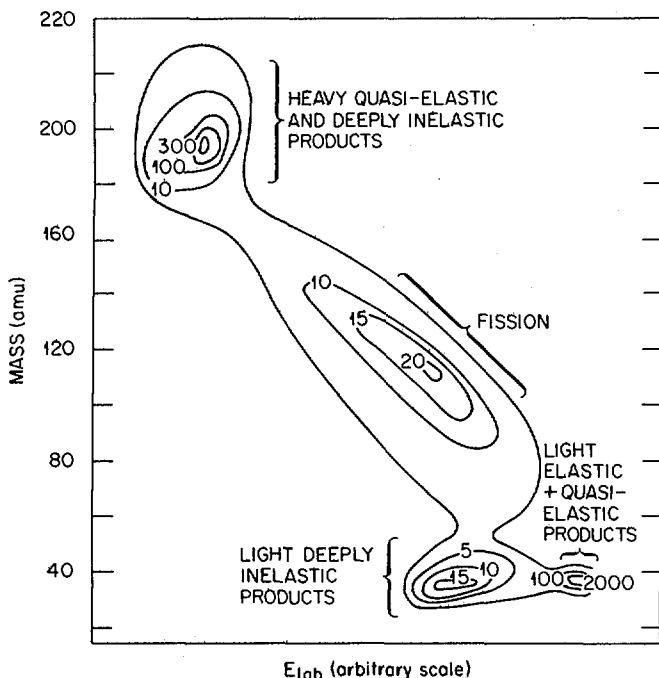


FIG. 7. Production cross-sections versus  $Z$  at various laboratory angles for the system  $\text{Ag} + ^{20}\text{Ne}$ . From Ref.[26].

Turning to reactions with heavier ions, it is possible, once again, to find examples in which a distinct fission component appears, as well as examples where yield at symmetric mass or charge splits may be associated with tails of distributions of DIC products. In Fig. 8, a mass-energy distribution is shown for the reaction 201-MeV  $^{40}\text{Ar} + ^{197}\text{Au}$  [27]. The various types of reaction products are identified in the figure, and it can be seen that fission events form a well-defined peak, separated from other events. This case may be contrasted with  $^{84}\text{Kr} + ^{209}\text{Bi}$  data shown in Fig. 9 [28]. Mass distributions derived from coincidence measurements are shown at 34° and 59°. Once again, there is no peak at near-symmetric mass divisions, and the yield in that mass region appears to be due to a tail of the DIC



*FIG.8. Kinetic energy versus mass contour diagram of products from the system  $^{197}\text{Au} + 201\text{-MeV } ^{40}\text{Ar}$ . Principal reaction-product groupings are labelled. From Ref.[27].*

events. The reason that the yield at symmetric mass division appears only at  $59^\circ$  and not at  $34^\circ$  is probably due to the fact that events appearing at  $59^\circ$  involve longer reaction times than those appearing at  $34^\circ$  and allow more mass transfer. This view is supported by the somewhat lower total kinetic energy associated with the  $59^\circ$  data (275 MeV, compared to 290 MeV at  $34^\circ$ ), which implies a greater degree of energy damping.

The final point we wish to make in this section concerns very fissile systems, in which the total fission cross section exceeds the  $B_f = 0$  limit. Two such examples are the  $^{20}\text{Ne} + ^{235}\text{U}$  system studied by Viola, et al. [23] using the angular correlation technique and the  $^{132}\text{Xe} + ^{56}\text{Fe}$  system of Heusch, et al. [29]. In both of these cases the fission events satisfy all criteria for FF listed earlier in this section, and in both cases the FF

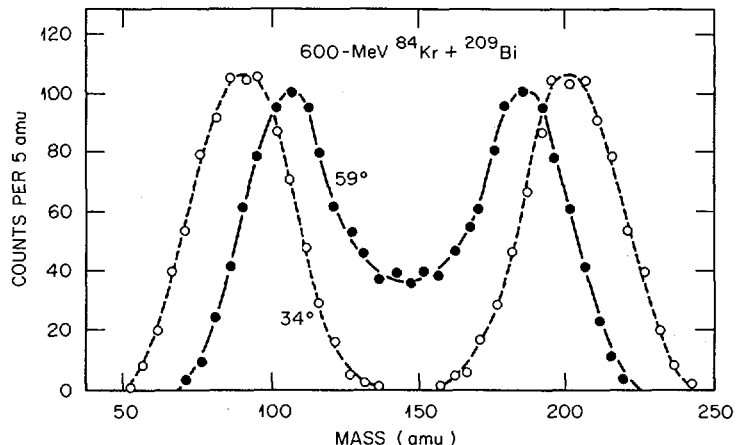


*FIG. 9. Relative mass yields for DIC products from the system  $^{209}\text{Bi} + 600\text{-MeV } ^{84}\text{Kr}$  at two laboratory angles. Average kinetic energies of products detected at  $34^\circ$  and  $59^\circ$  are 290 MeV and 275 MeV, respectively. From Ref. [28].*

cross section exceeds substantially the  $B_f = 0$  limit discussed in section 2. The three possible conclusions that can be drawn from these results are: (i) while all of the fragments observed result from FF, only some are the products of CNF; (ii) compound nuclei with  $B_f = 0$  are able to exist; and (iii) the calculated  $B_f = 0$  limit is inaccurate, and the true  $B_f = 0$  limit corresponds to a higher fission cross section. Of the three alternatives given above, (iii) seems unlikely to be correct in view of the considerations given in section 2. On the other hand, alternative (i), namely, that not all observed fission fragments result from CNF, is very likely to be true, and thus the description of a "new type of strongly damped collision" evoked in Ref. 29 to explain the Xe + Fe data is not necessary.

We conclude this section by pointing out that if we wish to restrict our attention to compound nucleus fission we should consider only fissioning systems with  $130 \leq A \leq 210$ , and only those cases in which fission was induced by ions with  $A \leq 40$ .

#### 4. Fission Barriers from Heavy Ion Reactions

In this section we examine problems associated with the extraction of fission barriers from excitation functions for heavy-ion-induced reactions. In view of the discussion of the previous section as to which cases constitute CNF, it is clear that considerable care must be exercised in choosing appropriate fissioning systems. First, systems to be used for the determination of fission barriers must not be dominated by DIC products. This excludes such light systems as the Ne + Ni case discussed in section 3, as well as the  $^{35}\text{Cl} + \text{Ni}$  case considered by Beckerman and Blann [30]. Systems in which target and projectile masses are similar are also unsuitable, since it is not possible in these cases to separate CNF from DIC products. An example of such a case is the  $^{65}\text{Cu} + ^{86}\text{Kr}$  data of Ref. 9. This same difficulty applies to cases in which fission-like events consist of a mixture of DIC and CNF products and in which the separation into two distinct components is ambiguous. Examples of such cases are the Ag + Ne data discussed in the previous section, as well as the  $^{40}\text{Ar} + ^{109}\text{Ag}$  data of Britt, et al. [9], which were used by Beckerman and Blann [30] to determine the fission barrier of the compound nucleus  $^{149}\text{Tb}$ . Finally, very fissile systems such as the  $^{20}\text{Ne} + ^{235}\text{U}$  of Viola, et al.<sup>23</sup> are also not appropriate. While they almost certainly involve FF, it is probable that not all of the events result from CNF, and thus they do not lend themselves to a statistical model analysis. With all of the above constraints, we are restricted to cases in which fission is induced by relatively light heavy ions such as C and Ne and to systems in the mass range  $130 \leq A \leq 210$ .

The most important region of the fission excitation function for the purpose of extracting fission barriers is, not surprisingly, the steep part of the excitation function in the threshold region. This point is discussed and illustrated in Ref. 31 and has been confirmed from an examination of a large number of systems for which data are available. It was found that the

value of  $B_f$  is determined primarily by the slope of the  $\sigma_f$  function and that poor fits at higher excitation energies did not affect extracted  $B_f$  values. It was also found by Moretto, et al. [32] that for  $^4\text{He}$ - and proton-induced-fission, fits to entire excitation functions can be obtained over a wide energy range, provided that level densities are based on realistic single particle schemes and that energy-dependent pairing effects are included. Fission barriers extracted by Moretto, et al. [32], however, do not differ substantially from those extracted by Khodai-Joopari [33] on the basis of a statistical model using Fermi gas level densities.

In this work, we have used Fermi gas level densities, and the angular momentum variation of the fission barriers (but not their absolute values) was assumed to be that given by the rotating liquid drop model [2]. The procedure of obtaining statistical model fits to heavy-ion-induced fission excitation functions allowing  $B_f^0$  and  $a_f/a_v$  to be free parameters has been described earlier [3,30]. In Refs. 3 and 30 the computer code ALICE [34] was used in this type of analysis. Here, we shall use a recently updated version of the code, ORNL ALICE [7]. Since ALICE-type calculations essentially divide the compound nucleus  $\sigma_{\text{CN}}$  cross section into its evaporation residue,  $\sigma_{\text{ER}}$ , and fission,  $\sigma_f$ , components, measured values of  $\sigma_{\text{ER}}$  are needed along with  $\sigma_f$  values. By assuming that  $\sigma_{\text{CN}} = \sigma_{\text{ER}} + \sigma_f$ , it is then possible to apply the statistical model treatment.

Finally, in order to isolate angular momentum effects and in order to provide a stringent consistency check, it is desirable to obtain excitation functions for two systems leading to the same compound nucleus. This motivated us to study the systems  $^{12}\text{C} + ^{14}\text{Pr}$  and  $^{20}\text{Ne} + ^{133}\text{Cs}$ , both leading to the compound nucleus  $^{153}\text{Tb}$  [35]. The fission data for these systems were discussed earlier [3], but it is only recently that we have succeeded in measuring the  $\sigma_{\text{ER}}$  values needed for an unambiguous statistical model

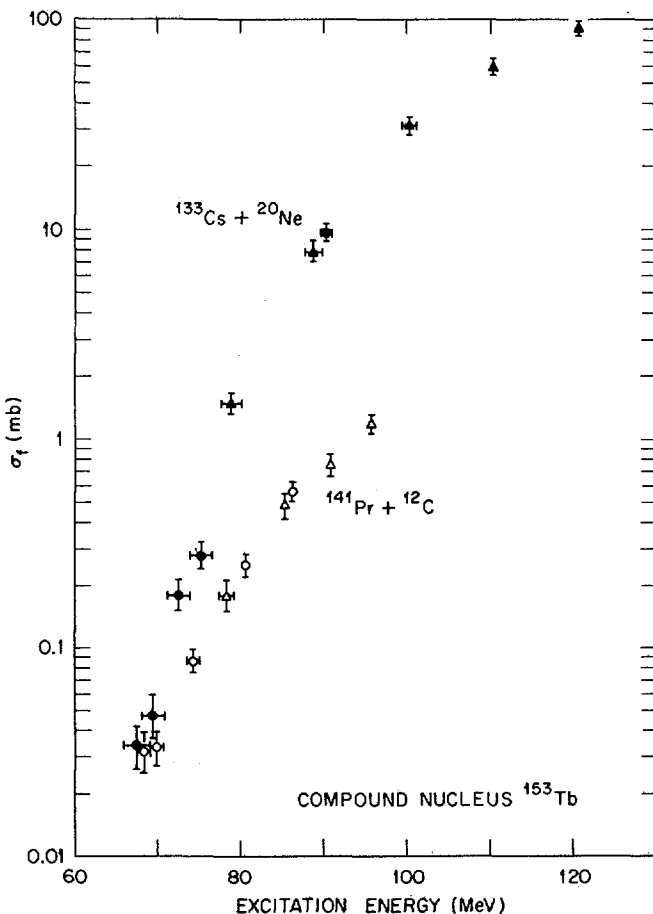


FIG.10. Fission excitation functions for fission of the  $^{153}\text{Tb}$  compound nucleus produced in two different reactions.

analysis. The  $\sigma_{ER}$  measurements indicate that for Ne + Cs  $\sigma_{CN}$  is approximately equal to the geometric cross section, while for C + Pr  $\sigma_{CN}$  is equal to about 63% of the geometric cross sections.

The fission excitation functions for the two systems are shown in Fig. 10. The effect of the increased angular momentum in the Ne + Cs case is clearly reflected in its enhanced fissility. As was stated above, the fission barrier for the non-rotating system,  $B_f^0$ , is determined from the

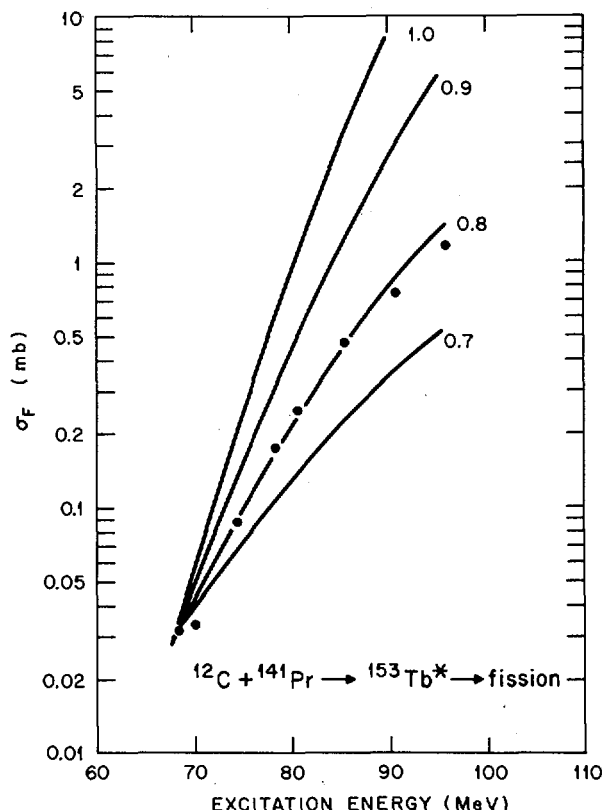


FIG.11. Experimental and theoretical fission excitation functions for the system  $^{141}\text{Pr} + ^{12}\text{C}$ . The curves, which are fit to the lowest energy point, are labelled with the fraction of the liquid-drop fission barrier used in the fit (see text). The best fit was obtained with  $0.8 B_{f,LD}^0$  and  $a_f/a_v = 1.06$ .

slope of the  $\sigma_f$  function. This is shown in Fig. 11. A number of different fits has been made to the data point at the lowest energy, with  $B_{f,LD}^0$  values ranging from the liquid drop value  $B_{f,LD}^0$  to  $0.7 B_{f,LD}^0$ . The corresponding  $a_f/a_v$  values needed to obtain the fits ranged from 0.985 for  $0.7 B_{f,LD}^0$  to 1.245 for  $B_{f,LD}^0$ . It is clear that a fission barrier of 80% of the liquid drop value best fits the observed results. For  $0.8 B_{f,LD}^0$ ,  $a_f/a_v$  was found to be 1.06. In Fig. 12 a fit with  $0.8 B_{f,LD}^0$  and  $a_f/a_v = 1.0$  is shown for the  $^{20}\text{Ne} + ^{133}\text{Cs}$  case. It can be seen that the fit is excellent, and, as in

the case of  $^{12}\text{C} + ^{141}\text{Pr}$ , it was also found to be unique. Thus it seems reasonable to conclude that the fission barrier of the  $^{153}\text{Tb}$  compound nucleus is 80% of the liquid drop value. This conclusion is consistent with the calculations of Krappe and Nix [36].

One troublesome feature of the above fits is that the value of  $a_f/a_v$  is not the same in the two cases; whereas it might have been expected to be identical. The reason for this may be due to errors arising from the  $\sigma_{\text{CN}}$  values used in the calculations. In our recent work, it was found that the ratio  $\sigma_{\text{CN}}/\sigma_{\text{geometric}}$  for  $\text{Ne} + \text{Cs}$  is approximately equal to 1.0, while for  $\text{C} + \text{Pr}$  it is equal to 0.63. The corresponding ratio of  $a_f/a_v$  for  $\text{C} + \text{Pr}$  to that for  $\text{Ne} + \text{Cs}$  is 1.06. In Ref. 3, in which  $\sigma_{\text{CN}}/\sigma_{\text{geometric}}$  was assumed to be 1.0 for both systems, the ratio of  $a_f/a_v$  for  $\text{C} + \text{Pr}$  to that for  $\text{Ne} + \text{Cs}$  was found to be 0.97. Thus neither here nor in Ref. 3 was  $a_f/a_v$  found to be the same for the two systems studied, but while it was calculated to be smaller for  $\text{C} + \text{Pr}$  than for  $\text{Ne} + \text{Cs}$  in Ref. 3, the reverse appears to be true in the more recent work. In any case, it is gratifying that the same conclusion was obtained in Ref. 3 as was obtained here: the fission barrier of  $^{153}\text{Tb}$  is 80% of the liquid drop value. The fits obtained in Ref. 3 are shown in Fig. 13.

The kinds of problems that may emerge when we attempt to fit data that consist of a mixture of CNF and DIC products are illustrated in Fig. 14 for the case of  $\text{Ne} + \text{Ag}$  [3,37]. Attempted fits to the lowest energy data point are shown with  $B_f^0$  values as low as 60% of  $B_{f,\text{LD}}^0$ . It is clear that it is not possible to obtain a fit to the data over a reasonable range (about 25 MeV) of excitation energy. (An earlier fit reported by Beckerman and Blann [30] to the  $\text{Ne} + \text{Ag}$  data made use of reported [3]  $\sigma_{\text{ER}}$  values that were recently found to be in gross error [38].) The reason for this failure is almost certainly that the DIC component, which has been shown to be present, does not vary with excitation energy at the same rate as CNF, and thus the data are not suitable for  $B_f^0$  extraction.

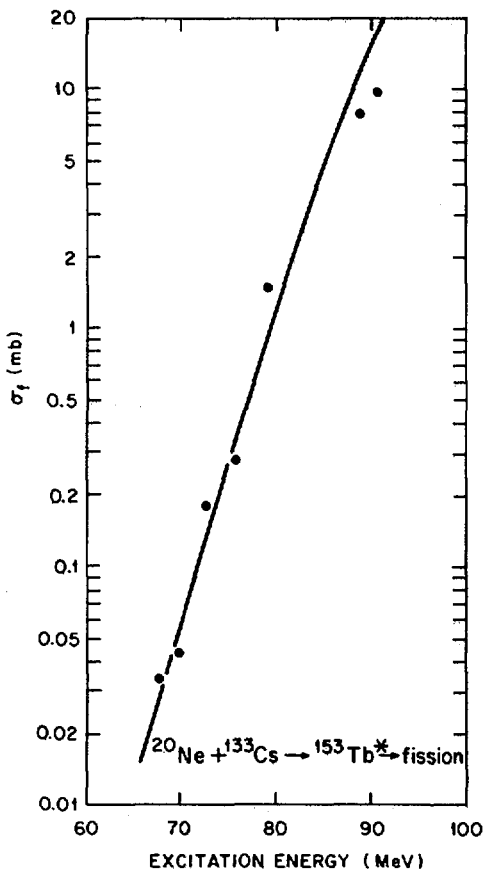


FIG.12. Experimental and theoretical fission excitation functions for the system  $^{133}\text{Cs} + ^{20}\text{Ne}$ . The theoretical curve is a fit to the lowest energy point using  $0.8B_{f,\text{LD}}^0$  and  $a_f/a_v = 1.0$ .

In Ref. 30, Beckerman and Blann have concluded that, based on an analysis of five different systems, fission barriers appear to be 50-70% of the liquid drop values. This discrepancy seems surprisingly large, and it is necessary to examine each system involved individually to determine its validity. We have already pointed out that in the case of three of the five systems, namely, Cl + Ni, Ne + Ag and Ar + Ag, there is a strong DIC component present that makes the analysis ambiguous at best.

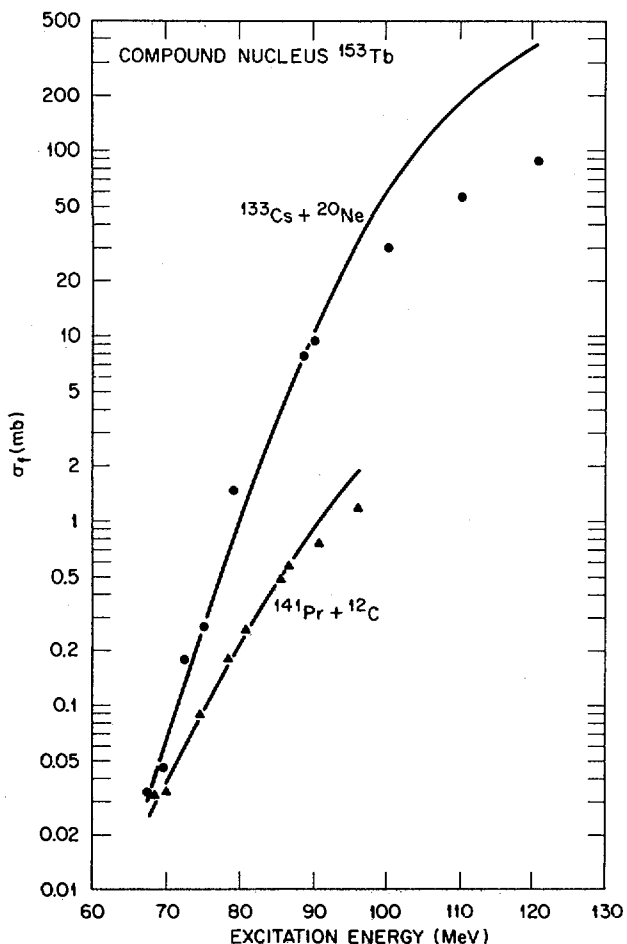


FIG.13. Experimental and theoretical fission excitation functions for fission of the  $^{153}\text{Tb}$  compound nucleus produced in two different reactions. The fits are those from Ref.[3] with the assumption that  $\sigma_{\text{ER}}/\sigma_{\text{geometric}} = 1.0$  for both systems (see text).

We have examined in some detail the case of  $^{35}\text{Cl} + ^{116}\text{Sn}$ , one of the two remaining systems of Ref. 30. The data are shown in Fig. 15 together with the MB-II fit of Ref. 30, in which final angular momentum states were treated explicitly (solid curve). While in ALICE calculations angular momentum is treated only approximately, it can be concluded from Ref. 30 that adequate fits can nevertheless be obtained with ALICE. This is also

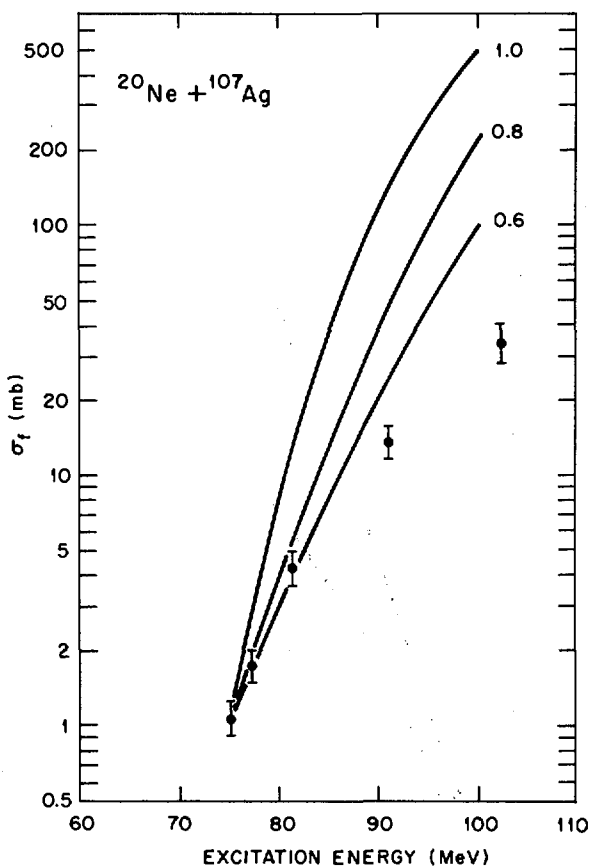


FIG. 14. Experimental and theoretical fission excitation functions for the system  $^{107}\text{Ag} + ^{20}\text{Ne}$ . Theoretical curves, fit to the lowest energy data point, are labelled with the fraction of the liquid-drop fission barrier used in the fit (see text). Experimental data are from Refs [3, 37].

shown in Fig. 15 (dashed curve), and we shall thus continue to use ALICE to illustrate the following point. In Ref. 3 it was pointed out that a possible severe source of error in the case of relatively light systems may be the sharp cutoff approximation. In Fig. 15 we show the results for a diffuse cutoff in the angular momentum distribution of the deexciting compound nuclei (dash-dot curve). It can be seen that this calculated fission excitation function lies above the sharp cutoff ALICE result, but that the slope

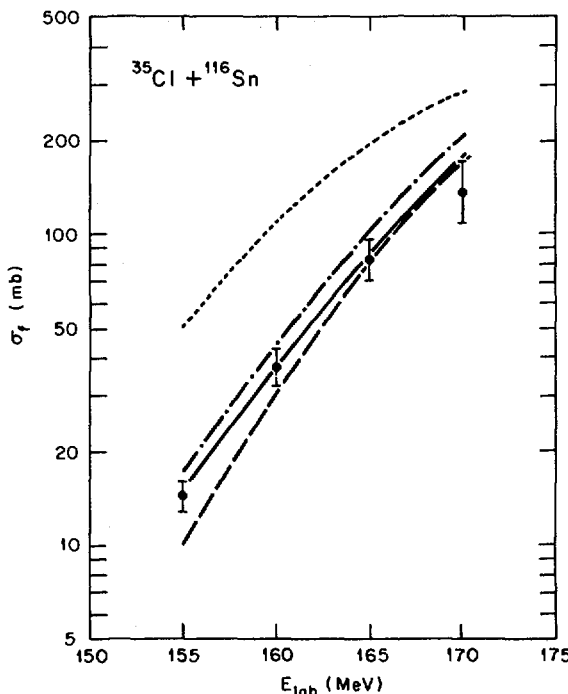


FIG. 15. Experimental and theoretical fission excitation functions for the system  $^{116}\text{Sn} + ^{35}\text{Cl}$ . The data and the solid curve (a fit using the program MB-II) are from Ref. [30]. The dashed curve is a fit using the program ALICE, and the dash-dot curve shows the result of using a diffuse cut-off in the angular-momentum distribution. The dotted curve represents a calculation using the program PACE of Ref. [40].

is changed only slightly. This implies that a diffuse cutoff does not lead to significantly different values of  $B_f^0$ . This same conclusion was reached by Blann [39] and co-workers.

Also shown in Fig. 15 is the result using a Monte Carlo-type program PACE, which does take final angular momentum states specifically into account [40] (dotted curve). Since all of the calculations of Fig. 15 involve the same parameters, the relatively large difference between our Monte Carlo-type calculation and that of Ref. 30 is not understood. Since the slope of our calculation is less steep than that of the fit of Ref. 30, it is possible that, if our results are correct, the  $B_f^0$  is not as low as the MB-II

calculation would imply. The final point to be made is that the Cl data considered by Beckerman and Blann span a rather narrow range of excitation energy (about 12 MeV), compared to an excitation energy range about twice as large for our  $^{153}\text{Tb}$  system.

In concluding this section, we wish to observe that, based on the study of the  $^{153}\text{Tb}$  system formed in two different ways and over a fairly large range of excitation energies, the fission barriers in this mass region are probably lower than those calculated from the liquid drop model, but only by about 20%, and not the 30-50% deduced earlier.

#### 5. Concluding Remarks

We have shown that the rapid decrease of fission barriers with increasing angular momentum has important implications for heavy-ion-induced fission. Currently, there appear to be no cases in which measured evaporation residue cross sections appreciably exceed the  $B_f = 0$  limit. This gives us considerable confidence in the quantitative aspects of current fission theory. The characterization of fission is complicated by the fact that experimentally it is impossible to distinguish between fission following fusion in general, and the fission of compound nuclei specifically. Furthermore, tails of deeply inelastic reactions may extend into the fission region, and these two types of products may also be indistinguishable from one another. Thus caution must be used when fission barriers are extracted from heavy-ion-induced fission data. However, we have concluded that, in the region of  $A \approx 150$ , fission barriers have values of about 80% of the liquid drop values and not the 50-70% indicated earlier.

#### 6. Acknowledgements

We are grateful to our colleagues, R. L. Hahn, F. E. Obenshain, F. Pleasonton, A. H. Snell, and G. R. Young for permission to use unpublished experimental data. We wish to thank A. Gavron for making available his program

PACE [40] and for adapting it to run in our computer environment. His helpful guidance in using the code is very much appreciated. Fruitful discussions with M. Blann and M. Beckerman are gratefully acknowledged.

Much of our own experimental work discussed in this paper was done when production of Ne beams at the Oak Ridge Isochronous Cyclotron was far from routine. The skill and dedication of Gene A. Palmer in operating the Cyclotron was especially appreciated, and his untimely death has saddened all of those who knew him.

#### REFERENCES

- [1] COHEN, S., PLASIL, F., SWIATECKI, W. J., Proceedings Third Conference on Reactions Between Complex Nuclei (GHIORSO, A., DIAMOND, R. M., CONZETT, H. E., Eds.), University of California Press, Berkeley (1963) 325; University of California Radiation Laboratory preprint UCRL-10775 (1963).
- [2] COHEN, S., PLASIL, F., SWIATECKI, W. J., Ann. Phys. 82 (1974) 557.
- [3] PLASIL, F., Proceedings of the International Conference on Reactions Between Complex Nuclei (ROBINSON, R. L., McGOWAN, F. K., BALL, J. B., HAMILTON, J. H., Eds.), North-Holland Publishing Co., Amsterdam (1974) 107.
- [4] PLASIL, F., FERGUSON, R. L., BRITT, H. C., ERKKILA, B. H., GOLDSTONE, P. D., STOKES, R. H., GUTBROD, H. H., Phys. Rev. C 18 (1973) 2603.
- [5] BLANN, M., PLASIL, F., Phys. Rev. Lett. 29 (1972) 303.
- [6] PLASIL, F., BLANN, M., Phys. Rev. C 11 (1975) 508.
- [7] PLASIL, F., ORNL ALICE A Statistical Model Computer Code Including Fission Competition, Oak Ridge National Laboratory Report ORNL/TM-6054 (1977).
- [8] PLASIL, F., Phys. Rev. C 17 (1978) 832.
- [9] BRITT, H. C., ERKKILA, B. H., STOKES, R. H., GUTBROD, H. H., PLASIL, F., FERGUSON, R. L., BLANN, M., Phys. Rev. C 13 (1976) 1483.
- [10] NATOWITZ, J. B., CHULICK, E. T., NAMBOODIRI, M. N., Phys. Rev. Lett. 31, (1973) 643.
- [11] NAMBOODIRI, M. N., CHULICK, E. T., NATOWITZ, J. B., KENEFICK, R. A., Phys. Rev. C 11 (1975) 401.
- [12] STOKSTAD, R. G., DAYRAS, R. A., GOMEZ DEL CAMPO, J., STELSON, P. H., OLMER, C., ZISMAN, M. S., Phys. Lett. 70B (1977) 289.

- [12] GOMEZ DEL CAMPO, J., DAYRAS, R. A., BIGGERSTAFF, J. A., SHAPIRA, D., SNELL, A. H., STELSON, P. H., STOKSTAD, R. G., Formation of  $^{26}\text{Al}$  by the Reactions  $^{10}\text{B} + ^{16}\text{O}$  and  $^{12}\text{C} + ^{14}\text{N}$ , preprint (1979).
- [14] VIGDOR, S. E., KOVAR, D. G., SPERR, P., MAHONEY, J., MENCHACA-ROCHA, A., OLMER, C., ZISMAN, M. S., Bull. Am. Phys. Soc. 23 (1978) 615, and preprint (1978).
- [15] GORDON, G. E., LARSH, A. E., SIKKELAND, T., SEABORG, G. T., Phys. Rev. 120 (1960) 1341.
- [16] SIKKELAND, T., HAINES, E. L., VIOLA, V. E., JR., Phys. Rev. 125 (1962) 1350.
- [17] VIOLA, V. E., JR., SIKKELAND, T., Phys. Rev. 128, (1962) 767.
- [18] VIOLA, V. E., JR., SIKKELAND, T., Phys. Rev. 130 (1963) 2044, and SIKKELAND, T., Phys. Lett. 31B (1970) 451.
- [19] SIKKELAND, T., Phys. Rev. 135 (1964) B669.
- [20] SIKKELAND, T., Phys. Lett. 27B (1963) 277.
- [21] SIKKELAND, T., CLARKSON, J. E., STEIGER-SHAFRIR, N. H., VIOLA, V. E., JR., Phys. Rev. C 3 (1971) 329.
- [22] DAVIES, K. T. R., SIERK, A. J., NIX, J. R., Phys. Rev. C 13 (1976) 2385.
- [23] VIOLA, V. E., JR., CLARK, R. G., MEYER, W. G., ZEBELMAN, A. M., SEXTRO, R. G., Nucl. Phys. A261 (1976) 174.
- [24] HALBERT, M. L., DAYRAS, R. A., FERGUSON, R. L., PLASIL, F., SARANTITES, D. G., Phys. Rev. C 17 (1978) 155.
- [25] OBENSHAIN, F. E., FERGUSON, R. L., HALBERT, M. L., HENSLEY, D. C., NAKAHARA, H., PLASIL, F., PLEASONTON, F., SNELL, A. H., STOKSTAD, R. G., Phys. Rev. C 18 (1978) 764.
- [26] BABINET, R., MORETTO, L. G., GALIN, J., JARED, R., MOULTON, J., THOMPSON, S. G., Nucl. Phys. A258 (1976) 172.
- [27] NGÔ, C., PÉTER, J., TAMAIN, B., BERLANGER, M., HANAPPE, F., Z. Phys. A 283 (1977) 161.
- [28] WOLF, K. L., UNIK, J. P., HUIZENGA, J. R., BIRKELUND, J., FREIESLEBEN, H., VIOLA, V. E., JR., Phys. Rev. Lett. 33 (1974) 1105.
- [29] HEUSCH, B., VOLANT, C., FREIESLEBEN, H., CHESTNUT, R. P., HILDENBRAND, K. D., PÜHLHOFER, F., SCHNEIDER, W. F. W., KOHLMAYER, B., PFEFFER, W., Z. Phys. A 288 (1978) 391.
- [30] BECKERMAN, M., BLANN, M., Phys. Lett. 68B (1977) 31.
- [31] BURNETT, D. S., GATTI, R. C., PLASIL, F., PRICE, P. B., SWIATECKI, W. J., THOMPSON, S. G., Phys. Rev. 134 (1964) B956.

- [32] MORETTO, L. G., THOMPSON, S. G., ROUTTI, J., GATTI, R. C., Phys. Lett. 38B (1972) 471.
- [33] KHODAI-JOOPARI, Ph. D. Thesis, University of California, Lawrence Radiation Laboratory Report UCRL-16489 (1966).
- [34] BLANN, M., PLASIL, F., ALICE: A Nuclear Evaporation Code, U.S.A.E.C. Report COO-3494-10 (1973).
- [35] PLASIL, F., FERGUSON, R. L., HAHN, R. L., OBENSHAIN, F. E., PLEASONTON, F., SNELL, A. H., YOUNG, G. R., to be published.
- [36] KRAPPE, H. J., NIX, J. R., Proceedings of the Third Symposium on the Physics and Chemistry of Fission 1, International Atomic Energy Agency, Vienna (1974) 159.
- [37] PLASIL, F., FERGUSON, R. L., PLEASONTON, F., Proceedings of the Third Symposium on the Physics and Chemistry of Fission 2, International Atomic Energy Agency, Vienna (1974) 319.
- [38] PLASIL, F., FERGUSON, R. L., OBENSHAIN, F. E., SNELL, A. H., YOUNG, G. R., to be published.
- [39] BLANN, M., private communication (1979).
- [40] GAVRON, A., PACE, adapted from HILLMAN, M., EYAL, Y., Proceedings of the European Conference on Nuclear Physics with Heavy Ions (FERNANDEZ, B., HARAR, S., JACMART, J. C., PÉTER, J., GUGENBERGER, Eds.), European Physical Society, Caen (1976) 109; private communication 1978.

## DISCUSSION

J.B. WILHELMY: Did you attempt to determine the  $a_f/a_v$  ratios using microscopic level densities? And do you think an analysis such as that would alter your conclusions regarding the height of the liquid-drop barrier?

R.L. FERGUSON: We have made calculations, based on a Monte-Carlo-type programme compiled by A. Gavron, of the fission excitation function for  $^{35}\text{Cl} + ^{116}\text{Sn}$  (see Fig.15 in the paper). Since we do not yet understand the discrepancies between the Monte-Carlo calculation and that of Beckerman and Blann for this same system, I would be reluctant to try to guess what the effect of such an analysis would be.

B. SCHRODER: Regarding the statement at the end of your paper that the 80% reduction in the rotating-liquid-drop model (RLDM) prediction agrees with the single Yukawa model proposed by Nix and co-workers, I would say that it is only true at the  $\beta$ -stability line. For a system beyond this line the liquid-drop model and the single Yukawa model yield much the same barrier values, for instance, for  $^{153}\text{Tb}$ .

W. REISDORF: As far as I can see, what you are actually doing is determining the fission barrier for the same average weighted angular momentum. Your conclusions regarding the absolute height of the fission barrier are also based on the angular momentum dependence predicted by the RLDM. How well is this dependence determined by the data?

R.L. FERGUSON: The barrier we calculated is, in fact, the one for the non-rotating-liquid-drop model. We feel that in the restricted range of reactions considered the rotating-drop model has been shown to agree reasonably well with experimental data.

E. CHEIFETZ (*Chairman*): In non-rotating-liquid-drop calculations there is a point in the fissility parameter ( $Z = 35-40$ ) below which the system tends to become asymmetric. What is the effect of angular momentum on this point, and can it explain some of the results for the light systems?

R.L. FERGUSON: The predicted effect of angular momentum on the Businaro-Gallone point is to transform it into a curve that increases with increasing angular momentum and decreasing fissility. Thus the expected asymmetric instability sets in at higher angular momentum values for lower values of the fissility parameter. I do not believe that any of the systems we considered were affected by the Businaro-Gallone asymmetry.

# MASS AND KINETIC-ENERGY DISTRIBUTIONS OF FRAGMENTS FORMED IN THE HEAVY-ION-INDUCED FISSION OF $^{208}\text{Po}$

J.G. CUNINGHAME, J.A.B. GOODALL  
Chemistry Division,  
AERE Harwell

J.E. FREEMAN, G.W.A. NEWTON, V.J. ROBINSON  
Department of Chemistry,  
Manchester University

J.L. DURELL, G.S. FOOTE, I.S. GRANT  
Schuster Laboratories,  
Manchester University

J.D. HEMINGWAY  
Universities Reactor,  
Risley, United Kingdom

## Abstract

MASS AND KINETIC-ENERGY DISTRIBUTIONS OF FRAGMENTS FORMED IN THE  
HEAVY-ION-INDUCED FISSION OF  $^{208}\text{Po}$ .

Fission fragments following the decay of a  $^{208}\text{Po}$  compound nucleus have been observed by using radiochemical and particle-counting techniques. The ( $\alpha + ^{204}\text{Pb}$ ), ( $^{12}\text{C} + ^{196}\text{Pt}$ ) and ( $^{16}\text{O} + ^{192}\text{Os}$ ) reactions were studied at two or three bombarding energies, covering overlapping ranges of excitation energies. — Radiochemical separations of As, Br, Y, Nb, Tc, Ag, Sb and I isotopes were made from catcher foils sandwiching isotopic targets, and their isotopic yield distributions determined. The distributions are used to estimate the average number of neutrons associated with each fission event, including neutrons emitted before and after fission. — Prompt coincidence measurements of fragments are used to derive the overall mass and kinetic-energy distributions of primary fragments, taking into account the effects of pre- and post-fission neutron emission. The mass distributions are well fitted by the statistical theory, at a temperature corresponding to an excitation about 10 MeV above that at the saddle point. No evidence is found for an increase of kinetic energy with increasing angular momentum of the compound nucleus.

## 1. INTRODUCTION

The compound nucleus  $^{208}\text{Po}$  can be produced in the ( $\alpha + ^{204}\text{Pb}$ ), ( $^{12}\text{C} + ^{196}\text{Pt}$ ) and ( $^{16}\text{O} + ^{192}\text{Os}$ ) reactions. We have studied fission products from these reactions at bombarding energies available from the

TABLE I. NUCLEAR PROPERTIES IN THE DECAY OF A  $^{208}\text{Po}$  (COMPOUND NUCLEUS)

Reaction	$E_{\text{lab}}$ (MeV)	$E_{\text{CN}}^*$	$E_S$	$\bar{I}^2$	TKE	$E_{\text{rot}}$	$\sigma_E$	$\sigma_A$				$\sigma_I$		$v_{\text{pre}}$	$v_{\text{tot}}$
								exp	saddle	10 MeV	20 MeV	exp	calc		
$\alpha + \text{Pb}$	50	44.4	17.1	384	147.0	0.4	9.4	11.2	10.6	11.8	12.7	-	-	0.7	5.9
	65	59.1	23.1	463	147.1	0.5	9.8	12.3	11.2	12.2	13.0	$1.6 \pm 0.1$	1.7	1.6	6.9
	80	73.8	28.1	561	147.1	0.6	10.1	13.0	11.6	12.5	13.3	$1.7 \pm 0.2$	1.8	2.4	7.3
$C + \text{Pt}$	93	70.9	26.7	1256	147.1	1.4	9.1	11.6	11.4	12.4	13.2	$1.6 \pm 0.1$	1.8	2.3	7.3
	105	85.0	29.8	1577	147.0	1.7	9.1	12.4	11.7	12.6	13.3	$1.5 \pm 0.1$	1.8	2.9	7.3
$O + Os$	106	76.3	27.2	1456	144.4	1.6	9.9	12.7	11.5	12.4	13.2	-	-	2.4	7.8
	119	88.3	31.1	1946	146.8	2.1	10.5	13.4	11.7	12.6	13.4	-	-	3.0	8.6

$E_{\text{CN}}^*$  is the excitation energy of the compound nucleus;

$E_S$  the average excitation of the fissioning nucleus above the saddle point;

$\bar{I}^2$  the mean square angular momentum of the fissioning nucleus;

TKE the mean total kinetic energy of primary fragments;

$E_{\text{rot}}$  the rotational contribution to TKE;

$\sigma_E$  the standard deviation of TKE for a particular mass ratio;

$\sigma_A$  the standard deviation of the overall mass distribution - the calculated values are for the saddle point temperature and for temperatures 10 and 20 MeV above the saddle point;

$\sigma_I$  the standard deviation of the mass distribution for a single element - the calculated values are for a temperature 10 MeV above the saddle point;

$v_{\text{pre}}$  the average number of pre-fission neutrons estimated with ALICE;

$v_{\text{tot}}$  the total number of neutrons per fission derived from radiochemical measurements.

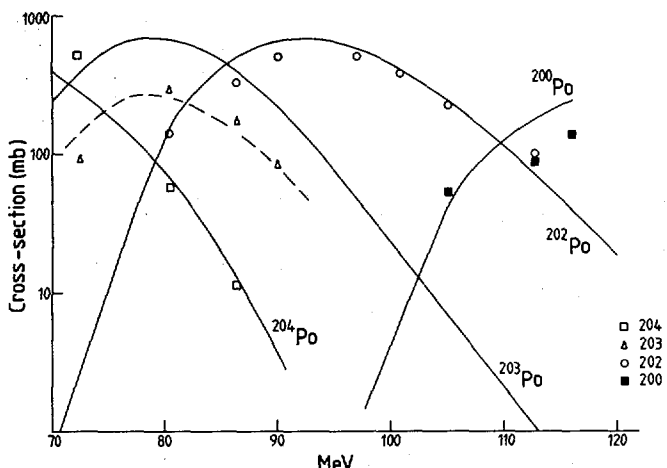


FIG.1. Comparison of measured  $^{196}\text{Pt} (^{12}\text{C}, xn)$  cross-sections with the predictions of the ALICE code.

Harwell Variable Energy Cyclotron. The excitation ranges of the  $^{208}\text{Po}$  nuclei resulting from the different reactions overlap, and cover a wide range of average angular momenta. The aim of the study is to learn, using a combination of radiochemical and particle counting techniques, how the properties of fission products depend on excitation and on angular momentum. Unfortunately, if the bombarding energy is high enough to overcome the Coulomb barrier, the  $^{208}\text{Po}$  nucleus is already at an excitation high enough for multichance fission to occur. Polonium nuclei are not very fissionable, and neutron emission is the most probable decay mode. The fission barrier is lower in the daughter nucleus, so that the loss of excitation is largely compensated, and fission competes effectively until the excitation energy is close to the barrier height. In order to measure the kinetic energy of primary fission fragments, we must know the number of neutrons emitted after fission, and it is therefore important to be able to make reliable estimates of multichance cross-sections.

The multichance fission cross-sections have been estimated with a modified version of the evaporation code ALICE(1). The level density in the code has the form described by Dössing and Jensen(2), in which shell and pairing effects are allowed to fade exponentially with increasing excitation. Collective enhancement of the saddle-point level density(3) is also allowed to fade exponentially, and the fission barrier is reduced to 95% of its liquid-drop value. The level density parameter is taken to be  $A/15$  both for ground-state and saddle-point deformations. At bombarding energies well above the Coulomb barrier, a small fraction of the reaction cross-section is in partial waves above the critical angular momentum for complete fusion proposed by Bass (4); all partial waves above the critical value are discarded.

To test the code, we have measured cross-sections for the  $2 + 0$  ground state band transitions in even-even Po nuclei in the ( $\alpha + ^{204}\text{Pb}$ ) and

( $^{12}\text{C} + ^{196}\text{Pt}$ ) reactions. The ALICE predictions are compared with the measured values in figure 1, which also includes the cross-section for the 641.3 keV transition in  $^{203}\text{Po}$  (clearly the  $^{203}\text{Po}$  nuclei do not all decay through this transition). The same set of parameters also gives a good fit to the  $^{204}\text{Pb}(\alpha, \text{xn})$  cross-sections and to the ratio  $T_f/T_t$  in the  $\alpha + ^{206}\text{Pb}$  reaction (5).

The code shows that fission following proton or  $\alpha$ -emission is negligible, but that fission does persist in the neutron evaporation chain to excitation energies close to the barrier. The average number of pre-fission neutrons, and the average angular momentum and excitation of the fissioning nucleus, are listed in Table I for all the systems studied. All these quantities are required in the analysis of the radiochemical and particle counting data.

## 2. RADIOCHEMICAL MEASUREMENTS

The same beam line at the A.E.R.E. Variable Energy Cyclotron is used for particle coincidence measurements and for the irradiations for radiochemical measurements. The beam (defined by a multistage  $\frac{1}{8}$ " diameter collimator) passes through a scattering chamber into a small chamber containing a target mounted between two magnesium catcher foils. The target and the catcher foils are mounted on separate cooled holders, and the catchers can be removed through a vacuum interlock without disturbing the target. The target itself can be withdrawn from the beam axis under vacuum, during particle measurements in the scattering chamber.

The  $^{204}\text{Pb}$  and  $^{196}\text{Pt}$  targets were self-supporting rolled metal foils. It proved very difficult to make satisfactory osmium targets. Some irradiations were carried out on targets consisting of  $^{192}\text{Os}$  powder pressed between Al foils, and others on  $^{192}\text{Os}$  electroplated onto a thin nickel backing from a solution of  $\text{OsO}_4$  dissolved in ammonia. The plated osmium is not very cohesive, and satisfactory targets could not be made thicker than  $1\text{mg/cm}^2$ . Comparison runs with the two types of targets gave similar mass distributions for chemically separated fission fragment activities, confirming that the particle size of the osmium powder was small enough not to introduce a bias in the mass distribution of fragments reaching the catcher foils. The magnesium catcher foils were thick enough to stop all fission fragments.

Irradiation times were between half an hour and three hours. The beam was collected in a Faraday cup, and monitored by a current integrator driving a chart recorder and printing the integrated count at frequent intervals. After an irradiation the catcher foils were removed and dissolved in acid, and the element of interest separated by conventional radiochemical techniques: As and Sb were separated by volatilisation of their hydrides (6) and all other elements by solvent extractions (7). In a typical run,  $\gamma$ -counting began 15-20 min after the end of the irradiation. Peak fitting was done with the SAMPO programme, and in all cases assignments of activities were based on half-lives as well as energies. Cumulative yields were derived from the fitted decay curves, making corrections where necessary for beam fluctuations. The contributions from feeding by  $\beta$ -decay precursors were calculated assuming that for each reaction the mass width before  $\beta$ -decay was the same for all elements, and requiring the yield of each element to be consistent with the overall mass distribution measured in the particle experiments.

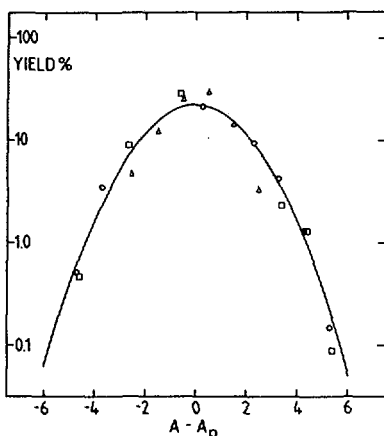


FIG.2. Isotopic mass distribution for the system  $^{12}\text{C} + ^{196}\text{Pt}$  at 93 MeV. Experimental points are normalized to 100% for each element.

The mass yield of Y, Sb and I, normalised to 100% yield for each element, is shown in figure 2 for the ( $\text{C} + \text{Pt}$ ) reaction at a mean bombarding energy of 93 MeV (corrections have been made to allow for energy loss in the target and the backward catcher foil). The most probable masses are shown for all the reactions in Table II and the mass widths  $\sigma_1$  for the  $\alpha + \text{Pb}$  and  $\text{C} + \text{Pt}$  reactions are shown in Table I. It is very striking that the width of the isotopic mass distributions is more or less independent of the excitation and angular momentum of the  $^{208}\text{Po}$  compound nucleus, even though up to six Po nuclei make comparable contributions to the multichance fission cross-section. This is in contrast with high energy proton-induced fission, in which pre-compound processes cause the fragment mass distributions to broaden with increasing excitation energy (8). In the heavy ion reactions, pre-fission and post-fission neutron evaporation are evidently associated with almost the same loss in excitation energy, and thus multichance fission is not a source of mass dispersion. Evidence from the coincidence experiments shows that the spread in excitation energy of the primary fragments is small enough not to contribute much to the mass dispersion of the chemically separated fragments: the observed mass widths are therefore close to the mass width of the primary fragments at any one stage of the multichance fission process. These widths are further considered in section 5.

In figure 3, the most probable mass  $A_p$  of chemically separated fragments is plotted (on an expanded scale) as a function of  $Z$ . Also plotted (curve (a)) are the values of  $A_p$  for the primary fragment, calculated on the MEESST prescription (maximum excitation energy sans shell) with the mass routine from ALICE; these  $A_p$  values are averages for the chain of Po nuclei, weighted by the multichance fission cross-sections. The data are consistent with the assumption that the average number  $v$  of post-fission neutrons emitted by the fragments is proportional to  $A_p$  - the line (b) through the points in the figure assumes  $v \propto A_p$ .

TABLE II. MOST PROBABLE MASSES  $A_p$  OF CHEMICALLY SEPARATED FRAGMENTS IN HEAVY-ION FISSION

Reaction	Element	Bombarding Energy (MeV)		
		50	65	80
$A_p$				
$\alpha + {}^{204}\text{Pb}$	As	-	77.2±0.5	77.1±0.3
	Br	83.0±0.7	83.7±0.4	83.1±0.3
	Y	93.4±0.4	93.1±0.1	92.8±0.1
	Ag	113.5±0.3	112.9±0.3	112.2±0.3
	Sb	125.5±0.5	123.8±0.1	123.2±0.1
	I	130.6±0.3	129.4±0.3	128.4±0.2
Bombarding Energy				
${}^{12}\text{C} + {}^{196}\text{Pt}$		79	93	105
	$A_p$			
	As	-	78.4±0.3	78.2±0.3
	Br	83.8±0.5	83.6±0.5	83.3±0.5
	Y	92.8±0.1	92.5±0.1	92.6±0.1
	Nb	98.0±0.5	97.7±0.2	97.4±0.2
${}^{16}\text{O} + {}^{192}\text{Os}$	Tc	103.2±0.5	102.9±0.4	102.8±0.5
	Ag	113.0±0.6	112.8±1.0	112.6±0.7
	Sb	123.3±0.1	122.6±0.1	122.6±0.4
	I	128.8±0.2	127.7±0.1	128.0±0.1
	Bombarding Energy			
		90	106	119
${}^{16}\text{O} + {}^{192}\text{Os}$	$A_p$			
	Y	92.5±0.1	92.5±0.2	-
	Nb	96.9±0.2	97.6±0.5	96.9±0.2
	Tc	102.5±0.4	102.2±0.6	102.1±0.3

### 3. FISSION FRAGMENT COINCIDENCES

A target ladder on the axis of the scattering chamber carries targets and a  ${}^{252}\text{Cf}$  source for calibrations: one of the ladder positions is left blank to allow high beams to pass during radiochemical irradiations. The two surface barrier counters used for measuring fission fragment coincidences are not mounted symmetrically with respect to the beam axis. This is because in heavy ion reactions the centre of mass velocity is not small compared with the fragment velocity, and the laboratory correlation angle between the

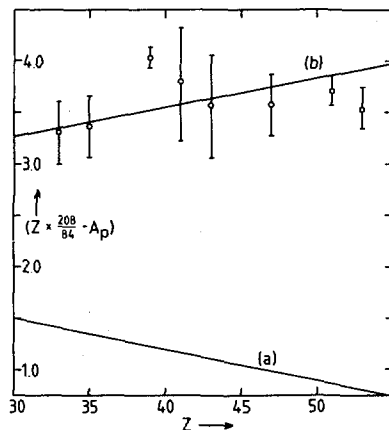


FIG.3. Most probable mass as a function of Z for the system  $^{12}\text{C} + ^{196}\text{Pt}$  at 93 MeV. The calculated distribution (a) is for primary fragments; (b) is for final fragments, assuming  $\nu \ll A_p$ .

fragments depends on the total kinetic energy of the fission event. The spread in correlation angles is reduced when the fragments are observed close to the beam axis. One counter is fixed at  $30^\circ$  to the beam direction, and the other is on a moveable arm. The forward counter is about 1m from the target and subtends a small solid angle, while the collimator on the backward counter is adjusted to select a solid angle large enough to ensure collection of almost all the complementary fragments in coincidence with fragments reaching the  $30^\circ$  detector. To minimise the electron and photon flux, the backward detector is protected by a ring magnet and a thin nickel foil.

For accurate measurement of fragment energies and masses in the heavy ion reactions, careful calibration procedures are essential. Preliminary calibrations were made with a precision pulse generator and  $\alpha$ -sources to establish the zero channel and amplifier gain, but the final counter parameters were determined with a  $^{252}\text{Cf}$  source on a thin nickel backing. Calibration runs were made with this source facing each counter in turn. Pulse heights from both counters, together with the pulse heights from a TAC registering coincidences, were recorded event-by-event. The parameters for both counters are fitted simultaneously to the coincidence data; the method of analysis is described in more detail in the next section. Calibrations of this kind were carried out before and after heavy ion runs. Singles calibrations were also taken from time to time, to check the calibration of the backward counter, which was subjected to a much higher particle flux than the  $30^\circ$  counter.

In the heavy ion runs, the mean angle between the fragments was up to  $90^\circ$  away from collinearity. The best setting for the backward detector was found by measuring the angular correlation at  $10^\circ$  intervals. In the ( $\alpha + \text{Pb}$ ) reactions the correlation function was clearly flat-topped, showing that all coincidences were detected. The correlations for the ( $\text{C} + \text{Pt}$ ) and ( $\text{O} + \text{Os}$ ) reactions did not have well-defined flat tops, and indeed the full analysis of the data shows that some events are missed in the extreme wings of the

fragment distributions, when energetic particles of very low mass reach the forward detector and the slow-moving complementary fragments are thrown forward of the acceptance angle of the other detector.

The  $^{204}\text{Pb}$  targets were evaporated onto thin carbon backings; both  $^{196}\text{Pt}$  and  $^{192}\text{Os}$  were electroplated onto nickel-plated copper, and the copper later dissolved away. As for the radiochemistry targets, osmium proved troublesome, and the  $^{192}\text{Os}$  targets, at about  $0.5\text{mg/cm}^2$ , were more than their optimum thickness. Important mass- and energy-dependent corrections have to be made for fragment energy loss in traversing target and backing. The target and backing thicknesses were therefore measured using the fission fragments themselves. Coincidence spectra were taken with the target at different angles to the fragment directions, with the backing towards each counter in turn. Interpolating Northcliffe and Schilling's tables to estimate the energy loss of symmetrical fragments, target and backing thicknesses were determined by a least-square fit to the mean energies in the two detectors.

#### 4. ANALYSIS OF THE EVENT-BY-EVENT DATA

The  $^{252}\text{Cf}$  source data are used to determine the best values of the counter parameters. Labelling the counters 1 and 2, the data for each event are the pulse heights,  $P_1$  and  $P_2$ .  $(P_1 + P_2)$  is a rough measure of the total kinetic energy (TKE) of the pair of fragments, and for a stationary source  $P_2/P_1$  is on average equal to the mass ratio of the primary fragments; thus the quantity  $P_2/(P_1 + P_2)$  indicates the mass of the primary fragment which, after emitting neutrons, reaches counter 1. Events are assigned to a cell in an equally spaced mesh using the co-ordinates  $(P_1 + P_2)$  and  $P_2/(P_1 + P_2)$ . The yield in each cell is converted to a point value at the centre of the cell by making second order finite difference corrections.

A grid is now set up with equal spacings in primary fragment mass and TKE. At each point on the grid, pulse heights are calculated for both counters. The pulse-height defect is estimated using the empirical expression of Kaufman et al (9), which is a one-parameter function valid for all masses, expressed in terms of the dimensionless energy units defined by Lindhard et al (10). The primary fragment energies are modified to allow for emission of the mean number of neutrons for each TKE and mass: the neutron data is taken from Bowman et al (11). The energy losses in the source backing and the nickel foil are estimated as in the target thickness measurement with an empirical stopping power function, using effective charges derived from the most probable atomic number for fragments of each mass. Each mesh point on the primary mass-TKE array is now located on the pulse-height grid, and yields and masses may be interpolated from one grid to another. The yield on the primary mass-TKE grid must be symmetrical, since both counters are observing the same source. The counter gains and the pulse-height defect parameters are then varied to give symmetrical yields and to reproduce the mean masses and energies of light and heavy fragments measured by Kaufman et al (9). (This procedure is analogous to the method of Schmitt, Lide and Pleasonton (12) for measuring neutron numbers in  $^{252}\text{Cf}$  fission. Time differences were recorded in our event-by-event data, and the counter parameters were also constrained to match the time differences. Excellent fits to the neutron number data were obtained by allowing the counters to have a small linear time-walk).

Exactly the same procedure is then applied to the data from the heavy ion runs. In the heavy ion reactions we have studied, the ratio of the

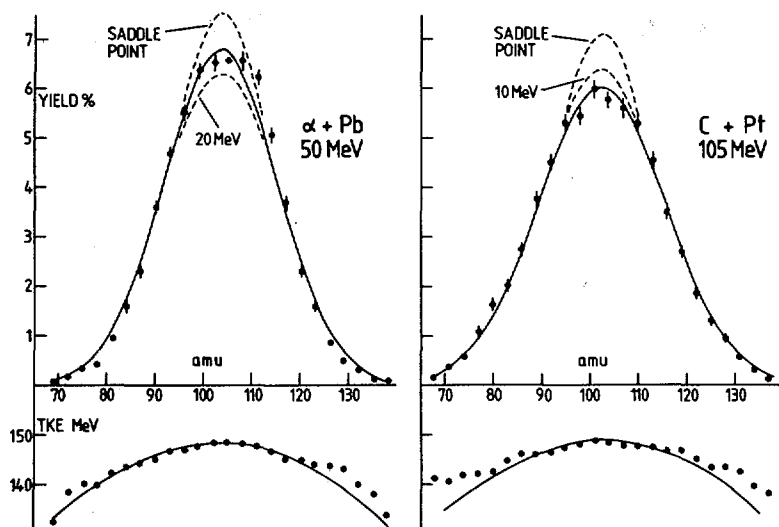


FIG.4. Overall mass and kinetic-energy distributions in  $^{208}\text{Po}$  fission. The full line assumes an excitation above the saddle point of 10 MeV for the  $\alpha + \text{Pb}$  data, 20 MeV for the  $\text{C} + \text{Pt}$  data.

energies of the forward and backward fragments is roughly two to one, and it is better to use  $(P_1 + P_2)$  and  $2P_2/(2P_2 + P_1)$  as the pulse-height coordinates. Kinematic corrections must be made to allow for the centre of mass motion, but once again yields can be found by interpolating between the two grids. In all cases, the forward fragment had an energy within the range covered by the  $^{252}\text{Cf}$  calibration. The backward fragment, however, has an energy below the heavy fragment peak in the  $^{252}\text{Cf}$  spectrum. In deriving the yields in the heavy ion fission reaction, the pulse-height defect parameter in the backward counter was again allowed to float, and the yield map constrained to be symmetrical about the central mass. The fissioning nucleus was assumed to have a fixed mass equal to the mass of the compound nucleus less the mean number of pre-fission neutrons. Post-fission neutron numbers were assumed to be proportional to fragment mass; an increase of 10 MeV in TKE is associated with a reduction of one in the sum of the neutron numbers of the two fragments. The total number of neutrons emitted before and after fission, and averaged over all energies, is required to agree with the radiochemical mass yields.

The final result of the analysis is a set of point yields on a regular grid of primary fragments masses and TKE values. Projections of the yields onto the mass axis, and average TKE for different masses, are shown in figure 4 for the ( $\alpha + \text{Pb}$ ) reaction at 50 MeV and for the ( $\text{C} + \text{Pt}$ ) reaction at 105 MeV. Mass widths and mean TKE values for all the systems studied are summarised in Table 1.

## 5. DISCUSSION

Most of the fissions in the heavy ion reactions occur at excitations far above the barrier. Statistical considerations apply and the mass and

charge distributions of the fragments are determined by the density of states. We have taken the view that the relevant density of states is for a nucleus which has moved beyond the saddle point, some way towards scission, and having a temperature greater than the saddle point temperature. The excitation energy of a fragment pair ( $Z_1, A_1$ ), ( $Z_2, A_2$ ), from which their temperature is derived, is assumed to be the excitation above the saddle point plus a fixed amount to allow for the change in potential energy in motion towards scission plus a Q-value correction plus a Coulomb correction. The Q-value correction, which is the difference between the Q-value for the fragment pair and for symmetric fragments, is calculated with liquid drop masses. The Coulomb correction is  $(1-4Z_1Z_2/Z^2)TKE_{max}$ , which applies if the fragment kinetic energy is simply proportional to  $Z_1Z_2$ . The full lines through the TKE data in figure 4 are based on this approximation, which accounts reasonably well for the variation of TKE with mass ratio.

The yield of each fragment pair is taken to be proportional to the product of level densities, which are calculated with a level density parameter  $A/15$ . The yield distributions for each step in the multichance fission are summed, with weightings according to the cross-sections given by the ALICE programme, with the results shown in figure 4. The data in the figure are well fitted over the whole mass range by a suitable choice of excess excitation beyond the saddle point. Overall mass variances are listed for all the systems in Table II, and in every case the saddle point temperature is too low. The biggest uncertainty in the analysis is the magnitude of the multichance fission cross-sections. In our judgement, however, the level densities used in ALICE are realistic, and our observations favour the notion that the fragment mass distributions are determined near an "exit" point (13) rather than at the saddle point.

The theoretical yields for different masses of the same element are shown for ( $C + Pt$ ) at 93 MeV by the full line in figure 2, assuming a temperature 10 MeV higher than the saddle point value. The experimental distribution is a little narrower than the calculated one, a finding which is repeated for all systems. A possible reason for this is that because the symmetry force is very strong,  $Z/A$  equilibration persists almost to scission, until a moment when the mass ratio is already roughly determined. It is known from deep inelastic scattering measurements that  $Z/A$  equilibration is a very rapid process (14).

The column in Table II labelled  $\sigma_E$  represents an average value for the standard deviation of the TKE values within one mass bin. In all cases  $\sigma_E$  is almost constant except in the extreme wings of the mass distribution, where it becomes smaller. The associated spread  $\frac{1}{2}\sigma_E$  in the excitation energy of a single symmetric fragment is about 5 MeV, or in terms of a mass distribution, about 0.5amu. The experimental observations have shown that the width of the post-neutron emission mass distribution is insensitive to compound nucleus excitation, and we may deduce that this width is almost the same as for the primary fragments.

The mean value of TKE does not reproduce the increase with angular momentum reported by Unik et al (15). However, Unik et al assumed only first chance fission, and did not allow for the reduction in energy available for neutron emission at high angular momenta. The  $^{208}Po$  nucleus is very elongated even at its saddle point, and the rotational energy is consequently small. The column headed  $E_{rot}$  in Table I is the rotational contribution to TKE expected with classical moments of inertia for the saddle point nucleus, i.e. its total rotational energy minus the collective rotational energy of each fragment. In each reaction the relative uncertainty in TKE to errors in

neutron number is estimated to be 0.4 MeV; in addition there may be systematic errors in the energy loss corrections. Apart from one of the osmium runs which appears to be anomalous, the TKE values are essentially constant. Since the target thickness measurements were based on the energies of the fission fragments themselves, it is unlikely that the energy loss measurements are in error by as much as the 1.6 MeV spread in rotational contributions to TKE. The data suggest that in the range of angular momenta covered by these experiments, the rotational contribution is roughly compensated by centrifugal stretching of the saddle point nucleus.

### ACKNOWLEDGEMENTS

We wish to thank R.W. McIlroy and the operating staff of the Harwell VEC for providing us with the irradiations. We also wish to acknowledge the work of the late Dr. J.E. Freeman in carrying out most of the radiochemical separations.

### REFERENCES

- [1] BLANN, M., PLASIL, F., Phys. Rev. Lett. 24 (1972) 103.
- [2] DØSSING, T., JENSEN, A.S., Nucl. Phys. A222 (1974) 493.
- [3] BJØRNHOLM, S., MOTTELSON, B.R., Physics and Chemistry of Fission (Proc. Int. Conf. Rochester, 1973) 1, IAEA, Vienna (1974) 367.
- [4] BASS, R., Phys. Lett., 47B (1973) 143.
- [5] MORETTO, L.G., Physics and Chemistry of Fission (Proc. Int. Conf. Rochester, 1973) 1, IAEA, Vienna (1974) 329.
- [6] FREEMAN, J.E., et al., J. Inorg. Nucl. Chem. 38 (1976) 941.
- [7] FREEMAN, J.E., NEWTON, G.W.A., ROBINSON, V.J., J. Rad. Chem. 24 (1975) 433.
- [8] GALINIER, J.L., YAFFE, L., J. Inorg. Nuc. Chem. 39 (1977) 1497.
- [9] KAUFMAN, S.B., et al., Nucl. Inst. Methods 115 (1974) 47.
- [10] LINDHARD, J., SCHARFF, M., SCHIØTT, H.E., Mat. Fys. Medd. Dan. Vid. Selsk. 33 14 (1963) 1.
- [11] BOWMAN, H.R., et al., Phys. Rev. 129 (1963) 2133.
- [12] SCHMITT, H.W., LIDE, R.W., PLEASONTON, F. Nucl. Inst. Methods 63 (1968) 237.
- [13] BRACK, M., et al., Rev. Mod. Phys. 44 (1972) 320.
- [14] GATTY, B., et al., Nucl. Phys. A253 (1975) 511.
- [15] UNIK, J.P., CUNINGHAME, J.G., CROALL, I.F., Physics and Chemistry of Fission (Proc. Int. Conf. Vienna, 1969) IAEA, Vienna (1969) 717.

### DISCUSSION

J. PETER: Just a short comment. We have also observed that there was no increase in the total kinetic energy with angular momentum (within an experimental accuracy of 1–2 MeV, which is much lower than the rotational energy), even for  $\ell$  up to 100 or 110. The only explanation we can give is that the increase normally due to the rotational energy is compensated here by the more elongated shape of the scission point and that this reduces the Coulomb repulsion.



# INFLUENCE DU MOMENT ANGULAIRE SUR LA LARGEUR DES DISTRIBUTIONS DE MASSE DE FISSION INDUITE PAR IONS LOURDS

*Existe-t-il un troisième mécanisme entre  
la fission et les collisions très inélastiques?*

F. HANAPPE\*, J. PETER, B. TAMAIN

Institut de physique nucléaire,  
Orsay,

C. LEBRUN, J.F. LECOLLEY, F. LEFEBVRES

Laboratoire de physique corpusculaire  
associé à l'IN2P3, ISMRA,  
Université de Caen,  
Caen,

C. NGÔ,  
DPh-N-MF,  
CEA, Centre d'études nucléaires de Saclay,  
Gif-sur-Yvette,  
France

## Abstract—Résumé

### INFLUENCE OF ANGULAR MOMENTUM ON THE WIDTH OF THE MASS DISTRIBUTION OF HEAVY-ION INDUCED FISSION: IS THERE A THIRD MECHANISM BETWEEN FISSION AND THE HIGHLY INELASTIC COLLISIONS?

The systems  $^{20}\text{Ne} + ^{\text{nat}}\text{Re}$  at 124 and 206 MeV and  $^{40}\text{Ar} + ^{165}\text{Ho}$  at 192 and 197 MeV were used to produce the  $^{205}\text{At}$  nucleus with different populations of angular momentum. The mass distributions of the fission products were measured. After allowing for the effects of temperature and neutron evaporation, it is found that the widths of the mass distributions increase considerably when the fission barrier disappears. Comparison of the results obtained here with those of other authors suggests that a third intermediate mechanism exists between fission and the highly inelastic collisions.

---

\* Fonds national de la recherche scientifique, détaché de Physique nucléaire expérimentale, CP229, Université libre de Bruxelles, Bruxelles, Belgique.

## INFLUENCE DU MOMENT ANGULAIRE SUR LA LARGEUR DES DISTRIBUTIONS DE MASSE DE FISSION INDUIITE PAR IONS LOURDS: EXISTE-T-IL UN TROISIÈME MÉCANISME ENTRE LA FISSION ET LES COLLISIONS TRÈS INÉLASTIQUES?

Les systèmes  $^{20}\text{Ne} + ^{\text{nat}}\text{Re}$  à 124 et 206 MeV et  $^{40}\text{Ar} + ^{165}\text{Ho}$  à 192 et 197 MeV ont été utilisés pour produire le noyau  $^{205}\text{At}$  avec différentes populations de moment angulaire. Les distributions de masse des produits de fission ont été mesurées. Après avoir tenu compte des effets de la température et de l'évaporation de neutrons, on observe que les largeurs des distributions de masse augmentent considérablement lorsque la barrière de fission a disparu. Une comparaison des résultats obtenus dans ce travail et par d'autres auteurs amène à penser qu'il existe un troisième mécanisme intermédiaire entre la fission et les collisions très inélastiques.

### INTRODUCTION

On admet pour le moment l'existence de deux mécanismes de réactions faisant intervenir un grand nombre de nucléons:

— *La fusion de deux noyaux en un noyau composé.* Ce dernier, lorsque sa masse est suffisamment élevée, peut avoir une probabilité non négligeable de se désexciter par fission. Cette probabilité augmente d'une part avec l'énergie d'excitation mais également avec le moment angulaire — les réactions induites par ions lourds présentent un grand intérêt pour étudier l'influence de ce dernier paramètre car de grandes valeurs de moment angulaire peuvent être mises en jeu. Les caractéristiques principales des produits de fission du noyau composé sont: une distribution de masse centrée à la masse moitié de celle du noyau composé en ce qui concerne les produits primaires et une distribution angulaire  $d\sigma/d\Omega$  très proche de  $1/\sin \theta$ .

— *Les réactions très inélastiques.* Dans ce cas, tous les nucléons ne participent pas à la réaction mais un grand nombre d'entre eux interagissent et l'on observe un haut degré d'inélasticité dans la réaction. La majorité des produits ont une masse proche des masses initiales des noyaux incidents et leur distribution angulaire est assez fortement focalisée dans un petit domaine d'angle. Toutefois on observe également des produits correspondant à des transferts de masse de plus en plus importants et donc à des temps d'interaction entre les deux noyaux de plus en plus grands, les produits ont alors une distribution angulaire qui se rapproche d'une distribution en  $1/\sin \theta$ .

— Dans le cas où l'on a *simultanément* les deux mécanismes précédents, il est possible de les distinguer si l'on part d'un système très asymétrique et si l'énergie de bombardement n'est pas trop élevée au-dessus de la barrière d'interaction [1]. En effet l'observation des distributions de masses permet de séparer

les contributions respectives de ces deux mécanismes. A haute énergie de bombardement, cette séparation ne devient plus possible car les distributions de masse des produits très inélastiques ainsi que celle des produits de fission s'élargissent et se mélangeant tellement qu'il n'est plus possible de distinguer deux composantes. Dans le cas d'un système symétrique, quelle que soit l'énergie de bombardement, il n'est pas possible de séparer les produits de fission des produits très inélastiques qui ont une distribution angulaire proche de  $1/\sin \theta$  [2].

L'évolution de la largeur de la distribution de masse des produits très inélastiques avec l'énergie de bombardement est à présent bien comprise: elle augmente d'une part à cause des fluctuations statistiques qui deviennent de plus en plus importantes mais aussi parce que le nombre de paramètres d'impact contribuant au processus très inélastique augmente. Au contraire l'évolution de la largeur des distributions de masse des produits de fission avec l'énergie d'excitation et le moment angulaire du noyau fissionnant reste encore mal connue. L'ensemble des résultats expérimentaux semble montrer que les largeurs augmentent avec la température du système fissionnant. En ce qui concerne l'influence du moment angulaire, lorsque celui-ci est assez important on observe une forte dépendance des largeurs, qui augmentent avec lui. Ceci a été constaté en utilisant des ions lourds comme projectiles pour former un noyau composé [3]. Toutefois, pour des valeurs de moment angulaire du noyau fissionnant plus faibles, la dépendance n'est pas aussi brutale et des résultats contradictoires ont été obtenus [4].

Nous nous sommes donc proposé d'étudier cet effet en formant le même noyau composé, le  $^{205}\text{At}$ , par deux voies d'entrée différentes de telle manière que la température soit à peu près la même mais que les populations de moment angulaire soient différentes. Deux expériences ont été effectuées: l'une en formant le noyau de  $^{205}\text{At}$  à la température d'environ 1,6 MeV, par les réactions  $^{20}\text{Ne} + ^{nat}\text{Re}$  à 124 MeV et  $^{40}\text{Ar} + ^{165}\text{Ho}$  à 192 MeV; l'autre en utilisant les mêmes systèmes mais des énergies incidentes de 206 MeV pour  $^{20}\text{Ne}$  et 297 MeV pour  $^{40}\text{Ar}$ . Dans ce dernier cas, le noyau composé est alors formé avec une température voisine de 2,2 MeV [5].

## RESULTATS

Les fragments de fission ont été détectés et identifiés par un télescope à temps de vol. L'énergie cinétique du fragment était mesurée à l'aide d'un détecteur à barrière de surface de  $900 \text{ mm}^2$  situé à 120 cm de la cible. Le temps zéro était donné par un système à galettes de microcanaux placé à 20 cm de la cible. La résolution en temps était de l'ordre de 500 ps alors que la résolution en masse, surtout limitée par la résolution en énergie du détecteur à semiconducteur évaluée à 2%, était de l'ordre de quelques unités de masse sur les fragments de fission.

TABLEAU I. ENERGIE DE BOMBARDEMENT DANS LES SYSTEMES DU LABORATOIRE ( $E_L$ ) ET DU CENTRE DE MASSE ( $E_{CM}$ ), ENERGIE D'EXCITATION MOYENNE ( $E^*$ ), ANGLE DE DETECTION DES FRAGMENTS ( $\theta$ ), LARGEUR A MI-HAUTEUR DES DISTRIBUTIONS DE MASSE, MESUREE (FWHM) ET CORRIGEE POUR L'EVAPORATION DE NEUTRON (FWHMC), MOMENT ANGULAIRE CRITIQUE CALCULE ( $\ell_c$ ) ET TEMPERATURE (T) DU NOYAU COMPOSE FISSIONNANT  $^{205}\text{At}$

Système	$E_L$ (MeV)	$E_{CM}$ (MeV)	$E^*$ (MeV)	$\theta$ (deg)	FWHM	FWHMC	$\ell_c$	T (MeV)
$^{20}\text{Ne} + ^{75}\text{Re}$	124	112	73	40	$29+3$ $38+3$	$30+3$	49	1,6
				27				
$^{40}\text{Ar} + ^{165}\text{Ho}$	206	186	149	40	$39+3$	$42+3$	86	2,2
				50	$39+3$			
				60	$37+3$			
$^{10}\text{Be} + ^{165}\text{Ho}$	192	154,5	68,5	30	$34+3$	$34+3$	55	1,6
				60	$33+3$			
	297	239	153	30	$52+4$	$56+4$	120	2,2
				60	$54+4$			

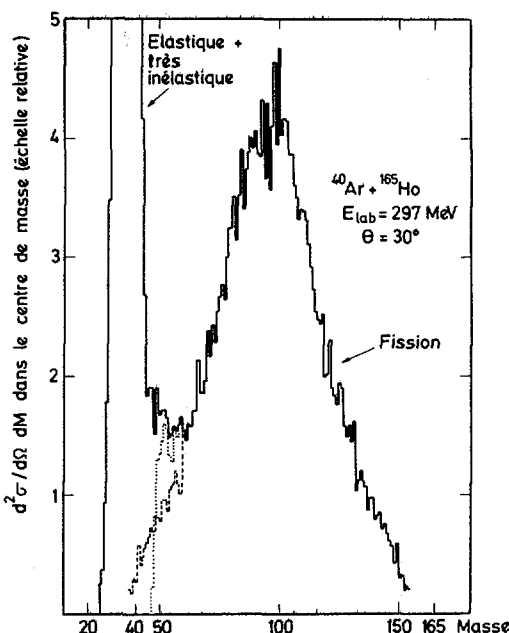


*FIG.1. Section efficace doublement différenciée en fonction de l'angle centre de masse et de la masse du fragment.*

Pour les systèmes què nous avons étudiés, il est aisé de séparer les produits très inélastiques des fragments de fission après fusion complète. Ceci est illustré à la figure 1 où est donnée une distribution de masse des produits dans un des cas pourtant parmi les plus défavorables. Les résultats expérimentaux concernant les largeurs de distribution de masse sont consignés dans le tableau I. La largeur à mi-hauteur de la distribution de masse des produits de fission correspond à celle des produits secondaires. On peut corriger l'effet dû à l'évaporation de neutrons par les fragments primaires au moins de manière moyenne, en supposant que l'énergie d'excitation (à laquelle on a soustrait l'énergie de rotation) se partage entre les fragments en proportion de leur masse [6]. Comme on peut le constater, l'évaporation a pour effet de diminuer les largeurs d'à peu près 1 uma à 1,6 MeV et 3 uma à 2,2 MeV. Les largeurs corrigées sont donc légèrement supérieures aux largeurs mesurées.

Les largeurs corrigées sont portées sur la figure 2 en fonction du moment angulaire maximum contribuant au processus de fusion  $I_c$ . Le moment angulaire critique ( $I_c$ ) a été calculé comme suit: à basse énergie incidente au-dessus de la barrière d'interaction, le processus de fusion est déterminé par la barrière de fusion du système. Lorsque l'énergie de bombardement augmente, cette barrière ne représente plus le paramètre déterminant pour que les deux noyaux fusionnent

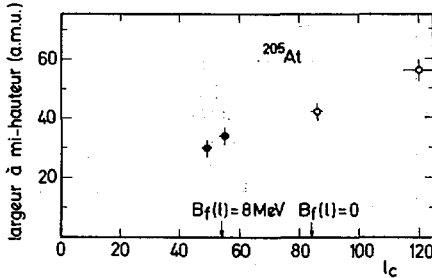


FIG.2. Largeur à mi-hauteur des distributions de masse de fission en fonction de  $l_c$ .

•  $T = 1.6 \text{ MeV}$ ; ○  $T = 2.2 \text{ MeV}$  [5].

et il est alors nécessaire de tenir compte du concept de distance critique [7]. Nous avons calculé le moment angulaire critique en utilisant ces concepts et le potentiel d'interaction des deux ions calculé par le formalisme de la densité d'énergie dans l'approximation soudaine [8]. Une fois le paramètre de distance critique choisi, il est aisément de voir dans quels cas la barrière de fusion ou la distance critique est le paramètre déterminant pour la fusion. Pour  $r_c$ , paramètre de distance critique, nous avons adopté la valeur de 1,05 fm obtenue par compilation des résultats expérimentaux [9]. L'utilisation de ce potentiel particulier permet de reproduire les moments angulaires avec une précision de l'ordre de 10 à 15% [10]. Pour les systèmes à haute énergie de bombardement, la fusion s'est avérée gouvernée par la distance critique, alors qu'à basse énergie on observe un régime transitoire entre la barrière de fusion et la distance critique.

## DISCUSSION

La variation de la largeur des distributions de masse des produits de fission est le reflet de deux effets: d'une part la température du système intrinsèque et d'autre part du moment angulaire du noyau fissionnant. L'effet de la température est d'augmenter la largeur de la distribution de masse [1,11]. On comprend qualitativement cet effet dans le cadre d'un modèle statistique: en effet les fluctuations statistiques augmentent avec la température. L'effet du moment angulaire est celui que nous voulons observer. Pour une température donnée, la figure 2 nous indique que l'effet est important et nous allons faire l'hypothèse que ces deux effets sont décorrélés. En d'autres termes nous allons supposer que, pour une température donnée, l'influence du moment angulaire est indépendante de la température choisie. Cette hypothèse semble plausible dans la mesure où l'effet du moment angulaire a une influence plus importante sur la largeur que la température. Ceci

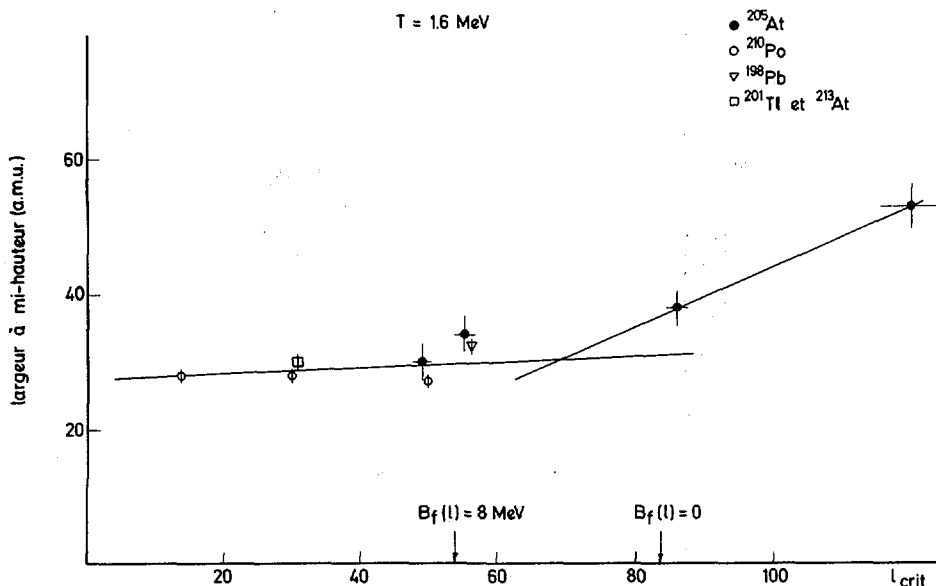


FIG. 3. Largeur à mi-hauteur des distributions de masse pour  $^{205}\text{At}$  (ce travail ●), et des noyaux composés voisins [13].

étant, il est possible d'estimer comment varie la largeur de la distribution de masse lorsque pratiquement aucun moment angulaire n'est mis en jeu, et ce à partir de résultats déjà existants dans la littérature et obtenus en utilisant des particules légères comme projectile [12]. Nous pouvons ainsi corriger les points obtenus pour 2,2 MeV et les ramener à une température de 1,6 MeV. La figure 3 donne le résultat de cette correction. Sur cette figure on a également porté les données d'autres mesures effectuées par d'autres auteurs et relatives à des distributions de masse des produits de fission de noyaux composés proches ou identiques à  $^{205}\text{At}$  [3,4]. On observe que jusqu'à  $l_c$  supérieur à 80, la largeur de la distribution reste à peu près constante ou n'augmente que très peu. Pour  $l_c$  supérieur à 80, on observe un très fort accroissement de la largeur. Cette brusque augmentation a lieu au voisinage de la valeur  $l_c$  pour laquelle la barrière de fission devient nulle [13]. Dans notre cas, ceci correspond à une valeur de  $l = 82$ . Cela signifie que lorsque  $l_c$  est supérieur à cette valeur, de plus en plus d'ondes partielles conduisent à un noyau composé ayant une barrière de fission nulle. Le résultat que nous mettons ici en évidence ne semble pas particulier au noyau de  $^{205}\text{At}$ . Des mesures effectuées par d'autres auteurs permettent de tirer la valeur de la largeur de distribution de masse des produits de fission d'autres noyaux composés [14]. Afin de comparer la largeur des distributions de masse des produits de fission provenant de noyaux

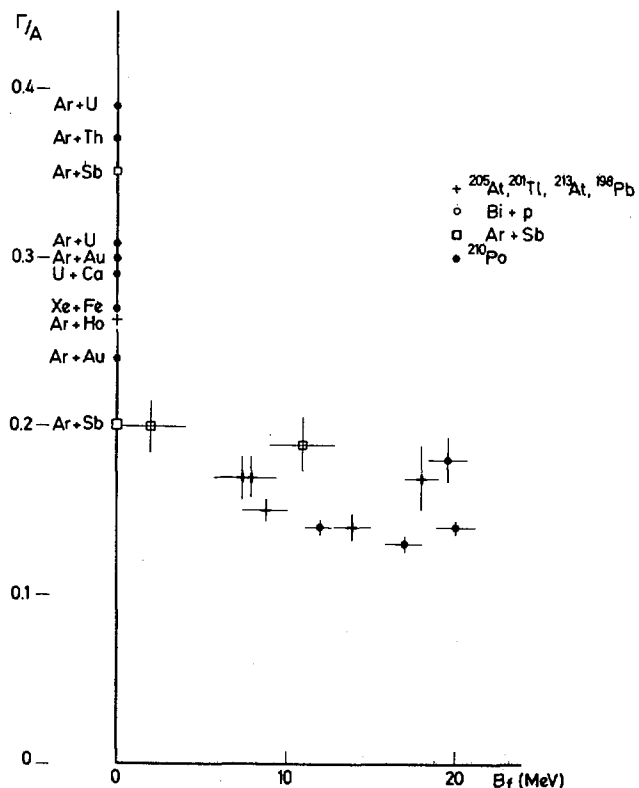


FIG. 4. Largeurs à mi-hauteur corrigées des distributions de masse en fonction de la barrière de fission pour différents systèmes [15].

composés différents, nous avons fait l'hypothèse simple que la largeur de la distribution est proportionnelle au nombre de nucléons  $A$ . Les largeurs sont préalablement corrigées pour l'effet de la température (elles sont ramenées à  $T = 1,6$  MeV), puis divisées par la masse du noyau composé considéré. Pour ces réactions, la valeur de la barrière de fission du noyau composé a été calculée selon le modèle de Cohen, Plasil et Swiatecki pour un moment angulaire du noyau composé égal au moment angulaire critique. Lorsque cette barrière est positive nous avons tracé  $\Gamma/A$  (rapport de la largeur au nombre de nucléons) en fonction de la valeur de la barrière. Lorsqu'elle est négative ou nulle, nous avons porté la valeur de  $\Gamma/A$  sur l'axe correspondant à une barrière nulle. Les résultats sont donnés à la figure 4. On observe que  $\Gamma/A$  reste constant lorsque pour toutes les ondes partielles conduisant à la fusion, la barrière de fission est supérieure à zéro. Au contraire, dès qu'il existe des ondes partielles pour lesquelles la barrière de fission est nulle, on observe une augmentation importante de  $\Gamma/A$ .

Ce résultat nous amène à nous demander si, lorsque la barrière de fission devient nulle, on forme un réel noyau composé et si, dans ce cas, la fission observée est celle qui correspond au noyau composé. En effet on conçoit fort bien que lorsque la barrière de fission est nulle, le temps de vie du noyau composé, s'il se forme, est très bref. Par conséquent, on s'attendrait qualitativement à une diminution des largeurs plutôt qu'à une brusque augmentation puisque le système n'aurait pas eu le temps d'atteindre l'équilibre que constitue le noyau composé. Cet argument suggère que nous observons plutôt un nouveau type de mécanisme, intermédiaire entre la formation du noyau composé et les collisions très inélastiques. Cette distinction se situe alors au niveau des temps de réactions: pour les collisions très inélastiques on a affaire à des temps courts ( $10^{-22}$  à  $10^{-20}$  s) tels qu'un grand nombre de variables collectives n'ont pas le temps de se relaxer dans un état d'équilibre. Au contraire le noyau composé fissionnant est caractérisé par un temps de vie long ( $10^{-18}$  à  $10^{-16}$  s) permettant l'oubli de la majeure partie de la voie d'entrée. Entre ces deux mécanismes, on peut en imaginer un troisième où le temps d'interaction est suffisant pour relaxer les degrés collectifs observés tels dans les collisions très inélastiques. Notamment, le degré d'asymétrie de masse aurait juste le temps d'atteindre un équilibre, ce qui explique les distributions de masse analogues aux distributions de masse de fission. Toutefois, le temps d'interaction est assez bref pour que l'identité des deux fragments ne soit pas perdue au cours de la réaction. On imagine alors un système composite symétrique se décomposant en deux fragments semblables aux fragments de fission. Le temps d'un tel système serait de l'ordre de  $10^{-20}$  à  $10^{-19}$  s, ce qui signifie que la transition entre une approximation soudaine et une approximation adiabatique du potentiel d'interaction entre les deux ions incidents est un phénomène relativement lent.

## REFERENCES

- [1] NGO, C., PETER, J., TAMAIN, B., BERLANGER, M., HANAPPE, F., Z.Physik A283 (1977) 161.
- [2] Voir discussion dans : HANAPPE, F., TAMAIN, B., Proceedings of the IPCR Symposium on Macroscopic Features of Heavy-Ion Collisions and Pre-equilibrium Process, Hakone, September 2-3, (1977) IPCR Cyclotron Progress Report, Supplement 6 (1977) 293.
- [3] PLASIL, F., BURNETT, D.S., BRITT, H.S., THOMPSON, S.G., Phys.Rev. 142 (1966) 696.
- [4] UNIK, J.P., CUNNINGHAM, J.G., CROALL, I.F., Proc.IAEA Symp. on Physics and Chemistry Fission, IAEA-SM- 122/58, Vienna, (1969) 717.
- [5] LEBRUN, C., HANAPPE, F., LECOLLEY, J.F., LEFEBVRES, F., NGO, C., PETER, J., TAMAIN, B., Nucl.Phys. Sous presse.
- [6] MORJEAN, M., NGO, C., PETER, J., TAMAIN, B., DAKOWSKI, M., LUCAS, B., MAZUR, C., RIBRAG, M., SIGNARBIEUX, C., BERLANGER, M., HANAPPE, F., CHECHIK, R., FUCHS, H., cette conférence.

- [7] GALIN,J., GUERREAU,D., LEFORT,M., TARRAGO,X., Phys. Rev. C9 (1974) 1018.
- [8] NGO,C., Thèse (1974) IPN-Orsay.
- [9] LEFORT,M., Lecture notes in physics, 33 (1975) 274.
- [10] LEFORT,M., NGO,C., Ann. de Phys. 3 (1978) 5.
- [11] BORDERIE,B., HANAPPE,F., NGO,C., PETER,J., TAMAIN,B., Nucl. Phys. A220 (1974) 93.
- [12] CHECHIK,R., communication privée.
- [13] COHEN,S., PLASIL,F., SWIATECKI,W.J., Ann. of Phys., 82 (1974) 557.
- [14] TAMAIN,B., Thèse (1974) IPN-Orsay.  
HEUSCH,B., VOLANT,C., FREIESLEBEN,H., CHESNUT,R.P., HILDENBRAND, K.D., PUHLHOFER,F., SCHNEIDER,W.F.W., KOHLMAYER,B., PFEFFER,W., Z.Physik A288 (1978) 391.  
OGANESSIAN,Ju.Tz., Preprint Joint Institute for Nuclear Research, E2/3942 DUBNA (1968).  
CHEIFETZ,E., FRAENKEL,Z., GALIN,J., LEFORT,M., PETER,J., TARRAGO,X., Phys. Rev. C2 (1970) 256.  
OLMI,A., SANN,H., LYNEN,U., METAG,V., BJORNHOLM,S., HABS,D., SPECHT,H.J., BOCK,R., GOBBI,A., STELZER,H., 15th Int. Meeting on Nuclear Physics, BORMIO (1978) 724.

## DISCUSSION

H.J. SPECHT: The fission properties of nuclei with a vanishing fission barrier are providing us with some very interesting information, as we shall doubtless continue to see during this session. Within this context I would personally like to see more data on fragment angular distribution for these non-compound fusion-fission reactions, not so much in terms of  $1/\sin \theta$ , but rather of quantitative deviations from  $1/\sin \theta$  close to  $0^\circ$ . Are you aware of any such data in connection with the nuclei that you have discussed?

F. HANAPPE: Although I would agree with you on the importance of studying the deviations from the  $1/\sin \theta$  angular distribution close to  $0^\circ$ , I do not think that there any experimental data available at the present time because of the obvious difficulty involved in detecting products at an angle near the beam direction without the use of a sophisticated experimental set-up permitting high detection efficiency.

J.B. WILHELMY: I should like to ask how you decide on the time limits given for this new process. If the system does not have a fission barrier, what enables it to stay together for such a long period of time?

F. HANAPPE: The time scales for this new process are given, first, by the upper limit imposed by the fissioning compound nucleus ( $10^{-18} - 10^{-16}$  s) and then by the time scales usually associated with deep inelastic collisions. A zero fission barrier does not imply the absence of a potential well, and before scission the system needs some time to find the fission direction for which the barrier has vanished.

E. CHEIFETZ (*Chairman*): I wonder if you could elaborate on that point. For example, let me put the question this way — what is the experimental evidence for lifetime associated with the process described?

F. HANAPPE: Well, firstly, since the fission barrier is zero, the lifetime must be shorter than that associated with the compound nucleus which has attained complete thermodynamic equilibrium. Secondly, in this process the initial relative motion is completely relaxed and the angular distribution is close to  $1/\sin \theta$ , which must correspond to the longest life-time of the composite system of deep-inelastic collision associated with an intermediate system of this kind. In addition, the mass-asymmetric degree of freedom is equilibrated, showing that the life-time is longer than that calculated for the composite system of deep-inelastic collisions in such systems where the deep-inelastic products are not mass equilibrated. The absolute value is difficult to obtain, but the range must be intermediate between those of the compound nucleus and the deep inelastic process.

H. FREIESLEBEN: Let me just comment on the time scale over which the "fission without a fission barrier" occurs. From our data for the  $^{132}\text{Xe} + ^{56}\text{Fe}$  (HEUSCH, B. et al., Z. Phys. A 288 (1978)) it can only be qualitatively calculated that two time limits apply to the process. The lower time limit is given by the period needed for at least half a revolution of the dinuclear complex, since the fragment distributions are proportional to  $1/\sin \theta$ . On the other hand, the system has no fission barrier, so it should be short-lived as compared with a fully equilibrated compound nucleus.



# FISSION PROPERTIES OF VERY HEAVY NUCLEI PRODUCED IN DEEP-INELASTIC COLLISIONS

D. v.HARRACH, P. GLÄSSEL, Y. CIVELEKOĞLU,

R. MÄNNER, H.J. SPECHT, J.B. WILHELMY\*

Physikalisches Institut, Universität Heidelberg,  
Heidelberg

H. FREIESLEBEN, K.D. HILDENBRAND

Gesellschaft für Schwerionenforschung,

Darmstadt,

Federal Republic of Germany

## Abstract

### FISSION PROPERTIES OF VERY HEAVY NUCLEI PRODUCED IN DEEP-INELASTIC COLLISIONS.

Kinematically complete experiments have been performed on the three-body exit channels in the reactions 7.5 MeV/u  $^{238}\text{U}$  on  $^{90}\text{Zr}$ ,  $^{238}\text{U}$  and  $^{248}\text{Cm}$  to investigate the fission properties of nuclei with a vanishing liquid-drop fission barrier. Thus far, no evidence was found for true instantaneous three-body break-up of the collision system. Instead, a seemingly sequential fission pattern in the sense of unperturbed fission-fragment kinetic energies (as found before for lighter systems) is observed even for the heaviest elements. However, a considerable broadening of the fragment mass distributions as well as angular distributions incompatible with the usual saddle-point concept are also observed in this region. Possible explanations in terms of non-equilibrium processes or a revision of the equilibrium liquid-drop picture near instability are discussed.

## 1. INTRODUCTION

The availability of very-heavy-ion beams like Pb and U at energies well above the Coulomb barrier for all elements has raised expectations for the observation of a new type of fission process [1] — ‘fast’ fission under the influence of strong Coulomb and nuclear forces exerted by a heavy reaction partner. The first experiments in this direction using Pb and U beams on Ni and Zr targets [2] did not find any evidence for such phenomena. Instead, all characteristics observed pointed to a sequential process which then proved to be a powerful probe for the investigation of angular-momentum transfer and angular-momentum

---

\* Visitor from Los Alamos Scientific Laboratory.

orientation in deep-inelastic collisions [2, 3]. In continuing these studies, we turned to the heaviest available target-projectile combinations, i.e.  $^{238}\text{U}+^{238}\text{U}$  and  $^{238}\text{U}+^{248}\text{Cm}$ . These systems are of particular interest because of their enhanced mass diffusion [4] and the strong external forces, combined with decreasing stability against fission. The behaviour of fission in this region has also important bearings on the possibility of super-heavy element production in heavy-ion collisions.

In the present experiments, we have specifically concentrated on the three-body exit channel which allows the investigation of the fission properties of nuclei extending into the super-heavy region. We find a strong increase in the width of the fission mass distribution in the region of the heaviest elements where the liquid-drop fission barrier is expected to vanish. We find, in addition, that the standard liquid-drop model [5], together with the usual statistical distribution of K-states at the saddle point [6], completely fails to describe the observed fragment angular correlations. It is not clear, at present, whether this failure is associated with more general deficiencies of the model for very heavy nuclei, or whether, indeed, non-equilibrium processes are observed for nuclei produced outside their fission saddle point.

## 2. EXPERIMENTAL PROCEDURE

$^{238}\text{U}$  and  $^{248}\text{Cm}$  targets of 100 to 200  $\mu\text{g}\cdot\text{cm}^{-2}$  were bombarded with a  $^{238}\text{U}$  beam of 7.5 MeV/u from the Unilac at GSI. Two- and three-body exit channels were investigated in a kinematically complete way. One heavy fragment was analysed in a  $40 \times 12 \text{ cm}^2$  position-sensitive  $\Delta E-E$  gas ionization chamber [7] centred at  $50^\circ$  (lab), spanning centre-of-mass (CM) angles between  $45^\circ$  and  $110^\circ$  (effectively,  $135^\circ$  for the symmetrical system U+U). The atomic number Z was deduced from  $\Delta E$  and time-of-flight rather than  $\Delta E-E$ , yielding a better separation for slow particles. In the region of  $60 < Z < 96$ , a Z-resolution of four to five units was achieved. The other binary reaction partner or its two fission fragments were detected in coincidence in a  $1 \times 1 \text{ m}^2$  position-sensitive parallel-plate avalanche counter [8] with an overall time-resolution of  $\leq 0.5 \text{ ns}$  (in connection with the bunched beam). Because of the high lab velocity of the fissioning nuclei as compared to the velocity of the fission fragments in the moving frame, the possible directions of the fragments are compressed into a narrow cone of less than  $60^\circ$  opening angle. Thus, one angle setting of the detector was sufficient to cover the entire cone, resulting in  $4\pi$ -efficiency for the investigation of the various fission parameters. For a certain fraction of the events, only one fission fragment was detected, owing to losses on the support structure of the counter window and on an adjustable beam stop located in front of the detector, shielding it against small-angle ( $< 6^\circ$ ) Rutherford scattering.

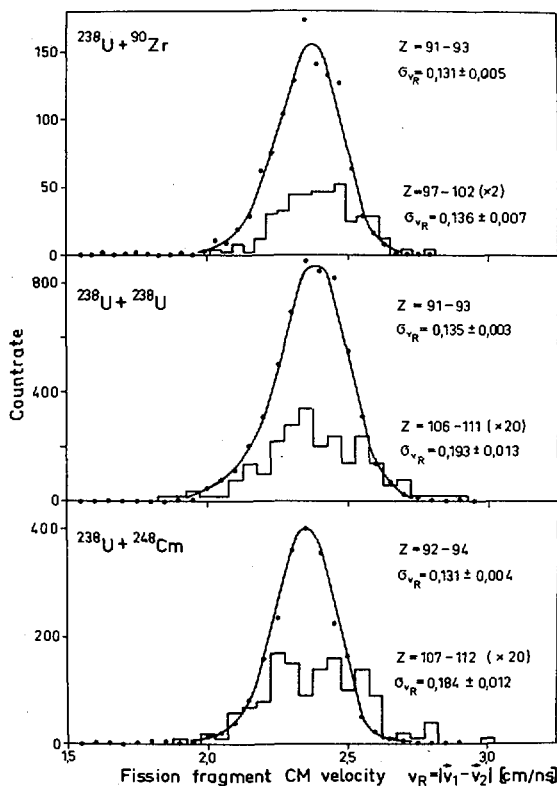


*FIG.1. Distribution of the vector difference  $|\vec{v}_1 - \vec{v}_2|$  of the fragment lab velocities for a Z-bin close to the entrance channel and for a high Z-bin in the systems  $^{238}\text{U} + ^{90}\text{Zr}$ ,  $^{238}\text{U} + ^{248}\text{Cm}$ .*

In the off-line analysis, a two-step procedure on the basis of the ionization chamber data was employed, yielding the charge Z and the mass M of the non-fissioning deep-inelastic collision fragment as well as the Q-value and the CM-angle of the first binary reaction step. With the data from the other detector, the fission direction in the frame of the fissioning nucleus can then be evaluated unambiguously, even in the case where only one fragment has been observed. With the detection of both, full information including total fission kinetic energy and fragment mass ratio is obtained. The background from four-body events stemming from double sequential fission is rejected very effectively by testing the coplanarity of the three observed particles in the CM-system. The possibility of confusing a light transfer product of the first reaction step with a heavy fission fragment of the second step is strongly reduced for three-particle coincidences compared to one-particle-inclusive measurements [4]. In Monte-Carlo

simulations of the system U+U we have verified that essentially no contamination occurs down to  $Z \approx 70$  for the non-fissioning partner, corresponding to  $Z \approx 114$  for the fissioning nucleus.

### 3. RESULTS

In a truly instantaneous break-up of the collision complex into three particles of comparable mass, one would expect strong Coulomb force influences of one particle on the total kinetic energies of the other two as well as specific directional correlations. Conversely, the non-existence of such effects in a sequential break-up process would allow some lower limit for the time difference between the two reaction steps to be extracted. We shall, therefore, first discuss the fission fragment total kinetic energies and their azimuthal angular correlations.

The distribution of the vector difference  $v_R = |\vec{v}_1 - \vec{v}_2|$  of the fragment lab velocities, integrated over all other observables, is shown in Fig.1 for two different bins for the charge  $Z$  of the fissioning nuclei (determined as the  $Z$ -complement to the particles in the ionization chamber). The quantity  $v_R$  essentially determines the total fragment kinetic energy  $E_K = 1/2 \mu v_R^2$ ,  $\mu$  being the reduced mass of the two fragments. All distributions clearly demonstrate the existence of intermediate fissioning nuclei as 'resonances'. Whereas unperturbed fragment energies for nuclei close to U are to be expected in view of large contributions from quasi-elastic reactions as well as sizeable fission barriers at very large deformations in this region, the persistence of a seemingly sequential pattern up to nuclei with a vanishing liquid-drop fission barrier is quite surprising. The only visible difference appears to occur in a significantly increased variance of the distributions. More quantitatively, the centre of gravity, transformed into average total kinetic energy  $\langle E_K \rangle$  and plotted versus the charge  $Z$  of the fissioning nuclei in Fig.2, very well follows the known Viola systematics [9]. It is also essentially independent of the fission direction and the energy dissipation in the first reaction step.

Taken together, these observations definitely rule out an instantaneous three-body break-up of the collision complex up to the heaviest nuclei. Simple Coulomb-trajectory calculations for the distortion of the fragment energies in the presence of the non-fissioning partner give a lower limit on the separation of the fissioning nucleus and the other partner at scission of 70 to 100 fm, corresponding to  $2$  to  $4 \times 10^{-21}$  s ('scission-to-scission time'). For smaller separations, a substantial distortion depending on the azimuthal fission angle should have been seen.

The fission fragment angular correlations are described in spherical co-ordinates in the rest frame of the fissioning nuclei [2, 3]. The normal to the reaction plane of the first step is chosen as the quantization axis ( $\theta = 0^\circ$ ). The reaction plane

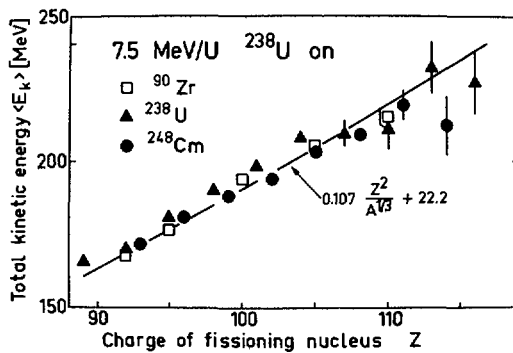


FIG.2. Average fission total kinetic energy release versus Z of the fissioning nucleus for the systems  $^{238}\text{U} + ^{90}\text{Zr}$ ,  $^{238}\text{U}$ ,  $^{248}\text{Cm}$ . The solid line is an empirical fit to older fission data (Viola, 1966 [9]).

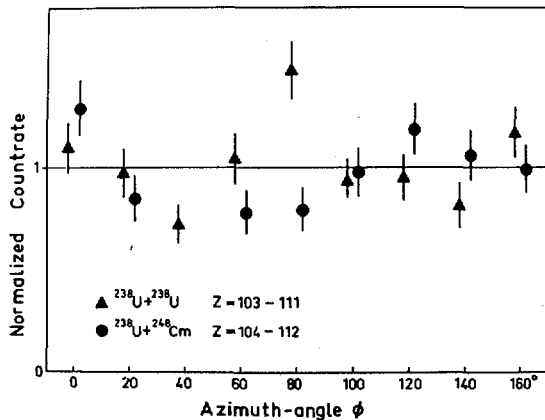


FIG.3. Azimuthal angular distributions of fission fragments for a high Z-bin integrated over all off-plane angles  $\theta$ . Systematical errors may double the indicated statistical errors.

itself then corresponds to the equator ( $\theta = 90^\circ$ ); the beam axis defines the zero direction of the azimuth angle  $\phi$  for  $\theta = 90^\circ$ . The overall fragment azimuthal distributions, integrated over all polar angles, are shown in Fig.3 for cuts in Z corresponding to the heaviest elements. Within our present accuracy, no significant dependences can be recognized.

For a really fast process, anisotropies like increased probabilities for fission parallel to the CM recoil axis of the first reaction step should have been observed. In qualitative agreement with the findings discussed above, the isotropy found

implies that the scission-to-scission time has to be comparable to or longer than the average rotational half-period of the fissioning system, assuming a symmetrical triangular angular momentum distribution. With an average angular momentum of  $50 \text{ h}$  (compare Fig. 5 below), the rotational half-period of a mass-280 nucleus amounts to times between  $7$  and  $25 \times 10^{-21} \text{ s}$ , where the lower limit applies to rotation of a rigid sphere, the upper to that of two mass-140 spheres sticking together (demonstrating some necessary increase in the lower limit by the increasing deformation attained during the descent towards scission). Quantitatively, these times are significantly longer than the limit obtained from the lack of Coulomb distortions. They are also longer than the usual saddle-to-scission time estimates of about  $4 \times 10^{-21} \text{ s}$  and up, depending on the type and strength of the friction force [10, 11]. It may, however, be premature to try to distinguish between different models on this basis. One should, in any case, expect very large fluctuations in the scission-to-scission time, considering the flat potential energy surface of a nearly spherical nucleus without a fission barrier (random walk with a superimposed path to scission).

On the other hand, the remaining aspects of the reactions investigated do not favour an interpretation as fission of a truly equilibrated system, either. Although upper limits for the scission-to-scission time cannot be given at this stage, both the fission fragment out-of-plane angular correlations and the behaviour of their mass distributions point, for the heaviest elements, to a process which is not described by the standard liquid-drop model.

As observed before for sequential fission of lighter elements [2, 3] the out-of-plane angular distributions exhibit the strong concentration within the reaction plane expected for the decay of a system with considerable angular momentum aligned perpendicularly to that plane. The half-width of these distributions as a function of the atomic number  $Z$  of the fissioning system is shown in Fig. 4 for all three reactions. Owing to the smaller mass diffusion in  $^{238}\text{U} + ^{90}\text{Zr}$ , a full comparison can only be made up to  $Z \approx 100$ . In this region, the behaviour is identical, i.e. the width decreases — within only 4 units of  $Z$  — from about  $110^\circ$  for nuclei close to U to a rather constant value of about  $75^\circ$ . As demonstrated before [12], this rapid drop basically reflects the rapidly increasing dissipation of kinetic energy and angular momentum (correlated with  $Z$ ) rather than a direct effect of  $Z$ .

From these widths, average-oriented spins  $\langle I \rangle$  of the fissioning nuclei can be deduced as in our previous work [2, 3], relying on empirical values for the variance  $K_0$  of the Gaussian distribution of the spin projection  $K$  on the symmetry axis of the fission saddle-point configuration, and assuming the same amount of randomly oriented spin components ( $M_0 = 13\text{h}$ ) as established for the system  $^{208}\text{Pb} + ^{90}\text{Zr}$  [2]. In all cases, a rise of  $\langle I \rangle$  from about  $15 \text{ h}$  for the quasi-elastic region to a plateau of  $40-50 \text{ h}$  is obtained, rather independent of the system (compare also Ref.[2]). This independence is due to an approximate

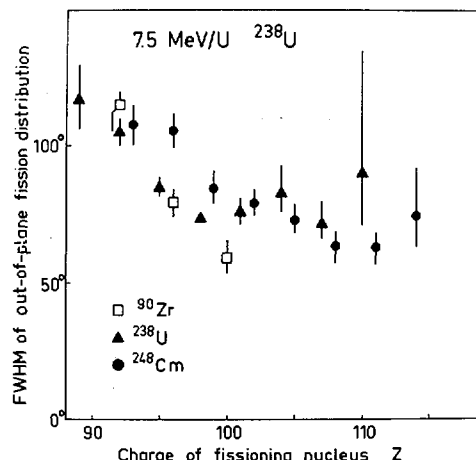


FIG. 4. FWHM of the out-of-plane fission fragment angular distributions for the systems  ${}^{238}\text{U} + {}^{90}\text{Zr}$ ,  ${}^{238}\text{U}$  and  ${}^{248}\text{Cm}$ . The higher values close to the entrance channel are due to a strong contribution from quasi-elastic events.

cancellation between the target mass dependences of the orbital angular momentum brought in by the entrance channel and that fraction of it as is transferred to the U-like nuclei in the sticking limit. Selecting only deeply inelastic events ( $\text{TKE} < 340$  MeV), the average spins  $\langle I \rangle$  deduced for  ${}^{238}\text{U} + {}^{90}\text{Zr}$  are shown in the upper part of Fig. 5 as a function of the atomic number  $Z$  of the fissioning system [12]; the values of  $K_0$  employed are given for comparison. A sticking dependence of  $\sim A^{5/3}$  describes the data reasonably well.

For nuclei with  $Z > 100$ , the observed widths of the out-of-plane distributions (Fig. 4) both for the  ${}^{238}\text{U}$  and  ${}^{248}\text{Cm}$  targets remain surprisingly constant up to the heaviest elements, irrespective of the fact that the rotating-liquid-drop model for rotationally symmetric nuclei at these angular momenta (40–50  $\hbar$ ) leads to a complete loss of stability and a corresponding divergence of  $K_0$  around  $Z = 107$  (Fig. 5, lower part). Empirical values for  $K_0$  are not known in this region. Any attempt to deduce spin values for elements with  $Z > 100$  (as successfully done before for  $Z < 100$ ) on the basis of the theoretical values of  $K_0$  obviously yields unphysical results. In the following, we, therefore, reverse the argumentation. Assuming, together with the previous value for  $M_0$ , the smooth sticking dependence of the average oriented spin  $\langle I \rangle$  established for  $Z < 100$  to remain valid up to  $Z > 110$ , ‘experimental’ values for  $K_0$  can be deduced from the measured widths. As shown in Fig. 5, only a very slow increase up to about 25  $\hbar$  is found, contrary to the theoretical divergence.

The heavy elements under discussion are characterized by a more or less spherical saddle-point shape with a near-degeneracy of levels with different  $K$ .

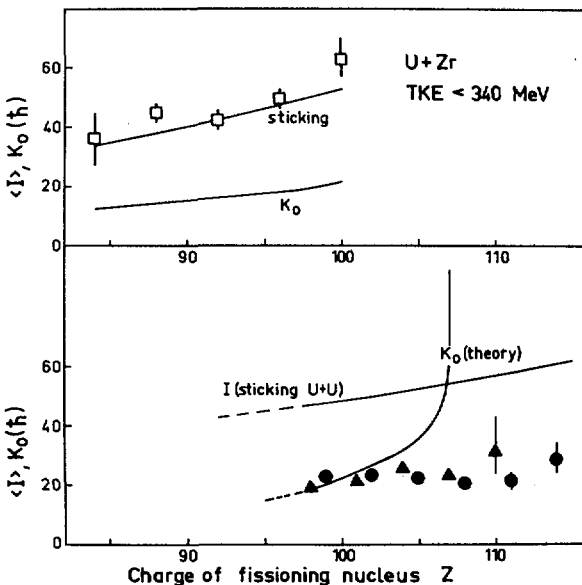


FIG. 5. Comparison of the sticking dependence with average oriented spins deduced for the deep-inelastic component of the reaction  $^{238}\text{U} + ^{90}\text{Zr}$ . The  $K_0$ -values used are also shown (top part).

The bottom part contains  $K_0$  values deduced from an assumed sticking behaviour of the spin for the systems  $^{238}\text{U} + ^{238}\text{U}$ ,  $^{248}\text{Cm}$ . The spin is normalized to  $42.5 \text{ hbar}$  at  $Z = 92$ . No points are evaluated up to  $Z = 96$  because sticking is not expected there to hold, owing to the quasi-elastic component. The liquid-drop model prediction for  $K_0$  is also shown.

Two alternative interpretations of our results are, therefore, possible. If we assume both (i) thermal equilibrium to be established at the saddle, and (ii)  $K$  to be conserved throughout the descent from saddle to scission, then, at least, an indication of the divergence of  $K_0$  should have been observed. Since this was not the case, either of the assumptions has to be incorrect.

- (i)  $K$ -non-conservation could solve the problem in the following way: During the descent towards scission, the near-degeneracy of levels with different  $K$  is removed. A strict conservation of  $K$  would drive the system away from thermal equilibrium. However, because of the long scission times, relatively small perturbations may tend to re-establish equilibrium. Such re-orientations will always favour small values of  $K$  because of the higher density of such levels, resulting ultimately in effective parameters  $K_0$  representative of nuclear shapes somewhere between spherical and scission. The influence of Coriolis forces will actually be increased for nearly spherical shapes because of the inverse relation between perturbation and moment of inertia.

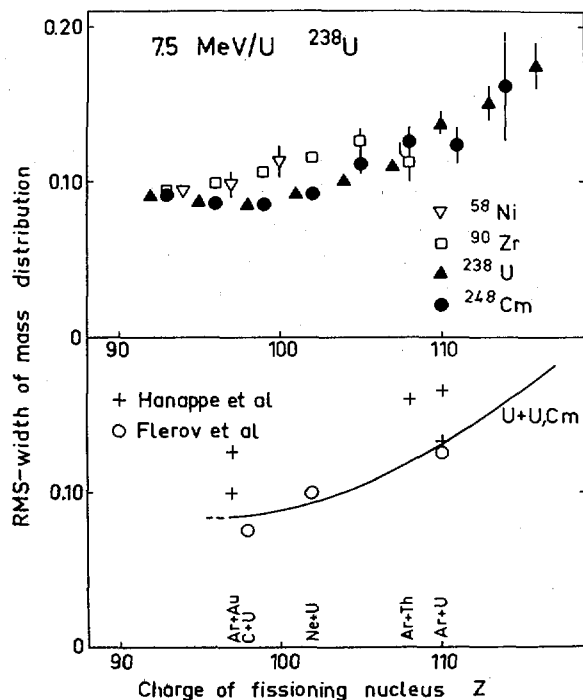


FIG. 6. Width of the fission fragment mass distributions (defined as RMS of  $A_1/(A_1 + A_2)$ ) for the systems  $^{238}\text{U} + ^{58}\text{Ni}$ ,  $^{90}\text{Zr}$ ,  $^{238}\text{U}$  and  $^{248}\text{Cm}$  (top). The bottom part shows a comparison of the trend of our data with fusion-fission data from Refs [15].

- (ii) A non-statistical, relatively 'fast' process could alternatively solve the problem. It is conceivable that the fissioning system, formed already beyond its saddle point, receives the information on the final fission direction from the collision partner of the first reaction step. In an extremely simple picture, an initial direction collinear with the separation axis of the first step may be expected [14]. If fluctuations are also considered, again effective parameters  $K_0$  may arise which now do not resemble properties of the fissioning nucleus, but rather those of the deep-inelastic collision (possibly related to  $M_0$ ).

We finally turn to a discussion of the fission fragment mass distributions. The well-known asymmetric mass split of U-like nuclei is only observed in the vicinity of U, whereas a rapid transition towards symmetric fission occurs for heavier elements, mainly caused by the larger average energy dissipation. The RMS-widths of the mass distributions as a function of the atomic number of the fissioning nuclei are plotted in the upper part of Fig.6. Rather system-independent, a strong increase is observed in the region of  $Z > 100$  up to the heaviest elements.

The slight differences between the light and the heavy targets visible around  $Z \approx 100$  are possibly due to a specific selection of excitation energies for the latter, originating from losses by four-particle events. In the lower part of Fig.6, the average trend of these data (solid line) is compared to various scattered results from heavy-ion fusion-fission reactions, compiled by Hanappe et al. [15]. Within the present accuracy, the overall behaviour appears to be rather universal.

The observed increase in the width of the mass distributions for heavy elements is much stronger than expected for a slight change in nuclear temperature [13], correlated with  $Z$  (see above). It is intriguing to speculate again about a relatively fast process, in which the shape of the observed mass distributions reflects an incomplete thermalization of the asymmetry mode, strongly excited in the first step of the reaction [14]. The apparent independence of the entrance channel, however, rather suggests these results to reflect inherent properties of the liquid-drop model, i.e. a close correlation between a decreasing stability against mass asymmetry and the loss of stability in the fission degree of freedom for nuclei with a vanishing fission barrier. Further support for this interpretation stems from a possibly related increase in the widths observed for lighter elements with fission barriers reaching zero because of very high angular momenta [15]. There does not seem to be a need to define a new reaction mechanism intermediate between fusion-fission and deep-inelastic collisions [15].

#### 4. CONCLUSIONS

In our present experimental investigations of the heaviest collision systems available, no evidence has so far been obtained for instantaneous three-body break-up. The observed kinetic energy release of fission as well as the absence of any fragment azimuthal anisotropies confirm the existence of a dominantly two-step process up to the heaviest elements produced, with a lower limit of the scission-to-scission time of  $\sim 10^{-20}$  s. The strong fragment out-of-plane anisotropies for these elements are, however, not compatible with the current picture of a statistical equilibrium at the liquid-drop saddle point, combined with strict K-conservation down to scission. In addition, the heaviest nuclei exhibit a considerable increase in the width of the fragment mass distributions. There is no way, at present, to decide whether these observations reflect deficiencies of the liquid-drop model for nuclei at the limits of stability or whether, truly, fast non-statistical processes are being observed.

## REFERENCES

- [1] DEUBLER, H.H., DIETRICH, K., Phys. Lett. **62B** (1976) 369; Z. Phys. **284** (1978) 237.
- [2] SPECHT, H.J., MPI H-1978-V26, to be published in Proc. Int. Conf. Nucl. Interactions, Canberra (1978); HARRACH, D.v., GLÄSSEL, P., CIVELEKOĞLU, Y., MÄNNER, R., SPECHT, H.J., submitted for publication.
- [3] DYER, P., PUIGH, R.J., VANDENBOSCH, R., THOMAS, T.D., ZISMAN, M.S., Phys. Rev. Lett. **39** (1977) 392.
- [4] HILDENBRAND, K.D., FREIESLEBEN, H., PÜHLHOFER, F., SCHNEIDER, W.F.W., BOCK, R., HARRACH, D.v., SPECHT, H.J., Phys. Rev. Lett. **39** (1977) 1065.
- [5] COHEN, S., PLASIL, F., SWIATECKI, W.J., Ann. Phys. **82** (1974) 557.
- [6] HALPERN, I., STRUTINSKY, V.M., Peaceful Uses of Atomic Energy (Proc. 2nd Int. Conf. Geneva, 1957) **15**, UN, New York (1958) 408.
- [7] SANN, H., DAMJANTSCHITSCH, H., HEBBARD, D., JUNGE, J., PELTE, D., POVH, B., SCHWALM, D., TRAN THOAI, D.B., Nucl. Instrum. Methods **124** (1975) 509.
- [8] HARRACH, D.v., SPECHT, H.J., submitted to Nucl. Instrum. Methods.
- [9] VIOLA, V.E., Jr., Nucl. Data Sect. **A1** (1966) 391.
- [10] SIERK, A.J., NIX, J.R., Phys. Rev. **C16** (1977) 1048.
- [11] NEGELE, J.W., KOONIN, S.E., MÖLLER, P., NIX, J.R., SIERK, A.J., Phys. Rev. **C17** (1978) 1098.
- [12] CIVELEKOĞLU, Y., thesis 1979, University of Heidelberg.
- [13] NIX, J.R., Nucl. Phys. **A130** (1969) 241.
- [14] DHAR, A.K., NILSSON, B.S., Phys. Lett. **77B** (1978) 50.
- [15] HANAPPE et al., these Proceedings; FLEROV, G.N., ORANESSIAN, Yu.Ts., Dubna preprint E7-6838 (1972).

## DISCUSSION

J. PETER: Your final 'universal' curve does not hold for  $Z < 90$ , where the maximum  $\ell$  is higher than the  $\ell$  value at which  $B_f(\ell) = 0$ .

D. von HARRACH: The broadening of the mass distribution seems to be fairly independent of the way in which we destabilize the liquid drop. So we mainly studied the influence of  $X(Z^2/A)$ , whereas in your work you increased the rotational parameter  $\gamma$  for lower  $Z$ .

H-G. CLERC: How did you disentangle the various effects of the large nuclear charge and angular momentum on the stability of the fissioning nucleus?

D. von HARRACH: Empirical  $K_0$  values are available for around  $Z \approx 92$ . By taking these values we can derive  $J$ . The additional assumption is that the dependence of  $J$  on  $Z$  is described fairly well by sticking model so that we can extrapolate to the high  $Z$  region, where no empirical  $K_0$  values are available. In this manner  $K_0$  can be derived and compared with theoretical predictions.

H-G. CLERC: Thank you. What was the angular momentum in your case?

D. von HARRACH: It was about  $45 \hbar$  at  $Z \gtrsim 92$  for deep inelastic events.

H.J. SPECHT: Perhaps at this point I could revert to the problem of the

conservation of K. We learnt from Dr. Tsigpenyuk (see SM-241/A2 in these Proceedings) that at excitations close to the barrier K may actually be known with accuracy better than 1% on the basis of photofission data. This might be associated with the apparently small coupling of the fission mode to qp excitations, as will be discussed later on at this meeting. What convincing evidence is there, however, that the conservation of K is not increasingly violated at higher energies, where that coupling presumably becomes much stronger? Mechanisms influencing K other than those associated with the saddle shape could be relevant not only for the work you have reported, but also for the systematics of the effective moments of inertia  $J_{\text{eff}}$ , which, after all, have been used for quantitative verification of the liquid drop model. In this connection I should also recall the very good experiments carried out by Dabbs and co-workers, and also by Postma and co-workers, with polarized neutrons on polarized targets, although they have unfortunately not been continued. In the case of  $^{235}\text{U} + n$ , a broad K distribution peaking around  $2 - 3 \text{ h}$  and with hardly any contribution from O was found. This is very different from the low fission channels one might have expected.

D. von HARRACH: I think that Dr. Kapoor is more qualified to comment on that point.

S.S. KAPOOR: As regards the possibility of non-conservation of K at medium excitation energies we can indicate two experimental observations which can be interpreted as showing that the K distribution further broadens during descent from saddle to scission. These are, first, a plot of  $J_0/J_{\text{eff}}$  versus X, i.e. data derived from fragment angular distribution analysis, and, second, values of  $J_{\text{eff}}$  versus excitation energy. Generally speaking, the  $J_0/J_{\text{eff}}$  values are found to be lower than those calculated for LDM shapes for actinides. In the past the LDM parameters have been adjusted and curvature correction has been introduced to account for this fact. Alternatively, the interpretation can be that  $K_0^2$  becomes larger during descent from saddle to scission. If this broadening is dependent on excitation energy, it will lead to an increase in  $J_{\text{eff}}$  with  $E_x$ , which was in fact observed in some work I did a few years ago at Berkeley.

F. DICKMANN: I would like to add with regard to the conservation of K between saddle and scission that due to dynamic effects the pairing correlations are reduced in a deforming nucleus. So I think that quasi-particle states are more easily excited and that this fact gives rise to K mixing.

# RELATIONS ENTRE LES PROPRIETES DES COLLISIONS TRES INELASTIQUES ET LA FISSION

J. PETER\*, B. TAMAIN  
Institut de physique nucléaire,  
Orsay, France

## Abstract—Résumé

### RELATIONSHIPS BETWEEN THE PROPERTIES OF HIGHLY INELASTIC COLLISIONS AND FISSION.

The second stage of a highly inelastic collision — separation of the fragments — resembles fission beyond the saddle point. The advantage of highly inelastic collisions for nuclear macrophysical studies is that the different combinations of projectiles, targets, energies, angles and masses of the nuclei detected enable one to study the behaviour of the different collective modes with time. Mass transfer between the two fragments takes place slowly ( $\text{several } 10^{-21} \text{ s}$ ), as in fission. The transfer from orbital angular momentum to spin angular momentum of the fragments is also slow; as in fission, the collective modes of rolling oscillation, gliding oscillation and torsion can be excited and modify the magnitude and direction of the angular momentum of the fragments. The other collective degrees of freedom — relative velocity, N/Z equilibrium and energy thermalization — are damped very quickly ( $\sim 10^{-22} \text{ s}$ ). Part of the charged-particle emission accompanying the highly inelastic collisions is very similar to ternary fission. The de-excitation of fragments by neutron evaporation is also similar to that of fission fragments, but in addition the high mass asymmetry ratios enable the energy of deformation at the scission point to be demonstrated. For heavy systems the transition between compound nucleus fission and quasi-fission is discrete, and an intermediate type of reaction is proposed, i.e. ‘beyond-the-barrier’ fission.

### RELATIONS ENTRE LES PROPRIETES DES COLLISIONS TRES INELASTIQUES ET LA FISSION.

La deuxième étape d'une collision très inélastique (CTI) — la séparation des fragments — ressemble à la fission au-delà du point selle. L'avantage des CTI pour les études de macrophysique nucléaire est que les différentes combinaisons de projectiles, cibles, énergies, angles et masses des noyaux détectés permettent d'étudier l'évolution des différents modes collectifs en fonction du temps. Le transfert de masse entre les deux fragments s'effectue lentement (plusieurs  $10^{-21} \text{ s}$ ), comme en fission. Le transfert de moment angulaire orbital en moment angulaire intrinsèque des fragments est également lent; comme en fission, les modes collectifs d'oscillation de roulement, d'oscillation de glissement et de torsion peuvent être excités et modifient la grandeur et la direction du moment angulaire des fragments. Les autres degrés de liberté collectifs sont amortis très rapidement ( $\sim 10^{-22} \text{ s}$ ): vitesse relative, équilibre N/Z, thermalisation de l'énergie. Une partie de l'émission de particules chargées accompagnant les CTI est très semblable à la tripartition. La déexcitation des fragments par évaporation de

---

\* En visite au Lawrence Berkeley Laboratory, Berkeley, Etats-Unis d'Amérique.

neutrons est également semblable à celle des fragments de fission, mais en plus, les rapports d'asymétrie de masse élevés permettent de mettre en évidence l'énergie de déformation au point de scission. Pour les systèmes lourds, la transition entre noyau composé-fission et quasi-fission est discrète, et un type de réaction intermédiaire est proposé: la fission «hors barrière».

## 1. INTRODUCTION

Pendant très longtemps — plus de 30 ans — l'étude de la fission est restée un domaine distinct du reste de la physique nucléaire. Ce processus est si différent qu'il requérait une approche différente de celles utilisées dans les autres secteurs. L'évolution qui amène un noyau à se scinder en deux noyaux représente une transformation d'une échelle qui n'était atteinte par aucune autre désintégration radioactive ou réaction nucléaire. Les physiciens nucléaires fascinés par l'étude de cette transformation devaient avoir un état d'esprit quelque peu différent. Ils n'hésitaient pas à employer des concepts aussi simples que celui de la goutte liquide [1] où les propriétés individuelles des nucléons étaient totalement négligées et le noyau considéré comme un ensemble de matière nucléaire dont seules les propriétés macroscopiques étaient prises en considération. Quelques beaux succès avaient été obtenus; en particulier l'étude dynamique de l'évolution depuis l'état du noyau initial jusqu'aux deux fragments séparés avait été capable de reproduire une grande partie des propriétés observables des fragments dans la fission à énergie d'excitation élevée. D'autres tentatives essayaient d'incorporer les effets de couches qui jouaient à l'évidence un grand rôle dans l'évolution de la fission spontanée ou thermique. La prise en compte de ces effets dans le tracé des cartes d'énergie potentielle dans l'espace des déformations à plusieurs dimensions [2] permit de faire un grand pas, ou plutôt de suivre les bons chemins.

Mais une grande gêne dans la compréhension résulte de ce qu'on doit à chaque fois considérer la totalité de l'évolution depuis le noyau initial jusqu'aux deux fragments finaux sans pouvoir isoler un état défini à un instant donné. L'état du noyau composé peut certes être changé, mais une fois que l'évolution vers la scission est commencée, on n'a aucune maîtrise du chemin qui est suivi. Pendant toute la durée de cette évolution, les différents degrés de liberté collectifs se modifient, chacun avec son temps caractéristique propre, sans qu'il soit possible d'en isoler un indépendamment des autres.

Les faisceaux d'ions lourds ne changèrent pas d'abord cette situation. Les réactions de fusion pouvaient certes être considérées comme l'inverse de la fission, mais cela n'apportait guère de renseignements, pour la même raison que pour la fission: une fois que les noyaux commencent à fusionner, le processus se poursuit sans que l'expérimentateur en ait la moindre vue. Donc les premiers

faisceaux d'ions lourds furent surtout utilisés comme outils supplémentaires pour compléter les données obtenues avec les particules chargées légères, en particulier dans les réactions de transfert.

C'est seulement au bout de dix ans que chacune des différentes réactions nucléaires induites par ions lourds conduisit, presque fortuitement, à découvrir un nouveau type de réactions communément appelées maintenant *collisions très inélastiques (CTI)*. Les appellations d'origine dépendaient de la préoccupation qui avait amené à leur découverte: en étudiant les réactions de transfert avec des ions de masse 10 à 20, on observe des *transferts très inélastiques* [3], en détectant les fragments de la fission consécutive à la fusion induite par des ions de masse 40, on trouve des produits *semblables à la fission* [4], et en cherchant si la fusion intervenait entre noyau lourd et ion de masse 84, on découvrit des *quasi-fissions* [5].

Ces dénominations font tout de suite pressentir la liaison entre cette nouvelle physique des ions lourds et la fission: les caractéristiques des produits de CTI ressemblent à celles de la fission, et donc une partie du processus est commune. En effet, une CTI peut schématiquement être scindée en deux étapes. Dans la première étape, les deux noyaux s'interpénètrent en perdant une grande partie — voire la totalité — de leur énergie cinétique relative. Ils forment ainsi un système dit composite ou binucléaire. Dans une deuxième étape, les deux parties du système s'écartent en raison de la répulsion coulombienne et finalement se séparent (fig.1)<sup>1</sup>. Cette deuxième étape représente une partie de l'évolution d'un noyau fissioneer entre le point selle et le point de scission. L'intérêt remarquable des CTI par rapport à la fission est de permettre de modifier l'état du système composite, donc le point de départ de l'évolution vers la scission. Pour cela il suffit de modifier la charge et la masse du projectile ou de la cible et l'énergie incidente.

Cette séparation en deux étapes ne correspond pas à la réalité, qui est à la fois plus complexe et plus riche. L'ensemble des degrés de liberté du système évolue au cours de la collision. Chacun a un temps propre qui peut être déterminé par comparaison avec les autres. En modifiant les conditions initiales et en choisissant les produits finaux, on peut étudier sélectivement l'évolution d'un degré de liberté particulier, ce qui est impossible en fission. Le développement constant des faisceaux d'ions lourds disponibles a permis d'élargir le domaine de la macrophysique nucléaire. Alors que les études détaillées sur la fission ont dû se limiter à la région des noyaux lourds, les systèmes étudiés en CTI vont de quelques dizaines de nucléons à plus de 400 uma (deux fois le nombre de masse de l'uranium 238).

---

<sup>1</sup> Les figures sont groupées en annexe.

Nous examinerons successivement les renseignements obtenus sur les différents degrés de liberté par les CTI en les comparant aux informations recueillies en fission et en nous attachant aux aspects expérimentaux. Une bibliographie plus complète pourra être trouvée dans les articles de revue sur les CTI [6]. Puis nous discuterons de la transition entre CTI et fusion suivie de fission. Nous ne parlerons pas des techniques de détection. Bornons-nous à rappeler qu'elles sont pour la plupart issues des techniques utilisées pour la fission, en particulier la fission induite par ions lourds; elles ont été adaptées à un domaine de noyaux détectés beaucoup plus large en énergie, masse et charge; ce sujet est bien décrit dans la réf. [7].

## 2. PROPRIETES DES COLLISIONS TRES INELASTIQUES

Le temps de réaction est défini par l'intervalle entre l'instant de contact des deux noyaux initiaux et l'instant de scission. Une très large gamme de temps de réaction est couverte dans les CTI, et chaque partie de cette gamme permet d'étudier particulièrement tel ou tel degré de liberté collectif ayant un temps de relaxation voisin. Pour suivre l'évolution, on utilise des «horloges» de différentes périodes qui sont fournies par d'autres aspects des réactions. En classant leur temps de relaxation par valeur approximativement décroissante, les modes étudiés concernent:

- l'asymétrie de masse (ou de charge)
- la déformation
- le moment angulaire relatif
- la vitesse relative
- l'énergie d'excitation
- l'asymétrie de la masse par rapport à la charge.

### 2.1. Temps de réaction et distribution angulaire

En fission, la distribution angulaire des fragments est symétrique par rapport à  $90^\circ$  c.m. Cette propriété manifeste la grande durée de vie associée au processus. En CTI, la situation est fondamentalement différente: le système a généralement gardé la mémoire de la direction de l'ion incident car sa durée de vie est beaucoup plus courte. Dans une collision quasi élastique, les produits sont retrouvés autour d'un angle appelé angle d'effleurement. Quand la collision est plus profonde, le potentiel nucléaire «retient» un instant supplémentaire les partenaires en contact. Pendant ce temps, le système composite tourne et les quasi-projectiles sont observés à  $\theta_{\text{ff}}$  plus en avant de l'angle coulombien  $\theta_{\text{ic}}$ .

Le temps de réaction  $t_\ell$  se déduit de l'angle de rotation  $\theta_r = (\theta_{f\ell} - \theta_{i\ell})$  et de la vitesse de rotation  $\omega_\ell$  (fig.1):

$$\omega_\ell = \frac{\ell \hbar}{\mu r_0^2} \quad (1)$$

où  $\mu$  est le moment d'inertie du système (supposé ici tournant comme un corps rigide (voir 2.4)) et  $\ell$  le numéro de l'onde partielle considérée.

$$t_\ell = \omega_\ell \cdot (\theta_{f\ell} - \theta_{i\ell}) \quad (2)$$

La relation n'est en fait pas toujours aussi simple, pour trois raisons: d'abord le système peut ne pas avoir atteint le stade du collage pour lequel la relation (1) est valable (voir 2.4); ensuite, il peut se faire qu'à certains angles, on trouve des produits venant de deux zones de moment angulaire donc de temps différents; enfin, le fait que de nombreuses ondes partielles conduisent souvent aux CTI induit des mélanges dans le cas des systèmes lourds. Sur la figure 2, on voit que pour le système Xe + Au, tous les CTI se retrouvent à peu près au même angle et que la correspondance temps de réaction - angle n'est plus valable.

## 2.2. Asymétrie de masse

Dans le cas du système  $^{63}\text{Cu}$  365 MeV +  $^{197}\text{Au}$  (figure 3) on observe que la distribution de masse s'élargit quand on s'éloigne de l'angle d'effleurement, donc pour des valeurs des angles de rotation  $\theta_r$  et du temps croissantes. On observe corrélativement un déplacement du maximum de cette distribution.

Cette évolution peut être simplement comprise comme étant due à un processus de diffusion en physique statistique. La même hypothèse avait été formulée en ce qui concerne les distributions de masse des fragments de fission [8]: on peut considérer que les fragments sont définis au départ (masses initiales en CTI, fragments égaux au point selle en fission) et qu'un transfert au hasard de nucléons, de la nature d'un processus de Markov, a lieu entre le point selle et le point de scission.

La probabilité  $P$  de trouver le système de masse totale  $M$  avec des fragments de masse  $M_1$  et  $M_2 = M - M_1$  à un instant  $t$  est l'intégrale des probabilités de transfert de nucléons entre les deux fragments entre  $t = 0$  et  $t$ ,  $t = 0$  étant l'instant où le transfert commence, c'est-à-dire l'instant de contact en CTI et le point selle en fission. Il en résulte que  $P(M_1, t)$  obéit à une équation de Fokker-Planck:

$$\frac{\partial P(M_1, t)}{\partial t} = -V \frac{\partial P(M_1, t)}{\partial M_1} + D \frac{\partial^2 P(M_1, t)}{\partial M_1^2} \quad (3)$$

où  $V$  représente la vitesse d'entraînement du maximum de la distribution de  $M_1$  et  $D$  le coefficient de diffusion lié à la largeur de cette distribution.  $V$  s'obtient à partir de la dérivée de l'énergie potentielle du système en fonction de la répartition des nucléons entre ses deux parties (fig.3c; l'allure régulière de la courbe vient de ce que sont pris en compte seulement les termes de goutte-liquide). L'expression (3) dépend explicitement du temps et permet donc de calculer la distribution de masse à chaque instant. C'est ce qui a été fait pour les CTI sur la figure 3b [9]. Une comparaison plus précise peut être faite sur la figure 4 où l'évolution de la variance avec le déplacement de masse a été tracée pour deux énergies de bombardement. Les points expérimentaux s'alignent sur des droites, comme le prévoit la théorie. Les pentes de ces droites renseignent sur les valeurs des paramètres  $V$  et  $D$ . En fission, un raisonnement semblable conduit à l'évolution en fonction du temps, représentée sur la figure 5 en même temps que la distribution de masse expérimentale pour la fission spontanée du  $^{252}\text{Cf}$ ; la stabilité des configurations en couches est simulée par une diminution de la probabilité de transfert lorsqu'une telle configuration est atteinte dans un fragment.

On voit clairement, en comparant ces deux exemples, combien les possibilités d'investigation du processus sont plus puissantes dans le cas des CTI. En fission, on doit faire une supposition sur les fragments de départ; la durée n'est pas connue; il y a un seul élément de comparaison avec la réalité, qui sert à la fois à établir les valeurs des probabilités de transfert et à vérifier la validité des hypothèses de base, ce qui n'est évidemment pas satisfaisant. A l'opposé, en CTI, on connaît bien les masses des fragments initiaux; on obtient les distributions à une série d'angles correspondant chacun à une distribution différente de temps de réaction, et une comparaison avec l'expérience peut être faite pour chacune.

De plus, on peut modifier les conditions initiales de manière à déterminer la dépendance de  $V$  et  $D$  avec le rapport de masse initial, le moment angulaire  $\ell_i$ , la température nucléaire ... Par exemple, en choisissant un rapport de masse initial correspondant au maximum ou au minimum de la courbe d'énergie potentielle de la fig.3c,  $V$  s'annule (ou est très faible, selon la valeur de  $\ell$ ) et l'équation de Fokker-Planck se réduit à une équation de diffusion: la distribution de masse doit s'élargir avec la durée de réaction sans que sa position moyenne varie. Ceci a été vérifié par exemple pour le système  $^{40}\text{Ar} + ^{197}\text{Au}$  [10].

Lorsque l'énergie incidente augmente, la variance de la distribution de masse doit augmenter comme le produit du déplacement du maximum par la température nucléaire, ce qui est également observé [11].

Les effets de couches, qui jouent un rôle dominant en fission à basse énergie, ont été jusqu'ici négligés dans les calculs de CTI, car la température nucléaire est élevée. Cependant, ces effets modifient quelque peu l'énergie potentielle du système (fig.6) ainsi que la densité de niveaux des fragments — et donc la probabilité de transfert de nucléons — jusqu'à une température de plus de

2 MeV. Leur prise en considération devrait permettre de mieux rendre compte des transferts de masse observés [9, 12, 13].

Le temps de relaxation en masse est de l'ordre de  $5 \text{ à } 10 \cdot 10^{-21} \text{ s}$ , beaucoup plus long que les temps de relaxation en mouvement relatif et en rapport  $Z/N$ . Dans les premiers calculs, cela permettait de considérer que ces degrés de liberté étaient relaxés lorsque la diffusion en masse commençait. Actuellement, les calculs effectués suivent simultanément la variation des différents degrés de liberté collectifs [13, 14].

En conclusion de ce paragraphe, on peut retenir que l'étude des collisions très inélastiques a permis de montrer l'importance des phénomènes d'ordre statistique dans l'évolution d'un ensemble important de nucléons. Tous les résultats ne sont cependant pas expliqués; par exemple, des données récentes obtenues à Darmstadt [15] indiquent que les phénomènes de diffusion en CTI peuvent s'inverser quand l'énergie incidente dépasse 10 MeV/n; aucune explication satisfaisante n'a pu encore être fournie.

### 2.3. La vitesse relative

La situation est, là aussi, beaucoup plus variée en CTI qu'en fission. Dans le cas de la fission la vitesse relative des deux fragments provient de la phase d'accélération due à la répulsion coulombienne. Dans les CTI il y a d'abord une phase de freinage des deux ions, puis une phase d'accélération. Cette seconde phase peut être assimilée à ce que l'on observe en fission (voir 2.6), mais la première partie du phénomène donne des renseignements fort originaux qui permettent de comprendre la seconde (observée en fission).

En regardant simplement la distribution corrélée d'énergie cinétique et d'angle pour des fragments voisins des noyaux initiaux (fig. 7), on voit que même à l'angle d'effleurement l'énergie cinétique finale dépasse à peine la répulsion coulombienne; donc dans le système composite, la vitesse relative a été réduite à moins de 20% de la vitesse initiale. D'après la relation (1), le temps nécessaire correspondant est de  $10^{-21} \text{ s}$ . La dissipation de l'énergie cinétique relative est donc un phénomène très rapide qui a conduit à penser que la matière nucléaire est très visqueuse.

On peut utiliser une autre « horloge » : nous avons vu que la distribution de masse ou de charge s'élargit selon un processus de diffusion (relation 3, 2.2). On a donc  $\sigma_Z^2$ , ou  $M = D_Z t$ , ou  $M \cdot t$ . On peut donc utiliser maintenant l'élargissement en  $Z$  ou  $M$  (fig. 8) comme une horloge grâce à laquelle on étudie la perte d'énergie. Dans cette approche, il ne faut pas négliger les effets de transferts de charge qui modifient l'énergie de répulsion coulombienne, mais la correction correspondante est aisée. A partir de tels résultats, on peut tirer la figure 9 qui montre que la plus grande partie de l'énergie cinétique est perdue en un temps très court. Ensuite une composante plus lente apparaît.

Cette perte d'énergie peut être comprise dans un modèle classique [16] (voir la relation 5), où les deux noyaux sont freinés par une force de viscosité à deux corps proportionnelle à leur vitesse et à leur recouvrement. Cependant, les pertes d'énergie obtenues sont trop faibles, ce qui conduit à admettre un autre mécanisme au début de la collision. L'éjection de particules légères a été envisagée mais des résultats récents [17–19] montrent que, au moins pour des énergies incidentes pas trop élevées, elle ne peut permettre de comprendre les résultats. Une autre alternative consiste à admettre l'excitation de résonances géantes au début de la collision. Les données expérimentales actuelles [20] supportant cette hypothèse sont encore trop fragmentaires pour permettre de conclure, mais il semble de toute façon peu probable qu'elle permette d'expliquer des pertes d'énergie de grande ampleur (100 MeV au plus).

Plus séduisante est l'hypothèse de la viscosité à un corps qui consiste à étudier l'effet des parois d'un système sur les nucléons qui y sont contenus. Ceci revient à étudier le comportement des nucléons dans un potentiel moyen de dimension finie. L'effet des parois de ce potentiel est dominant si le libre parcours moyen des nucléons dans le noyau est de l'ordre ou plus grand que la dimension de ce noyau, ce qui est tout à fait le cas en CTI ou en fission. Le gros intérêt de ce concept est qu'il est le seul à pouvoir unifier les résultats obtenus en fission et en CTI.

En effet, si on utilise le concept de la viscosité à deux corps, les résultats concernant les énergies cinétiques de fission ne peuvent être expliqués que si le coefficient de viscosité est faible. C'est tout à fait l'inverse en CTI. Cette contradiction est levée si l'on admet que la viscosité est à un corps [21]. Dans ce cas les modes multipolaires de déformation d'ordre élevé sont amortis nettement plus vite que les modes multipolaires d'ordre inférieur qui sont supposés prédominer en fission. Notons que cette explication permet aussi de comprendre les deux régions notées sur la figure 9: la perte d'énergie est très rapide au début du processus du CTI, puis devient faible lorsque les effets de déformation des deux fragments se font sentir et conduisent le système dans une configuration voisine de celle obtenue en fission.

#### **2.4. Moment angulaire relatif et modes collectifs d'oscillation et de rotation**

*Comment un moment angulaire apparaît-il dans les fragments en fission et en CTI?* Nous distinguerons trois cas: d'abord, le cas de la fission spontanée ou induite par particules légères pour laquelle le noyau fissioneerant n'a pas ou peu de moment angulaire; ensuite, le cas de la fission induite par ions lourds pour laquelle le noyau fissioneerant a un moment angulaire important; enfin, le cas des CTI.

*Dans le premier cas*, on sait que l'on observe que les fragments émettent des rayonnements gamma. L'étude de leur distribution angulaire a permis de montrer que les fragments de fission disposent d'un moment angulaire perpendiculaire à leur direction de vol. Deux processus sont utilisés pour expliquer ces résultats:

- D'une part, l'excitation du mode collectif de pliage (oscillation de roulement, ou *bending* [22] des deux fragments autour du col les séparant; les rotations de torsion des deux fragments l'un par rapport à l'autre (*twisting*) et d'oscillation de glissement (*wriggling*) ont aussi été prises en compte (fig. 10); pour les noyaux lourds, la période propre de ces modes va de  $\sim 10^{-21}$  s pour le pliage à plusieurs  $10^{-21}$  s pour les autres [22].

- D'autre part, des excitations de quasi-particules lors de l'échange de nucléons entre les deux fragments.

La contribution relative de ces deux processus dépend des hypothèses faites sur le caractère adiabatique, partiellement statistique ou complètement statistique de la fission entre le point selle et le point de scission [23].

*Dans le cas de la fission d'un noyau disposant d'un important moment angulaire*, le moment angulaire observé dans les fragments peut avoir deux origines: une partie du moment angulaire initial du système (2/7 pour une fission symétrique) est convertie en spin des fragments; par ailleurs on peut s'attendre à observer les mêmes effets du mode de pliage observés dans la fission sans moment angulaire.

De fait, il faut faire appel à ces deux origines pour expliquer le seul résultat obtenu à ce jour: il s'agit de la fission du noyau de  $^{237}_{97}\text{Bk}$  formé dans la réaction  $^{40}\text{Ar} + ^{197}\text{Au}$  à 227 MeV [24]. La valeur de multiplicité  $\gamma$  obtenue conduit à un spin total des fragments de  $23,5 \pm 4 \text{ h}$  qui ne peut être expliquée à partir du moment angulaire initial seulement et qui conduit à une valeur de moment angulaire due au mode de pliage de  $10 \text{ h}$ . Cette valeur est semblable à celle observée en fission spontanée du  $^{252}\text{Cf}$  ( $\sim 7,5 \text{ h}$ ), et permet de rendre compte également de la distribution angulaire des gamma.

Supposons en effet qu'il n'y ait aucun effet du mode de pliage, donc que tout le moment angulaire observé dans les fragments soit dû au moment angulaire initial apporté dans la voie d'entrée. Le moment angulaire final dans les fragments serait alors grossièrement aligné avec le moment angulaire initial, donc perpendiculaire au plan de la réaction. Or, par analogie avec la désexcitation du noyau composé et des fragments de fission thermique, la plupart des  $\gamma$  sont des E2 (*stretched*) dont la distribution angulaire est:

$$w(\theta) = \frac{5}{4} (1 - \cos^4 \theta) \quad (4)$$

où  $\theta$  est l'angle d'émission par rapport à la direction du moment angulaire.

On s'attendrait donc à observer une forte anisotropie des gamma émis, ce qui n'est pas le cas. Ce résultat semblerait confirmer l'existence d'une composante additionnelle du moment angulaire.

*En CTI, la différence essentielle avec le cas de la fission avec moment angulaire (§ précédent) vient du fait que le temps de vie du système composite est beaucoup plus court. Il peut donc ne pas avoir atteint le stade d'une rotation globale (rigide) du système composite, comme c'est sûrement le cas en fission. Mais examinons plus formellement la situation:*

Soit  $\ell_i$  le moment angulaire initial (dans la voie d'entrée). Le transfert de moment angulaire  $\Delta\ell$  s'effectue pendant toute la durée de collision et sa valeur finale dépend du degré de cohésion atteint par le système à la scission. L'interaction entre les deux noyaux peut être comprise classiquement en introduisant dans les équations du mouvement un terme dissipatif dû à la friction entre les deux ensembles de nucléons dans la zone d'interaction. En distinguant la friction radiale de la friction tangentielle, on obtient deux équations:

$$\mu \frac{d^2 r}{dt^2} = - \frac{\partial V N(r)}{\partial r} + \frac{Z_1 Z_2 e^2}{r^2} + \frac{\ell(\ell+1)\hbar^3}{\mu r^3} - C_r - f(r) \frac{dr}{dt} \quad (5)$$

et

$$\frac{d}{dt} \ell \hbar = - C_t \cdot f(r) \frac{d\theta}{dt} r^2 \quad (6)$$

(5) décrit le mouvement radial, alors que (6) décrit le mouvement de rotation. La friction tangentielle  $C_t$  peut être décomposée en une friction de frottement qui intervient au début de l'interaction et induit une rotation relative des deux noyaux (les noyaux roulent l'un sur l'autre), et une friction de roulement qui réduit cette rotation et bloque les deux partenaires l'un sur l'autre: le système est alors un corps rigide en mouvement de rotation global.

Si la séparation intervient quand les deux noyaux roulent l'un sur l'autre, le transfert de moment angulaire est

$$\Delta\ell_r = \frac{2}{7} \ell_i \quad (7)$$

et la répartition entre les deux fragments de masses  $M_1$  et  $M_2$  est proportionnelle à leur rayon

$$\frac{\Delta\ell_{r1}}{\Delta\ell_{r2}} = \left( \frac{M_1}{M_2} \right)^{1/3} \quad (8)$$

Si la séparation intervient après que le système a atteint le stade ultime (rotation d'un corps rigide), les moments angulaires des deux partenaires sont

$$\Delta\ell_{s1} = \frac{\mathcal{J}_1}{\mathcal{J}_1 + \mathcal{J}_2 + \text{orb}} \ell_i \quad (9)$$

$$\Delta\ell_{s2} = \frac{\mathcal{J}_2}{\mathcal{J}_1 + \mathcal{J}_2 + \text{orb}} \ell_i \quad (10)$$

Le moment angulaire total des deux fragments est

$$\Delta\ell_s = \Delta\ell_{s1} + \Delta\ell_{s2} \quad (11)$$

$\mathcal{J}_1$  et  $\mathcal{J}_2$  sont les moments d'inertie des noyaux autour de leurs axes de rotation, et  $\text{J}_{\text{orb}}$  est le moment d'inertie de ces deux fragments relativement au centre de gravité du système. Si les deux fragments ont la même déformation, le rapport des moments angulaires intrinsèques varie comme

$$\frac{\Delta\ell_{s1}}{\Delta\ell_{s2}} = \left( \frac{M_1}{M_2} \right)^{5/3} \quad (12)$$

La mesure la plus précise de l'état de cohésion du système serait donnée par le rapport  $\Delta\ell_1/\Delta\ell_2$ , qui varie très rapidement (relations 8 et 12). Il faudrait mesurer simultanément le moment angulaire de chaque fragment. Ceci n'a pas été fait et on utilise seulement la mesure de  $\Delta\ell$  globale, par la multiplicité  $\gamma$  associée à chaque événement, ou  $\Delta\ell_1$  du fragment lourd, par la distribution angulaire de fission séquentielle [25].

La difficulté dans l'interprétation des expériences vient de la mauvaise connaissance que l'on a généralement de  $\ell_i$ . Par ailleurs,  $\Delta\ell_s/\ell_i$  varie avec le moment d'inertie des fragments (relations 9 à 11). Il dépend donc de l'état de déformation des fragments. La figure 11 donne une idée de l'influence des déformations sur le résultat: la courbe intermédiaire correspond à des déformations compatibles avec les énergies cinétiques des produits finaux observés. C'est en particulier la courbe qui s'applique à la fission puisque les deux fragments sont dans ce cas liés rigidement.

En CTI, la première observation est que  $\Delta\ell$  augmente rapidement avec le degré d'inélasticité (fig. 12). Les transferts d'énergie cinétique partiels correspondent à toute une gamme de temps d'interaction qui couvre toutes les étapes depuis le glissement jusqu'au roulement. Si on sélectionne les événements complètement amortis en énergie, leur degré de cohésion augmente avec le temps de réaction, depuis une valeur correspondant au moins à l'étape du roulement jusqu'à l'étape

du corps rigide. Le temps de relaxation associé à  $\Delta\ell$  est long ( $\sim 5 \times 10^{-21}$  s), et seule une partie des événements de quasi-fission atteignent un état de cohésion du système équivalent à la fission, ceci en particulier lorsque l'énergie de bombardement du système dépasse 1,5 fois la barrière d'interaction.

En fait une grande partie des résultats obtenus en multiplicité  $\gamma$  associée aux CTI n'offrent pas une interprétation aisée. Prenons pour exemple le cas du système Cu + Au à 365 MeV; la valeur moyenne de multiplicité  $M_\gamma$  obtenue pour les événements relaxés en énergie mais ne correspondant pas à de grands transferts de masse est tout à fait compréhensible dans l'hypothèse du collage. Il semblerait établi que ce stade ultime est atteint pour ces événements. Pourtant, l'évolution de  $M_\gamma$ , lorsque l'on considère des événements pour lesquels le transfert de masse a eu lieu, est tout à fait opposée à ce que prévoit le calcul (figure 13). Diverses interprétations ont été données de ces résultats, mais aucune n'est pleinement satisfaisante.

Dans la première [12], on utilise les propriétés des courbes d'énergie potentielle du type de celles tracées sur la figure 3c. On voit sur ce schéma que les forces d' entraînement conduisant le système vers une configuration symétrique sont d'autant plus grandes que le moment angulaire dans la voie d'entrée est grand. Les événements symétriques seraient donc associés préférentiellement à des grandes valeurs de  $\ell_i$ . La figure 11 a été tracée pour une valeur donnée de  $\ell_i$ . Pour un ensemble de valeurs de  $\ell_i$ , cet effet de force d' entraînement peut inverser la tendance et conduire à une variation telle que celle observée expérimentalement (fig. 13). Cette interprétation se heurte à deux problèmes: le premier concerne les estimations quantitatives indiquant que dans le cas du système Cu + Au cet effet n'est pas suffisant pour inverser la variation de  $M_\gamma$  avec l'asymétrie de masse; le second est que les propriétés relatives aux transferts des nucléons entre les deux fragments sont interprétées en admettant au contraire que les événements symétriques correspondent à des valeurs faibles de  $\ell_i$  pour lesquelles la durée de vie du système composite est grande.

La seconde interprétation [26] consiste à admettre que le stade de collage n'est atteint que très lentement. On n'atteindrait donc la courbe théorique de la figure 11 que pour de grands temps d'interaction, donc pour des masses égales des deux produits (degré de liberté asymétrie de masses équilibré). Pour des valeurs supérieures du rapport des masses, donc pour des temps de vie plus courts, le collage serait loin d'être atteint et le transfert de moment angulaire  $\Delta\ell$  serait beaucoup plus petit. L'effet serait assez violent pour inverser la tendance de la figure 11. Cette interprétation a été retrouvée quantitativement, mais elle se heurte au fait que les valeurs de multiplicité obtenues dans le calcul sont plus faibles que les valeurs mesurées.

On peut donner de cette divergence deux explications: D'abord, on peut admettre que la multipolarité de la plupart des gamma émis n'est pas deux, comme on l'admet toujours. Cette question est encore aujourd'hui très contro-

versée [27, 28]. On peut aussi voir dans cette divergence un effet du mode de pliage, comme nous l'avons noté en fission. Cette seconde interprétation nous paraît très plausible si l'on remarque que le temps nécessaire pour exciter ce mode est de l'ordre de  $10^{-21}$  s, donc compatible avec la durée de vie des CTI. Notons que l'excitation de ce mode est très favorisée si le système présente une symétrie non axiale [29], ce qui est bien évidemment le cas en CTI. L'ordre de grandeur du moment angulaire de pliage serait de 18  $\hbar$  pour le système Cu + Au, valeur tout à fait comparable aux valeurs obtenues en fission. Enfin, on explique également ainsi comment la distribution angulaire des gamma associés aux CTI est isotrope comme en fission [24, 30].

Les expériences de fission séquentielle peuvent donner une information intéressante sur cette question. Les résultats actuels [25] indiquent que la dépolarisat<sup>ion</sup> dans les CTI n'est sûrement pas totale, mais ils sont en désaccord pour ce qui concerne l'importance de la dépolarisat<sup>ion</sup>. Certains indiquent qu'elle serait nulle; d'autres qu'elle ne serait pas négligeable et explicable par un mode de pliage mais que le moment angulaire supplémentaire apporté par ce mode serait relativement faible. De nouvelles expériences sont nécessaires pour clarifier la situation. Notons que la comparaison de différents résultats entre eux doit être réalisée avec prudence. Ainsi les résultats de fission séquentielle ont tous été obtenus pour des valeurs de  $\ell_{\max}$  (valeur de moment angulaire correspondant à une trajectoire rasante de l'ion incident) beaucoup plus grandes que les valeurs correspondantes impliquées dans les expériences de multiplicité gamma telles que l'expérience Cu + Au 365 MeV. L'effet du mode de pliage pouvant être le même en valeur absolue dans les deux cas sera beaucoup plus nettement ressenti à bas  $\ell_{\max}$  où il sera relativement plus important.

En conclusion de ce paragraphe, les transferts de moment angulaire dans les CTI ne sont pas clairement connus. Ce qui est certain est que le temps de relaxation associé à ce mode est grand. Ce qui est probable, c'est que le mode de pliage, comme en fission, joue un rôle dans le processus.

## 2.5. Emission de particules accompagnant les CTI et la fission

Une des premières questions qui se sont posées à la découverte des CTI était: où passe l'énergie cinétique perdue entre les voies d'entrée et de sortie? Puisque le caractère essentiellement binaire de la réaction a été bien établi, il faut que cette énergie soit dissipée par émission de particules légères (et en  $\gamma$ , mais ceux-ci n'ont que 1 MeV en moyenne).

On peut imaginer plusieurs étapes où cette émission a lieu: une ou des particules peuvent être éjectées, par friction, de la zone de contact au début de la collision; ensuite une partie de l'énergie cinétique relative est transformée en énergie d'excitation interne qui peut rester concentrée dans la zone du col, auquel cas une émission de prééquilibre peut avoir lieu soit depuis le col, soit

depuis la zone du col appartenant à chaque fragment après la scission; ou bien, cette énergie d'excitation est thermalisée sur l'ensemble du système composite, la température nucléaire atteinte ne dépasse pas quelques MeV et, après séparation, les fragments se désexcitent par évaporation de particules, essentiellement des neutrons (ou par fission dans le cas des fragments très lourds).

Pour distinguer entre ces différentes possibilités, il suffit en principe de mesurer la distribution angulaire et en énergie des particules émises en coïncidence avec les fragments de CTI. Si la vitesse du (ou des) centre émetteur n'est pas faible devant celle de la particule émise, la reconstruction cinématique indiquera la direction et la vitesse moyenne du (ou des) centre émetteur. On peut ainsi déterminer si la majorité des particules vient d'un fragment avant ralentissement complet, du système composite, d'un ou deux des fragments accélérés après scission. Mais une émission de faible importance relative apparaît difficilement.

Lorsqu'une seule particule est émise en coïncidence avec les deux fragments principaux, on peut utiliser les lois de conservation du mouvement pour distinguer entre émission directe (simultanée) des trois fragments et émission séquentielle par un fragment sans influence de l'autre. Dans les deux cas, les lois de conservation sont satisfaites sur la somme des énergies cinétiques et des quantités de mouvement des trois fragments. Dans le deuxième cas, on a une relation supplémentaire: les  $Q$  de formation du fragment intermédiaire (qui émet la particule) et de l'autre fragment sont en moyenne indépendants de l'angle de détection de la particule [31].

### 2.5.1. Emission de neutrons

En fission, les particules émises sont presque exclusivement des neutrons. Seules quelques particules chargées très peu nombreuses sont observées. La raison de cet état de chose est que les fragments de fission sont toujours riches en neutrons.

Dans le cas des CTI, l'émission de neutrons n'est nettement dominante que si les énergies de liaison correspondantes favorisent leur émission: c'est systématiquement le cas pour les systèmes lourds. Dans ce cas il a pu être montré [18, 19] que l'essentiel de l'énergie dissipée dans les CTI se retrouve sous la forme de neutrons évaporés par les fragments. Ceci apparaît très nettement sur la figure 14 qui donne en coordonnées polaires les nombres de neutrons détectés à différents angles laboratoires et avec des vitesses  $v$ . Il s'agit du système Cu + Au à 400 MeV [18].

Aucune contribution du col ou d'un point chaud n'est visible [32]. Cette analyse est confirmée par une analyse cinématique détaillée où l'origine possible de chaque neutron détecté est prise en compte. Deux conclusions se dégagent: 1) la totalité de l'énergie cinétique perdue se retrouve en énergie d'excitation des fragments (compte tenu du  $Q$  de réaction lorsqu'il y a transfert de masse),

qui évaporent des neutrons et émettent des  $\gamma$ ; 2) l'énergie d'excitation est répartie entre les fragments proportionnellement à leur masse, et les spectres en énergie des neutrons émis par chaque fragment correspondent à la même température. On en conclut qu'à la scission la température nucléaire est uniforme dans l'ensemble du système. Le temps de thermalisation est donc inférieur à quelques  $10^{-21}$  s. Une valeur plus précise peut être obtenue. On utilise la dissipation d'énergie cinétique comme horloge rapide puisqu'on sait que la première partie de l'amortissement en énergie cinétique est très rapide (voir figure 9). On a donc sélectionné les fragments de masse voisine de celles des noyaux initiaux et on a examiné le rapport des nombres de neutrons émis par chaque fragment en fonction de la perte d'énergie cinétique (fig. 15). Ce rapport est constant et égal au rapport des masses dès une diminution d'énergie cinétique de 30 MeV: pour ce degré de liberté intrinsèque, l'équilibre est atteint même pour des durées de contact de quelques  $10^{-22}$  s. On peut en conclure que pour des durées de vie aussi longues que celles impliquées dans la fission, il est certain que la température du système fissioneer reste uniforme.

### *2.5.2. Emission de particules chargées*

Dans le cas des CTI, un résultat est clair: l'émission de particules chargées croît fortement avec l'énergie incidente, ce qui signifie que les mécanismes d'éjection de particules sont plus importants à haute énergie. D'une façon générale, les particules chargées peuvent être classées en deux catégories: les particules chargées évaporées par les fragments pleinement accélérés et les particules chargées directes. Les particules chargées évaporées ne concernent que les systèmes légers, car dans le cas de systèmes lourds l'émission de neutrons ne laisse aucune place à l'évaporation de particules chargées (à cause des effets de barrières coulombiennes). C'est ainsi que des composantes d'évaporation ont été notées pour les systèmes  $^{14}\text{N} + ^{93}\text{Nb}$  à 110 MeV [33],  $^{16}\text{O} + ^{58}\text{Ni}$  à 94 MeV [34], Ar + Ni à 280 MeV [35]. Par contre, pour le système Kr + Au [36], une partie des particules détectées sont éjectées au moment de la collision.

#### *Composante d'évaporation*

Le point le plus frappant concerne ici les températures des noyaux émetteurs. Dans le cas du système O + Ni, les auteurs ne peuvent expliquer leurs résultats qu'en admettant l'existence d'un point chaud pendant la collision. Ceci implique que la conductivité thermique de la matière nucléaire serait très faible, résultat complètement opposé aux conclusions de toutes les études d'émission de neutrons.

*Composante directe*

Les résultats sont encore très fragmentaires sur cette question et l'origine de cette composante est inconnue. Cependant, une conclusion intéressante semble pouvoir être tirée qui est très proche de celle concernant l'émission de particules  $\alpha$  accompagnant la fission [37]: la direction d'émission est perpendiculaire à la direction d'émission des fragments. On en conclut qu'il y a émission d' $\alpha$  de faible vitesse à partir du col puis accélération et focalisation par le champ coulombien des deux fragments naissants. Cette description s'applique à l'émission de particules chargées accompagnant la fission. La différence apparente est dans le taux d'émission, qui serait voisin de 0,1 donc de deux ordres de grandeur supérieur à celui de la fission spontanée. Cependant, en fission, le taux d'émission croît avec le  $Z/A$  et l'énergie d'excitation du noyau fissioneer, ceci jusqu'au  $^{252}\text{Cf}$  et à 50 MeV d'énergie d'excitation. L'extrapolation de ces données au système  $^{283}115$  excité à plus de 300 MeV est donc quelque peu hasardeuse. Néanmoins, le taux observé n'est pas en désaccord avec la systématique de fission. Cette similitude entre fission et CTI n'est guère surprenante, car l'émission  $\alpha$  a lieu au point de scission. En ce point, les propriétés des fragments de CTI et de fission peuvent être voisines.

**2.6. La déformation au point de scission**

On ne peut obtenir sur ce paramètre que des renseignements indirects concernant les énergies cinétiques des produits finaux et les désexcitations de ces produits.

**2.6.1. Energies cinétiques des produits finaux**

On sait qu'en fission les énergies cinétiques totales des fragments sont inférieures à la répulsion coulombienne de deux noyaux sphériques. Ce résultat implique une déformation des fragments au point de scission que l'on est capable de calculer dans un modèle hydrodynamique [38]. La situation est tout à fait similaire dans le cas de la plupart des CTI et les fragments naissants sont donc largement déformés [39]. Des comparaisons précises entre les énergies cinétiques obtenues en fission et les valeurs correspondantes pour les CTI sont difficiles à réaliser. En effet, la distinction entre les deux mécanismes ne peut être faite que dans le cas de couples cible-projectile très asymétriques conduisant à des fragments de CTI très asymétriques que l'on doit comparer à des fragments de fission symétrique obtenus pour le même système composite; la correction due à l'asymétrie de masse et à l'émission de neutrons n'est pas évidente à évaluer et on ne peut conclure que le résultat suivant: les valeurs des énergies cinétiques finales des fragments de CTI et de fission sont voisines (peut-être un peu supé-

rieures pour les CTI). Ces deux processus conduisent donc à des fragments déformés de déformation voisine. Les chemins suivis en fin de CTI et en fin de fission pourraient donc être similaires si l'on ne considère que ce résultat.

### 2.6.2. Désexcitation des fragments

Il est connu que les courbes  $\nu(M)$  donnant la multiplicité de neutrons en fonction de la masse du fragment de fission émetteur traduisent la déformation dudit fragment. En effet l'énergie d'excitation d'un fragment accéléré est la somme de deux termes: l'énergie d'excitation + l'énergie de déformation au point de scission. Dans la fission à basse énergie, le premier terme est négligeable devant le second qui est donc déterminant. La même analyse peut être faite en CTI si l'énergie de bombardement est suffisamment faible. Une seule mesure de multiplicité neutrons a été réalisée dans ce cas [40]. Elle a montré que l'énergie de déformation du fragment léger est relativement beaucoup plus grande que celle du fragment lourd. Ce résultat est très intéressant car il semble indiquer que les formes des fragments mises en jeu en CTI sont différentes de celles mises en jeu en fission. De nouvelles mesures sont clairement nécessaires, et en fission à haute énergie d'excitation, et en CTI, pour préciser ce résultat.

## 2.7. Le rapport N/Z des nombres de neutrons et de protons

Il s'agit là d'un domaine où les CTI ont apporté beaucoup à l'étude de la fission. On sait en effet qu'en fission, les distributions de charges peuvent être interprétées dans trois contextes: UCD (*unchanged charge density*), ECD (*equal charge displacement*) [41] et MPE (énergie potentielle minimale) mais qu'on ne peut pas trancher entre les trois approches. Il a été montré que l'évolution du rapport N/Z était associée à un temps propre suffisamment court pour que les propriétés des fragments influent beaucoup sur les résultats, mais la situation est restée floue.

En CTI, on bénéficie encore une fois du grand choix de couples cible-projectile qui ont permis d'étudier d'abord le temps propre associé à l'équilibrio-  
tion N/Z. Il a été montré il y a plusieurs années [42, 43] que ce temps propre est très court, tellement court qu'il est équilibré pour tous les événements de CTI dès que la dissipation d'énergie a commencé. On peut donc penser que la situation est tout à fait similaire en CTI et en fission.

Or il a été montré en CTI que la valeur d'équilibre atteinte correspond au N/Z qui minimise l'énergie potentielle du système composite (MPE) mais pas celle prévue dans l'interprétation ECD. La raison pour laquelle on a pu facilement trancher en CTI et pas en fission est que les fragments de fission sont toujours tous les deux déficients en neutrons, ce qui n'est pas le cas en CTI.

Une autre donnée intéressante concerne la largeur des distributions en N/Z [44]. En fission, on sait que ces largeurs n'augmentent pas quand on augmente l'énergie d'excitation. Récemment un résultat tout à fait similaire [45] a été obtenu en CTI. On voit en effet sur la figure 16 comment la largeur  $\Gamma_z$  de la distribution en charge varie avec le degré d'inélasticité. Dès que l'énergie dissipée atteint 30 MeV,  $\Gamma_z$  ne varie plus, contrairement à ce que l'on attendrait dans un traitement statistique. En fission comme en CTI, ce résultat serait le reflet de fluctuations quantiques.

## 2.8. Conclusion

La fission et les CTI présentent manifestement de grandes analogies. En première approximation on peut admettre que les stades finaux des deux mécanismes sont voisins, bien qu'il existe certaines évidences qu'ils ne sont pas superposables (§ 2.7). Les différences essentielles entre les deux mécanismes résident dans les temps de réaction qui sont généralement très différents (voir § 2.1 et § 3). Cette propriété a pu être utilisée en CTI pour obtenir des informations sur les propriétés nucléaires qui avaient été noyées dans le cas de la fission à cause de la trop grande durée de vie associée. Un autre avantage des CTI réside dans la grande gamme de couples projectile-cible, propriété qui permet de s'affranchir de telle ou telle difficulté selon la caractéristique étudiée.

Un inconvénient des CTI réside par contre dans le fait qu'il est dans ce cas impossible de s'affranchir de l'effet du moment angulaire  $\ell_i \hbar$ . Souvent, on a affaire à toute une plage de valeurs de  $\ell_i$  qui rend difficile les interprétations de données telles que les spins des fragments finaux ou leur énergie cinétique, puisque le terme centrifuge correspondant est mal connu. Dans ce cas la fission a apporté et apportera des renseignements précieux pour interpréter les données en CTI.

## 3. EVOLUTION DES CTI A LA FISSION SUIVANT FUSION

Quand on bombarde un noyau cible avec un projectile, on observe soit des phénomènes élastiques ou quasi élastiques, soit des CTI, soit de la fusion.

La fusion des noyaux projectile et cible aboutit soit directement à la formation du noyau composé, soit à une émission de prééquilibre qui conduit à la formation d'un noyau de masse et d'énergie d'excitation inférieures à celles du noyau composé mais qui a atteint l'équilibre thermodynamique. Ne pouvant généralement pas faire la distinction, nous utilisons le terme de «noyau de fusion complète» qui est moins restrictif que le terme de «noyau composé». Ce noyau se désexcite par évaporation de particules, émission  $\gamma$  ou par fission. Sa forme dépend du moment angulaire: dans le cadre du modèle de la goutte

liquide, à faible  $\ell$ , il est pratiquement sphérique, et au fur et à mesure que  $\ell$  croît, il devient de plus en plus allongé [46]. Pour des valeurs pas trop élevées de  $\ell$ , cette forme est moins allongée que celle du point de déformation critique conduisant à la fission en deux fragments égaux (point selle).

La fission d'un noyau de fusion consiste en l'évolution du système depuis cette configuration relativement « ramassée » jusqu'au point de scission. En CTI, nous avons vu que la situation est généralement inverse, le système restant au-delà de ce point critique. C'est la raison pour laquelle le temps associé aux CTI est beaucoup plus court.

Le problème est que, expérimentalement, il semble pourtant qu'il y ait souvent une évolution continue entre fission suivant fusion et CTI. De fait, si la distribution de masse de la plupart des CTI reste marquée par la mémoire des masses initiales (§ 2.2), un faible pourcentage d'événements a vécu assez longtemps pour que le degré de liberté asymétrie de masse soit équilibré. C'est le cas des événements détectés à  $26^\circ$  sur la figure 3a. Ces événements peuvent constituer une traîne de CTI à durée de vie plus longue (il y a une évolution continue quand l'angle de détection diminue), mais ils peuvent aussi être attribués à de la fission suivant fusion et l'on ne peut trouver aucun critère expérimental permettant de trancher. Par exemple, la distribution angulaire associée aux événements symétriques de la figure 17 est en  $1/\sin \theta$ , comme en fission, et on voit sur la figure l'évolution continue entre les distributions angulaires pour ces événements et les événements clairement attribuables aux CTI (autour de la masse 63).

Les bandes de temps associées aux CTI et à la fission suivant fusion sont-elles donc assez longues pour se recouvrir? La réponse est non. Il existe en effet des systèmes pour lesquels la distinction entre CTI et fission suivant fusion est absolument sans équivoque: c'est le cas du système Ar + Au à 220 MeV pour lequel chacune des bosses de la figure 18 est associée à l'un des processus. Dans ce cas la distinction est claire et montre sans ambiguïté la discontinuité en temps entre les deux mécanismes.

Sur un plan théorique, cette distinction est clairement visible dans des calculs tels que ceux de Nix (fig. 19) relatifs à la collision entre deux ions de  $^{110}\text{Pd}$  à une énergie supérieure de 20 MeV à la barrière coulombienne [47]. Dans l'espace des déformations (représentées ici par l'interdistance des noyaux et leur élongation), la trajectoire du système passe à l'intérieur de la position du point de déformation critique entre  $\ell = 0$  et  $\ell = 45$ , et la fusion peut avoir lieu. Au-dessus de  $\ell = \ell_{\text{Cfu}} = 45$ , le système reste au-delà du point selle et seule une CTI a lieu.

Les deux réactions sont caractérisées par des temps différents: la durée du système composite varie dans le domaine  $10^{-22}$  à  $10^{-21}$  s alors que la durée de vie du noyau de fusion complète dépasse  $10^{-20}$  s avant la fission.

A ce stade du raisonnement, il subsiste une difficulté dans le modèle de la goutte liquide tournante déjà mentionné [48]: la barrière de fission s'annule au-delà d'une certaine valeur  $\ell_{Bf=0}$  du moment angulaire initial  $\ell_i$ . Il est clair que, dans ce cas, la durée de vie du noyau composé diminue fortement et on peut se demander si elle ne rejoint pas celle des CTI. Dans une telle interprétation,  $\ell_{Bf=0}$  serait la frontière entre la fission suivant fusion et les CTI.

Ceci n'est pas le cas: en effet, une série de données expérimentales peut être utilisée pour indiquer que, entre la fission suivant fusion et les CTI, il existe un troisième mécanisme. Nous allons d'abord faire le tour de ces données puis nous donnerons l'interprétation.

### 3.1. Données

Si l'on découpe la plage de moment angulaire conduisant à des réactions inélastiques profondes, on s'attendrait à ce que la zone attribuable à la fission ne dépasse pas  $\ell = \ell_{Bf=0}$ . Des résultats concernant par exemple les systèmes Ar + Sb, Ar + Tb, Ar + U [48] ont montré que la zone de  $\ell$  associés à des événements symétriques de type fission excède en fait largement ce moment angulaire limite. Au-delà de  $\ell_{Bf=0}$ , les événements obtenus sont donc de type symétrique, relaxés en masse et clairement résolus des CTI; la limite au-delà de laquelle apparaissent les CTI est donc largement supérieure à  $\ell_{Bf=0}$ . Elle a souvent été appelée  $\ell_{crit}$ . Entre  $\ell_{Bf=0}$  et  $\ell_{crit}$ , les événements observés ont une durée de vie sûrement beaucoup plus courte que celle associée à la fusion, mais sûrement beaucoup plus longue que celle des CTI.

Si l'on étudie la distribution de masse de ces événements intermédiaires, il apparaît qu'elle est beaucoup plus large que celle des événements de fission [49,50]. Il est donc clair que ces événements ont eu une histoire différente.

Une troisième donnée expérimentale indique aussi l'existence de ce troisième mécanisme, mais arrive à des conclusions un peu différentes: il s'agit de l'analyse des fonctions d'excitation de fission. Ces fonctions d'excitation ont été mesurées pour 5 systèmes formés avec des ions lourds  $^{20}Ne$ ,  $^{35}Cl$  ou  $^{40}Ar$  sur des cibles  $^{63}Ni$ , Ag,  $^{116}Sn$  et  $^{141}Br$  [51]. En utilisant le modèle statistique de la compétition entre fission et évaporation tenant compte de l'effet du moment angulaire, on se heurte à une difficulté: quel que soit le choix de paramètres de densité de niveaux, on ne peut reproduire à la fois le seuil de la fonction d'excitation et la valeur qu'elle atteint à quelques dizaines de MeV au-dessus du seuil (fig.20). Pour parvenir à un accord, les auteurs utilisent des barrières de fission «effectives» qui atteignent seulement 50 à 65% des valeurs des barrières goutte liquide pour les ondes partielles où la fission intervient, c'est-à-dire plus de 40 à 45 h. Ceci impliquerait que la diminution de la barrière de fission avec le moment angulaire est beaucoup plus importante que ne le prévoit le modèle de la goutte liquide. Une autre possibilité est d'admettre qu'au moins une partie

des événements attribués à « noyau composé — fission» sont en fait issus d'un autre processus. La courbe en tirets de la figure 20 montre que ces événements supplémentaires sont ceux qui apparaissent au seuil de la fonction d'excitation. Ceux-ci ne correspondent donc pas aux ondes partielles pour lesquelles la barrière de fission est nulle (et qui sont d'ailleurs inclus dans la section efficace de fission calculée) puisque celles-ci n'interviennent qu'aux grandes énergies incidentes.

### 3.2. Interprétation

Il semble au premier abord difficile de concilier cette troisième donnée (qui semble ne rien avoir affaire avec  $\ell_{Bf} = 0$ ) et les deux précédentes. En fait il n'en est rien.

Pour comprendre la situation, il faut remarquer qu'une carte telle que celle de la figure 19 est tracée pour une asymétrie de masse donnée. Supposons que le système dans la voie d'entrée soit asymétrique et que, pour des considérations d'énergie potentielle, il ait tendance à évoluer vers la symétrie (voir § 2.2). Si l'énergie de bombardement est relativement faible il peut franchir le point critique de la figure 19 avec une faible vitesse. Par la suite, à cause du transfert de nucléons, la carte de la figure 19 évolue; en particulier, le point critique se déplace; plus précisément, il se rapproche de la configuration sphérique. L'évolution est donc double: le point de configuration du système S et le point critique C évoluent tous les deux vers la configuration quasi-sphérique du noyau composé. Il peut se faire que, au cours de cette évolution, le point critique C dépasse le point S. Le système se retrouve alors au-delà du point selle et évolue irrémédiablement vers la scission. Cette image explique très bien les résultats de [51] exposés plus haut: on observe la fission suivant fusion ou le 3<sup>e</sup> mécanisme selon les vitesses de déplacement relatives des points S et C.

Examinons maintenant la situation lorsque le moment angulaire incident  $\ell_i$  croît. Lorsqu'on atteint  $\ell_{Bf}=0$ , le point critique C pour une configuration symétrique disparaît. Cela ne signifie pas qu'il n'existe pas pour la configuration asymétrique de la voie d'entrée. Ce système peut donc dépasser ce point critique, rester en deçà du point critique (configuration plus ramassée) tant que le système n'a pas évolué vers la symétrie. Quand il se rapproche de la configuration symétrique, le point C disparaît et le point S évolue à nouveau irrémédiablement vers la scission: comme dans le cas précédent, on assiste à une «fission» sans passage de point selle. Le système a une durée de vie qui est juste celle permettant de réaliser suffisamment l'équilibration en masse.

Si on augmente encore  $\ell_i$ , ou si le système incident est très lourd, le point C n'existe même plus dans la voie d'entrée (voir les calculs réalisés dans l'approximation soudaine). Dans ce cas, le système évolue directement vers le point de scission; il n'est à aucun moment piégé: on n'observera que des CTI, pas de fission, pas de 3<sup>e</sup> mécanisme. Ceci est le cas des systèmes Cu + Au ou Kr + Bi.

Ce troisième mécanisme est une fission sans passage de point selle. Le nom de «quasi-fission» semblerait adapté, mais ce terme a déjà été utilisé pour les collisions d'ions très lourds relaxées en énergie. Aussi l'appellerons-nous «fission hors barrière».

Sa mise en évidence expérimentale n'est pas facile car:

- elle n'existe pas pour les couples projectile-cible identiques; aux grands  $\lambda_i$ , le système reste au-delà de la déformation critique, et on a des CTI; lorsque  $\lambda_i$  diminue, il franchit cette déformation et évolue alors vers la fusion complète (l'absence possible de fusion aux faibles  $\lambda_i$  est une autre question);
- lorsque le noyau de fusion a une faible barrière de fission, les événements de fission par le point selle et de fission hors barrière sont mélangés.

On ne peut donc étudier ces événements que pour des systèmes initiaux asymétriques. On peut alors choisir soit un système lourd, soit un système moyen. Avec un système lourd, on bénéficie de la possibilité d'atteindre une grande plage de  $\lambda$  supérieurs à  $\lambda_{Bf=0}$  aux énergies de bombardement élevées; en faisant croître l'énergie incidente, la proportion relative des événements dus à la fission hors barrière augmente, et ses caractéristiques peuvent être mises en évidence. C'est ce qui a été fait dans la réf. [49]. Avec un système moyen, au contraire, la fission hors barrière est une faible partie de la fission par le point selle aux énergies incidentes élevées, mais son seuil est un peu inférieur et c'est là qu'elle apparaît dans la réf. [51].

L'étude de ce troisième mécanisme ne fait que commencer et il n'est pas encore possible de le comparer précisément à la fission conventionnelle et aux CTI. Les expériences les plus intéressantes seront celles qui montreront les effets de formes des fragments. En effet, dans le cas du 3<sup>e</sup> mécanisme, on s'attend à ce que le système reste toujours bi-nucléaire, par opposition à ce qui se passe en fission. Des indications intéressantes concernant ce point ont déjà été obtenues [40].

#### REMERCIEMENTS

Cet exposé a été en partie préparé pendant le séjour d'un auteur (Jean Péter) au Lawrence Berkeley Laboratory qu'il remercie pour son hospitalité et son aide.

**Annexe**

**FIGURES 1 A 20**

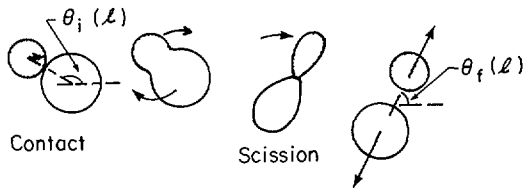


FIG.1. Représentation schématique d'une collision très inélastique.

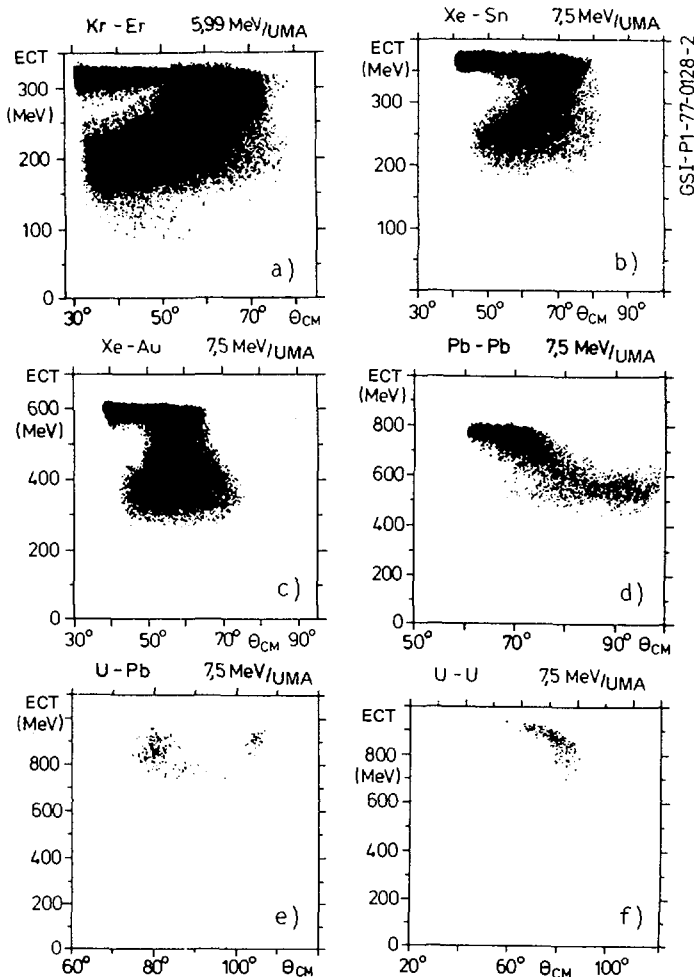
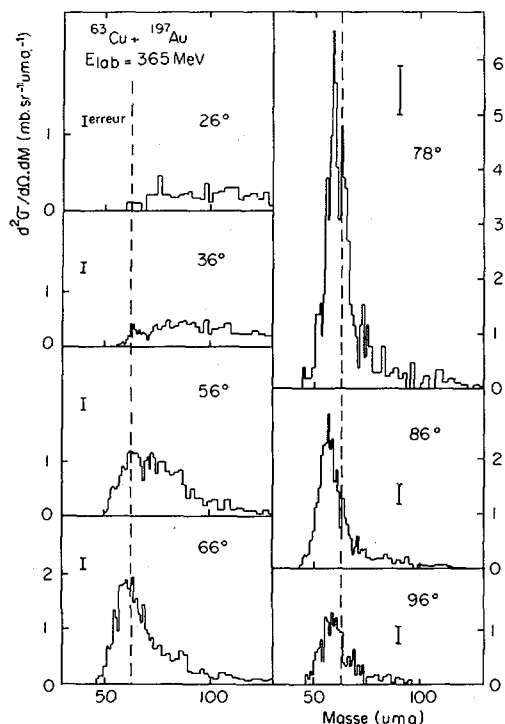
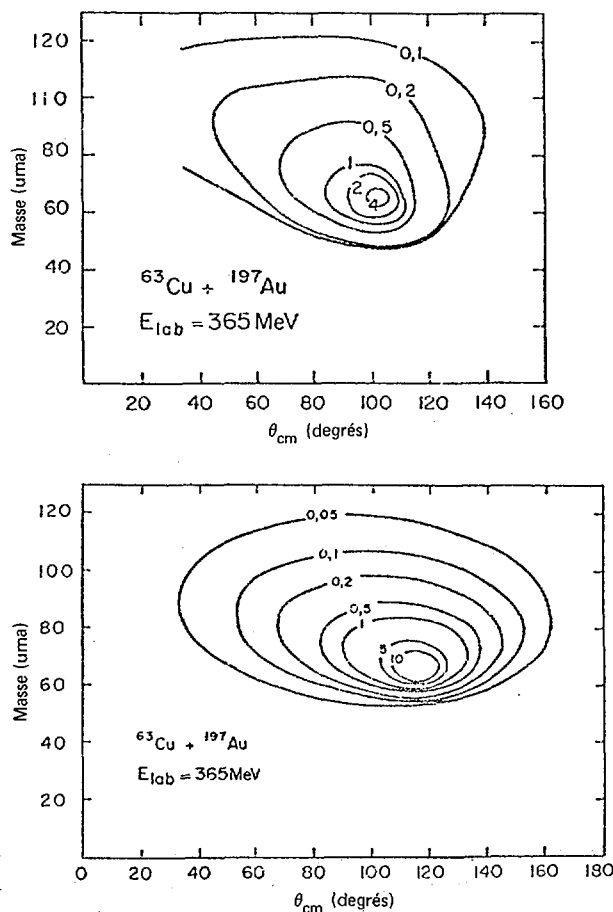


FIG.2. Diagrammes de Wilczynski pour 4 cas. On remarquera l'allure très différente selon que le système est relativement léger, ou très lourd. Extrait de la réf. [52]. ECT = énergie cinétique totale.



*FIG.3a. Distributions de masses expérimentales à divers angles pour le système Cu + Au à 365 MeV. La mémoire des masses initiales est perdue quand on s'éloigne de l'angle d'effleurement ( $90^\circ$ ). Extrait de la réf. [11].*



*FIG.3b. Comparaison expérience-théorie pour les cartes des distributions de masse – angle d'observation. Système Cu + Au à 365 MeV identique à celui de la figure 3a. Résultats extraits de la réf. [9].*

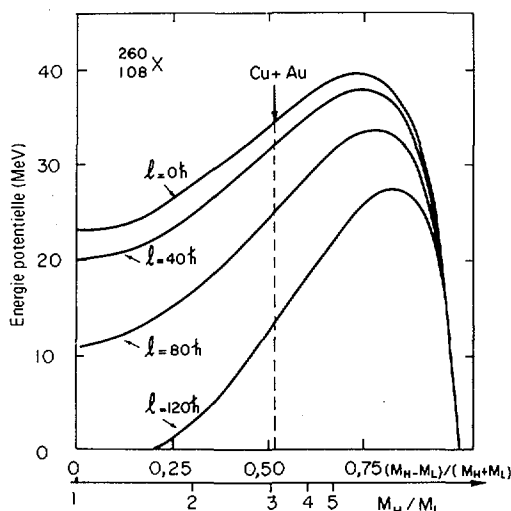


*FIG.3c. Courbes d'énergie potentielle d'un système de 108 protons et 152 neutrons répartis en deux gouttes liquides sphéroïdales en contact en fonction de l'asymétrie de masse de ces deux gouttes. Les différentes courbes correspondent à des moments angulaires totaux différents.*

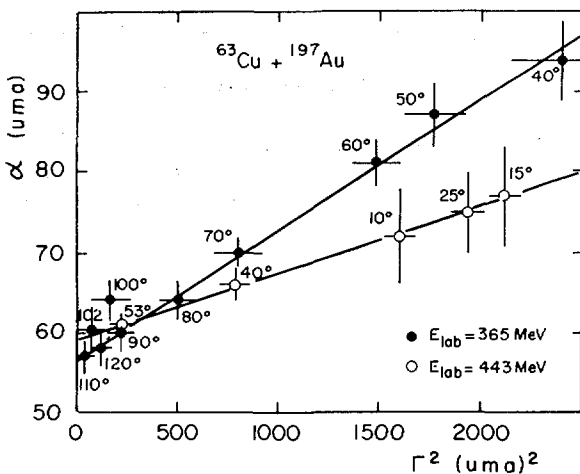


*FIG.4. Système Cu + Au à 365 MeV et 443 MeV. Variations de la masse moyenne des fragments détectés à un angle en fonction de la variance de la distribution de masse au même angle. Les points s'alignent sur des droites en accord avec le modèle de diffusion. Extrait de la réf. [53].*

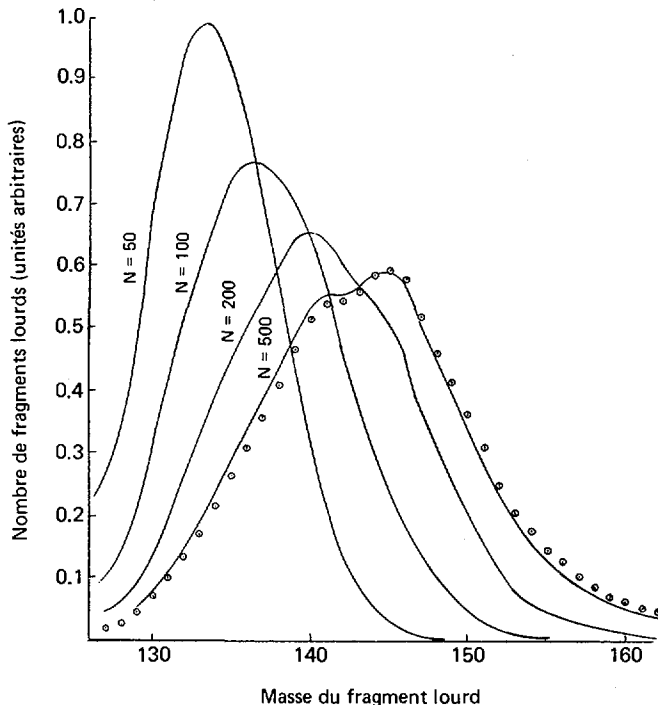


*FIG. 5. Calcul de la distribution de masse dans la fission spontanée du  $^{252}\text{Cf}$  basé sur un transfert de masse aléatoire entre les fragments.  $N$  représente le nombre d'étapes d'échanges de nucléons. Une situation d'équilibre est atteinte pour  $N = 500$ . Extrait de la réf. [8].*

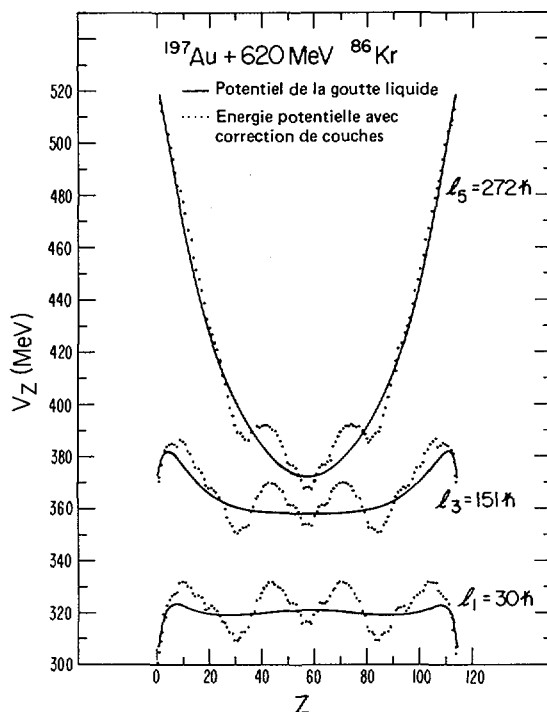


FIG. 6. Energie potentielle calculée pour un système de 115 protons et 168 neutrons à différents moments angulaires, en fonction de la charge nucléaire d'un fragment.  
Ligne continue: potentiel de goutte liquide.  
Pointillés: goutte liquide + corrections dues aux effets de couches.  
Remarquez le minimum au voisinage du point d'injection ( $Z = 36 - 79$ ). Extrait de la réf. [14].

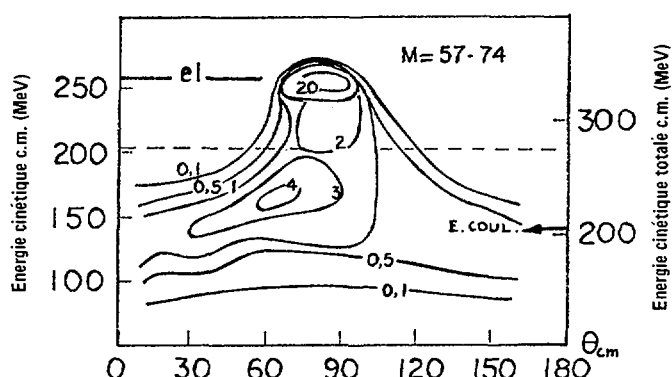
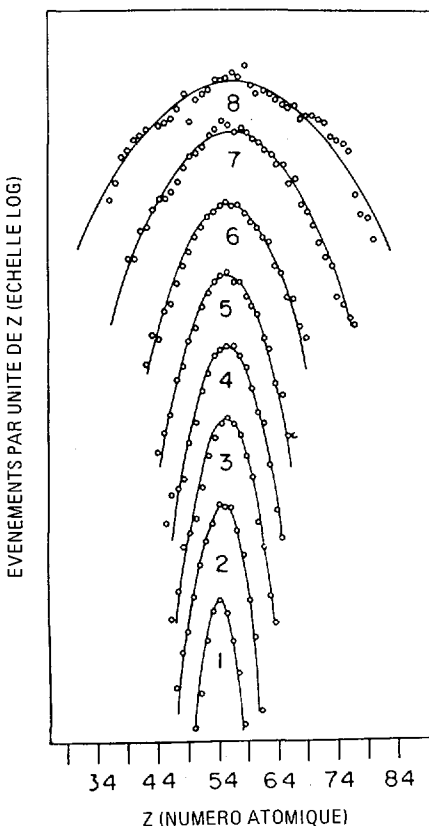
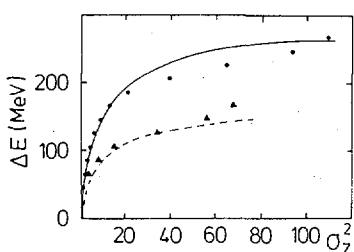


FIG. 7. Système  $^{63}\text{Cu}$  de 443 MeV +  $^{197}\text{Au}$ . Distribution corrélée en énergie cinétique et angle c.m. des fragments légers voisins du projectile. Extrait de la réf. [53].



*FIG. 8. Système Xe + Bi. Distributions de Z des fragments pour différentes valeurs de l'énergie cinétique totale. Les nombres croissants correspondent à des valeurs croissantes de la perte d'énergie (réf. [54]).*



*FIG. 9. Relation entre la perte d'énergie cinétique relative (corrigée pour la variation d'énergie potentielle) et l'élargissement de la distribution de Z. Les points expérimentaux proviennent de la réf. [55]. Les courbes ont été calculées (réf. [56]).*

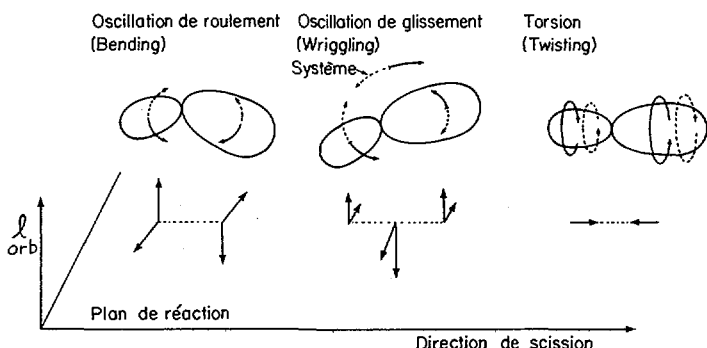


FIG.10. Illustration des modes d'oscillation, de roulement, de glissement, et de torsion, au point de scission. Les deux premiers modes sont doublement dégénérés et le moment angulaire résultant peut être décomposé en deux parties, respectivement parallèle et perpendiculaire au moment angulaire orbital initial. La torsion provoque une rotation uniforme plutôt qu'oscillatoire.

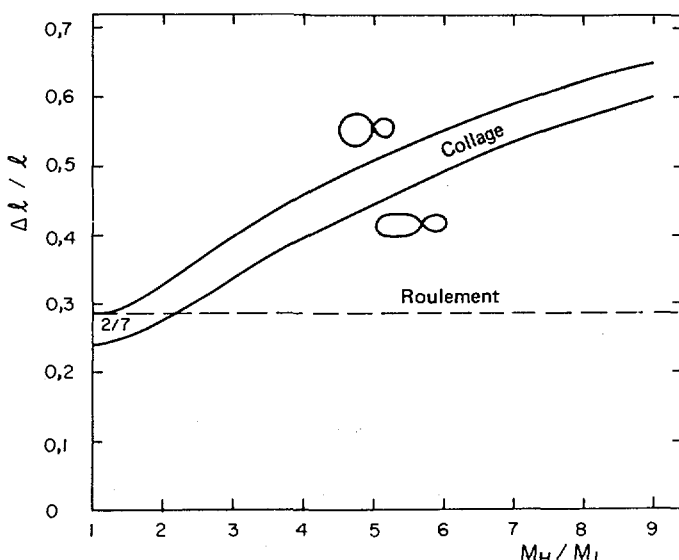


FIG.11. Rapport du moment angulaire transféré aux fragments ( $\Delta\ell$ ) au moment angulaire orbital initial ( $\ell_i$ ), en fonction du rapport de masses des fragments finaux. Trois situations possibles à la scission sont indiquées:  
tirets: les fragments roulent librement l'un sur l'autre.  
courbes en traits pleins: les noyaux sont liés rigidement.  
courbe supérieure: les noyaux sont deux sphères en contact.  
courbe inférieure: les noyaux sont deux sphéroïdes allongés en contact; le rapport des axes de 1,3 rend compte des énergies cinétiques de fission et de quasi-fission pour les systèmes lourds.

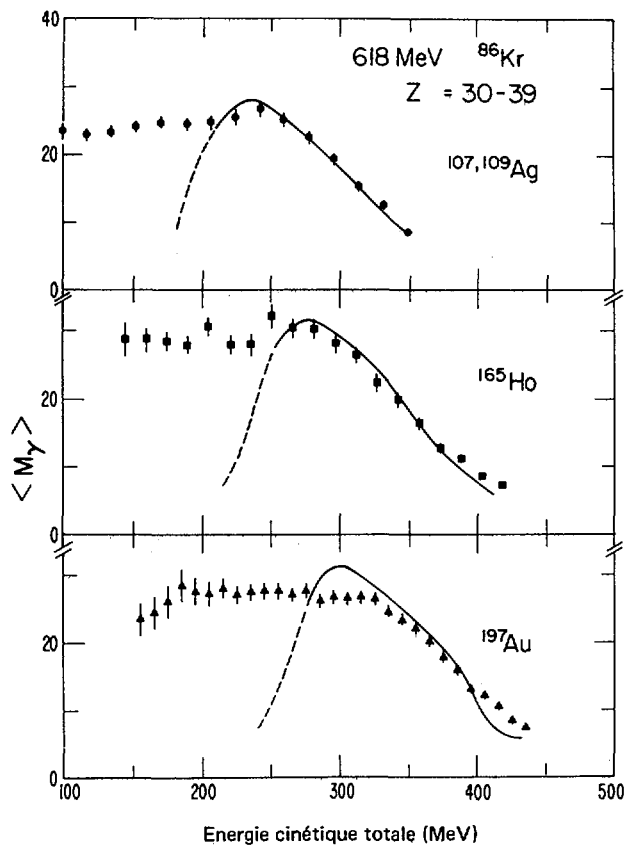


FIG.12. Variation de la multiplicité  $\gamma$  avec l'énergie cinétique finale des fragments légers pour les CTI de trois systèmes lourds. Les courbes ont été obtenues par un modèle de diffusion où la perte d'énergie cinétique et le transfert de moment angulaire résultent tous deux du transfert de nucléons entre les deux fragments. Extrait de la réf. [57].

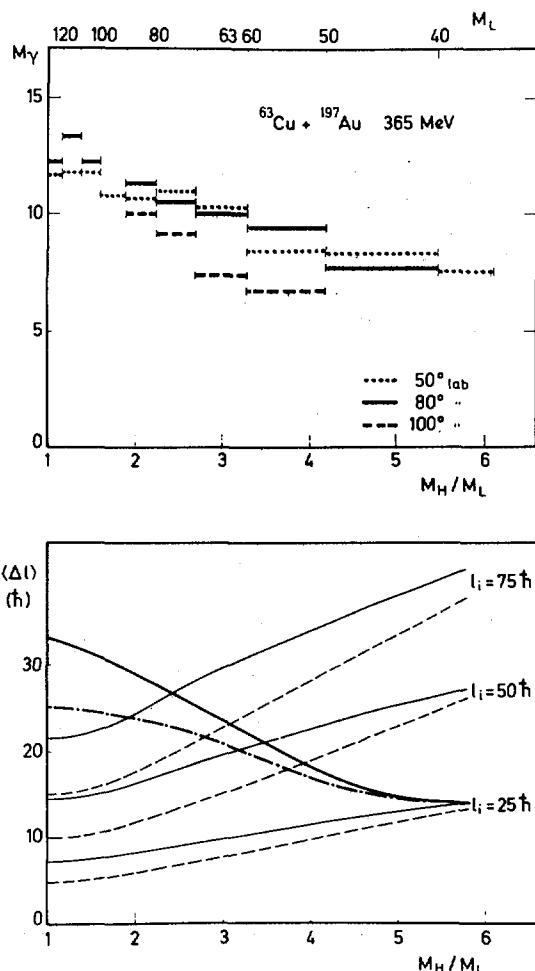
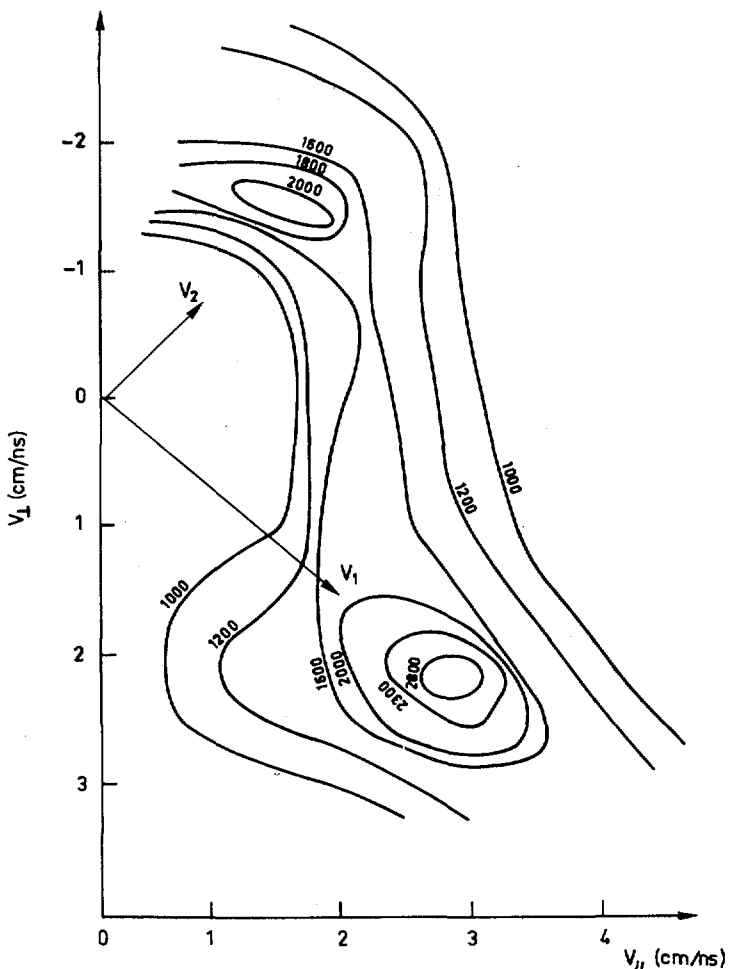
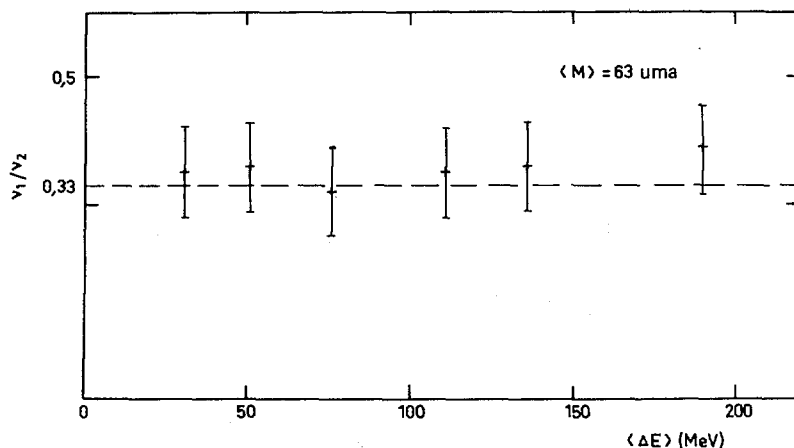


FIG.13. Partie supérieure: multiplicité  $\gamma$  en fonction de la masse du fragment léger final (ou du rapport de masse des fragments) pour les quasi-fissions du système  $^{63}\text{Cu}$  de 365 MeV sur  $^{197}\text{Au}$ . Partie inférieure: comparaison entre le moment angulaire transféré déduit de la figure supérieure (pentes négatives) et le moment angulaire calculé avec l'hypothèse du corps rigide (pentes positives) pour des fragments sphériques (traits continus) ou allongés (tirets) à différents moments angulaires correspondant aux CTI de ce système ( $\sim 0$  à  $75 \hbar$ ). Extrait de la réf. [24].



*FIG.14. Système  $^{63}\text{Cu}$  de 400 MeV  $^{197}\text{Au}$ . Distribution bidimensionnelle  $d^2\sigma/(dv_{\parallel}dv_{\perp})$  des neutrons détectés en coïncidence avec les fragments de CTI.  $v_{\parallel}$  et  $v_{\perp}$  sont les composantes de la vitesse du neutron respectivement parallèle et perpendiculaire à la direction du faisceau.  $V_1$  et  $V_2$  représentent la direction et la grandeur des vecteurs vitesse des fragments léger et lourd respectivement (réf. [18]).*



*FIG.15. Système  $^{63}\text{Cu}$  de 400 MeV +  $^{197}\text{Au}$ . Rapport du nombre de neutrons émis par les fragments léger et lourd, respectivement, en fonction de la perte d'énergie cinétique. La ligne en tirets est le rapport de masse des fragments léger et lourd respectivement et correspond donc à l'équilibre de température dans le système composite (réf. [18]).*

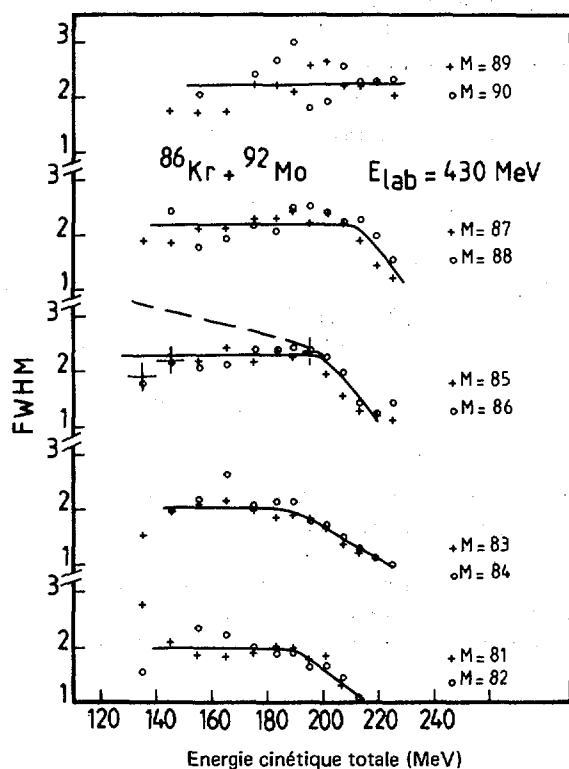


*FIG.16. Système  $^{86}\text{Kr}$  de 430 MeV +  $^{92}\text{Mo}$ . Largeur de la distribution de Z en fonction de la perte d'énergie cinétique, pour différentes masses finales. La diffusion élastique correspond à 229 MeV (réf. [45]).*

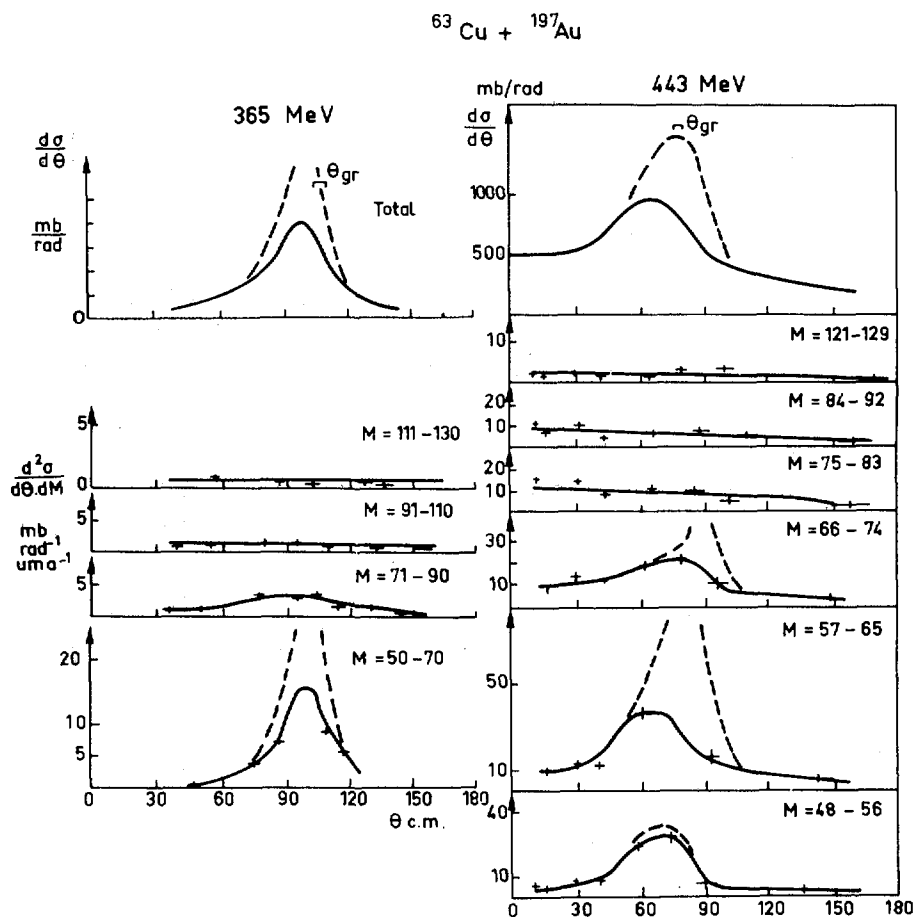


*FIG. 17. Distributions angulaires c.m. des CTI pour le système Cu + Au à deux énergies. Les courbes supérieures concernent l'ensemble des masses. Au fur et à mesure que la masse s'éloigne de la masse initiale, la distribution angulaire s'aplatis et tend vers  $1/\sin \theta$  pour les événements symétriques. La mémoire de la direction initiale est alors totalement perdue. Les courbes en traits pleins sont tracées en excluant les événements partiellement amortis en énergie. Ils sont inclus pour les courbes en pointillés. Extrait de la réf. [53].*

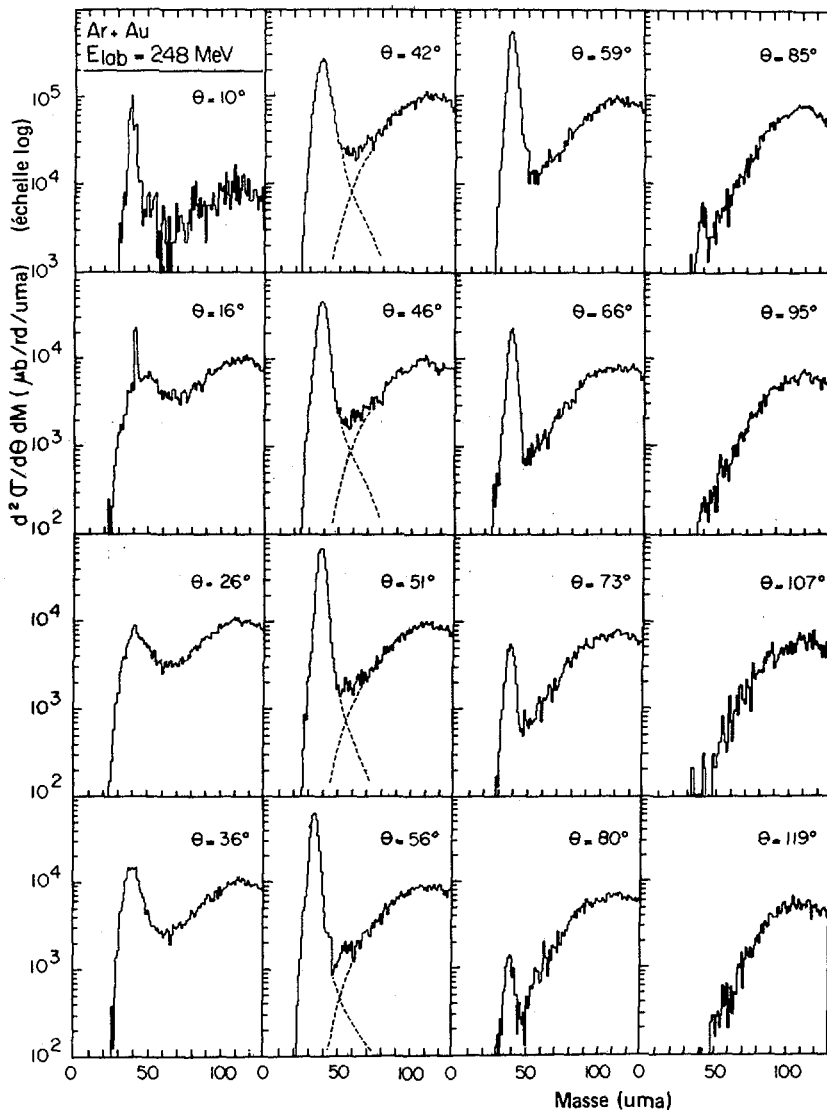


*FIG.18. Distributions de masses des événements relaxés en énergie pour le système Ar + Au à 248 MeV. Les angles sont des angles laboratoires. On remarque les deux composantes obtenues: l'une attribuable aux CTI autour de la masse 40; l'autre à la fission et au troisième mécanisme. L'échelle des ordonnées est logarithmique. Extrait de la réf. [10].*

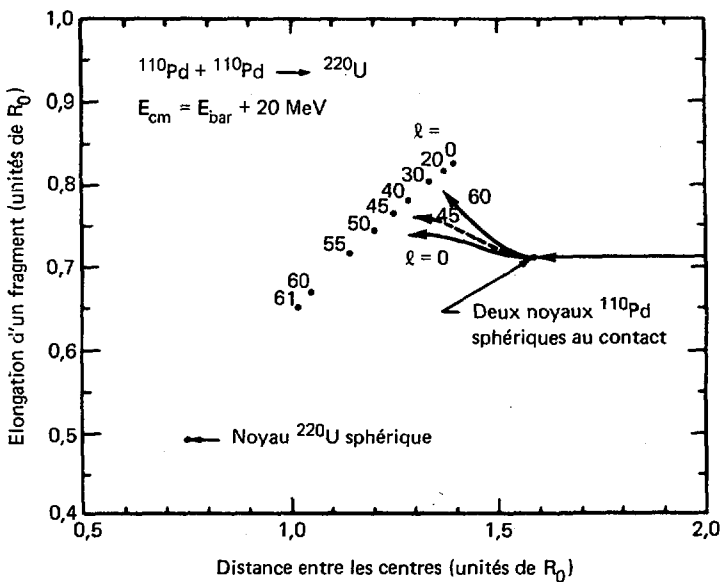


FIG.19. Trajectoires dynamiques pour la fusion entre deux noyaux  $^{110}\text{Pd}$  à 20 MeV au-dessus de la barrière d'interaction. Les points représentent la forme du point de déformation critique pour différentes valeurs du moment angulaire orbital, de  $\ell = 0$  à 60. A l'énergie considérée, seules les trajectoires des ondes de  $\ell \leq 45$  amènent le système à la fusion (réf. [47]).

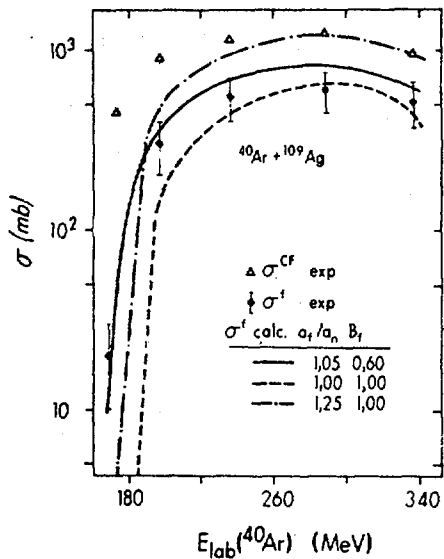


FIG.20. Fonctions d'excitation de «fission» mesurées (points) et calculées (courbes) pour le système  $^{40}\text{Ar} + ^{109}\text{Ag}$ . Les triangles représentent les sections efficaces mesurées de «fusion complète». Pour chaque courbe calculée sont indiqués: le rapport des paramètres de densités de niveau au point selle et pour le noyau résiduel après émission de particules:  $a_f/a_n$ , et le rapport de la barrière de fission effectivement utilisée à la barrière calculée par le modèle de la goutte liquide incluant l'effet du moment angulaire:  $B_f$  (réf. [51]).

## REFERENCES

- [1] BOHR, N., WHEELER, A., Phys. Rev. **56** (1939) 42.
- NIX, J.R., SWIATECKI, W.J., Nucl. Phys. **71** (1965) 1.
- [2] STRUTINSKY, V.M., Nucl. Phys. **A95** (1967) 426.
- [3] GREDNEV, G.F., VOLKOV, V.V., WILCZYNISKI, J., Nucl. Phys. **A142** (1970) 385.
- [4] GALIN, J., GUERREAU, D., LEFORT, M., PETER, J., TARRAGO, X., BASILE, R., Nucl. Phys. **A159** (1970) 461.  
MORETTO, L.G., HEUNEMANN, D., JARED, R.C., GATTI, R.C., THOMPSON, S.G., «Study of a fission-like environment in reactions with very heavy ions», Physics and Chemistry of Fission 1973 (C.R. Coll. Rochester, New York, 1973) II, AIEA, Vienne (1974) 351.
- [5] HANAPPE, F., LEFORT, M., NGÔ, C., PETER, J., TAMAIN, B., Phys. Rev. Lett. **32** (1974) 738.
- [6] PETER, J., Nucl. Instrum. Methods **146** (1977) 225.  
MORETTO, L.G., SCHMITT, R., NÖRENBERG, W., GALIN, J., J. Phys. (Paris) **C5** (1976) 109, 141, 83.  
VOLKOV, V.V., Sov. J. Nucl. Phys. **6** (1976) 420.  
SCHRÖDER, W.V., HUIZENGA, J.R., Ann. Rev. Nucl. Sci. (1977).  
LEFORT, M., NGÔ, C., Ann. Phys. (Paris) **3** (1978) 5.
- [7] ARMBRÜSTER, P., J. Phys. (Paris) **C5** (1976) 161.
- [8] RAMANNA, R., SUBRAMANIAN, R., AIYER, R.N., «Nuclear fission as a Markov process», Physics and Chemistry of Fission (C.R. Coll. Salzbourg, 1965) I, AIEA, Vienne (1965) 85.
- [9] NGÔ, C., Cours donné à l'INSTN, février 1979, Saclay.  
NGÔ, C., HOFMANN, H., Z. Phys. A **282** (1977) 83.
- [10] NGÔ, C., PETER, J., TAMAIN, B., BERLANGER, M., HANAPPE, F., Z. Phys. **A283** (1977) 161.  
GALIN, J., GATTI, B., GUERREAU, D., LEFORT, M., TARRAGO, X., AGARWAL, S., BABINET, R., CAUVIN, B., GIRARD, J., NIFENECKER, H., Z. Phys. **A283** (1977) 173.
- [11] NGÔ, C., PETER, J., TAMAIN, B., BERLANGER, M., HANAPPE, F., Nucl. Phys. **A 267** (1976) 181.
- [12] MORETTO, L., Communication personnelle.
- [13] SCHURMANN, B., NÖRENBERG, W., SIMBEL, M., Z. Phys. **A286** (1979) 263.
- [14] BEHKANI, A.N., MORETTO, L.G., LBL Report 8151 (1978) 175.
- [15] DOLL, P., GOBBI, A., STELZER, H., BOCK, R., LYNEN, U., NATOWITZ, J.B., OLMI, A., SANN, H., PELTE, D., RUDOLF, G., Spring Meeting of the Nuclear Physics Sections of the DPG, NNV, DFS, BNV, SBP, 26–30 Mars 1979, Gand, Comptes rendus, p.723.
- [16] GROSS, D.H.E., KALINOWSKI, H., Phys. Lett. **48B** (1974) 302.  
GROSS, D.H.E., KALINOWSKI, H., J.N.D.E.: Proc. Symp. on Heavy Ion Reactions, Heidelberg, 1974, Lecture notes dans Physics, **33** (1975) 194.  
KALINOWSKI, H., thèse (1975).
- [17] HILSCHER, D., BIRKELUND, J.R., HOOVER, A.D., SCHRÖDER, W.U., WILCKE, W.W., HUIZENGA, J.R., MIGNEREY, A., WOLF, K.L., BREUR, H.F., VIOLA, V.E., Jr., Rapport interne UR. NSRL 189, Rochester (1979).
- [18] TAMAIN, B., CHECHIK, R., FUCHS, H., HANAPPE, F., MORJEAN, M., NGÔ, C., PETER, J., DAKOWSKI, M., LUCAS, B., MAZUR, C., RIBRAG, M., SIGNARBIEUX, C., soumis à Nucl. Phys., IPN RC.79–02 (1979) Orsay.

- [19] GOULD, C.R., BASS, R., CZARNECKI, J.V., HARTMANN, V., STELZER, K., ZITZMANN, R., EYAL, Y., *Z. Phys. A* **284** (1978) 353.  
PETER, J., BERLANGER, M., NGÔ, C., TAMAIN, B., LUCAS, B., MAZUR, C., RIBRAG, M., SIGNARBIEUX, C., *Z. Phys. A* **283** (1977) 413.  
EYAL, Y., GAVRON, A., TSERRUYA, I., FRAENKEL, Z., EYSEN, Y., WALD, S., BASS, R., GOULD, C.R., KREYLING, G., RENDFORDT, R., STELZER, K., ZITZMANN, R., GOBBI, A., LYNNEN, U., STELZER, H., RODE, I., BOCK, R., *Phys. Rev. Lett.* **41** (1978) 625.
- [20] FRASCARIA, N., STEPHAN, C., COLOMBANI, P., GARRON, J.P., JACMART, J.C., RIOU, M., TASSANGOT, L., Rapport interne IPNO PhN - 77.15 (1977); *Phys. Rev. Lett.* **39** (1977) 918.
- [21] SWIATECKI, W.J., Rapport LBL 4296 (1975).  
KRAPPÉ, H.J., NIX, J.R., «Modified definition of the surface energy in the liquid drop formula», Physics and Chemistry of Fission 1973 (C.R. Coll. Rochester, New York, 1973) I, AIEA, Vienne (1974) 159.  
RANDRUP, J., *Nucl. Instrum. Methods* **146** (1977) 214.  
KOONIN, S.E., RANDRUP, J., *Nucl. Phys. A* **289** (1977) 475.
- [22] NIX, J.R., SWIATECKI, W.J., *Nucl. Phys.* **71** (1965) 1.
- [23] DIETRICH, K., Problèmes théoriques actuels de la fission et de la physique des ions lourds, Université Libre de Bruxelles (1978).
- [24] BERLANGER, M., DELEPLANQUE, M.A., GERSCHEL, C., HANAPPE, F., LEBLANC, M., MAYAULT, J.F., NGÔ, C., PAYA, D., PERRIN, N., PETER, J., TAMAIN, B., VALENTIN, L., *J. Phys. Lett.* **37** (1976) L 323.  
GERSCHEL, C., DELEPLANQUE, M.A., ISHIHARA, M., NGÔ, C., PERRIN, N., PETER, J., TAMAIN, B., VALENTIN, L., PAYA, D., SUGIYAMA, Y., BERLANGER, M., HANAPPE, F., à paraître dans *Nucl. Phys.*
- [25] DYER, P., PUIGH, R.J., VANDENBOSCH, R., THOMAS, T.D., ZISMAN, M.S., *Phys. Rev. Lett.* **39** (1977) 392.  
CIVELEKOGLU, Y., GLÄSSEL, P., HARRACH, D.V., MÄNNER, R., PELTE, D., SANN, H., SPECHT, H.J., Spring Meeting of the Nuclear Sections of the DPG, NNV, DFS, BNV.SBP, 26-30 Mars 1979, Gand, Comptes Rendus, p.680.
- [26] BERLANGER, M., GRANGE, P., HOFMANN, H., NGÔ, C., RICHERT, J., *Z. Phys. A* **286** (1978) 207.
- [27] DELEPLANQUE, M.A., Communication privée.  
FEENSTRA, S.J., VAN KLINKEN, J., PIJN, J.P., JANSENS, R., MICHEL, C., STEYAERT, J., VERVIER, J., CORNELIS, K., HUYSE, M., LHERSONNEAU, G., Spring Meeting of the Nuclear Sections of the DPG, NNV, DFS, BNV.SBP, 26-30 Mars 1979, Gand.  
NEWTON, J.O., SIE, S.H., DRACOULIS, G.D., *Phys. Rev. Lett.* **40** (1978) 62.
- [28] PERRIN, N., PETER, J., Proc. Winter School on Nuclear Physics, Zakopane, Pologne (1977).
- [29] STRUTINSKY, V.M., Sov. Phys.-JETP **10** (1960) 613.
- [30] WOZNIAK, G.J., SCHMITT, R.P., GLÄSSEL, P., JARED, R.C., BIZARD, G., MORETTO, L.G., *Phys. Rev. Lett.* **40** (1978) 1436.
- [31] OHLSEN, G.G., *Nucl. Instrum. Methods* **37** (1965) 240.
- [32] BABINET, R., CAUVIN, B., GIRARD, J., NIFENECKER, H., GATTY, B., GUERREAU, D., LEFORT, M., TARRAGO, X., *Nucl. Phys. A* **296** (1978) 160.  
SCHMITT, R.P., BIZARD, G., WOZNIAK, G.J., MORETTO, L.G., Rapport LBL 6571 (1978).  
PLASIL, F., FERGUSSON, R.L., BRITT, M.C., STOKES, R.M., ERKKILA, B.H., GOLDSTONE, P., BLANN, M., GUTBROD, M., *Phys. Rev. Lett.* **40** (1978) 1164.

- [33] SHIMODA, T., ISHIHARA, M., KAMITSUBO, M., MOTOBAYASHI, T., FUKUDA, T., IPCR Cyclotron Report 46 (1978).
- [34] ALBRECHT, Ho(H), DUNNWEBER, W., GRAW, G., STEADMANN, S.G., WURN, J.P., DIDDIER, D., RAUCH, V., SCHEIBLING, F., Z. Phys. A 283 (1977) 235.
- [35] GALIN, J., GUERREAU, D., BABINET, R., Communication privée, IPNO-RC 77-08 (1977) Orsay.
- [36] MILLER, J.M., CATCHEN, G.L., LOGAN, D., ROJAGOPALAN, M., ALEXANDER, J.M., KAPLAN, M., ZISMAN, M.S., Phys. Rev. Lett. **40** (1978) 100.
- [37] VANDENBOSCH, R., HUIZENGA, J.R., Nuclear Fission, Academic Press, New York and London (1973).
- [38] NIX, J.R., Nucl. Phys. A **130** (1969) 241.
- [39] DEUBLER, M.M., DIETRICH, K., Phys. Lett. **56B** (1975) 241.  
BECK, F., Phys. Lett. **62B** (1976) 385.  
ABUL-MAGD, A.Y., SIMBET, M.M., WEIDENMÜLLER, M.A., Z. Phys. A **285** (1978) 41.
- [40] DAKOWSKI, M., CHECHICK, R., HANAPPE, F., LUCAS, B., MAZUR, C., RIBRAG, M., PETER, J., SIGNARBIEUX, C., TAMAIN, B., à publier.
- [41] GLENDENING, L.E., CORYELL, C.D., EDWARDS, R., Radiochemical Studies: the Fission Products (C.D. CORYELL, N. SUGARMAN, Eds), Nat. Nucl. Energy Ser., Plutonium Project Rec, Paper 52, McGraw-Hill, New York.
- [42] KRATZ, V., AHRENS, M., BÖGL, W., BRÜCHLE, N., FRANZ, G., SCHODEL, M., WARNECKE, I., WIRTH, G., KLEIN, G., WEISS, M., Phys. Rev. Lett. **39** (1977) 984.  
BROGLIA, R.A., DASSO, C.H., WINTHER, A., Phys. Lett. **61B** (1976) 113.
- [43] GATTY, B., GUERREAU, D., LEFORT, M., TARRAGO, X., GALIN, J., CAUVIN, B., GIRARD, J., NIFENECKER, H., Nucl. Phys. A **278** (1976) 347.
- [44] SWIATECKI, W.J., BLANN, H.M., Communication privée (1961).
- [45] BERLANGER, M., GOBBI, A., HANAPPE, F., LYNEN, U., NGÔ, C., OLMI, A., SANN, M., STELZER, H., RICHEL, M., RIVET, M.F., Proc. VIIth Int. Workshop, Mirschegg (1979).
- [46] COHEN, S., PLASIL, F., SWIATECKI, W.J., Ann. Phys. (US) **82** (1974) 557.
- [47] NIX, J.R., SIERK, A.J., Phys. Rev. **C15** (1977) 2072.
- [48] TAMAIN, B., NGÔ, C., PETER, J., Nucl. Phys. A **252** (1975) 187.
- [49] LEBRUN, C., CHECHICK, R., HANAPPE, F., LECOLLEY, J.F., LEFEBRES, F., NGÔ, C., PETER, J., TAMAIN, B., Nucl. Phys. (à paraître).
- [50] HEUSCH, B., VOLANT, C., FREIESLEBEN, H., CHESTNUT, R.P., HITDENBRAND, K.D., PÜHLHOFER, F., SCHNEIDER, W.F.W., KOHLMAYER, B., PFEFFER, W., Z. Phys. A **288** (1978) 39.
- [51] BECKERMANN, M., BLANN, M., Phys. Rev. **C17** (1978) 1615.
- [52] SANN, H., OLMI, A., CIVELOKOGLU, Y., PELTE, D., LYNEN, U., STELZER, H., GOBBI, A., EYAL, Y., KOHL, W., RENFORDT, R., RODE, I., RUDOLF, G., SCHWALM, D., BOCK, R., Meeting on Heavy Ion Collisions, Fall Creek Falls, 13-17 juin 1977, Rapport interne GSI Bericht P.S.77, Phys. Rev. **111** (1978) 688.
- [53] PETER, J., NGÔ, C., TAMAIN, B., BERLANGER, M., HANAPPE, F., Nucl. Phys. A **279** (1977) 110.
- [54] SCHRÖDER, W.U., BIRKELUND, J.R., HUIZENGA, J.R., WOLF, K.L., UNIK, J.P., VIOLA, V.E., Tiré à part (1977).
- [55] RUDOLF, G., GOBBI, A., STELZER, H., LYNEN, U., OLMI, A., SANN, H., STOKSTAD, R.G., PELTE, D., Rapport GSI-VP-12-78 (déc.1978).
- [56] RIEDEL, C., WOLSCHIN, G., NÖRENBERG, N., Rapport GSI-VI-10-78 (oct.1978).
- [57] REGIMBART, R., BEHKAMI, A.N., WOZNIAKI, G.J., SCHMITT, R.P., SVENTEK, J.S., MORETTO, L.G., Rapport LBL 7751 (1978).

## DISCUSSION

H. FREIESLEBEN: I have a question regarding the angular momentum transfer in deep-inelastic collisions and its connection with the bending, wriggling and twisting modes in fission. If you use the sticking model to explain the angular momentum transfer in deep-inelastic collisions, you can hardly add a bending mode, since you then destroy the sticking. In other words, are you not trying to mix two concepts?

J. PETER: No, the system can attain cohesion close to the sticking limit, and the bending and/or wriggling modes can still be excited. To achieve the minimum angular momentum due to these modes, we compare the experimental angular momentum with the maximum orbital angular momentum transferred to the fragments, i.e. the value obtained in the limiting case of sticking.

C.R. GUET: Can you distinguish experimentally between the different mechanisms for light-charged particle emission in deep inelastic collisions? If so, with how much confidence?

J. PETER: Yes, their origin can be deduced from their angular and energy distributions relative to the direction and velocity of the heavy fragments. We can distinguish with a high degree of confidence between sequential and non-sequential processes, but I grant you the identification of the process or processes occurring in a specific case is much more difficult.

J.B. WILHELMY: Does the wide mass distribution associated with reactions for which the fission barrier has been calculated to vanish require a longer time for the process than the characteristic deep inelastic times? Do we have to invoke a new time scale for this process or can it be fitted into our current concept?

J. PETER: "Fission outside the barrier" requires full damping of the relative motion and of mass transfer (towards mass symmetry) and is observed to correspond to full angular momentum transfer and to at least one half-rotation. The time required is then the upper limit of deep-inelastic collision (DIC). In a reaction time distribution, "fission outside the barrier" would appear as the upper tail of DIC times when it corresponded to a narrow range of initial  $\ell$  values, and as a peak when it corresponded to a broad range of  $\ell$  values.

P. SCHUK: Giant resonance widths are due to one-body dissipation. You mentioned that higher multipolarities dissipate more rapidly. Are there any experimental data on the way in which the giant resonance widths vary with angular momentum?

J. PETER: No, not as far as I know.

## **CHAIRMEN OF SESSIONS**

Session A	A.F. MICHAUDON	France
Session B	S.S. KAPOOR	India
Session C(1)	K.M. DIETRICH	FRG
Session C(2)	H.C. PAULI	FRG
Session D	E. CHEIFETZ	Israel
Session E	E. CHEIFETZ	Israel
Session F(1)	P. ARMBRUSTER	FRG
Session F(2)	B.G. YANKOV	USSR
Session F(3)	G.F. HERRMANN	FRG
Session G	B.G. YANKOV	USSR
Session H	P. FONG	USA

## **SECRETARIAT OF THE SYMPOSIUM**

Scientific Secretary:	J. DOLNICAR	Division of Research and Laboratories, IAEA
Administrative Secretary:	Edith PILLER	Division of External Relations, IAEA
Editor:	J.W. WEIL	Division of Publications, IAEA
Records Officer:	J. RICHARDSON	Division of Languages, IAEA



# HOW TO ORDER IAEA PUBLICATIONS

**An exclusive sales agent for IAEA publications, to whom all orders  
and inquiries should be addressed, has been appointed  
in the following country:**

UNITED STATES OF AMERICA UNIPUB, 345 Park Avenue South, New York, NY 10010

**In the following countries IAEA publications may be purchased from the  
sales agents or booksellers listed or through your  
major local booksellers. Payment can be made in local  
currency or with UNESCO coupons.**

ARGENTINA	Comisión Nacional de Energía Atomica, Avenida del Libertador 8250, RA-1429 Buenos Aires
AUSTRALIA	Hunter Publications, 58 A Gipps Street, Collingwood, Victoria 3066
BELGIUM	Service du Courrier de l'UNESCO, 202, Avenue du Roi, B-1060 Brussels
CZECHOSLOVAKIA	S.N.T.L., Spálená 51, CS-113 02 Prague 1
FRANCE	Alfa, Publishers, Hurbanovo námestie 6, CS-893 31 Bratislava Office International de Documentation et Librairie, 48, rue Gay-Lussac, F-75240 Paris Cedex 05
HUNGARY	Kultura, Hungarian Trading Company for Books and Newspapers, P.O. Box 149, H-1389 Budapest 62
INDIA	Oxford Book and Stationery Co., 17, Park Street, Calcutta-700 016 Oxford Book and Stationery Co., Scindia House, New Delhi-110 001
ISRAEL	Heiliger and Co., Ltd., Scientific and Medical Books, 3, Nathan Strauss Street, Jerusalem
ITALY	Libreria Scientifica, Dott. Lucio de Biasio "aeiou", Via Meravigli 16, I-20123 Milan
JAPAN	Maruzen Company, Ltd., P.O. Box 5050, 100-31 Tokyo International
NETHERLANDS	Martinus Nijhoff B.V., Booksellers, Lange Voorhout 9-11, P.O. Box 269, NL-2501 The Hague
PAKISTAN	Mirza Book Agency, 65, Shahrah Quaid-e-Azam, P.O. Box 729, Lahore 3
POLAND	Ars Polona-Ruch, Centralna Handlu Zagranicznego, Krakowskie Przedmiescie 7, PL-00-068 Warsaw
ROMANIA	Ilexim, P.O. Box 136-137, Bucharest
SOUTH AFRICA	Van Schaik's Bookstore (Pty) Ltd., Libri Building, Church Street, P.O. Box 724, Pretoria 0001
SPAIN	Díaz de Santos, Lagasca 95, Madrid-6 Díaz de Santos, Balmes 417, Barcelona-6
SWEDEN	AB C.E. Fritzes Kungl. Hovbokhandel, Fredsgatan 2, P.O. Box 16356, S-103 27 Stockholm
UNITED KINGDOM U.S.S.R.	Her Majesty's Stationery Office, P.O. Box 569, London SE 1 9NH Mezhdunarodnaya Kniga, Smolenskaya-Sennaya 32-34, Moscow G-200
YUGOSLAVIA	Jugoslovenska Knjiga, Terazije 27, P.O. Box 36, YU-11001 Belgrade

**Orders from countries where sales agents have not yet been appointed and  
requests for information should be addressed directly to:**



**Division of Publications  
International Atomic Energy Agency  
Wagramerstrasse 5, P.O. Box 100, A-1400 Vienna, Austria**

79-8041/1

INTERNATIONAL  
ATOMIC ENERGY AGENCY  
VIENNA, 1980

SUBJECT GROUP: III  
Physics/Nuclear Physics, Reactor Physics, Fission  
PRICE: Austrian Schillings 900.-